Deutsche Gesellschaft für Kristallographie

22. Jahrestagung

17. bis 20. März 2014

Berlin

Abstracts

Deutsche Gesellschaft für Kristallographie

22. Jahrestagung

17. bis 20. März 2014

Berlin

Abstracts

Table of Content

IYCr 2014 Celebration

The past, present and future of crystallography

S. Larsen[1]
[1]*University of Copenhagen, Department of Chemistry, Copenhagen, Denmark*

In the International Year of Crystallography 2014 that celebrates the now more than the centennial of modern crystallography, it is natural to look back and forward on the development of our science. In the historical perspective it is interesting to note that the theoretical foundation of crystallographic science was developed within a very short period (around 20 year) after Max von Laue's seminal experiment with X-rays in 1912. Though the theory was in place it was not before the advent of computers in the mid 1960es that X-ray crystallography became the most powerful tool for accurate structure determination at atomic resolution of crystalline materials. The computers were driving the development of experimental equipment and software that enabled structure determination by “direct methods”, leading to an exponential growth of the crystal structures of inorganic and organic compounds. The success of crystallography and its impact on other sciences that depend on structural information were so great that it almost threatened its role as an independent scientific area.

The availability of new neutron and X-ray sources (synchrotrons) opened new exciting avenues for crystallography with the ability to study very small (micron-sized) crystals and to combine different X-ray/neutron based techniques. This can be exemplified by the development of structural biology that experienced a similar exponential growth in known protein structures as seen earlier for the smaller molecules, and a steadily increasing use of methods complementary to diffraction. It has been interesting to note how the advanced instrumentation at the large facilities has had a great impact on the development of the instrumentation for in house equipment.

The International Union of Crystallography (IUCr) has as a learned society publisher for the last 65 years been a leading in publishing crystallographic results but it has also had an important role in maintaining and developing the identity of the crystallographic community. The crystallographic conferences and meetings show the richness and diversity of crystallography as a science in itself and how it underpins related sciences.

We can already predict that the new neutron and X-ray sources including the free electron lasers will advance our science even further enabling the study of structural dynamics, large macromolecular assemblies, and extrapolating from the past also the future will bring exciting new developments to crystallography.

Growth of Si- and Ge-Nanocrystals

T. Boeck[1]
[1]*Leibniz-Institut für Kristallzüchtung, Max-Born-Str. 2, 12489 Berlin, Germany*

Crystallography in science management

Y. Tomm[1]
[1]*Helmholtz Zentrum für Materialien und Energie Berlin, Department Third Party Funding, Hahn-Meitner-Platz 1, 14109 Berlin, Germany*

Macromolecular Crystallography in drug discovery

U. Egner[1]
[1]*GDD - GCGE - Lead Discovery - Structural Biology*
Bayer Pharma, 13342 Berlin, Germany

At Bayer, Structural Biology together with Protein Technologies is responsible for protein X-ray crystallography and fragment screening. A crystallographer in Structural Biology supports projects in lead generation and optimization and works closely together with colleagues from Screening, Medicinal Chemistry and different indication areas. Team work and setting of clear priorities are a key part of the job - a structural biologist is often involved in 5-10 projects in parallel. Communication skills are essential both within the company and with academic or industrial external partners. Expect the unexpected! Discovering a new inhibitor binding mode or a new protein conformation may contribute towards the next successful lead compound.

Crystallography and public relations

M. Tovar[1]
[1]*Helmholtz Zentrum für Materialien und Energie Berlin, Department Crystallography, Hahn-Meitner-Platz 1, 14109 Berlin, Germany*

Laue Prize 2013

Detection of pressure-induced phase transitions using second harmonic generation

L. Bayarjargal[1]
[1]*Goethe-Universität, Institut für Geowissenschaften, Abt. Kristallographie , Frankfurt am Main, Germany*

Phase transitions are extensively studied in physics, chemistry, material science, and geoscience. In addition to changes in temperature and pressure, the occurrence of a phase transitions also depends on numerous further parameters, such as electromagnetic fields, grain size, strain fields and many other factors. This complicates the investigation of phase transitions at high pressures, and therefore the development of novel techniques, which are complementary to the established X-ray diffraction and spectroscopic methods, is desirable.

Here I present the possibility to use of the second harmonic generation (SHG) for the detection of pressure-induced phase transitions. SHG is allowed only in acentric structures and hence can be used to study phase transitions involving the loss or appearance of a center of inversion. A typical example is the phase transition from the B4 phase to the B1 phase in ZnO and AlN, where the influence of pressure and the grain size could be determined using SHG in a straightforward fashion. Depending on the pressure conditions, ZnO and AlN can go through different intermediate phases [1]. Non-hydrostatic pressures cause a decrease of the transition pressure of bulk and nanocrystals. The transition pressures of ZnO are significantly higher for nanocrystals than for bulk crystals. In contrast, AlN nanocrystals have lower transition pressures than bulk samples. The difference in the behavior can be explained by the surface stress and the surface energy. The main reason for the decrease of the transition pressure is that the surface energy of the B4 phase is higher than that of the B1 phase. The surface energy of AlN influences the change in the transition pressure more than the surface stress. Another significant parameter is the morphology of the nanocrystals [2-3].

Further examples that will be discussed include the phase transitions in KIO_3 and quartz. On increasing pressure the SHG signal of quartz decreases while it increases for ZnO. This different pressure dependence can be explained by correlating it to the ratio between the average coherence length and the average particle size. Further examples, e.g. our studies of Cr_2O_3 and ice VII show that the SHG method is complementary to X-ray diffraction and provides additional information about the presence of a inversion center for unknown or controversially discussed structures at high pressure or for pressure-induced magnetic phase transitions [4-5].

Financial support from the DFG (SPP1236)and the FOKUS program (Goethe University)is gratefully acknowledged.

[1] L. Bayarjargal, B. Winkler, E. Haussühl, R. Boehler, *Appl. Phys. Lett.*95, 061907 (2009)
[2] L. Bayarjargal, B. Winkler, *Appl. Phys. Lett.*100, 021909 (2012)
[3] L. Bayarjargal, L. Wiehl, B. Winkler, *High Pressure Res.*33, 642 (2013)
[4] L. Bayarjargal, B. Winkler, *Appl. Phys. Lett.*102, 182403 (2013)
[5] L. Bayarjargal, B. Winkler, *Z. Kristallogr.* 229, 1 (2014)

Plenary Talks

P01

Metal nanoparticles in energy catalysis; the role of structure and dynamics

R. Schlögl[1,2]
[1]*Fritz-Haber-Institut der MPG, Department AC, Berlin, Germany*
[2]*Max-Planck-Institut für Chemische Energiekonversion, Mülheim an der Ruhr, Germany*

The chemical conversion of energy is the largest application of catalysis and requires thus the best possible design of its reactions. The splitting of water through electrocatalysis, the synthesis of ammonia and the reduction of CO2 are the most urgent target reactions that require metals as active functional materials.

In all reactions we find that it is not the property of the metal itself nor the geometric size of it that determines the catalytic function but rather the ability of the functional material to undergo chemical dynamics. The material transforms under reaction conditions from a pre-cataylst into the active phase that brings about active sites by dynamical processes. The distinction between static and dynamical sites will be discussed using examples of the aforementioned reactions and a combination of in-situ analytical techniques of diffraction, spectroscopy and microscopy.

P02

New Opportunities for X-ray Crystallography: Fourth Generation Lightsources and Computational Advances

A. T. Brunger[1]
[1]*Stanford University, Howard Hughes Medical Institute, Departments of Molecular and Cellular Physiology, Neurology and Neurological Sciences, Structural Biology, and Photon Science, Stanford, United States*

X-ray diffraction plays a pivotal role in revealing atomic structures of macromolecules and their complexes. Since crystals of large complexes or membrane proteins often diffract weakly, new experimental tools and computational methods need to be developed. For example, the first hard X-ray XFEL has been operational at Stanford University (Linac Coherent Light Source, LCLS, at SLAC) for over two years, and pioneering studies of sub-micron crystals have been performed. LCLS produces ten orders of magnitude higher peak photon brilliance, compared to third generation lightsources. There is promise that it may be possible to solve a new crystal structure that is currently intractable by other lightsources, although this remains to be shown. These and other experimental advances are complemented by new computational tools in the analysis of X-ray diffraction data at low resolution. As an example, the DEN (Deformable Elastic Network) refinement method will be discussed. It adds specific information from a known reference structure but allows global and local deformations of this reference model. Cross-validation with R_{free} determines the optimum deformation and influence of the reference model. For test cases at 3.5 - 7 Å resolution with known structures at high resolution, the method improves the refined model, as monitored by coordinate accuracy, the definition of secondary structure, and the quality of electron density maps.

References:

1. A.T. Brunger, P.D. Adams, P. Fromme, R. Fromme, M. Levitt, G.F. Schröder. Improving the accuracy of macromolecular structure refinement at 7 Å resolution. *Structure* 20, 957-966 (2012).
2. G.F. Schröder, M. Levitt, A.T. Brunger. Super-resolution biomolecular crystallography with low-resolution data. *Nature* 464, 1218-1222 (2010).
3. G.F. Schröder, A.T. Brunger, M. Levitt. Combining efficient conformational sampling with a deformable elastic network model facilitates structure refinement at low resolution. *Structure* 15, 1630-1641 (2007).

P03

Enhanced nucleation of the fcc phase during solidification of alloys by 5-fold symmetry icosahedral quasicrystals

M. Rappaz[1]
[1]*Ecole Polytechnique Fédérale de Lausanne, Institute of Materials, Lausanne, Switzerland*

In the 1980's, 5-fold symmetry icosahedral quasicrystals (iQC) were discovered in Al-alloys: they inherit the local icosahedral arrangement of atoms in the liquid already predicted by Frank in the 1950's, but without exhibiting translation invariance. This icosahedral arrangement of atoms is also retrieved in the building blocks of the unit cell of the corresponding approximant intermetallic phase. Recently, we have shown that minute Cr additions (typically 0.1 wt%) to Al-Zn alloys solidified in a uniform temperature field spontaneously lead to the formation of fine equiaxed fcc Al grains. Furthermore, these grains exhibit an unexpectedly large number of twin relationships and some of them even show a 5-fold symmetry multi-twin relationship with a common á110ñ direction. Similar observations have been made for yellow gold alloys inoculated with a few ppm of Ir. These results become fully consistent when one considers that the primary fcc phase forms on facets of iQC's, or alternatively on nuclei of the parent approximant phase, with the following heteroepitaxy relationship: $\{111\}_{fcc}$ ^ 3-fold i-QC axes, á110ñ$_{fcc}$ ^ 2-fold i-QC symmetry axes. This new nucleation mechanism is consistent with the fact that the interfacial energy of iQC with the liquid is about 10 times lower than that of the fcc phase. It also brings an explanation for a long-standing problem of the origin of twinned dendrites in Al alloys, a morphology discovered more than 60 years ago and consisting in á110ñ dendrites split in their center by coherent {111} twin planes. Furthermore, from a practical point of view, it also sets guidelines for the quest of new solute elements acting as grain refiners for fcc, and possibly hcp metallic alloys.

P04

Photosystem II: Crystal Structure and Functional Studies Using Serial Femtosecond X-Ray Laser Microcrystallography

W. Saenger[1]
[1]*Freie Universität Berlin, Institut für Chemie und Biochemie/Kristallographie, Berlin, Germany*

The multisubunit protein complex photosystem II (PSII) contains numerous cofactors and is located in the photosynthetic thylakoid membrane of plants, green algae, and cyanobacteria. PSII initiates photosynthesis by oxidizing water to protons, electrons and oxygen according to $2\ H_2O \rightarrow 4\ H^+ + 4e^- + O_2$. Whereas O_2 is "waste" and populates the atmosphere, the H^+ drive ATP synthesis and e^- reduce NADP to NADPH, and both ATP and NADPH are used in the Calvin cycle to convert CO_2 to carbohydrates. The oxidation of water molecules occurs at the unique Mn_4CaO_5 cluster of PSII in four steps called S_0, S_1, S_2, and S_3 according to the Kok cycle.

We extracted (solubilized) PSII from the thylakoid membrane of the cyanobacterium *Thermosynechococcus elongatus* using the detergent dodecylmaltoside. The crystal structure featured one PSII homodimer in the asymmetric unit and was determined at 2.9 Å resolution [1]. This led to the assignment per PSII monomer of all 20 protein subunits and of 35 chlorophyll *a*, 2 pheophytins, 2 cytochromes, 2 plastoquinones, 12 carotenoid molecules, 25 integral lipids, 1 chloride ion and the unique Mn_4CaO_5 cluster. This was confirmed by the crystal structure of PSI from the related cyanobacterium *Thermosynechococcus vulcanus* at higher resolution of 1.9 Å [2]. The structure of PSII is well known, but the events occurring during the Kok cycle remained elusive, and the application of conventional protein crystallography is problematic as X-rays reduce oxidation states Mn(IV) and Mn(III) to Mn(II), thereby inactivating the Mn_4CaO_5 cluster.

This problem can be avoided when femtosecond pulse X-ray diffraction patterns from PSII microcystals are collected using X-ray free-electron lasers at Hamburg or Berkeley. For this, crystal suspensions of PSII are illuminated stepwise by visible light to bring the crystals into the desired S-state of the Kok cycle. Since the high energy of an X-ray pulse destroys a crystal, a large number of fresh microcrystals has to pass the X-ray laser beam. The obtained diffraction patterns from the heterogeneous microcrystal population, one for each microcrystal, are evaluated in terms of crystal orientation and size [3,4].

[1] Guskov A., Kern, J., Gabdulkhakov A., Broser M., Zouni A., Saenger W. Nat. Struct. Mol. Biol. 16, 334-342 (2009).
[2] Umena,Y., Kawakami, K., Shen, J.-R., Kamiya, N. Nature 473, 55-60 (2011).
[3] Kern, J., and 40 coauthors, Science 349, 491-495 (2013).
[4] White, T. A., Barty, A., Stellato, F., Holton, J. M., Kirian, R. A., Zatsepin, N. A., Chapman, H. N. Acta Cryst. D69, 1231-1240 (2013).

P05

Ten years of charge flipping

L. Palatinus[1]
[1]*Institute of Physics of the AS CR, Prague, Czech Republic*

It is almost exactly ten years since the publication of the dual-space phasing algorihm called the charge-flipping algorithm [1-3]. Since the publication the algorithm has found a broad range of applications in many fields of crystallography.

Charge flipping is a member of the diverse family of dual-space iterative phasing algorithms [e.g. 4-7]. These algorithms use alternating modifications in direct and reciprocal space to find a solution to the phase problem. Unlike other algorithms from the diverse family of *ab initio* structure solution methods, in dual space algorithms neither of the two spaces is dominant in the structure solution, but it is the iteration between the two that makes the structure solution possible. The dual space algorithms bear strong relationship to the convex feasibility problem, but the constraint sets used in crystallography are not convex and therefore the convergence properties of the convex problems cannot be directly transferred to the solution of the phase problem in crystallography.

Dual space algorithms, and charge flipping in particular, have met considerable interest in the crystallographic community. Apart from the standard structure solution of small-molecule or inorganic compounds, the dual space algorithms, especially charge flipping, have been applied to specialized problems like the solution of complex structures from powder diffraction data, the solution of incommensurately modulated crystals and quasicrystals or solution of protein structures and heavy-atom substructures in macromolecular crystallography [8].

[1] Oszlányi, G. & Sütö, A. (2004). *Acta Cryst*. A60, 134-141.
[2] Oszlányi,G. & Sütö,A. (2008). *Acta Cryst*. A64, 123-134.
[3] Oszlányi, G. & Sütö, A. (2011). *Acta Cryst*. A67, 284-291.
[4] Shiono, M. & Woolfson, M. M. (1992). *Acta Cryst.* A48, 451-456.
[5] Elser, V. (2003). *Acta Cryst*. A59, 201-209.
[6] Bauschke, H. H., Combettes, P. L. & Luke, D. R. (2004). *J. Approx. Theory* 127, 178-192.
[7] Luke, D. R. (2005). *Inverse Probl.* 21, 37-50.
[8] Palatinus, L. (2013). *Acta Cryst.* B69, 1-16.

Keywords: charge flipping, phase problem, structure solution

P06

Characterizing intermolecular interactions from the topological analyses of the electrostatic potential and the Laplacian of the electron density

E. Espinosa[1]

[1]*Université de Lorraine, Faculté des Sciences et Technologies, Laboratoire de Cristallographie, Résonance Magnétique et Modélisations (UMR CNRS 7036), Vandoeuvre-lès-Nancy, France*

Charge density analysis is a useful tool for understanding chemical bonding in molecular systems. Nowadays, one of the most widely used methods to analyze the electron density $\rho(\mathbf{r})$ is the Quantum Theory of Atoms in Molecules (QTAIM) developed by Bader and collaborators.[1] This theory is based on the topological analysis of the scalar field $\rho(\mathbf{r})$ and permits to deeply characterize interatomic and intermolecular interactions within the framework of the Quantum Theory. In addition, other scalar fields also bring important information on these interactions and they should be considered as a complementary source of information. They are the electrostatic potential $\varphi(\mathbf{r})$ and the Laplacian of the electron density $\tilde{N}^2\rho(\mathbf{r})$. As in the case of $\rho(\mathbf{r})$, the topological analyses of $\varphi(\mathbf{r})$ and $L(\mathbf{r}) = -\tilde{N}^2\rho(\mathbf{r})$ permit to extract significant information on the interactions taking place in chemical systems. Thus, (i) Influence zones of electrophilic/nucleophilic sites,[2] (ii) regions mainly involved in electrostatic interactions,[3] (iii) understanding anion-anion interactions and the morphological meaning of electric field lines,[4] and (iv) atomic electrostatic sites responsible for molecular orientations[5] have been concepts developed in our research.

References

1. R.F.W. Bader, Atoms in Molecules: A Quantum Theory, International Series of Monographs on Chemistry, Clarendon Press (1994).
2. I. Mata, E. Molins, E. Espinosa, J. Phys. Chem. A (2007), 111, 9859.
3. I. Mata, E. Molins, I. Alkorta, E. Espinosa, J. Phys. Chem. A (2007), 111, 6425.
4. (a) I. Mata, I. Alkorta, E. Molins, E. Espinosa, ChemPhysChem (2012), 13, 1421 ; (b) I. Mata, I. Alkorta, E. Molins, E. Espinosa, Chem. Phys. Lett. (2013), 555, 106. (c) I. Mata, I. Alkorta, E. Molins, E. Espinosa, in preparation.
5. (a) T.T.T. Bui, S. Dahaoui, C. Lecomte, G.R. Desiraju, E. Espinosa, Angew. Chem., Int. Ed. (2009), 48, 3838; (b) M.E. Brezgunova, E. Aubert, S. Dahaoui, P. Fertey, S. Lebègue, C. Jelsch, J.A. Ángyan, E. Espinosa, Cryst. Growth Des. (2012), 12, 5373; (c) M.E. Brezgunova, J. Lieffrig, E. Aubert, S. Dahaoui, P. Fertey, S. Lebègue, C. Jelsch, J.A. Ángyan, M. Fourmigué, E. Espinosa, Cryst. Growth Des. (2013), 13, 3283.

Talks

MS01 – Crystallography of pharmaceutically active compounds & halogen and hydrogen bonds in crystal engineering

MS01-T1

Small-molecule crystallography: applications to pharmaceuticals

E. Boldyreva[1,2]
[1]*Novosibirsk State University, Institute of Solid State Chemistry, Novosibirsk, Russian Federation*
[2]*Institute of Solid State Chemistry and Mechanochemistry, SB Russian Academy of Sciences, Novosibirsk, Russian Federation*

The role that crystallography plays in drug design and development is difficult to overestimate. In most cases, however, this role is associated with macromolecular crystallography. In the present contribution I shall try to give a concise overview of different applications of small-molecule crystallography in design of new drug forms and in optimising the methods of obtaining the pharmaceutical formulations with desirable characteristics. The following topics will be discussed:

1. Analysis of molecular packing and intermolecular interactions in the crystal structures of small-molecule drugs as a tool of designing forms with improved dissolution profile.

2. Polymorphism of small-molecule drug crystals - expected vs. non-expected, desirable vs. non-desirable.

3. Non-ambient small-molecule crystallography and pharmaceuticals.

4. Different properties of melts and solutions prepared from different polymorphs - reality or artefacts?

The work was supported by several programs and grants from the Russian Academy of Sciences and Ministry of Education, and by a RFBR grant 13-03-00795.

MS01-T2

Absolute Configuration Determination for Light Atom Structures using a Liquid Metal Jet X-ray Source with Ga Kα Radiation

J. Graf[1], M. Ruf[2], B. Noll[2], S. Freisz[3], A. Gerisch[3], H. Ott[3], B. Dittrich[4], A. Kleine[1], C. Michaelsen[1]
[1]*Incoatec GmbH, Geesthacht, Germany*
[2]*Bruker AXS Inc., Madison, United States*
[3]*Bruker AXS GmbH, Karlsruhe, Germany*
[4]*Georg-August-Universität Göttingen, Göttingen, Germany*

The determination of the absolute configuration for light-atom structures has become central to research in pharmaceuticals and natural products synthesis [1, 2, 3]. In the absence of elements heavier than silicon, it is often problematic to make a significant assignment of absolute configuration. Traditionally, heavy-atom derivatives were prepared which have a stronger anomalous signal compared to the native compound. However, this is not always feasible.

The assignment of the absolute structure configuration of light atom compounds has become somewhat easier with the advent of high-brightness microfocus sources in combination with multilayer mirrors. The increased flux density of these sources allows for the collection of high quality data, even on small samples, and improves the anomalous signal by improvements in counting statistics [4].

With the recent introduction of a liquid-metal-jet X-ray source, which uses a high-speed jet of a molten Gallium alloy as target, unprecedented beam intensities can be achieved [5]. The shorter wavelength of the Ga Kα radiation compared to Cu Kα radiation leads to a slightly weaker anomalous signal for typical light atom structures. However, due to the shorter wavelength, the highest resolution achievable with the metal-jet X-ray source is typically at about 0.70 Å, compared to about 0.80 Å for Cu Kα. Hence, about 50% more unique reflections can be recorded. These additional reflections significantly improve the quality of the Flack parameter.

In this contribution, we will be demonstrating the improvement in data quality from the metal-jet X-ray source.

[1] H. D. Flack, G. Bernardinelli, *Chriality* (2008), 20, 681 - 690.
[2] A. L. Thompson, D. J. Watkin, *Tetrahedron: Asymmetry* (2009), 20, 712 - 717.
[3] H. D. Flack, G. Bernardinelli, *J. Appl. Cryst.* (2000), 33, 1143 - 1148.
[4] T. Schulz, K. Meindl, D. Leusser, D. Stern, J. Graf, C. Michaelsen, M. Ruf, G. M. Sheldrick, D. Stalke, *J. Appl. Cryst.* (2009), 42, 885 - 891.
[5] M. Otendal, T. Tuohimaa, U. Vogt, H. M. Hertz, *Rev. Sci. Instrum.* (2008), 79, 016102.

MS01-T3

Refinement of Macromolecular Structures against Neutron Data with SHELXL-2013

T. Gruene[1], H. W. Hahn[1], A. V. Luebben[1], F. Meilleur[2], G. M. Sheldrick[1]
[1]*Anorganische Chemie/Georg-August-Universitaet, Strukturchemie, Goettingen, Germany*
[2]*Oak Ridge National Laboratory, Oak Ridge, United States*

The refinement program SHELXL [1] is well known for its reliability, robustness, and flexibility. Thanks to its flexibility, SHELXL has long been capable of refining against neutron data. The previous release SHELXL-97 [2] included improvements to make the program more convenient to use with macromolecular structures, e.g. the availability of Engh & Huber restraints [3] in SHELX syntax. Some of the unique features of SHELXL make it particularly well suited for the refinement of macromolecular structures against neutron data, e.g. the automated analysis of non-standard hydrogen bonding (via the HTAB keyword), the main point of interest in macromolecular single crystal neutron diffraction. SHELXL also allows the refinement of deuterium / hydrogen occupancies in a chemically sensible way and hence avoids pathological entries to be submitted to the PDB [4] e.g. with variable occupancies for every single deuterium atom. In this work we re-refined several of the protein structures from the PDB for which neutron data were available with the beta version of SHELXL. Our results were incorporated into the latest release SHELXL-2013 [5]. They include improvements to make sophisticated refinement of macromolecular structures against neutron data available even to less experienced crystallographers and promote the sophistication of SHELXL to the world of macromolecular neutron crystallography. The NEUT keyword automatically replaces X-ray scattering factors with neutron scattering lengths without further ado of the user and also adapts the hydrogen bond lengths for the AFIX keyword to correctly place hydrogen atoms in riding position. However as one of the main results, our work also shows that using (correct) restraints for hydrogen positions significantly improves the quality of the structure compared to riding position, a result which may be unexpected to many (X-ray) crystallographers. To our knowledge this work presents the first publication for Engh & Huber-like restraints for the hydrogen atoms for all 20 standard amino acids. Fig. 1 shows the hydrogen bonding network from a beta sheet from PDB ID 2ZOI and highlights incomplete hydrogen exchange during the deuteration procedure.

[1] Sheldrick, G.M. (2008) Acta Cryst. A65, 222-122
[2] Schneider, T. R. and Sheldrick, G. M. (1997) Methods Enzymol. 277, 319-343
[3] Engh, R. A. and Huber, R. (1991) Acta Cryst. A47, 392-400
[4] Berman, H. M. et al. (2000) Nucleic Acids Res. 28, 235—242
[5] Gruene, T. et al (2014) J. Appl. Cryst. 47

Figure 1

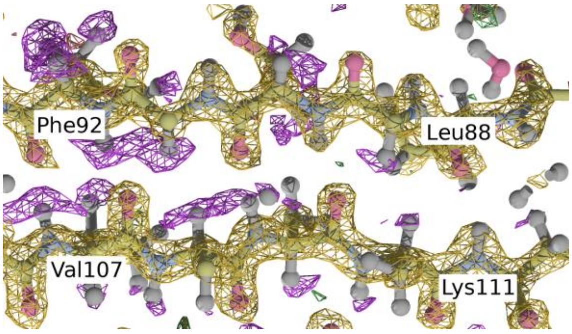

MS01-T4

Influence on crystallisation process of amino acids from solution

K. Merz[1], A. Kupka[1], H. Gies[1]
[1]*Ruhr Universität Bochum, Bochum, Germany*

The famous Miller experiment to model the primordial soup demonstrated that amino acids can form spontaneously as the essential building blocks of life in solutions. It is, however, still an open question how self-recognition processes influence the transformation of these spontaneously formed amino acids in solvents into higher ordered structures in the solid state, thereby creating chiral materials and catalytically competent structures. The understanding of the first steps of molecular self-assembly processes in such environments will thus give important clues towards the understanding of biological evolution.

Most of intermolecular interactions are not very strong and their formation is related to and affected by small changes in the molecular structure and the crystallisation conditions. Continuing our investigations on aggregation of substituted aromatic molecules in the solid state, we studied the influence and boundaries of weak directing substituents like deuterium on the aggregation of small molecules [1-3]. Hydrogen/deuterium (H/D)-exchange, the smallest possible modification of a molecule, is generally seen as a non dominating parameter in the formation of crystal structures of chemical compounds. On the other hand, it could already be shown that the aggregation of molecules in the solid state of polymorphic N-heterocycle systems like pyridine-N-oxide or acridine can be very sensitive to small changes of the isotopic substitution pattern of the selected molecules [4-7].

Within our project, the molecular aggregation of amino acids in solution with the formation of molecular aggregates and pre-nucleation clusters in deuterated and non-deuterated systems, and in particular the role of the solvent in these processes, will be studied in both experiment and theory.

[1] V. Vasylyeva, K. Merz, *J. Fluor. Chem.*, 2010, *131(3)*, 446
[2] V. Vasylyeva, K. Merz, *Cryst. Growth & Des.* 2010, *10*, 4250
[3] V. Vasylyeva, O. V. Shishkin, A. V. Maleev, K. Merz, *Cryst. Growth Des.*, 2012, *12*, 1032
[4] O. V. Shishkin, S. V. Shishkina, A. V. Maleev, R. Zubatyuk, V. Vasylyeva, K. Merz, *ChemPhysChem*, 2013**,** *14***,** 847
[5] V. Vasylyeva, T. Kedziorski, N. Metzler-Nolte, C. Schauerte, K. Merz, *Crystal Growth & Design* 2010; *10*, 4224.
[6] K. Merz, V. Vasylyeva, *CrystEngCom*. 2010; *12*, 3989.

[7] A. Kupka, V. Vasylyeva, D. W. M. Hofmann, K. Merz, *Cryst Growth Des*, 2012, *12*, 5966

Keywords: molecular aggregation, amino acids, deuteration effect

Figure 1

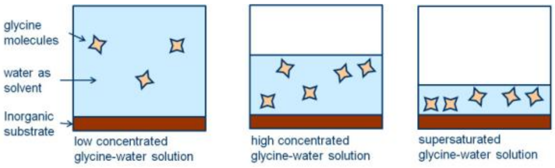

MS01-T5

Crystal Engineering Involving Ditopic Ligands of Modified Acetylacetones

C. Merkens[1], F. Pan[2], U. Englert[1]
[1]*RWTH Aachen University, Institute of Inorganic Chemistry, Aachen, Germany*
[2]*University of Jyväskylä, Nanoscience Center, Department of Chemistry, Jyväskylä, Finland*

Bimetallic coordination polymers represent an area of very active studies and provide an attractive meeting ground for basic research and applied materials science. [1, 2] Suitably substituted acetylacetone derivatives represent attractive ditopic ligands for crystal engineering of bimetallic coordination polymers. In particular the nitrile substituted ligand HacacCN [3] and the pyridine derivative HacacPy [4] are suitable candidates for the stepwise construction of bimetallic networks *via* initial building block formation.

HacacCN has been used to construct building blocks based on trivalent transition metal cations [5], main group [6] and rare earth cations. [7, 8] These building blocks can be used for further crosslinking reactions using the weakly coordinating nitrile functionality. Crosslinking reactions were only successful for Ag(I) and result in bimetallic networks of complex architectures.

In contrast to HacacCN the ligand HacacPy offers a strong N-donor functionality, which is used for additional modes in terms of crystal engineering: the design of extended structures is not limited to coordinative bonds towards metal cations. Rather, halogen bonds have been established as a powerful tool for the construction of expanded architectures.[11] High resolution X-ray diffraction has provided experimental access to the charge density and hence information about the nature and strength of chemical bonds and intermolecular interactions. [12]

Figure 1

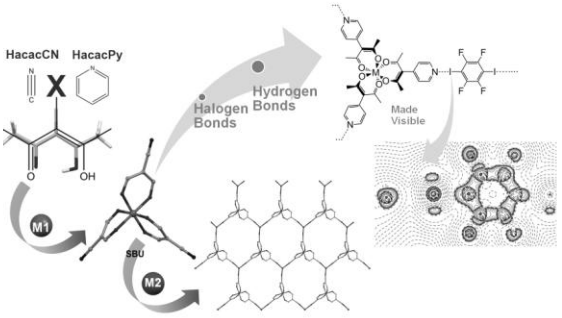

MS01-T6

Pair distribution function analysis of organic compounds: improving the modelling of the atomic vibrations

D. Podgorski[1], P. Juhas[2], S. J. L. Billinge[2,3], M. U. Schmidt[1]
[1]*Goethe University, Institute of Inorganic and Analytical Chemistry, Frankfurt am Main, Germany*
[2]*Brookhaven National Laboratory, Condensed Matter Physics and Materials Science Department, Upton, New York, United States*
[3]*Columbia University, epartment of Applied Physics and Applied Mathematics, New York, United States*

The pair distribution function (PDF) of molecular solids contains information about intramolecular as well as intermolecular atom-atom distances[1,2]. The amplitudes of the intramolecular vibrations are much smaller than those of the intermolecular vibrations[3]. To date, the resulting mixture of sharp and broad peaks in a PDF-curve could not be modelled appropriately. We have developed a new modelling approach using two different isotropic displacement parameters for intramolecular and intermolecular vibrations. The method was implemented within the Program SrFit[4]. Paracetamol and quinacridone were used as test compounds (Fig. 1).

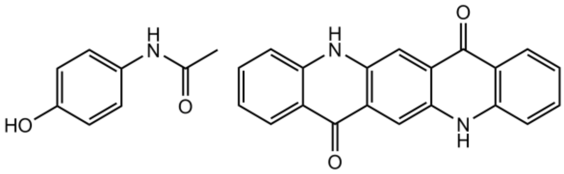

Paracetamol Quinacridone

Fig. 1: Structural formula of paracetamol and quinacridone.

The new modelling approach results in a significantly better fit of the calculated PDFs to the experimental PDFs, especially in the region from 3-15 Å which consists of intramolecular and intermolecular distances[5]. This development is a significant step in the investigation of structures of nanocrystalline and amorphous organic compounds.

[1] T. Egami, S. J. L. Billinge, *Underneath the Bragg peaks: Structural analysis of complex materials,* (2012). Kidlington, Oxford, UK: Pergamon.

[2] M. U. Schmidt, S. Brühne, A. K. Wolf, A. Rech, J. Brüning, E. Alig, L. Fink, C. Buchsbaum, J. Glinnemann, J. van de Streek, F. Gozzo, M. Brunelli, F. Stowasser, T. Gorelik, E. Mugnaioli, U. Kolb (2009), *Acta Cryst., B6**5***, 189-199.
[3] I. K. Jeong, T. Proffen, F. Mohiuddin, S. J. L. Billinge (1999), J. Phys. Chem., A103, 921-924.
[4] X. Yang, C. Farrow, P. Juhas, S. J. L. Billinge, SrFit-a program for full-profile fitting of the atomic pair distribution function (PDF) derived from x-ray or neutron diffraction data, in preparation.
[5] D. Podgorski, P. Juhas, S. J. L. Billinge, M. U. Schmidt, Pair distribution function analysis of organic compounds, submitted.

MS02 – Functional materials and technologies for energy conversion and catalysis

MS02-T01

Wet chemical synthesis andcharacterisation of $SrTiO_3$-Ruddlesden-Popper-films for photoelectrochemical water splitting

D. Karsch[1], D. Eger[1], E. Mehner[1], H. Stöcker[1], D. Meyer[1]
[1]*TU Freiberg, Institut für experimentelle Physik, Freiberg, Germany*

The photoinduced watersplitting promises a considerable simplification for hydrogen production. Therefore, the energy of photons, e.g. from sunlight, is used for splitting water into its molecular components, Oxygen and Hydrogen. This is realised by irradiation of light of suitable wavelength on a semiconductor.

Four samples of thin films of $SrTiO_3$-Ruddlesden-Popper-Phases on Niobium-doped $SrTiO_3$ are produced by Sol-Gel synthesis and are characterized regarding phase content and morphology. For comparison of phase composition additionally one sample with equal stoichiometric relations is produced by ion beam implantation in a $SrTiO_3$ single crystal. The crystalline phases in the films are investigated with *in-situ* X-ray diffraction.

All samples show delicate, spongy structures on the surface, which are visible by electron scanning microscopy and have a relevant part of impurity phases in addition to the RP-phases. Furthermore, photoelectrochemical measurements with Sol-Gel synthesized thin layers have been executed for the first time. The results show that the thin layer working electrodes are suitable for water splitting. The highest photo currents are achieved by irradiating with UV light. Irradiation with a conventional Neon tube including also visible wavelengths reveals an improvement for coated samples compared to the pure substrate.

MS02-T02

Cu/SBA-15 catalysts for methanol steam reforming (MSR): Increase in intrinsic activity due to redox pretreatment

G. Koch[1], T. Ressler[1]
[1]*TU-Berlin, Inorganic and Analytical Chemistry, Berlin, Germany*

Questions

Cu based catalysts play a significant role in methanol steam reforming (MSR) [1]. Cu catalysts showed strong deactivation in the beginning of MSR. However, temporary addition of O_2 to reaction feed resulted in increased H_2 formation for Cu/ZrO_2 [2], Cu/SiO_2 [3] and Cu/ZnO [4] catalysts. After O_2 addition, Cu/ZnO catalysts showed increased crystallite sizes and increased disorder. The disorder was attributed to CuZnO interface [5] and may lead to microstrain in Cu particles. Therefore model catalysts without ZnO were investigated to understand structure activity correlation and to elucidate changes in catalytic activity.

Methods

Oxidic precursors, CuO/SBA-15, were synthesized as described in [3]. Besides reduction in H_2 of CuO/SBA-15, the oxidic precursors were reduced and reoxidized and then again reduced, followed by MSR. MSR activity was measured in 2 % H_2O and 2 % methanol atmosphere at 250 °C. Cu surface area was determined using N_2O. Furthermore, *in situ* measurements at the Cu K edge of activated Cu particles were performed at beamline X at HASYLAB, Hamburg. Catalysts were measured in laboratory *in situ* XRD.

Results

During reduction in H_2, XAS measurements at the Cu K edge revealed, that oxidic precursors were reduced to metallic Cu via a Cu_2O intermediate. During pretreatment the reduction of oxidic precursors in H_2 was followed by reoxidation and subsequent 2nd reduction. Using *in situ* XAS during pretreatment, the reduction of oxidic precursors to metallic Cu and subsequent oxidation to CuO/SBA-15 were measured. The 2nd reduction in H_2 started at lower temperatures. Reduction of Cu particles took place via Cu_2O to metallic Cu particles, too. After pretreatment, catalysts exhibited increased activity in MSR (Fig. 1). N_2O chemisorption showed that pretreatment increased dispersion of Cu. Interestingly, neither *in situ*: XAS nor *in situ* XRD revealed significant decrease in Cu particle size and strain due to pretreatment. Moreover, deactivation of catalysts was similar during MSR independent of pretreatment (Fig. 1).

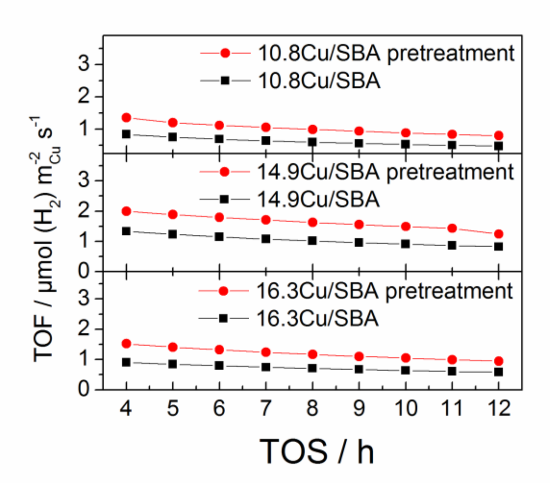

Fig. 1 Activity in methanol steam reforming at 250 °C for Cu/SBA-15 catalysts with different loadings as a function of time on stream (TOS). Loading increases from top to bottom. Squares show turn over frequency after simple activation in H_2. Circles show turn over frequency after redox pretreatment and reduction in H_2. Number before *Cu/SBA* represents weight % of Cu in oxidic precursors.

[1] S. Sá, H. Silva, L. Brandão, J. M. Soua, A. Mendes *Appl. Catal., B Environmental* 2010, *99*, 43-57.
[2] H. Purnama, F. Girgsdies, T. Ressler, J. H. Schattka, R. A. Caruso, R. Schohmäcker, R. Schlögl *Catal. Lett*. 2004, *94*, 61-68.
[3] G. Koch, K. Meurisch, T. Ressler *Z. Anorg. Allg. Chem.* 2010, *636*, 2094.
[4] M. M. Günter, B. Bems, R. Schlögl, T. Ressler *J. Synchrotron Rad*. 2001, *8*, 619-621.
[5] M. M. Günther, T. Ressler, R. E. Jentoft, B. Bems *J. Catal.* 2001, *203*, 133-149.

MS02-T03

Structure determination of the first example of a metal-interlayer expanded zeolite

H. Gies[1], B. Yilmaz[2], T. De Baerdemaeker[3], M. Feyen[4], U. Müller[4], F.- S. Xiao[5], D. De Vos[3]
[1]*RU Bochum, Institut für Geologie, Mineralogie und Geophysik, Bochum, Germany*
[2]*BASF Coorp., Iselin, United States*
[3]*KU Leuven, Centre for Surface Chemistry and Catalysis, Leuven, Belgium*
[4]*BASF SE, Ludwigshafen, Germany*
[5]*Zhejiang University, Chemistry, Hangzhou, China*

Interlayer expansion using silylating agents to connect layer silicates to 3D framework structures has proofed to be a versatile synthesis route to new micro-porous frameworks (1). We show here that also Me-cations can be used as linker agents. An acidic Fe-chloride solution was used in a hydrothermal reaction to convert the hydrous layer silicate RUB-36 into an interlayer expanded zeolite, containing Fe at the linker site. Structure analysis of the new material Fe-COE-3, $Si_{19.14}Fe_{0.86}O_{42}$, showed that the porous framework is stable after calcination and contains Fe on T-sites at the linker position which connects the two silicate layers. From chemical analysis it is confirmed that every other linker site is occupied by iron.
The material crystallizes in space group Pm witha = 12.200(9) Å, b = 13.981(8) Å, c = 7.369(2) Å, ß = 106.9(1)°.Fig. 1 and 2 show the results of the final Rietveld analysis (chi^2 = 8.8) and a projection of the framework structure along [001]. Because of the limited crystallinity of the material also the quality of the structure refinement is constricted. However, including complementary information from adsorption experiments, IR-, and UV-spectroscopy the structure model is confirmed without any doubt. Besides, the Rietveld analysis of the XRD data is the analytical tool to gain more detailed geometric information of the metallosilicate framework.

The synthesis procedure is flexible and can be extended to other Me-cations as linker sites. We have prepared isostructural interlayer expanded metallosilicates of similar crystallinity with Ti, Sn, Zn, Eu, and Al as active centers. This method of inserting Me-cations as linkers in hydrous layer silicates shows for the first time that the active sites in the generated microporous silicate framework can be obtained in a controlled manner on well defined T-sites.

References:
Hermann Gies, Ulrich Muller, Bilge Yilmaz, Takashi Tatsumi, Bin Xie, Feng-Shou Xiao, Xinhe Bao, Weiping Zhang, Dirk De Vos: Interlayer Expansion of the Layered Zeolite Precursor RUB-39: A Universal Method To Synthesize Functionalized Microporous Silicates.
Chem. Mater. 23(10), 2545-2554(2011)

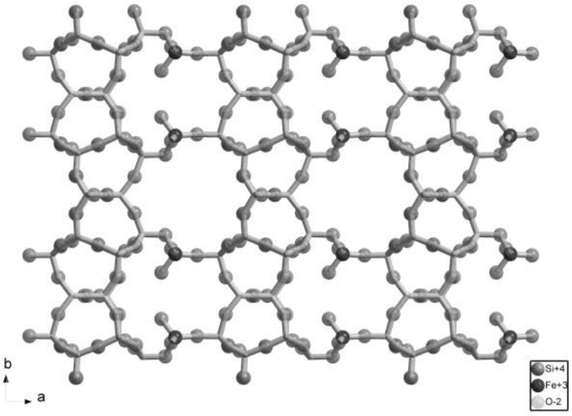

Fig. 1: Projection of the Fe-interconnected (dark spheres) zeolite framework

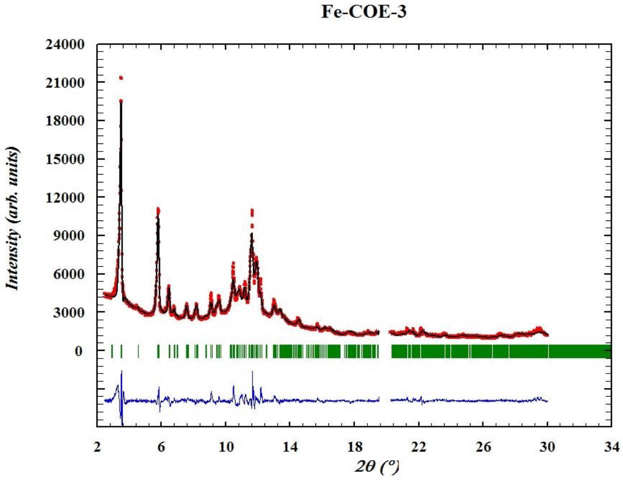

Fig. 2: Final results of the Rietveld analysis of the PXRD data.

MS02-T04

Absorption Behavior of H_2 in Three-dimensional CAU Metal Organic Framework Structure

M.- C. Schlegel[1], M. Russina[1], N. Stock[2], H. Reinsch[3], D. Többens[1], M. Krüger[2]
[1]*Helmholtz-Zentrum Berlin (HZB), Berlin, Germany*
[2]*Christian-Albrecht Universität, Kiel, Germany*
[3]*Centre for Surface Chemistry and Catalysis, Leuven, Belgium*

Hydrogen gas storage in bulk materials is an advanced alternative to storage in compressed or liquid form. The ideal hydrogen storage material should have a relative high specific surface, high porosity , fast kinetics of hydrogenation and dehydrogenation near ambient temperature, long-term stability and good thermal conductivity for removing the reaction heat. A fundamental knowledge of gas adsorption behavior and therefor storage processes is crucial for optimal material design. Though some progress has been made towards understanding of the conditions needed, but many questions remain unanswered. In particular questions of the mechanism by which H_2 binds at different sites, hydrogen mobility and impact of confinement geometry needed to be addressed in details and are the topics of the presented study.

Metal organic frameworks (MOFs) are materials of great interest due to their large variety of structure types, as well as low density and very high specific surface. Newly synthesized CAU compounds are MOFs based on aluminum polyhedral connected by different organic linker molecules. Using this organic linker molecules offer opportunities to form tunable structures with channels of various geometries and allow in this way to study the impact of confinement dimension and geometry on the absorption of the molecular hydrogen in the systematic way. In-situ structure analyses allow information about adsorption mechanism of hydrogen in such materials and provide the basis for the future study of the dynamics of hydrogen inside the MOFs.

Here we report the first results of the high resolution neutron diffraction study of CAU compounds, which we conducted using neutron diffractometer E9 at the BER II in Berlin, Germany. Two different types of CAU metal organic framework structures at various gas pressures using D_2-gas were analyzed. The chosen experimental setup allowed us to observe changes in the relative intensities of the reflections. The refinement of the structure and determination of the positions of absorbed D_2 was obtained using thermodynamic modeling and crystal structure analysis (Figure 1). Based on our results we were able to characterize the adsorption process in detail. The comparison will give us the opportunity to understand the influence of various cavity shapes to the adsorption properties, especially the differences between three-dimensional cage (CAU-1) and one-dimensional tunnel (CAU-8) structures [1, 2].

References
[1] T. Ahnsfeld, N. Guillou, D. Gunzlemann, I. Margiolaki, T. Loiseau, G. Ferey, J. Senker, N. Stock, Angew. Chem. Int. Edit., 48, (2009), 5163-5166.
[2] H. Reinsch, M. Krüger, J. Marrot, N. Stock, Inorg. Chem., 52, (2013), 1854-1859.

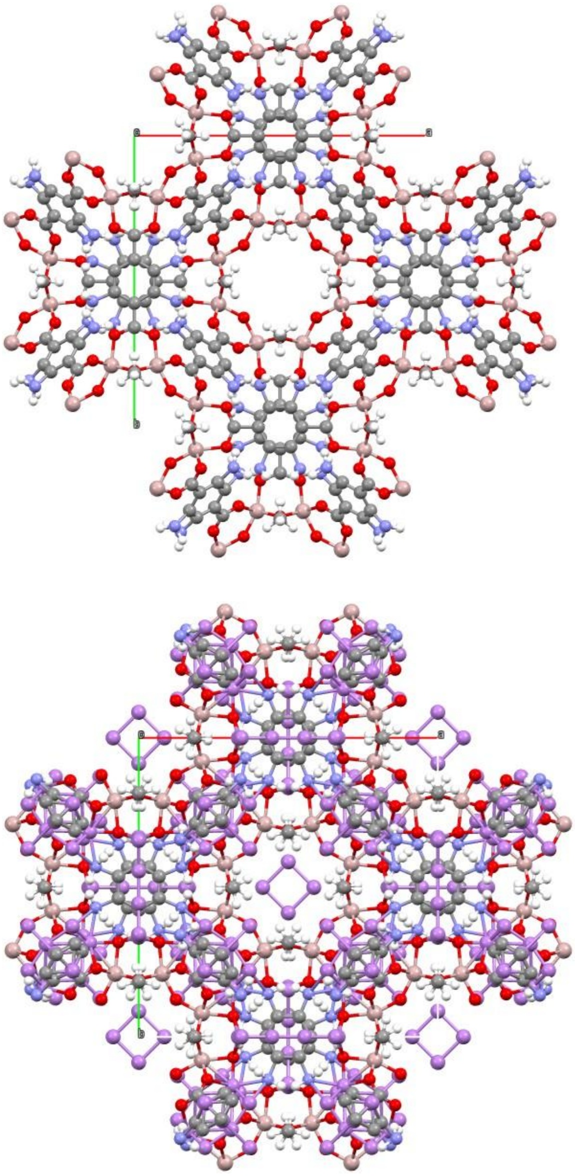

Figure 1: Crystal structure of CAU-1 along ***c***, empty (left) and totally filled with D2-guest molecules (right).

MS02-T05

The hydrogenation of Zintl phases by *in situ* neutron powder diffraction

H. Kohlmann[1], P. Wenderoth[2]
[1]*Universität Leipzig, Anorganische Chemie, Leipzig, Germany*
[2]*Universität des Saarlandes, Anorganische Festkörperchemie, Saarbrücken, Germany*

By taking up hydrogen Zintl phases may either form polyanionic or Zintl phase hydrides [1]. In polyanionic hydrides hydrogen in covalently bound to the polyanion, thus often reducing its connectivity. In Zintl phase hydrides, however, hydrogen is incorporated in interstitials and increases the connectivity of the polyanion by oxidizing it chemically. In view of the reversibility of these reactions and the potential of such materials for hydrogen storage, reaction pathways and possible intermediates are of importance. We have therefore studied the hydrogenation (deuteration) of Zintl phases MGa_2 (M = Sr, Eu, Yb) and CaSi *in situ* by neutron powder diffraction [2]. By using a sapphire gas pressure cell [3] at 60 bar deuterium pressure and temperatures of 550 K it was shown that $SrGa_2$ reacts does not incorporate deuterium into interstitials, but reacts directly to the polyanionic deuteride $SrGa_2D_2$ with covalent Ga-D bonds of 186.6(8) pm. The crystal structure of an earlier study [4] was confirmed. $EuGa_2$ and $YbGa_2$ react to the binary hydrides EuH_2 and $YbGa_{2.67}$, respectively, and gallium rich intermetallic compounds. CaSi first forms a deuterides, in which the CaSi structure is distorted and deuterium occupies interstitial voids. The reaction from the Zintl phase CaSi to the deuterides $CaSiD_x$ is very fast and completes within less than two minutes. At 600 K both compounds can be switched one into the other by changing the deuterium pressure between 1 and 55 bar. Prolonged reaction times at higher temperatures lead to the formation of $CaSiD_{1+x}$, which was described before [5]. Such reaction intermediates can only by detected by *in situ* studies, underlining their importance. They may also help to classify hydrogenation reactions according to their reversibility, which is of importance for hydrogen storage.

[1] U. Häußermann, V. F. Kranak, K. Puhakainen, *Struct. Bond*. 2011, *139*, 143-162
[2] P. Wenderoth, H. Kohlmann, *Inorg. Chem*. 2013, *52*, 10525-10531
[3] H. Kohlmann, N. Kurtzemann, T. C. Hansen, *Powder Diffr*. 2013, *28*, S242-S255
[4] T. Björling, D. Noréus, U. Häussermann, *J. Am. Chem. Soc.* 2006, *128*, 817-824
[5] H. Wu, W. Zhou, T. J. Udovic, J. J. Rush, T. Yildirim, *Phys. Rev. B: Condens. Matter Mater. Phys.* 2006, *74*, 224101

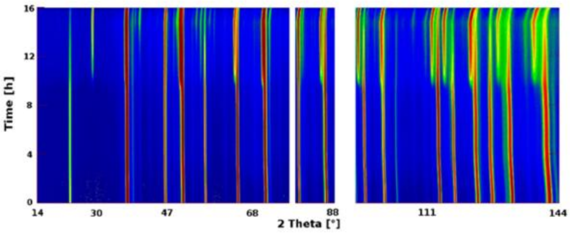

Fig. 1: *In situ* neutron poweder diffraction investigation of the formation of $SrGaD_2$ at 550 K and 60 bar deuterium presure

MS02-T06

Chalcopyrite semiconductors: atomic-scale structure and band gap bowing

C. S. Schnohr[1], S. Eckner[1], H. Kämmer[1], T. Steinbach[1], M. Gnauck[1], A. Johannes[1], C. A. Kaufmann[2], C. Stephan[2], S. Schorr[2,3]
[1]*Friedrich-Schiller-Universität Jena, Institut für Festkörperphysik, Jena, Germany*
[2]*Helmholtz-Zentrum Berlin für Materialien und Energie, Berlin, Germany*
[3]*Freie Universität Berlin, Institut für Geologische Wissenschaften, Berlin, Germany*

$Cu(In,Ga)Se_2$ is one of the most promising material systems for thin film photovoltaics with record efficiencies above 20% on laboratory scale. The material crystallizes in the chalcopyrite type crystal structure where the anion is typically displaced from the ideal tetrahedral lattice site due to the different properties of the neighbouring cations. This subtle structural variation has a strong influence on the energy band gap. Therefore, we have studied the atomic-scale structure of $Cu(In,Ga)Se_2$ as a function of composition using extended X-ray absorption fine structure spectroscopy and valence force field simulations [1]. The element-specific In-Se, Ga-Se and Cu-Se bond lengths are strikingly different from each other and remain close to the values of the ternary parent compounds despite the significant change of the lattice constants. The local atomic arrangements thus deviate significantly from the long-range crystallographic structure. Furthermore, the material is characterised by structural inhomogeneity on the atomic scale even if compositional fluctuations or secondary phases are absent. Regarding the anion position, two different displacement mechanisms have to be distinguished both of which influence the nonlinear change of the band gap with material composition. Similar results were also obtained for $Cu(In,Ga)S_2$ indicating that our findings represent general features of these highly relevant yet complex chalcopyrite semiconductors [2].

[1] C. S. Schnohr, H. Kämmer, C. Stephan, S. Schorr, T. Steinbach, and J. Rensberg, Phys. Rev. B 85, 245204 (2012).
[2] S. Eckner, H. Kämmer, T. Steinbach, M. Gnauck, A. Johannes, C. Stephan, S. Schorr, and C. S. Schnohr, Appl. Phys. Lett. 103, 081905 (2013).

MS02-T07

The influence of sodium on the defect characteristics in off stoichiomteric $Cu(In, Ga)Se_2$

C. Stephan[1], C. Kaufmann[1], D. Greiner[1], S. Schorr[1]
[1]*Helmholtz-Zentrum Berlin für Materialien und Energie, Berlin, Germany*

Off stoichiometric $Cu(In,Ga)Se_2$ materials are highly efficient absorber layers in thin film solar cells and sodium is generally supplied during thin film fabrication. Native point defects within the materials are influencing the electronic properties of such a device, sensitively. The introduction of sodium is advantageous for the device, whereby it is expected that it has an effect on the defect chemistry of the material. The influence of sodium addition was investigated by neutron powder diffraction and subsequent Rietveld analysis using two different types of samples. Powder material, with a well-defined chemical composition, and thin films produced by a multi-stage co-evaporation process.The resulting structural parameters such as cation site occupancies show differences compared to off stoichiometric Cu(In, Ga)Se_2 samples without sodium studie previously [1,2]. The structural results will be discussed in terms of the beneficial effect on the resulting solar absorber material caused by providing sodium during material preparation.

[1] C. Stephan, S. Schorr, M. Tovar, and H. W. Schock, Appl Phys Lett 98 (9), 091906 (1) (2011).
[2] C. Stephan, T. Scherb, C.A. Kaufmann, S. Schorr, and H. W. Schock, Appl Phys Lett 101 (10), 101907(1) (2012).

MS02-T08

In-situ XRD investigation of thin film growth by thermal co-evaporation

G. Schuck[1], M. Kastowsky[1], G. Kaune[2], S. Hartnauer[2], R. Scheer[2]
[1]*EFG GmbH, Berlin, Germany*
[2]*Martin-Luther-Universität Halle-Wittenberg, Fachgruppe Photovoltaik, D-06120 Halle (Saale), Germany*

The growth of a $Cu_2ZnSnSe_4$ (CZTSe) thin film deposited with a multi-stage co-evaporation process is investigated with time-resolved in-situ X-ray diffraction [1]. The X-ray diffractometer is a custom-made system manufactured by EFG GmbH Berlin (Fig. 1). A novel setup intended for in-situ growth studies is used for the experiment. The X-ray data confirm the former observation that CZTSe growth is delayed with deposition of only $Cu_{2-x}Se$ and ZnSe in the initial process stage and provide new insight into the evolution of the appearing phases. In Zn-rich deposition conditions, ZnSe deposited at the beginning may not be consumed by the growing CZTSe but remain as an unreacted layer at the interface to the Mo back contact. $Cu_{2-x}Se$ growth starts with the formation of a Cu rich phase which is reduced to a Cu poor phase in the process. Furthermore, our results show that in-situ XRD at elevated temperatures is able to distinguish between ZnSe and CZTSe and that it can be used for the detection of ZnSe as secondary phase.

[1] Gunar Kaune, Stefan Hartnauer, and Roland Scheer, In-situ XRD investigation of $Cu_2ZnSnSe_4$ thin film growth by thermal co-evaporation, submitted for publication, 2013, Physica Status Solidi A: Applications and Materials Science

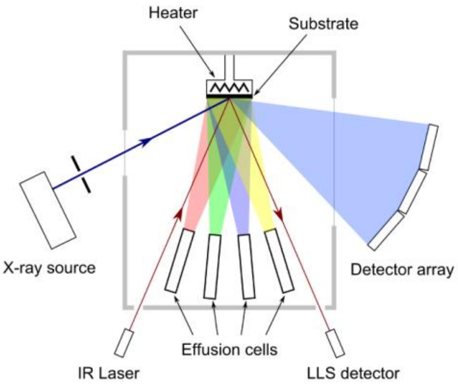

Figure 1 Schematic representation of the setup for in-situ XRD growth studies.

MS03 – Temperature, pressure and field induced processes/phase transitions

MS03-T1

EosFit7: A new program for equation of state analyses and calculations

J. Gonzalez-Platas[1], R. Angel[2], M. Alvaro[2], F. Nestola[2]
[1]*University of La Laguna, Fundamental Physics II, La Laguna, Tenerife, Spain*
[2]*University of Padua, Geosciences, Padua, Italy*

Equations of state (EoS) describe how the volume or density of a material changes with pressure and temperature. They also define how the elastic properties of the material change in response to compression and expansion. Equations of state therefore provide not only fundamental thermodynamic data that is required for the calculation of equilibrium phase diagrams, but they also give insights in to the details of interatomic interactions within the solid state, as it is these that resist the externally-applied compressive stresses and control the dynamics that lead to thermal expansion.

The ready availability of a variety of spread sheets and algebraic software makes it relatively easy, *in principle*, to fit any EoS formulation to data. However, the complex nature of some equation of state functions has led to their algebraic forms being given incorrectly in the literature. The additional possibility of errors in coding the complex equations, and the requirement to implement specific (non-standard) weighting methods to overcome correlation problems, makes imperative the provision of a validated set of publicly-available self-consistent algorithms for EoS calculations. We have now translated the original code of EosFit (Angel, 2000) to Fortran-95, fully revalidated it, and have built it in to a module that we have integrated into the *Crystallographic Fortran Modules Library* CrysFML (Rodriguez-Carvajal & Gonzalez-Platas, 2003). With this module we have developed a new console program, EosFit7c, to perform EoS calculations and fitting for both volume and linear isothermal data, isobaric data and *P-T* data (Angel et al. 2014). New features all easy handling and analysis of phase transition data. We will also present a completely new full GUI program that allows for the first time the integrated analysis, fitting and display of EoS data, and thus provides a new tool for both teaching and research.

This work was supported by ERC starting grant 307322 to Fabrizio Nestola.

Angel RJ (2000) *Reviews in Mineralogy and Geochemistry*, 41:35-60.

Angel RJ, Gonzalez-Platas J, Alvaro M (2014) *Zeitschrift für Kristallographie*, submitted.

Rodriguez-Carvajal J, Gonzalez-Platas J (2003) *IUCr Computing Commission Newsletter*, 1:50-58.

MS03-T2

Pressure-induced spin transition in henritermierite, a tetragonal Mn^{3+} hydrogarnet

A. Friedrich[1], W. Morgenroth[1], B. Winkler[1], A. Perlov[2], V. Milman[2]
[1]*Goethe University Frankfurt am Main, Institute for Geosciences, Frankfurt am Main, Germany*
[2]*Accelrys, Cambridge, United Kingdom*

Henritermierite is a rare Mn^{3+} silicate hydrogarnet with the end-member formula $Ca_3Mn_2[SiO_4]_2[OH]_4$. Due to the Jahn-Teller distortion of octahedrally coordinated Mn^{3+} and the ordered arrangement of small SiO_4 and large O_4H_4 tetrahedra henritermierite is tetragonal (space group $I4_1/acd$) [1]. While no phase transition was reported on compression up to 8.7 GPa [1], we were interested whether octahedrally-coordinated Mn^{3+} shows a high spin-to-low spin transition in henritermierite at considerably higher pressures.

Single-crystal synchrotron x-ray diffraction experiments were carried out at beamline P02.2 at PETRA III (DESY, Hamburg, Germany) using 42.8 keV radiation and a PerkinElmer XRD1621 area detector. Natural crystals with a composition close to the end member [1] and of sizes down to 20 × 10 × 5 μm^3 were pressurized in diamond anvil cells up to 79(1) GPa using neon as pressure-transmitting medium and ruby for pressure determination [2]. Images were converted [3] and further processed with the CrysAlis software [4]. Crystal structures were refined with the Shelx software [5]. Raman spectra were collected at high pressure with a Renishaw micro-Raman spectrometer. Complementary spin-polarized quantum mechanical calculations based on density functional theory were performed using the CASTEP program [6].

The calculations predicted an isosymmetric high spin-to-low spin transition at about 58 GPa. Experimental results showed a strongly enhanced reduction of the Jahn-Teller distortion of the $Mn^{3+}O_6$ octahedra above 55 GPa until suppression was reached at about 65-70 GPa. The suppression of the Jahn-Teller distortion is in agreement with the theoretically predicted high-pressure structures with Mn^{3+} in low-spin configuration. This confirms the occurrence of the pressure-induced high spin-to-low spin transition in henritermierite.

We gratefully acknowledge financial support from the DFG, Germany, (project Fr2491/2-1 within SPP1236) and the BMBF, Germany (projects 05K10RFA, 05KS7RF1, 05K13RF1). Portions of this research were carried out at the light source PETRA III at DESY, a member of the Helmholtz Association (HGF). We thank J. Gutzmer (Bergakademie Freiberg) for donation of the crystals.

[1] T. Armbruster et al., Am. Mineral. 86, 147 (2001)

[2] H.K. Mao, J. Xu, and P.M. Bell, J. Geophys. Res. 91, 4673 (1986)

[3] A. Rothkirch et al., J. Synchr. Rad. 20, 711 (2013)

[4] Agilent Technologies, *CrysAlis RED*, version 171.36.28 (2013)

[5] G.M. Sheldrick, Acta Crystallogr. A 64, 112 (2008)
[6] S.J. Clark et al., Z. Kristallogr. 220, 567 (2005)

MS03-T3

The Behaviour of SiO_2 under Dynamic Loading and Unloading

E.- R. Carl[1], A. Danilewsky[2], G. Trullenque[1], T. Kenkmann[1], H.-P. Liermann[3]
[1]*Institut für Geo- und Umweltnaturwissenschaften, Geologie, Freiburg i. Br, Germany*
[2]*Institut für Geo- und Umweltnaturwissenschaften, Kristallographie, Freiburg i. Br., Germany*
[3]*DESY, Hamburg, Germany*

Little is known about phase transitions in the SiO_2 system under non-equilibrium conditions that occur at highly dynamic geological processes such as meteorite impacts. In a meteorite impact, the high pressure polymorphs coesite and stishovite are formed at pressures which differ significantly from the hydrostatic stability field of 2 GPa and 10 GPa, respectively.

For the investigation of the conditions of their formation during a meteorite impact, dynamic experiments were carried out at the PETRA III "Extreme Conditions Beamline" (ECB) P02.2 at DESY, Hamburg at a wavelength of ~ 0.29 Å. Thereby, quartz powder (grain size < 1 micrometer) and a Gold grain for pressure calibration were placed in a membrane driven Diamond anvil cell (mDAC). Powder diffraction pattern were monitored every second by a detector flat panel XRD1621 from Perkin Elmer. The results from various pressure rates under non-hydrostatic conditions and at room temperature will be presented: The compression rate on the sample ranges from 0.08 GPa/s to 3.0 GPa/s with a maximum pressure of 60 GPa.

The results indicate that stishovite is formed only at the slowest compression rate. On the other hand, coesite has not been determined in the experiments yet due to the small intensities of the modelled peaks and, furthermore, strong overlapping with peaks of other phases. Since the phases are identified by peak-fitting, a Rietveld analysis will be carried out to scan for coesite and determine details about the formed phases.

Figure 1 shows two phase transitions occurring at a slow compression rate of 0.08 GPa/s. The first one is observed at ~ 25 GPa indicated by a peak splitting of the low-quartz (100) reflection as well as one appearing peak at low refraction angles (3 - 11 °2θ) (Figure 1a). These peaks cannot be fitted to any known high pressure phase of quartz indicating an unknown phase. The second one is observed at ~ 58 GPa characterized by two peaks splitting (Figure 1b). This pattern correlates with a modelled pattern of stishovite at equivalent pressures.

Besides gaining knowledge of the phase transformations of quartz dynamically, the performed experiments establish a basis to analyse phase transformations under conditions closer to a meteorite impact as will be offered by X-ray laser in the future.

Figure 1: Detail of a Stack of approx. 1600 diffractograms of SiO_2- powder during loading at 0.08 GPa/s. The starting materials are alpha-quartz (Qt) and gold (Au) for pressure calibration: The phase transition to an unknown phase (np) at ~ 25 GPa (a) and the formation of stishovite (St) at ~ 58 GPa (b) are observed. The details are limited to low diffraction angles (3 - 11 °2θ).

Figure 1

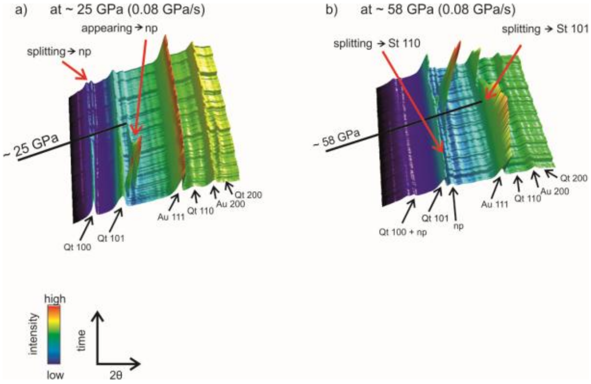

MS03-T4

Pressure-induced first-order phase transitions in ion-conducting anion-excess fluorite KY_3F_{10} studied with single-crystal x-ray diffraction

A. Grzechnik[1], K. Friese[1]
[1]*RWTH Aachen, Institute for Crystallography, Aachen, Germany*

Ternary fluorides with yttrium or lanthanide ions are commercially used materials for solid state lasers. Some of them are the most efficient materials for green and blue up-conversion known to date [1]. In the last few years, we have performed a series of studies on the AMF_4 and MF_3 compounds (A = Li, Na, K; M = Y, lanthanide) at different pressure-temperature conditions. Our work on the fluorite-related materials provides information on their structural instabilities as a function of temperature and pressure that could further be used to better understand and control their properties [2].

In the system KF - YF_3, we have studied not only KYF_4 [3] but also KY_3F_{10} (Fm-3m, Z = 8). At atmospheric pressure, KY_3F_{10} is an anion-excess *2×2×2* superstructure of fluorite with two building blocks Y_6F_{36} and Y_6F_{32}. In the Y_6F_{36} block, six square YF_8 antiprisms share their edges to form an empty F_{12} cubooctahedron. In the Y_6F_{32} block, six square YF_8 antiprisms share their edges to form an empty F_8 cube. Earlier investigations on the electrical conductivity have shown two thermally activated processes which can be attributed to increased fluorine ion mobility [4,5].

We investigated the stability of KY_3F_{10} with single-crystal x-ray diffraction to 9.5 GPa in a diamond anvil cell under hydrostatic conditions. Upon compression, there occur two phase transitions at about 5 and 7 GPa. The isostructural phase transition at about 5 GPa is due to an instability of the empty F_{12} cubooctahedra in the *2x2x2* superstucture. At about 7 GPa, the cubooctahedra collapse completely due to a further first-order phase transition to a high-pressure structure (Pm-3m, Z = 1) in which all the cations are surrounded by cubes of the F atoms. The excessive fluorine is located in the F_8 cubes. This is remarkable as earlier observations concerning the fluorine mobility in KY_3F_{10} as a function of temperature suggested that the centric site inside the F_8 cube might be involved in the underlying mechanism of fluorine ion conduction [5]. At hydrostatic conditions, all the transformations are reversible. Our findings suggest that at high pressures the anion-excess fluorite superstructures tend to transform to the ideal CaF_2 structure.

1. M. Haase, H. Schäfer, Angew. Chem., Int. Ed., 2011, 50, 5808.
2. A. Grzechnik, K. Friese, Dalton Trans., 2012, 41, 10258.
3. A. Grzechnik, K. Friese, Dalton Trans., 2013, 42, 441.
4. A.P. Ayala, M.A.S. Oliveira, J.-Y.Gesland, R.L. Moreira, J. Phys.: Condens. Matter, 1998, 10, 5161.
5. K. Friese, H. Krüger, V. Kahlenberg, T. Balic-Zunic, H. Emerich, J.-Y. Gesland, A. Grzechnik, J. Phys.: Condens. Matter, 2006, 18, 2677.

MS03-T5

Decomposition of SF_6 in the presence of glassy carbon in the laser heated diamond anvil cell

N. Rademacher[1], L. Bayarjargal[1], W. Morgenroth[1], A. Friedrich[1], B. Winkler[1]
[1]*Goethe University Frankfurt, Institute of Geosciences, Frankfurt am Main, Germany*

Chemical reactions at high pressures and temperatures are of interest because extreme conditions can lead to reaction pathways which result in novel compounds with unusual structural features [1]. Well-known examples are the polymerisation of CO_2 [2], N_2 [3] or CO [4]. This study presents the decomposition of the less well studied molecule SF_6 in the presence of glassy carbon in the laser heated diamond anvil cell as well as an extension of the known phase diagram of SF_6.

The behaviour of SF_6 at high pressures up to 10 GPa has been studied by Sasaki et al. [5] using Raman spectroscopy. The authors found two crystalline phases, denoted as phase I and phase II and SF_6 was stable up to the highest applied pressure of 10 GPa. We explored the stability field of SF_6-He mixtures with 10 and 20 vol% SF_6 up to pressures of 32 GPa and induced the decomposition of SF_6 in the presence of glassy carbon at 10-11 GPa and around 2000-2500 K by laser heating. SF_6 as well as the amorphous and crystalline reaction products were analysed using powder X-ray diffraction (including total scattering analysis) at the *Extreme Conditions Beamline* P02.2 [6] at PETRA III (DESY) and micro-Raman spectroscopy in Frankfurt.

We found two additional phase transformations of SF_6 at around 10(1) and 19(1) GPa. Moreover, the compressibilities of the phases I and II were determined to be 6.3(2)GPa and 12.6(3) GPa, respectively, by fitting equations of state to the *p*-*V*-data. Figure 1 shows the sample chamber before and after laser heating. Clearly, a chemical reaction must have occurred, since the black glassy carbon was no longer visible after the heating but a yellow and red coloured material instead. The reaction products were determined to be elemental sulfur and C_xF_y compounds.

The authors gratefully acknowledge financial support from the BMBF (project 05K10RFA) and the DFG (projects WI1232/25-1 and FR2491/2-1 within SPP1236). Part of this research was carried out at PETRA III (DESY), a member of the Helmholtz Association HGF. We thank the beamline scientist of P02.2 H.-P. Liermann and his team.

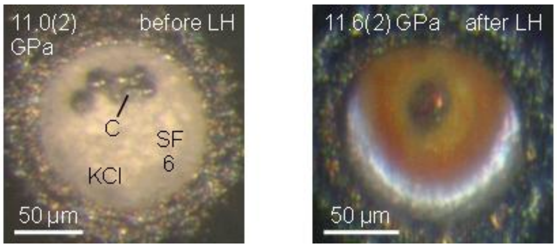

Figure 1: Glassy carbon and SF_6-He in the DAC before laser heating (left) and the reaction products after heating (right).

References

[1] R. Bini, M. Ceppatelli, M. Citroni, and V. Schettino, Chemical Physics 398, 262 (2012).
[2] V. Iota, C. S. Yoo, and H. Cynn, Science 283, 1510 (1999).
[3] M. I. Eremets, A. G. Gavriliuk, I. A. Trojan, D. A. Dzivenko, and R. Boehler, Nat. Mater. 3, 558 (2004).
[4] W. J. Evans, M. J. Lipp, C.-S. Yoo, H. Cynn, J. L. Herberg, R. S. Maxwell, and M. F. Nicol, Chem. Mater. 18, 2520 (2006).
[5] S. Sasaki, Y. Tomida, and H. Shimizu, J. Phys. Soc. Jpn. 61, 514 (1992).
[6] H.-P. Liermann, W. Morgenroth, A. Ehnes, A. Berghäuser, B. Winkler, H. Franz, and E.Weckert, J. Phys. Conf. Ser. 215, 012029 (2010).

MS03-T6

Structure-property relations of orthorhombic $[(CH_3)_3NCH_2COO]_2(CuCl_2)_3 \cdot 2\ H_2O$

E. Haussühl[1], J. Schreuer[2], L. Wiehl[1], N. Paulsen[1]
[1]*Goethe Universität Frankfurt, Kristallographie, Frankfurt, Germany*
[2]*Ruhr-Universität Bochum, Institut f¨ur Geologie, Mineralogie und Geophysi, Bochum, Germany*

Betaine adducts have been considered as a potential source of crystal species possessing low-dimensional magnetic structures [1]. With $[(CH_3)_3NCH_2COO]_2 (CuCl_2)_3 \cdot 2H_2O$ a novel quasi-2-dimensional quantum spin system was discovered [2].

Large single crystals of orthorhombic $[(CH_3)_3NCH_2COO]_2 (CuCl_2)_3 \cdot 2H_2O$ with dimensions up to 40 x 40 x 30 mm^3 were grown from aqueous solutions. The elastic and piezoelastic coefficients were derived from ultrasonic resonance frequencies and their shifts upon variation of pressure, respectively, using the plate-resonance technique. Additionally, the coefficients of thermal expansion were determined between 95 K and 305 K by dilatometry.

The elastic behaviour at ambient conditions is dominated by the 2-dimensional network of strong hydrogen bonds within the (001) plane leading to a corresponding pseudo-tetragonal anisotropy of the longitudinal elastic stiffness. The variation of elastic properties with pressure, however, as well as the thermal expansion show strong deviations from the pseudo-tetragonal symmetry. These deviations are probably correlated with tilts of the elongated tri-nuclear betaine-$CuCl_2$-water complexes. Neither the thermal expansion nor the specific heat capacity give any hint on a phase transition in the investigated temperature range.

[1] Wiehl L, Schreuer J, Haussühl E, Winkler B, Removic-Langer K, Wolf B, Lang M & Milman V, 2006 *J. Phys.: Condensed Matter* 18, 11067-11079.
[2] Removic-Langer K, E. Haussühl, E.and Wiehl L, Wolf B, Sauli F, Hasselmann N, Kopietz P & Lang M, 2009 *J. Phys.: Condens. Matter* 21, 185013.

MS03-T7

Cancrinite-groupminerals at non-ambient conditions: The role of the extraframework population

P. Lotti[1], G. D. Gatta[1], V. Kahlenberg[2], M. Merlini[1], N. Rotiroti[1]
[1]*Università degli Studi di Milano, Scienze della Terra - Earth Sciences, Milano, Italy*
[2]*Leopold Franzens Universität, Institut für Mineralogie und Petrographie, Innsbruck, Austria*

The minerals of the cancrinite group are zeolite-like compounds, sharing the [CAN]-topology of the framework. Their structure shows large 12-ring channels along [0001], bound by columns of cages, the so-called *can* units. Natural and synthetic compounds exhibit a remarkable chemical variability. Among the natural species, the majority shows an aluminosilicate framework. Two subgroups can be identified according to the extraframework content of the *can* units: the cancrinite- and the davyne-subgroups, showing Na-H_2O and Ca-Cl chains, respectively. The channels are stuffed by cations, anions and molecules. In Nature, cancrinite-group minerals occur in the late/hydrothermal stages of alkaline (SiO_2)-undersaturated magmatism and in related effusive or contact rocks. Cancrinite-group compounds have been proposed as stable storage form for alkaline wastes.

The characterization of the phase-stability fields, thermo-elastic behavior and structure response to applied (P,T) is needed to evaluate and predict their behavior in natural and industrial processes.

Methods
We aimed to model the thermo-elastic behavior and the mechanisms of (P,T)-induced structure evolution of cancrinite-group minerals, paying a special attention to the role played by the extraframework population. The study was restricted to the following (CO_3)-rich and (SO_4)-rich end-members: cancrinite $\{[(Na,Ca)_6(CO_3)_{1.2-1.7}][Na_2(H_2O)_2][Al_6Si_6O_{24}]\}$, vishnevite {[(Na,Ca,K)6(SO4)][Na2(H2O)2][Al6Si6O24]}, balliranoite {[(Na,Ca)6(CO3)1.2-1.7][Ca2Cl2][Al6Si6O24]} and davyne {[(Na,Ca,K)6((SO4),Cl)][Ca2Cl2][Al6Si6O24]}. Their high-P and low-T (T < 293 K) behavior was investigated by means of *in situ* single crystal X-ray diffraction, using diamond-anvil cells and (N_2)-cryosystems, respectively.

Results
Though sharing a similar volume compressibility and thermal expansivity, these minerals have a different thermo-elastic anisotropy, more pronounced in the cancrinite-subgroup compounds. This behavior is governed by different deformation mechanisms, which reflect the different coordination environments of the cage population between the minerals of the two subgroups. The davyne sample studied at high-P showed a displacive phase transition from $P6_3/m$ to $P6_3$ after the load of pressure [$0.0001 \leq P$ (GPa) $\leq 0.38(2)$]. In vishnevite, a P-induced re-organization of the extraframework population took place at $P > 3.5$ GPa, suggesting that the channel-constituents can also play an active role at non-ambient conditions.

Conclusions
Besides common features likely ascribable to the [CAN]-topology, the nature of the extraframework population appears to control significantly the (P,T)-induced structure evolution and thermo-elastic behavior of the cancrinite-group compounds.

MS03-T8

Comparative elasticity of cordierite: Effect of heavy-ion irradiation on the compressibility of H_2O- and CO_2-rich cordierite

K. S. Scheidl[1], M. Schmitt[2], G. D. Gatta[3], C. Trautmann[4], B. Schuster[5,4], R. Miletich[1]
[1]University of Vienna, Vienna, Austria
[2]University of Innsbruck, Innsbruck, Austria
[3]Universitá degli Studi di Milano, Milano, Italy
[4]GSI Helmholtzzentrum für Schwerionenforschung, Darmstadt, Germany
[5]Technische Universität Darmstadt, Darmstadt, Germany

The effect of ion-beam irradiations on the elastic properties of natural H_2O- and CO_2-rich cordierite $(Mg,Fe)_2Al_4Si_5O_{18}$ was investigated by means of high-pressure X-ray diffraction experiments on single crystals pressurized in the diamond-anvil cell (DAC). Oriented single crystals were exposed to Au ions to a fluence of 1 × 10^{12} ions/cm^2. The experimental findings suggest the linear CO_2 molecules to sustain irradiation-induced breakdown with small CO_2-to-CO conversion rates relative to the distinct irradiation-induced loss of H_2O. The irradiation-induced unit-cell contraction of the H_2O-rich as well of the CO_2-rich sample is anisotropic with the *c*-axis to shrink only half as much as the axes within the *ab* plane. Lattice parameters for CO_2-rich cordierite reveal, however, a less pronounced irradiation-induced contraction such as for hydrous cordierite. The fitted 3rd-order Birch-Murnaghan equation-of-state parameters for both of the irradiated cordierite specimens reveal obvious higher compressibilities (H_2O: bulk modulus K_0 = 117.1±1.1 GPa; CO_2: K_0 =109.7) compared to the non-irradiated (H_2O: K_0 = 137.8±1.5 GPa; CO_2: K_0 = 120.3 ±3.7 GPa) (Fig. 1). The difference is attributed to the irradiation-induced loss of H_2O (CO_2-rich cordierite also contains H_2O in the channels) which causes a lower stability of the framework. It is remarkable that the difference in the compressibilities between non-irradiated and irradiated samples for H_2O-rich cordierite is higher than for CO_2-rich cordierite. It appears that the CO_2 molecule intercalated inside the channels might contribute to stabilize the structure to a certain degree. The compression and decompression experiments for irradiated CO_2-rich cordierite suggest a hysteresis with smaller volumes changes per pressure unit for decompression relative to the volumes changes on compression (Fig. 2). In addition, the volume at room pressure varies between the measurements before being loaded in the DAC and the recovered samples from high pressure measurements. A second discrepancy can be observed, which matches the observation described by Likhacheva et al. (2013). At around 4 GPa the molar volume increases and appears to be constant over the pressure between 4 and 5 GPa. This effect is ascribed to overhydration due to the extra H_2O of the pressure medium is stuffed inside the channels and causes a structural expansion and stabilisation of the structure. As the samples of hydrous cordierite have been compressed in argon, which is absolutely free of water, the equivalent effect could not have been observed.

References:

Likhacheva, A.Yu, Goryainov, S.V., and Bul'bak, T.A., (2013) An X-ray diffraction study of the pressure-induced hydration in cordierite at 4-5 GPa. American Mineralogist, 98, 181-186

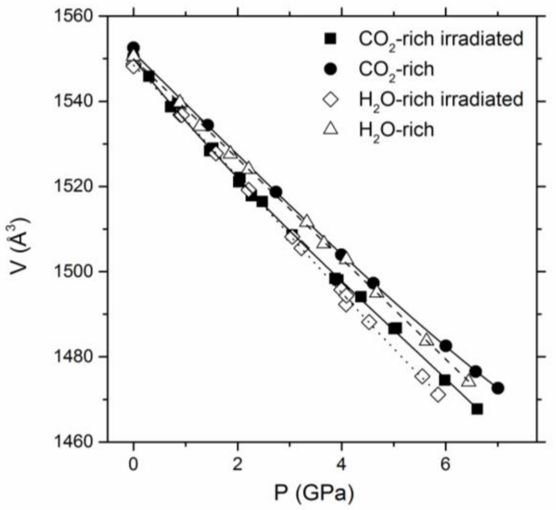

Figure 1: Volume compressibility of non-irradiated and irradiated CO_2-rich cordierite in comparison to H_2O-rich cordierite

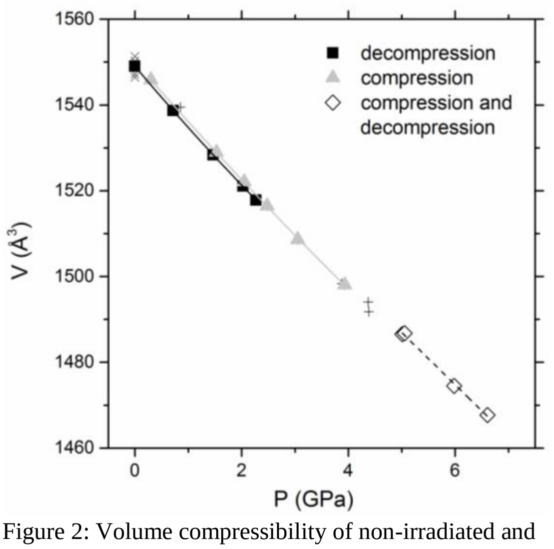

Figure 2: Volume compressibility of non-irradiated and irradiated CO_2-rich cordierite

MS04 – Hot new structures I

MS04-T1

RNA polymerase I structure and transcription regulation

C. Engel[1]
[1]*Gene Center Munich, Munich, Germany*

Transcription of ribosomal RNA by RNA polymerase (Pol) I initiates ribosome biogenesis and regulates eukaryotic cell growth. The crystal structure of Pol I from the yeast Saccharomyces cerevisiae at 2.8A resolution reveals all 14 subunits of the 590-kilodalton enzyme, and shows differences to Pol II. An ‘expander’ element occupies the DNA template site and stabilizes an expanded active centre cleft with an unwound bridge helix. A ‘connector’ element invades the cleft of an adjacent polymerase and stabilizes an inactive polymerase dimer. The connector and expander must detach during Pol I activation to enable transcription initiation and cleft contraction by convergent movement of the polymerase ‘core’ and ‘shelf’ modules. Conversion between an inactive expanded and an active contracted polymerase state may generally underlie transcription. Regulatory factors can modulate the core-shelf interface that includes a ‘composite’ active site for RNA chain initiation, elongation, proofreading and termination.

MS04-T2

Structural Studies of Spliceosomal B-Complex Proteins

A. Ulrich[1], T. Schütze[1], M. Seeger[1], M. C. Wahl[1]
[1]*FU Berlin, Biochemistry, Berlin, Germany*

Pre-mRNA splicing is catalyzed by a large and highly dynamic RNA-protein (RNP) molecular machine, the spliceosome, which is composed of five small nuclear (sn) RNPs and numerous non-snRNP proteins. For each round of splicing, a spliceosome is assembled, catalytically activated and, after splicing catalysis, disassembled in a stepwise fashion [1]. Transitions between functional stages in this reaction pathway are characterized by the ordered recruitment and release of specific snRNPs and non-snRNP proteins [2]. Initially, U1 and U2 snRNPs recognize the 5’ splice site and branch point region of an intron, respectively, forming the A-complex. Subsequently, the U4, U5 and U6 snRNPs join as a pre-formed tri-snRNP, giving rise to the pre-catalytic B-complex. The B-complex is then catalytically activated, yielding the B*-complex that can carry out the first of two transesterification reactions of a splicing event. After step one of splicing the C-complex catalyses the second transesterification reaction, subsequent to which the spliceosome is disassembled in an ordered fashion. In higher eukaryotes a group of B-complex-specific non-snRNP proteins joins the spliceosome at the stage of B-complex formation [3]. Their restriction to higher eukaryotes and the implication of several members in alternative splicing [4] suggest that B-complex proteins are key splicing regulators. However, their precise functions and the underlying molecular mechanisms are presently unknown. We have characterized the interactome of the RS-repeat containing B-complex protein Prp38 and have identified and structurally analyzed stable sub-complexes centered on Prp38. Our results suggest that B-complex proteins are recruited as a pre-formed complex through Prp38 and that they may be involved in tri-snRNP incorporation. Our structures now pave the way for further interrogating the proteins’ functions by interfering with their interactions in a rational manner.

References

1. Wahl, M.C., Will, C.L., and Lührmann, R. (2009). The spliceosome: design principles of a dynamic RNP machine. Cell *136*, 701-718.
2. Brow, D.A. (2002). Allosteric cascade of spliceosome activation. Annu. Rev. Genet. *36*, 333-360.
3. Agafonov, D.E., Deckert, J., Wolf, E., Odenwalder, P., Bessonov, S., Will, C.L., Urlaub, H., and Lührmann, R. (2011). Semiquantitative proteomic analysis of the human spliceosome via a novel two-dimensional gel electrophoresis method. Mol Cell Biol *31*, 2667-2682.
4. Park, J.W., Parisky, K., Celotto, A.M., Reenan, R.A., and Graveley, B.R. (2004). Identification of alternative splicing regulators by RNA interference in Drosophila. Proc Natl Acad Sci U S A *101*, 15974-15979.

MS04-T3

Structure and function of a novel RNA-binding domain

S. Liu[1], M. C. Wahl[1]
[1]*Free University of Berlin, Structural Biochemistry, Berlin, Germany*

Spliceosomal protein Prp3 is a component of the U4/U6 di-snRNP and of the U4/U6-U5 tri-snRNP (1). The protein is an essential pre-mRNA splicing factor that is required for the assembly of an active spliceosome (2). Prp3 is conserved from yeast to human. Mutations in human Prp3 have been linked to the RP18 form of autosomal dominant retinitis pigmentosa (3). Prp3 interacts with a number of other spliceosomal proteins (4) and human Prp3 has been suggested to directly bind the U4/U6 di-snRNA (5). We have experimentally defined a folded unit within yeast Prp3, which interacts stably with U4/U6 di-snRNA. Using electrophoretic gel mobility shift analyses, we found that both a U4/U6 duplex region and a single-stranded U6 3’-overhang are required for efficient binding of Prp3 to U4/U6 di-snRNA. To understand the mechanism of RNA binding by yPrp3, we have determined the crystal structure of its RNA-binding domain alone and in complex with RNA. The structure of the Prp3 RNA-binding domain differs markedly from known RNA-binding folds. The RNA complex structure shows how the sequence of the single-stranded U6 3’-overhang is specifically recognized by yPrp3. Both RNA and protein mutagenesis studies further confirmed our structural findings.

References
(1) J. Lauber, G. Plessel, S. Prehn, C.L. Will, P. Fabrizio, K. Gröning, W.S. Lane, R. Lührmann, *RNA*, 3, (1997), 926
(2) M. C. Wahl, C. L. Will, and R. Lührmann, *Cell*, 136, (2009), 701.
(3) C.F. Chakarova et al., *Hum. Mol. Genet*., 11, (2002), 87.
(4) S. Liu, R. Rauhut, H.P. Vornlocher, R. Lührmann, *RNA*, 12, (2006), 1418.
(5) S. Nottrott, H. Urlaub, R. Lührmann, *EMBO J*., 21, (2002), 5527.

MS04-T4

Eukaryotic translation initiation factors 3 subunit b (eIF3b) contains a novel nine-bladed WD40 domain

Y. Liu[1], P. Neumann[1], B. Kuhle[1], T. Monecke[1], R. Ficner[1]
[1]*Goettingen university, Department of Molecular Structural Biology, Göttingen, Germany*

The hetero-oligomeric eukaryotic translation initiation factor 3 (eIF3) plays an essential role in protein synthesis by associating with other initiation factors and promoting their attachment to the 40S ribosomal subunit [1,2]. Among this multi-subunit complex, eIF3b/Prt1 is the major scaffold protein. According to the yeast eIF3 interaction map, b/Prt1 can independently assemble two distinct subcomplexes *in vivo* composed of a/Tif32-b/Prt1-c/Nip1 and b/Prt1-i/Tif34-g/Tif35, respectively [3].

Here we report the 2.7 Å resolution crystal structure of the central WD40 domain of eIF3b from *Chaetomium thermophilum*. The structure represents a novel WD40 β-propeller fold as it consists of nine blades. Besides its unique nine-bladed architecture, the eIF3b-WD40 exhibits several unusual folding properties, namely a “3_N + 1_C velcro” closure, a clear *circular-truncated-cone-like* central channel and large overall dimensions. Both multiple sequence alignments and secondary structure predictions indicate that this new β-propeller fold is universally adopted by eIF3b orthologs. The *ct*eIF3b-WD40 structure reveals highly conserved surface regions that could play an important role in binding other proteins.

[1] Hinnebusch AG. *Trends Biochem Sci*. 2006, 31(10):553-62.
[2] Valasek L. *Curr Protein Pept Sci*.2012, 13(4):305-30.
[3] Valasek L, Nielsen KH, Hinnebusch AG. *EMBO J*, 2002, 21 (21), 5886 - 5898.

Figure 1

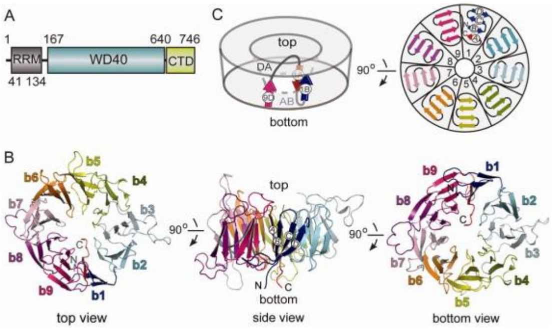

MS04-T5

Specific molecular targeting of oncofetal fibronectin by Anticalins

A. Schiefner[1]
[1]*Technische Universitaet Muenchen, Lehrstuhl Biologische Chemie, Freising-Weihenstephan, Germany*

Human fibronectin (Fn) is a ubiquitous extracellular matrix protein that plays a crucial role in cell adhesion, migration, growth, and differentiation during processes such as wound healing and embryonic development. Its so-called oncofetal isoform, which exhibits the extra-domain B (ED-B) and is exclusively expressed in neovasculature, has gained considerable attention for tumor diagnosis and therapy. Based on the human lipocalin 2, a small and robust non-immunoglobulin scaffold, we have selected ED-B specific Anticalins by phage display selection from a combinatorial library and ELISA screening using the three-domain Fn fragment Fn7B8 as target. Four different Anticalins were isolated and biochemically characterized, revealing low nanomolar affinities for ED-B. BIAcore measurements indicated distinct modes of epitope recognition by the three Anticalins N7A, N7E and N9B, which were subjected to X-ray structural analyses. From the crystal structures of the different complexes it appears that Anticalins recognize the most exposed structural feature, that is the *cc'* loop of ED-B, with their calyx-like binding pocket shaped by four variable loops. Nevertheless, the orientation of ED-B with respect to the β-barrel axis of each Anticalin differs remarkably by 90 or 180°. These distinct modes of interaction are facilitated by conformational changes of the four structurally hyper-variable loops on top of the conserved β-barrel and illustrate the broad potential for molecular recognition offered by the lipocalin scaffold. Structural and biochemical data on the isolated Fn fragment Fn7B89 as well as the Anticalin complexes N7A•Fn7B8, N7E•Fn7B8 and N9B•ED-B will be presented.

MS04-T6

Structural insights into PROPPINs, a family of phosphoinositide binding proteins

K. Kühnel[1]
[1]*Max-Planck-Institute for biophysical Chemistry, Neurobiology, Göttingen, Germany*

PROPPINs (β-propellers that bind polyphosphoinositides) interact specifically with PtdIns3P and PtdIns(3,5)P_2. There are three PROPPINs in yeast: Atg18, Atg21 and Hsv2 (homologous with swollen vacuole phenotype 2) which play an important role in autophagy. We determined the crystal structures of Atg18 and Hsv2. Together with comprehensive in vivo and in vitro mutagenesis studies these structures give new insights into how PROPPINs bind to membranes.

MS05 – Inorganic structural chemistry – synthesis, structure, properties and applications I

MS05-T1

In-situ PDF Study on the Nucleation of ZnO Nanoparticles in Ethanolic Solution

M. Zobel[1], R. B. Neder[1]
[1]*Institute of Crystallography and Structural Physics, University Erlangen, Erlangen, Germany*

Semiconductor nanoparticles such as zinc oxide (ZnO) are commonly produced in sol-gel processes. A variety of synthesis strategies exists and the final products are well characterized with respect to their crystallinity, which fundamentally governs their physical and chemical properties. Nevertheless, the nucleation process and, above all, the evolution of crystallinity of the nucleating and growing nanoparticles is not yet understood [1].

Pair-distribution function (PDF) analysis of high-energy x-ray diffraction data is a powerful tool to study local atomic order and crystallinity as well as particle size on a mesoscopic length scale of up to 40 nm in particle diameter. With the advent of the Rapid Acquisition PDF method [2], time-resolved PDF studies have become possible, and the distinction between molecular clusters and nanoparticles in 1 M aqueous solutions of metal oxide nanoparticles [3] has been demonstrated. However, nucleation in dilute sol-gel processes in more complex organic solutions remains untackled [1].

Our experiments are, to our knowledge, the first study to measure in-situ PDFs in organic solvents. We used a 30 mM ethanolic solution of zinc acetate dihydrate, which forms rather monodisperse ZnO nanoparticles upon the addition of the organic base tetramethylammonium hydroxide [4, 5]. In Fig. 1, the experimental PDFs of the solutions at different times after base addition are compared to the PDF of a 3 nm ZnO nanoparticle powder: the left panel shows precursor structures after 3 and 100 min, the right one growing nanoparticles after 150 and 400 min.

It is known from EXAFS that zinc and acetate ions form the tetrahedral precursor Zn_4OAc_6 [6]. We can see this in our solutions 3 min after base addition, but and more important, we detect metastable precursor structures of about 1 nm in diameter (green curve), which have not been observed before. They remain in this state for a dwell time of about 2 hours before they spontaneously nucleate to wurtzite-structured nanoparticles of 2 nm in diameter after about 150 min. Subsequently, growth sets in. Multiphase fits of structural models of the precursors, the nanoparticles and the complex ethanolic background show that precursors co-exist in the solution for all times (8 hours). Based upon this finding, we suggest a nucleation and growth model differing from classical nucleation theory.

[1] B. Ludi and M. Niederberger, Dalton Trans. 42 (2013), 12554
[2] P. J. Chupas, et al. J. Appl. Cryst. 36 (2003), 1342
[3] K. M. O. Jensen, et al. J. Am. Chem. Soc.134 (2012), 6785
[4] L. Spanhel and M. A. Anderson, J. Am. Chem. Soc. 113 (1991), 2826
[5] Ch. Chory, et al., phys. stat. sol. c 4 (2007), 3260
[6] M. S. Tokumoto, et al., J. Phys. Chem. B 107 (2003), 568

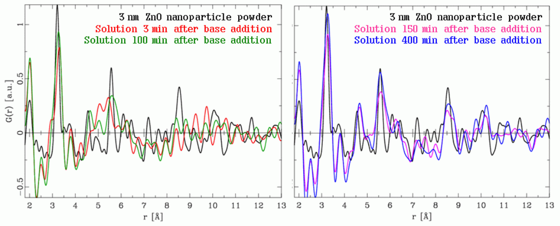

Fig. 1: Nucleation of ZnO nanoparticles in a 30 mM ethanolic solution after base addition compared to ZnO nanoparticle powder; left: precursor stages; right: growing nanoparticles

MS05-T2

Twinning structure and phase analysis of TiN/ nanoparticles by high-resolution transmission electron microscopy (HRTEM)

I. V. Luzhkova[1], A. N. Ermakov[1], A. M. Murzakaev[2], Y. G. Zainulin[1]
[1]*Institute of Solid State Chemistry, Ural Branch of the Russian Academy of Sciences, Ekaterinburg, Russian Federation*
[2]*Institute of Electrophysics, Ural Branch of the Russian Academy of Sciences, Ekaterinburg, Russian Federation*

TiN nanoparticles with metal shell from Ni [1, 2] were synthesized processing of titanium nickelide in the low-temperature nitrogen plasma [3]. The starting material is more fine-crystallized fraction, which has been obtained with unloading from the standard filter cloth. It has NaCl structure type and consists of crystal particles having sizes up to 27 nm.

Using combination of high-resolution transmission electron microscopy (HRTEM) and image analysis by Fast Fourier Transform (FFT), we investigated the structural and morphological features of nanoparticles. HRTEM was performed by JEM-2100 microscope of JEOL Ltd. with point to point limit resolution of 1,9 Å. Image analysis was carried out by Digital Micrograph 3.5 (Gatan Inc.,USA).

Twinning is widespread in crystalline materials of various origin and nature [4]. In figure 1, ananoparticle is exhibited in the form of cuboctahedral shape with distinct crystallographic facets. Phase composition of selected area (Fig. 1a) of particle can be determined according to FFT spectrum (Fig. 1a′). Points 1 and 2 corresponds to a plane [200] of phase TiN (*sp.g: Fm-3m*) with parameter of lattice a = 4.2417 Å and one of [-200] of α - phase $TiN_{0.61}$ (*sp.g: I41/amd*) with parameter of lattice a = 4.1980 Å. Points 3 and 4 corresponds to a plane [020] of phase TiNi (*sp.g: P21/m*) with parameter of lattice a = 2.885Å and one of [0-20] of phase TiNi (*sp.g: P21/m*) with parameter of lattice a = 2.8840Å.

Using filtration of selected area of image (Fig. 1a) we obtain twin plane or twin boundary in which the twinned sub-units are disposed in mirror symmetry to each other.

References:
I.G. Grigorov, O.N. Ermakova, A.N.Ermakov, I.V. Misharina, Zainulin Y.G., Malashin S.I., Dobrinskii E.K. Structural-morphological transformations in titanium nickelide treated in a nitrogen plasma// Russian Metallurgy (Metally). Vol. 2010. 2010. №1. p. 71 - 75
Patent for an invention: «Method of producing titanium nitride nanopowders» 2010101652/05, from 19.01.2010
P.A. Storozhenko, Sh. L. Guseinov, S.I. Malashin. Nanodispersed Powders: Synthesis Methods and Practical Applications // Nanotechnologies inRussia, Vol. 4. №.5-6. 2009. p. 262-274.
H. Hofmeister. High-resolution electron microscopy studies of metal nanoparticles: shape and twin defects, and surface stress effects// J. of optoelectronics and advanced materials. Vol. 9. № 1. 2007. p. 99 - 105.

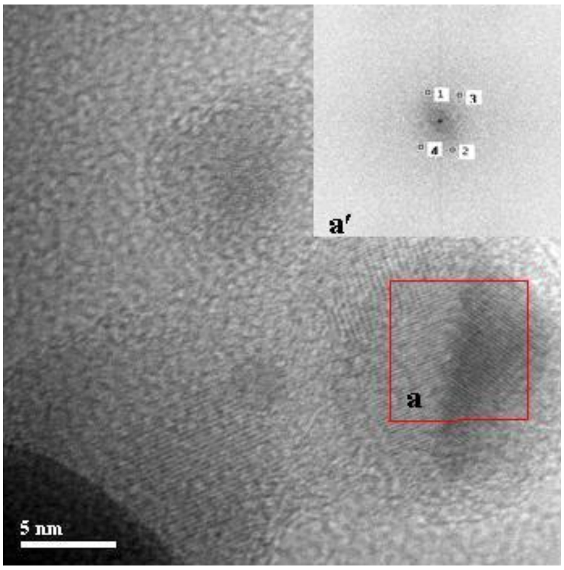

Fig. 1: HRTEM image of TiN/Ni nanoparticles: **a** selected area of nanopowder; **a′** Fast Fourier Transform (FFT) of area a.

MS05-T3

ICSD Desktop - The new interface to ICSD

S. Rühl[1]
[1]*FIZ Karlsruhe, Eggenstein-Leopoldshafen, Germany*

The new, locally installable version of ICSD - ICSD Desktop - has reached the beta stage. It will be shipped to users of the current desktop version with the next release of the well-known FindIt version in order to collect some feedback and to provide an early view on this development.

The interface is based on the ICSD Web interface [1], which combines a modern graphical user interface with unique features. ICSD Desktop will comprise all of these features, for example

- Visualization as an interactive, customizable browser applet (Jmol [2]) which offers suitable features for displaying crystal structures.
- Simultaneous display of up to six standardized crystal structures or powder pattern diagrams generated on the fly from the CIF files in a synoptic view.
- Quality ranking for easier identification of relevant entries.

In addition, the search engine has been rewritten and now includes the option to combine queries employing Boolean logic (Fig. 1). This feature allows for much more specific searches.

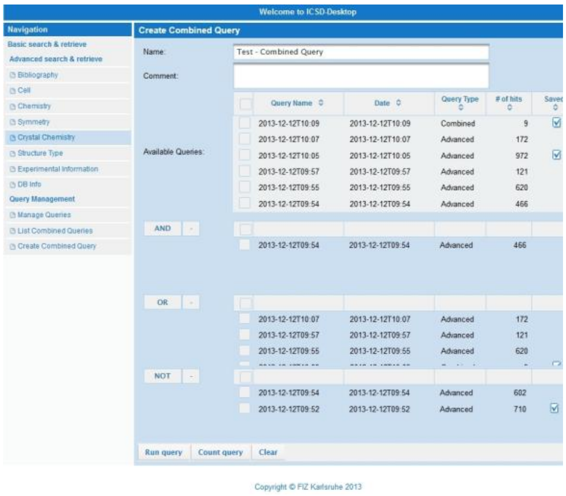

Name: Test - Combined Query
Comment:
Available Queries:

☐	Query Name	Date	Query Type	# of hits	Saved
☐	2013-12-12T10:09	2013-12-12T10:09	Combined	9	☑
☐	2013-12-12T10:07	2013-12-12T10:07	Advanced	172	
☐	2013-12-12T10:05	2013-12-12T10:05	Advanced	972	☑
☐	2013-12-12T09:57	2013-12-12T09:57	Advanced	121	
☐	2013-12-12T09:55	2013-12-12T09:55	Advanced	620	
☐	2013-12-12T09:54	2013-12-12T09:54	Advanced	466	

AND

☐					
☐	2013-12-12T09:54	2013-12-12T09:54	Advanced	466	

OR

☐					
☐	2013-12-12T10:07	2013-12-12T10:07	Advanced	172	
☐	2013-12-12T09:57	2013-12-12T09:57	Advanced	121	
☐	2013-12-12T09:55	2013-12-12T09:55	Advanced	620	

NOT

☐					
☐	2013-12-12T09:54	2013-12-12T09:54	Advanced	602	
☐	2013-12-12T09:52	2013-12-12T09:52	Advanced	710	☑

Fig. 1: The “Create Combined Query” mask

Especially the structure type search has been significantly improved and now offers an interactive way of setting the structure type descriptors during the search.
The current version of the ICSD [3] contains more than 166,000 entries including about 131,000 fully determined crystal structures derived from experimental data and 29,000 crystal structures with atom coordinates derived from the corresponding structure types. About 7,000 new entries are included each year.

[1] ICSD is available online at http://icsd.fiz-karlsruhe.de. More details can be found on http://www.fiz-karlsruhe.de/icsd_web.html.
[2] Jmol: an open-source Java viewer for chemical structures in 3D. http://www.jmol.org/
[3] Bergerhoff G., Brown I.D., „*Crystallographic Databases*“, 1987, Allen F.H. (Editor) Chester, International Union of Crystallography.

MS05-T4

Solid solutions of $CdIn_2Te_4$ and silver indium tellurides: structure and element distribution by resonant X-ray scattering

S. Welzmiller[1], F. Hennersdorf[1], T. Schröder[2], G. Wagner[1], O. Oeckler[1]
[1]Leipzig University, Faculty of Chemistry and Mineralogy, Leipzig, Germany
[2]LMU Munich, Department of Chemistry, Munich, Germany

Chalcopyrite-like compounds such as $CdIn_2Te_4$, $AgInTe_2$ and $AgIn_5Te_8$ show low thermal conductivities of down to ~0.5 $Wm^{-1}K^{-1}$ at 900 K for $AgIn_5Te_8$ or $CdIn_2Te_4$. For $AgInTe_2$, for example, thermoelectric figures of merit of up to ZT = 0.06 were attributed to low electrical conductivity. [1,2,3] The similar scattering factors of all elements involved impede unequivocal atom type assignments in conventional X-ray experiments and led to some discussion about the correct structure models.[4,5]

The miscibility of $CdIn_2Te_4$ with $AgInTe_2$, $AgIn_3Te_5$ and $AgIn_5Te_8$ is limited as the end members exhibit different space groups; however there are broad ranges of mixed crystals whose lattice parameters show Vegard-like behavior. In order to distinguish the elements with similar electron count, resonant X-ray powder diffraction data were measured at the K absorption edges of the elements involved (beamline ID31, ESRF, Grenoble). The anomalous dispersion correction terms were calculated from X-ray fluorescence data of each sample via the Kramers-Kronig transform. The structures were refined in joint multi-dataset Rietveld calculations.

There is a solid solution between $(CdIn_2Te_4)_x(Ag_2In_2Te_4)_{1-x}$ (formulae are normalized with respect to the Te content) [2] for x=0 - 0.45, whose members form the chalcopyrite structure type like $AgInTe_2$ (*I-42d*). $CdIn_2Te_4$ was described with a completely ordered structure ($HgCu_2I_4$-type; *I-42m*), [6] and lower symmetry ($CdGa_2S_4$-type; I-*4*) was also discussed.[7] The structure refinement of $CdIn_2Te_4$ as well as those of mixed crystals, however, unambiguously show mixed occupied cation positions.

Solid solutions $(CdIn_2Te_4)_x(Ag_{0.8}In_{2.4}Te_4)_{1-x}$ (x=0 - 0.75) exhibit the structure type of $Ag_{0.8}In_{2.4}Te_4$ = $AgIn_3Te_5$ (space group *P-42c*). In the latter (x = 0), vacancies are located on two cation positions (20% and 60%) and mixed with Ag and In while both other cation positions are fully occupied. For x = 0.75, the vacancies are ordered on only one Wyckoff position and the cations are uniformly distributed.

As $CdIn_2Te_4$ and $AgIn_5Te_8$ have the same anion/cation ratio (3:4) and crystallize in the same space group *I-42m*, a complete solid solution series $(Cd_2In_4Te_8)_x(AgIn_5Te_8)_{1-x}$ is possible. The absence of reflections with h+k+l=2n+1 in powder diffraction and SAED patterns confirms the space group *I-42m* in contrast to *P-42m* as reported earlier.[5] The cations are uniformly distributed over two Wyckoff positions while vacancies are completely ordered as shown for $(Cd_2In_4Te_8)_{0.5}(AgIn_5Te_8)_{0.5}$.

Our investigations show that vacancies strongly tend to order in a regular fashion but that Cd, In and Te are almost uniformly distributed and occupy mixed positions in chalcopyrite-like telluride materials.

[1] T. Suriwong, K. Kurosaki, S. Thongtem, A. Harnwunggmoung, T. Plirdpring, T. Sugahara, Y. Ohishi, H. Muta, S. Yamanaka, *J. Alloys Comp.* 2011**,** *509*, 7484.
[2] Y. Aikebaier, K. Kurosaki, T. Sugahara, Y. Ohishi, H. Muta, S. Yamanaka, *Mater. Sci. Eng. B* 2012**,** *177*, 999.
[3] A. Charoenphakdee, K. Kurosaki, H. Muta, M. Uno, S. Yamanaka, *Mater. Trans.* 2009**,** *50*, 1603.
[4] A. J. Mora, G. E. Delgado, C. Pineda, T. Tinoco, *Phys. Stat. Sol. (a)* 2004**,** *201*, 1477.
[5] G. Marín, J. M. Delgado, S. M. Wasim, C. Rincón, G. Sánchez Pérez, A. E. Mora, P. Bocaranda, J. A. Henao, *J. Appl. Phys.* 2000**,** *87*, 7814.
[6] J.-C. Launay, J.-F. Lambert, B. Darriet, P. Gravereau, *J. Mater. Chem.* 1995**,** *5*, 165.
[7] H. Hahn, G. Frank, W. Klingler, A. D. Störger, G. Störger, *Z. Anorg. Allg. Chem.* 1955, *279*, 241.

MS05-T5

New insights in the pseudobinary system $(SnSe)_nBi_2Se_3$

P. Urban[1], C. Fraunhofer[2], G. Wagner[1], O. Oeckler[1]
[1]Leipzig University, Faculty of Chemistry and Mineralogy, Leipzig, Germany
[2]LMU Munich, Department of Chemistry, Munich, Germany

Compounds $(SnSe)_nBi_2Se_3$ are promising candidates on the way to novel thermoelectric materials. Only some of the compounds suggested by the phase diagram have been charcaterized so far. Layered structures like $(SnSe)_{0.5}Bi_2Se_3$ = $SnBi_4Te_7$ [1,2] with a defect $GeSb_2Te_4$-type structure may coexist with '$(SnSe)_2Bi_2Se_3$ = $Sn_2Bi_2Se_5$', whose structure type was unknown. In addition, there is a cubic high temperature phase $(SnSe)_{\sim 2.5\text{-}4}Bi_2Se_3$ which upon quenching yields a metastable pseudocubic one.[3] This variety of structure types may offer a good chance to obtain heterostructured materials with good thermoelectric figures of merit.

The present overview over the system $(SnSe)_nBi_2Se_3$ focuses on single-crystal structure determinations. For instance, the phase $Sn_{4.68}Bi_{3.33}Se_9$ (which corresponds to '$(SnSe)_2Bi_2Se_3$' in the phase diagram) exhibits a heyrovskite-type structure (*Cmcm*, a = 4.1934(3) Å, b = 13.8656(14) Å, c = 32.006(2) Å, R1(obs) = 0.0397). It consists of a herringbone pattern of distorted rocksalt-type slabs, in which the cation coordination is (distorted) octahedral. These slabs are interconnected via cations in trigonal prisms. Chemical vapor transport further afforded a new phase $Sn_{2.79}Bi_{2.19}Se_6$ with a structure related to lillianite (*Pnma*, a = 21.0989(18) Å, b = 4.1970(3) Å, c = 13.7378(11) Å, R1(obs) = 0.0424). It also consists of a herringbone pattern of distorted rocksalt-type slabs, which are interconnected by tetrahedrally coordinated selenium atoms. These form irregular cation coordination polyhedra, which explain the symmetry reduction from *Cmcm* of lillianite itself.

The layered structure of $(SnSe)_{0.5}Bi_2Se_3$ was also investigated by transmission electron microscopy to verify the unusual $GeSb_2Te_4$ structure type confirmed by single-crystal structure analysis (*R*-3*m*, a = 4.1724(6) Å, c = 38.861(8) Å, R1(obs) = 0.0246). It exhibits a 21*R* stacking sequence, whereas from the stoichiometry a 12*P* stacking would be expected. Stacking disorder is a characteristic feature of $(SnSe)_{0.5}Bi_2Se_3$ bulk material. An isotropic disordered rocksalt-type structure is present in quenched $(SnSe)_4Bi_2Se_3$ (*Fm*-3*m*, a = 5.9359(7) Å, R1(obs) = 0.0473). Although the phase has a broad existence range ~2.5 < n < 4 a small amount of SnSe precipitates can be identified in $(SnSe)_{4-x}Bi_2Se_3$ bulk material, whose structure remains unchanged. This heterostructure shows an exceptionally low thermal conductivity of 0.83 W/(m·K) at room termperature, while it keeps electrical conductivity (167.3 S/cm at 50 °C). This is promising regarding the development of new thermoelectrics.

[1] K. Adouby, M. L. Elidrissi Moubtassim, C. P. Vicente, J. C. Jumas, A. A. Touré, *J. Alloys Compd.* 2008, *453*, 161.
[2] C. Pérez-Vicente, J. L. Tirado, K. Adouby, J. C. Jumas, A. Abba Touré, G. Kra, *Inorg. Chem.* 1999, *38*, 2131.
[3] K. Adouby, C. Pérez-Vicente, J. C. Jumas, *Z. Kristallogr.* 1998, *213*, 343

MS05-T6
Bridgman-Stockbarger growth and characterization of tin (II) sulfide

F. Hofherr[1]
[1]*Universität Freiburg, Freiburg, Germany*

Solar energy is usually converted by commercial silicon solar cells. Despite this, thin film solar cells are very attractive, ecofriendly, and more efficient technique for converting solar energy. Due to their properties, especially the chalcogenide thin film solar cells are one seminal development. Thin film solar cells based on $Cu(In,Ga)(Se,S)_2$ and CdTe as absorber material, are today one of the most popular materials. However they are/or toxic and very uneconomical in price compared to other materials. One alternative pioneering non strategic IV-VI compound material is tin (II) sulfide. SnS crystallizes in orthorhombic layer structure. Its lattice parameter are a = 3.98 Å, b = 4.33 Å, and c = 11.18 Å. Particularly interesting for photovoltaics, is the direct energy band gap (E_g) in the range of 1.2 - 1.3 eV, therefore a high absorption coefficient ($\alpha > 10^5$/cm) for photons [1]. This material was only produced and characterized in the form of thin sputtered films so far. In contrast to this for the growth of bulk material from the melt, the results are rare. In order to increase the understanding why the theoretically light conversion efficiency of >24% [2] has not been reached yet bulk growth and characterization is necessary. The material synthesis, bulk growth, and characterization of tin (II) sulfide were investigated. For the synthesis of SnS with highly purified material (Sn (5N) and S (6N)) new results could be achieved. Also new results for the bulk growth with the Bridgman-Stockbarger method will be presented [2]. Nevertheless the material has some challenges. A low hardness (Mohs hardness 2) and a solid-solid phase transition at 600 °C, with an elongation of the b-axis (≈ 0.5 Å), impede the bulk growth [3]. Methods to reduce the stress to the crystal during the growth will also be presented. Photoluminescence measurements revealed a value for the energy band gap of 1.22 eV, which is in a good accordance to literature. With high resolution X-ray diffraction the structural quality of the material was investigated. Through the Laue method the growth direction of the bulk material was elucidated. Furthermore energy dispersive X-ray measurements were done to make a point about the elemental composition and whether the bulk material shows segregation. Measurements with the four point probe method showed values in the range of 35.71 - 45.23 Ω cm. These values are in a good agreement with reported values for thin sputtered films.

[1] Sajeesh, T.H., et al., *Thin Solid Films*, 2010. 518(15): p. 4370-4374.
[2] Loferski, J. J., *J. Appl. Phys*. 1956. 27, p. 777.
[3] Sorgenfrei, T., Hofherr, F., Jauß, T. & Cröll, A., *Cryst. Res.Technol.*, 2013. 48 p. 193-199.
[4] Wiedemeier, H. and F.J. Csillag, *Crystalline Materials*, 1979. 149(1-2): p. 17-29.

MS05-T7
A New Compound in the System $Na_{3-x}Ag_xSbS_3$ (0≤x≤3) - Crystal Structure of Na_2AgSbS_3

C. Pompe[1], A. Pfitzner[1]
[1]*Universität Regensburg, Institut für Anorganische Chemie, Regensburg, Germany*

Recently we reported structural details and properties of the compounds Na_3SbQ_3 (Q = S, Se).[1, 2] Based on this work we substituted Na^+ gradually by Ag^+ and synthesized compositions $Na_{3-x}Ag_xSbS_3$ (0≤x≤3). The samples were obtained by solid state reactions of the elements at 650 °C. They were characterized by powder diffraction and single crystal X-ray diffraction. Thus, the new material Na_2AgSbS_3 was obtained as a phase pure product. The structure of Na_2AgSbS_3 was determined by single X-Ray diffraction. It crystallizes monoclinic in the space group $P2_1/n$ with the cell parameters a=5.8536(3) Å, b=17.9897(9) Å, c=6.956(7) Å, β=113.68°, and V=670.91(7) Å^3 with Z=4. The unit cell is shown in Fig.

1. Antimony and silver are coordinated by three sulfur atoms. The resulting trigonal pyramids [SbS_3] are isolated from each other, whereas the units [AgS_3] are linked to strands along the [101]. The Na1 cations are six-coordinate by sulfur. The distorted $Na1S_6$ octahedra share common edges and create layers perpendicular to the *ab*-plane. Na2 creates square pyramids with the five nearest sulfur atoms.

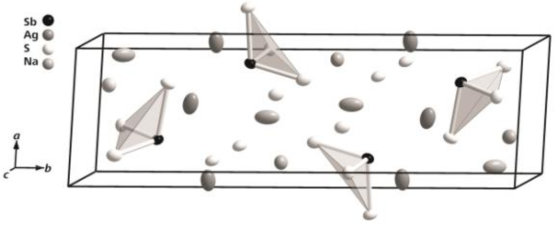

Fig1: The unit cell of the title compound Na2AgSbS3.

[1] C. Pompe, A. Pfitzner, *Z. anorg. allg. Chem.*, 2012, 638, 2158.
[2] C. Pompe, A. Pfitzner, *Z. anorg. allg. Chem.*, 2013, 639, 296.

MS05-T8

Investigation of sodium insertion into Fe[Fe(CN)6] and Fe[Co(CN)6]

S. Schmid[1], T. Godfrey[1], C. J. Kepert[1], L. Cameron[1], J.- C. Pérez-Flores[1,2], F. García-Alvarado[1,2], A. Kuhn[1,2]
[1]*The University of Sydney, School of Chemistry, Sydney NSW, Spain*
[2]*Universidad CEU San Pablo , Departamento de Química, Facultad de Farmacia , Boadilla del Monte, Spain*

The growing interest in the use of rechargeable batteries in electric vehicles and the storage of energy from renewable sources, has led to an increased focus on sodium ion (Na-ion) batteries as a viable alternative to Li-ion batteries in some applications. [1] The flexible open framework structures of metal organic frameworks (MOFs) are highly suited to hosting alkali ions, such as Na^+ in their large interstitial sites, [2] and there is a growing interest in their use as electrode materials in rechargeable Na-ion batteries. [3]

The Prussian blue type compounds Fe[Fe$(CN)_6$] and Fe[Co$(CN)_6$] are investigated as cathode materials for use in rechargeable Na-ion batteries. The sodium insertion chemistry of Fe[Fe$(CN)_6$] and Fe[Co$(CN)_6$] is examined both chemically and electrochemically. The structural changes following Na^+ ion insertion are followed using X-ray and neutron powder diffraction techniques.

Synchrotron X-ray diffraction data confirm that Fe[Fe$(CN)_6$] and Fe[Co$(CN)_6$] crystallise in the space group *Fm*-3*m* which is retained upon drying under vacuum at 110 °C. From Rietveld refinement, the cell parameters were found to be a = 10.1952 and = 10.1885 Å, respectively. Further, each structure retains the *Fm*-3*m* space group upon chemical Na^+ ion insertion, with the only change being the expected increase in the size of the unit cell parameters. Synchrotron X-ray and neutron powder diffraction techniques allow the accurate structural characterisation of each framework material before and after the chemical insertion of Na^+ ions.

This contribution will address the structural changes, which occur following chemical and electrochemical Na^+ ion insertion of Fe[Fe$(CN)_6$] and Fe[Co$(CN)_6$].

References

[1] Alcantara, R.; Jimenez-Mateos, J. M.; Lavela, P.; Tirado, J. L., “Carbon black: a promising electrode material for sodium-ion batteries.” *Electrochem. Commun.* Vol. 3, No. 11, (2001), pp 639-642.
[2] Huggins, R. A., “Mixed-conducting host structures into which either cations or anions can be inserted.” *Solid State Ion* Vol. 113 (1998), pp 533-544.
[3] Wu, X.; Deng, W.; Qian, J.; Cao, Y.; Ai, X.; Yang, H., “Single-crystal FeFe(CN)6 nanoparticles: a high capacity and high rate cathode for Na-ion batteries.” *Journal of Materials Chemistry A* (2013).

MS06 – Structure-property relations in materials sciences I

MS06-T1

Hydrogen positions and their effect on exchange couplings of Cu-minerals

H. Rosner[1], S. Lebernegg[1], O. Janson[1,2], A. Tsirlin[2]
[1]*MPI CPfS Dresden, Dresden, Germany*
[2]*NICPB, Tallinn, Estonia*

Exotic magnetic properties and the possibility of challenging our understanding of collective quantum phenomena are the reasons why low-dimensional spin-1/2 quantum magnets attract so much attention. Cu(2+) minerals belong to this class of compounds, and several hundredths of them are provided by nature. However, only very few of these materials have ever been investigated with respect to their magnetic properties. Thus, the Cu-minerals keep a high potential for the discovery of new effects and interesting properties. However, many of these compounds contain crystal water or OH-groups where the position of hydrogen in the crystal structure crucially affects the magnetic behavior. Since the experimental determination of H-positions is highly elaborate - if possible at all - these positions are usually not available in the structural data of minerals. Here, we will present a viable density functional calculation-based alternative for determining the respective hydrogen positions. The importance of the hydrogen positions for the magnetic properties and the evaluation of reliable microscopic magnetic models will be discussed for selected Cu-minerals which have been investigated by combining several experimental and computational techniques.

MS06-T2

Using the concept of natural tilings to identify promising zeolite frameworks for CO2/N2 separation: A computational study

M. Fischer[1], R. Bell[1]
[1]*University College London, Chemistry, London, United Kingdom*

Recently, considerable research efforts have been directed towards the application of microporous materials, such as zeolites or MOFs, as adsorbent materials for the removal of carbon dioxide from exhaust gases. In addition to experimental investigations, computational studies at different levels of theory have provided important insights into the microscopic interactions governing adsorption. However, relatively few systematic studies addressing the connections between particular structural features and the CO_2 adsorption properties have been reported. In this contribution, we use the concept of natural tilings [1] to define selection criteria that permit the identification of zeolite frameworks that could exhibit a high affinity for CO_2. We then perform grand-canonical Monte Carlo (GCMC) simulations of CO_2 adsorption and CO_2/N_2 mixture adsorption to test our hypothesis.

In previous work, we used GCMC simulations to predict the CO2 adsorption properties of 18 zeolite frameworks, assuming a purely siliceous composition.[2] Adsorption sites at which the interaction is particularly strong were identified in a few systems. Usually, such “strong” adsorption sites are located in narrow cages (e.g. in the gismondine cage in GIS) or at eight-ring windows. The increased interaction with CO_2 leads to higher CO_2 uptakes at low pressures and higher CO_2/N_2 selectivities.

The concept of natural tilings decomposes a zeolite framework into fundamental three-dimensional building units, the natural tiles. It is easy to develop a connection between the adsorption sites, identified above, and the natural tile representing their atomic environment. Based on our findings for the 18 framework types, we define a series of criteria which a tile should match in order to provide strong adsorption sites.[3] Among the total number of zeolites included in the IZA database, we find 37 systems which contain at least one tile that conforms to these criteria. Additional simulations for these systems reveal very high affinities for CO_2 in some of these systems.

Due to the use of mostly hypothetical materials (only a limited number of topologies are synthetically accessible as all-silica systems), our findings cannot directly be translated into real-world applications. Nevertheless, our study shows how the crystallochemical concept of natural tilings can help to judiciously select candidate topologies for a given task, provided that some initial information on the relationships between zeolite structure and the property in question is available.

References

[1] N. A. Anurova et al., J. Phys. Chem. C 114 (2010) 10160-10170.
[2] M. Fischer, R. G. Bell, J. Phys. Chem. C 116 (2012) 26449-26463.
[3] M. Fischer, R. G. Bell, J. Phys. Chem. C 117 (2013) 17099-17110.

MS06-T3

In situ Powder Diffraction meets Breaking Crystals

T. Runcevski[1], R. E. Dinnebier[1]
[1]*Max Planck Institute for Solid State Research, Stuttgart, Germany*

Following chemical reactions and physical processes, by observing the atoms moving, stands as one of the main interest of science. When the reactant and the product are single crystals, single crystal diffraction is the method of choice for detailed *in situ* studies of many single-crystal-to-single-crystal reactions. These reactions employ the necessity of minimum atomic movements and geometrical changes. On contrary, sometimes the structure profoundly changes by twisting, bending, flopping of molecular fragments, and/or jumping or hoping of atoms and alterations of the crystal packing. An unfortunate fact is, in many cases, that when the geometrical movements during the reaction are significant, the crystal cannot withstand the stress generated and therefore disintegrates. The disintegration hampers the applicability of single crystal diffraction, making these single-crystal-to-powder reactions very loosely and sporadically studied. The breaking of the crystals, however, is all but an obstacle for powder diffraction. Taken the recent advances of instrumentation and software for structure solution, powder diffraction calls the challenge to study these reactions in great detail. The power of powder diffraction is shown via two examples. First we focus on the study of jumping crystals: Very few solid-state compounds exhibit an extremely rare propensity to be self-actuated by an active ballistic event when taken over a thermally induced phase transition, whereby soft mechanically responsive crystals break and jump for great distances. To understand and explain why, detailed structural information at the molecular level before and after the phase transition is needed. The second example focusses on photoinduced breaking of crystals, where *in situ* powder diffraction can be used not only to describe the structural changes, but also to give the mechanistic, kinetic picture of the reaction of the crystal when subjected to UV light, allowing the kinetic and growth rates to be determined. Finally, a perspective of the applicability of *in situ* powder diffraction in studying the astonishing crystal chemistry of many single-crystal-to-powder systems is outlined.

Figure 1

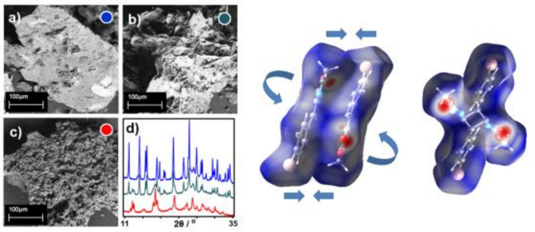

MS06-T4

In situ X-ray diffraction study of InAlN-based heterostructure during annealing

L. Grieger[1], A. Kharchenko[1], J. Woitok[1]
[1]*PANalytical, Application Competence Center, Almelo, Netherlands*

In the present work, we carry out an in situ X-ray analysis during annealing of a nitride heterostructure and determine the activation energy for thermal detoration in ambient air. The samples are grown using a typical GaN-AlN-Sapphire buffer stack, a 1 nm AlN spacer layer on a 16 nm $Al_{0.84}In_{0.16}N$ barrier. An AIXTRON MOVPE reactor was used for growth while a PANalytical X'Pert PRO MRD 4-circle diffractometer equipped with a PIXcel detector was used for characterization by means of reciprocal space maps (RSM of (20.4)) and ω-2θ scans (00.2). These were measured, while annealing the sample under ambient air at temperatures between 400°C and 850°C in the Anton Paar DHS 900 Domed Hot Stage. Since the structural fidelity of the layers and their interfaces is critical for device performance, a detailed knowledge of further process steps like thermal annealing and their effects on these properties is crucial. The time resolved data allowed to determine the activation energy and the diffusion kinetics of the thin AlN and AlInN layers. The diffracted intensity of the layer peak and pendellösung oscillations decreases exponentially over time with a temperature dependent prefactor. The Arrhenius evaluation of this prefactor yields an activation energy of 2.05 eV employing formulas based on the Cahn-Hillard formalism. Comparing non-ambient X-ray reflectometry data, the same value is evaluated within 5% deviation. Also the development of layer thickness, relaxation and composition is accessible by in situ measurements. In summary, our results provide valuable information about the heterostructure layer and interface stability for further thermal processing, for instance ohmic contact annealing or dopant activation.

Figure 1

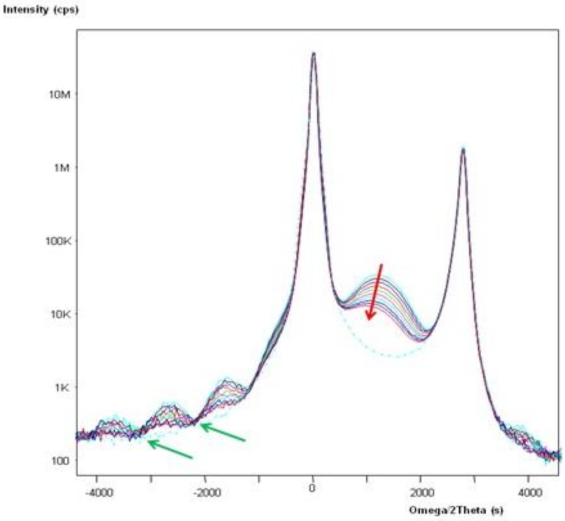

Figure 2

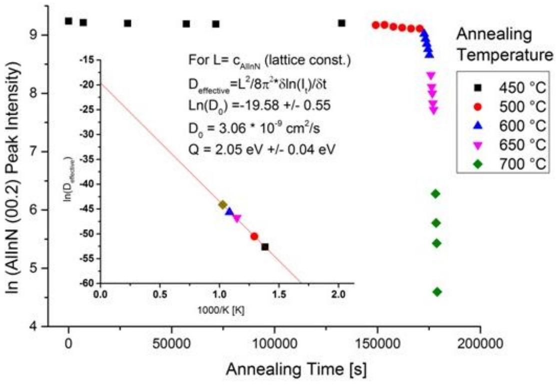

MS06-T5

Pyroelectricity in strontium titanate single crystals?

E. Mehner[1], J. Hanzig[1], S. Jachalke[1], F. Hanzig[1], M. Zschornak[1], H. Stöcker[1], D. C. Meyer[1]
[1]*TU BA Freiberg, Institut f Experimentelle Physik, Freiberg, Germany*

The temperature dependence of a ferroelectric's spontaneous polarisation constitutes the pyroelectric effect. A crystal structure that allows for pyroelectricity cannot have an inversion center, if it had a polar axis would not exist. Hence the well-known perovskite strontium titanate, crystallizing in the space group *Pm-3m*, is known to be dielectric. An external electric field (1MV/m) applied to a strontium titanate single crystal can coerce charged defects like oxygen vacancies to redistribute, leading to a distortion of the unit cell and subsequently to the formation of a defect structure called the migration-induced field-stabilized polar (MFP) phase [1]. Raman scattering shows that the MFP phase of strontium titanate may exhibit broken centrosymmetry, suggesting the existence of a polar axis. Here, we investigate the pyroelectric properties of strontium titanate single crystals at room temperature during these electroformation cycles with a modified Sharp-Garn method [2]. Our measurements clearly indicate the pyroelectricity of the MFP phase. Additionally the measurement method elucidates the kinetics of the oxygen vacancy migration as well as electric properties during electroformation. The presented method to induce pyroelectricity in a centrosymmetric crystal structure opens the scope for a new class of pyroelectric materials.

1 Hanzig,J.; Zschornak, M.; Hanzig, F.; Mehner, E.; Stöcker, H.; Abendroth, B.; Röder, C.; Talkenberger, A.; Schreiber, G.; Rafaja, D.; Gemming, S.; Meyer, D.C.; Phys.Rev.B.2013,88,24104-1-24104-10
2 Garn, L.; Sharp, E.; J.Appl.Phys.1982,53,8974-8976

MS06-T6

Extension of Crystal Structure Prediction to Hydrates, Organometallic and Inorganic Compounds

L. N. Kuleshova[1], D. W. M. Hofmann[1]
[1]*CRS4, Pula, Italy*

It is well known that lattice of organic crystal structures can be predicted very accurately and allows to predict the right polymorph in dependence of temperature and pressure. The lattice energy is crucial to predict other properties like the solubility or the logP and is in QSPR methods one of the most important descriptors. The question rises, if it is possible to extend existing approaches to predict the crystal structures of organometallic and inorganic compounds.

We extended the approach of data mining to parametrize force fields for organic compounds to organometallic and inorganic compounds. The basic idea of the data mining approach is that experimental crystal structures are a local minimum [1]. Therefore it holds that any distorted crystal structure (virtual crystal structure) must be higher in energy. The parameters of nay model can be obtained by solving the system of inequalities G(experiment) < G(virtual). However, the application of this method for these kind of compounds requires several changes. The prediction of inorganic crystal structures requires a bigger amount of atoms and molecules in the asymmetric cell has organics, commonly organic crystals contain one or two molecules in the asymmetric unit. The crystal structure prediction is extended to till 15 units in the asymmetric cell. In organometallic the coordination of the metal is very often the interest of a prediction rather than to be assumed. To allow this kind of predictions we removed the common division of potentials in intra and intermolecular interactions and joined the potential as we did already in former time for the description of water [2].

The improved algorithm did allow the determination of effective potentials for compounds not accessible. This concerns hydrates, organometallic and inorganic compounds. An analysis of predicted crystal structures, shows that complex coordination schemes of inorganic substances like in Ga_2O_3 can be reproduced correctly.

References
[1] Data Mining in Crystallography, ed. D.W.M. Hofmann and L.N. Kuleshova, Structure & Bonding, Vol. 134, Springer Verlag 2010.
[2] A new reactive potential for the molecular dynamics of liquid water, D.W.M. Hofmann and L.N. Kuleshova, Chem. Phys. Lett., 448, 138-143, 2007.

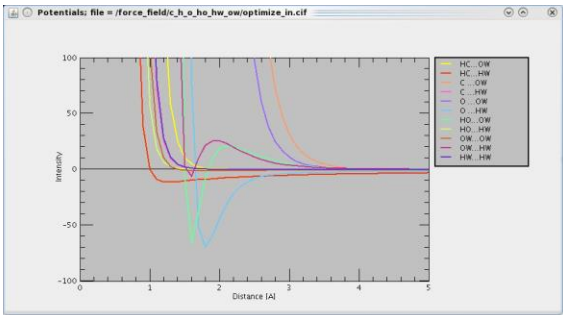

The complex interaction potentials for hydrates with CxHyOz compounds.

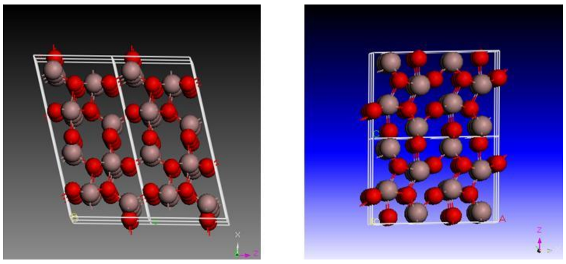

A comparison between the experimental crystal structure and the predicted crystal structure of Ga_2O_3

MS06-T7

Structural and magnetic phase transitions in antiferromagnetic $PrCaFeO_4$

N. Qureshi[1], M. Valldor[1,2], L. Weber[1], A. Senyshyn[3], Y. Sidis[4], M. Braden[1]
[1]*Universität zu Köln, II. Physikalisches Institut, Köln, Germany*
[2]*MPI für Chemische Physik fester Stoffe, Dresden, Germany*
[3]*Technische Universität München, FRM-II, Garching, Germany*
[4]*Laboratoire Léon Brillouin, C.E.A., Saclay, France*

We present a comprehensive study on $PrCaFeO_4$ using macroscopic methods, neutron and x-ray diffraction as well as inelastic neutron scattering. Two single crystals have been grown which exhibit a structural phase transition from a presumably high-temperature tetragonal phase to an intermediate orthorhombic phase (space group *Bmeb*, see Fig.1) as seen from single differential thermal analysis measurements. At 300 K a further structural phase transition takes place into a second orthorhombic phase (space group *Pccn*) which was deduced by neutron powder (see Fig.2) and single crystal diffraction. In contrast, the very closely related compound $LaSrFeO_4$ stays tetragonal (*I4/mmm*) throughout the whole temperature range [1]. Due to strong diffuse scattering at high temperatures neutron powder diffraction may only safely state that T_N is above 330 K. A magnetic phase transition has been observed in both samples where the magnetic moments turn from an in-plane configuration (like in $LaSrFeO_4$) to align along the *c* axis upon cooling. However, the transition temperatures and especially the transition regime of the magnetic transition are strikingly different between the two samples suggesting a strong influence of the crystal quality on the magnetic properties. Inelastic neutron scattering was employed in order to reveal the magnon dispersion along the main symmetry directions. The dispersion relation was derived using an antiferromagnetic next-neighbour coupling, an antiferromagnetic interplane coupling and an effective magnetic anisotropy field. The global fit of the magnon cross section to the raw data taking into account the instrument resolution [2] reveals a smaller anisotropy gap in the low temperature magnetic phase, whereas the coupling constants only change for the interplane interaction between the two phases. The spin reorientation and the decreasing gap result from an interplay between magnetostriction and spin-orbit coupling closely connected to the temperature-induced structural changes of lattice constants and octahedral tilts.

References:
[1] N. Qureshi et al., Phys. Rev. B **87**, 054433 (2013).
[2] A. Zheludev, RESLIB 3.4c (Oak Ridge National Laboratory) (2006).

Figure 1

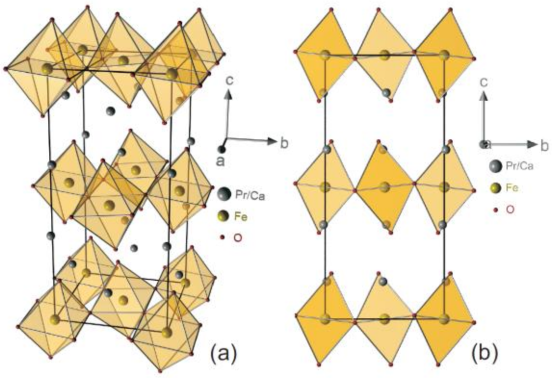

Figure 2

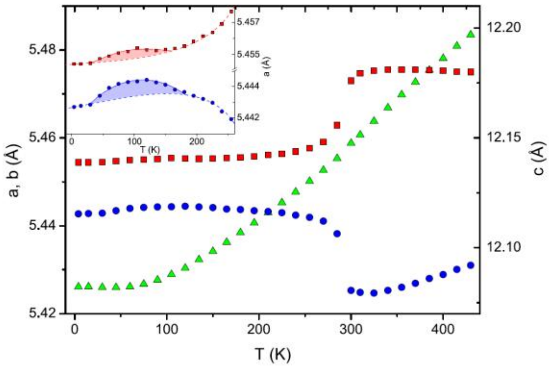

MS06-T8

Point Defects and Diffusion in Crystalline Oxides

J. Shi[1], K.- D. Becker[1]
[1]*Technische Universität Braunschweig, Braunschweig, Germany*

Nonstoichiometry or impurity/doping ions in oxides produce electronic and ionic defects on sublattices in the crystal structure. These point defects play a decisive role in diffusion processes in oxide crystals. Information on point defects in equilibrium and defect kinetics is of importance for the understanding of reactivity, degradation mechanisms of functional materials as well as for the development of new materials with improved ionic or electronic transport properties.

Due to the sensitivity to electronic transitions of ions and defects, optical spectroscopy in the UV-vis-NIR range is one of the versatile spectroscopic techniques for the study of point defects, reaction kinetics and diffusion, in particular, under in-situ conditions, Fig. 1.

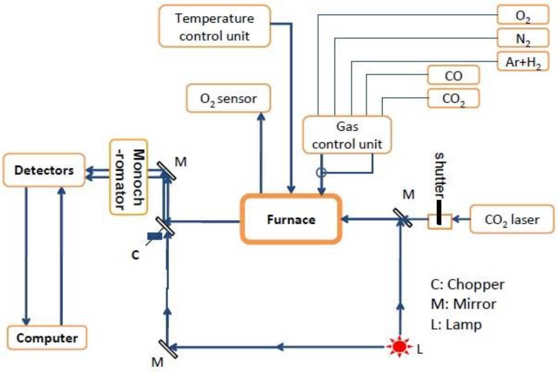

Fig. 1. Schematics of optical in-situ spectroscopy

In this presentation we will demonstrate the applications of optical in-situ spectroscopy into the investigation of defect chemistry, chemical kinetics and diffusion at high temperatures in oxides. Examples under consideration are: 1) the oxidation kinetics of nitrogen doped titania (N-doped TiO_{2-d}) thin films which can be well described by a parabolic rate law; 2) Optical absorption of electronic defects, and kinetics of redox reaction, as well as diffusion in lithium niobate single crystals under reducing conditions.

References

1. J. Shi, H. Fritze, G. Borchardt and K.-D. Becker, “Defect chemistry, redox kinetics, and chemical diffusion of lithium difficient lithium niobate,” *Phys. Chem. Chem. Phys.*, 2011, 13: 6925-30.
2. J. Shi, H. Fritze, A. Weidenfelder, C. Swanson, P. Fielitz, G. Borchadt, K.-D. Becker, “Optical absorption of electronic defects and chemical diffusion in vapor transport equilibrated lithium niobate at high temperatures,” *Solid State ionics*, 2013, in press, http://dx.doi.org/10.1016/j.ssi.2013.11.025
3. J. Shi, D.-K. Lee, H.-I. Yoo, J. Janek, K.-D. Becker, “Oxidation kinetics of N-doped TiO_{2-x} thin films”, *Phys. Chem. Chem. Phys.*, 2012, 14: 12930-12937

MS07 – Synchrotron opportunities and challenging structure determinations I (Bio)

MS07-T1

Update on the facilities for macromolecular crystallography at BESSY II in Berlin of HZB

U. Mueller[1]
[1]*Helmholtz Zentrum Berlin, Macromolecular Crystallography, Berlin, Germany*

The facilities for macromolecular crystallography (MX) at the Helmholtz-Zentrum Berlin (HZB) has been in operation since 2003. Since then, three state-of-the-art synchrotron beam lines (BL14.1-3) for MX have been built up on a 7T-wavelength shifter source. Currently, the three beam lines represent the most productive MX-stations in Germany, with more than 1000 PDB depositions. BLs14.1 and 14.2 are energy tuneable in the range 5.5-15.5 keV, while BL14.3 is a fixed-energy side station (13.8 keV). BL14.1 has been upgraded with an PILATUS-6M detector (DECTRIS) recently. The beam lines BL14.2+3 are equipped with MX-225 CCD-detectors (RAYONIX). All beam lines are in regular user operation providing about 200 beam days per year and about 600 user shifts to approximately 50 research groups across Europe. BL14.3 has been equipped with a HC1 crystal dehydration device and has been set back to user operation as a screening and test beam line in 2010. BL14.1 is acting as a high throughput station and is equipped with an MD2-microdiffractometer including a kappa-geometry option and an automated sample changer. Within the next years we will upgrade the experimental station of BL14.2 to a dedicated beamline for synchrotron based fragment screening. This infrastructure is complemented by an fragment library, which we are developing together with AG Klebe from Marburg university an will be offered to interested users for collaborations.

Figure 1

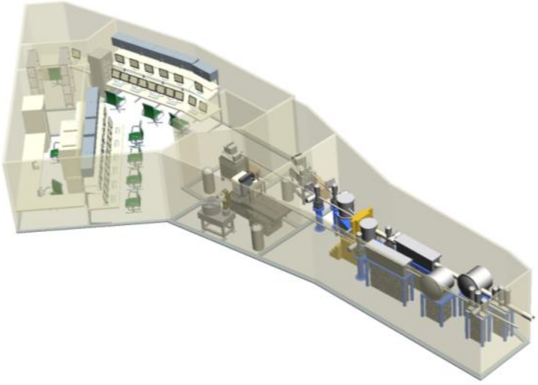

Figure 2

MS07-T2

Structural Biology beam lines at the ESRF: new developments

D. von Stetten[1]
[1]*European Synchrotron Radiation Facility, Structural Biology, Grenoble, France*

The portfolio of Structural Biology beam lines at the ESRF is currently being upgraded: while the last of the originally four ID14 beam lines was closed at the end of 2013, four new experimental end stations for Structural Biology are being built on ID30. Three fixed-energy end stations were built and are in their commissioning phase on the first branch of the ID30 slot and named MASSIF (Massively Automated Sample Selection Integrated Facility). The second branch of the canted setup, ID30B, is an energy tunable beam line currently under construction and foreseen to be opened to users from the beginning of 2015.

The MASSIF set of beam lines focuses on high-throughput sample evaluation based on user-defined criteria (resolution, presence of ligands or heavy atoms, *etc*.), as well as on fast diffraction data collection, *e.g.*, serial crystallography. The aim is to evaluate a large number of samples in an automated manner prior to diffraction data collection. This then allows users to focus their efforts on collecting diffraction data only from the most promising of many crystals. All beam lines will be equipped with a newly developed sampler changing robot which is also used as goniometer in conjunction with a high capacity sample dewar system.

The current status of MASSIF and ID30B as well as future plans for all ESRF Structural Biology beam lines will be presented.

MS07-T3

New capabilities for Macromolecular X-ray Crystallography at beamline P11 at PETRA III

A. Meents[1], A. Burkhardt[1], B. Reime[1], T. Pakendorf[1], S. Panneerselvam[1], N. Stuebe[1], J. Roever[1], J. Meyer[1], M. Warmer[1], P. Fischer[1], D. Goeries[1]
[1]*DESY, Hamburg, Germany*

The macromolecular crystallography beamline P11 at the PETRA III synchrotron has started regular user operation in spring 2013. Beamline P11offers state-of-the-art hardware such as a very precise goniometer, a Pilatus 6M detector, and a fast sample changing robot in combination with the extremely high X-ray high flux densities available at the PETRA III synchrotron. This makes P11 an ideal instrument for structure determinations especially from microcrystals and many successful experiments have already been performed at P11.

However such a brilliant machine as PETRA III has more potential than only performing 'standard' macromolecular crystallography. From spring 2014 to spring 2015 the PETRA III ring will be shut down in order to extend the facility by several more beamlines. At beamline P11 we will make of use this year to also extend the experimental capabilities of beamline P11. The planned upgrade includes among other things the utilization of the 'pink beam' for Micro-focus Laue crystallography, the introduction of an in-vacuum diffractometer for the investigation of very small crystals, and the introduction of a chopper system for time-resolved experiments. The results from first experiments carried out at P11 and the new possibilities arising from these upgrades for the user community will be presented.

MS07-T4

EMBL Beamlines for Macromolecular Crystallography at PETRA III

T. Schneider[1], G. Bourenkov[1], M. Cianci[1], J. Kallio[1], G. Pompidor[1], I. Karpics[1], S. Fiedler[1]
[1]*EMBL c/o DESY, Hamburg, Germany*

Since 2012, EMBL Hamburg operates two new beamlines for macromolecular crystallography - P13 and P14 - at the high-brilliance synchrotron radiation source PETRA III at DESY (Hamburg, Germany).

P13 offers a photon flux of >10^{13} ph/sec from 16 keV to 6 keV (0.8 - 2.0 Å). Energies between 4 and 6 keV (3.1 - 2.0 Å) are accessible with a photon flux between >10^{12} ph/sec providing unique conditions for experimental phasing. Using adaptive focusing mirrors, the full beam (~1.5 x 1 mm^2) can be focused to sizes between 30 x 20 μm^2 and 150 x 100 μm^2. An MD2 diffractometer with a mini-kappa goniostat allows for rapid and accurate rotation of crystals in the X-ray beam. A MARVIN-robot is installed for rapid (< 30 s cycle time) loading and unloading of crystals.

P14 offers a photon flux of >10^{13} ph/sec between 7 and 20 keV (1.8 - 0.6 Å). Using adaptive focusing mirrors, a beamsize of 5 x 4 μm^2 with a total flux of >10^{12} ph/sec can be used for crystallographic experiments. The focusing mirrors can be moved into and out of the beam in less than half a minute allowing to rapidly toggle between a fully focused small beam and an unfocused large (~1.5 x 1 mm^2) beam to optimize data collection parameters for differently sized crystals. A high-precision vertically mounted MD3 diffractometer with a sphere of confusion of less than 100 nm is available for data collection.

Both MX beamlines are equipped with PILATUS 6M-F detectors and dedicated data processing computers. The beamlines are embedded into the 'Integrated Facility for Structural Biology' offering facilities for sample preparation and characterization, a laboratory specifically equipped for the preparation of heavy atom derivatives, and downstream facilities for data evaluation. Applications for beamtime can be made at smis.embl-hamburg.de. Access support can be obtained via www.biostruct-x.eu.

We will report about the status of the beamlines and describe typical experimental situations (small crystals, serial crystallography, low-energy phasing and others).

MS07-T5

The Long-Wavelength Macromolecular Crystallography Beamline at Diamond Light Source

A. Wagner[1], V. Mykhaylyk[1], R. Duman[1]
[1]*Diamond Light Source, Chilton, Didcot, United Kingdom*

The Long-Wavelength MX Beamline I23 at Diamond Light Source will be the first dedicated beamline for long-wavelength phasing experiments from macromolecular crystals. By exploiting the weak anomalous differences from sulfur or phosphorous present in proteins or RNA/DNA molecules the crystallographic phase problem can be experimentally solved by anomalous diffraction methods based on their intrinsic signal without labeling the crystals with additional anomalous scatterers. Additionally, anomalous contrast can be used to unambiguously identify biologically important ions such as Ca2+, K+ or Cl-. The beamline will operate in a core wavelength range from 1.5 to 4 Å, offering a complementary setup to the suite of already five existing MX beamlines at Diamond. To minimize absorption effects, the complete beamline including sample, goniometer and detector will be operated in vacuum. An X-ray tomography setup will be integrated into the experimental end station to determine the crystal shape and size as a basis for an analytical absorption correction. A large curved Pilatus 12M detector will allow access to diffraction data up to 2theta = ±100º. Sample cooling is realized by a conductive path from a pulse tube cryo-cooler through the kappa goniometer.

The beamline is currently in its construction phase with first users being expected in May 2014. The challenges of in-vacuum long-wavelength macromolecular crystallography and the opportunities by extending the wavelength range towards the sulfur and phosphorous K-absorption edges will be discussed and an overview on the current status of the project will be given.

MS07-T6

Serial crystallography using synchrotron radiation - novel strategies for macromolecular microcrystallography

C. Gati[1], G. Bourenkov[2], M. Klinge[3], D. Oberthür[1], D. Rehders[3], M. Heymann[1], C. Seuring[1], F. Stellato[1], O. Yevanov[1], C. Betzel[3], T. Schneider[2], H. Chapman[1], L. Redecke[3]
[1]*DESY, Center for Free-Electron Laser Science, Hamburg, Germany*
[2]*EMBL, Hamburg Outstation, Hamburg, Germany*
[3]*University of Hamburg, Structural Biology, Hamburg, Germany*

Protein crystallography continues to be the most frequently used technique to solve macromolecular structures to atomic resolution. To yield high resolution diffraction images from microcrystals, 3rd generation synchrotrons with high intensity X-ray beams focused below 10 µm are generally available. The high intensity beam in a small focus quickly damages even cryo-cooled microcrystals within fractions of a second so that only few diffraction patterns can be obtained per crystal. Accordingly diffraction patterns from many crystals need to be combined into one dataset. Thus, it is already standard to combine data from dozens of deliberately centered crystals. Here we adopt the approach of serial crystallography, first developed at X-ray Free-Electron Lasers (Chapman et al. 2011) to be used at microfocus synchrotron beamlines, where thousands of crystals are measured in random orientation.

CathepsinB is a medically and pharmaceutically relevant protein, involved in the life cycle of *T. brucei*, the parasite causing sleeping sickness. The structure of TbCatB has recently been solved by serial femtosecond crystallography using 180.000 indexed patterns (Redecke et al. 2013), representing an ideal reference for the evaluation of our technique. Using a standard cryogenic loop for sample delivery we applied a series of helical line scans and solved the structure of TbCatB using *in vivo* grown microcrystals (TbCatB, Koopmann et al. 2012) with an average size of 9 μm^3. In this study we combined the data of 80 TbCatB microcrystals to assemble a dataset of 3.0 Å resolution. The data allowed the refinement of a structural model that is consistent with that previously obtained using FEL radiation, providing mutual validation.

Our strategy exploited the combination of a micron-sized X-ray beam, high precision diffractometry and shutterless data acquisition with a pixel-array detector. We conclude that our serial crystallography approach can easily be implemented at any microfocus beamline, which enables the utilization and outcome of the limitations by inherent radiation damage to microcrystals at high intensity beams.

Gati, C.*, Bourenkov, G.* et al. Serial crystallography on in vivo grown microcrystals using synchrotron radiation. IUCrJ (In press).
Chapman, H.N. et al. Femtosecond X-ray protein nanocrystallography. Nature 470, 73-77 (2011).
Redecke, L. et al. Natively inhibited Trypanosoma brucei cathepsin B structure determined by using an X-ray laser. Science 339, 227-230 (2013).

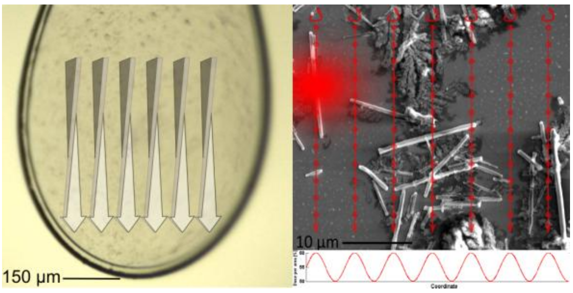

Experimental setup of the serial macromolecular crystallography experiment. (a) Schematic illustration of serial helical line scans in a cryoloop. (b) SEM image showing microcrystals. (red arrows) Illustration of the helical line scans (red flare) Calculated 2D Gaussian function (FWHM 4 x 5 µm) depicting non-finite size of the beam (lower part) Delivered dose (50-60%) per are

MS08 – Quasicrystals and incommensurate structures

MS08-T1

Crystal structure and modulation of Λ-Co(sepulchrate)-trinitrate at low temperatures

A. Schönleber[1], S. Dey[1], S. van Smaalen[1], F. K. Larsen[2]
[1]University of Bayreuth, Laboratory of Crystallography, Bayreuth, Germany
[2]Aarhus University, Department of Chemistry, Aarhus, Denmark

The organic salt Λ-Co(sepulchrate)-trinitrate, $C_{12}H_{18}N_8Co^{3+}\cdot\ 3(NO_3)^-$ crystallizes at room temperature in symmetry $P6_322$ [1,2]. The Co(sepulchrate) cation and two of the nitrate anions, centred on threefold rotation axes, are linked to each other by a N-H···O hydrogen bond network. The third nitrate anion shows orientational disorder.

Two phase transitions have been observed at T_1 = 133 K and at T_2 = 107 K, respectively, by means of light microscopy and spectroscopic measurements [1,3]. Temperature dependent single crystal neutron diffraction revealed the appearance of satellite reflections in the diffraction pattern at T_1, which vary their positions continuously with temperature. Next to the second phase transition at T_2 also a third one was observed at T_3 = 98 K [4].

We have performed single crystal X-ray diffraction at beamlines F1 and D3 of Hasylab (DESY, Hamburg) at different temperatures 115 K, 104 K and 100 K. Some first inspections of the data have shown, that the main reflections are regularly surrounded by satellite reflections up to third order. All observed peaks can be indexed in an hexagonal unit cell with lattice parameters of $a = b \approx 8.45$ Å and $c \approx 15.75$ Å and two **q**-vectors (σ, σ, 0) and (-2σ, σ, 0) with σ ≈ 0.088 (T = 115 K) in superspace group $P6_322(\sigma\sigma0)000(-2\sigma\sigma0)000$. This represents a two-dimensional modulation of the crystal structure and its description in (3+2)-dimensional superspace. However, it is also noticed that mixed hexagonal satellite reflections of second or third order are absent, indicating a possible lowering of symmetry. As also observations by low temperature Raman spectroscopy claim a reduction of the trigonal symmetry [3], we propose to describe the diffraction pattern at T = 115 K by a threefold orthorhombic twin in superspace group $C222_1(2\sigma00)000$ with $a \approx 8.45$ Å, $b \approx 14.63$ Å and $c \approx 15.75$ Å, reducing the modulation to one dimension and resulting in a structure description in (3+1)-dimensional superspace.

[1] L. Dubicki, J. Ferguson, B. Williamson, *J. Phys. Chem.* 88 (1984) 4254 - 4258.
[2] A. Schönleber, S. van Smaalen, F. K. Larsen, *Acta Crystallogr. C* 66 (2010) m107 - m109.
[3] L. Dubicki, J. Ferguson, R. J. Geue, A. M. Sargeson, *Chem. Phys. Lett.* 74 (1980) 393 - 397.
[4] F. K. Larsen, P. Jørgensen, R. Grønbæk Hazell, B. Lebech, R. Thomas, R. J. Geue, A. M. Sargeson: Phase transitions in Λ-Co(sepulchrate)$(NO_3)_3$, Chapter 49 in *Molecular structure: Chemical reactivity and biological activity*, J. J. Stezowski *et al.* (*ed.*) IUCr, Oxford University Press (1988) 499 - 504.

MS08-T2

The 3+1D modulated structure of $InMo_4O_6$, a molybdenum cluster compound hosting In_6 and In_7 oligomers

P. Schultz[1], O. Oeckler[1]
[1]IMKM, Chemistry, Leipzig, Germany

The chemistry of metal-rich cluster compounds is well known; it is dominated by M_6X_{12} and M_6X_8 clusters (M = metal, X = halogen or chalcogen) which require different electrons counts to stabilize them. Groups of condensed clusters (e. g. chains) reduce the number of bonding electrons per cluster unit. Metal-rich indium molybdates can be described with the formula $In_{1+n}Mo_{4n+2}O_{6n+4}$ (n = 4,[1] 5,[2] 6, ∞[3]) where n is the number of condensed octahedral clusters. The compounds with n = 4, 5, 6 crystallize with monoclinic or orthorhombic symmetry and contain finite zigzag chains of indium atoms between the molybdenum cluster chains. The phase $InMo_4O_6$ was identified by chemical analysis, powder diffraction data were indexed with tetragonal or orthorhombic symmetry,[4] and the structure was claimed to be isostructural with $NaMo_4O_6$.[3]

Single crystal data yield a primitive tetragonal cell with a = 9.673(1) Å, c = 2.8615(4) Å as mentioned in the literature; however, additional satellite reflections are present and can be indexed in 3+1D assuming a refined q-vector 0.003(1) a* - 0.002(1) b* - 0.1536(4) c*. The basic structure solved and refined from the main reflections is similar to the $NaMo_4O_6$ structure type[5]; however, indium seems to be coordinated in a (distorted) tetragonal planar fashion instead of the cubic coordination found for the cation in $NaMo_4O_6$. The structure was refined in the 3+1D super space group $P4/mbm$ (00g) 00ss with a = 9.673(1) Å, c = 2.8615(4) Å and q = (0 0 1/6.5). The fraction 1/6.5 is within one standard deviation equivalent to the measured c^* component 0.1536(4) of q. Harmonic and saw tooth displacement modulation functions were used in the refinement, taking into account first-order satellites.

The basic building blocks are edge-sharing M_6X_{12}-type Mo_6 octahedra, with oxygen atoms over every non-shared edge. Between the resulting infinite molybdate chains parallel [001], indium atoms form alternating 6- and 7-membered oligomers. The In-In distances within the oligomers are refined to ~2.7 Å, the gap between two chains amounts to ~3.7 Å.

The examination of reconstructed reciprocal lattice sections revealed that first-order satellites lie within diffuse planes perpendicular to [001], which suggests 2D, i. e. rod disorder of the indium oligomers. Very weak second-order satellites are visible but could not be included in the refinement.

Literature
[1] E. Fais, H. Borrmann, Hj. Mattausch, Z. Anorg. Allg. Chem. 621 (1995) 1178.
[2] R. Dronskowski, Hj. Mattausch, A. Simon, Z. Anorg. Allg. Chem. 619 (1993) 1397.
[3] R. E. McCarley, K. H. Lii, P. A. Edwards, L. F. Brough, J. Solid State Chem. **57** (1985) 17.
[4]R. L. Gitzendanner, F. J. DiSalvo, J. Alloys Compd. 218 (1995) 9.
[5]C. C. Toradi, R. E. McCarley, J. Am. Chem. Soc. 101 (1979) 3963

MS08-T3
(3+2) incommensurately modulated structure of K2Sc[Si2O6]F

C. Hejny[1], V. Kahlenberg[1], T. Eberhard[1], H. Krüger[1]
[1]*Universität Innsbruck, Mineralogie und Kristallographie, Innsbruck, Austria*

Due to a growing interest in rare earth silicates with specific luminescent properties and potential use as phosphor materials several scandium silicate phases have recently been studied (Vidican et al 2002, Kolitsch et al 2004). Single crystals of $K_2Sc[Si_2O_6]F$ have been grown from KF flux in a Pt capsule at 1100 °C. A first structural model was sketched in space group $P4_2/mnm$ with lattice parameters a = 8.9939(5), c = 8.2776(5) Å. However, additional satellite reflections at ca. $(\pm\mathbf{a^*}+\mathbf{b^*})/3$ were not accounted for by this model. This information and the observation of unusually large ADP´s for some of the atoms lead to the assumption that $K_2Sc[Si_2O_6]F$ has an incommensurately modulated structure. The modulation appears to be (3+2)-dimensional, similar to the one observed for the tetragonal phases fresnoite (Bindi et al 2006) and related compounds (Höche et al 2002). Refinement was subsequently performed for main and satellite reflections together in space group $P4_2/mnm(\alpha,\alpha,0)000s(-\alpha,\alpha,0)0000$ and the modulation vectors $\mathbf{q_1}$ = 0.2982(4)($\mathbf{a^*}$ + $\mathbf{b^*}$), $\mathbf{q_2}$ = 0.2982(4)(-$\mathbf{a^*}$ + $\mathbf{b^*}$) to R_o = 0.0467 for the main reflections and R_o = 0.0404 for the first order satellite reflections. The refinement includes a modulation of the atomic positions and displacement parameters and gives a reasonably good structure model. However, the R_o value of 0.1678 for satellite reflections with mixed indices for m and n and unusually large intensity spread of symmetrically equivalent reflections of up to 27% from the mean value indicate that this model could be still improved.

The structure is a mixed octahedral-tetrahedral framework containing four-membered rings of SiO_4-tetrahedra and columns of corner-sharing ScO_4F_2-octahedra; K atoms are in open irregular cavities. Mainly O and K atoms are affected by the modulation resulting in K atoms to occur in coordination from four-fold to six-fold up to a distance of 3.1 Å. As can be expected the SiO_4 tetrahedra show a stiff behaviour with the modulation affecting the spatial orientation of the SiO_4 tetrahedra relative to each other, e.g. the angle Ot-Ob-Ot formed by terminal oxygen atoms Ot around a bridging atom Ob varies by over 23° from 107.2(1) to 130.6(1)°.

The modulation wavevector is temperature independent within 1σ but the intensities of the satellite reflection show pronounced temperature dependence: They decrease with increasing temperature, disappear at 150(5) °C and reappear reversibly on cooling. Figure 1 shows satellite reflections with the strongest recorded intensities at -150 °C.

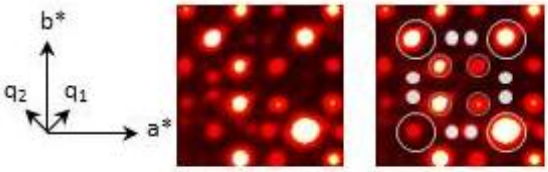

Fig. 1: Part of the reconstructed *hk*1 layer of $K_2Sc[Si_2O_6]F$ recorded at -150 °C. Large circles for main reflections *hk*100, medium circles for 1st order satellite reflections *hk*1*mn* with *m* or *n* = ±1, small circles for satellite reflections with mixed indices *m* and *n* = ±1.

References
Bindi L., Dusek M., Petricek V., Bonazzi P. (2006)
Acta Crystallographica B62 1031
Höche, T., Neumann, W., Esmaeilzadeh, S., Uecker, R., Lentzen, M., Rüssel c. (2002)
J Solid State Chem 166, 16
Kolitsch U., Tillmanns E. (2004)
EJM 16, 143
Vidican, I., Smith, M., & zur Loye, H. (2003). J Solid State Chem 170, 203

MS08-T4
On the triangle wave function

C. J. Müller[1], S. Lidin[1]
[1]*Lund University, Centre for Analysis and Synthesis, Lund, Sweden*

Incommensurate modulated structures are an interesting and often challenging research problem for crystallographers. Using the superspace approach for their description, several kinds of structural modulations may be used; displacive modulations, occupational modulations and modulations of thermal displacement parameters. While displacive modulations can be present exclusively, occupational modulations hardly occur without the accompaniment of displacive modulations. [1]

One common way to describe occupational modulation mathematically, are harmonic wave functions. A special feature of occupational modulations is that each harmonic wave will take care of only one pair of satellites in the model. However, Petricek et.al. showed that Crenel functions are an alternative to the harmonic functions. [2] Their benefits are that they are less prone to correlations than are the combinations of several harmonic waves and they are easier to interpret from a chemist's point of view, meaning it is easy to understand that one atom is either there or not. But, the square wave also has other less known properties: The intensity of the observed satellite reflections decreases by a factor of 1/N, where N is the satellite order, and only odd harmonics are needed to model it. This is leading to odd order satellites only.

Another function to model the observation of only odd order satellites is the triangle wave. Theoretically, this results in a decrease of the intensities by a factor of $1/N^2$. We are showing how the triangle wave can be constructed using the harmonic waves in Jana2006. Further, we are presenting their use for structures with dominating occupational modulation functions and odd order satellites only.

References
[1] S. van Smaalen: Incommensurate Crystallography, Oxford University Press, New York, 2007.
[2] V. Petricek, A. van der Lee, M. Evain, Acta Crystallogr. A, 1995, 51, 529-535.

MS08-T5
Non-crystallographic lattice restrictions in order-disorder structures

B. Stöger[1]
[1]*Vienna University of Technology, Institute of Chemical Technologies and Analytics, Vienna, Austria*

The order-disorder (OD) theory [1] was conceived in the 1950s to explain diffuse scattering of the mineral wollastonite [2]. Since then it has been developed into a versatile theory explaining the universal occurrence of polytypism in all classes of materials and generalizing the concept of space groups to families of polytypic structures [3].

According to the OD theory, if layers possess higher symmetry than the overall structure, the layer stacking becomes ambiguous. There then exists an infinity of locally geometrically equivalent polytypes. If long-range interactions are neglected, these polytypes are energetically equivalent.

Such an ambiguous stacking can for example be caused by different translational groups of adjacent layers as in $K_2HAsO_4 \cdot 2.5H_2O$ [4]. Nevertheless, OD structures composed of layers with different lattices have received virtually no attention. While developing computer routines to analyze such OD structures it became necessary to introduce layer lattice restrictions which are a generalization of the five two-dimensional Bravais lattices. The three kinds of lattice restrictions (1-3 free parameters) and human-readable as well as software-internal representations will be presented.

[1] K. Dornberger-Schiff, H. Grell-Niemann *Acta Crystallogr.* 1961, *14*, 167-177.
[2] J. W. Jeffery *Acta Crystallogr.* 1953. *6*, 821-825.
[3] G. Ferraris, E. Makovicky, S. Merlino Crystallography of Modular Materials, volume 15 of *IUCr Monographs on Crystallography*. Oxford University Press, 2004.
[4] B. Stöger, M. Weil, E. Zobetz *Z. Kristallogr* 2012, 227, 859-868.

MS08-T6
Dendritic growth of tenfold twins from an undercooled melt of glass-forming NiZr

W. Hornfeck[1], R. Kobold[1], M. Kolbe[1], D. Herlach[1]
[1]*German Aerospace Center, Cologne, Germany*

Samples of the glass-forming intermetallic compound NiZr were processed by the electrostatic levitation technique (ESL) on which occasion the nucleation and growth of tenfold dendritic microtwins was observed for large undercoolings of about 320 K. The highly correlated dendritic growth is accompanied by a decagon-shaped solidification front moving on top of the samples' surface which was directly observed via a high-speed camera. The resulting microstructure after complete solidification was studied by means of a scanning electron microscope employing energy-dispersive X-ray spectrometry (EDX) as well as electron backscatter diffraction (EBSD) in combination. A detailed picture of the solidification process was gained, correlating the macroscopic decagon-shaped growth front to the microscopic dendrite growth into a tenfold twinned microstructure and eventually to the crystal structure, whose metrical properties explain the mechanism of twinning, at the atomic scale. Thus, NiZr offers a deep understanding of the solidification process from atomic to macroscopic scales, which is a prerequisite for the experimental measurement and a challenge for the theoretical modelling of dendritic growth velocities.

MS08-T7
Quasicrystal and its periodic approximant - do they fit to each other?Epitaxial crystal growth experiments in the Al-Co-Ni system

B. Meisterernst[1], L. Grossmann[1], K. Scheidl[1], P. Gille[1]
[1]*Ludwig-Maximilians-Universität München, Department of Earth and Environmental Sciences, Crystallography section, Munich, Germany*

As soon as large enough quasicrystals became available, the deposition of thin layers of various elements that usually crystallize in periodic structures was investigated on crystallographically well-defined quasicrystalline substrates. The main focus of these studies has been the question whether or not it is possible to force monolayers or even multiple layers of periodic phases into a quasiperiodic structure [1].

In general, epitaxy is defined as the oriented growth of one crystal onto another and a lattice mismatch of less then 5 % is regarded as a prerequisite. Since quasicrystals are aperiodic and therefore no unit cell can be defined in the direct space, according to the classical definition of epitaxy an epitaxial intergrowth between a periodic phase and a quasicrystal should not be possible.

A more general definition of epitaxy has been proposed by Franke et al. [2] based on the concept of locking into registry at the interface. Accordingly, the essence of epitaxy is not the existence of a common interface unit cell, but whether the interface energy reaches a local minimum concerning lateral shifts of the crystals with respect to each other [3]. This can be achieved, if the interface of the two half-crystals has at least two projected non-collinear reciprocal lattice vectors in common [2]. This definition can be applied to all crystals including quasicrystals.

Using the Czochralski method we investigate if it is possible to grow a (bulk) quasicrystal onto a periodic seed (approximant) - or the other way around. For these experiments the system Al-Co-Ni has been chosen because the decagonal quasicrystal and its monoclinic approximant Y-$Al_{13}(Co,Ni)_4$ can be grown from Al-rich melts of only slightly changed composition. First experiments will be presented and discussed.

[1] V. Fournée, J. Ledieu, M. Shimoda, M. Krajčí, H.-R. Sharma, R. McGrath, Isr. J. Chem. 51 (2011) 1314 - 1325.
[2] K. J. Franke, P. Gille, K.-H. Rieder, W. Theis, Physical Review Letters 99 (2007) 036103.
[3] A. Zangwill, Physics at Surfaces,CambridgeUniversityPress,Cambridge(1990).

MS08-T8
Fulleranes and Frank-Kasper polyhedra in intermetallics

J. Dshemuchadse[1], W. Steurer[1]
[1]*ETH Zurich, Laboratory of Crystallography, Department of Materials, Zurich, Switzerland*

The study of the structure of metals has kept crystallographers busy for the past century: starting with the simplest of structures - sphere packings, such as found in aluminium or copper - up to some of the most complex inorganic structures known to date with more than 20000 atoms per unit cell [1]. But knowing all the atomic positions does not yet provide us with a deeper understanding of the design of the structure.

Different cluster interpretations of the atomic arrangement in an intermetallic can provide us with recurring motifs in the form of atomic environments, i.e. coordination polyhedra, or larger, endohedral clusters, such as dual Frank-Kasper polyhedra and fullerene-like shells (e.g., [2]). These cluster descriptions illustrate common features in structures either within the same intermetallic system or of related structures with entirely different constituents. However, they do not necessarily represent chemical entities and their meaningfulness is usually derived from their repeated occurrence in diverse compounds.

We will present possible ways of structure description for complex intermetallic phases and clues toward their significance. Hereby, we will focus on complex intermetallic structures [3]. (Adhering to chemical nomenclature, we will term the fullerene-shaped, metallic polyhedra “fulleranes”, considering the assumed absence of double bonds.)

[1] T. Weber, J. Dshemuchadse, M. Kobas, M. Conrad, B. Harbrecht, W. Steurer, Acta Cryst. B 65, 308-317 (2009).
[2] J. Dshemuchadse, S. Bigler, A. Simonov, T. Weber, W. Steurer, Acta Cryst. B 69, 238-248 (2013).
[3] J. Dshemuchadse, W. Steurer, MRS Proceedings 1517 (2012), doi:10.1557/opl.2012.1584

MS09 – Crystallography in geology – microstructures as indicators of rock forming processes

MS09-T1

Roch formation processes constrained by host-inclusion crystallography

R. Angel[1], S. Milani[1], P. Nimis[1], M. Bruno[2], J. Harris[3], F. Nestola[1]
[1]*University of Padua, Geosciences, Padua, Italy*
[2]*University of Torino, Earth Sciences, Torino, Italy*
[3]*University of Glasgow, Geographical & Earth Sciences, Glasgow, United Kingdom*

Inclusions of one mineral in another are a special kind of microstructure, but they are common and can provide vital constraints on the formation conditions of the minerals. We have adapted the methods of high-pressure single-crystal diffraction to characterize host-inclusion pairs *in-situ,* in order to place constraints on rock-forming processes. The methods will be illustrated by our recent studies of olivine inclusions in diamonds.

Inclusions in diamonds are the only direct samples we have of the Earth’s interior below the crust, apart from the diamonds themselves. Twenty-one diamonds, all from the same kimberlite source (Udachnaya, Yakutia), containing a total of 51 olivine inclusions with diamond-imposed morphology, were measured. Each diamond contained up to nine individual olivines. Most of these inclusions are single crystals, or clusters of a few single crystals. The orientations of both inclusion crystals and diamonds were determined simultaneously by single-crystal diffraction. Appropriate manipulation of the orientation matrices allows the orientation of the inclusion crystals relative to their diamond host crystal to be determined unambiguously. On a statistical basis, no preferential orientation could be found between the olivines and their diamond hosts. In particular, only 3 olivines show an orientation previously claimed to be dominant, (101)oli // (101)dia *and* (010)oli // (111)dia, and claimed to result from epitactic syngenetic growth. Our crystallographic data show that this special orientation does not appear to be “typical” of olivines included in our diamonds. But groups of olivine inclusions in individual diamonds often exhibit a common orientation. Taken together, these two observations allow us to constrain the mechanism by which these olivine-bearing diamonds grew in the Earth’s mantle.

This work was supported by ERC starting grant 307322 to Fabrizio Nestola.

MS09-T2

In-situ monitoring of spinel reaction band formation using synchrotron radiation

L. Götze[1], S. Schorr[1,2], R. Milke[1], R. Abart[3], R. Dohmen[4], R. Wirth[5]
[1]*FU Berlin, Berlin, Germany*
[2]*Helmholtz-Zentrum Berlin für Materialien und Energie, Berlin, Germany*
[3]*Universität Wien, Wien, Austria*
[4]*Ruhr-Universität Bochum, Bochum, Germany*
[5]*Helmholtz-Zentrum Potsdam - Deutsches GeoForschungsZentrum GFZ, Potsdam, Germany*

We used synchrotron X-rays and a heating attachment in energy-dispersive as well as angle-dispersive diffraction experiments to monitor *in-situ* the growth of nm-scale spinel ($MgAl_2O_4$) reaction bands that developed in diffusion reaction couples. Two different starting assemblies were used with either (0001) oriented single crystalline corundum substrates covered with a thin film of amorphous MgO or (111) oriented single crystalline periclase substrates covered with a thin film of amorphous Al_2O_3. The thin films were prepared using pulsed laser deposition (PLD; [1]), and they were always less than 300 nm thick. During annealing of the assemblies at temperatures in the range of 800 to 1000°C at ambient pressure for 5-120 min, a layer of spinel formed at the substrate/thin film interfaces.

At 1000°C, a linear increase of spinel layer thickness with time was observed suggesting that layer growth was interface-reaction controlled. At 900°C the layer growth is linear during the initial stages (first 10 minutes) and then changes to a non-linear, parabolic behavior indicating a transition from an interface-controlled to a diffusion-controlled kinetic reaction regime. The results were evaluated using a thermodynamic model that accounts for both, localized interface reactions and long range diffusion of chemical components across a growing reaction layer [2].

The crystallographic orientation of the *in-situ* grown, polycrystalline spinel reaction band was subsequently determined by constructing pole figures. These texture measurements show that the spinel reaction band grows topotactically into the substrates. As a complementary high-resolution analytical technique, TEM was used to reveal microstructures, microtextures and to determine absolute reaction rim widths. The initial Al_2O_3/MgO phase boundary can be seen as a natural planar microstructure inside the reaction band. Along with the texture measurements, this position confirms a counterdiffusion of cations through a relatively rigid oxygen sublattice as the diffusion mechanism in this system.

References:
[1] Dohmen et al. (2002). Eur. J. Min. 14: 1155
[2] Abart and Petrishcheva (2011). Am. J. Sci. 311: 517

MS09-T3

A perspective on magnesite reactivity

U.- N. Berninger[1,2], Q. Gautier[2], G. Jordan[1], M. Lindner[1], E. H. Oelkers[2], J. Schott[2]
[1]*LMU München, Dept. f. Geo- & Umweltwiss., München, Germany*
[2]*Géosciences Environnement Toulouse, Toulouse, France*

Although surface seawater is supersaturated with respect to calcite, dolomite and magnesite, no direct (abiotic) precipitation of these minerals can be observed in modern marine surface environments. Whereas calcite can be precipitated from aqueous solutions at room temperature and pressure in laboratory experiments, such attempts fail for dolomite and magnesite so far. Instead hydrous magnesium carbonates and disordered calcium magnesium carbonates are commonly obtained (Lippmann, 1973). This failure has been explained by the different dehydration energy of the calcium and magnesium ions (Pokrovsky and Schott, 2002). The difference in dehydration energy causes a different ligand-exchange rate of the aqueous cation complex which has been shown to directly correlate with the dissolution rate of the respective carbonate.

However, previous high resolution studies showed that magnesite dissolution kinetics is not only controlled by the stability of the cation complex in the bulk liquid but also by mechanisms taking place at the crystal surface (Jordan et al., 2001). Mixed control was also detected for the promoting effect of additives on magnesite dissolution (Jordan et al., 2007). In order to examine the effect of additives on magnesite growth and to test whether mixed kinetic control is also valid for precipitation, a combination of macroscopic reactor experiments and high resolution microscopy experiments have been conducted. Anionic molecules with carboxyl groups (citrate, oxalate, EDTA) and Ca^{2+} have been used as additives. Whereas the anionic additives are interesting due to their effects as ligands for magnesium ions, the investigation of Ca^{2+} is especially important because of its general implications for crystal growth in the Ca-Mg-carbonate system. Furthermore, the study might give insight whether the effect of calcium on magnesite growth correlates with the effect of strontium on calcite growth. The later has been identified as both growth promoting and inhibiting (Wasylenki et al., 2005).

Within the investigated range of conditions, macroscopic reactor experiments did not reveal any growth promotion of magnesite by anionic additives. High resolution microscopy experiments revealed several effects: anionic additives modified the morphology and inhibited the advance rate of steps on the (104) surface. Citrate, for instance, inhibited the kinematics of acute steps (Gautier et al., 2014). On the contrary, low concentrations of Ca^{2+} promoted obtuse step velocity. But growth promotion of these steps did not yield an accelerated macroscopic growth rate - suggesting that obtuse step advance is not controlling the overall growth kinetics of magnesite.

References:

Gautier Q et al. (2014) In prep.
Jordan G et al. (2001) *Geochim. Cosmochim. Acta*, 65, 4257.
Jordan G et al. (2007) *Chem. Geol.*, 242, 487.
Lippmann F (1973) *Sedimentary carbonate minerals*. Springer.
Pokrovsky OS, Schott J (2002) *Environ. Sci. Technol.*, 36, 426.
Wasylenki LE et al. (2005) *Geochim. Cosmochim. Acta*, 69, 3017.

MS09-T4

Experimental growth of radiaxial-fibrous calcite

F. Wiethoff[1], J. Schreuer[1]
[1]*Ruhr-Universität Bochum, GMG / Kristallographie, Bochum, Germany*

Radiaxial fibrous calcite (RFC) and fascicular optical calcite (FOFC) crystals show diverging and converging, respectively, *c*-axes which results in characteristic optical anomalies. Carbonates containing RFC and/or FOFC cements are considered to be one of the best proxies for the geochemistry of ancient oceans [1]. However, in contrast to their importance for climate reconstruction their formation and the structural origin of their unusual properties are only poorly understood.

In order to shed light into the formation of radiaxial-fibrous calcites we conducted gel-based crystal growth experiments at room temperature with strong concentration gradients in time and space. The experiments covered a wide range of final molar Mg/Ca ratios from 0:1 up to 5:1. At the beginning of crystallization rhombohedra (mostly {104}) dominated whereas over time with increasing Mg/Ca ratio new crystals with more and more complex and/or pathological morphologies nucleated leading finally to aggregates with pronounced RFC-FOFC-like optical behaviour (see figure below). The optical, morphological, chemical and structural properties of the obtained crystals were studied employing a combination of methods including optical microscopy, scanning electron microscopy, X-ray diffraction, electron microprobe and cathodoluminescence microscopy.

Our preliminary results show a clear correlation between the growth morphology of the investigated calcites and the Mg content of the fluid as well as the amount of Mg incorporated into the growing crystal. In particular, all crystals with a step like increase of the Mg content exhibit strong undulous optical extinction. Different zones (e.g. core, transition, rim) of optical anomalies are correlated to the changing local Mg/Ca ratio.

References:

[1] Richter, D. K., Neuser, R. D., Schreuer, J., Gies, H. and Immenhauser, A.: Radiaxial-fibrous calcites: A new

look at an old problem. Sediment. Geol. 239 (2011) 23-36.

Figure 1

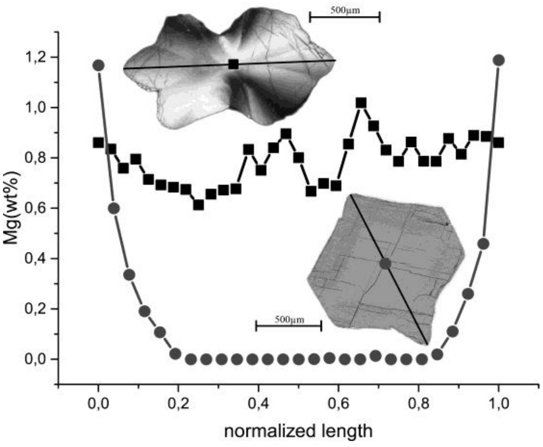

MS09-T5

Lattice strain across Na-K-interdiffusion fronts in alkali feldspar: an EBSD study

A.- K. Schäffer[1], T. Jaepel[2], S. Zaefferer[2], R. Abart[1]
[1]*University of Vienna, Department for Lithospheric Research, Vienna, Austria*
[2]*Max-Planck Institute for Iron Research, Duesseldorf, Germany*

Cation exchange between gem quality sanidine from the Eifel (X_{Or} = 0.85) and KCl melt lead to the formation of a chemically altered surface layer with X_{Or} = 1.00. The transition between the exchanged surface layer and unexchanged core of the crystal can be interpreted as a diffusion front, which propagates inwards by Na-K-interdiffusion on the alkali sublattice. These diffusion fronts are highly anisotropic with fronts normal to (010) being significantly sharper than fronts normal to (001).

Due to the composition dependence of the lattice parameters of alkali feldspar any shift in composition leads to coherency stress and elastic strain. The chemically induced eigenstrain is highly anisotropic; changes in *a* being about 5-times higher than in *b* and *c* (Kroll et al., 1986).

Electron back-scatter diffraction combined with the cross correlation technique was employed to determine the strain distribution across the Na-K-interdiffusion fronts in partially exchanged single crystal plates of alkali feldspar with polished (010) surfaces. This technique uses shifts in Kikuchi patterns relative to a reference pattern recorded in an unstrained part of the crystal to determine the full strain tensor with a resolution of 0.5 pixels and a strain sensitivity of up to 1.3 x 10^{-4} (Wilkinson et al., 2006).

Patterns were recorded in a 50 x 1 µm area which was moved in 1 µm steps along a 40 µm profile from the edge of the crystal, across the diffusion front and into the unexchanged core. The last pattern in the core was chosen as reference pattern. The software Cross Court 3 by BLG productions was used to determine the strain tensor. Several measurements across both the sharp and shallow fronts showed good reproducibility of the extracted strain pattern.

The strain changes gradually across the shallow front normal to (001) with a successive dilation primarily in the *a*-direction, which is in accordance with composition strain in an unstressed alkali feldspar. For the sharp diffusion fronts however, a pronounced dilation in the *b*-direction is localised at the diffusion front and is followed by a slight expansion in the *a*-direction in the exchanged orthoclase-rich rim.

This strain distribution does not confer with what would be expected from the anisotropy of the composition dependence of the lattice parameters. It can be explained by the mechanical coupling of the thin misfitting surface layer and the mechanically much stronger substratum. It can be hypothesized that the localisation of the lattice distortion at the diffusion front may have an influence on diffusion pathways, and possibly reduces component mobility across the diffusion front, leading to a self-sharpening feedback.

References
Kroll, H., Schmiemann, I. and von Cölln, G. (1986):Feldspar solid solutions. American Mineralogist, 71:1-16.
Wilkinson, A.J., Meaden, G. and Dingley, D.J.(2006): High-resolution elastic strain measurement from electron backscatter diffraction patterns: New levels of sensitivity. Ultramicroscopy, 106: 307-313.

MS09-T6

Crystal-plastic deformation of zircon from strained natural rocks

E. Kovaleva[1], G. Habler[1], U. Klötzli[1]
[1]*University of Vienna, Lithospheric Research, Vienna, Austria*

Crystal-plastic deformation of zircon hosted in various types of natural rocks has been examined by electron backscatter diffraction analysis (EBSD), allowing crystal lattice orientation mapping at high-spatial resolution.

One of the most important controlling factors of zircon plastic deformation represents its crystallographic and elastic anisotropy, related with the elementary crystal directions [001], [100] and [010]. Based on approximately 60 deformed grains from different geological settings, we have created misorientation-axes density distribution map (fig. 1), which shows at least six maxima in the pole figure. In the most common case, the misorientation axes are parallel to the [001] or [100] crystallographic axes. This is consistent with the most abundant slip systems in zircon, <100>{010} and <001>{010}, which have been documented previously by TEM and EBSD analyses [1],[2].

These common slip systems are preferably activated when zircon is hosted in a rheologically relatively softer phase, for instance biotite, where zircon acts as a rigid clast. This is due to a higher strain rate and elevated deviatoric stress on the zircon tips and rims, as derived from numerical modeling. If zircon has internal heterogeneities, such as a xenocryst core or inclusions, strain concentration also occurs around these features, leading to the activation of one or both of the main slip systems. Residing in a soft mica host, zircon deformation is controlled by its crystallography, whereas the deformation of zircon enclosed in a more rigid host phase is strongly controlled by the host phase microstructural arrangement / the phase boundary geometry.

Zircon hosted by a soft phase (mostly biotite) developed a crystallographic preferred orientation (CPO), which has not been documented for zircon so far. The C-axis of zircon is inclined 45 degrees with respect to the stretching lineation. The CPO formation is a consequence of dynamic recrystallization by a subgrain rotation mechanism. Subgrains rotate according to crystallographically controlled slip systems in order to accommodate deviatoric stress. Furthermore CPO formation is accompanied by the development of a characteristic zircon grain shape forming “two lobes”.

This in situ study of accessory zircon provides new information on its rheological behavior and allows constraining relatively early deformation stages in polymetamorphic rocks.

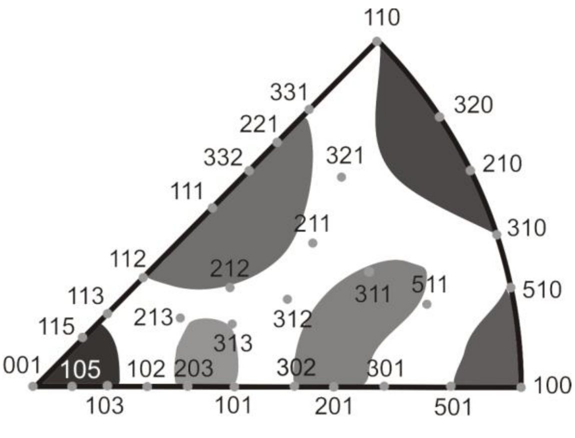

Figure 1. Collective misorientation-axes density distribution map. The intensity of the color corresponds to the misorientation axes density. The gray dots with labels are the positions of the crystallographic axes.

References:
[1] Leroux, H., Reimold, W.U., Koeberl, C., Hornemann, U., Doukhan, J.C., 1999. Experimental shock deformation in zircon: a transmission electron microscopic study. Earth and Planetary Science Letters, 169, 291-301.
[2] Reddy, S.M., Timms, N.E., Pantleon, W., Trimby, T., 2007. Quantitative characterization of plastic deformation of zircon and geological implications. Contributions to Mineralogy and Petrology 153, 625-645.

MS09-T7

High-stress crystal-plasticity of quartz and olivine

C. Trepmann[1]
[1]*Ludwig-Maximilians Universität München, Geo- und Umweltwissenschaften, München, Germany*

High-stress crystal-plasticity plays an important role during episodic creep in shear zones, i.e. deep continuations of seismic active fault zones. In this study, high-stress crystal-plasticity of olivine and quartz is investigated in deformation experiments performed in a triaxial solid-medium Griggs-type deformation apparatus. Peridotites experimentally deformed at temperatures of 300 and 600°C and strain rates of 10^{-4} s^{-1} show evidence of low-temperature plasticity of olivine by pronounced undulatory extinction on the light-optical scale associated with high dislocation densities at the TEM-scale. Pile-up of dislocations leads to the formation of either fracture arrays at 300°C or deformation lamellae parallel (100) at 600°C, indicating intragranular work hardening. Cellular structures characterized by domains of low dislocation densities bound by dislocation tangles are characteristic TEM-scale microstructures after deformation at 600°C. Natural vein quartz experimentally deformed at temperatures of 400°C and strain rates of 10^{-4} s^{-1} shows evidence of low-temperature plasticity by pronounced undulatory extinction and deformation bands associated with high dislocation densities, microfractures and cellular structures. The tested peridotites show a lower strength (< 2GPa) than the tested vein quartz samples (>2GPa) at comparable experimental conditions. A lower strength of olivine during dislocation glide-controlled deformation in comparison to quartz is interpreted to be related to crystallographic differences of the neosilicate olivine and the tectosilicate quartz. In nature the high-stress deformation microstructures are characteristically modified during a prolonged thermal history at low stresses. This modification is simulated in experiments by a high-temperature low-stress stage after high-stress deformation. The resulting microstructures are similar for quartz and olivine: small isometric grains without specific crystallographic relationship to the strain field or the host grains replace highly-damaged zones. Coarsening of new grains by grain boundary migration during the high-temperature low-stress stage is driven by the reduction in surface and strain energies. Extrapolation to natural conditions suggests that the observed characteristic microstructure may develop within as little as tens of years and less than ten thousands of years. These microstructures have a great diagnostic potential for past seismic activity because they are expected to be stable over geological time scales, since driving forces for further modification are not sufficient to erase the characteristic heterogeneities.

MS09-T8

Torsional deformation of calcite under high confining pressure

R. Schuster[1], R. Abart[1], E. Schafler[2], G. Habler[1]
[1]*University of Vienna, Department of Lithospheric Research, Vienna, Austria*
[2]*University of Vienna, Physics of Nanostructured Materials, Faculty of Physics, Vienna, Austria*

Torsional deformation is one of the most important methods of experimental rock deformation, where the Paterson type apparatus is the most commonly used torsional deformation machine. It allows for deformation of cylindrical samples at temperatures up to 1600 K and at pressures up to 500 MPa (Paterson & Olgaard, 2000). A different torsional deformation method that is currently hardly used in the earth sciences is High Pressure Torsion (HPT). HPT was developed in materials science to synthesize and investigate bulk nanostructured or ultrafine-grained materials. It permits deformation experiments under substantially higher pressures than the Paterson apparatus. The machine used in this study provides the possibility to perform experiments under pressures up to 8 GPa and at temperatures up to about 800 K. HPT is known from various studies, in particular on pure metals and alloys, to lead to pronounced grain refinement and to very high defect densities (Zhilyaev & Langdon, 2008). This deformation method is applied to calcite to study the microstructural evolution during deformation under pressure in the GPa range to high strains. Calcite is particularly suitable for HPT deformation, since it can be plastically deformed at relatively low temperatures and undergoes two phase transitions in the pressure range that can now be reached with HPT.

For the analysis of the grain refinement and the evolution of lattice preferred orientations due to the deformation by HPT as well as the underlying microphysical mechanisms, such as twinning and dislocation glide, that facilitate the plastic deformation both scanning electron microscopy and x-ray diffraction are used. Scanning electron microscopy, in particular Electron Backscatter Diffraction (EBSD), is utilized for the characterization of the microstructures and the investigation of the lattice preferred orientations that result from the deformation process. With EBSD both the general orientation relationships among different grains as well as the misorientations and the boundaries between neighbouring grains were investigated. It also allowed us to investigate the grain size dependence of the orientation relationships in the microstructures with a bimodal grain size distribution.

Additionally x-ray diffraction experiments were performed both in the home lab and at the synchrotron to investigate lattice preferred orientations and microstructural properties through x-ray line profile analysis. Although these measurements do not give the spatial information and the information on neighbour relationships of the grains that EBSD provides, it delivers complementary information and, due to the larger volume investigated, a better statistical reliability.

References:
Paterson M.S., Olgaard. D.L. (2000): Journal of Structural Geology, 22(9), 1341-1358
Zhilyaev A. P., Langdon T. G. (2008): Progress in Materials Science, 53(6), 893-979

MS10 – Protein function and regulation

MS10-T1

Structural and biochemical analysis of the RNA-binding protein roquin

A. Schütz[1], U. Heinemann[1]
[1]*Max Delbrück Center for Molecular Medicine, Helmholtz Protein Sample Production Facility, Berlin, Germany*

The lifespan of messenger RNAs (mRNAs) is increasingly recognized as an important determinant of gene expression levels. For example, the expression of ICOS (inducible T-cell co-stimulator), an essential receptor for follicular T-cells, is restricted by the roquin protein, which promotes the degradation of ICOS mRNA, thereby playing an important role in autoimmunity [1]. More recently, roquin proteins were reported to initiate mRNA degradation by specifically binding to a constitutive decay element (CDE) in the 3’ untranslated region (UTR) of various mRNAs, many of which encode proteins important for development as well as inflammation and immunity [2].

Roquin, also known as RC3H1 (ring finger and CCCH-type zinc finger domains 1) is a 1,133 amino-acid protein, containing a RING-type zinc finger, a roquin (ROQ) domain, a CCCH-type zinc finger, and a poorly defined C-terminal proline-rich domain. Roquin binding to CDE-like RNA stem-loop motifs was shown to be mediated by the ROQ domain [1], potentially acting together with the zinc finger [3], while the C-terminal effector domain recruits the Ccr4-Caf1-Not complex, resulting in Caf1a-dependent deadenylation and consecutive degradation of CDE-containing mRNAs [1].

We present the first crystal structure of a roquin domain, revealing a new protein fold capable of RNA-binding. By combining protein structure analysis with biochemical and mutational analyses we gain insight into the mode of RNA binding.

[1] Yu D, Tan AH, Hu X, Athanasopoulos V, Simpson N, Silva DG, Hutloff A, Giles KM, Leedman PJ, Lam KP, Goodnow CC, Vinuesa CG (2007) Roquin represses autoimmunity by limiting inducible T-cell co-stimulator messenger RNA. *Nature* 450:299-303.
[2] Leppek K, Schott J, Reitter S, Poetz F, Hammond MC, Stoecklin G (2013) Roquin promotes constitutive mRNA decay via a conserved class of stem-loop recognition motifs. *Cell* 153:869-81.
[3] Glasmacher E, Hoefig KP, Vogel KU, Rath N, Du L, Wolf C, Kremmer E, Wang X, Heissmeyer V (2010) Roquin binds inducible costimulator mRNA and effectors of mRNA decay to induce microRNA-independent post-transcriptional repression. *Nat Immunol.* 11:725-33.

MS10-T2

S-SAD structure determination of the N-terminal domain of human Prp38 reveals a novel folded domain that anchors alternative splice factors to the spliceosome

T. Schütze[1], L. Apelt[2], G. Weber[1], M. S. Weiss[3], U. Stelzl[2], M. C. Wahl[1]
[1]*Freie Universität Berlin, Laboratory of Structural Biochemistry, 14195 Berlin, Germany*
[2]*Max-Planck Institute for Molecular Genetics (MPI-MG), Otto-Warburg Laboratory, 14195 Berlin, Germany*
[3]*Helmholtz-Zentrum Berlin für Materialien und Energie, Macromolecular Crystallography (HZB-MX), 12489 Berlin, Germany*

The removal of introns from eukaryotic pre-mRNA is a crucial step in transcript maturation, which is carried out by the spliceosome. For each splicing reaction, a spliceosome is assembled *de novo* on its substrate by the stepwise recruitment of five small nuclear ribonucleoprotein particles (snRNPs) and many non-snRNP proteins [1]. Initially, the spliceosome is assembled as an inactive particle that undergoes major conformational and compositional rearrangements upon conversion to a catalytically active complex. Spliceosome activation in yeast requires the Prp38 protein [2]. While yeast Prp38 is a stable subunit of the U4/U6-U5 tri-snRNP, the human counterpart (hPrp38) joins the spliceosome independent of the tri-snRNP [3]. In addition to a yeast-like N-terminal domain (NTD), hPrp38 contains a C-terminal RS-domain, a signature of serine/arginine (SR)-rich splicing regulatory proteins. While in canonical SR proteins the RS domain is preceded by one or two RNA recognition motif (RRM) domains [4], the fold and function of the Prp38 NTD is unknown. We have obtained orthorhombic crystals of $hPrp38^{NTD}$ (179 amino acids, four cysteines, six methionines), which we used for anomalous diffraction data collection on the HZB-MX beamline BL14.2. Anomalous differences in diffraction data collected at an X-ray wavelength of 2.0 Å were used to solve the $hPrp38^{NTD}$ structure *via* S-SAD. The core of $hPrp38^{NTD}$ is formed by stacked pairs of anti-parallel alpha-helices connected by long β-hairpins. Using a comprehensive yeast 2-hybrid (Y2H) library of human spliceosomal proteins [5], we identified twelve splicing factors, including several proteins implicated in alternative splicing decisions, that interact with $hPrp38^{NTD}$, and mapped four distinct interaction sites using a surface-scanning Y2H approach. Our results suggest that hPrp38 is an unusual SR-protein, whose NTD serves as an interaction hub that recruits splicing regulatory proteins to influence the functional pairing of splice sites.

References:

[1] Wahl MC, Will CL, Luhrmann R. The spliceosome: design principles of a dynamic RNP machine. Cell 2009;136:701-18.
[2] Xie J, Beickman K, Otte E, Rymond BC. Progression through the spliceosome cycle requires Prp38p function

for U4/U6 snRNA dissociation. The EMBO journal 1998;17:2938-46.
[3] Agafonov DE, Deckert J, Wolf E, Odenwalder P, Bessonov S, Will CL, et al. Semiquantitative proteomic analysis of the human spliceosome via a novel two-dimensional gel electrophoresis method. Molecular and cellular biology 2011;31:2667-82.
[4] Long JC, Caceres JF. The SR protein family of splicing factors: master regulators of gene expression. The Biochemical journal 2009;417:15-27.
[5] Hegele A, Kamburov A, Grossmann A, Sourlis C, Wowro S, Weimann M, et al. Dynamic protein-protein interaction wiring of the human spliceosome. Molecular cell 2012;45:567-80.

MS10-T3

Crystal structure of Muskelin's Discoidin and LisH-domain provides the basis to understand the mechanism and impact of its oligomerization

C. Delto[1], F. Heisler[2], J. Kuper[1], M. Kneussel[2], H. Schindelin[1]
[1]*Rudolf Virchow Center, University of Würzburg, Structural Biology, Würzburg, Germany*
[2]*University of Hamburg Medical School , Center for Molecular Neurobiology (ZMNH) , Hamburg, Germany*

Muskelin is a ubiquitously expressed multi-domain protein involved in a diverse set of cellular functions, among them the regulation of the intracellular transport of ionotropic GABA$_A$ receptors containing the α1-subunit. It has a unique domain composition, consisting of an N-terminal Discoidin domain followed by a Lis1-homology (LisH) domain, a C-terminal to LisH (CTLH) domain, a Kelch-repeat domain with six repeats of the kelch motif and a non-annotated C-terminal module. Muskelin so far was rather poorly characterized with no structural information available at all.

We solved the first crystal structure of an N-terminal fragment of muskelin, comprised of its Discoidin and LisH domains. Phasing was accomplished via a single-wavelength anomalous diffraction experiment using muskelin’s intrinsic sulfur atoms with tetragonal crystals featuring one molecule in the asymmetric unit, however, the structure could not be successfully refined. A slight truncation of the N-terminus resulted in orthorhombic crystals containing a homodimer in the asymmetric unitwhich could be easily refined to final R-values of R=0.1562 and R_{free}=0.1931. The crystal structure formed the basis for an extensive analyses of muskelin’s oligomerization. These studies finally revealed that muskelin’s oligomerization determines its sub-cellular localization, providing vital information about a putative regulation of muskelin’s function.

MS10-T4

Crystal structure of AibA/AibB, a novel decarboxylase in alternative myxobacterial isovalerate biosynthesis

T. Bock[1], E. Luxenburger[2], R. Müller[2], W. Blankenfeldt[1]
[1]*Helmholtz Centre For Infection Research, Structure and Function of Proteins, Braunschweig, Germany*
[2]*Helmholtz Institute for Pharmaceutical Research Saarland, Microbial Natural Products, Saarbrücken, Germany*

Myxobacteria are of great pharmaceutical interest due to their ability to produce a large spectrum of secondary metabolites with conceivable antibiotic activity. A number of myxobacterial metabolites are produced from the common precursor isovaleryl CoA, which is normally derived from the degradation of leucine. Facing harsh conditions or leucine starvation an alternative pathway starting with acetoacetyl CoA is used. This pathway branches from the well-known mevalonate biosynthesis. It includes, in addition to three characterized proteins, a so far unknown protein complex assigned to AibA/AibB, which was based on sequence alignment annotated as a CoA-transferase (1). However, Li and coworkers clearly demonstrated that AibA/AibB is indeed a decarboxylase that converts 3-methylglutaconyl CoA to 3,3-dimethylacrylyl CoA. This leads to questions about the mechanism of this reaction (2).

Here we report the expression, purification, crystallization and structure determination of the heterodimer AibA/AibB. Using our tailor made plasmid p10$ and the commercially available pET26b, the two proteins were recombinantly co-expressed in *E. coli* and purified to homogeneity by a three step purification protocol. Crystals were obtained using a surface-engineered AibA/AibB and diffraction data were collected. The structure was solved using anomalous diffraction of a mercury derivative and has been refined to a resolution of 1.4 Å. The heterodimer shows a typical CoA-transferase-like fold and is arranged as a dimer of heterodimers within the crystal and in solution. The interface of the AibA and AibB subunit forms a mainly hydrophobic funnel pointing towards cysteine 56, which has been identified as required for catalysis (2). Interestingly, this cysteine is replaced by a conserved glutamic acid in other, structurally similar CoA-transferases, corroborating its importance in the different catalytic mechanism of AibA/AibB (2).

In order to get closer insights into the catalytic mechanism of this novel decarboxylase, further crystallographic as well as biochemical experiments are in progress.

References:
1) H. B. Bode, M. W. Ring, G. Schwär, M. O. Altmeyer, C. Kegler, I. R. Jose, M. Singer, R. Müller (2009) ChemBioChem 10: 128-140.
2) Y. Li, E. Luxemburger, R. Müller (2012) Angew. Chem. Int. Ed, 52: 1304-1308.

MS10-T5

Structural basis for a Kolbe-type decarboxylation catalysed by a glycyl radical enzyme

B. Selvaraj[1], M. Blaser[2], M. Feliks[3], G. M. Ullmann[3], T. Selmer[4,5], W. Buckel[2,5], B. M. Martins[1]
[1]*Humboldt-Universität zu Berlin, Strukturbiologie/Biochemie, Berlin, Germany*
[2]*Max-Planck-Institu Terretrische Mikrobiologie, Marburg, Germany*
[3]*Universität Bayreuth, Bayreuth, Germany*
[4]*Fachhochschule Aachen-Jülich, Jülich, Germany*
[5]*Philipps-Universität Marburg, Marburg, Germany*

4-Hydroxyphenylacetate decarboxylase (4Hpad: E.C. 4.1.1.83) is a structurally more complex glycyl radical enzyme with an extra small subunit essential for catalysis that binds two Fe/S clusters. Furthermore, the respective activating-enzyme (AE) contains an additional 50-60 amino acid insert after the SAM-binding cluster motif (CX_3CX_2C) with two ferredoxin $CX_2CX_2CX_3C$ patterns suggesting the binding of up to two additional Fe/S clusters most likely of cubane type. Albeit extensive studies, the understanding of how the GRE family, and especially the new subclass of *Fe/S cluster containing GREs* regulate the generation and reactivity of the functional radical dyad at a molecular level is still poor. Moreover, the functional roles of the additional small subunit and extra Fe/S cluster(s) in the AEs are not completely understood. 4-Hydroxyphenylacetate decarboxylase catalyzes the last reaction in the fermentative production of *p*-cresol (4-methylphenol) from tyrosine in clostridia. *p*-Cresol is a virulence factor of the human pathogen *Clostridium difficile*. The decarboxylase component is a functional $(\beta\gamma)_4$ heterotretramer (~ 440 kDa) composed of a 100 kDa catalytic β-subunit harboring the glycyl/thiyl active radical dyad and a small 9.5 kDa γ-subunit binding two [4Fe-4S] cluster. We have solved the crystal structures of wild-type and variants of 4Hpad from *C. scatologenes* with and without substrate-bound between 2.1 and 1.75 Å resolution. These are the first structures of a Fe/S clusters containing glycyl radical enzyme and provide unexpected insights into its mechanism. The structures show a $(bg)_4$ tetramer of heterodimers composed of a catalytic b-subunit harboring the putative glycyl/thiyl dyad and a distinct small g-subunit with two [4Fe-4S] clusters at 40 Å distance from the active site. The g-subunit comprises two domains displaying pseudo-twofold symmetry that are structurally related to the [4Fe-4S] cluster-binding scaffold of high-potential iron-sulfur proteins. The N-terminal domain coordinates one cluster with 1 histidine and 3 cysteines and the C-terminal domain coordinates the second cluster with 4 cysteines. The N-terminal cluster is directly involved in the complex interface and the C-terminal cluster is buried in the (bg) heterodimer interface. In contrast to expectation, the substrate-bound state shows a direct interaction between the substrate's carboxyl group and the putative active site Cys503 residue, while His536 and Glu637 at the opposite side of the active site pocket anchor the hydroxyl group. This state captures a possible catalytic competent complex and suggests a Kolbe-type decarboxylation for *p*-cresol formation.

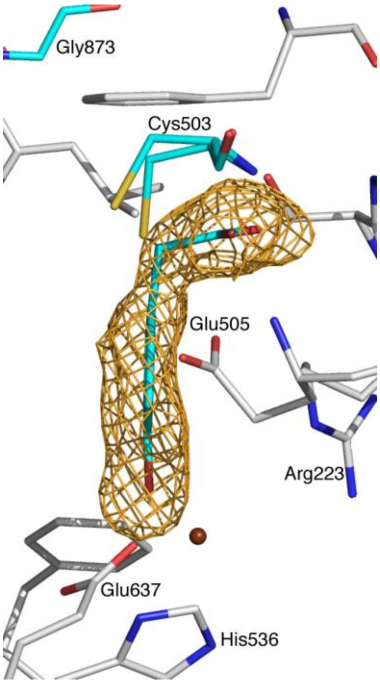

fig.: 1: Active site with 4-hydroxyphenylacetate bound. Yellow mesh: omit F_{obs}-F_{cal} map contoured at 0.35/Å.

MS10-T6

Structural and chemical transformation of the [4Fe3S]-cluster in the oxygen-tolerant [NiFe] hydrogenase of *Ralstonia eutropha*

A. Schmidt[1], J. Kalms[1], P. Scheerer[1]
[1]*Charite-Universitätsklinikum, Institute for medical physics and biophysics, Berlin, Germany*

Since hydrogen is one of the most promising clean energy carrier for the future, hydrogenases are on special interest for science as well as for industry. Still today the major part of the hydrogen production is based on fossil fuels, thus coupled with the pollution of carbon dioxid. The enzymatic H_2-production is an auspicious and clean alternative provided by nature. Hydrogenases are metallo-enzymes that catalyze the interconversion of hydrogen into two protons and two electrons. To use hydrogenases as a tool e.g. in renewable energy technologies, the retention of their activity in the presence of O_2 is required [1]. We investigate via protein X-ray crystallography the membrane-bound [NiFe] hydrogenase (MBH) from *Ralstonia eutropha*, belonging to a small subgroup of hydrogenases, which have evolved this feature. The MBH consists of a large subunit bearing the [NiFe] active site and a small subunit containing three different [FeS] clusters that direct electron flow to the respiratory chain (**Fig.1**). In case of MBH, O_2-tolerance mainly relies on the exceptional redox-properties of a unique six cysteine coordinated [4Fe3S]-cluster located proximal to the active site [2]. This novel [4Fe3S]-cluster operates as an electronic switch depending on the nature of the gas molecule entering the active site. Redox-dependent structural and chemical rearrangements in the cluster enable the bidirectional transfer of two electrons within a physiologically relevant potential range [3]. Compared to the four cysteine coordinated proximal [4Fe4S]-cluster in O_2-sensitive hydrogenases, the scaffold of the [4Fe3S]-cluster of MBH shows two additional cysteines, C19^S and C120^S. A double-mutation at the two cysteines to glycine (G) leads to a “standard cubane” cluster found in O_2-sensitive hydrogenases such as *Desulfovibrio vulgaris* Miyazaki F and an inactivation by dioxygen [4]. Structural changes at the cluster scaffold due to mutations of these two coordinating cysteines were examined under aerobic and anaerobic conditions. Single- and double-mutations at either C19^S or/and C120^S show similarities to O_2-tolerant hydrogenases for C120^{S}G and O_2-sensitive hydrogenases for C19^{S}G and C19^{S}G/C120^{S}G. The structures indicate that the additional cysteines are important for cluster stability and architecture, thus O_2-tolerance.

References:
Fritsch J, Lenz O, and Friedrich B (2013) NatRevMicrobiol. *2*, 106-114.
Fritsch J*, Scheerer P*,§, Frielingsdorf S, Kroschinsky S, Friedrich B, Lenz O§, Spahn CMT§ (2011) Nature *479 (7372)*, 249-52.
Frielingsdorf S, Fritsch J, Schmidt A, Hammer M, Löwenstein J, Siebert E, Pelmenschikov V, Jaenicke T, Kalms J, Rippers Y, Lendzian F, Zebger I, Teutloff C, Kaupp M, Bittl R, Hildebrandt P, Friedrich B, Lenz O§, and Scheerer P§. (2013) *in revision*.
Goris, T., Wait, AF., Saggu, M., Fritsch, J., Heidary, N., Stein, M., Zebger, I., Lendzian, F., Armstrong, FA., Friedrich, B.&Lenz, O. (2011). A unique iron-sulphur cluster is crucial for oxygen tolerance of a [NiFe]-hydrogenase. NatChemBiol. *5*, 310-318.

Figure 1

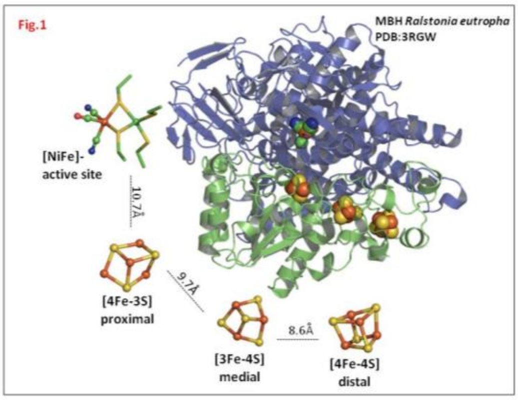

MS11 – Synchroton opportunities and challenging structure determinations II (Other)

MS11-T1

Mesoscopic relaxations in nanoscale systems: Experimental verification by surface x-ray diffraction and x-ray absorption spectroscopy

H. Meyerheim[1], V. S. Stepanyuk[1], O. Brovko[1], J. Kirschner[1,2]
[1]*MPI Halle, Halle, Germany*
[2]*Institut f. Physik, Martin-Luther-Univ., Halle, Germany*

Nanosized systems often exhibit strongly modified atomic structures and physical properties. Quite a while ago theory has predicted that in metallic nanoislands of 1 to 2 nm in diameter and monoatomic thickness (approx. 20-40 atoms) substantial atomic relaxations are induced involving contraction of the interatomic distance by up to 10% relative to the bulk distance [1]. In this study we report on direct experimental observations [2, 3, 4] which have confirmed theoretical predictions, clearly showing that mesoscopic relaxations are important and are also responsible for substantial modifications of the electronic, magnetic and geometric properties of nanostructures.

Experimental verifications of the bond length contraction within monoatomic nanoislands were carried out for a prototype heteroepitaxial [Co/Cu(001)] and homoepitaxial surfactant [Fe/O/Fe(001)-p(1x1)] adsorption system. Surface x-ray diffraction (SXRD) [2,4] and polarization dependent surface x-ray absorption fine structure (SEXAFS) measurements [3] were used for the structure analysis. While SXRD probes the relative misfit induced shift of the adatoms out of the substrate hollow sites by accurate determination of the atomic displacement factor, SEXAFS is directly sensitive to the local structure in terms of interatomic distance (R) and effective coordination number (N*).

Experiments accurately confirm theoretical predictions. For instance, in Co nanoislands on Cu(001) the nearest neghbour distance (RCo) is equal to RCo=0.245 (2) nm as compared to RCo=0.251 nm in bulk Co. In the more complex surfactant system Fe/O/Fe(001) also the adsorption height of oxygen atoms above the plane of Fe atoms was found to be affected by the Mesoscopic Misfit [4]. While it is 0.04 nm on flat large Fe(001) terrace (left side of Fig.1), it is 0.07 nm on the mesoscopic misfitted Fe islands (right side of Fig.1). This goes in parallel with a reduced Fe-Fe interlayer spacing [d=0.162 nm for O/Fe(001) in the case of a large Fe(001) terrace and d=0.143 nm in the case of Fe nanosilands, see Fig.1]. Our results provide a straightforward explanation for the oscillating surface magentic moment with Fe coverage observed by second harmonic generation experiments [5].

References:
[1] V. S. Stepanyuk, D. I. Bazhanov, A. N. Baranov, W. Hergert, P. H. Dederichs, and J. Kirschner, Phys. Rev. B 62, 15398 (2000)
[2] O. Mironets, H. L. Meyerheim, C. Tusche, V. S. Stepanyuk, E. Soyka, P. Zschack, H. Hong, N. Jeutter, R. Felici and J. Kirschner, Phys. Rev. Lett. 100, 096103 (2008)
[3] H. L. Meyerheim, E. D. Crozier, R. A. Gordon, Q. F. Xiao, K. Mohseni, N. N. Negulyaev, V. S. Stepanyuk, and J. Kirschner, Phys. Rev. B 85, 125405 (2012)
[4] W. Feng, H.L. Meyerheim, K. Mohseni, O. Brovko, V.S. Stepanyuk, N. Jedrecy, R. Felici, and J. Kirschner, Phys. Rev. Lett. 235503 (2013)
[5] M. Nyvlt, F. Bisio, J. Franta, C.L. Gao, H. Petek, and J. Kirschner, Phys. Rev. Lett. 95, 127201 (2005)

Figure 1

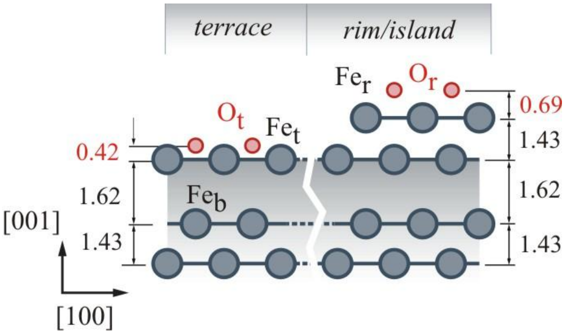

MS11-T2

Submicrosecond X-ray Crystallography: New Technique, Challenges and Opportunities

S. Gorfman[1], M. Ziolkowski[1], H. Choe[1], M. al Taani[1], U. Pietsch[1]
[1]*University of Siegen, Physics, Siegen, Germany*

Investigation of structural dynamics of crystals under external perturbation is one of the major challenges for modern X-ray structure analysis. The interest to structural dynamics is motivated by both fundamental and material sciences, since sensitivity of a structure to a perturbation predefines the number of macroscopic physical properties. In this work we developed the method and data-aquisition system (DAQ) for a broad range of time-resolved diffraction experiment with a point detector. It applies to probing the reversible submicro-, micro- or millisecond dynamics under periodically modulated external electric field such as a) dynamics of domains in ferroelectrics and multiferroic; b) piezoelectrically induced elastic vibrations; c) dynamics of field induced phase transitions, etc. The DAQ is constructed on the basis of a Field Programmable Gate Array (FPGA-board), which distributes the point detector signals in 10000 time channels, synchronized with an applied electric perturbation. It allows for a flexible change of the channel width (> 100 ns), i.e. the time resolution of the experiment.

We will demonstrate *in-situ* X-ray diffraction study of resonance-enhanced vibrations of α-quartz (the figure above shows the example: -3 2 0 Bragg rocking curve collected while the crystal was vibrating at the resonance frequency). The position, width and integrated intensity of the rocking curve can be extracted, thus the dynamics of elastic deformation, mosaicity and atomic position can be analyzed as a function of time and applied electric field. We will also present the time-resolved diffraction study of domain switching in uniaxial ($Sr_{0.5}Ba_{0.5}Nb_2O_6$) ferroelectric under alternating electric field. The dynamics of field induced Bragg peak splitting and dispalcements quantifies lattice and domains contribution into the piezoelectric deformation in ferroelectris. Finally, we used the DAQ to reveal the ferroelectric switching in magnetite (Fe_3O_4) below the Verwey transition temperture. We applied 1 kHz periodic electric field field: the single period included two 10 ms switching pulses and two longer periods without voltage. The small intensity contrast (the contrast between the Friedel pairs) between the two zero-field periods (straight after positive and after negative pulses) was observed.

Figure 1

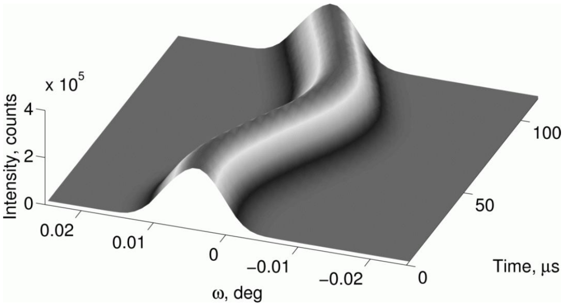

MS11-T3
Coherent diffraction imaging from semiconductor nanowires

A. Davtyan[1], A. Biermanns[1], O. Loffeld[1], U. Pietsch[1]
[1]*University of Siegen, Siegen, Germany*

The distribution of rotational twins within single semiconductor nanowires (NWs) has been studied using the nanobeam x-ray diffraction setup at ID1 beamline at ESRF [1]. Together with planar stacking faults, twins are the major defects in NWs. Their detailed analysis is crucial for the control of electronic and optical properties of future NW-devices. Coherent x-ray diffraction imaging (CDI) using a nano-focussed synchrotron beam provides a destruction free probe of the defect structure. However, as x-rays probe intensity distributions in reciprocal space, the electron density distribution in real space can only be accessed using an iterative inversion of the diffraction pattern using phase retrieval algorithms. In case of a highly defective NW structure, this approach is challenging as the planar defects lead to a complex speckle pattern along certain directions in reciprocal space (fig 1a), whose inversion has up to now not been shown. Here, we present a novel approach to retrieve the arrangement of twin domains within single GaAs nanowires. For this purpose we apply a combination of the phase retrieval algorithms and methods such as Error-Reduction (ER), Hybrid Input-Output (HIO) and Shrink Wrap (SW)[2, 3]. In addition, we consider the fact that the nanowire of finite size has constant density and is structurally homogeneous perpendicular to the growth axes. Therefore, the NW can be modeled by a number of phase domains with a relative phase change of and to each other (fig 1b). Probing about 10^4 different trial phases the arrangement and the length of particular phase segments is different but the average number of phase changes is rather constant (fig. 2). This leads to the conclusion that one can determine the defect density by CDI but still not the detailed phase arrangement. In present case the calculated defect density is 0.216 defects/nm.

References
1. Biermanns, A., et al., *Individual GaAs nanorods imaged by coherent X-ray diffraction.* Journal of Synchrotron Radiation, 2009. 16: p. 796-802.
2. Marchesini, S., et al., *X-ray image reconstruction from a diffraction pattern alone.* Physical Review B, 2003. 68(14).
3. Fienup, J.R., *Phase retrieval algorithms: a personal tour.* Applied Optics, 2013. 52(1): p. 45-56.

Figure 1

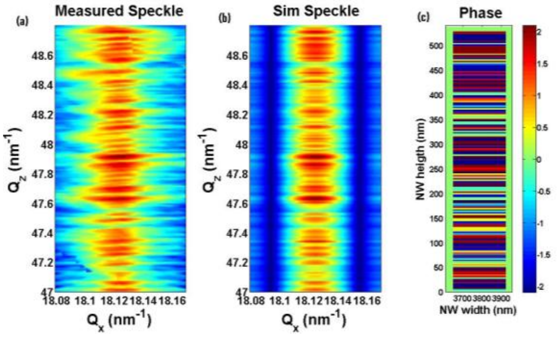

Figure 2

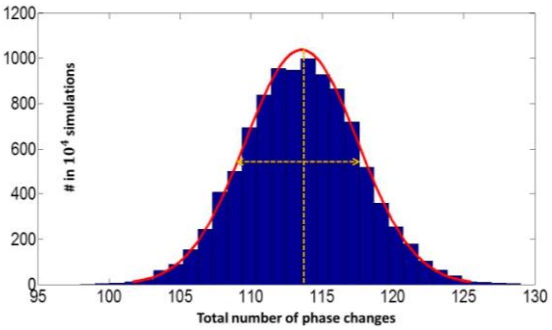

MS11-T4

Temperature-driven growth of ultra-small ZnO nanoparticles

R. Neder[1], H. Chatterjee[1], K. Datta[1]
[1]*Universität Erlangen, Kristallographie, Erlangen, Germany*

Temperature driven growth of ZnO nanoparticles (< 2 nm), stabilized by organic ligands, was followed by studying pair distribution functions (PDF) obtained from fast in-situ high energy x-ray powder diffraction experiments. PDFs of the nanoparticles were modelled as a function of temperature in order to extract development of structural parameters on the onset of temperature. It was noticed that nanoparticles start to grow bigger slowly until around 600 K, however, after that when most of the organics went off the surface, the process of coalescence became much faster. Besides, an apparent decrease in the unit cell volume of the Wurtzite type structure was seen with the increase of temperature, where Zn moves to a more symmetric position with respect to oxygens. Significant differences exist in the temperature dependent behavior for different ligand molecules.

MS11-T5

Combination of TEM and microfocus synchrotron diffraction for the structure determination of micro- and nanocrystalline materials

F. Fahrnbauer[1], T. Rosenthal[2], A. Marchuk[2], P. Urban[1], G. Wagner[1], W. Schnick[2], O. Oeckler[1]
[1]*Leipzig University, IMKM, Leipzig, Germany*
[2]*University of Munich (LMU), Department of Chemistry, Munich, Germany*

Solid-state syntheses which involve quenching melts or high-pressure conditions often lead to inhomogeneous microcrystalline samples that contain unknown and intriguing structures.[1,2] Multinary systems with nanoscopic heterostructures are also favorable for applications, e. g. as thermoelectrics.[3] Such samples cannot be studied efficiently by conventional X-ray methods, whereas electron crystallography often lacks the precision required for a detailed analysis of structure and bonding.

Selected-area electron diffraction (SAED) and X-ray spectroscopy (EDX) are ideal for the discovery of new microcrystalline compounds - especially side phases or components heterostructures. SEM images of TEM sample grids facilitate the optical recovery of pre-selected crystallites. Using sub-micron synchrotron beams (ID11, ESRF, Grenoble), complete single-crystal datasets can be collected after locating and centering the crystals characterized by TEM by means of fluorescence line-scans. This approach proved successful in a broad range of different material classes which include:

1.) $(Ca,Mg)_7P_{18}ON_{34}$ is a novel oxonitridophosphate that has been obtained as a microcrystalline side-phase in high-pressure synthesis. It consists of a hexagonal network with channels of corner-sharing PN_4 tetrahedra and Ca/Mg ions for charge compensation.

2.) The novel sulfide telluride $Pb_8Sb_8S_{15}Te_5$, a side phase in quenched melts of "$Pb_5Sb_4S_6Te_5$", is isostructural to Tl_3PbCl_5. It exhibits chains of distorted, single-side capped "heterocubane-like" units. The structure model ($P4_1$, a = 8.0034(11) Å, c = 15.022(3) Å, R_{int} = 0.040, R1 = 0.043) is as precise as structure determinations by standard single-crystal methods using macroscopic crystals. The atom distribution could be confirmed by bond-valence calculations as well as by the simulation of high-resolution electron micrographs.

3.) Metastable layered Ge/Sb/Te materials were analyzed by irradiating very small well-crystallized parts of poor platelet-shaped crystals. For example, the structure of $Ge_{3+x}Sb_{2-x}Te_6$ can be refined with R1 = 0.049. It is characterized by rocksalt-type slabs with van der Waals gaps between two anion layers.

4.) In heterostructures of skutterudite-type precipitated in a Ge/Sb/Te matrix, single-crystal data of both components were measured at the edge of an Ar-ion thinned sample. The matrix consists of rocksalt-type $(GeTe)_{10.5}Sb_2Te_3$ (R1 = 0.020) with Ge, Sb and vacancies randomly distributed over the cation position. The skutterudite-type precipitates $CoSb_2(GeTe)_{0.5}$ (R1 = 0.032) show a pronounced distortion of the characteristic Sb_4 units. No residual electron density could be found in the structural voids, so substitution effects do only take place on the anion position.

[1] S. J. Sedlmaier, J. Schmedt auf der Günne, W. Schnick, *Dalton Trans.* 2009, 4081-4084.
[2] E. Mugnaioli, S. J. Sedlmaier, O. Oeckler, U. Kolb, W. Schnick, *Eur. J. Inorg. Chem.* 2012, 121-125.
[3] K. F. Hsu, S. Loo, F. Guo, W. Chen, J. S. Dyck, C. Uher, T. Hogan, E. K. Polychroniadis, M. G. Kanatzidis, *Science* 2004, *303*, 818-821.

MS11-T6

Synchrotrons, pixel detectors and diffuse scattering - a great team for real structure determination

T. Weber[1]
[1]*ETH Zurich, Materials , Zurich, Switzerland*

Requirements for obtaining high quality diffuse scattering data sets for real structure investigations go far beyond the capabilities of standard in-house diffractometers. The locally very weak diffuse scattering is sensitive to artifacts and background scattering, it is measured next to strong Bragg reflections and the profiles of the diffuse features must be determined with high accuracy since they carry substantial structural information. Usage of synchrotron radiation is therefore a prerequisite for measuring high quality diffuse scattering data sets. In the past, however, the outstanding properties of synchrotron radiation could not be fully exploited, because popular area detectors like image plates or CCDs are not designed to support the diffuse scattering requirements in synchrotron experiments. Read-out times of image plates are one to two orders of magnitude longer than typical synchrotron exposure times and CCDs show significant intrinsic background that is frequently in the magnitude of the diffuse intensity. In addition, both detector types are very sensitive to overexposures from strong Bragg peaks. Modern pixel detectors like the Pilatus are able to overcome most of the problems. They are very fast, they have a large dynamic range, the detector intrinsic resolution function is only one pixel broad even in the case of strong overexposures and they allow suppression of fluorescence scattering. The latter is very crucial for the investigation of disorder in metallic compounds.

In this contribution we will show examples of diffuse scattering experiments, where the combination of synchrotron radiation with Pilatus detectors allowed obtaining structural information that was not accessible before. With the examples we will introduce new modeling techniques and computer programs for analyzing diffuse scattering.

MS12 – Inorganic structural chemistry – synthesis, structure, properties and applications II

MS12-T1

Polymorphism of dolomite-type structures: The C2/c high-pressure form of $BaMg(CO_3)_2$

R. Miletich[1], T. Pippinger[1], G. Hofer[1], H. Effenberger[1]
[1]*Universität Wien, Institut für Mineralogie und Kristallographie, Wien, Austria*

Within the scope of a better understanding of the global carbon cycles, carbonate minerals and their structure-property relationships are currently in the focus of ongoing studies at non-ambient conditions. The double carbonate norsethite, $BaMg(CO_3)_2$ (space group R-32/*c*, Z = 6, *a* = 5.0212 Å and *c* = 33.581 Å), crystallizes in a structure type related to that of dolomite with the Ba atoms in a *di*trigonal prismatic [6+6] and the Mg atoms in an octahedral coordination. Synthetic single crystals have been investigated by means of in-situ high pressure X-ray diffraction and Raman spectroscopy using the diamond-anvil cell technique. Static compression reveals a first-order phase transition appearing between 2.28 and 2.36 GPa according to a trigonal-to-monoclinic structural transition (2 1 0 / 0 1 0 / -⅔ -⅓ ⅓). The high-pressure phase crystallizes in space group *C*2/*c*, Z = 4, *a* = 8.647 Å, *b* = 4.909 Å, *c* = 10.785 Å, ß = 105.57°, *V* = 440.96 $Å^3$ (at 6.53 GPa). Fitting the equation of state to the obtained volume data the compressibility appears equal for both forms considering some apparent elastic softening for the high-pressure form (bulk moduli: K_0= 64.6 GPa, dK/dP=4 and K_0= 41.9 GPa, dK/dP=6.1). The axial compressibilities reveal a remarkable anisotropy: the *c*-axis becomes the softest, a higher compressibility of the *b*-axis in comparison to the *a*-axis is observed. This behavior could be related to the displacement of the Ba atoms along the two-fold axis. The transformation from space-group symmetry *R*-32/*c* to that of *C*2/*c* was investigated by in-situ high-P/T Raman spectroscopy up to 550 K and 5 GPa, the phase boundary between the low- and high-P form could be established in the P,T space with a distinct positive slope.

MS12-T2

Temperature dependent X-ray diffraction study of the transformation of studtite, $UO_4 \cdot 4\ H_2O$, to metastudtite, $UO_4 \cdot 2\ H_2O$

J. D. Bauer[1], S. Labs[2], B. Winkler[1], H. Curtius[2], D. Bosbach[2]
[1]*Goethe-Universität Frankfurt am Main, FB Geowissenschaften, Abt. Kristallographie , Frankfurt am Main, Germany*
[2]*Forschungszentrum Jülich GmbH, Inst. f. Energie- und Klimaforschung - Nukleare Entsorgung (IEK-6), Jülich, Germany*

The minerals studtite ($UO_4 \cdot 4\ H_2O$) and metastudtite ($UO_4 \cdot 2\ H_2O$) are the only naturally occurring peroxide minerals. The combination of slow flowing groundwater and a high alpha dose rate can lead to formation of enough H_2O_2 to trigger a reaction with UO_2 [1], the major component in spent nuclear fuel (SNF), even if overall conditions are reducing. Studtite could therefore form as a secondary uranium phase in a deep geologic repository for nuclear waste. Studtite and Metastudtite have been identified by Hanson et al. [2] in corrosion experiments on SNF. Taking data on these secondary phases into consideration can strongly benefit the long-term safety assessment of a final repository. Most studies on mineral reactions in nuclear waste repositories after an accidental water intrusion emphasize the role of the silicates, oxides and oxyhydroxides. However, Forbes et al. [3] were able to demonstrate that some of the phases formed initially are susceptible to an alteration to studtite. However, little data on the phase transition from studtite to metastudtite and further to amorphous UO_3 is available and the relevant mechanisms have not been investigated in any detail. Rey et al.[4] investigated the thermal decomposition of uranium peroxide with DSC-TG measurements and determined the reaction $UO_4 \cdot 4\ H_2O \rightarrow UO_4 \cdot 2\ H_2O$ (studtite to metastudtite) to take place at 353 K, while the decomposition, $UO_4 \cdot 4\ H_2O \rightarrow UO_3 \cdot x\ H_2O$ (x <2) occurred at 523 K.

X-ray diffraction pattern were collected in the temperature range 303 - 527 K, covering the transition from studtite to metastudtite as well as the subsequent amorphization. We show that the reaction already starts at 311 K. At T > 329 K studtite can no longer be detected in the pattern. The dimensions of the unit cell of studtite change only slightly during the heating process. The structure of studtite is characterized by long chains of edge-sharing $[UO_8]$-polyhedra, which are connected via the peroxide groups. These chains are oriented parallel to the c-axis. They remain essentially unchanged during the transition into metastudtite and are responsible for the negligible thermal expansion along the c-axis. The elongation of the a-axis can be explained by the strong increase of the thermal motion of the crystal water, which is located between the chains. The lattice parameters of metastudtite [5] above 333 K are insensitive to a further temperature increase and remain essentially constant until the amorphization process starts.

Financial support from BMBF, Germany, grants 02NUK019C and 02NUK019E is gratefully acknowledged.

References:

[1] K.-A. Kubatko et al. *Science* 2003, 302, 1191-1193
[2] B. Hanson et al. *Radiochim. Acta* 2005, 93, 159-168
[3] T. Forbes et al. *Amer. Min.* 2011, 96, 202-206
[4] A. Rey et al. *J. Nucl. Mater.* 2009, 385, 467-473
[5] P. Weck et al. *Dalton Trans.* 2012, 41, 9748-9752

MS12-T3

Determination of the nuclear and magnetic structure of $HoNi_2B_2C$ at room temperature and 2.2 K

K. Friese[1], V. Hutanu[2], M. Meven[2], A. Sazonow[2], O. Zaharko[3]
[1]Research Centre Jülich GmbH, Jülich Centre for Neutron Science 2, Jülich, Germany
[2]RWTH Aachen University, Institute for Crystallography, JCNS Outstation, Garching, Germany
[3]Paul Scherrer Institut, Villingen, Switzerland

Quarternary intermetallics of general composition $LnNi_2B_2C$ (Ln = La - Lu) have arisen much interest due to their superconducting and magnetic properties. Their structures are described in the literature in the tetragonal space group *I*4/*mmm* with lattice parameters $a_{\text{tet}} = b_{\text{tet}} \approx$ 3.5 Å and $c_{\text{tet}} \approx$ 10.5 Å [1]. Much attention has been focused on $HoNi_2B_2C$ due to its complex behaviour at low temperatures. The compound becomes superconducting at ~ 8 K, then reenters the normal state at ~ 5 K and becomes superconducting again at lower temperatures [2-3]. Below 8 K magnetic peaks develop indicating the co-existence of a commensurate antiferromagnetic structure and an incommensurate spiral state. An additional incommensurate magnetic phase develops at 6.25 K. Below ~5 K the incommensurate magnetic phases are suppressed and only the commensurate antiferromagnetic phase is observed.

We investigated the nuclear and commensurate magnetic structure of $HoNi_2B_2C$ at room temperature and 2.2 K, respectively, with x-ray and neutron diffraction, as well as spherical neutron polarimetry. Neutron measurements were performed on the 4-circle single crystal diffractometer HEiDi [4] and the polarized neutron single crystal diffractometer POLI [5] at MLZ in Garching. X-ray diffraction data were measured in-house using a STOE IPDS II diffractometer.

Refinements of the room temperature in different space groups were performed with the program Jana2006 [6], taking into account x-ray and neutron single crystal data simultaneously. A detailed comparison of the results showed the polar space group *I*4*mm* to be the best choice. The main difference in the structure with respect to previously published models is the significant displacement of the Ni and C atom from the mirror plane perpendicular to the *c* axis.

In the neutron data of the magnetically ordered phase at 2.2 K reflections $h + k + l = 2n + 1$ are clearly visible. Several trial refinements using different magnetic space groups were carried out and showed the magnetic space group $Cmm'2'$ ($a_{\text{ortho}} \approx b_{\text{ortho}} \approx \sqrt{2}\, a_{\text{tet}} \approx 4.97$ Å, $c_{\text{ortho}} \approx c_{\text{tet}} \approx 10.52$ Å) to be the best choice. The magnetic moments of Ho (refined to 7.98(10) μ_B) are coupled ferromagnetically in the *a*,*b* plane forming ferromagnetic sheets which are then stacked antiferromagnetically along the *c* axis. Spherical neutron polarimetry measurements show that the spins of Ho are aligned in the [110] direction.

[1] T. Siegrist, H. W. Zandbergen and R. J. Cava, Nature 367, 254 (1994).
[2] H. Eisaki, H. Takagi, R. J. Cava *et al.*, Phys. Rev. B 50, 647 (1994).
[3] J. W. Lynn, S. Skanthakumar, Q. Huang *et al.*, Phys. Rev. B 55, 6584 (1997).
[4] M. Meven, V. Hutanu and G. Heger, Neutron News 18, 19 (2007).
[5] V. Hutanu, M. Meven, E. Lelièvre-Berna and G. Heger, Physica B 404, 2633 (2009).
[6] Jana2006 - Computer Program, V. Petricek, M. Dusek, L. Palatinus, Institute of Physics, Prague, Czech Republic.

MS12-T4

Synthesis and characterisation of (La,Pr) monazite solid solution series

A. Hirsch[1], A. Neumann[1], A. Wätjen[2], J. Heuser[3], A. Thust[4], L. Peters[1], G. Roth[1]
[1]RWTH Aachen University, Institute of Crystallography, Aachen, Germany
[2]RWTH Aachen University, Institute of Mineral Engineering, Aachen, Germany
[3] Forschungszentrum Jülich GmbH, Institute for Energy and Climate Research IEK-6 Nuclear waste waste management , Jülich, Germany
[4]Goethe University Frankfurt am Main, Department of Geosciences, Frankfurt am Main, Germany

Monazite type ceramics are investigated for their application as a ceramic storage for nuclear waste forms, because natural monazite is known to be a host mineral for radioactive elements like U and Th without becoming metamict due to radiation damage. In this context, a solid solution series of $(La,Pr)PO_4$ was synthesised and characterised. La and Pr were used as surrogates for the minor actinides Am, Cm and Np, which pose a particular problem to safe long term storage due to their long half-life.

For the solid solution of (La,Pr) monazites, powder samples were prepared in a similar way to [1]. Ln_2O_3 were mixed with $NH_4H_2PO_4$ in excess. Powders were ground, pressed, and heated for one day at 1250 °C in air.

Powder X-ray diffraction analysis (PXRD) showed that all samples were single phase. The lattice parameters and volume showed a decrease with increasing Pr content. This was expected due to the smaller radius of Pr (Pr^{3+} = 1.179 Å, La^{3+} = 1.216 Å [2]). The monoclinic angle instead showed a linear increase.

Electron microprobe analysis (EMPA) showed that the average deviation from the nominal composition was calculated to be about 4 mol%. The stated deviations cover both, the inhomogeneity of the samples and the experimental uncertainties due to sample porosity and inadequate grain size/shape.

All samples showed a comparable behaviour in thermal gravimetric analysis (TGA) and differential scanning calorimetry (DSC) curves, except for the Pr end member, which revealed a higher weight loss after an additional heating cycle. It is conceivable that the redox system Pr^{+3}-Pr^{+4} was a possible source of the observed discrepancies in the TGA measurements. This is subject to ongoing investigations.

Vibrational modes observed with infrared spectroscopy revealed linear trends to higher wave numbers for the different P-O-bond stretching and bending modes as a function of the composition. This behaviour was also reported for *Ln*PO_4 (*Ln* = La-Gd) [3]. The shift of the modes with increasing atom number is due to stronger interactions between the [PO_4] tetrahedron and the rare earth ion [4].

References:
[1] Bregiroux, D., Audubert, F., Charpentier, T., Sakellariou, D., & Bernache-Assollant, D, 2007. Solid-state synthesis of monazite-type compounds *Ln*PO 4 (*Ln* = La to Gd). Solid State Sciences, 9(5), 432-439.
[2] Shannon, R. D., 1976. Revised effective ionic radii and systematic studies of interatomic distances in halides and chalcogenides. *Acta Crystallographica Section A, A32*, 751-767.
[3] Heuser, J., Bukaemskiy, A. A., Neumeier, S., Neumann, A., & Bosbach, D., 2013. Raman and infrared spectroscopy of monazite-type ceramics used for nuclear waste conditioning. *Progress in nuclear energy, Elsevier, in press; http://dx.doi.org/10.1016/j.pnucene.2013.09.003*.
[4] Chunhua, L., Jie, H., Zhongzie, X., Yaru, N., 2007. Preparation and IR spectra study of rare earth orthophosphates. *Journal of rare earth*, 25, 273-276.

MS12-T5

Optimization of crystal and morphological parameters of wet chemical synthesized $LiNbO_3$-films

D. Eger[1], D. Karsch[1], E. Mehner[1], H. Stöcker[1], D. Meyer[1]
[1]*TU Freiberg, Institut für experimentelle Physik, Freiberg, Germany*

Lithium niobate is a versatilly applicable material. Some applications require thin films on substrates, which can be produced only with high effort until now. The wet chemical synthesis is an environmentally friendly alternative for coating. In this work the influence of processing parameters on coating of silicon substrates is investigated.

For a systematic investigation 30 thin layer samples were produced in total. The samples were dip-coated using three different solutions. One route is water based, the others are sols established by different precursors. Three samples are analyzed with *in-situ* X-ray diffraction. The others are annealed at 400, 600 or 800 °C for 1, 4 or 7 h. For morphology analysis of these films mainly confocal light and scanning electron microscopy are used. The portions of crystalline lithium niobate and other phases are investigated by grazing incidence X-ray diffraction.

The coating by a sol based on $NbCl_5$ precursor shows the best results. The annealing at about 800 °C for 4 h yields the maximum amount of crystalline Lithium niobate with in parallel minimal impurity phases.

MS12-T6

Study on the Preparation of NiFe2O4 Ceramic Nanometer Powder and and its Microstructure

Y. Liu[1], X. Cheng[1], G. Song[1], J. Zhang[1]
[1]*Northeastern University, Shenyang, China*

The $NiFe_2O_4$ ceramic nanometer powder prepared by solid-phase chemical reaction from the ferrous sulfate ($FeSO_4 \cdot 7H_2O$), nickel sulfate ($NiSO_4 \cdot 6H_2O$) and sodium hydroxide（NaOH）is studied. The procedure for preparing $NiFe_2O_4$ ceramic powder precursor is grinding the solid reactants and dispersant sufficiently at ambient temperature first, and then calcined to obtain ultrafine powder. The effects of the dispersant content, preparation technology, calcining temperature and holding time on the ceramic powder's phase composition, particle distribution and morphology were studied emphatically through single-factor experiment.

The optimum parameters for preparation of $NiFe_2O_4$ ultrafine powder is determined, and the results showed that the powder, prepared under the optimum conditions behaves single phase, high crystalline and polyhedral in shape with the particle size range of 30-65 nm. The mechanism for low-temperature solid-phase reaction of $FeSO_4 \cdot 7H_2O$, $NiSO_4 \cdot 6H_2O$ and NaOH at room temperature is also discussed, and the factors, such as the crystal water captained in reactants, grinding and the grain distribution of the reactants could also promote the reaction take place.

MS12-T7

Crystal Structures of Alkaline Earth Glycolates and their Application as Cement Admixtures

R. Kaden[1], H. Pöllmann[1]
[1]*Institute of Geosciences and Geography, Mineralogy/Geochemistry, Halle (Saale), Germany*

Organic and inorganic admixtures are used to control the setting of calcium aluminate cements (CAC). While LiCl and Li_2CO_3 typically act as accelerators, organic acids like citric, formic, benzoic, oxalic, tartaric or chlorinated acetic acid and their Ca-salts retard the hydration reaction, depending on the concentration [1-7]. Glycolic acid was reported to retard the setting of brushite forming Ca-phosphate cement and improve the mechanical performance [8]. The present study focuses on the effect of glycolic acid and the alkaline earth salts on the setting behaviour of CAC and their crystal structures.

Mg-, Ca-, Sr-, Ba-glycolates/hydrates were synthesised by the reaction of glycolic acid with the carbonates in aqueous solution and following crystallisation by slow evaporation of the solvent water. PXRD attests $Mg(C_2H_3O_3)_2{\cdot}2H_2O$ a neso-type crystal structure isotypic to $Co(C_2H_3O_3)_2{\cdot}2H_2O$ [9]. The dimensions of the monoclinic unit cell (SG $P2_1/c$) are determined to be a = 11.5012(4) Å, b = 5.8537(2) Å, c = 12.4584(4) Å, β = 91.13(1)°, V = 838.6(1) Å^3, Z = 4. $Ca(C_2H_3O_3)_2{\cdot}nH_2O$ forms voluminous assemblies thin fibres. Structural data of Ca-, Sr- and Ba-glycolates are not available, yet. Moreover, the solutions of Sr- and Ba-glycolates tend to gel-like stiffening. In case of Sr-glycolate the gel recrystallises within 2 days at 25°C. The recrystallisation of Ba-glycolate was observed after several weeks. A following second dissolution of both crystalline materials in water, than results in a direct crystallisation of anhydrous $Sr(C_2H_3O_3)_2$ or $Ba(C_2H_3O_3)_2$. The crystal structures possess a 3-dimensional framework with complex connectivity between the cations and the glycolate ligands.

$Sr(C_2H_3O_3)_2$ (SG Pbca):

a = 9.505(1) Å, b = 9.740(1) Å, c = 15.88(1) Å, V = 1470.5(2) Å^3, Z = 4.

$Ba(C_2H_3O_3)_2$ (SG Cc), Fig. 1:

a = 10.2669(8) Å, b = 10.3702(8) Å, c = 7.6025(6) Å, β = 119.92(1)°, V = 701.6(1) Å^3, Z = 4.

Isoperibolic heat flow calorimetry of the hydration of a CAC (Secar 51) and aqueous solutions of alkaline earth glycolates shows an increasing retardation with increasing molarity. Small admixture concentrations below 0.001 mole/l affect only a week delay. Higher molarities up to 0.1 mole/l strongly delay the setting of Secar 51, up to 140 hours in case of Mg-glycolate. The dominant hydration product after 7 days was found to be CAH$_{10}$.

References:
[1] K.L. Scrivener, A. Capmas, in P.C. Hewlett: LEA´s Chemistry of Cements and Concrete. Oxford, 2004
[2] S. Stöber, H. Pöllmann, Proc. of the 11th Int. Congr. Chem. Cem. 2003, 719
[3] H. Pöllmann, Proc. 10th Int. Conf. Cem. Micr. 1988, 324
[4] H. Pöllmann, Proc. 11th Int. Conf. Cem. Micr. 1989, 286
[5] H. Pöllmann, Proc. 12th Int. Conf. Cem. Micr. 1990, 303
[6] M. Schmidt, H. Pöllmann, Proc. Cent. Conf. 2008, 93
[7] H. Pöllmann, P. Sturm, R. Kaden, Proc. 35th Int. Conf. Cem. Micr. 2013, 302
[8] F.T. Mariño, *et al.* Biomed. Mater. Res. 2007, B83, 571
[9] R. Carballo *et al.* Acta Cryst. 2003, E59, m588

Figure 1

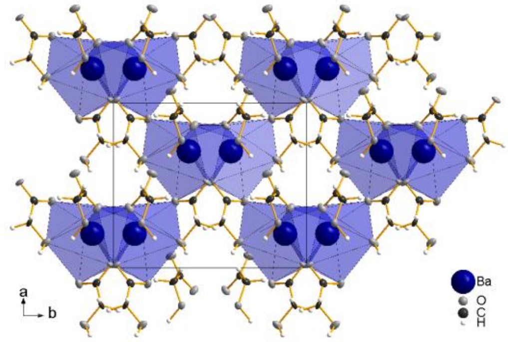

MS12-T8

Introducing the $X - |\psi|^2$ difference electron density in the study of3-D metal complexes

B. Dittrich[1]
[1] *Universität Hamburg, Institute for Inorganic and Applied Chemistry, Hamburg, Germany*

Topological analysis of the electron-density distribution (EDD) according to Bader’s QTAIM is a central outcome of charge density studies in single-crystal X-ray diffraction (XRD). The accuracy that can be reached in XRD, and the nature of the approximations involved in fitting experimental intensities with pseudoatom scattering factors, rarely allows full independent insight into chemical bonding in 3-D metal complexes. For that purpose chemists still need to rely on outcomes of theoretical computations, which is why many such studies only culminate in topology comparisons of theory and experiment. Insight provided by such studies has rightly been criticized [1] as insufficient.

Chemical questions raised in 3D coordination chemistry often aim at a conceptual understanding of the nature of unusual bonding situations. Fortunately, analytical techniques like EPR, cyclic voltammetry and magnetic measurements provide a wealth of complementary information on spin and oxidation states and on magnetic behavior, which are related to the EDD. However, disagreements frequently remain between different sources of information.

Detailed knowledge of the EDD from XRD can be of use in many such cases. Fitting a set of valence-density multipole parameters [2] really requires ideal datasets (rare especially for reactive species), and an alternative approach is required; simple $X-|\psi|^2$ difference density (analogous to X-N or X-X difference densities) can provide helpful information even with normal-resolution (d = 0.83 Å) data. For obtaining $X-|\psi|^2$, multipole parameters are predicted from Fourier transform of a single-point wavefunction, using tools developed for and used in invariom modeling [3]. Pre-refinement of a structural model using invariom X-H distances and scattering factors for the ligand environment gives a starting point. Whole-molecule scattering factors then replace the initial model until convergence is reached. Note that this procedure is conceptually similar to Hirshfeld-atom refinement [4].

The X-$|\psi|^2$ approach permits an indirect validation of theoretical predictions. Several assumptions can be probed. We illustrate possible outcomes on three examples of recently determined crystal structures of similar two-coordinated nickel, copper and zinc compounds with the cyclic alkyl amino carbene ligand.

[1] J.D. Dunitz, A. Gavezzotti, Angew. Chem. Int. Ed. (2005), 44, 1766-1787.
[2] N. Hansen, P. Coppens, Acta Cryst. (2013). A34, 909-921.
[3] B. Dittrich, C. B. Hübschle, K. Pröpper, F. Dietrich, T. Stolper and J. J. Holstein, Acta Cryst. (2013). B69, 91-104.
[4] D. Jayatilaka, B. Dittrich, Acta Cryst. (2008). A64, 383 - 393.

Figure 1

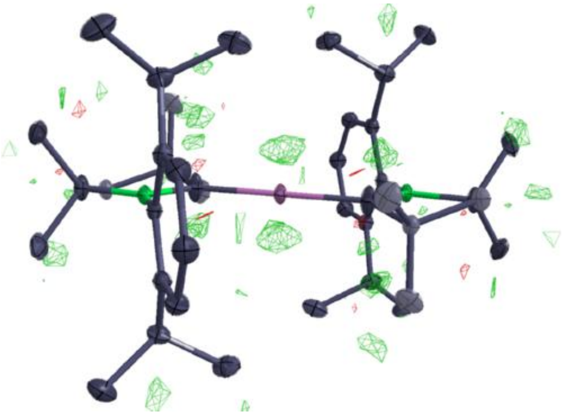

MS13 – Therapeutic targets and fragment-based drug discovery

MS13-T1

X-Ray Crystallography as Gold Standard of Fragment Screening

J. Schiebel[1], N. Radeva[1], A. Park[1], H. Köster[1], T. Craan[1], M. Krug[2], M. Ühlein[2], M. Weiss[2], K. Sparta[2], A. Heine[1], U. Müller[2], G. Klebe[1]
[1]*University of Marburg, Department of Pharmaceutical Chemistry, Marburg, Germany*
[2]*Helmholtz-Zentrum Berlin für Materialien und Energie, Macromolecular Crystallography, Berlin, Germany*

In recent years, fragment-based approaches have become increasingly popular to identify lead compounds for relevant drug targets (1). One advantage of the usage of fragments is their low molecular weight (< 300 g/mol), which leaves sufficient space for subsequent chemical modifications before the pharmaceutically reasonable limit of 500 g/mol is reached (2). However, the inherent low binding affinity of fragment-like molecules (typically μM to mM range) poses a challenge to current biophysical and biochemical screening methods (3). We therefore asked the important question whether typical pre-screening methods are able to reliably detect all putative fragments that can be successfully crystallized with the target protein, which is an essential prerequisite for fragment-based drug discovery.

To answer this question, we designed a fragment library consisting of 364 compounds and used the aspartic protease endothiapepsin as a model system (2). In an initial biochemical assay, 55 of these fragments were identified as putative inhibitors of endothiapepsin and the subsequent crystallographic analysis of these hits led to 11 crystal structures. To test whether all fragments with the capability to bind to endothiapepsin were already identified, we also screened our library using biophysical methods such as STD-NMR, ESI-MS and thermal shift analysis. Disappointingly, each individual screening method revealed varying hits with only a minimal overlap between the different techniques. To be able to analyze this phenomenon unbiased, we decided to perform a crystallographic screening of the entire fragment library with endothiapepsin. As expected based on the deviating results with the different screening methods, we were able to solve over 25 additional crystal structures of fragment-bound complexes. Thus, less than one third of all fragments that could be crystallized with endothiapepsin was identified by the initial biochemical assay. Stimulated by these findings, we suggest that crystallographic studies should rather be performed with relatively large fragment libraries than with only a limited subset suggested by a single pre-screening method, particularly because the determination of fragment-bound structures is pivotal and allows for a much larger selection of the most promising candidates for the subsequent fragment-to-lead optimization.

1. S. D. Roughley, R. E. Hubbard, *J Med Chem* 54, 3989 (Jun 23, 2011).
2. H. Koster *et al.*, *J Med Chem* 54, 7784 (Nov 24, 2011).
3. L. Englert *et al.*, *ChemMedChem* 5, 930 (Jun 7, 2010)

MS13-T2

Lead Discovery by Fragment Screening: a new Opportunity in Industrial Drug Research

M. Schäfer[1]
[1]*Bayer Health Care, Berlin, Germany*

Over the last 10 to 15 years fragment-based screening (FBS) has attracted great attention in industry as well as in academia. The first application was the use as an alternative approach to standard HTS campaigns to identify smaller, more lead-like molecules. Med Chem optimization was guided mainly by X-ray Crystallography and Computational Chemistry. The first drugs derived from pure fragment-based approaches are already on the market (e.g. vemurafenib, a B-Raf^{V600E} cancer inhibitor) or are in late development.

The most important success factor of a FBS is the composition of the fragment library. On one hand fragments must be small (<300Da) to allow optimization towards the ‘rule-of-five’ space. On the other hand they must be chemically attractive to stimulate the fantasy and interest of Medicinal Chemists. Therefore we developed a stringent selection process to cherry pick the most suitable and most attractive fragments.

Serine proteases have been explored extensively as drug discovery targets. Inhibitors of serine proteases tend to be large with peptidic elements. In particular, the discovery of orally available drugs has been turned out to be challenging. We applied fragment screening with our ownFragment Library to identify probes for the S1 specificity pocket as well as for other sub sites for several serine proteases applying surface plasmon resonance (SPR), high-concentration screening (HConcS) and thermal shift assay (TSA) as primary filters. The results of different filter methods are compared especially with respect so successful X-ray structure determination.

MS13-T3

Design of Novel Aspartic Protease Inhibitors from Fragments Exploiting Dynamic Combinatorial Chemistry

N. Radeva[1], M. Mondal[2], H. Koester[1], A. Park[1], C. Potamitis[3], M. Zervou[3], A. Hirsch[2], G. Klebe[1]
[1]*University of Marburg, Department of Pharmaceutical Chemistry, Marburg, Germany*
[2]*University of Groningen, Stratingh Institute for Chemistry, Groningen, Netherlands*
[3]*National Hellenic Research Foundation, Medicinal Chemistry & Biotechnology, Athen, Greece*

Over the past decade, dynamic combinatorial chemistry (DCC) has emerged as an innovative and efficient approach to accelerate identification of small-molecule inhibitors from small fragment precursors for biological targets [1,2]. We used a dynamic combinatorial library (DCL) of aldehyde and hydrazide fragments to generate new molecules formed by reversible reactions [3]. The connecting bonds between the building blocks are steadily being made and broken until all components are in equilibrium.

The composition of a DCL will respond to the addition of a target protein that selectively binds one or more library members and will extract such member(s) from the DCL. We selected endothiapepsin as target protein for our studies, as this enzyme belongs to the notoriously challenging class of pepsin-like aspartic proteases that are involved in numerous diseases such as hypertension, Alzheimer’s disease and malaria. Using the crystal structures of protein-ligand complexes as a reference, we designed a library of potential inhibitors (acylhydrazones) by structure-based design. We have used the DCC approach to identify the best binder(s) using a DCL generated from five aldehydes and five hydrazides. Exploiting ^{1}H-STD-NMR spectroscopy, we identified the binders from the dynamic combinatorial libraries and were able to confirm the predicted binding modes of the most potent inhibitors by X-ray crystallography. Applying a soaking protocol of varying concentration we succeeded to populate concentration dependent more than one inhibitor molecules in the binding site.

The identified ligands were synthesized separately and tested for their biological activity using an enzyme-based fluorescence assay. They showed to exhibit IC50 values in the double-digit micromolar range. This proof-of-concept study holds a lot of potential and represents an efficient starting point for lead-compound identification and, at the same time, it can support the optimization of novel inhibitors. It should be applicable to a large range of medicinal-chemistry projects, in particular during the early stages of the drug-discovery process.

[1] J.-M. Lehn, *Chem. Soc. Rev.* 2007, *36*, 151−160.
[2] P. T. Corbett, J. Leclaire, L. Vial, K. R. West, J. Wietor, J. K. M. Sanders, S. Otto, *Chem. Rev.* 2006, *106*, 3652-3711.
[3] M. Mondal, N.Radeva, H. Köster, A. Park, C. Potamitis, M. Zervou, G. Klebe, A. K. H. Hirsch, *Angew. Chem.* 2014, *in press*

MS13-T4

X-ray structures of human Furin in complex with competitive inhibitors

S. O. Dahms[1], T. Steinmetzer[2], H. Brandstetter[3], M. E. Than[1]
[1]*Leibniz Institute for Age Research - Fritz Lipmann Institute (FLI), Protein Crystallography, Jena, Germany*
[2]*Philipps University Marburg, Department of Pharmaceutical Chemistry, Marburg, Germany*
[3]*University of Salzburg, Department of Molecular Biology, Salzburg, Austria*

Furin is a member of the pro-hormone/pro-protein convertase family (PCs) of subtilisin-like endoproteinases. PCs are required for activation and maturation of many secreted proteins. Target proteins include peptide hormones, growth factors, matrix metalloproteases, blood coagulation factors, regulators of the cholesterol metabolism, bacterial toxins and viral capsid proteins. Therefore furin and other PCs are intensively investigated as pharmacological targets for the treatment of many diseases, e.g. cancer as well as viral- and bacterial infections [1].

The aim of this study is the structure based development of competitive and allosteric non-covalent Furin inhibitors and their optimization for pharmaceutical and biochemical applications. This approach requires an in-depth structural understanding of furin-inhibitor complexes. So far, structures of mouse furin [2] and of its yeast homologue kexin [3] are available in complex with covalently attached peptides. Here we describe a novel preparation of human furin and crystal structures of this enzyme in complex with competitive, non-covalent inhibitors. Our data elucidates so far enigmatic specificity determinants, resulting in Ki-changes of more than two orders of magnitude as well as in strong changes of the specificity for different PC family members upon variation of the P5 position. We also demonstrate exchange of the initially co-crystallized compound by soaking, allowing the investigation of additional inhibitors and substrate analogues. Thus, our work provides the basis for rational design of next-generation furin inhibitors.

References

[1] Seidah, N.G. and Prat, A. (2012) The biology and therapeutic targeting of the proprotein convertases. *Nat Rev Drug Discov*, 11, 367-383.
[2] Henrich, S., Cameron, A., Bourenkov, G.P., Kiefersauer, R., Huber, R., Lindberg, I., Bode, W. and Than, M.E. (2003) The crystal structure of the proprotein processing proteinase furin explains its stringent specificity. *Nat Struct Biol*, 10, 520-526.
[3] Wheatley, J.L. and Holyoak, T. (2007) Differential P1 arginine and lysine recognition in the prototypical proprotein convertase Kex2. *Proc Natl Acad Sci U S A*, 104, 6626-6631.

MS13-T5

From SARS to MERS: Structure-Based Design of Antivirals Against Middle-East Respiratory Syndrome Coronavirus

R. Hilgenfeld[1,2], Y. Xiao[1,2], Y. Kusov[1,2], S. George[1,2], L. Zhang[1,2], L. Zhu[1,2], D. Muth[3,4], M. A. Müller[3,4], C. Drosten[3,4], J. Lei[1,2], Q. Ma[1,2]
[1]*University of Lübeck, Institute of Biochemistry, Lübeck, Germany*
[2]*German Center for Infection Research (DZIF), Lübeck, Germany*
[3]*University of Bonn Medical Center, Institute of Virology, Bonn, Germany*
[4]*German Center for Infection Research (DZIF), Bonn, Germany*

2013 marked the 10th anniversary of the outbreak of Severe Acute Respiratory Syndrome (SARS), the first pandemic of the 21st century. Soon after the onset of the epidemic in southern China, a novel coronavirus, SARS-CoV, was identified as the causative agent of the disease. Since 2012, another, related coronavirus, Middle-East Respiratory Syndrome coronavirus (MERS-CoV), has been emerging. The case/fatality ratio of SARS was about 10%, while that of MERS is almost 50% (see (1) for a review).

Within weeks of the identification of SARS-CoV, we have shown that its main protease is a suitable target for the design of anticoronavirus drugs (2). Since then, a number of inhibitor leads have been developed (e.g., (3)), although the efforts were limited because only few virologists and policy-makers believed that SARS-CoV had the potential to return. After it had been shown that bat coronaviruses (bat-CoVs) were the origin of SARS-CoV (4), we embarked on a small research program on structure-based inhibitors of bat-CoV main proteases, in order to contribute to better preparedness against future zoonotic transmission. For example, we showed that our broad-spectrum antivirals, SG85 (5) and SG98, are good inhibitors of the mainprotease of bat-CoV HKU4. When MERS-CoV was sequenced in late 2012 (6), it became clear that it was similar to HKU4, and accordingly, our compounds were shown to have activity against MERS-CoV. In addition to this "predictive" work on the coronaviral main protease, we will present structures of some other potential MERS-CoV drug targets.

(1) Hilgenfeld, R., Peiris, M.: From SARS to MERS: 10 years of research on highly pathogenic human coronaviruses. *Antiviral Res.* 100, 286-295 (2013).

(2) Anand, K., Ziebuhr, J., Wadhwani, P., Mesters, J.R., Hilgenfeld, R.: Coronavirus main proteinase ($3CL^{pro}$) structure: basis for design of anti-SARS drugs. *Science* 300, 1763-1767 (2003).

(3) Zhu, L., George, S., Schmidt, M.F., Al-Gharabli, S.I., Rademann, J., Hilgenfeld, R.: Peptide aldehyde inhibitors challenge the substrate specificity of the SARS-coronavirus main protease. *Antiviral Res.* 92, 204-212 (2011).

(4) Li, W., Shi, Z., Yu, M., Ren, W., Smith, C., Epstein, J.H., Wang, H., Crameri, G., Hu, Z., Zhang, H., Zhang, J., McEachern, J., Field, H., Daszak, P., Eaton, B.T., Zhang, S., Wang, L.F.: Bats are natural reservoirs of SARS-like coronaviruses. *Science* 310, 676-678 (2005).

(5) Tan, J., George, S., Kusov, Y., Perbandt, M., Anemüller, S., Mesters, J.R.,Norder, H., Coutard, B., Lacroix, C., Leyssen, P., Neyts, J., Hilgenfeld, R.: 3C protease of enterovirus 68: Structure-based design of Michael acceptor inhibitors and their broad-spectrum antiviral effects against picornaviruses. *J. Virol.* 87, 4339-4351 (2013).

(6) van Boheemen,S., de Graaf, M., Lauber, C., Bestebroer, T.M., Raj, V.S., Zaki, A.M., Osterhaus, A.D., Haagmans, B.L., Gorbalenya, A.E., Snijder, E.J., Fouchier, R.A.:Genomic characterization of a newly discovered coronavirus associated with acute respiratory distress syndrome in humans.MBio. 3. doi:pii: e00473-12. 10.1128/mBio.00473-12 (2012).

MS13-T6

Exploring a mycobacterial thiolase - FadA5

C. Schäfer[1], R. Lu[2], N. Nesbitt[2], N. Sampson[2], C. Kisker[1]
[1]*Rudolf Virchow Center for Experimental Biomedicine, Structure Biology, Würzburg, Germany*
[2]*Stony Brook University, Chemistry, Stony Brook, United States*

Mycobacterium tuberculosis, the causative agent of tuberculosis, is one of the most dangerous pathogens of the world, and caused approx. 1.4 million deaths worldwide in the year 2011. Furthermore it is estimated that 1/3 of the world’s population is infected by the so-called latent tuberculosis. In these patients the disease can break out anytime if their immune system is compromised, for example by impaired living conditions, in combination with other diseases such as HIV and diabetes-type-2, or simply by ageing. As the number of drug-resistant strains of *M. tuberculosis* is increasing, new drugs are urgently needed and the search for new drug targets therefore plays an important role in this process.(1)

The cholesterol metabolism pathway in *M. tuberculosis* is a potential target for developing new drugs against this disease. Many studies have shown that the knockout of different genes which encode enzymes responsible for cholesterol import into the bacterium or for cholesterol metabolism negatively influences proliferation and survival of the bacteria in the chronic stage of infection. However, the exact function of cholesterol and its metabolites for *M. tuberculosis* survival is still under debate.(2,3)

FadA5 is a thiolase which has been proposed to be involved in the side chain metabolism of cholesterol. This thiolase catalyze the reverse Claisen condensation of a 3-ketoacyl-CoA, to liberate metabolites such as acetyl-CoA and propionyl-CoA. FadA5 is therefore important as the supplier of 2- and 3-carbon metabolites and in the biosynthesis of androsten-4-en-3,17-dione, an intermediate in cholesterol metabolism.(4)

The aim of this project is the first structural characterization of apo FadA5 as well as its interaction with ligands, substrates and products. Development of first inhibitory lead structures will follow subsequently.

We have solved five different FadA5 structures, wild type and active site mutants of the enzyme as well as the protein in complex with acetyl-CoA, CoA and a cleaved product. All FadA5 structures form homodimers, the predominant oligomeric state of thiolases. Intriguingly this enzyme is structurally very rigid, as hardly any changes in the dimer structure can be observed upon ligand binding, which may be a common feature among thiolases(5). Based on the active site analysis as well as the ligand-protein-interactions initial drug lead development will be pursued.

References:
(1) WHO, 2013, Tuberculosis-Fact sheet N°104,
(2) Van der Geize, R., et al., 2007, PNAS, 104: 1947
(3) Ouellet, H., et al., 2011, Trends in Microbiology, 19: 530
(4) Nesbitt, N.M., et al., 2010, Infect Immun, 78: 275
(5) Modis, Y., 2000, J. Mol. Biol, 297: 1171

MS14 – Structure-property relations in materials sciences II

MS14-T1

Elastic Constants in Crystals with Point Defects considering the example of Cluster Crystals, a Reciprocal Space approach

C. Walz[1], M. Fuchs[1], T. Ras[1], J. Häring[1], A. P. Gantapara[2], M. Dijkstra[2]
[1]*Universität Konstanz, Fachbereich Physik, Konstanz, Germany*
[2]*Utrecht University, Department of Physics and Astronomy, Utrecht, Netherlands*

We present applications of a reciprocal space approach to crystal elasticity [1] to multiple occupancy (cluster) crystals of the fourth order Generalized Exponential Model (GEM4) [2]. There, the large range of the average lattice site occupation number can be interpreted as a large range in point defect concentration. The high self diffusion linked to hopping processes therefore renders a real space definition of the displacement field u(q) impossible.

Based on Monte-Carlo-Simulation respectively classical Density functional theory (DFT) we obtain the dispersion relations at finite temperature. Discussion of mechanical instabilities provides new insight into the critical temperature for coexistence of differently occupied crystal phases versus a homogeneous average occupation number. This was previously discussed in [3] and [4] from an analytical respectively simulation point of view with hugely discrepant results. With simple DFT approximations, we are able to qualitatively reproduce the simulation results.

DFT is especially powerful in describing inhomogeneous states like crystalline solids. There exists an extensive body of work, using DFT to obtain the elastic constants of periodically ordered solids [5,6]. Yet application of DFT to this problem previously required an ad hoc ansatz of the inhomogeneous density field as expressed by the coarse-grained fields of elasticity theory.

Our analysis of the hydrodynamic equations for nonideal crystals in reciprocal space now provides a motivated ansatz for the coarse grained density fluctuations. This yields within DFT an expression for the elastic free energy which is based on the microscopic particle interactions including the influence of point defects.

From the simulation side, equilibrium configurations can be used to compute the displacement field fluctuations. The inverse correlations $\langle u_\alpha u_\beta \rangle^{-1}(q)$, give the dynamical matrix whose $q \to 0$ eigenvalues yield the constants of elasticity. As our expression for u(q) is based on a rapidly decaying reciprocal space Bragg peak summation, it is insensitive to self diffusion mediated by point defects [7]. Work in progress includes the extension of the formalism to quasiperiodic structures.

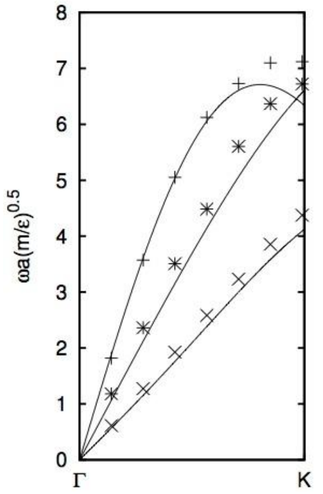

Figure 1 shows the [110] dispersion relation of a GEM4 cluster crystal at finite temperature from DFT (lines) and Monte Carlo data (points) that could not be obtained from conventional real space elasticity theory.

[1] Walz C. and Fuchs M., *Phys. Rev. B*, 81 (2010) 134110.
[2] Mladek B. M. et al., *J. Phys.: Cond. Matter* 20 (2008) 494245.
[3] Neuhaus T. and Likos C. N, *J. Phys.: Cond. Matter* 23 (2011) 234112.
[4] Wilding N. B. and Sollich P., *EPL* 101 (2013) 10004.
[5] Kirkpatrick T. et al., *J. Chem. Phys.* 92 (1990) 3768.
[6] Masters A. J., *Mol. Phys.* 99 (2001) 907.
[7] Fuchs M., *Proceedings of Course CLXXXIV 'Physics of Complex Colloids' of the International School on Physics 'Enrico Fermi'* (2013).

MS14-T2

In-situ Neutron Diffraction of monoclinic NiTi B19' revealing Components of its Elastic-Constant-Tensor

P. M. Kadletz[1], M. Hoelzel[2], W. W. Schmahl[1]
[1]*LMU, Section for applied Crystallography, Munich, Germany*
[2]*FRM II, Garching n. Munich, Germany*

NiTi shape memory alloys (SMAs) are used for medical and engineering applications with increasing commercial success. [1] Despite their technological importance, the elastic-constant-tensor and thus the orientation-specific Young’s moduli of the monoclinic B19’ martensite phase are still unknown as martensite single crystals are not available for resonant ultrasound spectroscopy or mechanical testing. DFT calculations have provided elastic constants for zero K involving a monoclinic angle of 108.5° [2] or 107° [3] instead of 98.5°, as we have observed experimentally at 4 K. Recently five of thirteen elastic constants of polycrystalline NiTi B19' have been determined experimentally [4]. However, the values for the remaining elastic-tensor-components and a complete picture of the elastic behavior of B19’ remain elusive.

In the present work we determined the elastic constants by in-situ neutron diffraction experiments using a load frame where the sample and load axis can be rotated in an Eulerian cradle [5]. This technique allows to separate the effects of elastic and inelastic deformation processes (detwinning). We recorded neutron diffraction patterns of a commercial, textured NiTi alloy ($M_f \approx 44°C$) at constant uniaxial loads.

Evaluation of previous neutron measurements showed the onset of the pseudoplastic plateau at a macroscopic strain of ~1% and indicated complex behavior with changes from constant-strain to constant-stress microstructures during loading to 4% strain. In our recent experiment diffractograms were recorded in the elastic regime at ~0.2, ~0.4 and ~0.6 % strain. Evaluating this data we obtained the evolution of the B19' texture and the orientation dependent elastic strain was isolated from textural changes (caused by variant reorientation). Finally, elastic-constant-tensor components are calculated which can be used for micromechanical modeling of NiTi B19' shape memory behavior.

[1] Otsuka K., Ren X. (2005) Progress in Materials Science 50: 511-678.

[2] Wagner M.F-X., Windl W. (2008) Acta Materialia 56: 6232-6245.

[3] Huang X., Ackland G.J., Rabe K.M. (2003) Nature Materials 2: 307-311.

[4] Stebner A.P., Brown D.W., Brinson L.C. (2013) Appl. Phys. Lett. 102: 211908.

[5] Hoelzel M., Gan W. M., Hofmann M., Randau C., Seidl G., Jüttner Ph., Schmahl W. W. (2013) Nucl. Instr. Meth. Phys. Res. A 711: 101-105.

MS14-T3

Possible piezoelectric materials $\mathbf{Cs}M\mathbf{Zr_{0.5}(MoO_4)_3}$ (M = V, Cr, Fe) and $\mathbf{CsCrTi_{0.5}(MoO_4)_3}$: structural considerations

D. Mikhailova[1], A. Sarapulova[1], B. Bazarov[2], T. Namsaraeva[2], S. Dorzhieva[2], J. Bazarova[2], V. Grossman[2], A. Bush[3], I. Antonyshyn[1], M. Schmidt[1], A. Bell[4], M. Knapp[5], H. Ehrenberg[5], J. Eckert[6]

[1]*Max Planck Institute for Chemical Physics of Solids, Dresden, Germany*

[2]*Baikal Institute of Nature Management, Siberian Branch, Russian Academy of Sciences, Ulan-Ude, Russian Federation*

[3]*Moscow State Institute of Radioengineering, Electronics and Automation (Technical University), Moscow, Russian Federation*

[4]*Hasylab/DESY, Hamburg, Germany*

[5]*Karlsruhe Institute of Technology (KIT), Institute for Applied Materials (IAM), Eggenstein-Leopoldshafen, Germany*

[6]*IFW Dresden, Institute for Complex Materials, Dresden, Germany*

A series of isostructural trigonal molybdates $\mathrm{Cs}M\mathrm{Zr_{0.5}(MoO_4)_3}$ with M = Cr, V, Fe, and $\mathrm{CsCrTi_{0.5}(MoO_4)_3}$ was synthesized by solid state reactions and characterized by synchrotron powder diffraction, differential scanning calorimetry, thermal conductivity measurements and magnetization measurements. The NASICON-type structure of these compounds (S. G. *R*-3) represents a three-dimensional framework of corner-sharing trigonal $\mathrm{MoO_4}$-pyramids and $M\mathrm{O_6}$-octahedra, in which M and Zr (Ti) ions are randomly distributed. The Cs ions occupy large channels along the *c*-axis. A combination of phenomena like a drastic increase of thermal conductivity, endothermic signals in the DSC curve and anomalies in the thermal expansion coefficients, observed for the compounds with M = Cr, V, Fe and $\mathrm{CsCrTi_{0.5}(MoO_4)_3}$ above 700 K, allows to propose a structural phase transition. The crystal structure of the high-temperature phase is very close to the low-temperature one.

The mechanism of this transition is very likely different for different transition metals. In contrast to $\mathrm{CsFeZr_{0.5}(MoO_4)_3}$ with no anomalies in reflection profiles in synchrotron diffraction patterns during increasing temperature a broadening of some reflections like the 220 one around the transition temperature allowed to suggest an intermediate phase formation for $\mathrm{CsCrZr_{0.5}(MoO_4)_3}$ and $\mathrm{CsCrTi_{0.5}(MoO_4)_3}$. For $\mathrm{CsVZr_{0.5}(MoO_4)_3}$ some decrease of the $\mathrm{FWHM_{(220)}}$ around transition temperature may point out a more complex structural behavior.

A significant hysteresis in high-temperature electronic and thermal conductivity was observed. A possible transition from the piezoelectric to the paraelectric state is discussed.

Figure 1

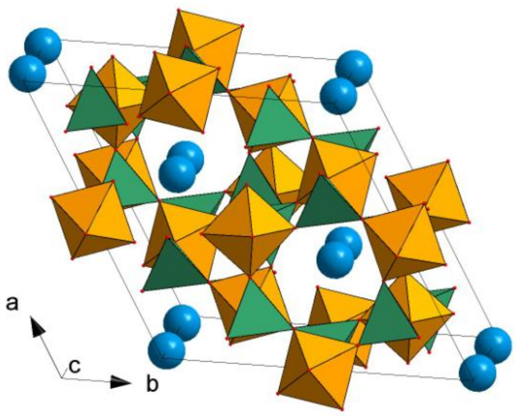

MS14-T4

Thermodynamic Properties of Hexaphenyldisilane from Experiment and DFT Calculations

T. Bernert[1], B. Winkler[1], V. Milman[2], L. Bayarjargal[1], L. Fink[3], M. Berger[3], H.- W. Lerner[3]
[1]*Goethe-Universität, Geowissenschaften, Abt. Kristallographie, Frankfurt am Main, Germany, Germany*
[2]*Accelrys, Cambridge CB4 OWN, UK, United Kingdom*
[3]*Goethe-Universität, Institut für Anorganische und Analytische Chemie, Frankfurt am Main, Germany, Germany*

Recently, we have determined the structure of hexaphenyldisilane, $Si_2(C_6H_5)_6$, by a combination of synchrotron X-ray diffraction and quantum mechanical model calculations (Bernert et al., in prep.). The temperature dependence of the heat capacity was measured with a low temperature microcalorimeter (Quantum Design PPMS) in the range of 2 K < T < 400 K (Fig. 1). From temperature dependent X-ray diffraction experiments in the range of 173 K < T < 298 K we have obtained the thermal expansion coefficients (Fig. 2). Complementary density functional theory calculations were performed with the CASTEP [1] and DMol^3 [2] packages. The experimentally determined temperature dependence of the heat capacity is shown in Fig. 1.

An approximate phonon density of states was derived by computing the phonon frequencies at the center of the Brillouin zone. The calculated heat capacity is in reasonably good agreement with the experimentally determined data (Fig. 1). The thermal expansion of hexaphenyldisilane is strongly anisotropic (Fig. 2). In fact, in two directions we observed negative thermal expansion for the temperature range investigated here. Negative thermal expansion is rare in organic compounds, and is often restricted to one direction only [3,4]. In the present case, the origin of the negative thermal expansion is due to the paddle wheel arrangement of the molecules. This kind of interlock in the (*a*,*b*)-plane leads to the temperature-induced decrease of the *c*-axis accompanied by an increase of the *a* and *b* axes.

References:

[1] S. J. Clark, M. D. Segall, C. J. Pickard, P. J. Hasnip, M. J. Probert, K. Refson, M. C. Payne, *Z. Kristallogr.*, 2005, 220, 567 - 570.

[2] B. Delly, *The Journal of Chemical Physics*, 1990, 92, 508 - 517.

[3] S. Bhattacharya, K. B. Saha, *Cryst. Growth Des.*, 2013, 13, 3299 - 3302.

[4] H. Birkedal, D. Schwarzenbach, P. Pattison, *Angew. Chem.*, 2002, 114, 780 - 782.

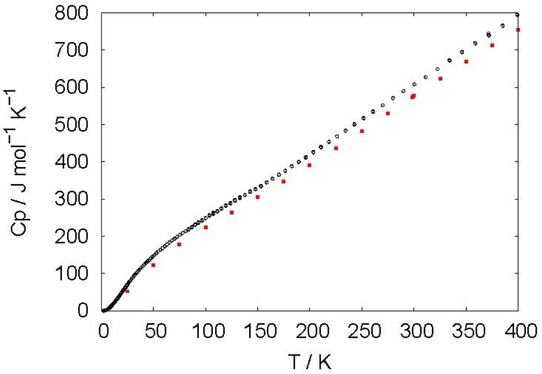

Figure 1: The heat capacity of hexaphenyldisilane was measured between 2 K and 400 K (black circles) and compared to the calculated heat capacity (red squares).

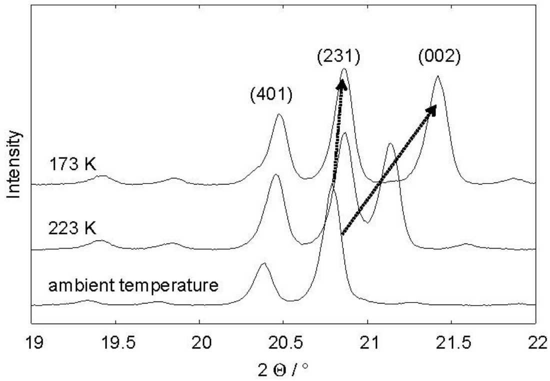

Figure 2: Diffractograms of hexaphenyldisilane at different temperatures from 19° - 22° in 2 θ. The arrows indicate the shift of the (002) and (231) reflections. They completely overlap at ambient temperature and split up at lower temperature due to strong anistropic thermal expansion.

MS14-T5

Coupling of Morphologic and Crystallographic Symmetry in Sea Urchins

B. Maier[1], P. Alexa[1], E. Griesshaber[1], F. Brümmer[2], W. Schmahl[1]
[1]*Ludwig-Maximillians-Universität München, Department für Geo- und Umweltwissenschaften, München, Germany*
[2]*Universität Stuttgart, Biologisches Institut - Abteilung Zoologie, Stuttgart, Germany*

Sea urchin teeth are a remarkable example of biomineralized multiplex composite crystals. Its hierarchical design of low and high Mg-calcite components enables a self-sharpening mechanism while the teeth are constantly regrown. This combination of design features allows these animals to use their teeth to grind off algae from rocks. Sea urchins exhibit five teeth and each tooth is hold in a jaw pyramid. Teeth and jaw pyramids are arranged in a lantern which exhibits a five-fold rotation symmetry with a parallel mirror plane through the middle of each pyramid-tooth segment. Electron back-scatter and X-ray diffraction data collected on Paracentrotus lividus reveal that the mirrored parts of the jaw pyramid each constitute a separate composite crystal, their c-axis enclosing an angle of about 72 degree and are mirrored by the morphologic mirror plane. The c-axis of the corresponding tooth lies in the mirror plane enclosing an angle of about 120 degree with each c-axis of the two pyramid parts. The five-fold rotation axis replicates this crystallographic arrangement every 72 degrees. Hence, the sea urchin mouth represents coupling of morphologic and crystallographic symmetry which highlights the high degree of biologic control over the crystallographic orientation of hierarchic substructures. In addition, the crystallographic orientation of the carapace with respect to the mouth part will be presented as well as a comparison of teeth from six different sea urchin species.

MS14-T6

Structural and Functional Characterization of Supported Vanadium Oxide Catalysts under Propene and Propane Oxidizing Conditions

J. Scholz[1], T. Ressler[1]
[1]*Technische Universität Berlin, Institut für Chemie, Berlin, Germany*

One of the most important ways to functionalize hydrocarbons is the selective oxidation of alkanes and alkenes with vanadium oxide based catalysts. One way to study the relation between catalytic performance and structure of a catalyst system is the investigation of suitable catalyst model systems. Such model systems often consist of metal oxides supported on nanostructured oxide materials possessing an ordered pore structure and a high specific surface area. The structure of the surface oxide catalyst is determined by the properties of the support material. Here, the preparation and detailed characterization of vanadium oxides supported on an alkaline oxide support (*MgO/SBA-15*) is presented. The catalysts were investigated by *in situ* spectroscopy under working conditions in selective oxidation reactions.

The high surface area support material was obtained by synthesis of silica SBA-15 and subsequent coating with MgO.[1] Vanadium oxide catalysts were formed by incipient wetness of the *MgO/SBA-15* support. Structural and functional characterization of the supported metal oxide catalysts was performed by a combination of various methods. *In situ* XAS experiments were performed at the V K edge at the Hamburg Synchrotron Radiation Laboratory, HASYLAB. *In situ* DR-UV-Vis measurements were conducted on a spectrometer equipped with a “Praying Mantis” *in situ* cell. Catalytic activity was tested in a laboratory fixed-bed reactor in 5% propene, 5% O_2 in He (SOP) or 7.5% propane, 5% O_2 in He (ODH).

In contrast to the highly oligomerized vanadium oxide units observed on SBA-15[2], low oligomerized $[VO_4]$ units could be stabilized on *MgO/SBA-15* at comparably high catalyst loadings. This was attributed to the alkaline surface of the *MgO/SBA-15* support. The degree of oligomerization of the $[VO_4]$ units depended on catalyst loading. With increasing surface coverage the degree of oligomerization increased from monomeric to oligomeric $[VO_4]$ tetrahedra. *In situ* XAS investigations revealed a correlation between partial reduction of the active metal oxide species and catalytic activity. Acrolein turnover frequency (TOF) as a function of surface coverage exhibited a "vulcano type" behavior (Fig. 1).[3] At optimal coverage the catalyst structure consisted of mainly $[V_2O_7]$ units. Eventually, the obtained structure activity correlation allowed a knowledge-based preparation of the optimal surface.

HASYLAB, Hamburg is acknowledged for providing beamtime and financial support. We are grateful to the Deutsche Forschungsgemeinschaft (DFG) for financial support.

[1] J. Scholz, A. Walter, A. H. P. Hahn, T. Ressler, *Microporous Mesoporous Mater.* 2013, *180*, 130-140.
[2] A. Walter, R. Herbert, C. Hess, T. Ressler, *Chem. Cent. J.* 2010, *4*, 3.
[3] J. Scholz, A. Walter, T. Ressler, *J. Catal.* 2014, *309*, 105-114.

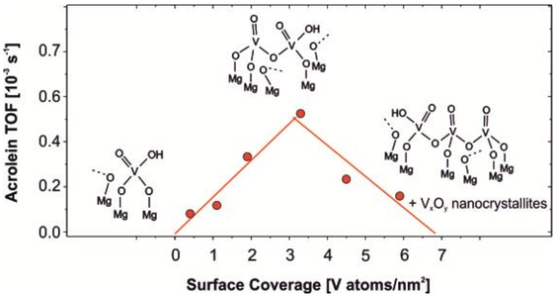

Fig. 1 Acrolein TOF of vanadium oxides supported on *MgO/SBA-15* as a function of surface coverage.

MS14-T7

Small angle Xray scattering of microcrystalline polymers and beyond

G. Nicoleta[1], P. Pierre[1], M. Fernadez-Martinez[1], F. Bossan[1], S. Rodrigues[1]
[1]*Xenocs, Sassenage, France*

Most polymer transformations from raw material towards finalized product necessitates, ad minima, a processing step involving a melt or close to molten state, with a first order phase transition, coupled to mechanical deformation and subsequent flow of macromolecular chains. Industrial processes being far from thermodynamic equilibrium, the macromolecular chains often trap their flow orientation during the cooling, inducing specific mechanical behaviors. Such orientation is appearing from the local phase to the mesophase and sometimes even up to the macroscopic phase.

Small Angle X-Ray Scattering (SAXS) is a technique well suited for investigating nano-materials and nano-structures of polymers. The technique gives information on sample structure parameters such as particle shape or size, size distribution, orientation, surface to volume ratio,… in the range from 1 nm to beyond 100 nm. In combination with Wide Angle X-ray Scattering (WAXS), the technique can provide information on length-scales down to 0.1 nm, thus allowing measuring both crystalline and nano-structure properties. Further, orientational functions of stretched matrices or of self assembled polymers can be derived from 2 dimensional x-ray patterns, leading to a deeper understanding of the behavior of macromolecular materials. Relationship between rheology and nanostructure has been demonstrated first in rheo-optical measurements and later with in-situ x-ray synchrotron studies [1-3, 5] and in-situ neutron studies [4]. As we describe in this paper, the progress in the performances of x-ray components and subsequent assembly enables to propose such characterization method in the laboratory [6]. Among others, recent results will be illustrating the capabilities of x-ray scattering, we will present investigation of microinjected semi crystalline polymers emphasizing the nanostructure orientation and processing relationships.

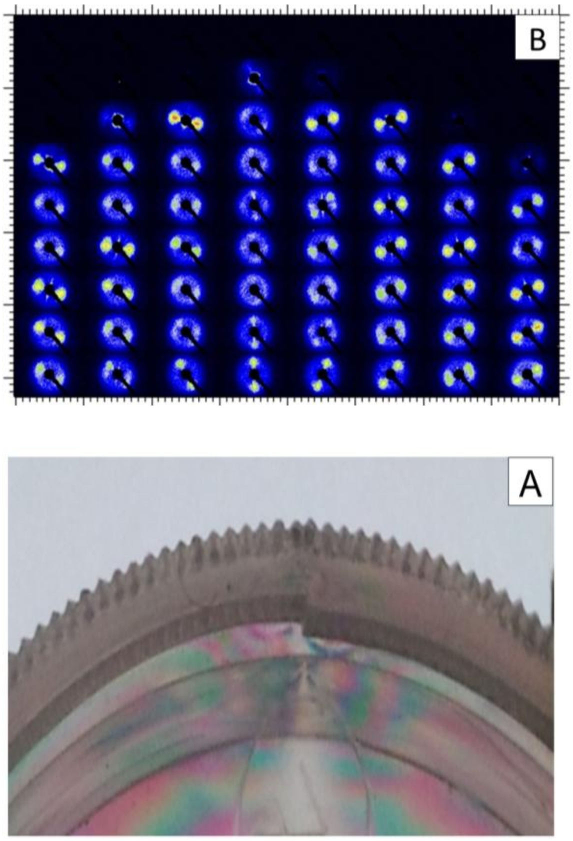

Figure 1: Rapid mapping of injection point of a polypropylene cap: A. Image between crossed polarizers, the scale bar corresponds to 5mm. B. Mosaic of SAXS images corresponding to the mapping of the plastic cap of same region as depicted in A. Geometry is transmission SAXS. Each pattern is a SAXS pattern collected every 3mm horizontally and every 0.7mm vertically. Injection point is clearly related to the lamellar long period orientation of the polypropylene macromolecular chain.

[1] Waldow, Han et al, Polymer 33, 4635 (1992)
[2] Balsara et al, Macromol. 25, 3896 (1992)
[3] Panine et al, Rev. Sci. Instrum. 74, 2451 (2003)
[4] Boué et al, Europhys Lett, 25, 421 (1994)
[5] Pignon et al, Phys. Rev. E 56, 3281 (1997)
[6] Bou Malhab N., (2012) PhD Thesis. Arts et Métiers ParisTech, Microinjection Moulding of semi-crystalline polymers.

MS14-T8

Evaluation of temperature-dependent X-ray diffraction data using the autocorrelation function

L. Robben[1], T. M. Gesing[1]
[1] *Universität Bremen, Chemische Kristallographie fester Stoffe, Bremen, Germany*

A concise treatment of the autocorrelation function application on data sets typically used for analytical methods in crystallography and solid state chemistry is presented. This function is applicable to all methods, in which data consists of peak shaped signals. The strength of this method is a quick and straightforward evaluation of multiple data sets depending on external parameters like temperature, pressure or composition. Originally the method was proposed for the evaluation of FTIR data [1] but is at all not limited to this energy range. The data evaluation process with the autocorrelation method contains the following steps: Extraction of data ranges, background correction, and calculation of the autocorrelation function for each data set and the selection and determination of the λ_{Corr} parameter. All these steps can easily be automatized thus enabling a very fast approach, even for data sets containing several dozens of single measurement steps. Typically occurring features of measured data, like background contributions, noise and window functions, and their expression in the autocorrelation function are considered to enable the detection of unwanted signal contributions. The limits of this method, regarding resolution criteria of the original data and the accessibility of the basic physical properties of the solid state systems under consideration, are shown. Direct access to physical properties is only possible if the peaks of the measured data set have an invariant, like the integrated peak area. Although this is not the case in temperature-dependent X-ray diffraction, due to the influence of the Debye-Weller factor, it is possible to pinpoint critical temperatures in such data sets. This feature is presented here for the first time for temperature-dependent X-ray powder data. An example is given in Figure 1: A discontinuity in the sodium occupancy, the micro-strain and the average crystal size around 633 K was observed from temperature-dependent X-ray powder pattern of the gallosilicate nitrite sodalite $|Na_8(NO_2)_2|[GaSiO_4]_6$ by Gesing [2]. This discontinuity is caused by domain formation due to a ordering of the sodalites cage filling and is reflected by the λ'_{Gauss}

parameter obtained from the autocorrelations of the X-ray diffraction data. The λ’$_{\text{Gauss}}$ parameter can be fitted by a modified Boltzmann distribution (see Figure 1) to determine the temperature of domain formation at 617±4 K.

[1] E.K.K.H. Salje, M.I.A. Carpenter, T.H. Malcherek, T. Boffa Ballaran, Autocorrelation analysis of infrared spectra from minerals, Eur. J. Mineral. 12 (2000) 503-519.
[2] T.M. Gesing, B.C. Schmidt, M.M. Murshed, Temperature dependent structural and spectroscopic studies of sodium gallosilicate nitrite sodalite, Mater. Res. Bull. 45 (2010) 1618-1624.

Figure 1

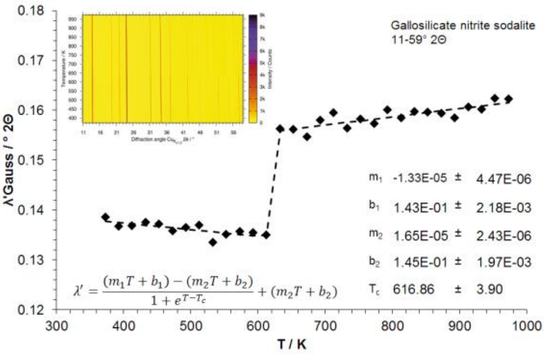

MS15 – Charge density for understanding chemical bonding in organic and inorganic structures (dedicated to Prof. Luger)

MS15-T1

New directions in pseudoatom modeling of X-ray charge densities

T. Koritsanszky[1]
[1]*Middle Tennessee State University, Computational Science, Tennessee, United States*

Through analyzing results of demanding computational experiments, we assess the feasibility and accuracy of extracting topological properties (TP) of the static electron density (ED) from the thermally smeared ED and from Bragg diffraction data. The following fundamental issues have been addressed and unraveled: (1) what is the uncertainty in local bond TPs of the static ED and how can they be quantitatively estimated from the anisotropic displacemet amplitudes of the vibrating nuclei? (2) what is the error introduced by the convolution approximation? (3) to what extent can vibration smearing be absorbed into static ED models? (4) can the topology of the static ED faithfully retrieved by the pseudoatom model? Using quantum-chemistry supported pseudoatom models we also critically reanalyze state-of-the-art X-ray diffraction data to explore some of the problems mention above.

MS15-T2

Low valent silicon - a carbon copy?

D. Stalke[1]
[1]*Universität Göttingen, Institut für Anorganische Chemie, Göttingen, Germany*

Silicon, the heavier congener of carbon, frequently shows different chemistry compared to its sister element. Different to $(RC)_6$ aromatic systems the $(RSi)_6$ silabenzene is not planar and contains silicon of different oxidation states in the Si_6 perimeter.[1] Allene type molecule A can also be rationalized along a structure of type B when the central C(0) atom is bonded by the ligand L, where L perform as donor ligands. B with the general formula $C(L:)_2$ which possess two lone pairs have been termed carbones whereas carbenes CR_2 accommodate only one lone pair.[2] When L is a carbene ligand in $C(L:)_2$, the compound is termed a carbodicarbene. A related situation may be envisaged for the silicon homologue of allene C.[3] Theoretical studies by Frenking et al.[4] suggested that the trisilaallene that was synthesized by Kira et al.[5] should rather be considered as a silylone $Si(L:)_2$ D which explains why the compound has a rather acute Si-Si-Si angle and why the substituents at the terminal silicon atoms are not orthogonal to each other which is typical for an allene structure.

The Si-C bonds in $[(L:)_2Si]$, L= cyclic-alkyl-amino-carbene (cAAC),[6] of 1.841 Å are shorter than typical Si-C_{aryl} single bonds (1.879 Å) but slightly longer than Si-C bonds in some recent Si-C_{sp3} systems (1.8174(14) Å) and much longer than Si=C double bonds (1.702 - 1.775 Å). Similarly they are marginally shorter than the calculated value for the silylone $Si(NHC)_2$ (1.869 Å). This leaves $[(L:)_2Si]$ a particularly interesting candidate for charge density investigations. Ways to synthesis $[(L:)_2Ge]$ will be presented.[7]

[1] D. Kratzert, D. Leusser, J. J. Holstein, B. Dittrich, K. Abersfelder, D. Scheschkewitz, D. Stalke, *Angew. Chem.* 2013, *125*, 4574-4578; *Angew. Chem. Int. Ed.* 2013, *52*, 4478-4482.
[2] K. C. Mondal, H. W. Roesky, M. C. Schwarzer, G. Frenking, S. Neudeck, I. Tkach, H. Wolf, D. Kratzert, R. Herbst-Irmer, B. Niepötter, D. Stalke, *Angew. Chem.* 2013, *125*, 3036-3040; *Angew. Chem. Int. Ed.* 2013, *52*, 2963-2967.
[3] S. Ishida, T. Iwamoto, C. Kabuto, M. A. Kira, *Nature* 2008, *421*, 725 - 727.
[4] N. Takagi, R. Tonner, G. Frenking, *Chem.-Eur. J.* 2012, *18*, 1772 - 1780.
[5] M. Kira, *Chem. Comunm.* 2010, *46*, 2893 - 2903.
[6] K. C. Mondal, H. W. Roesky, F. Klinke, M. C. Schwarzer, G. Frenking, B. Niepötter, H. Wolf, R. Herbst-Irmer, D. Stalke *Angew. Chem. Int. Ed.* 2013, *52*, 1801-1805.
[7] Y. Li, K. C. Mondal, H. W. Roesky, H. Zhu, P. Stollberg, R. Herbst-Irmer, D. Stalke, D. M. Andrada, *J. Am. Chem. Soc.* 2013, *135*, 12422−12428.

Figure 1

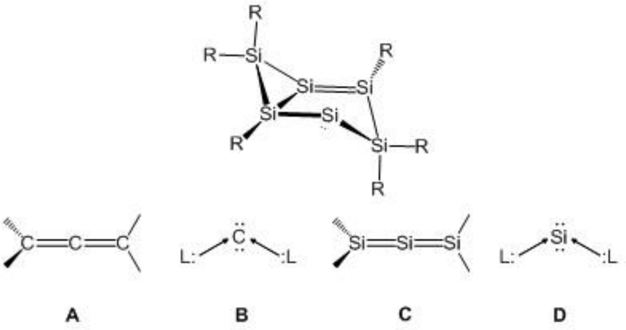

MS15-T3

Charge Density - an experimentalist's view

A. Wagner[1]
[1]*Diamond Light Source, Chilton, Didcot, United Kingdom*

The field of charge density has changed tremendously over the last two decades. While twenty years ago state-of-the-art experiments required more than a week of collecting accurate diffraction data from sealed tubes and point detectors, the combination of 2nd generation synchrotrons with CCD area detectors opened the field to much faster experiments with complete high-resolution data collected in only a day [1]. Moving to 3rd generation synchrotrons this time could be reduced even further to 3 - 4 hours per project [2]. With the advent of the Pilatus pixel detectors [3] nowadays complete accurate data sets can be collected even within minutes. In this talk I will review how recent hardware developments have enabled the method to become mature and will show examples from Peter Luger's group being on the forefront of these developments.

[1] T. Koritsanszky, R. Flaig, D. Zobel, H.-G. Krane, W. Morgenroth, P. Luger *Science* 1998 (279), 356-358.
[2] P. Luger, A. Wagner, C.B. Huebschle, S.I. Troyanov *J. Phys. Chem. A* 109 (2005), 10177-10179.
[3] Ch. Broennimann, E.F. Eikenberry, B. Henrich, R. Horisberger, G. Huelsen, E. Pohl, C. Schulze-Briese, M. Suzuki, T. Tomizaki, H. Toyokawa, A. Wagner *J. Synchrotron Rad.* 13 (2006), 120-130.

MS15-T4

Geometry versus Topology: Combined AIM, ELI-D and ASF Analysis of Hapticities and intramolecular H...H Contacts in asymmetric Zincocenes

S. Mebs[1], M. Chilleck[2]
[1]*Leibniz-Institut für Kristallzüchtung, Berlin, Germany*
[2]*Humboldt-Universität zu Berlin, Institut für Chemie, Berlin, Germany*

The molecular structures of asymmetric zincocenes (zinc cyclopentadienyl complexes) immediately raise two fundamental questions: 1. What is the nature of the metal-ligand interaction, or in other words: how to unambiguously determine the hapticities and metal-ligand bond characteristics? 2. What is the nature of the ligand-ligand interaction, or in other words: how to determine the number and types of weak intramolecular interactions (e.g. dihydrogen bonds)? For both questions the exclusive inspection of the geometrical parameters (distances and angles) may lead to arbitrary decisions and ambiguous concepts. However, the combined analysis of the topological and integrated properties of the electron density, its virial field (both according to the Atoms-In-Molecules, AIM[1], theory), and the electron localizability (according to the electron localizability indicator, ELI-D[2]) in conjunction with the analysis of fragmental surfaces (e.g. aspherical stockholder fragments, ASF[3]) provides a self-consistent interpretation scheme for the number and kind of metal-ligand and ligand-ligand interactions. For both questions the topological results can indeed be traced back to geometrical parameters: 1. For Zn-C distances shorter than 2.3 Å a Zn-C virial path and a disynaptic Zn-C ELI-D basin is observed, whereas for longer distances none of these are found. The ASF surfaces show characteristic shapes for η^1, η^2, and η^5 types of bonding.[3] 2. For the intramolecular H...H contacts a dependency of the AIM and ELI-D topology against the C_1-H_1...H_2 and H_1...H_2-C_2 angles is found. For sharp angles (both <100°) no H...H saddle points are found, neither in AIM nor in ELI-D. With increasing angle, H...H saddle points are observed first in ELI-D, then in the electron density and finally in the virial field if at least one angle becomes larger than ca. 130° and the other also being broad (>120°).[4] A dependency against the H...H distance is not observed. Exceptions are found in cases in which one H atom is involved in more than one H...H contact, because the close appearance of several H and C atoms can prevent the formation of a saddle point, although electron density is accumulated between the H atoms.

1. R.F.W. Bader, *Atoms in Molecules: A Quantum Theory*, Cambridge University Press, Oxford U.K., 1991.
2. M. Kohout, *Int. J. Quantum Chem.* 97 (2004) 651.
3. S. Mebs, M.A. Chilleck, S. Grabowsky, T. Braun, *Chem. Eur. J.* 18 (2012) 11647.
4. S. Mebs, M.A. Chilleck, *Chem. Phys. Lett.* 591 (2014) 1.

Analysis of the electron density, the potential energy density (virial field) and the electron localizability for the determination of the hapticities (Zn-C connectivity) and the intramolecular H...H contacts.

Figure 1

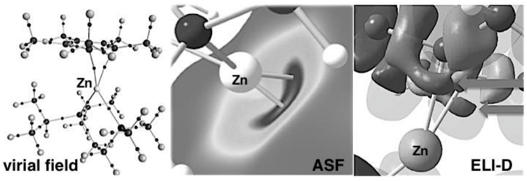

Figure 2

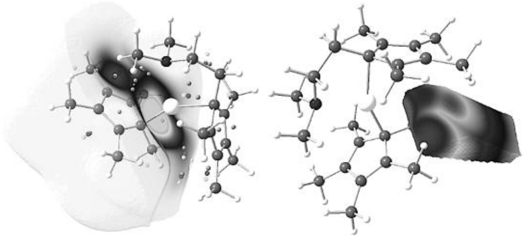

MS15-T5

Synchrotron data collection in five minutes, automatic model building and H-ADP estimation using the invariom database streamlines charge density research of organic molecules

J. Luebben[1], B. Dittrich[1,2], A. Meents[3]
[1]*Georg-August-University Goettingen, Institute of Inorganic Chemistry, Goettingen, Germany*
[2]*Universität Hamburg, Institut für Anorganische und Angewandte Chemie, Hamburg, Germany*
[3]*DESY, Petra III Beamline P11, Hamburg, Germany*

The synchrotron Petra III provides high flux at photon energies of 20-25 keV. Such energies, when combined with the Pilatus 6M pixel for shutterless data collection, expand the possibilities of high-resolution data collection in charge density research.

To illustrate this point we have collected crystal structure data (d=0.5 Å) of the antibiotic lincomycin at beamline P11 at Petra III in a five-minute experiment on a specimen approximately the size of the beam. A sample temperature of 11(3) K was set with a helium open flow

low-temperature device. The detector distance was 134.6 mm and allowed reaching high resolution with a single detector setting. A similar second measurement at 100(1) K with a nitrogen gas flow cooling device was also performed to allow comparison to an earlier experiment on the home diffractometer. The in-house data collection to d=0.45 Å at 100(1) K used a Bruker D8 goniometer equipped with an Apex II detector and an Incoatec Mo K microsource. It will be shown that fast, shutterless data collection is giving data quality comparable to the several day-long measurement at home. Problems of detector dead-time correction will be addressed and discussed. Careful data analysis with invariomtool [1] relied on automated model building for initial invariom- and subsequent charge-density refinement. The automatically assigned scattering factors of the generalized invariom database [2] ensured deconvolution of electron density and thermal motion parameters in pre-refinement. The database also provides individual bond-distances to hydrogen atoms from DFT geometry optimizations. Invriomtool generates a reproducible multipole model for free parameter refinement. A novel aspect of this study is that the invariom notation is now also used in a new procedure to obtain estimates for ADPs of hydrogen atoms that was inspired by TLS+ONIOM [3] and the shade server [4]. It combines an automated segmented rigid-body (TLS) fit [5] - to get external modes - with internal modes derived from computed invariom model-compound frequencies. Summing both contributions (subtracting the internal modes prior to the TLS fit) provides hydrogen ADPs in good agreement with those of the shade2 server.

A new program, APD-toolkit, was coded to do these tasks. The benefit for charge density research is that Uiso for hydrogen atoms become unnecessary, thereby minimizing the number of least-squares parameters, which helps to faithfully retrieve molecular properties like dipole moments or electrostatic potentials.

References
[1] C. B. Hübschle, P. Luger et al., J. Appl. Cryst. (2007), 40, 623-627.
[2] B. Dittrich, C. B. Hübschle et al., Acta Cryst. (1013), B69, 91-104.
[3] A. E. Whitten and M. A. Spackman, Acta Cryst. (2006), B62, 875-888.
[4] A. O. Madsen, J. Appl. Cryst. (2006), 39, 757-758.
[5] V. Schomaker and K. N. Trueblood, Acta Cryst. (1998), B54, 507-514.

MS15-T6

Is the R-factor resulting from my model refinement adequate?

J. Henn[1]
[1]*Universität Bayreuth, Fakulty I, Bayreuth, Germany*

It is possible to predict the R value from experimental data. When the experimental standard uncertainties are correct and the model is adequate, the predicted R value and the R value obtained after specifying and refining a model, the de facto R value, will be very close to each other. In this case the difference between predicted and de facto R value is due to random statistical fluctuations. Larger differences indicate systematic errors. This procedure is completely general and can be applied to any scientific field. Application to crystallographic problems will be discussed.

Literature: J. Henn and A. Schönleber, Acta Cryst. (2013). A 69, 549-558

MS16 – Hot new structures II

MS16-T1

Moving ions across membranes

W. Kühlbrand[1], D. Wöhlert[1], î Yildiz[1]
[1]*Max-Planck-Institut für Biophysik, Department of Structural Biology, Frankfurt am Main, Germany*

Membrane proteins are essential to transport molecules across biological membranes. This gateway task makes them important drug targets. About 60% of all approved drugs target membrane proteins (*1*). Transport of ions across membranes is essential for every cell to maintain physiological salt concentrations and to keep pH homeostasis. In the past years X-Ray structures of various secondary transporters have provided insight into the mechanisms of membrane transport. However, difficulties in expression, purification and crystallization of membrane proteins still restrict the number of available structures. For well-characterized secondary transporters such as LeuT (*2*), BetP (*3*) and Ca^{2+}/H^{+}-exchangers (*4*) crystal structures in different conformations and substrate binding states have been obtained. However, for many important classes of transport proteins, detailed structures are urgently needed to understand their mechanism of action and to guide drug development. We report crystal structures of 2 homologues of a new secondary transporter in different states, with or without substrate bound. These structures shed light on the transport mechanism of this important class of membrane transport proteins.

1. M. A. Yildirim, K. I. Goh, M. E. Cusick, A. L. Barabasi, M. Vidal, Drug-target network. *Nat Biotechnol* 25, 1119 (Oct, 2007).
2. H. Krishnamurthy, E. Gouaux, X-ray structures of LeuT in substrate-free outward-open and apo inward-open states. *Nature* 481, 469 (Jan 26, 2012).
3. C. Perez, C. Koshy, O. Yildiz, C. Ziegler, Alternating-access mechanism in conformationally asymmetric trimers of the betaine transporter BetP. *Nature* 490, 126 (Oct 4, 2012).
4. T. Nishizawa *et al.*, Structural basis for the counter-transport mechanism of a H+/Ca2+ exchanger. *Science* 341, 168 (Jul 12, 2013).

MS16-T2

Structural basis of substrate specificity of outer membrane channels from Acinetobacter baumannii

M. Zahn[1], B. van den Berg[1]
[1]*Newcastle University, Institute for Cellular and Molecular Biosciences, Medical School, Newcastle upon Tyne, United Kingdom*

Bacterial resistance against antibiotics is an increasing and serious global health problem. An important reason for antibiotics resistance is the inefficient passage of the antibiotics through the outer membrane (OM) of Gram-negative bacteria. In general, OM substrate uptake is achieved by protein channels within the OM. Pathogenic bacteria with a low-permeability OM such as *Acinetobacter baumannii* are intrinsically resistant towards antibiotics due to the fact that the OM contains exclusively substrate-specific channels with small pores. This is in contrast to e.g. *Escherichia coli*, which has large, non-specific OM pores that facilitate antibiotic uptake. Knowledge of OM channel structures will be essential for structure-guided development of new drugs that can penetrate the bacterial cell more efficiently. We have elucidated X-ray crystal structures of several outer membrane channels from *Acinetobacter baumannii* and have determined their substrate specificities. These studies form the starting point towards understanding small-molecule OM permeation for this notorious drug-resistant human pathogen.

MS16-T3

Entrapment of DNA in an intersubunit tunnel system of a single-stranded DNA-binding protein

H. Ghalei[1,2], H. von Moeller[1,3], D. Eppers[1], D. Sohmen[4], D. Wilson[4], B. Loll[1], M. Wahl[1]
[1]*Free University Berlin, Structural Biochemistry, 14195, Germany*
[2]*Max-Planck-Institute for Biophysical Chemistry, Department of Cellular Biochemistry, Goettingen, Germany*
[3]*moloX GmbH, Berlin, Germany*
[4]*University of Munich, Gene Center, Department of Biochemistry and Center of integrated Protein Science Munich (CiPSM), Munich, Germany*

All organisms contain essential ssDNA-binding proteins (SSBs) to protect and stabilize ssDNA during replication, recombination and repair. Most SSBs form oligomers and bind ssDNA on their outsides *via* one of four types of classical ssDNA-binding domains. Instead of a classical SSB, some hyperthermophilic crenarchaea harbor a non-canonical SSB termed ThermoDBP. Two related but poorly characterized groups of proteins, which share the ThermoDBP N-terminal DNA-binding domain, have a broader phylogenetic distribution and co-exist with ThermoDBPs and/or other SSBs. We have investigated the nucleic acid binding properties and crystal structures of representatives of these groups of ThermoDBP-related proteins (ThermoDBP-RPs) 1 and 2. ThermoDBP-RP 1 and 2 oligomerize by different mechanisms and only ThermoDBP-RP2 exhibits strong single-stranded DNA affinity *in vitro*. A crystal structure of ThermoDBP-RP2 in complex with DNA reveals how the NTD common to ThermoDBPs and ThermoDBP-RPs can contact the nucleic acid in a manner that allows a symmetric homo-tetrameric protein complex to bind single-stranded DNA molecules asymmetrically. While single-stranded DNA invariably wraps around classical SSBs, it traverses an internal, intersubunit tunnel system of a ThermoDBP-RP2 tetramer. Our results indicate that some archaea have acquired special SSBs for genome maintenance in particularly challenging environments.

MS16-T4

Ultra-high affinity chitin binding by LysM domain dimerization in fungal effectors prevents host PAMP signaling

J. Mesters[1], R. Saleem-Batcha[1], A. Sánchez-Vallet[2], B. Thomma[2]
[1]*University of Lübeck, Institute of Biochemistry, Lübeck, Germany*
[2]*Wageningen University, Laboratory of Phytopathology, Wageningen, Netherlands*

While host immune receptors detect microbial patterns (PAMPs) to activate immunity, pathogens deregulate immunity through secreted effectors. Fungi employ LysM domain-containing effectors to prevent recognition of cell wall chitin fragments by host LysM domain-containing immune receptors, although the mechanism how fungal LysM effectors compete for chitin binding remained unclear until recently. With combined crystallographic (structure to 1.6Å resolution) and isothermal titration calorimetric analysis we demonstrated a novel mode of chitin binding that evolved in fungi based on substrate induced intrachain LysM dimerization[1], leading to ultra-high (pM) chitin binding affinity. Meanwhile we obtained another fungal LysM effector structure that displays an intermolecular dimer of two LysM domains, providing further evidence that fungal LysM domains can cooperate to form a single high-affinity chitin binding site.

[1]Sánchez-Vallet et al. (2013) Fungal effector Ecp6 outcompetes host immune receptor for chitin binding through intrachain LysM dimerization. eLife **2**, e00790.

Figure 1

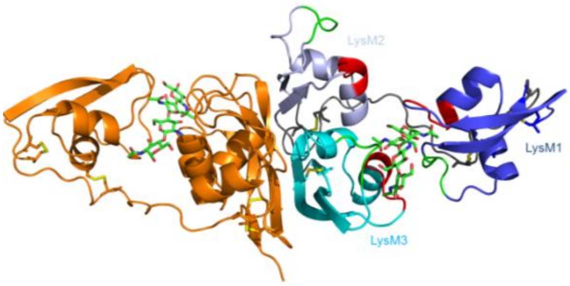

MS16-T5

Crystal structure of the first bacterial diterpene cyclase and structure-based engineering of plasticity residues

R. Janke[1], C. Görner[2], M. Hirte[2], T. Brück[2], B. Loll[1]
[1]*FU Berlin, Berlin, Germany*
[2]*TU Munich, Industrielle Biokatalyse, Garching, Germany*

Terpene molecules represent one of the most diverse groups of natural biomolecules. Sesqui- and diterpenes are a versatile class of secondary metabolites predominantly derived from plants, marine invertebrates, fungi and some prokaryotes. Properties of these natural products include anti-tumor, anti-inflammatory, antibiotic, neuroprotective and even insecticidal activities, which makes these compounds high value commercial targets for the chemical and pharmaceutical industry. Since terpenes are difficult to access by chemical synthesis, production can be alternatively performed in engineered microorganism. Here we present the first crystal structure of a bacterial diterpene cyclase CotB2 at 1.64 Å resolution by single wavelength anomalous dispersion. CotB2 catalyzes the cyclization of linear geranylgeranyl diphosphate to tri-cyclic cyclooctat-9-en-7-ol. Subsequent oxidation of cyclooctat-9-en-7-ol by two cytochrome P450 monooxygenases leads to bioactive cyclooctatin. Plasticity residues that decorate the active site of CotB2 have been mutated, resulting in altered, novel mono-, di- and tri-cyclic compounds.

MS16-T6

Structure of human α-2,6 sialyltransferase:Complex glycans, substrate specificity, and catalysis

M. Rudolph[1], B. Kuhn[1], J. Benz[1], M. Greif[2], A. Engel[2], H. Sobek[2]
[1]*F. Hoffmann-La Roche, Molecular Design & Chemical Biology, Basel, Switzerland*
[2]*Roche Diagnostics GmbH, Penzberg, Germany*

Human β -galactoside α-2,6-sialyltransferase I (ST6Gal-I) establishes the final glycosylation pattern of many glycoproteins by transferring a sialyl moiety to a terminal galactose. The sialyl moiety boosts the activity of therapeutic immunoglobulins (IgG) that are currently used to combat more than 30 different inflammatory diseases including rheumatoid arthritis and morbus Crohn. Complete sialylation is essential for IgG anti-inflammatory activity, but is difficult to achieve *in vitro* owing to the limited sialylation of certain galactose acceptors by ST6Gal-I. No structural information on ST6Gal-I that could help to improve its enzymatic properties for biotechnological purposes was hitherto available.

In order to understand the molecular reasons for the incomplete sialylation activity of ST6Gal-I, the crystal structure of the human enzyme in complex with the reaction product cytidine 5'-monophosphate was determined by SIRAS phasing using data from an iodide soak. The nucleotide complex allows the rationalization of the inhibitory activity of cytosine-based nucleotides by modeling of their binding modes. ST6Gal-I differs from related sialyltransferases by several large insertions and deletions that determine its regiospecificity and substrate specificity. An important feature of the structure is a large glycan contributed from a symmetry mate, which localizes to the active site of ST6Gal-I in an orientation that is compatible with catalysis. Because there are no protein-protein interactions the glycan binding mode can be generalized to any glycoprotein that is a substrate of ST6Gal-I. The structure also reveals why IgG are incompletely sialylated and illustrates avenues towards improving the enzymatic properties of ST6Gal-I. Comparison with a bacterial sialyltransferase in complex with a modified sialyl donor lends exciting insight into the Michaelis complex of ST6Gal-I catalysis. The results support an S_N2 reaction mechanism with inversion of configuration at the sialyl residue and suggest substrate-assisted catalysis with a charge-relay mechanism that bears a conceptual similarity to serine proteases.

Figure 1

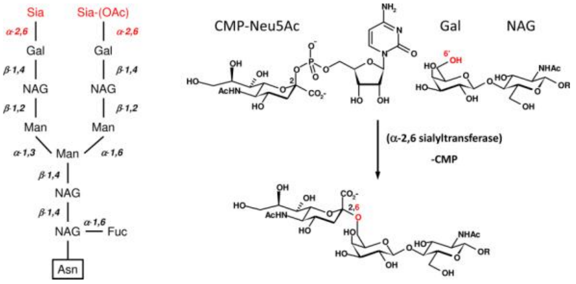

Figure 2

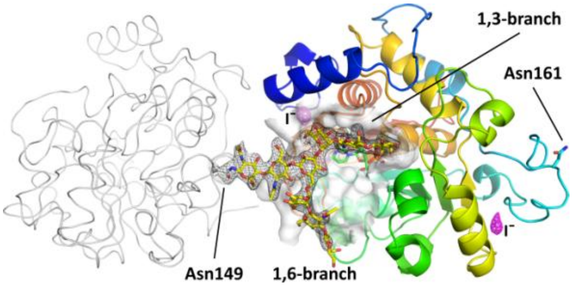

MS17 – Spectroscopy as supporting method in structure determination

MS17-T1

Surface-near modifications of $SrTiO_3$ local symmetry due to nitrogen implantation investigated by grazing incidence XANES

H. Stöcker[1], M. Zschornak[1], C. Richter[1], J. Walter[1], D. Meyer[1]
[1]*TU Bergakademie Freiberg, Institut für Experimentelle Physik, Freiberg, Germany*

Strontium titanate $SrTiO_3$ is an oxidic semiconductor and crystallizes in the perovskite-type of structure; however, several methods have been shown to induce distortions of this perfect cubic lattice. One of the key parameters is the oxygen stoichiometry that on the one hand acts as doping and has great influence on the electric conductivity but on the other hand also couples to the crystal structure. A common way to tune the real structure of surfaces is the implantation of ions. Therefore, we tested several species and found a strong impact of nitrogen implantation on the Ti-K absorption edge fine structure of $SrTiO_3$. X-ray absorption near-edge spectroscopy (XANES) in grazing incidence geometry was used to characterize the nitrogen implanted samples and revealed a slight shift of the Ti-K edge position and a strong increase of the second pre-edge peak compared to pure $SrTiO_3$. As both of these observations showed a dependence on the angle of incidence, clear evidence of a distorted surface layer is given. This layer is characterized by a shift of the Ti-K edge from the Ti^{4+} state of $SrTiO_3$ towards Ti^{3+} in the layer phase, which may be related to an increased concentration of oxygen vacancies or the formation of Ti-N bonds. The strong increase of the second pre-edge feature in the distorted phase can be explained by a static displacement of the Ti atom relative to the surrounding oxygen octahedron. Finally, the replacement of oxygen by implanted nitrogen may be the reason for both observations. This has been checked by comparing the measured spectra with simulations of the XANES region for different possible scenarios. Further photoelectron spectroscopy measurements were carried out to verify the results.

MS17-T2

Thermogravimetric, temperature dependent infrared and XRD investigations on $NaBO_2.xH_2O$ system

Z. Assi[1], C. H. Rüscher[1]
[1]*Institut für Mineralogie, Leibniz Universität, Kristallographie, Hannover, Germany*

Sodium metaborates , $NaBO_2.xH_2O$, with x the excess dehydration factor[1], form stable phases x=4, 2 (constituted of $B(OH)_4^-$ anions); x= 1/3 (Fig. 1) and x=0 (constituted of $[B_3O_6]^{3-}$ rings). These phases gain some attention as by-products of the reaction of $NaBH_4$ with water for hydrogen storage applications

$NaBH_4 + (2+x)\ H_2O \Rightarrow NaBO_2.xH_2O + 4H_2$

Therefore, the dehydration products of $NaBO_2.xH_2O$ with $4 \leq x \leq 2$ were further reinvestigated in more details.

Thermogravimetric analyses (TGA) were carried out under N_2 from room T to 400°, 200°, 120° and 75°C (20h) separately using a heating rate of 5°K/min. The end-product was then characterized by IR. Temperature dependent infrared (TIR) absorptions were measured in the range 25-420°C. Different isothermals were conducted under N_2 at temperatures 70° (20h), 120°, 120° (2h) and 400°C (5h). The end-product of each isothermal was then subjected to XRD and IR.

The starting product $NaBO_2.4H_2O$ (Riedel-de-Häen, >98%) was actually a mixture of x=4 and x=2 as evidenced by XRD and IR. The heating curve of TGA heated to 400°C shows five principal steps which are peaked in dTGA/dT at 66°, 95°, 115°, 156° and 280°C. According to the literature[2], the two first steps were associated to the release of crystalline water, and the other three steps at higher temperature were attributed to the release of structural water. However, characterizing the end- products of other TG at lower T than 400°C could give more explanations for these steps. TGA with heating to 200°C led to the 1/3 hydrate. The 120°C TGA reveals IR spectra with broad bands indicating an insofar not described phase, say x=n. This phase obviously preceded the formation of polymerized ring form. The 75°C 20h TGA experiment shows the formation of $NaB(OH)_4$.

TIR experiments (Fig. 2) elucidated more these steps and evidenced spectra of five different phases obtained during heating at 65°, 70° after 24h, at 115°, 160° after 43h and at 400°C. The spectra are assigned as follows: rearrangement of the water molecules (*spectrum 1)*, formation of the dihydrate (*spectrum 2)*, the phase x=n (*spectrum 3)*, the 1/3-hydrate (*spectrum 4)* and finally formation of $NaBO_2$ (*spectrum 5)*.

The different isothermals validated the different observations. Thus XRD analyses evidenced the formation of $NaBO_2$, $NaBO_2.1/3H_2O$, $NaB(OH)_4$ respectively from the isothermal at 400°C, 120°C (2h) and 70°C (20h). Three broad peaks with maxima at 3258, 3377, 3442 cm^{-1} and one sharp peak at 3640 cm^{-1} in the IR spectra of dihydrate were found characteristics of its framework and associated respectively to OH participating in hydrogen bonds and without such contribution. At 120°C the sample became gel-like after short time of heating, but then turns over to a white powder identified as the 1/3 hydrate.

In conclusion, the system $NaBO_2.xH_2O$ has been reinvestigated during heating showing a new gel type phase as the transferring state between the dihydrate into the 1/3 hydrate.

[1]E.Y. Marrero-Alfonso, J.R. Gray, T.A. Davis, M.A. Matthews, Int. J. Hydrogen Energy, 32, 4723 (2007)
[2]A. Kanturk, M. Sari, S. Piskin, Korean J. Chem. Eng., 25(6), 1331-1337 (2008)

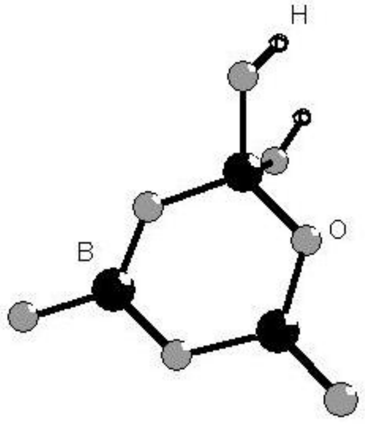

Fig.1 anionic part in NaBO2.1/3H2O

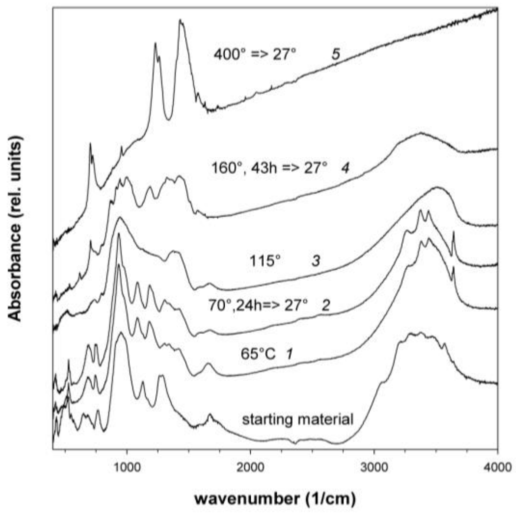

Fig.2 Temperature dependant IR on $NaBO_2.4H_2O$

MS17-T3

Resonant ultrasound spectroscopy: A non-destructive innovative technique to determine all independent elastic moduli

C. S. Pandey[1], J. Schreuer[1]
[1]*Ruhr University Bochum, Institute of Geology, Mineralogy and Geophysics, Bochum, Germany*

Resonant ultrasound spectroscopy (RUS) is an innovative non-destructive technique for determining elastic and piezoelectric constants of solids (minerals, materials, and thin films). Unlike other conventional methods for example pulse-echo method, where one requires a number of independent measurement of different samples, RUS require only one sample to determine all its independent elastic and piezoelectric constants in one single run with high internal consistency. The RUS technique measures the natural frequencies or free oscillations of a freely vibrating the sample, which are then used to solving an inverse problem for determining its complete set of independent elastic moduli. These frequencies depend on the sample's size, density, shape and elastic constants.

Here we describe RUS technique in detail, and using this technique we report some preliminary results on micrometer sized GaN sample for the first time. GaN is widely known because of its high technological importance. It has always been available as thin films, and therefore, its elastic moduli have not been measured reliably. Theoretically derived values of GaN elastic moduli as well as recently measured elastic constants on tiny GaN crystals using Brilliouin Zone spectroscopy and on several hundreds of micrometer sized GaN single crystal, all differ vastly from each other.

MS17-T4

Mechanisms behind the para- to ferroelectric phase transition in RbH2PO4 probed bymeans of purely resonant X-ray diffraction

C. Richter[1], D. Novikov[1], E. N. Ovchinnikova[2], K. Akimova[2], A. Oreshko[2], V. Dmitrienko[3], M. M. Borisov[4], M. Zschornak[5], E. Mehner[5], D. C. Meyer[5], J. Strempfer[1]
[1]*DESY, Photon Science, Hamburg, Germany*
[2]*Moscow State University, Physical Department, Moscow, Russian Federation*
[3]*A. V. Shubnikov Institute of Crystallography, Moscow, Russian Federation*
[4]*Kurtchatov Institute, Moscow, Russian Federation*
[5]*TU Bergakademie Freiberg, Experimentelle Physik, Freiberg, Germany*

Resonant X-ray diffraction was used to study the proton jumps in hydrogen-bonded rubidium dihydrogen phosphate (RDP) crystals. In the paraelectric RDP phase, hydrogen is delocalized between two crystallographically equivalent positions. At lower temperatures, this symmetry can be broken, which defines the processes that lead to the para- to ferroelectric phase transition. We have measured the energy spectra of the forbidden reflections 006 and 550 at incident radiation energies close to the Rb K-edge in a wide temperature range, down to the temperature of the ferroelectric phase transition. In the paraelectric phase we observed a growth of integrated intensity for both forbidden reflections with temperature. This behavior is opposite to conventional non-resonant Bragg reflections, where intensity decreases in accordance with the Debye-Waller factor. The developed theoretical model explains this effect with the thermal motion induced (TMI) scattering mechanism and also confirms the adiabatic approximation stating that electrons instantly follow the nuclei movements. In the 550 energy spectra, we have observed an additional contribution to the resonant structure factor which could be associated with the presence of transient Slater-type proton configurations (PC) in the half-filled hydrogen position.

Figure 1

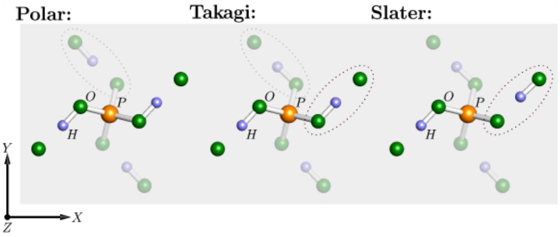

MS17-T5

High-temperature phase transitions. Spectroscopic properties and dimensionality reduction in rubidium thorium molybdate family

B. Xiao[1], T. Gesing[2], E. Alekseev[1]
[1]*Forschungszentrum Jülich GmbH, Jülich, Germany*
[2]*Universität Bremen, Institut für Anorganische Chemie, Bremen, Germany*

Molybdenum is one of the high yield fission products created in a nuclear reactor. The chemical reaction between Mo and the fuel materials such as UO_2, PuO_2 can lead to the formation of complex compounds and in turn to affect the behavior of spent fuel. The knowledge of the chemical characteristics of these molybdates compounds is hence crucial for evaluating the properties of nuclear reactors. Due to the chemical similarities of Th^{4+} and U^{4+}/Pu^{4+}, the less-radioactive and more stable Th^{4+} is often used as an alternative to study the chemical properties of these compounds. Therefore, detailed investigation were carried out on Th(IV)-Mo systems with a variety of cations (alkali metals and alkaline earth metals). These studies have led to 4 new Rb−Th−Mo phases which adopt the whole range of possible structural dimensionalities from 0D to 3D. The crystal structure of $Rb_8Th(MoO_4)_6$ is built upon infinite $[Th(MoO_4)_6]^{8-}$ clusters. 1D chain structure of $Rb_2Th(MoO_4)_3$ can be seen as being based on scheelite-typed $CaWO_4$. 2D sheets and 3D framework construct $Rb_4Th(MoO_4)_4$ and $Rb_4Th_5(MoO_4)_{12}$, respectively. Despite appearing complex dimensional hierarchy, the Th and Mo each only has one type of coordination configuration (ThO_8 anti-prism and MoO_4 tetrahedral) in all these 4 phases that shows the flexible property of Th−O−Mo linkages. Using the concept of “dimensional reduction”, the dimensionality changing in these phases is discussed. The result shows that by incorporating Rb cations, the Th−O−Mo connections can be broken and thus lead to lower dimensionality. Their physicochemical properties were characterized by a series method such as high-temperature powder diffraction, Raman and FTIR spectroscopy as well as DSC. The vibrational spectra which can be roughly divided into stretching and bending regions were analyzed by the means of nuclear-site group theory.[1] The DSC shows that two phases, $Rb_8Th(MoO_4)_6$ and $Rb_4Th_5(MoO_4)_{12}$, remain stable until melting points. The temperature-dependent X-ray powder diffraction data analysis confirms phase-transitions in $Rb_2Th(MoO_4)_3$ and $Rb_4Th(MoO_4)_4$ corresponding to the first endothermic peaks on DSC. Nevertheless, the deviations are really small and the high-temperature structures could not be finally evaluated from powder data.

1. Rousseau, D. L.; Bauman, R. P.; Porto, S. P. S., Normal mode determination in crystals. *J. Raman Spectrosc.* 1981, *10* (1), 253-290.

MS17-T6

Application of a Difference Electron Nanoscope (DEN): 3D Magnetical Structures of Synthetic Fayalite from the Combination of Synchrotron and Neutron Diffraction and Mössbauer Spectroscopy

W. Lottermoser[1], K. Steiner[2], G. Scharfetter[3], S.- U. Weber[4], M. Grodzicki[1], A. Kirfel[5], G. Amthauer[1]
[1]*University of Salzburg, Materials Engineering and Physics, Salzburg, Austria*
[2]*HBLA Ursprung, Salzburg, Austria*
[3]*University of Salzburg, Computer Sciences, Salzburg, Austria*
[4]*Technical University of Braunschweig, Physical and Theoretical Chemistry, Braunschweig, Germany*
[5]*University of Bonn, Mineralogy and Palaeontology, Bonn, Germany*

The evaluation of a 3-dimensional orientation of magnetic moments in solids is still a challenging problem in modern physics and crystallography. Common methods to arrive at this goal are neutron diffraction (in particular with polarized n.), magnetometry and Single Crystal Mössbauer Spectroscopy (SCMBS). However, each of these methods have their limitations, viz. antiphase domains, magnetical impurities, the confinement to special nuclides a.s.o.. X-ray and synchrotron diffraction may provide valuable information on crystallographic structures, but the separation of the magnetically effective electrons (in our case: 3d) is hardly possible with the latter experiments.

However, we are in the favourite situation that in the case of synthetic fayalite we dispose of data sets of most of the methods mentioned above and can try to combine the collected physical informations of each one. By the recently presented Difference Electron Nanoscope (DEN) we dispose of a powerful tool to display the 3-dimensional distribution of very accurately determined difference electrons from synchrotron diffraction measurements and to correlate them to the size and direction of the electric field gradient (efg) of Mössbauer spectroscopy and DFT calculations. This had been demonstrated successfully elsewhere [1,2]. Since Mössbauer spectroscopy is also capable of providing informations on the size and direction of the internal magnetic field H(0) with respect to the efg, we can now correlate the difference electron distribution mentioned above with H(0) and the magnetic moments’ orientation from neutron diffraction [3]. On the DEN images amazing details are visible, viz. difference electrons around special oxygens that have been identified as most probably bearing superexchange coupling.

New results will be presented with special emphasis on the M2 position that previously has not been taken into full account [2].

[1] W. Lottermoser, S.-U. Weber, M. Grodzicki, A. Kirfel, G. Amthauer. Eur.J.Min. 24/5, 791-797 (2012).
[2] W. Lottermoser, K. Steiner, G. Scharfetter, S.-U. Weber, M. Grodzicki, A. Kirfel, G. Amthauer. Cryst. Res. and Technology, published online: 29 Oct 2013, DOI: 10.1002/crat.201300208 (2013)
[3] W. Lottermoser, K. Forcher, G. Amthauer, W. Treutmann, S. Hosoya. Phys.Chem.Minerals 23, 432-438 (1996).

MS17-T7

A Crystal Chemical Study using 71Ga MAS NMR of the fast-ion conductor Li7La3Zr2O12 doped with Ga

G. Amthauer[1], D. Rettenwander[1], C. A. Geiger[1]
[1]*University of Salzburg, Dept. Material Research & Physics, Salzburg, Austria*

$Li_7La_3Zr_2O_{12}$ (LLZO), a garnet-like structure, has a high ion conductivity of approximately 10^{-4} S·cm^{-1} and good chemical stability against Li metal [1]. It is therefore a promising candidate as an electrolyte for secondary all-solid-state Li-ion batteries. At room temperature end-member LLZO is tetragonal ($I4_1/acd$) and it has a lower conductivity compared to the cubic modification (Ia-$3d$), which is only stable above approximately 150 °C [2]. Geiger et al. showed that the higher conducting cubic phase could be stabilized at room temperature through the incorporation of small amounts of Al^{3+}. Because gallium is directly below aluminum in the periodic table, Ga could show a similar crystal chemical behavior in LLZO as the latter. Initial work on Ga-bearing LLZO has been done by El Shinavi and Janek [3] and Howard et al [4]. A systematic NMR study of the whole chemically well characterized solid solution series was not performed.

Thus, we synthesized a series of $Ga^{3+}_xLi_{7-3x}La_3Zr_2O_{12}$ solid solutions with x = 0.06-0.72 by sintering oxides at high temperatures. The synthetic products were characterized by X-ray powder diffraction and were determined to be single-phase garnet. Compositions were determined by electron microprobe (La, Zr, Ga) and inductively coupled plasma (ICP) optical emission spectroscopy (OES) measurements (Li). We used ^{71}Ga MAS NMR spectroscopy to investigate the crystal-chemical role of Ga^{3+}. The NMR spectra show that Ga^{3+} occupies a distorted 4-fold coordinated 96*h* site in the garnet framework of cubic LLZO.

We thank Michael Fechtelkord, Ruhr Universität Bochum, for taking the spectra.

(1) Murugan, R.; Thangadurai, V.; Weppner, W. *Angew. Chem.* 2007, *119*, 7925.
(2) Geiger, C. A.; Alekseev, E.; Lazic, B.; Fisch, M.; Armbruster, T.; Langner, R.; Fechtelkord, M.; Kim, N.; Pettke, T.; Weppner, W. *Inorg. Chem.* 2011, *50*, 1089.
(3) El Shinawi, H.; Janek, J. *J.Power Sources* 2013, 225, 13.
(4) Howard, M. A.; Clemens, O.; Kendrick, E.; Knight, K. S.; Apperly, P. A.; Anderson, P. A.; Slater, P. R. *Dalton Trans.* 2012, 41, 12048.

MS18 – Crystallography in archeometry

MS18-T1

X-ray and Raman Studies on biotic and abiotic calcite decorations on celtic fibulae

K. Bente[1]
[1]*Universität Tübingen, Angewandte Mineralogie , Tübingen, Germany*

Aims: In general, bead decorations on celctic fibulae [1] are archaeologically defined as recent corals related to trade roads from the mediterranean sea to central Europe [2, 3]. Because of doubts [4, 5] about these interpretations, we systematically studied calcites due to biotic and abiotic mineralogical and sedimentary characteristics. These data are used as references for to check bead materials of fibulae from late La-Tène times in Germany.

Methods: Non-destructive X-ray diffraction studies were carried out by locally high resolving D8 discovery (Bruker AXS) using Co radiation. Raman data were non-destructively collected by Micro-Raman machines using a HeNe-Laser 633 nm and an Argon Laser 457 nm respectively and compared with literature data [6, 7]. In our comparison studies, recent red and white corals from different sources and also abiotic calcites and additional aragonite corals were used.

Results: The (104) x-ray reflection of the studied calcites as well as the related refined lattice parameters revealed MgCO3 contents up to 16.0% verified by XRF data. Raman spectroscopic data showed relatively simple fingerprints for abiotic, but complicated spectra for biotic materials represent organic pigments as polyenes. The resulting two groups of spectra significantly represent recebt or fossil coral and non-coral materials, respectively. Additionally, shifts of the Raman spectra related to Mg contents of the calcite were detected in agreement with XRD and XRF data [8].

The data are applied to bead decorations and their archaeological interpretations concerning celtic fibulae [9] provided by Kreismuseum Bitterfeld, Landesmuseum Stuttgart, Naturkundemuseum Leipzig and Landesamt für Vorgeschichte Halle.

Reference

[1] R. Müller: Die Grabfunde der Jastorf- und Latènezeit an unterer Saale und Mittelelbe.Veröff. Landesmuseum für Vorgeschichte Halle, Saale 38 Berlin (1985).

[2] F. Fleischer, M. Schrickel, J. Frase: Das Gräberfeld bei Leipzig-Hänichen i. V. (2012)

[3] R. Schorpp: Entstehung und Blüte der Keltischen Kultur (2009)

[4] T. Schüler: Röntgendiffraktometrische Untersuchungen an drei latènezeitlichen Schmuckeinlagen. Alt-Thüringen 31, 57 - 63 (1997)

[5] V. Moucha: Einlagen in bronzener Zierrosette Gehäuse Mittelmeerschnecke *Cypraecassis rufa* (1969)

[6] J. Unvros, S. K. Sharma, F. T. Mackenzie: Characterization of some biogenic carbonates with Raman spectroscopy - American Mineralogist, Volume 76, pages 641-646, 1991

[7] S. Fürst: Die südwestdeutschen Korallenfunde der Hallstatt- und Frühlatènezeit im Spiegel Raman-spektroskopischer Analysen - Mag. Art. Mainz (2010)

[8] J. B. Ries: Skeletal mineralogy in a high-CO_2 world - J. Exper. Marine Biolog. Ecolo. 403 54 -64 (2011)

[9] M. Schrickel, K. Bente, Ch. Berthold, W, Grill, U. Teschner, T. Sarge, T. Hoppe: Vergleichende archäometrische Untersuchungen an Fibeln mit Korallenzier: Fragestellungen und methodischer Überblick - Otzenhausen (2014)

MS18-T2

Non destructive chemical imaging of archaeological artifacts with the SLcamα®, an X-ray color camera

C. Berthold[1], O. Scharf[2], K. Bente[1], K. G. Nickel[1], R. Wedell[3], A. Bjeoumikhov[2]
[1]*University of Tübingen, Applied Mineralogy, Tübingen, Germany*
[2]*IFG-Institute for Scientific Instruments GmbH, Berlin, Germany*
[3]*IAP-Institut für angewandte Photonik e.V., Berlin, Germany*

The development of modern X-ray detector systems in the last decade gives meanwhile the opportunity to perform a direct locally highly resolved chemical image of a sample if a pnCCD detector (developed by PNSensor GmbH, Munich) is used with its image area of 12,7mm x 12,7mm and a 264x264 pixel resolution with a energy resolution of 152eV (MnKα) for each pixel. With this type of detector it is now possible to measure a full-field energy-resolved X-ray image (FF-XRF) of a sample surface if an X-ray optic is mounted in front of the detector (1,2). Using different types of such X-ray polycapillary optics with varying magnification it is also possible to change simply the magnification of the camera setup to increase or decrease the local resolution or vice versa the area, which is measured. Moreover, using a non magnifying 1:1 optic 3-dimensional objects can be characterized chemically for the first time without any focussing effort due to the almost infinite depth of sharpness of this kind of optic (3). This unique advantage of the SLcam® is a big step forward for an efficient chemical imaging of 3-dimensional surfaces. The opportunity of a nondestructive and time efficient locally resolved chemical analysis of sample surfaces in a common laboratory setup is a breakthrough in the characterization of not only sensitive archaeological artifacts objects independent from their size and morphology but also any kind of other materials.

In our presentation we will show results from different archaeological artifacts and other samples to demonstrate the potential of the X-ray color camera.

(1) Scharf, O. et al., (2011) *Compact pnCCD-Based X-ray Camera with High Spatial and Energy Resolution: A Color X-ray Camera*, Anal. Chem., Vol. 83(7), pp. 2532-2538

(2) Ordavo, I, et al., (2011) *A new pnCCD-based color X-ray camera for fast spatial and energy-resolved measurements,* Nucl. Instrum. Methods Phys. Res. Sec. A 654(1) pp. 250 - 257.

(3) Berthold, C, Bente, K., Scharf, O., Bjeoumikhov, A., Ordavo, I. (2011) *Fast chemical mapping of archaeological objects with a novel x-ray color camera.* Metalla Sonderheft 5 (Tübingen 2011)

MS18-T3

Microstructural analysis of bone apatite in archeological finds by XRD full line profile analysis

B. Kocsis[1], A. Toncala[2], M. Kaliwoda[3], B. Maier[1], G. Gruppe[2], W. Schmahl[1]

[1]*Ludwig Maximilinas Universität, Geo-und Umweltwissenschaften, München, Germany*

[2]*Ludwig Maximilian University Munich, Department of Biology I, Martinsried, Germany*

[3]*Mineral State Collection Munich, München, Germany*

The DFG cooperative research project FOR1670 in Munich connects archeologic, anthropologic, cultural and geographic aspects of transalpine human migrations in the bonze and iron age. The isotopic investigation of human bones and those of domesticated and wild animals from archeologic finds is a key method in this project. Applying XRD, SEM, Raman and IR spectroscopy we examine diagenetic alteration of the buried bone and thermal alteration occurring during the cremation of the deceased which was applied in certain cultural epochs. Both processes affect the crystalline state of the bone apatite and its trace element and isotope signatures. Thus the materials analysis is needed as a prerequisite to the interpretation of the isotope data.

To understand the crystalline state of the bone apatite we carefully analysed the XRD full profile shape of numerous fresh samples and samples from different archeological sites by model calcultations with the Rietveld method. The profile can be described with a monoclinic apatite structure and crystallite sizes in the range of 15-25 nm. Experimental heat treatment (at 800°C and 60 minutes for preparation for isotope analyses) results in grain growth to about 150 nm, and sometimes, but not always, CaO is formed. The CaO displays a crystallite size of about 60nm and it is conserved in air in the cremated bone at least over weeks, such that we assume it is encapsulated in the apatite nanocrystals. The carbonate in the bone apatite is sustained at these temperatures, as judged form the IR- and Raman signatures. In the archeologic context the CaO reacts to calcite in the soil environment. The CaO weight fraction in the experimentally cremated bone material depends significantly on the archeologic site from which the bone was taken. We suspect a relation to the Ca/P ratio of the bone. An experimental time-temperature-transformation diagram is under construction.

MS18-T4

The Eternal City, but non-eternal coins: Dezincification in an ancient Roman brass coin

G. Eisenblätter[1], A. Franz[1,2], N. Kardjilov[2], S. Zander[2], G. Kloess[1]

[1]*Leipzig University, Institute of Mineralogy, Crystallography and Materials Science, Leipzig, Germany*

[2]*Helmholtz-Zentrum Berlin for Materials and Energy, Berlin, Germany*

Today non-invasive methods are of special interest in historical and archaeological sciences to understand and preserve the cultural heritage. Many archaeometallurgic analyses were done on silver or gold coins due to their value and well preserved state. Copper objects in contrast are highly corrosive. The corrosion takes not only place at the surface but also in the inside showing different paths of corrosion and depletion of alloying elements. With surface analysis only a small amount of the real existing corrosion could be described. The archaeometric studies are carried out on 120 ancient Roman copper coins that are dated to the Julio-Claudian dynasty. The coins are stored at the Leipzig University Library and the Herzog Anton Ulrich Museum Brunswick.

Of a special interest are coins which contain defects or depletion inside. By using X-ray or Neutron computed microtomography (µXRCT or NCT) the corrosion inside the copper coins can be visualized. For example there is a strong depletion inside the sestertius of Tiberius with the object number BS181 (see figure 1). Riederer [1] stated a copper content of 86.75 wt% and zinc content of 13.08 wt%. Usually a ratio of about 80 to 20 would be expected for this brass coin so it had to be discussed whether the coin is authentic or not.

The circumstance of placing the drill hole for atomic absorption spectroscopy analysis in a depleted area is revealed by visualizing the coin using imaging data (see figure 1). As our work has also shown there is a strong depletion in parts of the bulk material which can be clearly visualized. In addition Neutron diffraction (ND) experiments were carried out to proof the dezincification by detecting α-brass as bulk material and plain copper in depleted areas. Neutron diffraction data states a copper to zinc ratio of about 75 to 25 for the brass, but clearly shows the shift of intensity for copper and brass in the bulk material and depleted area (see figure 2). Using Neutron techniques like NCT or ND the ancient copper coins could be investigated in a non-destructive, non-invasive and sensitive way. Volume information given by NCT and ND proofed the assumed dezincification. There are two co-existing phases inside the sestertius: copper and brass while smithsonite as zinc-bearing mineral is spread over the complete surface of the coin.

Many thanks to Professor Dr. Wolfgang Leschhorn from Herzog Anton Ulrich Museum Brunswick and the Helmholtz-Zentrum Berlin for Materials and Energy for beamtime on V7 (ART-04-2208) and on E9 (ART-01-3252).

[1] J. Riederer: Die Metallanalyse römischer Münzen aus Kupferlegierungen des Herzog Anton Ulrich-Museums in Braunschweig. In: W. Leschhorn (2006): Die römischen Münzen. Herzog Anton Ulrich-Museum Braunschweig.

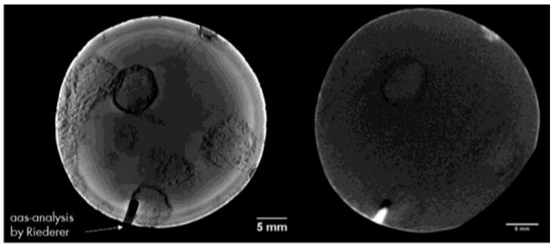

Figure 1: Visualization of the inner part of BS181 with drill hole and depleted areas
left: µXRCT (48.3 µm pixel size; measured at IMKM, Leipzig)
right: NCT (30 µm pixel size; measured at CONRAD-beamline (V7), HZB)

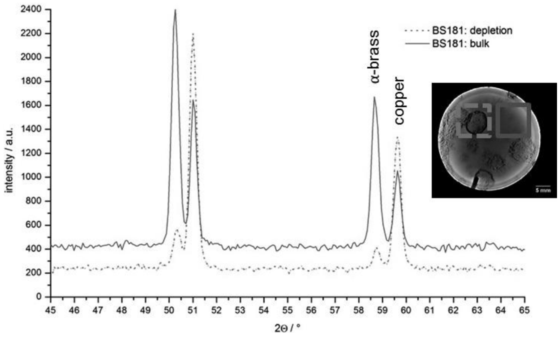

Figure 2: Neutron diffraction pattern for the depleted region (upper left coin part) and the bulk material (upper right coin part) of BS181 measured at FIREPOD-beamline (E9), HZB

MS18-T5
Chlorargyrite on attic silver coins

O. Baehre[1], G. Eisenblätter[1], G. Kloess[1]
[1]*Leipzig University, IMKM, Leipzig, Germany*

XRD measurements were performed on nine attic silver coins to determine surface contaminations and corrosion products. The silver coins are dated to the 5th century BC. The XRD experiments with high lateral resolution show significant lateral changes in the intensity of identified surface phases. This applies to single coins as well as between the coins. Diffraction patterns of two areas measured on coin 865 are showing this circumstance (see figure 1). The chlorargyrite (AgCl) peaks are surprisingly high. Beside the silver from the bulk and the chlorargyrite, acanthite (Ag_2S) could be detected on each coin. The peak intensity of all detected phases strongly depends on the measured area. Therefore we restricted the focal-spot size to 1 x 2 mm^2. To determine the chlorargyrite layer thickness the angle of the incident beam is varied. Other identified phases on the coins are quartz, calcite, akaganeite, litharge, and massicot.

In addition to XRD, XRF measurements were carried out. The measured content of silver, lead and copper reveal a typical composition of this mint. A significant amount of bromine could be detected on one coin. It is assumed that the bromine is located in the chlorargyrite. Precision lattice constant measurements are in progress to verify this expectation. Peak shifts of the chlorargyrite peaks to lower diffraction angles should be measured in dependence of the bromine content. The archaeometrical challenge is where the bromine does come from? Is this an evidence of underwater storage?

Many thanks to Professor Dr. Ulrich Johannes Schneider, Dr. Christoph Mackert and Jörg Graf from Leipzig University Library.

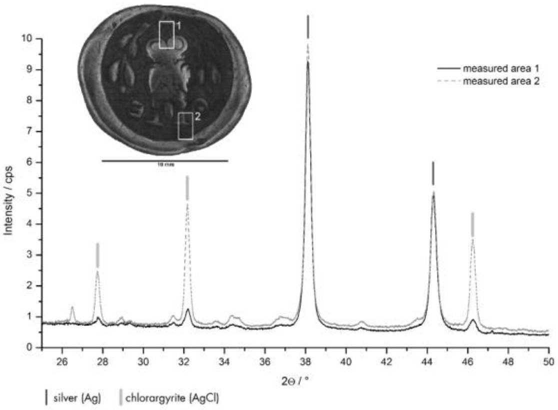

Figure 1: Diffraction patterns of two measured areas on coin 865. Not labelled peaks of lower intensity refer to acanthite, calcite and/or quartz. Data acquisition was done using a Bruker D8-Discover X-ray diffractometer (Cu-K_α; 300 s/frame; frame centre at 2Theta 30°, 45° and 60°; 40 kV and 40 mA; spot size: 1x2 mm^2; VÅNTEC-500 area detector).

MS18-T6
Surface phase analysis on a Classic Kerma tulip beaker

T. Muenster[1], G. Eisenblätter[1], A. Franz[2], D. Raue[3], G. Kloess[1]
[1]*Leipzig University, Institute of Mineralogy, Crystallography and Materials Science, Leipzig, Germany*
[2]*Helmholtz-Zentrum Berlin for Materials and Energy, Berlin, Germany*
[3]*Leipzig University, Egyptological Institute / Egyptian Museum - Georg Steindorff, Leipzig, Germany*

The Classic Kerma tulip beaker is stored at the Egyptian Museum -Georg Steindorff- Leipzig. The red and black ware is made of Nile silt (typ II B) and has a variegated grey-purple band on the exterior as a special decor. Besides of the egyptological classification of the Kerma beaker the mineral phase composition should be investigated to discuss details of the production process, the raw materials and what is so special on the grey-purple band.

As far as investigated by XRD, iron oxides like hematite, goethite, and magnetite are detected in the red part of the beaker but not in the black one. In contrast, graphite is detected in the black part only. XRF studies proofed that the typical red and black colouring is not the result of a different element contribution but rather due to the firing process. The matrix consists of only one material stating quartz and feldspar as main phases. The grey-purple band seems to be made of the same or very similar material, probably stone dust.

X-ray tomography is additionally used to image density differences within the beaker and the band.

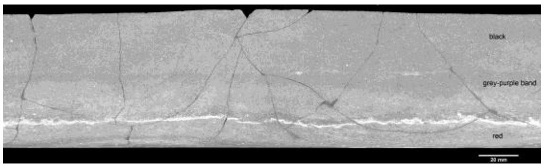

Figure 1: Visualization of the Classic Kerma tulip beaker (No. 3858) by µXRCT cylindrical projection (53.1 µm pixel size; measured at IMKM, Leipzig)

Poster

MS01 – Crystallography of pharmaceutically active compounds and halogen and hydrogen bonds in crystal engineering

MS01-P01

Erythromycin A dimethylsulfoxide disolvate 1.43-hydrate

J. Brüning[1,2], T. K. Trepte[1], E. Alig[1], J. W. Bats[3], M. U. Schmidt[1]
[1]*University of Frankfurt, Institute of Inorganic and Analytical Chemistry, Frankfurt am Main, Germany*
[2]*Aeropharm GmbH, Rudolstadt, Germany*
[3]*University of Frankfurt, Institute of Organic Chemistry and Chemical Biology, Frankfurt am Main, Germany*

Erythromycin A is a well-known macrolid antibiotic [1]. A new solvate-hydrate was found for this antibiotic. The new solvate-hydrate (I, [2,3]) exhibits better abilities to penetrate into skin as comparable erythromycins [4].

Compound I crystallizes in a layer structure in $P2_1$ with $Z = 2$ and $a = 11.1716(7)$, $b = 19.4025(12)$, $c = 12.0025(7)$Å, $\beta = 106.245(1)°$. The asymmetric unit of this solvat-hydrate contains one erythromycin A molecule, two dimethylsulfoxide (DMSO) molecules, one fully occupied and one partially occupied water molecule. The occupation factor of the partially occupied water molecule is 0.432 (11).

The conformation of the 14-membered ring of the macrolid considerably differs from the one in the known structure of erythromycin A dihydrate.

One of the two DMSO molecules is disordered over two positions; the orientation depends on the occupation of the partially occupied water molecule.

Within the crystal structure erythromycin exhibits hydrogen bonds from a hydroxy group to the fully occupied water molecule and thus forms layers parallel to (010).

[1] R. B. Woodward, E. Logusch, K. P. Nambiar, K. Sakan, D. E. Ward, B. W. Au-Yeung, P. Balaram, L. J. Browne, P. J. Card, and C. H. Chen (1981) *J. Am. Chem. Soc.* **103**, 3210-3213.
[2] J. Brüning, T. K. Trepte, J. W. Bats, and M. U. Schmidt (2012) *Acta Cryst.* **E68**, o700-o701.
[3] M. U. Schmidt, J. Brüning, T. K. Trepte, and J. W. Bats (2011) German Patent Appl. 102011117874.4.
[4] G. A. Stephenson, J. G. Stowell, P. H. Toma, R. R. Pfeiffer, and S. R. Byrn (1997) *J. Pharm. Sci.* **86**, 1239-1244.

Figure 1

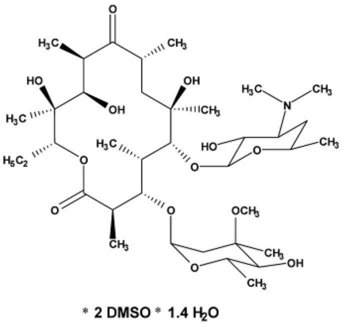

MS01-P02

Investigating cyclodextrin complex formation at high pressure

S. Saouane[1], W. Morgenroth[2,3], H.- P. Liermann[2], F. P. A. Fabbiani[1]
[1]*Georg-August-Universitaet Goettingen, GZG, Abt. Kristallographie, Goettingen, Germany*
[2]*Deutsches-Elektronen Synchrotron , Photon Science , Hamburg, Germany*
[3]*Goethe-Universität Frankfurt, Institut für Geowissenschaften, Abt. Kristallographie, Frankfurt am Main, Germany*

Native cyclodextrins are cyclic oligosaccharides with a low chemical toxicity.[1] They are widely used as “molecular cages”[2] in both the solid and solution states, especially in the pharmaceutical field.[3,4] Thanks to their hydrophilic outer surface, cyclodextrins are known to improve the aqueous solubility and bioavailability of hydrophobic active pharmaceutical ingredients (APIs) by trapping them temporarily into their inner cavity, which is more lipophilic in character.[3] The formation of cyclodextrin inclusion complexes in the solid state has been pioneered by Saenger and Steiner.[5,6] The wealth of structures available in the literature has been obtained by experiments performed under ambient-pressure conditions. High-pressure techniques are proving to be a suitable method for obtaining novel crystal forms of pharmaceutical compounds, in particular for exploring the phenomenon of polymorphism and solvate formation more thoroughly.[7,8] Investigating inclusion complex formation of cyclodextrins would be an interesting extension of the technique: can cyclodextrin complex formation be achieved at high pressure or would individual crystal components crystallise separately, and if so, which ones? Examples of successful *in-situ* complex formation as well as unexpected results are presented herein for α- and β-cyclodextrin with APIs using water as crystallisation medium. The crystals have been characterised by means of polarised optical microscopy and single-crystal X-ray diffraction using both home and synchrotron sources.

[1] T. Irie and K. Uekama, *J. Pharm. Sci.*, 1997, 86, 147-162. [2] M. Roux, B. Perly, and F. Djedaïni-Pilard, *Eur. Biophys. J.*, 2007, 36, 861-867. [3] T. Loftsson and M. E. Brewster, *J. Pharm. Sci.*, 1996, 85**,** 1017-1025. [4] K. Uekama, F. Hirayama, and T. Irie, *Chem. Rev.*, 1998, 98, 2045-2076. [5] W. Saenger, *Angew. Chemie*, 1980, 92,

343-361. [6] W. Saenger and T. Steiner, *Acta Crystallogr. Sect. A*, 1998, 54, 798-805. [7] F. P. A. Fabbiani and C. R. Pulham, *Chem. Soc. Rev.*, 2006, 35, 932-42. [8] E. V Boldyreva, *Acta Crystallogr. A.*, 2008, 64, 218-31.

MS01-P03

Downsizing material and efforts: do microfluidic approaches work for small molecules?

P. Piechon[1], T. Wagner[1], I. Dix[1]
[1]*NOVARTIS Pharma AG, Novartis Institutes for BioMedical Research, Basel, Switzerland*

In the pharmaceutical industry a large number of novel compounds is synthesized during the drug development process. One important method to characterize those molecules is x-ray structure determination which not only delivers a proof of constitution when other methods are non-conclusive but also but also provides the absolute configuration of chiral entities and a three-dimensional model of the molecule which can then be the starting point for structure activity studies. The inherent draw-back of the method, however, is the necessity to grow single crystals suitable for diffraction experiments.

Our standard crystallization protocol comprises classical techniques such as room temperature evaporation with a fixed set of solvents and solvent/anti-solvent mixtures. For the majority of cases this simple approach already leads to suitable crystalline material. In many cases, however, we obtain oily films, glass-like crusts or amorphous precipitation, and usually this can be taken as a sign for a tedious crystallization process. To extend our portfolio of experimental approaches we recently purchased a Microcapillary Crystallization System, the Emerald BioSystems PlugMaker, which was originally designed for protein applications. This instrument allows us to use much less material (1 instead of 20 mg), make use of water as an anti-solvent and screen up to 400 different concentration conditions in a single experiment. Starting the evaluation we noticed that some groups also investigate Microcapillary Technique for small molecule application [1,2]

First results and findings of our evaluation of this technology will be presented and will be the foundation for further systematic investigations. After the firsts test we already consider the microfluidic approach as a valuable addition to the traditional methods of crystallization: the crystals we have been able to grow are often of exceptional quality and, equally important, can be directly be harvested from the CrystalCards. For 20% of the test cases we have successfully demonstrated that a microfluidic system (even without further customization) can significantly reduce the time and material spent on the crystallization process. Ideas to adapt the instrument to the specific needs of the small molecule space will be discussed.

Keywords**:** crystallization

http://alphabiotech.co.uk/pdfs/MCPS_Plug_Maker_3-14-11.pdf
[1] Leng J., Salmon J.B. (2009). Lab Chip, 9, 24-34.
[2] Teychené S., Biscans B. Microfluidic Toolbox for the Crystallization of Organic Molecules. 18th International Symposium on Industrial Crystallization (ISIC 18), Zurich (2011)

MS01-P04

The only hydrogen bond - two ways to build a structure. The role of N-H···O hydrogen bond in crystal structures of N,N-dimethylglycine

E. Kapustin[1], V. Minkov[2,1], E. Boldyreva[2,1]
[1]*Novosibirsk State University, Novosibirsk, Russian Federation*
[2]*Institute of Solid Sate Chemistry and Mechanochemistry SB RAS, Novosibirsk, Russian Federation*

Crystal structures of amino acids are considered to mimic important interactions in peptides, therefore the studies of the structure-forming factors in these systems attract much attention. N,N-dimethylglycine is an interesting model compound that was used to test the role of the N-H···O hydrogen bonds in forming the head-to-tail chains - the main structural unit - in the crystals of amino acids. It was hypothesized previously [1] that additional side N-H···O hydrogen bonds play an important role in forming the head-to-tail chains of amino acid zwitterions linked via N-H···O hydrogen bonds between the charged $-NH_3^+$ and $-COO^-$ terminal groups. Twice methylated amino group of N,N-dimethylglycine is able to form only one N-H···O hydrogen bond in the crystal structure, so that this hypothesis could be tested. In the present work we describe the crystal structures of two polymorphs of N,N-dimethylglycine, in which the zwitterions are packed in two different ways. In one polymorph (orthorhombic, *Pbca*) they form finite four member ring motifs not linked to each other via any hydrogen bonds, but only by weak van der Waals interactions. However, in the second polymorph (monoclinic, $P2_1/n$, which was never described before) the zwitterions do form infinite head-to-tail chains though the N-H···O bond is the only one and is not assisted via any additional H-bonds. The effect of cooling on the two crystal structures was followed by single-crystal X-ray diffraction combined with polarized Raman spectroscopy of oriented single crystals, in order to compare the response of the N-H···O bonds to temperature variations. The crystal structure of the monoclinic polymorph with infinite chain motifs compresses anisotropically on cooling, whereas that of the orthorhombic polymorph with finite cycles undergoes a reversible single-crystal to single-crystal phase transition at ~200 K accompanied by non-merohedral twinning, reducing the space symmetry to monoclinic ($P2_1/b$), and doubling the asymmetric unit up to 4. This phase transition does not manifest in the Raman spectra and DSC data.

[1] Kolesov, B.A., Boldyreva, E.V. Self-trapped N-H vibrational states in the polymorphs of glycine, L- and DL-alanine // J. Raman. Spectrosc. - 2010. - Vol.41. - 670-677.

MS01-P05

A chiral polyiodide with four symmetry independant tyrosinate molecules

K. Lamberts[1], P. Handels[1], U. Englert[1]
[1]*Inorganic Chemistry, RWTH Aachen, Aachen, Germany*

Polyiodides are of high interest not only because of their structural diversity and interesting bonding situations but also with respect to application[1]. Oftentimes the specific connectivity around the iodides cannot be assigned with final certainty and several investigations cover the determination of bonding criteria for Iodine-Iodine bonds[1-5]. Even the connectivity within elemental Iodine is not trivial and already includes covalent bonds as well as contacts significantly below and contacts similar to the sum of the Van-der-Waals radii. Although, the formation of higher iodides is defined by equilibrium reactions in solution, the formation of crystalline solids is favoured if larger cations are used (*e.g.* alkali cations coordinated by suitable crown ethers[6]).

Introducing chirality in form of amino-acids yields a polyiodide structure from L-tyrosine. Single crystal X-ray diffraction revealed the unusually large asymmetric unit of the product: it contains four L-tyrosinate cations, one water molecule and 16 Iodine atoms arranged in a polyiodide layer. It will be discussed which interactions are present within this layer and how it can be described with respect to discrete higher iodides like tri- or penta-iodide. Secondary interactions between the organic residues may be evaluated as well as some chemical properties of the bulk product.

[1] P. H. Svensson, L. Kloo, *Chem. Rev.* 2003, *103*, 1649-1684.
[2] F. Van Bolhuis, P. B. Koster, T. Migchelsen, *Acta Crystallogr.* 1967**,** *23,* 90-91
[3] N. W. Alcock, *Adv. Inorg. Chem. Radiochem.* 1972**,** *15,* 1.
[4] A. J. Blake, R. O. Gould, W-S. Li, V. Lippolis, S. Parsons, M. Schröder, *Cryst. Eng.* 1999, *2*, 153-170.
[5] L. Kloo, J. Rosdahl, P. H. Svensson, *Eur. J. Inorg. Chem.* 2002, 1203-1209.
[6] See for example: a) K.-F. Tebbe, M. El Essawi, *Z. Anorg. Allg. Chem.* 1998 b) A. J. Blake, R. O. Gould, W.-S. Li, V. Lippolis, S. Parsons, C. Radek, M. Schröder, *Angew. Chem.* 1998, *110*, 305-308.

Figure 1

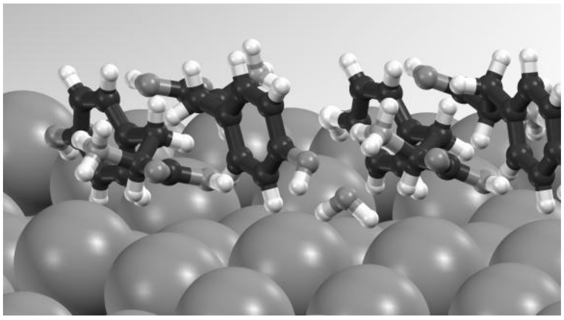

MS01-P06

The role of detergent in crystal packing upon dehydration of photosystem II crystals

M. Bommer[1], J. Hellmich[1]
[1]*Humboldt Universität Berlin, Berlin, Germany*

As is the case for many complex biological membrane proteins, photosystem II (PSII) crystals, while often simple to obtain, present a nightmare in optimisation. In an attempt to produce consistently highly diffracting crystals, we explore the interplay of detergent and crystal packing.

Membrane proteins are most commonly extracted into detergent (hemi)micelles that remain bound around the transmembrane surface of the protein in a belt-like fashion during purification and crystallisation. They thus form part of the protein crystal and mediate rather unstable crystal contacts and prevent direct protein-protein interactions.

We have purified and crystallised PSII in an alternative detergent and this made crystals more malleable by controlled dehydration and chemical treatment. At least five distinct crystal states with 25% difference in unit cell size could be produced by post crystallisation treatment alone. While the initial untreated crystals show diffraction to a maximum of only 6 Å, diffraction up to 2.4 Å was observed in one dehydration state. At the same time crystal packing changed from a Type II to a Type I like state that potentially mimics packing inside the biological membrane.

MS02 – Functional materials and technologies for energy conversion and catalysis

MS02-P01

Automated set-up for measurement and evaluation of pyroelectric properties

S. Jachalke[1], E. Mehner[1], H. Stöcker[1], D. C. Meyer[1]
[1]*TU Bergakademie Freiberg, Experimentelle Physik, Freiberg, Germany*

Pyroelectric materials offer a great potential of low-temperature waste heat recovery by utilizing e.g. the Olsen-Cylce to convert residual heat into electric energy. By using the pyroelectric effect, a change in temperature alters the materials polarization, which further chages the charge density on the material's surface. This results in a current flow trough an external circuit. This work focuses on a set-up for the characterization of pyroelectric materials with the help of a computer controlled thermal/electrical stimulation and a simultaneously recording of the electrical response of the material, including e.g. ferro- to paraelectric phase transitions, discharge of thermal traps and Curie temperature between 270 to 420 K. Data analysis with the Shap-Garn-method [1] yields temperature depended pyroelectric coefficients (accuracy 1-5%) and polarization, by separating the pyroelectric from disturbing non-pyroelectric signal. With the setup a broad spectrum of materials (single crystals, ceramics, polymers, …) and geometries can be measured to in order to evaluate their potential for waste heat recovery. The set-up is also able to realize and evaluate the Olsen Cycle, which will be part of future development.

[1] I. Lubomirsky and O. Stafsudd, "Invited Review Article: Practical guide for pyroelectric measurements.," Rev Sci Instrum, vol. 83, no. 5, p. 051101, May 2012.

MS02-P02

The low-temperature sodium-sulphur secondary battery: materials and structure

W. Münchgesang[1], F. Meutzner[1], T. Schucknecht[2], M. Kohl[3], H. Althues[3], B. Abendroth[1], T. Leisegang[4], D. Rafaja[2], D. C. Meyer[1]
[1]*TU Bergakademie Freiberg, Institut für Experimentelle Physik, Freiberg, Germany*
[2]*TU Bergakademie Freiberg, Institut für Werkstoffwissenschaf, Freiberg, Germany*
[3]*Fraunhofer-Institut für Werkstoff- und Strahltechnik, Dresden, Germany*
[4]*Fraunhofer-Technologiezentrum Halbleitermaterialien , Freiberg, Germany*

Sodium (Na) - sulphur (S) secondary batteries are economically very attractive, due to the low cost of the active materials Na and S and the corresponding high energy densities. Commercially available systems are stationary high-temperature batteries, with an operating temperature of about 350 °C and a power of about 1 MW, respectively. The high operating temperature substantially increases operating costs. Within the BMU-financed joint project 'BaSta' a low-temperature design of a Na-S battery is evaluated to overcome this disadvantage.

To develop and optimize a design for a low-temperature Na-S battery, the investigation of the structural, morphological and chemical changes of the individual components i. e. materials is of great relevance. In order to prevent a battery breakdown, the influence of these changes on mechanical, electrical and kinetic properties of the used materials on different scales have to be evaluated.

In this work, we present the first results on a new design of a low-temperature Na-S battery, addressing in particular the structural, morphological and chemical changes of the cathode material. This is investigated with ex- and in-situ X-ray diffraction, scanning electron microscope and electrochemical impedance spectroscopy measurements.

MS02-P03

Defect separation in strontium titanate single crystals - a concept for electrochemical energy storage

J. Hanzig[1], M. Zschornak[1,2], M. Nentwich[1], F. Hanzig[1], E. Mehner[1], C. Röder[3], B. Abendroth[1], T. Leisegang[1], H. Stöcker[1], S. Gemming[2], D. C. Meyer[1]
[1]*TU Bergakademie Freiberg, Institut für Experimentelle Physik, Freiberg, Germany*
[2]*Helmholtz-Zentrum Dresden Rossendorf, 2 Institut für Ionenstrahlphysik und Materialforschung, Dresden, Germany*
[3]*TU Bergakademie Freiberg, Institut für Theoretische Physik, Freiberg, Germany*

Stoichiometric perovskite-type strontium titanate acts as an insulator because of its wide electronic band gap and has therefore great potential as high-k dielectric and storage material in memory applications. Degradation phenomena of insulating properties of transition metal oxides occur during long time voltage application. From the defect chemistry point of view the question arises how mobile species react on an external electric field and which impact redistribution of mobile species has on the stability of the crystal structure. In $SrTiO_3$ oxygen vacancies are well-known charged defects to migrate during electroformation and to establish a concentration gradient through the bulk.

Here, we discuss near-surface reversible structural changes in $SrTiO_3$ single crystals caused by oxygen vacancy redistribution in an external electric field. We present in-situ X-ray diffraction measurements during and after electroformation. Several reflections are monitored and show a tetragonal elongation of the cubic unit cell of strontium titanate. In-situ Raman investigations were carried out to verify that the expansion of the unit cell involves a transition from the centrosymmetric to a less symmetric structure. Regarding a whole formation cycle, two different time scales occur: a slow one during the increase of the lattice constant and a fast one at the end. Based on the experimental data we suggest a model containing the formation of a polar strontium titanate unit cell stabilized by the electric field, which is referred to as migration induced field stabilized polar (MFP) phase at room temperature.

Furthermore, we show that intrinsic defect separation establishes a non-equilibrium state in the transition metal oxide accompanied by an electromotive force. A comprehensive thermodynamic deduction in terms of theoretical energy and entropy calculations indicate an exergonic electrochemical reaction after the electric field is switched off. Based on that driving force the experimental and theoretical proof of concept of an all-in-one rechargeable $SrTiO_3$ single crystal battery is reported here.

MS02-P04

FEM-simulation of energy conversion and storage concepts based on oxide crystals

C. Cherkouk[1], M. Zschornak[1], J. Hanzig[1], M. Nentwich[1], F. Meutzner[1], M. Ureña de Vivanco[1], T. Leisegang[2], D. C. Meyer[1]

[1]Technische Universität Bergakademie Freiberg, Institute of Experimental Physics, Freiberg, Germany

[2]Fraunhofer-Technologiezentrum, Halbleitermaterialien, Freiberg, Germany

Recent development on global warming and in particular a change in energy policy in Germany have renewed interest on green power based energy and material conversion, and solutions for efficient storage in respect to short and long term power generation applications. Unused power sources exist on various forms such as vibrations, flowing water, as well as wind and waste heat energy. Whereas the use of the latter form can increase the efficiency of the corresponding processes such as charge and discharge of batteries, the conversion of waste heat energy into chemical or electrical energy can be realized by using the pyroelectric effect, for instance.

Two kinds of concepts based on oxide materials are presented: The first concept describes a system converting waste heat energy into chemical energy by pyrocatalytic water splitting, which in turn can be used for electricity generation from fuel cells. The second concept aims to use oxygen defects migration inside a crystal as electromotive force to store and release electrical energy. Another application based on oxygen migration uses a temperature gradient, which can result in material properties similar to the first concept described.

However, the physical and electrochemical governing processes inside these conversion and storage devices are often complex. A mathematical modeling based on a finite element method was utilized using the Comsol Multiphysics code in order to investigate underlying processes under various conditions up to device design.

In this work, different energy conversion and storage concepts are described. Comsol Multiphysics simulations of corresponding devices, which include important physical and electrochemical characteristics, are presented, describing the basic functionality of these devices.

Keywords**:** Energy, Conversion, storage systems, simulation, comsol Multiphysics

MS02-P05

Categorization of electrodes and separators in electrochemical energy storage devices - evaluating new concepts

F. Meutzner[1], T. Nestler[1], J. Hanzig[1], M. Zschornak[1], M. Nentwich[1], R. Schmid[1], M. Ureña de Vivanco[1], C. Cherkouk[1], B. Störr[1], W. Münchgesang[1], T. Leisegang[2], D. C. Meyer[1]

[1]TU Bergakademie Freiberg, Experimentelle Physik, Freiberg, Germany

[2]Fraunhofer-Technologiezentrum Halbleitermaterialien, Freiberg, Germany

Energy storage and conversion is an important, still growing sector of research and economy. It provides technologies for a very broad field of applications ranging from mobile devices to stationary applications for grid stabilization. The latter is essential for compensating the capricious nature of renewable energies. Due to high achievable energy densities, electrochemical storage devices are of great relevance. Apart from electrochemistry, materials science and related disciplines have had a major influence on research and development. Especially lithium-ion batteries, which - besides the lead sulphuric acid system - are the main sellers of secondary batteries, have largely undergone material and electrochemistry optimization and are still under intense research.

Within the project ‘CryPhysConcept’ (financed by the BMBF - Federal Ministry of Education and Research), crystallographic and crystal physical methodology is applied to develop new electrochemical energy storage materials and concepts. It is therefore the aim to deepen the understanding of relevant processes at the atomic scale. In the first stage, a categorization for the electrodes and separators - which for the most part are in the solid state - has been developed. Economic, ecologic and technological aspects are taken into consideration in order to evaluate promising materials. The next stages will focus on a thorough screening of materials and processes under a crystallographic perspective revealing underlying principles.

Here we present a systematization of electrodes and separators and show especially eligible candidates for crystallographic investigations.

MS02-P06

Crystals as the heart of thermal-into-chemical-energy conversion devices

M. Ureña de Vivanco[1], M. Sonntag[1], C. Forman[2], M. Gootz[2], E. Mehner[1], S. Jachalke[1], H. Stöcker[1], R. Strohmayer[1], D. Scheithauer[2], I. Muritala[2], B. Störr[1], M. Zschornak[1], J. Hanzig[1], M. Herrmann[1], M. Koitsch[1], R. Pardemann[2], T. Leisegang[3], B. Meyer[2], D. C. Meyer[1]
[1]*TU Bergakademie Freiberg, Institut für Experimentelle Physik, Freiberg, Germany*
[2]*TU Bergakademie Freiberg, Institut für Energieverfahrenstechnik und Chemieingenieurwesen, Freiberg, Germany*
[3]*Fraunhofer-Technologiezentrum Halbleitermaterialien, Freiberg, Germany*

An estimated 58 % of the total energy production in the USA in 2012 was lost in the form of waste heat [1]. This exemplifies the paramount importance of reducing heat losses for increasing the process efficiency of various industries, ranging from coal power stations to microelectronics. Especially low-temperature waste heat should be dealt with, as this form of energy is neither usable for heating, nor for running turbines.

Pyroelectric materials pose great potential for this task [2]. These are crystalline, non-centrosymmetric materials such as $LiNbO_3$, $BaTiO_3$ or even some organic polymers like polyvinylidenefluoride (PVDF), that display a polar axis. When pyroelectric crystals are subjected to a temperature gradient, the macroscopic polarisation of the crystal is altered and charges are created over its surface. The surface charges can be used to drive chemical reactions, to run an external current circuit or to treat wastes, to mention a few possibilities.

After presenting an energetic assessment for waste gains with the use of pyroelectricity, this work focuses on possible materials and approaches for the conception of technologies for waste heat reuse based on pyroelectric materials. A pilot reactor for the generation of hydrogen gas has been built and patented. Therein, a temperature gradient is used to pyrocatalytically dissociate water. As a source of heat, a hot waste stream can be used. The generated gases can afterwards be fed into a fuel cell to generate an electrical current. If there is no immediate electricity demand, the gases can be stored or used as raw material to supply industries, as an example.

In addition, an outlook for the conception of new pyroelectric materials based on defect migration as well as further fields of application for pyromaterials is provided.

[1] Estimated U.S. Energy Use in 2012, Lawrence Livermore National Laboratory.

[2] Gutmann, E.; Benke, A.; Gerth, K.; Böttcher, H.; Mehner, E.; Klein, C.; Krause-Buchholz, U.; Bergmann, U.; Pompe, W.; Meyer, D.C. 2012; Pyroelectrocatalytic disinfection using the pyroelectric effect of nano- and microcrystalline $LiNbO_3$ and $LiTaO_3$ particles; J. Phys. Chem. C; 116, 5383-5393.

MS02-P07

Comprehensive collection of pyroelectric properties of organic and inorganic materials: database and categorization

B. Störr[1], R. Schmid[1], H. Stöcker[1], E. Mehner[1], S. Jachalke[1], J. Hanzig[1], M. Sonntag[1], T. Leisegang[2], D. C. Meyer[1]
[1]*TU Bergakademie Freiberg, Institut für Experimentelle Physik, Freiberg, Germany*
[2]*Fraunhofer-Technologiezentrum Halbleitermaterialien, Freiberg, Germany*

In 2012, approximately 58 % of U.S. total energy production was emitted as residual heat back to the environment by various sources, ranging from coal power stations to microelectronic devices [1]. The transformation of low-temperature waste heat into higher-class energy, like electrical or chemical, is of main interest for increasing the efficiency of corresponding processes and devices. Furthermore, the demand of novel so-called “green” power generation techniques increases due to imminent climate changes. An excellent opportunity is offered by utilizing pyroelectric materials for electric power generation out of low-temperature waste heat. The waste heat can be converted into an electric current that in turn can be used for pyrocatalytic hydrogen production from water. Hence, this technology offers the opportunity to store the waste heat energy as chemical energy.

Pyroelectricity can only occur in crystals belonging to specific crystal classes. It is required that these crystals do not have a symmetry center and either have only one axis with rotational symmetry that is not included in the inversion axis or do not have an axis with rotational symmetry at all [2].

Pyroelectric materials possess spontaneous polarization, which can be altered by temperature fluctuations leading to charge separation. Characteristic for a pyroelectric material is its pyroelectric coefficient that indicates how many charges emerge per surface area and temperature difference. In order to develop a high-efficiency technology for energy conversion a material with a high pyroelectric coefficient is of choice. Since typically the highest pyroelectric coefficient is found directly below the Curie temperature of the material, the right selection of materials with an appropriate Curie temperature is additionally required.

In order to find suitable pyroelectric materials we extensively collected data of pyroelectric substances reported in the literature and categorized them. This database of organic and inorganic pyroelectric materials in single crystalline, powder or ceramic state allows the evaluation and prediction of materials properties.

Since there is no comprehensive collection of pyroelectric materials covering all materials reported so far, it is the aim to provide a dedicated database for all areas of science and industry.

[1] Lawrence Livermore National Laboratory. Estimated U.S. Energy Use in 2012: 95.1 Quads. url: https://flowcharts.llnl.gov/
[2] S. Lang: Sourcebook of Pyroelectricity. Gordon and Breach Science Publishers, New York 1974

MS02-P08

In situ Grazing Incidence Diffraction in electrochemical catalysis

- from theory to experiment

M. Scherzer[1], F. Girgsdies[1], M. Behrens[1], R. Schlögl[1]
[1]*Fritz Haber Institute of the Max Planck Society, Inorganic Chemistry, Berlin, Germany*

The method of X-ray diffraction at very low incident angles was developed in the late 1970´s. Since the well known paper of Marra, Eisenberger and Cho[1] the application of this technique has widely spread over different areas of solid state-chemistry and -physics. In the last years GIXRD becames an established method for investigation of thin films and layers in many material research areas like magnet recording materials[2], semiconductor industry and catalysis.

A particularly interesting approach is the investigation of the in-situ oxidation of catalytically active metal surfaces like Pt or Ir during the water splitting reaction. Oxidations under anodic potential of such surfaces lead to the formation of very thin oxide-layers during the oxygen evolution reaction (Fig. 1A). Due to their surface sensitivity, the GIXRD and XRR (X-ray reflectivity) techniques are very suitable for a structural investigation of these thin layers, because phase analysis, lattice parameter and layer orientation can be analyzed. Such investigations need a very precise mounting and adjustment of the sample and its environment. The first step towards an in-situ experiment is to define the sensitivity of the method applied to very thin layers. This can be done by using different metal foils with, at ambient conditions, stable layers on top, like oxides, nitrides or other deposited metals.

Fig. 1A:The metastable material formed on top (Pt - oxo - hydroxo-layer on a polycrystalline Pt-foil) decomposes (reduces) to form Pt nanoparticles under open circuit conditions.

Fig. 1B: Sensitivity : A common symmetric measurement (Parallel beam) compared with GID technique on a Ti/TiN sample system.

During experiments with such a Ti/TiN model system (Fig. 1B), we found a clear dependency of the phase composition with GI confirming the identification as a very thin layer (Titaniumnitride) besides dominant substrates (Titanium). This allows the extraction of precise phase ID´s (Ti2N, $TiN_{0.9}$, $TiN_{0.26}$) and depth profiling. This is a crucial knowledge for sample adjustment and further measurements on the choosen deposited layer(s).

References:
[1] W.Marra, P.Eisenberger, A.Cho; J.Appl.Phys. 50, 6827 (1979)
[2] V. R. Reddy et al., J.Cond.Mat, 21, (2009)

Mail to the corresponding author: scherzer@fhi-berlin.mpg.de

Figure1

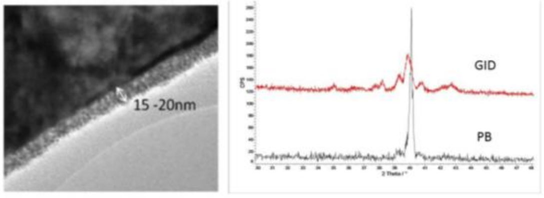
Fig. 1A Fig. 1B

MS02-P09

Magentron Sputter Deposition and Crystallization of $Ba_xSr_{1-x}TiO_3$ thin films

R. Strohmeyer[1], B. Abendroth[1], H. Stöcker[1], E. Mehner[1], M. Franke[2], D. C. Meyer[1]
[1]*TU Bergakademie Freiberg, Institut Experimentelle Physik, Freiberg, Germany*
[2]*TU Bergakademie Freiberg, Institut für Elektronik- und Sensormaterialien, Freiberg, Germany*

Barium Titanate (BTO) as well as Strontium Titanate (STO) are both oxides with a perovskite-like structure. Above 120°C both materials are cubic and centrosymmetric with quite similar lattice constants. At lower temperatures (down to room temperature) STO remains cubic while BTO shifts into a tetragonal phase and thereby breaks the inversion symmetry. This leads to a polar unit cell which implies pyroelectricity in BTO with diverging pyroelectric coefficient at the phase transition temperature. It is known that this transition temperature can be shifted in $Ba_xSr_{1-x}TiO_3$ (BST) with varying composition ratio of Ba and Sr. So it is expected that the pyroelectric coefficient divergence shifts as well.

The BST was sputtered as a thin film by RF magnetron sputtering from BTO and STO ceramic targets in confocal geometry. The film thickness and stoichiometry were adjusted by varying the sputter times of the correspondent targets and verified using x-ray reflectometry (XRR) and x-ray fluorescence (XRF) respectively. XRD data showed no crystal phases after deposition. The crystallization began with annealing the thin films in air above 600°C.

MS02-P10

In situ X-Ray Diffraction Studies on $LiNi_{0.5}Mn_{1.5}O_4$ and also Fe substituted $LiNi_{0.5}Mn_{1.5}O_4$ Spinel Cathodes during Electrochemical Cycling

N. Kiziltas-Yavuz[1], A. Bhaskar[1], M. Yavuz[1], M. S. D. Darma[1], M. Knapp[1], S. Indris[1], H. Ehrenberg[1]
[1]*Karlsruhe Institute of Technology (KIT), Karlsruhe, Germany*

The lithium-ion batteries are particularly suitable energy storage systems because of their high energy densities. Many cathode materials such as layered oxides ($LiMO_2$, M= V, Cr, Co and Ni), olivines (LiFePO4) and spinels (LiM_2O_4, M= Ti, V, and Mn) have been studied over the past years [1]. Among all these compounds the Mn-based spinel (LiMn2O4) and its derivatives such as spinel $LiNi_{0.5}Mn_{1.5}O_4$ are promising cathode materials because of their facile synthesis route, non-toxicity, abundance and high operating voltage. Additionally, they have good ionic/electronic transport properties. The spinel $LiNi_{0.5}Mn_{1.5}O_4$ cathode shows impressive electrochemical performance like large reversible capacity at a high operating voltage around 4.7 V where the reversible Ni2+↔ Ni4+ redox reactions take place which makes it a promising and suitable cathode material for high energy battery applications [2]. However, the electrochemical performance of spinel $LiNi_{0.5}Mn_{1.5}O_4$ still needs to be improved to meet the required power density especially at high charge/discharge rates (C-rates) and at elevated temperatures. Furthermore, in the ideal $LiNi_{0.5}Mn_{1.5}O_4$ spinel, the oxidation state of Mn is 4+ but usually a small amount of Mn3+, which is well-known as Jahn-Teller ion causing structural instability, remains in the compound as a result of oxygen deficiency after the high temperature synthesis process [3]. Cationic doping such as Fe on $LiNi_{0.5}Mn_{1.5}O_4$ is one of the techniques to improve the electrochemical performance. It has been reported that Fe doping exhibits a better electrochemical performance than $LiNi_{0.5}Mn_{1.5}O_4$ [4]. It is also reported that Fe doping gives better thermal stability and can also suppress the formation of a thick SEI (Solid electrolyte interface) layer which is an important benefit to improve the electrochemical performances [5,6]. Therefore, the multiple substitution of Fe for Ni and Mn on the crystallographically interesting transition metal sites 16d with three different compositions will be investigated. Electrochemical and structural data, including in-situ XRD, will be presented.

[1] M.Yoshio, R.J. Brodd, A. Kozawa, Lithium-Ion Batteries, Science and Technologies.
[2] A. Bhaskar, N. N. Bramnik, A. Senyshyn, H. Fuess, H. Ehrenberg, Synthesis, Characterization, and Comparison of Electrochemical Properties of LiM0.5Mn1.5O4 (M = Fe, Co, Ni) at Different Temperatures J. Electrochem. Soc., 157 (6), A689-A695, 2010
[3] Q. Zhong, A. Bonakdarpour, J.R. Dahn, Synthesis and Electrochemistry of LiNixMn2-xO4 J., Electrochem. Soc., 144,205, 1997
[4] G.B. Zhong, Y.Y. Wang, Y.Q. Yu, C.H. Chen, Electrochemical investigations of the LiNi0.45M0.10Mn1.45O4 (M = Fe, Co, Cr) 5 V cathode materials for lithium ion batteries, J.Power Sources, 205,385-393 (2012).
[5] A. Bhaskar, PhD Dissertation, Investigations on LiM0.5Mn1.5O4 (M=Fe, Co, Ni) Spinels as High-Volt Cathode Materials for Rechargeable Lithium- Ion Batteries (2011)
[6] T.F. Yi, Y. Xie, M.F. Ye, L.J. Jiang, R.S. Zhu, Y.R. Zhu, Recent developments in the doping of LiNi0.5Mn1.5O4 cathode materials for 5 V lithium-ion batteries, Ionics, 17, 383-389 (2011)

MS02-P11

Material Concepts for Designing an Aluminum-Ion Thin-Film Battery

T. Nestler[1], W. Förster[2], S. Braun[2], W. Münchgesang[1,2], F. Meutzner[1], J. Hanzig[1], M. Zschornak[1], M. Nentwich[1], R. Schmid[1], M. Ureña de Vivanco[1], C. Cherkouk[1], T. Leisegang[3], D. C. Meyer[1]
[1]*TU Bergakademie Freiberg, Institut für Experimentelle Physik, Freiberg, Germany*
[2]*Frauenhofer IWS, Frauenhofer-Institut für Werkstoff- und Strahltechnik, Dresden, Germany*
[3]*Frauenhofer Gesellschaft, Technologiezentrum Halbleitermaterialien, Freiberg, Germany*

The constantly increasing demand for high-energy density batteries for mobile devices, electronic vehicles and the storage of renewable energy, as well as the shortage of lithium resources, spur the research on new battery materials utilizing other elements than lithium as active species. Especially multivalent-ions, such as Mg^{2+}, Ca^{2+} and Al^{3+}, have become popular candidates for post-lithium systems, as they can transfer more electrons per atom. Indeed, batteries based on aluminum can reach higher energy densities than conventional lithium-ion batteries, which has been recently demonstrated for electronic vehicles run by a primary Al-air battery. However, there have been only a few reports on rechargeable aluminum batteries [1]. All of them employ ionic liquids for Al^{3+}-conduction, as aqueous electrolytes would generate a passivating oxide film upon the aluminum anode that hinders the battery operation. Cathode materials have been adopted from lithium-batteries, however, often without investigating the intercalation process from a crystallographic point of view. Besides the already mentioned high energy density, the high natural abundance of aluminum as well as the improved safety compared to lithium-batteries make it worth to have a closer look on possible electrode and electrolyte materials.

In addition to high specific capacities, a long cycle lifetime is a main aspect for future energy storage materials. One way to satisfy both demands and simultaneously ensure a highest level of safety is to build thin film batteries (TFBs), which could be used in all sorts of autonomous devices. As they utilize a non-flammable solid electrolyte, TFBs do not suffer from possible passivation of the surface of the electrodes during cycling, which expands their lifetime. Furthermore, investigable cathode/anode systems are not limited by a decomposition voltage, as is the case for liquid electrolytes, which could improve the energy density. Moreover, the electrodes can be investigated in unmixed condition, as there is no need for binders or additives in TFBs, which make them a suitable model system to investigate the material´s intrinsic ionic transfer and insertion.

Within the project CryPhysConcept (financed by the Federal Ministry of Education and Research -BMBF), suitable cathode and electrolyte materials meeting the structural requirements for aluminum-ion thin-film batteries are identified. The presented materials, as e.g. the 3D electrolyte $(Al_{0.2}Zr_{0.8})_{20/19}Nb(PO_4)_3$ and MnO_2 as electrode material, are discussed in terms of their crystal structure and a battery concept is suggested.

[1] Jayaprakash, N.et al. "The rechargeable aluminum-ion battery." *Chemical Communications* 47.47 (2011): 12610-12612.

MS02-P12

Structural Defects in β-TaON

S. Cosgun[1], M. Rohloff[1], M. Lublow[1], T. Lunkenbein[2], A. Senyshyn[3], S. Müller[4], A. Bartelt[4], A. Fischer[1], M. Lerch[1]
[1]*Institut für Chemie der TU Berlin, Berlin, Germany*
[2]*Fritz-Haber-Institut, Abteilung Anorganische Chemie, Berlin, Germany*
[3]*FRM II, TU München, München, Germany*
[4]*Helmholtz-Zentrum Berlin für Materialien und Energie, Institut Solare Brennstoffe, Berlin, Germany*

Tantalum-based oxide nitride materials are promising candidates as efficient photocatalysts for water splitting under visible light.[1] The compound β-TaON which crystallizes in the monoclinic baddeleyite-type structure is well known. In our study two synthesis routes to phase pure β-TaON powders were developed: 1) Ta_2O_5 was treated for 12 h at 900 °C in an atmosphere consisting of NH_3 and O_2. 2) The same procedure was applied at 1050 °C, followed by a subsequent treatment at 700 °C (15 min., air). The crystal structure of samples prepared via the first route can be refined easily. In contrast, the additional treatment used in route 2 leads to severe refinement problems (Fig. 1a). Neutron diffraction measurements clearly point out that this is not an effect of O/N ordering. Interestingly, applying an anisotropic strain broadening model[2] (X-rays) leads to a considerable increase of the refinement quality (Fig. 1b). This anisotropic strain broadening is suggested to be caused by stacking faults which are also observed by transmission electron microscopy, rather than by a particle shape effect. The influence of such structural defects on the photocatalytic properties and on the lifetimes of photogenerated charge carriers in β-TaON is currently under investigation.

Figure 1:
a) Rietveld refinement of β-TaON (route 2) without microstructural analysis
b) Rietveld refinement after applying an anisotropic strain broadening model

[1] K. Maeda, K. Domen, *J. Phys. Chem. C*, 2007, 111
[2] P. W. Stevens, *J. Appl. Cryst.* 1999, 32, 281-298
[3] J. Rodriguez-Carvajal, *Commision on Powder Diffraction Newsletter* 2001, 26

Financial support from the Deutsche Forschungsgemeinschaft (SPP 1613) is gratefully acknowledged.

Figure 1

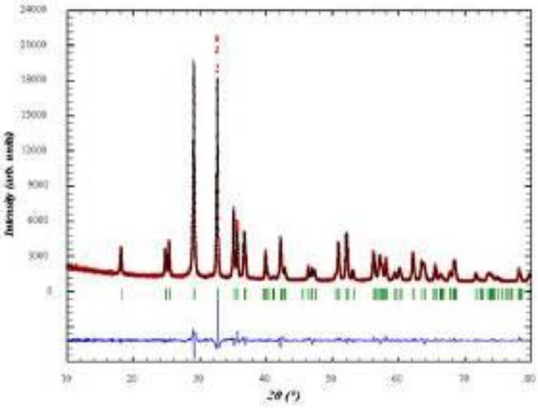

Figure 2

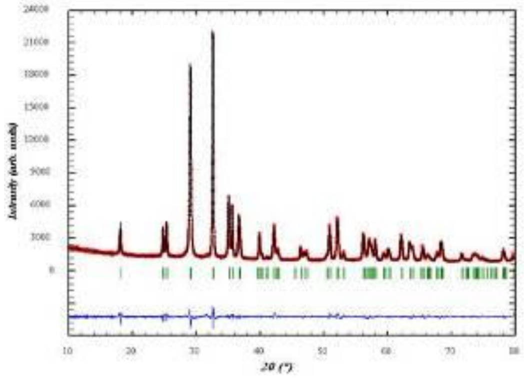

MS02-P13

Synthesis and Crystal Structure of $ScTa_2O_5N$

S. Cosgun[1], M. Rohloff[1], M. Lublow[1], A. Fischer[1], M. Lerch[1]
[1]*Institut für Chemie der TU Berlin, Berlin, Germany*

Transition metal oxide nitrides are interesting materials with outstanding potential as photocatalysts for water splitting or as nontoxic color pigments.[1,2] A new phase in the system Sc-Ta-O-N was synthesized. Tantalum and scandium citrate solutions were mixed with ethylene glycole and polymerized at 200 °C. After calcination at 500 °C an amorphous oxide was obtained. This precursor was treated with a gaseous mixture of NH_3 / O_2 at 800 °C for 2h in a tube furnace with flow rates of 10 $l\cdot h^{-1}$ ammonia and 0.1 $l\cdot h^{-1}$ oxygen. Crystal structure determination of the new phase was performed with X-ray powder data. The results of the Rietveld refinement are depicted in Figure 1, pointing to anisotropic reflection broadening. Unfortunately, the new compound could not be prepared as a pure phase yet. A maximum yield of ~90 % was hitherto obtained. This was respected for the calculation of the chemical composition out from hot gas extraction data. $ScTa_2O_5N$ crystallizes in the tetragonal space group $P4_2/mnm$ (rutile-type structure, Fig. 2) and shows a brilliant yellow color.

[1] K. Maeda, K. Domen, *J. Phys. Chem. C,* 2007, 111
[2] M. Jansen, H. P. Letschert, *Nature*, 404, 2000, *27*, 980-982

Financial support from the Deutsche Forschungsgemeinschaft (SPP 1613) is gratefully acknowledged.

Figure 1

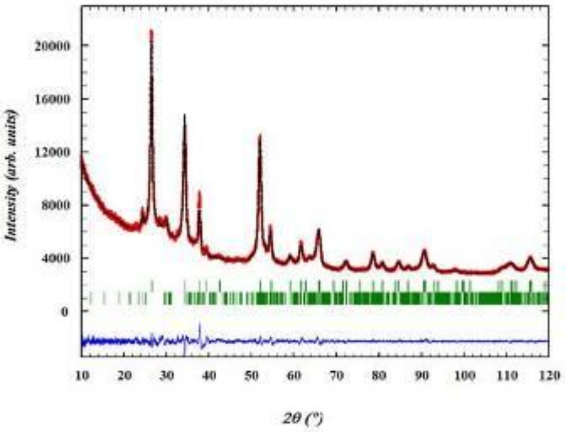

Figure 1: Results of the Rietveld refinement of $ScTa_2O_5N$. The product exhibits small amounts of an additional wodginite-type phase.

Figure 2

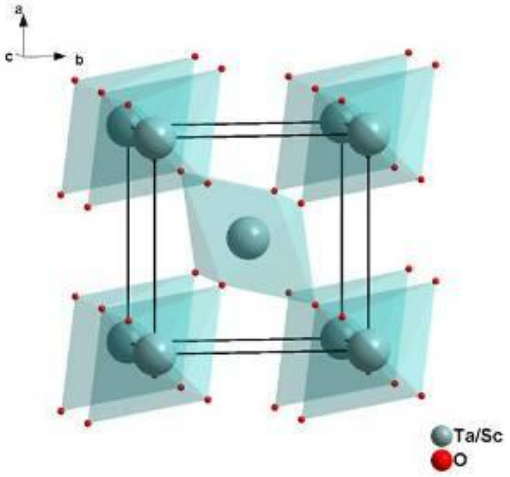

Figure 2: Crystalstructure of the new rutile-type phase $ScTa_2O_5N$.

MS02-P14

In situ characterization of mechanically treated MoO_3 and its oxide nitrides as model catalysts for selective propene oxidation

S. Kühn[1], C. D. Feldt[1], S. Orthmann[1], M. Lerch[1], T. Ressler[1]
[1]*TU Berlin, Berlin, Germany*

Introduction

Molybdenum-based oxides represent well-known model systems for selective oxidation of light alkenes [1]. According to the redox mechanism it is assumed that oxygen availability may play a distinguished role for catalytic activity. Furthermore catalytic properties are affected by the crystallinity of the bulk catalysts. Real catalysts mostly consist of a complex structure. Instead, simplified model catalysts are required to elucidate structure activity relationships. Oxide nitrides of MoO_3 represent a suitable model system for studying correlations between oxygen mobility and catalytic performance [2]. In this work we studied the influence of a modified crystallinity of MoO_3 and its corresponding oxide nitrides on structural behavior under catalytic conditions.

Experimental

Commercially available MoO_3 was ground in a planetary mill in order to vary its crystallinity. Corresponding oxide nitrides of MoO_3 were produced by ammonolysis of these catalysts. A structural characterization was conducted by ex situ and in situ XRD. Catalytic performance was investigated by GC-MS of the oxidation products.

Structural characterization

XRD measurements and IR spectra of the grounded MoO_3 and its corresponding oxide nitrides showed that the structure of MoO_3 was preserved. Hence, a slightly increased lattice parameter *b* after ammonolysis was determined due to the incorporation of nitrogen. Additionally, determination of crystallite size and lattice strain was carried out by using a single-line method to analyze line broadening [3]. The size and strain analysis revealed a decrease of crystallite size after milling process. The ammonolysis of MoO_3 resulted in a significant increase of lattice strain.

In situ investigations of MoO_3 and oxide nitrides In situ XRD experiments were conducted to investigate structural properties under catalytic conditions. Determination of lattice strain resulted in an increase of lattice strain at the onset of catalytic activity. On-line GC-MS analysis of propene oxidation products showed little effect on propene conversion caused by ammonolysis. Additionally, a decrease of lattice strain in molybdenum oxide nitrides was calculated at the same temperatures as the removal of nitrogen, observed in the equivalent MS ion currents.

Oxide nitrides are suitable model systems to study correlations between lattice oxygen mobility, electrical properties, crystallinity, and catalytic activity.

Acknowledgement

The authors gratefully acknowledge financial support from the Deutsche Forschungsgemeinschaft, DFG.

[1] J. Haber, E. Lalik, *Catal. Today*, 1997, *33*, 119-137.
[2] S. Kühn, P. Schmidt-Zhang, A.H.P. Hahn, M. Huber, M. Lerch, T. Ressler, *Chemistry Central Journal* 2011, 5:42.
[3] Th.H. De Keijser, E.J. Mittemeijer, H.C.F. Rozendaal, *J. Appl. Cryst.* 1983, *16*, 309-316.

MS02-P15

Skull Melting for growing $Y_{0,2}Zr_{0,2}Ce_{0,6}O_{2-\delta}$ single crystals

G. Ulbrich[1], M. Lerch[1]
[1]*Technische Universität Berlin, Institut für Chemie, Berlin, Germany*

The number of methods for growing single crystals of refractory oxides with decent quality is limited. For example the crystals growing by the Czochralsky method at high temperatures usually contain impurities coming from the crucible. The Skull Melting method is an alternative possibility for receiving very clean single crystals with, in theory, no limitation concerning the melting temperature[1,2]. It can be described as quasi-crucible-free high frequency process where the material is included in a water cooled Container (Fig.1). Power transfer occurs via a HF-Field. By putting a small amount of characteristic Metal in the material, it can be coupled to the HF-Field and heated up to the melting point. Between the molten material and the cool crucible a thin ceramic layer remains protecting the melt from impurities. After the whole material is molten, the crucible is slowly moved out of the HF-Field and the crystals grow in a Bridgman like process.

The $Y_{0,2}Zr_{0,2}Ce_{0,6}O_{2-\delta}$ crystal is interesting because of its ability to restore a large amount of oxygen. For synthesis we fill a stoichiometric mixed amount of the different Oxides (together around 2 Kg) in the crucible. After passing through the process we receive single crystals with dimensions of (6 x 6 x 15 mm^3). The crystals were analyzed by XRD, WDX, EBSD and gravimetric analysis.

Fig.1 Schematic presentation of the setup (1: cooled bottom, 2: cooled fingers, 3: cooled induction coil)[3].
[1] W. Assmus, N. Whippey, *Chem. Ing. Tech.* 1983, 55, 716-717
[2] M. Lerch et al, *Progress in Solid State Chemistry* 2009, 37 (2-3), 81-131
[3] S. Gutzov et al, *Phys. Chem. Chem. Phys.* 2009, 11, 636-640

Figure 1

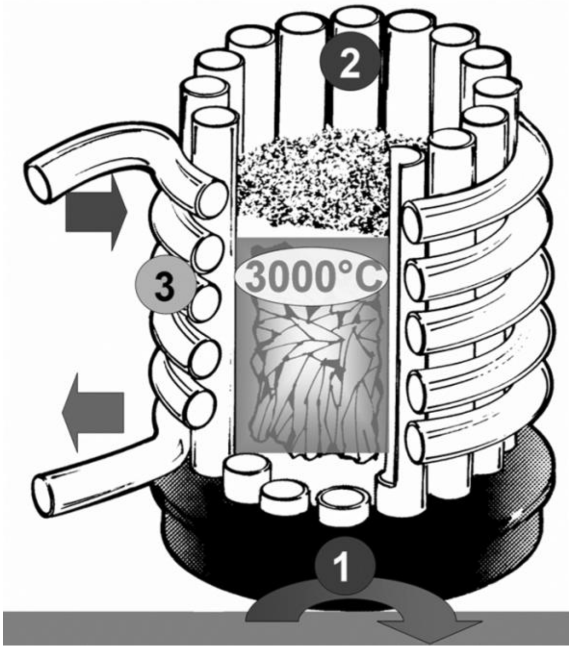

MS02-P16

Microstructural and defect analysis of metal nanoparticles in functional catalysts by diffraction and electron microscopy: The Cu/ZnO catalyst for methanol synthesis

T. Kandemir[1], R. Schlögl[1], M. Behrens[1]
[1]*Fritz-Haber-Institut, Anorganische Chemie, Berlin, Germany*

The application of different methods for a microstructural analysis of functional catalysts is reported for the example of different Cu/ZnO-based methanol synthesis catalysts. Transmission electron microscopy and diffraction were used as complementary techniques to extract information on the size and the defect concentration of the Cu nano-crystallites. The results, strengths and limitations of the two techniques and of different evaluation methods for line profile analysis of diffraction data including Rietveld-refinement, Scherrer- and (modified) Williamson-Hall-analyses, single peak deconvolution and whole powder pattern modeling are compared. It was found that in comparison with a macrocrystalline pure Cu sample, the catalysts were not only characterized by a smaller crystallite size, but also by a high concentration of lattice defects, in particular stacking faults. Neutron diffraction was introduced as a valuable tool for such analysis, because of the larger number of higher-order diffraction peaks that can be detected with this method. An attempt is reported to quantify the different types of defects for a selected catalyst.

MS02-P17

CuZnO nanoparticles supported on nanostructured silica as catalysts for methanol steam reforming (MSR)

G. Koch[1], K. Pavel[1], T. Ressler[1]
[1]*TU-Berlin, Inorganic and Analytical Chemistry, Berlin, Germany*

Questions

Because H_2 may play an important role as energy carrier, it is of interest to investigate possibilities to store H_2 in small molecules like ammonia or methanol. Conversion of methanol and water (MSR) may achieve subsequent H_2 release. MSR is catalyzed by Cu containing catalysts under ambient pressure at 250 °C. The chemical composition as well as synthesis route of the catalyst influence catalytic activity [1]. Besides a large Cu surface area microstrain in Cu crystallites increased the H_2 production for bulk Cu/ZnO catalysts [2]. In order to further elucidate structure activity correlations, a series of CuZnO/SBA-15 catalysts was synthesized. During preparation, the sequence of deposition of Cu and Zn precursors was varied while the ratio of Cu/Zn atoms was kept invariant.

Methods

Using incipient wetness method nanostructured silica was treated with metal citrate solutions. Calcinations in air resulted in *oxidic precursors*. Structures of catalysts were examined using *in situ* X-ray absorption spectroscopy (XAS) at Cu K edge and Zn K edge at beamline X at HASYLAB, Hamburg, and laboratory *in situ* XRD. Furthermore, temperature programmed reductions in H_2 were performed prior to catalytic tests. MSR activity was tested in 2 % methanol and 2 % H_2O balanced with He at 250 °C. Reactants and products were analyzed using a gas chromatograph.

Results

Independent of synthesis sequence, XRD identified small CuO crystallites in the oxidic precursor. XAS at the Zn K edge showed Zn^{2+} ions in the oxidic precursor. During activation in H_2, time resolved XAS at the Cu K egde showed a reduction of CuOZnO particles supported on SBA-15 via a Cu^{1+} intermediate to CuZnO/SBA-15. Reduction to Cu started at different temperatures. Deposition of Zn precursors on already supported CuO resulted in retarded reduction. XRD patterns of the working catalysts revealed Cu crystallites, which differed in size and microstrain. For ZnO containing catalysts more strained Cu crystallites were found. CuZnO/SBA-15 catalysts showed good catalytic activity in MSR. A correlation between H_2 production and microstrain was found (Fig. 1).

Conclusions

In total, CuZnO nanoparticles supported on SBA-15 were successfully prepared independent of preparation sequence. In ZnO containing catalysts smaller and more strained Cu crystallites were found. When Cu and Zn precursors were deposited simultaneously, the resulting catalyst exhibited a superior activity, which correlated with the microstrain in the Cu crystallites.

[1] S. Sá, H. Silva, L. Brandão, J. M. Soua, A. Mendes *Appl. Catal., B Environmental* **2010**, *99*, 43-57.
[2] B. L. Kniep, T. Ressler, A. Rabis, F. Girgsdies, M. Baenitz, F. Steglich, R. Schlögl *Angew. Chem.* **2004**, *116*, 113-117.

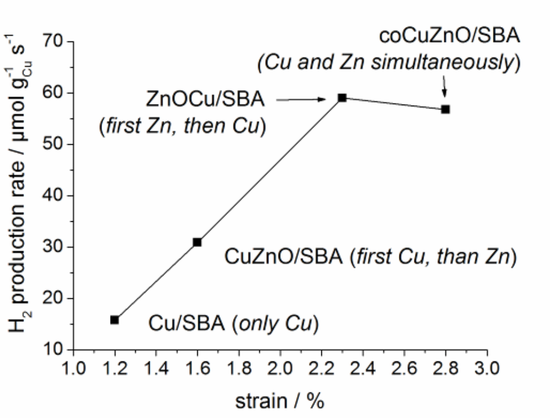

Fig 1. H_2production rate of CuZnO/SBA-15 catalysts after 10 h time on stream is shown as function of Cu crystallite microstrain. Preparation sequence of metal deposition on SBA-15 is given in brackets.

MS02-P18

Role of V and P in PV_2Mo_{10} supported on silica SBA-15 during oxidation of propene with gas phase oxygen

R. Zubrzycki[1], T. Ressler[1]
[1]*TU Berlin, Institut für Chemie, Berlin, Germany*

Introduction

Heteropolyoxomolybdates (HPOM) with Keggin structure exhibit a broad compositional range while maintaining their characteristic structural motifs. Substituting Mo atoms with addenda atoms (i.e. V, W, Nb) make Keggin type HPOM suitable model system to study structure-activity relationships. Additionally, supported HPOM exhibited a high dispersions and an improved surface to bulk ratio. However, the structural evolution and role of V and P in supported $H_5[PV_2Mo_{10}O_{40}]$ (PV_2Mo_{10}) under catalytic conditions is largely unknown. Here, the structure and the catalytic performance of PV_2Mo_{10} supported on nanostructured silica SBA-15 were investigated. The resulted activated structure of PV_2Mo_{10}-SBA-15 was compared to a reference $V_2Mo_{10}O_x$-SBA-15 which was synthesized from various vanadium and molybdenum precursors.

Experimental

Supported PV_2Mo_{10} was investigated with respect to catalytic activity in selective oxidation of propene with gas phase oxygen. PV_2Mo_{10} was deposited via incipient wetness on the support material SBA-15 with a loading of 10 wt.% Mo. The supported HPOM were characterized by XRD, EXAFS-, and ^{31}P-NMR-spectroscopy. Quantitative catalysis measurements were performed using a fixed bed laboratory reactor connected to an online gas chromatography system and a non-calibrated mass spectrometer

Results and discussion

Strong interaction effect of the support material SBA-15 resulted in a further decreased thermal stability of the supported Keggin ions during oxidation of propene with gas phase oxygene [1]. Mo and V atoms were connected via Mo-O-V bonds in substituted Keggin type precursors. This bond persisted during thermal treatment under catalytic conditions. Comparison of the pseudo radial distribution showed connected Mo-O-V species in act. PV_2Mo_{10}-SBA-15 in contrast to the reference $V_2Mo_{10}O_x$-SBA-15. Apparently, the proximity of V and Mo atoms in an identical metal oxide source was necessary to obtain connected metal oxide species on the support material. Phosphorus in PV_2Mo_{10}-SBA-15 formed a P-O-Si bond to the support material SBA-15 during propene oxidation. Moreover, P appeared to be bond to molybdat- and/or vanadat-species comparable to those observed in supported VPO-SBA-15 catalysts [2]. Furthermore, availability of dimeric or oligomeric $[(V,Mo)O_x]$ units increased selectivity towards oxygenates in contrast to isolated $[MoO_4]$ units [3].

Acknowledgment

Hamburg Synchrotron Radiation Laboratory, HASYLAB is acknowledged for providing beamtime. We are grateful to DESY and the Deutsche Forschungsgemeinschaft for financial support.

References

[1] T. Ressler, U, Dorn, A. Walter, S. Schwarz, A.H.P. Hahn, *J. Catal.* 275 (2010) 1-10.

[2] J. Frey, C. Lieder, T. Schölkopf, T. Schleid, U. Nieken, E. Klemm, M. Hunger, J. Catal. 27 (2010) 131-139.

[3] J. Scholz, A. Walter, A.H.P.Hahn, T Ressler, Microporous Mesoporous Mater. 180 (2013) 130-140.

MS02-P19

Solid state kinetic investigations of corundum type V_2O_3 under catalytic reaction conditions

A. Müller[1], D. Weber[1], M. Lerch[1], T. Ressler[1]

[1]*Technische Universität Berlin, Institut für Chemie, Berlin, Germany*

Motivation

Large ranges of physical properties of transition metal oxides are mainly determined by their crystal structure, electronic band structure, and concentration of defects in the crystal lattice. Furthermore, many transition metals and oxides have a huge importance in the field of catalysis. Here, we focus on potential catalytic properties of metastable transition metal oxide nitrides and oxides. Hence, V_2O_3 with corundum structure (trigonal rhombohedral lattice) is used as model system for solid-state kinetic investigations under catalytic conditions. Different solid state kinetic models were evaluated to describe the early stage of the oxidation of V_2O_3 with corundum structure during selective oxidation of propene.

Experimental

XANES (X-ray Absorption Near Edge Structure), in situ X- ray diffraction (XRD) and gas chromatography (GC) were used for structural and functional analysis. During XRD and XAFS measurements selective and total oxidation products in the gas phase were detected with a non-calibrated mass spectrometer. Measurements under catalytic conditions were conducted in 5 vol% propene and 5 vol% oxygen.

Results

For V_2O_3 with corundum structure isothermal XANES measurements under catalytic conditions were performed up to a maximum temperature of 633 K and 643 K. The material was heated in a He atmosphere to suppress initial oxidation of V_2O_3 to rutile type VO_2. After reaching the corresponding temperature, propene and oxygen gases were added into the in situ cell. A change in the XANES region indicating structural changes in the material was observed. In situ XRD experiments under catalytic conditions showed only the forming of rutile type VO_2. Using reference materials (V_3O_7, V_6O_{13}) the amount of formed rutile type VO_2 as a function of time at 633 K and 643 K was evaluated and transformed into $\alpha(t)$ conversion curves (Figure 1a). The increasing $\alpha(t)$ conversion curves at 633 K and 643 K can be descript with a parabolic curve segment. $\alpha(t)$ conversion curves are linearized at 643 K and at 633 K with a one dimensional and with a two dimensional diffusion model, respectively (Figure 1b). During isothermal and nonisothermal in situ XRD measurements in 2 vol% oxygen in Helium the formation of rutile type VO_2, V_3O_7 and V_2O_5 was observed. This indicates a much fast reduction of potentially formed V_3O_7 to rutile type VO_2 under catalytic conditions.

References

[1] S. Nakhal, W. Hermes, T. Ressler, R. Pöttgen and M. Lerch, *Z. Naturforsch*. 2009, *64b*, 281-286

[2] A. Khawam, D. R. Flanagan, *J. Phys. Chem. B* 2006, *110*, 17315-17328

Figure 1: a) Increasing amount of rutile type VO_2 at 633 and 643 K measured during oxidation of V_2O_3 under catalytic conditions (5 vol% propene, 5 vol% oxygen) and b) with corresponding kinetic models.

Figure 1

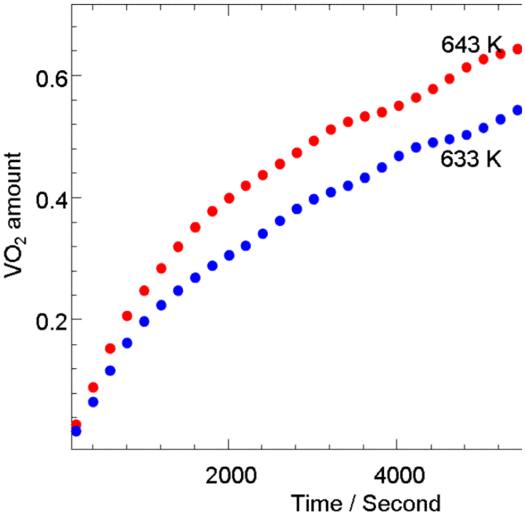

Figure 2

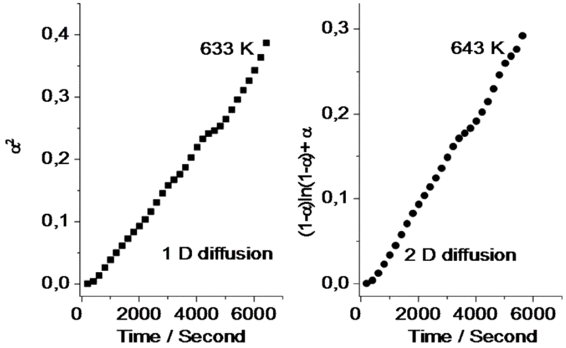

MS03 – Temperature, pressure and field induced processes/phase transitions

MS03-P01

Parametric Rietveld refinements combined with the new approach of rotational rigid body symmetry modes: Investigation of high pressure powder diffraction data

M. Etter[1], M. Müller[1], M. Hanfland[2], R. E. Dinnebier[1]
[1]*Max Planck Institute for Solid State Research, Stuttgart, Germany*
[2]*European Synchrotron Radiation Facility, Grenoble, France*

The typical procedure to investigate high pressure powder diffraction data obtained by X-ray or neutron diffraction methods is to use least square iteration processes such as the Rietveld method[1] to analyze structural and magnetic changes of the crystal structure. However the limiting factor for this type of investigation often is anisotropic peak broadening which occurs for instance due to the onset of non-hydrostatic conditions.

This anisotropic peak broadening is one reason, why the Rietveld refinement process is not always able to determine the global minimum. A stabilization of the Rietveld refinement process and therefore an optimization of the least squares iteration process can be obtained, by applying accurate structural models with as few as possible refineable parameters. In order to reduce the number of refineable parameters, different approaches can be applied e.g. rigid bodies, symmetry modes or the recently developed method of rotational rigid body symmetry modes[2], which is a combination of the aforementioned approaches. In all these approaches the number of required atomic coordinates is decreased by either the introduction of rigid connections between atoms or the fact that some symmetry modes are negligible. A further decrease in the number of refined parameters can be obtained by parametric Rietveld refinement[3], which means that physical or empirical equations are applied to refineable parameters as constraints over a set of simultaneously treated data. The combined application of one of the above mentioned approaches and the parametric treatment normally lead to a stabilization of the refinement process even for high pressure values, where the traditional sequential atomic coordinate refinement is no longer reliable.

In the present work, four competitive approaches, namely the traditional atomic coordinate refinement, a refinement with a deformable body using the method of rigid bodies, a symmetry mode refinement and a refinement with rotational symmetry modes of a rigid body were sequentially and parametrically carried out in a case study of $LaFeO_3$, with special focus on rotational rigid body symmetry modes.

Fig 1: Example of a deformable body (FeO_6 octahedron + 2 dummy atoms) combined with rotational rigid body symmetry modes in $LaFeO_3$[4].

References:
[1] Rietveld, H.M.**:** *A Profile Refinement Method for Nuclear and Magnetic Structures.* Journal of Applied Crystallography, **2**, 65, (1969)

[2] Müller, M.; Dinnebier, R.E.; Dippel, A.-C.; Stokes, H.T.; Campbell, B.J.**:** *A symmetry-mode description of rigid-body-rotations in crystalline solids: a case study of $Mg[H_2O]_6RbBr_3$.* Submitted to Journal of Applied Crystallography.
[3] Stinton, G.W.; Evans, J.S.O.: *Parametric Rietveld refinement.* Journal of Applied Crystallography, 40, 87, (2000)
[4] Etter, M; Müller, M; Hanfland, M; Dinnebier, R.E.**:** *Possibilities and limitations of parametric Rietveld refinement on high pressure data: The case study of $LaFeO_3$.* Zeitschrift für Kristallographie in press.

Figure 1

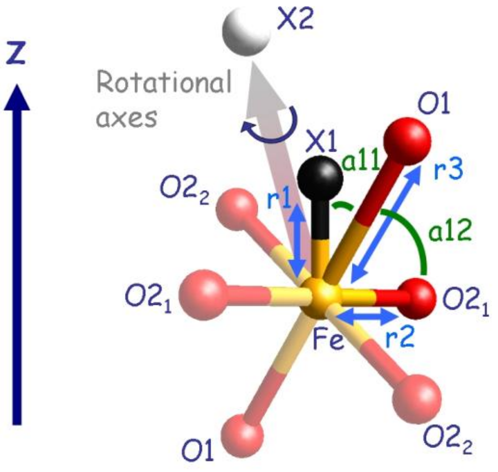

MS03-P02

Structural compression of $Sm_2Ti_2O_7$ and $Er_2Ti_2O_7$ pyrochlores up to 50 GPa from single crystal x-ray diffraction and DFT calculations

A. Friedrich[1], W. Morgenroth[1], B. Winkler[1], E. Haussühl[1], M. Hanfland[2], V. Milman[3], C. Stanek[4], K. McClellan[4]
[1]*Goethe University Frankfurt am Main, Institute for Geosciences, Frankfurt am Main, Germany*
[2]*ESRF, Grenoble, France*
[3]*Accelrys, Cambridge, United Kingdom*
[4]*Los Alamos National Laboratory, Los Alamos, United States*

The cubic pyrochlore group with composition $A_2Ti_2O_7$, with A = lanthanide, displays a large variety of interesting electronic properties, including exotic spin states (such as spin ices) at low temperatures and high pressures [1,2]. Based on powder x-ray diffraction and Raman spectroscopy using aluminium as a pressure medium it has been proposed that $Sm_2Ti_2O_7$ forms a distorted pyrochlore structure showing pressure-induced anion disorder above 40 GPa, and starts to amorphise at 51 GPa [3,4]. Here, we investigate the high-pressure structures of $Sm_2Ti_2O_7$ and isotypic $Er_2Ti_2O_7$ by single-crystal x-ray diffraction and quantum mechanical calculations.

Large crystals were grown by the optical floating zone method in a 4-lamp (halogen) furnace. Small crystals of sizes down to 20 × 20 × 5 μm^3 were pressurized in diamond anvil cells up to 50 GPa using neon as pressure-transmitting medium and ruby for pressure determination [5]. Single-crystal synchrotron x-ray diffraction experiments were carried out at PETRA III (beamline P02.2, DESY, Hamburg, Germany) and at ESRF (beamline ID09A, Grenoble, France) using 42.86 keV or 29.91 keV radiation and a PerkinElmer XRD1621 or MAR555 area detector, respectively. Images were converted [6] and further processed with the CrysAlis software [7]. Crystal structures were refined with the Shelx software [8] and with the Jana package [9]. Complementary quantum mechanical calculations based on density functional theory were performed using the CASTEP package [10].

In contrast to earlier reports [3,4] we observed no pressure-induced amorphisation or anion disorder up to 50 GPa. The current results are more reliable due to the use of neon as pressure medium, which provides a more hydrostatic pressure than the aluminium which had been employed as a pressure medium in the earlier study. A comparative analysis of the compression of $Sm_2Ti_2O_7$ and $Er_2Ti_2O_7$ pyrochlores will be given.

We gratefully acknowledge financial support from the DFG, Germany, (project Fr2491/2-1 within SPP1236) and the BMBF, Germany (projects 05K10RFA, 05KS7RF1, 05K13RF1). Portions of this research were carried out at the light source PETRA III at DESY, a member of the Helmholtz Association (HGF). We thank ESRF for beamtime and financial support.

[1] D. Pomaranski et al., Nature Physics 9, 353 (2013)
[2] I. Mirebeau et al., Nature 420, 54 (2002)
[3] F.X. Zhang and S.K. Saxena, Chem. Phys. Lett. 413, 248 (2005)
[4] F.X. Zhang et al., Appl. Phys. Lett. 86, 181906 (2005)
[5] H.K. Mao, J. Xu, and P.M. Bell, J. Geophys. Res. 91, 4673 (1986)
[6] A. Rothkirch et al., J. Synchr. Rad. 20, 711 (2013)
[7] Agilent Technologies, *CrysAlis RED*, version 171.36.28 (2013)
[8] G.M. Sheldrick, Acta Crystallogr. A 64, 112 (2008)
[9] V. Petricek, M. Dusek, and L. Palatinus, Jana2006, Institute of Physics, Praha, Czech Republic (2006)
[10] S.J. Clark et al., Z. Kristallogr. 220, 567 (2005)

MS03-P03

Structural, spectroscopic and computational studies on the monoclinic polymorph (form I) of potassium hydrogen disilicate ($KHSi_2O_5$)

D. Schmidmair[1], V. Kahlenberg[1], L. Perfler[1], D. M. Többens[2]
[1]Institute of Mineralogy and Petrography / University of Innsbruck, Innsbruck, Austria
[2]Helmholtz-Zentrum Berlin für Materialien und Energie GmbH, Department of Crystallography, Berlin, Germany

Hydrothermal treatment of quartz with 2 M K_2CO_3 solutions at 350°C and 1 kbar resulted in the formation of single-crystals of the monoclinic polymorph of potassium hydrogen disilicate ($KHSi_2O_5$ or $KSi_2O_4(OH)$). Basic crystallographic data of this so-called phase I at room conditions are as follows: space group $C2/m$, a = 14.5895(10)Å, b = 8.2992(3)Å, c = 9.6866(7)Å, β = 122.756(10)°, V = 986.36(10)$Å^3$, Z = 8. The structure was determined by direct methods and refined to a residual of R(|F|) = 0.0224 for 892 independent observed reflections with $I > 2\sigma(I)$. The compound belongs to the group of chain silicates. It is based on crankshaft-like *vierer* double-chains running parallel to [010]. The hydrogen atoms are associated with silanol groups. Hydrogen bonding between neighbouring double-chains results in the formation of about 5 Å wide slabs. The three crystallographically independent potassium cations with six to eight oxygen ligands provide linkage (i) between the chains of a single slab or (ii) between adjacent slabs. Structural investigations have been supplemented by micro-Raman spectroscopy. The interpretation of the spectroscopic data including the allocation of the bands to certain vibrational species has been aided by DFT-calculations.

MS03-P04

$P2_1/c$ to $C2/c$ phase transition in metamict titanite

T. Beirau[1], B. Mihailova[1], T. Malcherek[1], C. Paulmann[1], L. A. Groat[2], U. Bismayer[1]
[1]University of Hamburg, Mineralogisch-Petrographisches Institut, Hamburg, Germany
[2]University of British Columbia, Department of Earth, Ocean and Atmospheric Sciences, Vancouver, Canada

In titanite actinides can occur as natural constituents of the crystal structure. After a period of time the long-range ordered crystal structure is destroyed by self-radiation damage resulting from α-decay events of the radiogenic impurities. This radiation induced structural amorphization process generates the metamict state, which is characterized by a high degree of structural disorder with coexisting defect-rich crystalline and amorphous regions. [1]

We present the results of recent in situ temperature-dependent Raman spectroscopic measurements of two different metamict titanite samples. The results provide evidence for a thermally induced transformation process analogous to the phase transition $P2_1/c \leftrightarrow C2/c$ in pure non-metamict titanite. Quantitative analysis of the temperature evolution of the wavenumbers and widths of Raman active vibrations reveals an anomaly near 500 K in both radiation damaged titanites, which matches the $P2_1/c \leftrightarrow C2/c$ phase transition temperature of crystalline titanite. The structural transformation near 500 K is observed by Raman spectroscopy even in heavily metamict and chemically inhomogeneous titanite. The temperature evolution of the Raman active phonon modes between RT and 800 K reveals the occurrence of a thermally induced phase transition near 500 K, which up to now has been observed only in highly crystalline titanite samples with low defect concentration. [2]

[1] Hawthorne, F.C. et al. (1991) Alpha-decay damage in titanite. American Mineralogist, 76, 370-396.
[2] Beirau, T. et al. Temperature-induced P21/c to C2/c phase transition in metamict titanite revealed by Raman spectroscopy. (submitted to The Canadian Mineralogist)

MS03-P05

Exploring the water-*tert*-butylamine system at high pressure

R. Granero-García[1], F. P. A. Fabbiani[1]
[1]*Georg-August-Universität Göttingen, GZG, Abt. Kristallographie, Göttingen, Germany*

Gas hydrates are water-based crystalline compounds in which non-stoichiometric amounts of small non-polar molecules (generally gases under normal conditions) are trapped [1]. Gas hydrates have been proposed as a possible way to store H_2 for industrial use, however pure H_2 hydrates are stable above 200 MPa at 273 K [2]. To allow for production and storage under milder conditions stabilizers, such as *tert*-butylamine (^{t}BA) or THF, can be used [3].

As a polar molecule, ^{t}BA interacts with water, forming semi-clathrates instead of true clathrates [4], leading to different solid phases depending on the relative amounts of water and ^{t}BA in the system. The ^{t}BA 9.75 hydrate [5] exhibits a type-VI structure in which the large cages are occupied by ^{t}BA and are responsible for the stability of the entire structure, whilst the small cages can be filled with other small molecules, like H_2. The crystallisation behaviour of ^{t}BA hydrates by means of temperature has been recently untangled [6,7] and seven different hydrates, of which five are completely new, have been obtained in the solid state (with 0.25, 1, 7.25, 7.75, 9.75, 11, and 17 water molecules); additionally the low-temperature structure of pure ^{t}BA has been reported.

High-pressure crystallisation has proved to be a very successful technique for accessingnew polymorphs and hydrates of organic substances [8]: the present work makes use of this technique to further explore the behaviour of the ^{t}BA-water system. The high-pressure crystallisation behaviour of solutions with different stoichiometries is reported. In addition, two novel phases, with structures refined from X-ray single-crystal diffraction data, have been fully characterised. First, a 5.38 hydrate crystallised inside a diamond anvil cell at a pressure of 0.76 GPa. Second, a new polymorph of pure ^{t}BA crystallised at 0.78 GPa. A full analysis of disorder, water cages and hydrogen-bond networks is presented.

[1] Sloan E. D. and Koh C. A., *Clathrate Hydrates of Natural Gases.* (3rd ed.) Boca Raton, FL: CRC Press; 2008.
[2] Dyadin Y. A., Larionov E. G., Manakov A. Y., Zhurko F. V., Aladko, E. Y., Mikina T. V. and Kornarov V. Y., *Mendeleev Commun.* 1999,9,209-210.
[3] Prasad P. S. R., Sugahara T., Sum A. K., Sloan E. D. and Koh A. C., *J. Chem. Phys. A* 2009, 113, 6540-6543.
[4] Alavi S., Udachin K. and Ripmeester J. A., *Chem. Eur. J.* 201**0**, 16, 1017-1025.
[5] McMullan R. K., Jeffrey G. A. and Jordan T. H., *J. Chem. Phys.* 1967, 47, 1229.
[6] Dobrzycki L., Cirkel S., Taraszewska P., Boese R. and Cyrański M. K., *The 28th Meeting of the European Crystallographic Association, Warwick, 2013.*
[7] Dobrzycki L., *personal communication.*
[8] Fabbiani F. P. A. and Pulham C. R., *Chem. Soc. Rev.* 2006, 35, 932-942.

MS03-P06

Phase relations between basic copper chlorides of the atacamite group

T. Malcherek[1], M. Welch[2], M. Sciberras[3], J. Schlüter[1], P. Williams[3]
[1]*Universität Hamburg, Mineralogisch-Petrogr. Institut, Hamburg, Germany*
[2]*Natural History Museum, Earth Sciences department, London, United Kingdom*
[3]*University of Western Sydney, Sydney, Australia*

Pure $Cu_2(OH)_3Cl$ can occur as the orthorhombic mineral atacamite, with Cu in entirely heterogeneous coordination by $(OH)^-$ and Cl^- anions. It can also occur with a pseudo-trigonal, monoclinic or triclinically distorted crystal structure. Especially clinoatacamite can accommodate substantial amounts of divalent cations such as Zn, Mg, Co or Ni substituting for Cu. These substitutions gradually reduce the Jahn-Teller distortion of Cu-sites coordinated only by hydroxyl anions. Thus, with increasing dilution of Cu-content, crystal structures of space group symmetry *R-3* (paratacamite) and *R-3m* (herbertsmithite) are stabilized. A central element ofthese crystal

structures is the two dimensional kagome topology of Cu atoms. In herbertsmithite, $Cu_3Zn(OH)_6Cl_2$, these kagome layers are undistorted and magnetically insulated from each other by intermediate layers of Zn atoms. Geometric frustration of antiferromagnetic ordering within the kagome layers enables the potential formation of exotic ground state structures. While the magnetic properties of herbertsmithite and other members of the atacamite group have attracted much attention in recent years, knowledge about the phase relations between the various polymorphs remains rather limited. Recently a temperature controlled, reversible structural phase transition between paratacamite and herbertsmithite [1] at a composition of $Cu_3(Cu_{0.71},Zn_{0.29})(OH)_6Cl_2$ has been observed. This contribution presents a symmetry mode analysis of the paratacamite - herbertsmithite transition and discusses possible further phase transitions to triclinic symmetry.

[1] M. D. Welch, M. J. Sciberras, P. A. Williams, P. Leverett, J. Schlüter, T. Malcherek (2013) Physics and Chemistry of Minerals, Published online: 03 September 2013.

MS03-P07

A new approach to experimental determination of orientation relationships in pressure-induced phase transformations

N. Pukallus[1], H. Klein[1], H. Sowa[1]
[1]*Georg-August-Universität Göttingen, Abteilung Kristallographie, Göttingen, Germany*

Under non-ambient conditions a crystal structure of a compound may become energetically unfavourable and a phase transformation occurs which can be driven by different mechanisms. The investigated phase transformations are considered to be reconstructive. It is assumed that the orientation relations of the unit cells of both phases give clues about the actual transformation path. During the phase transformation the single crystal turns into a polycrystalline material with a highly preferred orientation. The investigated materials include indium arsenide, copper indium selenide, cadmium sulfide, and cadmium selenide.

The experiments were carried out at the beam lines BW5 and P02.1 at DESY, Hamburg. High-pressure experiments were performed in diamond anvil cells. Before and after the phase transition pole figures were measured in a range -42°£w£42° of the orientation angle w. The data were recorded with either a mar345 or a Perkin Elmer 1621 area detector.

Attempts were made to evaluate the data by using the Rietveld-texture analysing program MAUD [1]. However, owing to strong powder rings caused by the gasket material and the reflections of the diamond anvils it was not possible to analyse weak sample reflections. Therefore, another approach was followed: For the determination of the experimental pole figures the detector images are cut into concentrical rings which only contain the texture information of one peak in the diffraction pattern. From the detected intensity distribution along these rings the experimental pole figures were determined from which the orientation distribution function (ODF) can be calculated. The ODFs of the starting and resulting phases of the considered material can be directly used to determine the orientation relationships. Additionally, non-measured complete pole figures calculated from ODF data provide the interpretation.

Literature:
[1] L. Lutterotti, S. Matthies, H. R. Wenk: Proceedings of the Twelfth International Conference on Textures of Materials (ICOTOM-12) Vol. 1, 159 (1999)

MS03-P08

Alternative ways of describing structural phase transitions: the case study of $[Mg(H_20)_6]RbBr_3$

M. Müller[1,2], R. E. Dinnebier[1], A.- C. Dippel[3], H. T. Stokes[4], B. J. Campbell[4]
[1]*Max Planck Institute for Solid State Research, Stuttgart, Germany*
[2]*University of Trento, Trento, Germany*
[3]*Deutsches Elektronen-Synchrotron DESY, Hamburg, Germany*
[4]*Brigham Young University, Provo, United States*

$[Mg(H_20)_6]RbBr_3$ undergoes a structural phase transition from monoclinic to cubic upon heating at 138 °C [1]. Structurally, this phase transition involves a substantial rotation of $Mg(H_2O)_6$ octahedra, which are embedded into a network of corner-sharing $RbBr_6$ octahedra.

Such rotations of a rigid arrangement of atoms can be followed using different approaches for structural description. In the present case, parametric and sequential Rietveld refinements were conducted using four model types: (1) traditional atomic xyz coordinates for each atom, (2) traditional rigid-body parameters, (3) purely displacive symmetry modes [2] and (4) rigid-body-rotational symmetry modes. Rotational rigid body symmetry modes were especially developed to describe rotations of groups of atoms, which can be constrained into a rigid body. Using this concept, rotations of rigid-bodies are treated as axial-vector order parameters and projected using group-theoretical methods. A comparison of the different approaches and their benefits and drawbacks will be presented [3].

References:
[1] R.E. Dinnebier, Y. Liebold-Ribeiro, M. Jansen, Z. Anorg. Allg. Chem. (2008), 634, 1857-1862.
[2] B.J. Campbell, H.T. Stokes, D.E. Tanner, D.M. Hatch, " J. Appl. Cryst. (2006) 39, 607-614.
[3] M. Müller, R.E. Dinnebier, A.-C. Dippel, H.T. Stokes, B.J. Campbell (submitted)

Figure 1: Comparison of the LT (left) and HT (right) crystal structures of $Mg(H_2O)_6RbBr_3$ viewed the c-axis. In HT phase, the new cubic unit cell is indicated in black.

Figure 1

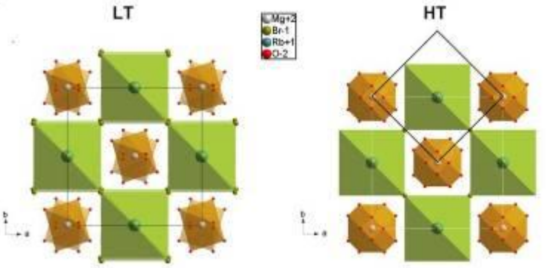

MS03-P09

Switching hydrogen bonds at high pressures in DL-alaninium semi-oxalate monohydrate

B. Zakharov[1,2], E. Boldyreva[1,2]

[1]*Institute of Solid State Chemistry and Mechanochemistry SB RAS, 15, Novosibirsk, Russian Federation*

[2]*Novosibirsk State University, REC-008, Novosibirsk, Russian Federation*

Hydrogen-bonded systems attract much attention. Even subtle changes in the hydrogen bonds can account for structural phase transitions with significant changes in physical properties of molecular materials, or for the conformational rearrangements of biopolymers. Hydrogen bonds may allow a crystal structure to resist significant strain without a collapse, and to be restored reversibly after the source of strain is removed. This property is important for the functioning of supramolecular devices or biological systems.

This work describes the first example of a single-crystal diffraction study of a high-pressure phase transition in a crystalline amino acid salt hydrate. The transition is accompanied by pronounced discontinuities in the changes of cell parameters and volume vs. pressure, although no radical changes in the molecular packing are induced.

A single-crystal to single-crystal transition in DL-alaninium semi-oxalate monohydrate at a pressure between 1.5 and 2.4 GPa was studied by single-crystal X-ray diffraction and Raman spectroscopy. Selected hydrogen bonds switch-over and become bifurcated, whereas the others are compressed continuously. Although, in contrast to DL-alanine, in the crystal structure of the salt there are short O-H…O hydrogen bonds, the structure of the salt is more compressible. At the same time, the structure of DL-alanine does not undergo pressure-induced phase transitions, whereas the structure of DL-alaninium semi-oxalate monohydrate does, and at a relatively low pressure. The anisotropy of lattice strain for the low-pressure phase differs from that on cooling at ambient pressure; interestingly enough, the anisotropy of the pressure-induced compression of the high-pressure phase is quite similar to the lattice strain of the low-pressure phase on cooling [1].

This work was supported by grants from RFBR (12-03-31541 mol_a), by the Ministry of Education and Science of Russia (project 14.B37.21.1093), and by a grant of President of Russia for State Support of Russian Leading Scientific Schools (project NSh-221.2012.3).

[1] Zakharov B.A., Boldyreva E.V. A high-pressure single-crystal to single-crystal phase transition in DL-alaninium semi-oxalate monohydrate with switching-over hydrogen bonds // Acta Crystallographica Section B. - 2013. - V. 69. - P. 271-280

MS03-P10

Serine co-crystals under extreme P-T conditions.

S. G. Arkhipov[1,2], B. A. Zakharov[1,2], E. V. Boldyreva[1,2]

[1]*Novosibirsk State University, REC-008, Novosibirsk, Russian Federation*

[2]*Institute of Solid State Chemistry and Mechanochemistry SB RAS, Novosibirsk, Russian Federation*

This work is devoted to the preparation and study of crystals of molecular complexes of amino acids. Co-crystals and salts of amino acids are very promising models to study the regularities in the formation of salts and co-crystals. The presence of amino-, carboxylic-groups, and also various side chains makes it possible to produce a rich variety of crystal structures with homomolecular and heteromolecular contacts. Multicomponent serine crystals can be considered as biomimetics when analyzing relation between crystal structures, hydrogen bonding, and side-chain mobility. Besides, some of them are promising as molecular materials with piezoelectric, ferroelectric, non-linear optical properties, or as biologically active compounds. The systems are also of fundamental interest for crystal engineering. Their structures can help to understand the role of the presence of several potential hydrogen-bond donors and acceptors, as well as of the shapes and flexibility of molecules in forming a certain molecular packing in multi-component crystals. Experiments with systematic temperature and pressure changes can provide valuable information about the behavior of the hydrogen bonds in the structures under study. These researches allow us to understand the relationship "structure-property" and in particular to compare the behavior of the hydrogen bonds in mixed crystals as compared with crystals of the individual components.

In the present contribution we describe crystallization of two new multi-component crystals (*L*-serinium semi-maleate (I), and DL-serinium semi-maleate (II), $C_3H_8NO_3^+$Ч$C_4H_3O_4^-$), and the results of solving their structures [1]. They provide the first example of the chiral and racemic anhydrous serine salts with the same organic anion. A comparison of their crystal structures with each other, and also with the structures of pure components (L-serine polymorphs, DL-serine, maleic acid, and other amino acids maleates) is important for understanding the formation of crystal structures, their response to variations of temperature and pressure, and structure-properties relations. Both in (I) and in (II), there are chains $C_2^2(12)$ and $C_2^2(12)'$. In (I) chains $C_2^2(12)'$ look like springs and account for interesting response of this structure with respect to P, T variations, which was followed by X-ray diffraction and Raman spectroscopy. Some data were compared with the existing data obtained for the individual components constituting the mixed crystal as well as with to some of the results obtained for other structures of serine.

This work was supported by a grant from Ministry of Education and Science of Russia (14.B37.12.1093), by RFBR (grant 12-03-31541 mol_a), by Department of Chemistry and Materials Sciences of the Russian Academy of Science (projects No. 5.6.4. and No. 22.44) and by a grant of President of Russia for Russian leading Scientific Schools (project NSh-221.2012.3).

[1] Arkhipov, S., Zakharov, B., Boldyreva E. (2013) *Acta Cryst.* C69, 517-521.

Keywords: mixed crystals, amino acids, high pressure, low temperature.

MS03-P11

In situ diamond anvil cell - Raman spectroscopy and nanoindentation study of the effect of pressure on γ- and δ-polymorphs of chlorpropamide

A. Ivanenko[1], V. Minkov[1], B. Janković[2], E. Boldyreva[1]
[1]*Novosibirsk State University, Institute of Solid State Chemistry and Mechanochemistry, Novosibirsk, Russian Federation*
[2]*University of Ljubljana, Department of Pharmaceutical Technology, Faculty of Pharmacy, Ljubljana, Slovenia*

Various properties of molecular solids account for the weak intermolecular interactions - hydrogen bonds and van der Waals interactions - which stabilize anisotropic crystal structures typical for molecular crystals. Molecular packing, slip planes and defects are directly related to mechanical properties of the molecular crystals. Studies of mechanical properties of molecular organic crystals either by hydrostatic loading, or by nanoindentation are not only of great fundamental interest but are also of significant practical importance. The majority of active pharmaceutical ingredients are crystalline molecular solids frequently having different polymorphic modifications with distinct physicochemical properties. As long as a pharmaceutical substance is subject to external influences during processing (milling, compressing, granulation), transportation and storage, the knowledge about the structure response to these actions and possible consequences for the mechanical properties appears to be very useful.

Sulfonylurea derivatives which have been used as antidiabetic agents for a long time are particularly interesting in terms of conformational polymorphism. Chlorpropamide belongs to the first generation of the antidiabetic drugs and can be crystallized in five different crystalline phases (α, β, γ, δ and ε). Existence of these polymorphs at ambient conditions is possible because of various packing of the conformationally flexible molecules which are connected with each other via the hydrogen bonds. Such hydrogen bonded motifs are preserved for all polymorphs of chlorpropamide, they are rigid and are directed along certain crystallographic axes in the crystal structure. Considering differences in the crystal structures of the polymorphs of chlorpropamide we can expect different response of the polymorphic single crystals to mechanical stress of various nature. It is also interesting to correlate mechanical properties with the features of crystal structure and to compare it for different polymorphs.

In this contribution we present the results of a comparative study of the mechanical properties of γ- and δ-polymorphs of chlorpropamide using Raman spectroscopy in a diamond anvil cell and nanoindentation measurements.

Samples of γ- and δ-chlorpropamide were obtained from the mixture of heptane and ethyl acetate by varying the solvents ratio, concentration of solution and temperature regime. Thin plates shape single crystals of γ- and δ-polymorphs of chlorpropamide for Raman spectroscopy as well as for nanoindentation were taken from the same batches respectively and had no visible imperfections as evidenced by observing the samples in the polarized microscope.

The effect of hydrostatic pressure was followed by Raman spectroscopy in a diamond anvil cell up to 5.0 GPa. Reversible phase transitions were observed in γ- and δ-polymorphs of chlorpropamide. Both phase transitions occurred at different pressures and gave different phases. It is worth to mention that pressure increase was accompanied by cracking of the single crystals as well as crystallization of the unknown phase in the diamond anvil cell. Single crystals of γ- and δ-polymorphs of chlorpropamide demonstrated significantly different plasticity (indentation hardness) which is related to different molecular packaging. The results are compared with the effect of hydrostatic pressure on the two forms.

The research was supported by a grant for Russia-Slovenia collaboration BI-RU-12-13-038, a grant from RFBR and the Integration project 108 of the SB RAS.

MS04 – Hot new structures

MS04-P01

Better Data Faster - Shutterless Data Collection Using a CMOS Detector

M. Adam[1], H. Ott[1], S. Freisz[1], J. Kaercher[1,2], G. Wachter[2], S. Leo[2]
[1]*BRUKER AXS GmbH, Karlsruhe, United States*
[2]*BRUKER AXS INC, Madison, WI, United States*

CMOS active pixel sensors for laboratory crystallography, such as the PHOTON 100 detector; are rapidly displacing imaging plate and CCD detectors as a large number of D8 QUEST and D8 VENTURE systems are now used in laboratories throughout the world.

CCD detectors and imaging plates operate in the conventional still-image mode involving numerous shutter-open/shutter-close, goniometer ramp-up/ramp-down and detector readout steps. Next to overhead-time this process introduces mechanical jitter. CMOS detectors can be operated in this mode but offer continuous read-out, which eliminates overhead-time and provides increased productivity.

The PHOTON 100 detector can now operate in a completely shutterless read-out mode. This enables continuous data collection without the need to frequently open and close the X-ray shutter; only accelerating and decelerating the goniometer at the beginning and the end of the scan. The Bruker Software Suite and in particular its integration engine SAINT now include the continuous scan, shutter-free integration for the D8 QUEST and D8 VENTURE systems. We will discuss the user benefit of continuous scan data and demonstrate the improvements to data quality achieved using the new shutterless data collection mode.

Figure 1

MS04-P02

Crystal Structure Determination of the Non-Classical 2-Norbornyl Cation

F. W. Heinemann[1], K. Meyer[1], F. Scholz[2], I. Krossing[2], D. Himmel[2], P. von Ragué Schleyer[3,4]
[1]*Friedrich-Alexander-Universität Erlangen-Nürnberg, Chemie und Pharmazie, Anorganische Chemie, Erlangen, Germany*
[2]*Albert-Ludwigs-Universität Freiburg, Insitut für Anorganische und Analytische Chemie, Freiburg, Germany*
[3]*University of Georgia, Department of Chemistry, Athens, United States*
[4]*Friedrich-Alexander-Universität Erlangen-Nürnberg, Chemie und Pharmazie, Erlangen, United States*

Question

Carbocations have been controversial throughout their eleven-decade history *(1, 2)*. Despite numerous arguments, ingenious “proofs” and “compelling evidence” for the non-classical structure that had been put forward over the years, definitive experimental evidence for the proposed symmetry of the non-classical norbornyl cation - namely the X-ray crystal structure determination - was still missing *(3)*. Although crystalline 2-norbornyl salts have been obtained earlier (*4*), numerous attempts by various research groups to solve the X-ray structure failed (*5*, *6*). Only now, 49 years after the first preparation of the 2-norbornyl cation under stable ion conditions *(7, 8)*, this vexing X-ray problem was solved *(9)*.

Methods

Suitable single crystals of the CH_2Br_2 solvate of the non-classical 2-norbornyl cation salt $[C_7H_{11}]^+[Al_2Br_7]^-$ were obtained by reaction of norbornyl bromide with aluminum tribromide in CH_2Br_2. These crystals undergo a reversible order-disorder phase transition at 86 K. A careful annealing procedure had to be applied to give a fully ordered lower temperature phase of the 2-norbornyl cation salt. Data collection at 40 K and refinement revealed the molecular structures of three independent 2-norbornyl cations in the unit cell.

Results

Multiple full single crystal XRD measurements at temperatures above 86 K always led to a high temperature phase with well-ordered anions, but completely disordered cations. Reversible ordering with phase transition takes place at 86 K and is completed upon cooling to approximately 50 K. Crystal parameters obtained from converged data recorded at 120 K and 40 K are: high temperature form, $T = 120$ K: $R_1 = 0.040$, $wR_2 = 0.082$; *orthorhombic* $Cmc2_1$: a 12.1499(5), b 14.0677(6), c 12.8625(5) Å; low temperature form, $T = 40$ K: $R_1 = 0.060$, $wR_2 = 0.121$; *orthorhombic* $Pna2_1$: a 14.040(4), b 36.042(9), c 12.851(3) Å. The well-ordered 40 K crystal structure of $[C_7H_{11}]^+[Al_2Br_7]^-$ is comprised of three independent ion pairs and co-crystallized CH_2Br_2 solvate molecules in the unit cell tripled along the crystallographic *b* axis

References
(1) F. C. Whitmore, *J. Am. Chem. Soc.* 54, 3274 (1932).
(2) H. C. Brown, *The Nonclassical Ion Problem*, with comments by P. v. R. Schleyer (Plenum Press, New York, 1977).
(3) H. C. Brown, *Acc. Chem. Res.* 19, 34 (1986).
(4) L. K. Montgomery, M. P. Grendze, J. C. Huffman, *J. Am. Chem. Soc.* 109, 4749 (1987).
(5) T. Laube, *J. Am. Chem. Soc.* 111, 9224 (1989).
(6) T. Laube, *Angew. Chem., Int. Ed. Engl.* 26, 560 (1987).
(7) P. v. R. Schleyer, W. E. Watts, R. C. Fort, M. B. Comisarow, G. A. Olah, *J. Am. Chem. Soc.* 86, 5679 (1964).
(8) M. Saunders, P. v. R. Schleyer, G. A. Olah, *J. Am. Chem. Soc.* 86, 5680 (1964).
(9) F. Scholz, D. Himmel, F. W. Heinemann, P. v. R. Schleyer, K. Meyer, I. Krossing, Science *341*, 62 (2013).

Figure 1

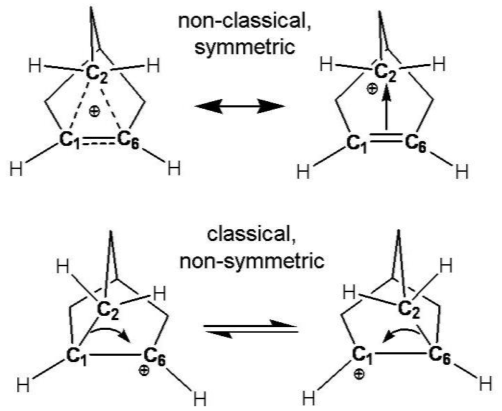

Proposed 2-norbornyl cation structures.

Figure 2

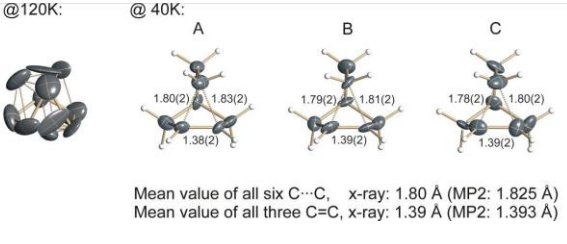

Molecular structure of the 2-norbornyl cation in crystals of $[C_7H_{11}]^+[Al_2Br_7]^-\cdot CH_2Br_2$

MS04-P03
Crystallisation and preliminary X-ray structure of a bacterial fatty acid synthase

K. Paithankar[1], M. Enderle[1], M. Grininger[1]
[1] *Goethe University Frankfurt, Buchmann Institute for Molecular Life Sciences, Frankfurt, Germany*

Important advances in the understanding of fatty acid synthase (FAS) type multi-enzyme complexes have been made during the last years by reports of X-ray crystallographic and cryo-electron microscopic (cryo-EM) structures of the fungal and mammalian complexes [1-3]. Cryo-EM structural characterisation of *Mycobacterium tuberculosis* FAS type 1 reveal high conformational flexibility that allow dynamic domain reorganisations during fatty acid synthesis [4]. Antibiotic therapy in response to *Mycobacterium tuberculosis* infections targets de novo fatty acid biosynthesis, which is orchestrated by a 1.9 MDa type I fatty acid synthase. A structural characterisation of this megasynthase is very relevant to anti-tuberculosis inhibition strategies, for example, to develop new inhibitory concepts based on the conformational flexibility of individual domains.

An homolog of M. tuberculosis FAS type I was chosen from Corynebacterium efficiens and subject to recombinant expression in E. coli and purified. The purified protein was crystallised by hanging drop vapour diffusion method. Initial diffraction experiments on the crystals using synchrotron radiation indicate crystals belong to hexagonal space group and likely to contain one molecule in the asymmetric unit.

[1] S. Jenni, M. Leibundgut, D. Boehringer, C. Frick, B. Mikolasek, N. Ban, Science 2007, 316, 254-261
[2] I. B. Lomakin, Y. Xiong, T. A. Steitz, Cell 2007, 129, 319-332
[3] P. Johansson, B. Wiltschi, P. Kumari, B. Kessler, C. Vonrhein, J. Vonck, D. Oesterhelt, M. Grininger, Proc Natl Acad Sci U S A. 2008, 105,
[4] L. Ciccarelli, S. R. Connell, M. Enderle, D. J. Mills , J. Vonck, M. Grininger, Structure 2013, 21, 1251-1257.

MS04-P04
Structure determination by Serial Femtosecond Crystallography

K. Nass[1]
[1]*MPIMF, Heidelberg, Germany*

X-ray crystallography is the most widely applied method for determining the structures of macromolecules using synchrotron or laboratory sources.

However, the method is hampered by the necessity to obtain crystals of sufficient size that withstand radiation damage. With the advent of hard X-ray free-electron lasers (FELs) it became possible to obtain interpretable high-resolution diffraction data from micro-sized crystals of only about 1 um on the side, that resulted in undamaged structures due to the intense ultra-short X-ray pulses (Chapman et al., Boutet et al., Redecke et al., Barty et al., Barends et al.).

I this talk I will present the general concepts and methods of serial femtosecond crystallography (SFX) at FEL sources. I will review the recently published results of the first unknown structure of natively inhibited cathepsin B from Trypanosoma brucei that has been determined using FEL diffraction data that extended up to 2.1 A resolution from in vivo grown micro-crystals and the first application of de novo phasing of the FEL data from the Lysozyme Gd derivative.

In contrast to the “diffraction-before-destruction” principle, our recent results suggest, that under highly intense FEL beam radiation sensitive systems may not provide damage free snapshots of the macromolecules assembled into crystals. The “hot spots” of radiation induced damage arise due to increase in the absorption coefficient of heavier elements in the crystal structure.

Chapman H. et al. “Femtosecond X-ray protein nanocrystallography” Nature 470, 73-77 (2011).
Boutet S. et al. “High-resolution Protein Structure Determination by Serial Femtosecond Crystalography” Science 337 (6092), 362-364 (2012).
Redecke L., Nass K. et al “Natively Inhibited Trypanosoma brucei Cathepsin B Structure Determined bby Using an X-ray laser” Science 339 (6116), 227-230 (2012).
Barty A. et al. “Self terminating diffraction gates femtosecond X-ray nanocrystallography measurements” Nature photonics 6, 35-40 (2012).
Barends T. et al. “De novo protein crystal structure determination from X-ray free-electron data” Science 10.1038/nature12773 (2013)

MS04-P05

Kryptoracemate: an example of a very rare class of racemic crystals crystallizing in a Sohnke space group

B. Braun[1], R. Laubenstein[1], T. Braun[1]
[1]*Humboldt Universität zu Berlin, Institute of Chemistry, Berlin, Germany*

We were fortunate to come across a racemic crystal structure crystallizing in a Sohnke space group, a so-called kryptoracemate. A review on this rare class of compounds was published by Fábián&Brock[1] in 2009.

Our compound crystallizes in the orthorhombic Sohnke space group $P2_12_12_1$ with one well-ordered enantiomeric pair in the asymmetric unit. The two enantiomeric molecules of opposite chirality differ significantly in conformation. There is no pseudosymmetry present in the crystal structure. p stacking interactions between electronically different substituted aryl rings of the (*R*)- and (S)- enantiomers amounts 3.495(18) Å. An infinite one dimensional chain occurs as a result of a classical hydrogen bond between one enantiomer and it’s neighbouring symmetry equivalents.

[1] L. Fa´bia´n and C. Pratt Brock, Acta Cryst. (2010). B66, 94-103.

MS04-P06

New Ce(III)-based metal-organic frameworks: Relevant Refinement Models.

A. Ellern[1], O. Ayhan[2], I. L. Malaestean[2], S. G. Baca[2], P. Kögerler[2]
[1]*Iowa State University, Chemistry, Ames, United States*
[2]*Institute Inorganic Chemistry, RWTH, Aachen, Germany*

Two new Ce(III)-based metal-organic frameworks (MOFs) with 2,2′-bipyridine-5,5′-dicarboxylic acid (bpdc), $\{[Ce_2(H_2O)(bpdc)_3(dmf)_2] \cdot 2(dmf)\}_n$ (**1**) and $\{[Ce_4(H_2O)_6(bpdc)_6] \cdot 6(dmf)\}_n$ (**2**), have been hydrothermally synthesized and characterized by a range of physical methods including IR spectroscopy, thermogravimetric and gas sorption analyses, and single-crystal X-ray diffraction. Both MOFs **1** and **2** are built from [Ce(solvent)] units (solvent = dmf (**1**), and H_2O (**2**)) bridged by water molecules in one-dimensional chains. The Ce(III)…Ce(III) separations in the chains are 4.269 and 4.835 Å in **1**, whereas in **2** the Ce(III)...Ce(III) distances equal 4.208; 4.394, 4.417, and 4.751 Å. Additionally, bpdc molecules connect these water-bridged Ce(III) chains into a 3D polymeric structure with cavities filled by dmf molecules.

This kind of abstract is typical for smooth publication of crystallographic data. Sometimes it is very difficult to find out what is hidden under this glossy cover. The reported in this presentation structures have typical complication which are very common for bulky 3d, 4f frameworks and huge POM clusters. There are well-known and widely used ways to “optimize” the results. Similarity restrains and SQUEEZE are the most common approaches to “massage” data for obtaining nice looking, geometrically relevant and CHECKCIF valid results. However even a very powerful tool should be used only when needed and by experienced person.

Different refinement models for variety of MOFs and POMs will be presented as illustration.

MS04-P07

Structural Studies on Ectonucleotidases Involved in Purinergic Signaling

C. Döhler[1], M. Zebisch[1,2], N. Sträter[1]
[1]*Universität Leipzig, Biotechnologisches Biomedizinisches Zentrum, Leipzig, Germany*
[2]*University of Oxford, Wellcome Trust Centre for Human Genetics, Oxford, United Kingdom*

Nucleotide pyrophosphatases/phosphodiesterases (NPPs) are a family of ectophosphodiesterases comprising 7 members in vertebrates. NPPs are glycoproteins and able to hydrolyze a wide range of molecules involved in different signaling pathways (e.g. in purinergic signaling). Whereas NPP1 and 3 are specific for nucleotides and dinucleotides, the natural substrates of NPP2, NPP5 and NPP7 are phospholipids. NPP1-3 include besides the catalytic domain a nuclease-like domain, which has no catalytic activity. Furthermore at the N-terminus of NPP1-3 two consecutive cysteinerich somatomedin B (SMB)like domains are located, which are involved in substrate binding (NPP2) and membrane anchoring (NPP1 and 3). NPP4-7 are only contain the catalytic domain. Apart from NPP2 all NPP family members are membrane associated [1]. Based ontheir involvement in many physiological functions and diseases NPPs are regarded as attractive drug targets. We aim to determine crystal structures of these proteins to characterize the structural basis of substrate specificity and the catalytic mechanisms.Structures of NPP1 and NPP2 from vertebrates revealed first insights in domain arrangement and ligand binding [2][3]. Neverthelessfor further investigations of the catalytic function of NPP enzymes high resolution structures in complex with substrates or substrate analogs are needed. We report on structural studies of rat NPP3, which was expressed in HEK293S cells.

References 1. Stefan C., Jansen S., Bollen M.,(2006). Modulation of purinergic signalling by NPP-type ectophosphodiesterases. Purinergic Signal *2*, 361-70
2. Nishimasu H., Okudaira S., Hama K., Mihara E., Dohmae N., Inoue A., Ishitani R., Takagi J., Aoki J., Nureki O., (2011) Crystal structure of autotaxin and insight into GPCR activation by lipid mediators. Nature Structural and Molecular Biology *18*, 205-12

MS04-P08

Improved Data Quality using the PHOTON 100 Detector in Shutterless Mode

V. Smith[1], S. Freisz[1], M. Benning[2]
[1]*Bruker AXS, Karlsruhe, Germany*
[2]*Bruker AXS, Madison WI, United States*

The PHOTON 100 detector can now operate in shutterless read-out mode. This capability eliminates errors in the diffraction data originating from shutter timing and goniometer stop and starts which are associated with traditional data collection leading to significant improvements in data quality.

Shutterless data collection eliminates frame-to-frame dead time, enabling more data to be collected within the same experiment time. High brightness in-house X-ray sources such as the METALJET™ and TURBO X-RAY SOURCE™ produce strong diffraction using exposure times of only a few seconds. Shutterless data collection thus makes possible the collection complete data in minutes.

SAD phasing experiments are experimentally challenging, requiring extremely accurate measurement of intensities. Recent, improvements in instrumentation and software have increased the number of structures solved using this method.

Here we show how the PHOTON 100 detector operating in shutterless mode can improve data quality and increase the number of successful solutions obtained from SAD phasing experiments.

MS04-P09

Solvent Effect on Crystal Structures

M. Abraham[1], I. Oppel[1]
[1]*RWTH Aachen University, Institute of Inorganic Chemistry, Aachen, Germany*

C_3-symmetric triaminoguanidinium based ligands $[H_6R_3L]Cl$ (R = H, Br) carrying a rigid backbone are an important building block for the preparation of supramolecular coordination cages as tetrahedra or trigonal bipyramides. [1] Understanding the chemical behavior of model compounds is a key for getting an insight in even more complex structures.

We reported the unexpected cyclization of the triaminoguanidinium based ligand forming a 1,2,4-triazole unit L' in the crystal structures of a protein-seized doughnut shaped coordination oligomer. [2] For the synthesis of a Pd(II)-based coordination capsule with octahedral shape, a $PdPPh_3$-triazole complex $[(PdPPh_3)(H_2L')]$ was observed. [3]

Recently, this oxidant induced intramolecular 1,2,4-triazole formation of $[(PdPEt_3)H_3R_3L]$ into $[Pd(PEt_3)H_2R_3L']$ was monitored successfully by NMR and X-ray-studies [3].

Due to numberless crystallisation experiments applying various solvents, we found up to now three different crystal structures of coordination compound $[(PdPEt_3)H_2Br_3L']\cdot$solvent: $P2_1$ (CCDC 942799), P-1, $P4/n$. Focusing on the coordination compound, its general position in all of the crystal structures allows comparison of the molecular bond length and bond angles. As the coordination geometry of Pd(II) is rather tight and therefore comparable in all of the structures, each of the corresponding ligand's backbone $[H_2Br_3L']^{2-}$ shows different torsion angles. Using single crystal X-ray diffraction we obtain insight into the flexibility of $[(PdPEt_3)H_2Br_3L']$ by three unique conformation isomers and their different crystal packing motives.

Figure 1. Molecular structure of $[(PdPEt_3)H_2Br_3L']$.

[1] A. C. Schulze, I. M. Oppel, *Top. Curr. Chem.*, 2012, *319*, 79.
[2] I. M. Müller, R. Robson, *Angew. Chem., Int. Ed.*, 2000, *39*, 4357.

[3] I. M. Müller, S. Spillmann, H. Franck and R. Pietschnig, *Chem. Eur. J.*, 2004, *10*, 2207.
[4] M. L. Abraham, A. C. Schulze, A. Korthaus, I. M. Oppel, *Dalton Trans.*, 2013, *42*, 16066.

Figure 1

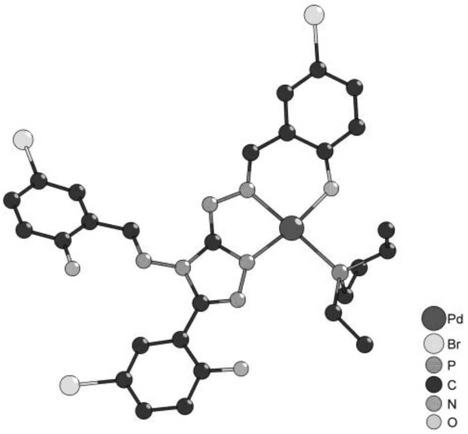

MS04-P10

The autofluorescence characteristics of chalcedony (a crystalline variety of silica) from skates

M. Prado Figueroa[1]
[1]*Universidad Nacional del Sur, Biología, Bioq. and Farmacia, Bahía Blanca, Argentina*

Aluminium and silicon accumulations have been detected in electrocytes (electric organ cells) from skates by a combination of scanning electron microscopy and X-ray spectrometry (EDS-SEM). Biosilicification is an evolutionarily old and widespread type of biomineralization. Chalcedony (SiO2) formation was also documented in Rajidae electric organs during oxidative stress. Chalcedony is a microcrystalline fibrous form of silica consisting of an intergrowth of silica polymorphs quartz and moganite on the nanoscale. In this work, we document the visualization and identification of chalcedony crystals and silica polymorphs from skates electric organ, using a Leica TCS - SP2 Laser Scanning Confocal Microscope (LSCM). The autofluorescent character of chalcedony allowed us to obtain images of crystals and a comparative topographic study was made. Chalcedony crystals have different dimensions. Crystals of great size measure about 30 micron while little crystallites are 5 micron. Silica polymorphs: quartz and moganite were also detected. They differ in their crystal structure which is described in this work with three-dimensional (3-D) images. Quartz nanocrystals have a trigonal crystal structure and are rhombohedral in shape. While moganite nanocrystals have a monoclinic crystal structure and are acicular (pinacoid) in shape. These nanocrystals can be differentiated by using an argon ion laser with two emission bands: 514 nm (yellow emission) and 458 nm (cyan emission). This communication provides the first experimental evidence of biologically produced crystalline silica mineral phase (i.e., chalcedony) and its growth (crystallinity) in electric organs from living electric fish.

MS04-P11

Crystal structures of the cytosolic 5’-nucleotidase IIIB explain its preference for m^{7}GMP

T. Monecke[1], J. Buschmann[2], P. Neumann[1], E. Wahle[2], R. Ficner[1]
[1]*University of Göttingen, Department for Molecular Structural Biology, Göttingen, Germany*
[2]*Martin Luther University Halle-Wittenberg, Institute of Biochemistry and Biotechnology, Halle, Germany*

5’-nucleotidases catalyze the hydrolytic dephosphorylation of nucleoside monophosphates and thus play a pivotal role in the regulation of cellular nucleotide levels. Misregulation of nucleotide metabolism and nucleotidase deficiencies are associated with a number of diseases like hemolytic anemia.

Recently, a novel cytosolic 5’-nucleotidase (cN-IIIB) has been discovered and characterized [1]. In contrast to known 5’-nucleotidases, cN-IIIB has a broad substrate spectrum including purines and pyrimidines but nevertheless exhibits a strong substrate preference for the modified nucleotide 7-methylguanosine monophosphate (m^{7}GMP). The structural reasons for these unusual features were unknown so far.

Here, we describe the crystal structures of the novel cytosolic 5’-nucleotidase IIIB from *Drosophila melanogaster* either bound to the reaction product 7-methylguanosine and the transition state analog MgF_3, or cytidine. We show that the substrate preference of cN-IIIB for m^{7}GMP can be explained by a unique m^{7}G-binding mode. The 7-methylguanine moiety of the product is stacked between two aromatic residues in a coplanar but off-centered position. 7-methylguanosine is bound through π-π interactions and distinguished from unmodified guanosine by additional cation-π coulomb interactions resulting from the stack of aromatic side chains and the positively charged 7-methylguanine. Notably, the base is further stabilized by T-shaped edge-to-face stacking of an additional tryptophan packing perpendicularly against the purine ring and forming, together with the other aromates, an aromatic slot. The structural data in combination with sited-directed mutagenesis and activity assays as well as docking simulations provide conclusive insight in the molecular basis for the broad substrate specificity of cN-IIIB but also explain its substrate preference for m^{7}GMP.

Figure 1**.** Crystal structure of *Drosophila melanogaster* cN-IIIB. The reaction product 7-methylguanosine is bound in a cavity between the cap domain (dark grey) and the HAD core domain (light grey). The positively charged base (defined by a mF_o-DF_c omit map at 3σ) is stacked by Trp120, Trp121 and Phe75 together forming an aromatic slot (inset).

[1] Buschmann J., Moritz B., Jeske M., Lilie H., Schierhorn A. et al. (2013) Identification of *Drosophila*

and Human 7-Methyl GMP-specific Nucleotidases. *J. Biol. Chem.* 288.

Figure 1

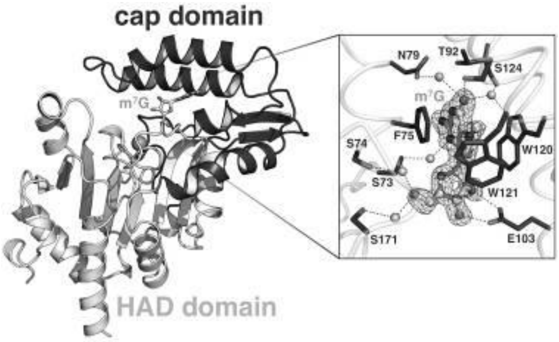

MS04-P12
Structural changes of Importin β in dependence of divergent crystallization conditions

M. Tauchert[1], A. Dickmanns[1], R. Ficner[1]
[1]*University of Göttingen, Molecular Structural Biology, Göttingen, Germany*

Transport of large biomolecules between the nucleus and the cytoplasm is mediated by nuclear transport receptors [1]. The majority of these receptors belong to the Importin β superfamily, which share a common structural motif. These so-called HEAT repeats are composed of two antiparallel α-helices which interact tightly. The repetitive arrangement enables a high degree of movement between neighboring HEAT repeats which results in a substantial overall flexibility as shown by crystal structures of Importin β either in the free form or bound to the small GTPase RAN or to various cargoes like SREBP-2 [2] and different import adaptors. We tried to crystallize Importin β under various conditions to gain insight into the intrinsic dynamic properties of free Importin β which have been suggested by molecular dynamics simulations [3]. Moreover, we will compare these structures with existing structures from the PDB with respect to the crystallization conditions and the contact areas within the crystal lattice.

1. Cook, A. (2007). Structural Biology of Nucleocytoplasmic Transport. Annu. Rev. Biochem. 76, 647-671.
2. Lee, S. J. (2003). The Structure of Importin-Bound to SREBP-2: Nuclear Import of a Transcription Factor. Science 302, 1571-1575.
3. Zachariae, U. (2008). Impβ: Structural and Dynamic Determinants of a Molecular Spring. Structure 16, 906-905.

MS04-P13
Structural analysis of the spliceosomal helicase Prp2 and its intrinsically disordered interaction partner Spp2

A. Schmitt[1], R. Ficner[1]
[1]*Georg-August-University Göttingen, Institute for Microbiology und Genetics, Department for Molecular Structural Biology, Göttingen, Germany*

mRNA splicing is a highly dynamic process by which non-coding sequences are removed from a pre-mature mRNA. It is catalyzed by the spliceosome, a huge and highly dynamic ribonucleoprotein complex consisting of up to five small nuclear RNAs and more than 100 proteins [1]. In this process, extensive rearrangements of RNA-RNA, RNA-protein and protein-proteininteractions are required in order to form the activated spliceosome.

The DEAH-box ATPase Prp2 and its interaction partner Spp2 play a key role in the activation of the spliceosome, as they promote the transition of the spliceosome from the Bact to the catalytically active B* complex [2, 3]. Prp2 exhibits an RNA-dependent NTPase activity and is active in the spliceosome after binding to its interaction partner Spp2. Spp2 contains a G-patch sequence motif which consists of a conserved glycine pattern and is mostly found in proteins involved in RNA processing. So far, the structure of a G-patch motif has been unknown and the function of the G-patch motif in general and in particular of Spp2 remained elusive.

After all attempts to crystallize Spp2 or the Spp2-Prp2 complex from yeast have failed, we used the orthologous proteins from the thermophilic fungus *Chaetomium thermophilum* (ctPrp2, ctSpp2). Thereby we were able to obtain well diffracting crystals of the ctPrp2 helicase in an ADP bound state and could refine this structure to a resolution of 2.1 Å. Moreover, we could solve the structure of ctPrp2 in complex with the G-patch motif of ctSpp2 at a resolution of 2.75 Å. Free Spp2 is intrinsically disordered as demonstrated by CD spectroscopy, but at least its G-patch region adopts a well-defined fold upon binding to Prp2. The interaction with Spp2 induces major structural changes in the β-hairpin of Prp2, a region which is supposed to move upon ATP binding. However, Spp2 does not affect the ATPase activity of Prp2 *in vitro*. Together, these findings give rise to the hypothesis that Spp2 might fulfill the function of an adaptor protein recruiting Prp2 to the spliceosome and transferring mechanical forces generated by ATP hydrolysis to other components of the spliceosome.

1. Will, C. L. & Lührmann, R. (2011) Spliceosome structure and function, *Cold Spring Harbor Perspectives in Biology.* **3**.
2. Edwalds-Gilbert, G., Kim, D. H., Silverman, E. & Lin, R. J. (2004) Definition of a spliceosome interaction domain in yeast Prp2 ATPase, *RNA.* **10**, 210-220.

3. Silverman, E. J., Maeda, A., Wei, J., Smith, P., Beggs, J. D. & Lin, R. J. (2004) Interaction between a G-patch protein and a spliceosomal DEXD/H-box ATPase that is critical for splicing, *Mol Cell Biol.* **24**, 10101-10.

Figure 1: G-patch motif of ctSpp2 (black) bound on the surface of ctPrp2 (light gray). Upon binding to ctPrp2 the formation of three α-helices is induced in the G-patch. Conserved glycine residues are shown as spheres in dark gray.

Figure 1

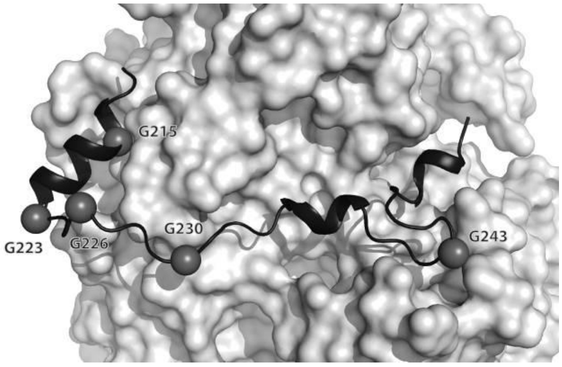

MS04-P14

Crystal structure of a 3D domain-swapped dimer of the Helicobacter pylori type IV secretion protein CagL

S. Barden[1], B. Schomburg[1], H. Niemann[1]
[1]*Universität Bielefeld, Fakultät für Chemie, Bielefeld, Germany*

3D domain swapping is a mechanism by which proteins exchange identical parts to form dimers or higher oligomers. Two recently reported crystal structures of the *Helicobacter pylori* type IV secretion system (T4SS) pilus protein CagL revealed a monomeric helix bundle with three helices forming a structural core, to which the N-terminal helix associates only loosely.

Here, we describe a third crystal structure, in which CagL forms a 3D domain-swapped dimer. Dimers of CagL can arise either during refolding from inclusion bodies or spontaneously from purified monomeric CagL in the crystallization conditions. In the CagL dimer structure the N-terminal helix is missing. The domain swap is formed by exchange of the C-terminal helix between the two protomers of a dimer. A loop-to-helix transition results in a long helix of 108 amino acids comprising the next-to-last and the last helix of the monomer. Apart from the 3D domain swap, there are no major structural differences between the monomer and the domain-swapped dimer.

The observed domain swap is most likely an *in vitro* artifact. A physiological relevance of CagL dimerization is questionable. Nevertheless, this new crystal form contributes to understanding the properties of CagL. Comparing the 3D domain-swapped dimer with the monomeric structures highlights rigid and flexible regions in the protein.

MS05 – Inorganic structural chemistry – synthesis, structure, properties and applications

MS05-P01

Hydrogen selective Graphite based Membranes

A. Schulz[1], F. Steinbach[1], J. Caro[1]
[1]*Institut für Physikalische Chemie und Elektrochemie, Hannover, Germany*

The use of graphite for hydrogen permeable membranes as well as for hydrogen adsorption interests were present for fusion reactor applications or as hydrogen storage material [1-5].

This work show another suitable application of easy pressed graphite based membranes for the hydrogen removal produced by catalytic steam reforming of bio-ethanol at ambient pressures and temperatures between 294 to 537 K ($C_2H_5OH + 3\ H_2O \leftrightarrow 2\ CO_2 + 6\ H_2$) [6]. Commercial graphite powders till flakes with average crystal sizes of 5 to 200 µm were easily pressed (~100 kN) to disks with a thickness of 1 mm and 18 mm in diameter.

First experiments using Wicke-Kallenbach technique coupled with a soap bubble meter for single-gas permeation of H_2 and CO_2 (feed pressures: 2-5 bar, “Sweep” pressures: 1 bar) show high permeances in the range of $0.5\text{-}1.7\text{x}10^{-3}$Mol/s m² Pa ($H_2$) combined with relative high separation factors (SF: H_2/CO_2) between 6.7 and 59.8 (Fig.: 1).

The Separation results from the molecular weight of the relative gaseous Phases (Knudsen-Diffusion) along the grain boundaries of the pressed graphite crystals.

$H_2 > He > CH_4 > N_2 > Ar >$ “CO_2”

In the case of CO_2 the structure depending properties of the strong anisotropic graphite crystals (S.G.: P 6_3/mmc) lead to van der Waals interactions and increase the experimental SF related to the theoretical SF of around 4.7 after the equation: $J_{H2}/J_{CO2} = (M_{CO2}/M_{H2})^{0.5}$ [7,8].

Further investigations to mixed-gas permeation experiments (molar ratios of H_2/CO_2, H_2/H_2O) and temperature depending experiments should give a better understanding for this complex interaction between mixed gaseous phases and crystal surfaces.

References:
[1] T. Kiyoshi, T. Namba, M. Yamawaki: J. Nuclear Materials. 155-157 (1988) 230-233.
[2] K. Yamaguchi, Y. Suzuki , S. Tanaka, M. Yamawaki: J. Nuclear Materials. 179-181 (1991) 242-245.
[3] H. Atsumi, K. Tauchi: J. Alloys Comp. 356-357 (2003) 705-709.
[4] A.Spitsyn, A. Pisarev, A. Skovoroda, V. Gureev, Yu Martynenko: J. Nuclear Materials. 363-365 (2007) 833-838
[5] A. V. Spitsyn, A.V. Golubeva, M. Mayer, A.A. Skovoroda: J. Nuclear Materials. 390-391 (2009) 701-704.
[6] M. Ni, D.Y.C. Leung, M.K.H. Leung, Int. J. Hydrogen Energy 32 (2007) 3238.
[7] A. K. Mishra, S. Ramaprabhu: I.J. Chemical Engineering and Aplications, Vol.1, No.3 October 2010. ISSN: 2010-0221.
[8] V. R. Deitz: Journal of Physical Chemistry. Vol. 71, No. 4, 830-837 (1967).

Figure 1: Separation factors from single-gas permeation experiments for different average crystal sizes of graphite depending from different pressure gradients.

Figure 1

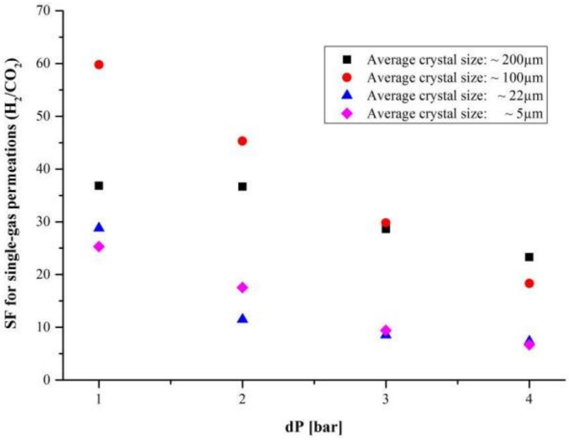

MS05-P02

Simulation of Pair Distribution Function of $CaCO_3$ polymorphs using DISCUS

M. Happel[1], A. Niedermayr[1], H. Gies[1]
[1]*Ruhr-University Bochum, Institute for Geology, Mineralogy and Geophysics, Bochum, Germany*

Calcium carbonates are one of the most abundant chemical compounds on earth. They occur as rock forming minerals, outer skeleton of invertebrates or amorphous as building units of sponges and cystolithes in plants. $CaCO_3$ forms six polymorphs, five crystalline phases (aragonite, calcite, vaterite, monohydrocalcite (containing H_2O), ikaite (containing 6 H_2O)) and one amorphous. Depending on the conditions during the synthesis and ageing processes like temperature, pressure, pH, humidity, amorphous calcium carbonate (ACC) crystallises to one of the five crystalline polymorphs.

A good method to determine structural information about amorphous phases like ACC is to analyse X-ray scattering experiments with the Pair Distibution Function (PDF). The PDF obtains information about atomic distances so that the short-range order of amorphous materials can be determined. Using the DISCUS program [1], among other things, it is possible to simulate ordered and disordered structures and calculate their PDFs.These simulations provide a basis for structural analyses of synthesized ACC. With this basis it is possible to identify the predominating crystalline structure within the short-range order of ACC by comparing experimental observed PDF of ACC with simulated PDFs of crystalline $CaCO_3$ polymorphs.

In this study PDF simulations of the five crystalline $CaCO_3$ polymorphs are presented. Various parameters as phase (one of the crystalline polymorphs), volume of the phase, computed range of the simulation, stepwidth, particle shape, value for correction of the limited resolution of the experiment (damping), which all affect the results of the simulation were considered and varied. This yields PDFs with differences in coherence length, proportion of atomic distances and shape.

Based on the simulated PDF of the crystalline $CaCO_3$ phases it is expected to identify the basic structural units in the different ACC materials which crystallise to one of the $CaCO_3$ polymorphs.

[1] Neder, R.B.; Proffen, T. (2007). Diffuse Scattering and Defect-Structure Simulations. Oxford University Press.

MS05-P03

Detailed studies on hydrogen bonds in various minerals using neutron single crystal diffraction

M. Meven[1], D. Gatta[2], A. Sazonov[1]
[1]RWTH Aachen, Institut für Kristallographie, Outstation at MLZ, Garching, Germany
[2]Universita` degli Studi di Milano, Dipartimento di Scienze Della Terra, Milano, Italy

Minerals of the silicate and phosphate families are is up to the present day an interesting topic of research. Various members from the epidote, lithium tourmaline and beryl group with very different crystallographic space groups were studied on the single crystal diffractometer HEIDI at the hot source of the Heinz Maier-Leibnitz Zentrum in Garching (MLZ) in the recent past. The combination of neutron and X-ray diffraction in combination with other methods revealed for each of the studied minerals - zoisite, elbaite, pezzottaite and brazillianite- valuable information about their structural details like its thermal evolutions, mixed occupancies and details of hydrogen bonds.

[1] F. Cámara, G.D. Gatta, M. Meven and D. Pasqual; Thermal expansion and high temperature structure evolution of zoisite by single-crystal X-ray and neutron diffraction; Physics and Chemistry of Minerals, 39(1):27-45 (2011).
[2] G. Diego Gatta, Rosa M. Danisi, Ilaria Adamo, Martin Meven and Valeria Diella; A single-crystal neutron and X-ray diffraction study of elbaite; Physics and Chemistry of Minerals, 39(7):577-588 (2012).
[3]G. Diego Gatta, Ilaria Adamo, Martin Meven and Erica Lambruschi, A single-crystal neutron and X-ray diffraction study of pezzottaite, Cs(Be2Li)Al2Si6O18, Physics and Chemistry of Minerals, (39):829-840 (2012).
[4] G. Diego Gatta,Pietro Vignola,Martin Meven and Romano Rinaldi,Neutron diffraction in gemology: Single-crystal diffraction study of brazilianite, NaAl3(PO4)2(OH)4;American Mineralogist,98(8-9):1624-1630 (2013).

MS05-P04

Synthesis, structural and optical characterizations of $(Cs,K)_3SmSi_6O_{15}$

M. Wierzbicka-Wieczorek[1], M. Göckeritz[1], C. Lenz[2], G. Giester[2]
[1]Friedrich-Schiller-Universität Jena, Institut für Geowissenschaften, Jena, Germany
[2]Universität Wien, Institut für Mineralogie und Kristallographie, Wien, Austria

The characterization of the title compound is part of a detailed study focusing on synthesis, structural and optical properties of novel silicates containing Sm, Tb, Dy and Pr cations. The silicate $(Cs,K)_3SmSi_6O_{15}$ forms as small, colorless, prismatic crystals from a high-temperature flux. The molybdate-carbonate-based flux solvent was heated to T_{max} = 950° C, held for 3 h, cooled at 2 °/h down to 850°C, then heated again at 17 °/h up to 900° C, held for 0.25 h and cooled at 2 °/h down to 700° C, followed by furnace shut-down and subsequent cooling. The reaction products were washed in distilled water, filtered and dried in air.

The crystal structure has been determined from single-crystal X-ray intensity data (Mo*K*α, 21° C; Bruker APEXII diffractometer) and refined in the orthorhombic space group *Cmca* (no. 64), with a = 14.474(3), b = 14.718(3), c = 15.231(3) Å, V = 3244.7(11) Å^3, to $R(F)$ = 2.44 %. The asymmetric unit of $(Cs,K)_3SmSi_6O_{15}$ contains two split mixed occupied K/Cs, a further K, one Sm, three Si and nine O atomic positions. The SiO_4 tetrahedra are interconnected to form zigzag layers parallel to (010) corner linked with SmO_6 octahedra building a three-dimensional framework with K^+ and Cs^+ atoms in between. The structural relationships between $(Cs,K)_3SmSi_6O_{15}$ and others silicates [1, 2] will be presented.

Photoluminescence spectra were obtained from random oriented crystals at room temperature using a Horiba Jobin Yvon LabRAM-HR 800 spektrometer with 473 nm laser-excitation. The emission of $(Cs,K)_3SmSi_6O_{15}$ is caused by Sm^{3+} cations, which shows two dominant luminescence transitions in the visible orange to yellow spectral range at 600 and 570 nm, which are interpreted as $^4G_{5/2} \rightarrow {}^6H_{7/2}$ and $^4G_{5/2} \rightarrow {}^6H_{5/2}$ transitions, respectively.

References
[1] S. M. Haile, B. J. Wuensch (2000) Structure, phase transitions and ionic conductivity of $K_3NdSi_6O_{15}$ x H_2O. II. Structure of β-$K_3NdSi_6O_{15.}$ Acta Cryst. **B**56, 349-362.
[2] A. Ziadi, H. Hillebrecht, G. Thiele, B. Elouad (2004) Structure determination of $Na_3DySi_6O_{15}$ and crystal chemistry of zektzerite related compounds. J. Solid State Chem. 177, 4777-4784.

Acknowledgements
This research was financially supported by DFG (WI 4132/1-1).

MS05-P05

Structure properties of the solid-solution $Mn_xZn_{2-x}SiO_4$ (0 < x < 0.6)

D. Behal[1,2], S.- H. Park[2]
[1]*Technische Universität München, Forschungs-Neutronenquelle Heinz Maier-Leibnitz (FRM II), Garching, Germany*
[2]*Ludwig-Maximilians-Universität München, Department for Earth and Environmental Sciences, München, Germany*

Introduction

Mn-doped α-Zn_2SiO_4 (willemite; **R**-3) is a well-known green phosphor. Its emission band at about 552 cm^{-1} is attributed to the 5d orbital electron transition of Mn^{2+} $^4T_1 \rightarrow {}^6A_1$ at two unique Zn sites [1, 2]. It has been assumed that the amount of defects along with metals cations could be the reason for the violet emission from Mn-doped α-Zn_2SiO_4 [3, 4]. To understand the influence of defects and metal cations on optical behaviors we have investigated a systematic Mn substitution in the willemite-type solid-solution $Mn_xZn_{2-x}SiO_4$ (0 < x < 0.6).

Experimental

The synthesis was conducted via a sol-gel route with ethanol solutions of $Si(OCH_3)_4$, $Zn(NO_3)_2$-$4H_2O$, and $Mn(NO_3)_2$-$4H_2O$. The mixture solution was heated first at 60°C for making a homogeneous gel and then the gel product was completely dried at 110°C. The crystallization from the dried gel was succeeded by calcination at 1200°C for 10 hours. X-ray powder diffraction (XPD) data was collected with 4 samples (Mn:Zn = 0, 10, 20, and 30%) on a GE-diffractometer (XRD3003) in Bragg-Brentano geometry with Cu$K\alpha_1$. The starting model from [4] was refined by Rietveld calculations.The contents of Zn, Si, and Mn were determined by electron microprobe (Cameca SX100).

Results

Rietveld analyses of $Mn_xZn_{2-x}SiO_4$ (0 < x < 0.6) show an increase of the lattice parameters **a** and **c**. This confirms Mn^{2+} substitution for Zn^{2+} due to their different ionic radii (0.66 Å Mn^{2+}; 0.60 Å for Zn^{2+}). Both Zn1 and Zn2 sites are surrounded by four of the same SiO_4 tetrahedra (Figure), but their bonding distances to oxygens are pretty different (Table). The averaged atomic distance d(Zn1-O) = 1.995(3) Å is much larger than d(Zn2-O) = 1.939(7) Å in the Mn-doped compound $Mn_{0.53(7)}Zn_{1.28(7)}Si_{1.00(2)\Box 0.19}O_4$. Considering this along with the presence of defects based on the chemical analysis (Mn + Zn < 2 per four oxygens) it can be concluded that Mn prefers to reside at Zn1 while defects are at Zn2. This tendency accords with the case in Zn_2SiO_4 showing d(Zn1-O) = 1.969(11) Å; d(Zn2-O) = 1.948(11) Å (Table). Interestingly, the amount of defects is correlated with increasing Mn replacement for Zn. Our previous single crystal diffraction study of 0.05Mn-doping Zn_2SiO_4 [4] also showed not perfect random distribution of defects [4]. Details of structural properties in this solid-solution system will be presented with their emission properties at DGK 2014 Berlin.

References
[1] Y.Hu, J.-P.Yand, J.-S.Liu, Luminescence, 27(2012) 437-440.
[2] Y.I.Kim,et al., Nuclear Inst. Methods Phys. Res., B268(2010) 346-351.
[3] R.P. SreekanthChakradhar, et al., J. Chem. Phys., V121-20(2004) 10250-10259.
[4] D. Behal, B. Röska, U. Gatterman, A. Reul, S-H. Park, J. Solid St. Chem., V210(2014), 144-149.

Figure Structure of Zn_2SiO_4 built with $Zn(1)O_4$-, $Zn(2)O_4$-, and SiO_4-tetrahedra.

Table Interatomic distances in Zn_2SiO_4 (left) and $Mn_{0.53(7)}Zn_{1.28(7)}Si_{1.00(2)\Box 0.19}O_4$ (right).

Figure 1

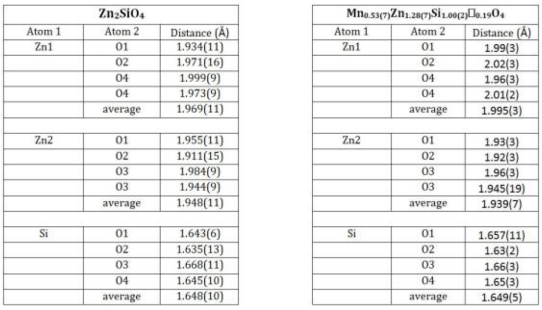

Zn_2SiO_4		
Atom 1	Atom 2	Distance (Å)
Zn1	01	1.934(11)
	02	1.971(16)
	04	1.999(9)
	04	1.973(9)
	average	1.969(11)
Zn2	01	1.955(11)
	02	1.911(15)
	03	1.984(9)
	03	1.944(9)
	average	1.948(11)
Si	01	1.643(6)
	02	1.635(13)
	03	1.668(11)
	04	1.645(10)
	average	1.648(10)

$Mn_{0.53(7)}Zn_{1.28(7)}Si_{1.00(2)}\Box_{0.19}O_4$		
Atom 1	Atom 2	Distance (Å)
Zn1	01	1.99(3)
	02	2.02(3)
	04	1.96(3)
	04	2.01(2)
	average	1.995(3)
Zn2	01	1.93(3)
	02	1.92(3)
	03	1.96(3)
	03	1.945(19)
	average	1.939(7)
Si	01	1.657(11)
	02	1.63(2)
	03	1.66(3)
	04	1.65(3)
	average	1.649(5)

Figure 2

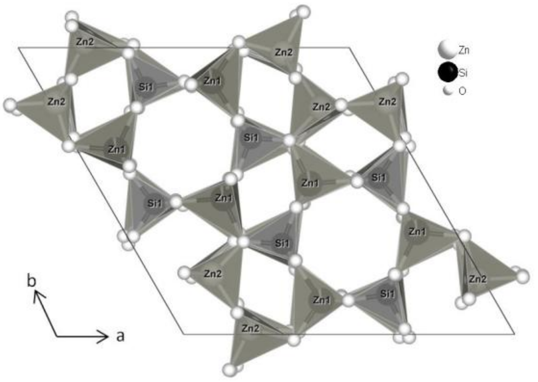

MS05-P06

$Tl_4Si_5O_{12}$ - a microporous thallium silicate

V. Kahlenberg[1], L. Perfler[1], P. Blaha[2]
[1]*University of Innsbruck, Institute of Mineralogy & Petrography, Innsbruck, Austria*
[2]*Vienna University of Technology, Institute of Materials Chemistry, Vienna, Austria*

Microporous thallium *alumo*silicates are known for a long time. Among the group of zeolites, for example, several synthetic compounds have been reported which can incorporate large amounts of Tl^+. Examples include the following zeolite framework types: ABW, FAU, LTA, LTL, MFI, RHO, SOD and ANA. In most cases they were prepared from the corresponding Na analogues by ion exchange using aqueous solutions of a thallium salt such as $TlNO_3$ or Tl(OH). Aluminum free thallium silicates with a three dimensional tetrahedral framework structure have not been reported so far. Actually, the whole crystal chemistry of the phases belonging to the binary system Tl_2O-SiO_2 is rather uncharted territory. Until now, only $Tl_6Si_2O_7$ has been characterized in detail [1]. This is even more surprising because a precise knowledge of the parameters that govern the stereochemical activity of the lone electron pairs in thallium(I) compounds is indispensable for the choice and design of complexing agents that can remove toxic thallium selectively from biological systems [2]. Recently, we succeeded in the preparation of microporous alkali silicates such as γ-$Na_2Si_2O_5$ [3] from low temperature devitrification of glassy precursors. As a first result of a research project aiming on the synthesis of pure and mixed thallium-sodium/potassium silicates with this synthesis approach a comprehensive characterization of the previously unknown framework compound $Tl_4Si_5O_{12}$ is reported in this contribution.

Single-crystal structure analysis resulted the following basic crystallographic data: monoclinic symmetry, space group $C2/c$, a= 9.2059(5), b=11.5796(6), c=13.0963(7) Å, b=94.534(5)°. From a structural point of view the compound can be classified as an interrupted framework silicate with Q^3- andQ^4-units in the ratio 2:1. Within the framework 4-, 6- and 12-membered rings can be distinguished. The framework density of 14.4 T-atoms/1000Å^3 is comparable with those observed in zeolitic materials like Linde type A, for example. The thallium cations show a pronounced one-sided coordination each occupying the apex of a distorted trigonal TlO_3 pyramid. Obviously, this reflects the presence of a stereochemically active $6s^2$ lone pair electron. The porous structure contains channels running along [110] and [-110], respectively, where the Tl^+-cations are located for charge compensation. Structural investigations have been completed by Raman spectroscopy. The interpretation of the spectroscopic data and the allocation of the bands to certain vibrational species has been aided by DFT-calculations, which were also employed to study the electronic structure of the compound.

[1] Y. Piffard, R. Marchand, M. Tournoux *Rev. Chim. Min.* 1975, *12*, 210.
[2] G. Meyer, D. Naumann, I. Wesemann Eds. *Inorganic Chemistry in Focus III*, Wiley-VCH, 2006.
[3] V. Kahlenberg, S. Rakić, C. Weidenthaler, *Z. Kristallogr.* 2003, *218*, 421.

MS05-P07

Analysis of lattice defects in silica zeolites of the structure type MFI

I. Großkreuz[1], H. Gies[1], B. Marler[1]
[1]*Ruhr-Universität Bochum, Institut für Kristallographie, Bochum, Germany*

Introduction

Characteristic framework defects of different types can be observed in silica ZSM-5: Vacancies, so called hydroxyl-nests (Fig. 1a) and non-bridging defects (Fig. 1b, c) [1]. The defects are mostly terminated by hydrogen-atoms. Whereas calcination heals defects of type 1b and c, type 1a remains.

In the current study, we synthesized various silica ZSM-5 materials using different procedures. They were partly defect-free in the as-made form, became defect-free after calcination or remained defect-loaded after calcination. To understand the processes and to predict the effect of calcination, NMR, IR, and XRD studies were carried out.

Experimental

Syntheses were carried out in Teflon lined steel autoclaves using TPA^+ as organic SDA. All-silica-ZSM-5 was prepared without any additives (180 °C, 14 d). For the synthesis of “defect-free” material (F-ZSM-5) the mineralizer NH_4F was added (200 °C, 15 d) [2]. H_3BO_3 has been introduced to a third synthesis (B-ZSM-5, 200 °C, 1 d) [3]. Post syntheses treatment included calcination in air (540 °C, 5 d), washing in H_2O_{dest} and drying in air. B-ZSM-5 has, in addition, been deborated. X-ray powder diffraction diagrams have been collected using a Siemens D5000. IR-spectra were recorded with a Nicolet Scientific IR spectrometer (400 to 4000 cm^{-1}). Using a Bruker Avance ASX-400 NMR spectrometer, ^1H MAS (defect tracing), ^{11}B MAS (deboration), ^{13}C CP MAS (organic cation) and ^{29}Si HP DEC (Si-connectivity) NMR spectra have been gathered.

Results

and discussionThe X-ray diagrams display minor intensity variations between all materials. Full pattern Rietveld structure refinements [4] yielded reasonable residuals for all materials indicating a high degree of long-range order. However, no conclusion on the local defects concerning type, sites or concentrations was possible (see Fig. 2a).

^{29}Si HP DEC NMR shows fully 4-connected Si Q^4 and 3-connected Si Q^3 signals (defect-site) for all-silica-ZSM-5 (Fig. 2b). While F-ZSM-5 exhibits no defects in neither form, all-silica-ZSM-5 and B-ZSM-5 show Q^3 defects in both forms, albeit in minor concentrations in the calcined/deborated state. ^1H MAS NMR experiments illustrate the existence of silanol-group-type defects (Fig. 2c). The signal at 10.4 ppm (♦) represents a healable non-bridging defect. After calcination, only sorbed water is detected at 4.5 ppm (**x**). IR spectroscopy supports these results. ^1H MAS spectra are in particular suitable to distinguish between healable and persistent defects since the spectra provide strong evidence for defects which can be healed (10.4 ppm) upon calcination.

References
[1] J.M. Chezeau, L. Delmotte, J.L. Guth, Zeolites, Vol. 11, 599, (1991).
[2] J. L. Guth, H. Kessler, J. M. Higel., J. M. Lamblin, J. Patarin, A. Seive, J. M. Chezeau, R. Wey, J. Am.Chem. Soc, 13, 176-195, (1989).
[3] M. Dicks, Diplomarbeit, Bochum, (2000).
[4] J. Rodriguez-Carvajal, Physica B., 192, 55, (1993).

Figure 1

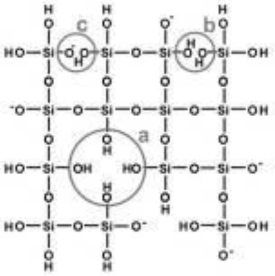

Figure 2

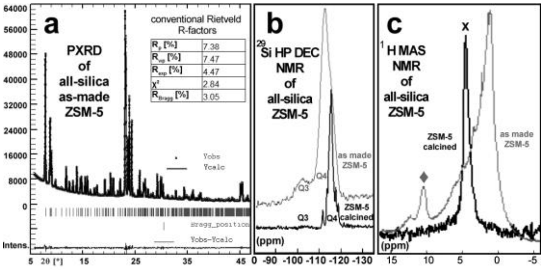

MS05-P08

Untersuchungen der Übergangsreaktion von Tobermorit zu Xonotlit unter dem Einfluss von Additiven und erhöhter Temperatur

A. Hartmann[1], D. Schulenberg[1], J.- C. Buhl[1]
[1]*Institut für Mineralogie, Leibniz Universität Hannover, Hannover, Germany*

Im Rahmen dieser Arbeit wurden Untersuchungen der Übergangsreaktion von Tobermorit zu Xonotlit unter dem Einfluss von Additiven bei erhöhter Temperatur (220°C) durchgeführt. Bereits in vorherigen Arbeiten wurde der Einfluss der Additive Sucrose [1], Ca- Format [2] und $CaCl_2x2H_2O$ [3] auf die Bildung von CSH-Phasen, bzw. Tobermorit, untersucht. Bei einer Synthesetemperatur von 200°C konnte jeweils ein Verzögerungseffekt der CSH-Bildung unter Verwendung von Sucrose und Ca-Format beobachtet werden. $CaCl_2x2H_2O$ hatte dagegen eine beschleunigende Wirkung auf die CSH-Bildung.

Als Edukte für die Synthesen der vorliegenden Arbeit wurden Quarzpulver und kalziniertes $CaCO_3$ ausgewählt. Es erfolgten drei Synthesen mit dem Zusatz der oben erwähnten Additive und eine Referenzsynthese ohne Additive im C/S-Verhältnis von 0,83. Die Edukte wurden zu Presslingen geformt und anschließend in Stahlautoklaven bei 220°C für 40,5 h einer Hydrothermalbehandlung unterzogen. Die Charakterisierung der CSH-Phasen erfolgte anhand röntgenographischer (XRD), elektronenmikroskopischer (REM und EDX) und IR-spektroskopischer (MIR) Methoden.

Die Ergebnisse zeigen bei der Referenzsynthese eine ausgiebige Bildung von Xonotlit neben Tobermorit, was aus der Literatur zu erwarten war [4]. Bei den Synthesen mit einem Zusatz an Sucrose erfolgte nur eine geringe CSH-Bildung, die Sucrose wirkte stark hemmend. Ein Zusatz an Ca-Format als Syntheseadditiv führte zu einer geringen Bildung von Xonotlit. Der Zusatz an Ca-Format wirkt ebenfalls hemmend auf die CSH-Bildung, aber nicht so stark wie der Zusatz an Sucrose. Die Verwendung des Additivs $CaCl_2x2H_2O$ führte dagegen zu einer beschleunigten CSH-Phasen Bildung. Hier zeigte sich Xonotlit neben Tobermorit.

Die Ergebnisse belegen, dass sich eine Abschätzung der beschleunigenden oder hemmenden Wirkung von Additiven auf die CSH-Phasenbildung durch Synthesen im Temperaturbereich des Übergangs Tobermorit-Xonotlit recht gut durchführen lässt. Bereits in den Röntgen-Pulverdiffraktogrammen sind die Abnahme der Signalintensitäten von Tobermorit und die Zunahme der Xonotlitpeaks besser zu unterscheiden, als es beim Übergang von CSH-Vorphasen zu Tobermorit bei geringerer Synthesetemperatur der Fall ist.

Abb. 1: REM-Abb. der Referenzsynthese
Abb. 2: REM-Abb. der Synthese mit $CaCl_2x2H_2O$

[1] Hartmann, A., Buhl, J.-C.: Materials Research Bulletin 45 (2010), 396-402
[2] Khakhutov, M.: Diplomarbeit. Institut für Mineralogie, Leibniz Universität Hannover, Hannover 2011
[3] Schulenberg, D.: Bachelorarbeit. Institut für Mineralogie, Leibniz Universität Hannover, Hannover 2012
[4] Mörtel, H.: Fortschr. Miner. 59 (1980) 37-67.

Figure 1

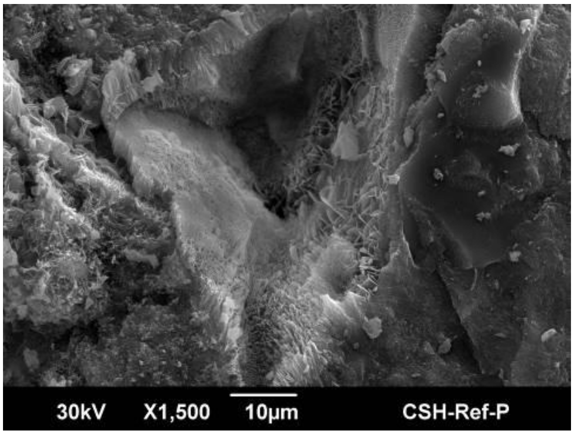

Figure2

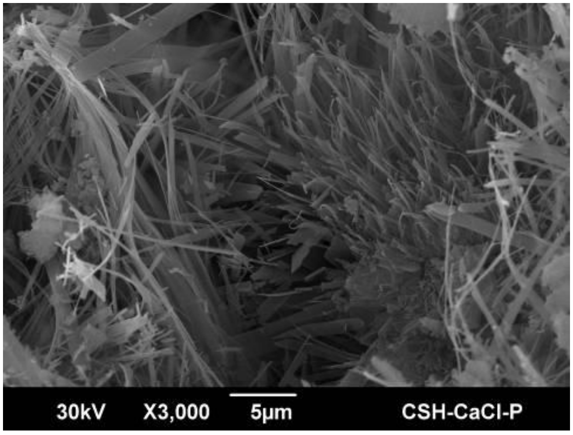

MS05-P09

Incorporation of Foreign Ions in C_2S - Synthesis, Characterization and Hydration

K. Pöhler[1]
[1]*Martin-Luther-Universität Halle Wittenberg, Mineralogie/Geochemie, Halle/Saale, United Kingdom*

The target is to investigate the incorporation of different foreign ions into dicalcium silicate (C_2S) and determine the hydraulic reactivity. Different elements like aluminium and potassium stabilize the high temperature modifications of C_2S /1,2/. These modifications improve the hydraulic reactivity at room temperature as well as under hydrothermal conditions. The results can help to optimize the production of the new possible CSH binder (Celitement). The results show a relation between the type and the size of the ions and the stabilization of the high temperature modifications of C_2S. The C_2S syntheses were done using the Pechini method /3/, which enables the production of a single phase by using only one sintering step without homgenization in-between. Further a lower sintering temperature and large specific surfaces of the resulting powder were achieved. Experiments at the SUL-X beamline at ANKA (Karlsruhe) made it possible to investigate the hydration behaviour at hydrothermal conditions (200°C, 16 bar) in a special designed reaction cell /4/. Supplementary examinations like Raman measurements and the determination of the density and lattice parameters allow an overall description of the synthesis products and their hydraulic behaviour. The results of the investigations show, that it is possible to produce highly reactive C_2S doped with foreign ions. Dependencies between the amount of incorporated foreign ions, the high temperature modification, the crystallinity of the synthesis product and the C-S-H phases (e.g. α-C_2SH see figure below: SEM micrograph from C_2S sample after hydrothermal treatment) after the hydration process were shown.

/1/ Lai, G.-C., Nojiri, T. & Nakano, K. (1992): *"Studies of the stability of β-Ca_2SiO_4 doped by minor ions"* Cement Concrete Research, 1992, 22, 743-754
/2/ Kim, Y. M. & Hong, S. H. (2004): *"Influence of minor ions on the stability and hydration rates of β-dicalcium silicate"* Journal American Ceramic Society, 2004, 87, 5, 900-905
/3/ Pechini, M. O. (1967): US Patent No. 3 330697, USA
/4/ Ullrich, P., Stemmermann, P., Garbev, K. & Gasharova, B. (2013): *"Development and Application of Reaction Cells for Synchrotron-based IR and XRD in situ Investigations: Hydrothermal Synthesis of Calcium Silicate Hydrates"* Building Materials Analysis, Halle/Saale, 2013

Figure 1

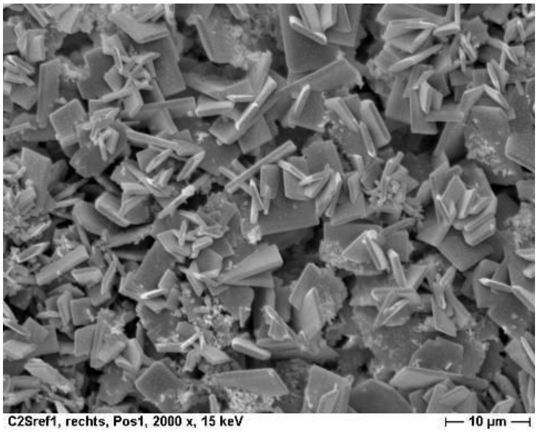

MS05-P10

Optimierung der Kristallisation von Zeolith Na-A aus Rückständen der Silanproduktion

A. Hartmann[1], V. Petrov[1], J.- C. Buhl[1], K. Rübner[2], M. Lindemann[2]
[1]*Institut für Mineralogie, Leibniz Universität Hannover, Hannover, Germany*
[2]*BAM, Fachbereich 7.4, Berlin, Germany*

Zeolithsynthesen unter stark alkalischen Reaktionsbedingungen bei 333 K werden unter Einsatz von Reststoffen der energetischen Verwertung der Destillationsrückstände der Silanherstellung in enger Zeitabstufung (1,5 h≤ t ≤ 3,5 h) in 30‘-Schritten, jeweils mit $NaAlO_2$ im Startansatz, untersucht. Aus den Ergebnissen werden optimierte Bedingungen zur Alkalinität und Synthesezeit abgeleitet.

Bei den Rückständen handelt es sich um Material mit sehr hohen Anteilen amorphen Silikats. Im Rahmen der vorliegenden Arbeit erfolgten Zeolithsynthesen mit zwei Rückständen (FR 2, ein Filterrückstand aus der Abwässerneutralisation der Rauchgaswäsche und FR 3, eine Flugasche des Verbrennungsprozesses). Die Rückstände weisen unterschiedliche SiO_2 Gehalte auf (FR 2: 92.3 M.-% SiO_2; 3.83 M.-% Al_2O_3, FR 3: 97.2 M.-% SiO_2; 0.3 M.-% Al_2O_3). Die Synthesemethode der hochalkalischen Niedertemperatursynthese kam dabei wegen der Energie-und Zeiteffizienz zur Anwendung [1-3].

Im Rahmen der vorliegenden Arbeit erfolgten in der Erweiterung bisher erarbeiteter Erkenntnisse [3] Zeolithsynthesen mit FR 2 und FR 3 bei kurzen Synthesezeiten in enger Zeitabstufung (1,5 h$\leq$ t $\leq$ 3,5 h in 30‘-Schritten), jeweils mit $NaAlO_2$ im Startansatz. Aus den Ergebnissen abgeleitet, wurde eine weitere Syntheseserie unter Verringerung der Molarität der NaOH bei einer Synthesezeit von 4 h durchgeführt.

Die Synthesen wurden unter offenen Bedingungen im Becher (Abdeckung mit Parafilm) unter Rühren bei 333 K durchgeführt. Nach Ablauf der jeweiligen Reaktionszeit wurde das Produkt durch Zentrifugieren abgetrennt. Die Lösungen werden zur Bestimmung der Reaktionskinetik chemisch analysiert. Die Analyse der Feststoffe erfolgte nach Waschen (H_2O dest.) und Trocknen im Wärmeschrank mittels XRD und REM/EDX.

Die Ergebnisse zeigen, dass unter Verwendung von FR 2 bei kurzen Synthesezeiten von 1,5- 3,5 h hauptsächlich Sodalith gebildet wurde. Ab einer Synthesezeit von 3 h erfolgte die Bildung von Zeolith Z 21. Bei der Synthese mit FR 3 wurde insgesamt im Zeitintervall von 1,5-3,5 h Zeolith LTA mit geringem Anteil an Sodalith gebildet. Eine Verringerung der Molarität der NaOH (4M) führte bei der Synthesereihe mit FR 2 zur Kristallisation von phasenreinem Zeolith LTA bei einer Synthesezeit von 4 h. Abb. 1 (links) zeigt die REM/EDX-Analyse dieses Produktes, das XRD Beugungsdiagramm zeigt Abb. 2 (oben). Bei der Synthese mit FR 3 für 2 h in 8 molarer NaOH kristallisierte fast reiner Zeolith LTA mit kleinem Anteil (ca. 10%) an Sodalith (REM/EDX-Analyse: Abb. 1 (rechts), XRD Beugungsdiagramm siehe Abb. 2, unten).

Abb. 1: REM/EDX Analyse der Produkte (FR 2 links, FR 3 rechts)

Abb. 2: Röntgen-Pulverdiffraktogramme (FR 2 oben, FR 3 darunter)

Literatur

[1] Hadan, M., Fischer, F.: Cryst. Res. Technol. 27 (1992) 343 - 350.

[2] Fischer, F., Hadan, M., Horn, A.: Chem. Tech. 43 (1991) 191 - 195.

[3] Hartmann, A., Petrov, V., Buhl, J.-Ch., Rübner, K.: 21. Jahrestagung der DGK, Freiberg 2013, Abstracts, PS 05-P55, S. 102-103.

Figure 1

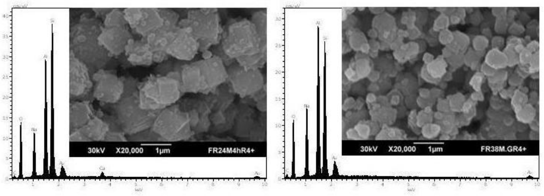

Figure 2

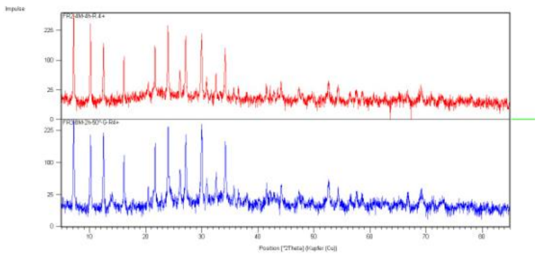

MS05-P11

Zeolithkristallisation bei simultanem Einsatz SiO_2- und CaO-reicher industrieller Reststoffe und alkalischer Aktivierung

V. Petrov[1], A. Hartmann[1], J.- C. Buhl[1], K. Rübner[2], M. Lindemann[2]

[1] *Institut für Mineralogie Hannover, Hannover, Germany*

[2] *Bundesanstalt für Materialforschung und -prüfung, Fachbereich 7.4, Berlin, Germany*

Zusammenfassung: Untersucht wird die Synthese der technisch wichtigen Zeolithe (Na, Ca)-LTA bei gleichzeitigem Einsatz SiO_2- sowie CaO-reicher industrieller Reststoffe. Dabei erfolgt der Umsatz der Reststoffe zu Zeolithen durch alkalische Aktivierung bei Raumtemperatur (RT) und nachfolgende Kristallisation bei nur 333 K in Abhängigkeit von der Aktivierungs- und Reaktionszeit. Die direkte Synthese von (Na, Ca)-LTA Zeolith mit minimiertem Anteil an Hydrosodalith gelang bei einer Aktivierungs- sowie Reaktionszeit von jeweils 3 h in 6 M NaOH.

Einleitung:Die Synthesemöglichkeiten von LTA-Zeolithen unter Einsatz SiO_2-reicher Filterrückstände (FR) aus der Aufbereitung industrieller Abwässer und simultanem Zusatz CaO-reicher Papieraschen (PA) aus der thermischen Verwertung von Rückständen der Altpapieraufbereitung wurden experimentell geprüft. Aufgrund der effizienten Energiebilanz der Kristallisation aus hochalkalischen Alumosilikat-Gelen bei nur 333 K [1-2], wird diese Methode hier in weiter modifizierter Form - erstmals mit vorangehender alkalischer Aktivierung bei RT - eingesetzt.

Experimentelles:Die Zeolithsynthesen erfolgten durch eine alkalische Aktivierung von PA und FR in NaOH (6M) sowie unter Zusatz von Natriumaluminat zur Einstellung des Si/Al Verhältnisses ist proportional 1. Nach dieser Behandlung bei RT erfolgte die Kristallisation bei 333 K. Syntheseparameter waren die Aktivierungs- und Synthesezeit (1,5 - 3 h). Die Reaktionsprodukte wurden zentrifugiert, gewaschen ($H_2O_{dest.}$) und getrocknet. Zur Analyse der Produkte diente die Röntgen-Pulverdiffraktometrie sowie die Rasterelektronenmikroskopie mit EDX-Analyse.

Ergebnisse:Die Syntheseansätze unter Variation der Aktivierungs- und Synthesezeiten bei konstanter Konzentration der Edukte, führten bei kurzer Synthesezeit (1,5 h) nur zu amorphem Material. Als günstige Reaktionsbedingungen konnten Aktivierungszeiten von 3h und nachfolgende Synthesen in 6 M NaOH, ebenfalls für 3 h, bei nur 333 K Reaktionstemperatur ermittelt werden. Es entstanden dabei (Na, Ca)-Zeolithe vom Typ LTA in guter Kristallinität. Abb. 1 zeigt die Röntgen-Pulverdiffraktogramme von Produkten unter Einsatz von FR (92 M.-% SiO_2) sowie einer calcitreichen PA-NL (61,19 M.-% CaO) und einer gehlenitreichen PA-DS (48,61 M.-% CaO). Abb. 2 zeigt in beiden Fällen Kristalle von Zeolith LTA mit typischer würfelförmiger Morphologie und einer Größe bis zu 1 µm. Die EDX-Analysen belegen die Anteile an (Na, Ca) in den Zeolithkristallen.

Abb**. 1:** Röntgen-Pulverdiffraktogramme der Zeolithe aus FR und gehlenitreicher PA-DS (oben) sowie FR und calcitreicher PA-NL (darunter).

Abb**. 2:** REM Aufnahmen der Zeolithe

Litheratur: [1] Hadan, M., Fischer, F.: Synthesis of fine grained NaA-type Zeolites from superalkaline solutions. Cryst. Res. Technol. 27 (1992) 343 - 350. [2] Hartmann, A., Petrov, V., Buhl, J.-Ch., Rübner, K.: Kristallisationsprozesse in stark alkalischen Aufschlusslösungen von Aschen aus der Verbrennung von Schlämmen der Altpapieraufbereitung. Abstracts 21. Jahrestagung der DGK, Freiberg 2013, PS 05-P55, S. 102-103.

Figure

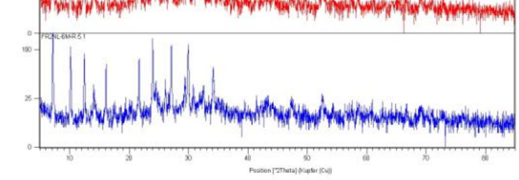

Figure 2

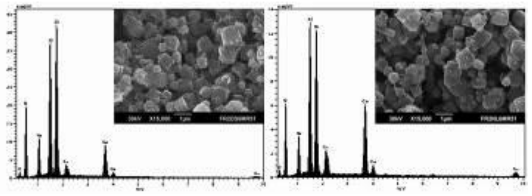

MS05-P12

Hydrothermal Synthesis of Fine-Crystalline Eulytite ($Bi_4(SiO_4)_3$) Powders in Supercritical Fluids.

E. Marina[1], I. Makhina[1], V. Balitsky[1]
[1]*Institute of Experimental Mineralogy RAS, LSMM, Chernogolovka, Russian Federation*

Eulytite ($Bi_4(SiO_4)_3$) is one of the rarest natural minerals. Eulytite crystals are applied as a scintillator in highenergy physics, computer tomography, and dosimetry. Monocrystalline bismuth orthogermanate with a eulytite-type structure is one of the most promising materials in this relation. However, Eulytite has better scintillative characteristics in comparison with bismuth orthogermanate (for example, its period of flashing (0.1 ms) is three times better), but due to the complexity of Eulytite single crystal growth from the melt (high viscosity) the problem of its synthesis is not yet solved.

There is a clear tendency in modern science and production toward replacement of monocrystalline materials by ceramics with the same or better functional characteristics. Ceramics of optical quality are produced by pressing of small (micro- and nanosized) natural or synthetic crystals. In addition, agglomeration of crystals (in contrast to agglomeration of powders of oxides) provides ceramics with a homogeneous distribution of dopants. We believe that ceramics produced from Eulytite crystals will have better characteristics than those obtained by direct agglomeration of the starting oxides.

Previously Eulytite was synthesized by the hydrothermal method at 260°Cand ~50 MPa. A stoichiometric mixture of Bi_2O_3 and SiO_2 was applied as a starting material. We performed a run series using different solvents: NaOH, NH_4F, and H_2O_2. Hydrogen peroxide is the best solvent, because it does not contain elements entering the composition of Eulytite..

Study of Eulytite crystals grown at different levels of an autoclave provides evidence for their size heterogeneity, which may have a negative influence on the quality of ceramics. Because of this, it was necessary to improve the methodology of synthesis. Unique properties of supercritical fluids (SCF), such as the high solvent power of solid materials and the high rate of transport, make the process of crystallization more intense, which provides size homogeneity of the synthetic crystals. In addition, we produced an instrument with active mixing of the solution during crystallization in order to solve this problem.

Growth of fine-crystalline Eulytite was carried out at a temperature of ~400°C and a pressure up to 100 MPa. We applied hydrogen peroxide aqueous solutions of various concentrations (from 1 to 10 vol %) as a solvent. Active mixing of the solution during crystallization was provided by a specially constructed oven with a horizontal position of four autoclaves around the central rotating rod. This allowed us to rotate autoclaves during synthesis at a rate of 1 rev/min and thus promote active mixing of the solution and charge. As a result, we synthesized fine-crystalline Eulytite with quite homogeneous crystal sizes (Fig. 1).

Fig. 1. Eulytite crystals synthesized in 5 vol. % H_2O_2 solution at a temperature of 400 º C.

Thus, the performed investigations allowed us to synthesize microcrystalline Eulytite powders, which may be applied for the production of highquality scintillative ceramics.

This study was supported by the Russian Foundation for Basic Research (project 09_02_00647)

Figure 1

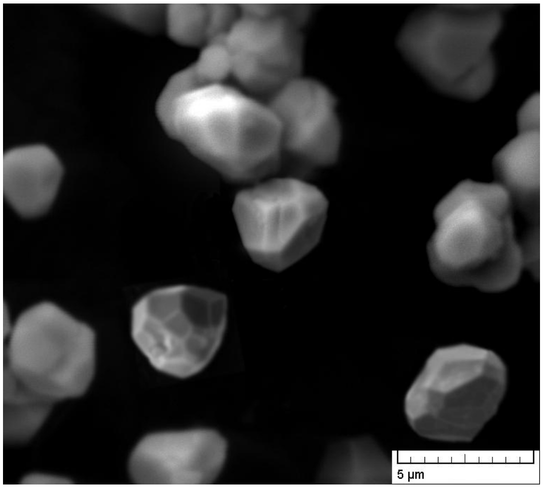

MS05-P13

The average structure of RUB-12: a new lithosilicate zeolite

B. Marler[1], A. Grünewald-Lüke[1], H. Gies[1]
[1]*Ruhr-Universität, Dept. of Geology, Mineralogy and Geophysics, Bochum, Germany*

Zeolites are important materials for industrial applications like catalysis, ion exchange or molecular sieving. Most zeolite frameworks are made up by interconnected $[SiO_4]$- and $[AlO_4]$-tetrahedra but other $[TO_4]$-units can as well be part of the 3-dim. frameworks. $[LiO_4]$-tetrahedra are in particular flexible and can form strain-free 3-rings together with $[SiO_4]$-tetrahedra not observed in alumosilicate zeolites. So far, zeolites with a framework containing 3-rings have been synthesized only rarely. Here we present a new microporous lithosilicate, RUB-12, $(Li,H)_6[Li_2Si_8O_{20}] \bullet 8\ H_2O$.

RUB-12 was synthesized under hydrothermal conditions in the system LiOH / SiO_2 / H_2O / SDA at 160°C. The small, colorless and densely intergrown crystals are of needle-like shape.

The crystal structure was solved by Direct Methods (program EXPO2009) from X-ray powder data in the space group Ccc2. A close inspection of the powder pattern shows weak reflexions contradicting the C-centered lattice and leading to a primitive lattice. Moreover, the powder pattern presents sharp and broad reflexions indicating a disordered structure. The structure model of the average structure could, nevertheless, successfully be refined by a Rietveld analysis using additional parameters to account for the anisotropic peak halfwidths. The best refinement which was performed in space group Pnc2 led to meaningful bond lenghts and angles and converged to R-values of $R_F = 0.049$, Rwp = 13.9, $Chi^2 = 2.86$.

RUB-12 has a unique structure with an 1-dimensional pore system of non-intersecting 10-ring channels running parallel to the c-axis of the orthorhombic unit cell (a_0 = 13.770 Å, b_0 = 8.809 Å, c_0 = 5.050 Å). The negative charge of the framework, $[Li_2Si_8O_{20}]^{6-}$, is compensated by non-framework lithium and/or hydrogen cations which could not be located from the XRD powder data. The pore system is occupied by water molecules.

The silicate framework (Fig. 1) can either be described as being constructed exclusively from interconnected spiro-5-units with Li^+ on T sites in the center of the units (Fig. 2a) or as silicate layers being interconnected by tetrahedrally coordinated Li cations (Fig. 2b).

The disorder is related to the positions of the Li cations. The given space group symmetry of the average structure (Pnc2) generates 4 symmetrically equivalent Li cations per unit cell (twice as much as should be present) and leads to 3-coordinated oxygen atoms (Fig. 2b). In the real structure actually only every second Li^+ can be present.

RUB-12 is related to other lithosilicate zeolites like RUB-23 [1] and RUB-29 [2]. All three zeolites contain spiro units with Li at the spiro position.

References:

[1] S.-H. Park, P. Daniels, H. Gies, Microporous Mesoporous Mater. 37, 129 (2000);
[2] S.-H. Park et al., J. Am. Chem. Soc. 122, 11023 (2000)

Fig. 1: The structure of RUB-12 as seen along the c-axis (purple: Si, red: Oxygen, orange: Li, blue: Water molecules).
Fig. 2: a) The spiro-5 unit made up by two interconnected 3-rings, b) the average structure of the lithosilicate layer.

Figure 1

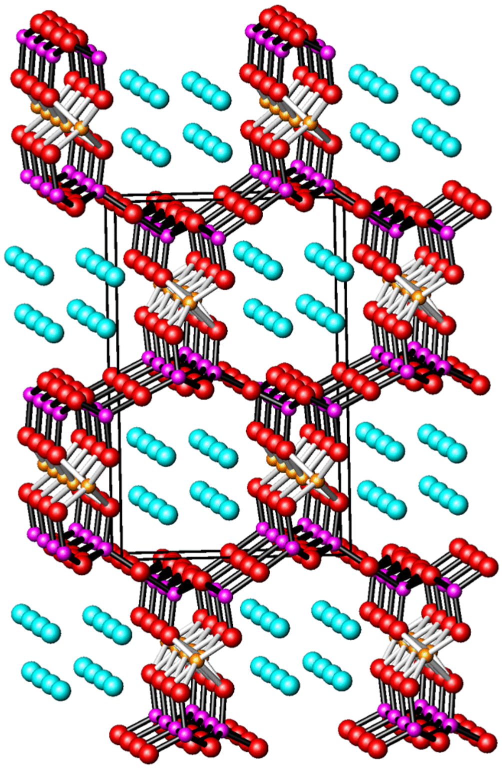

Figure 2

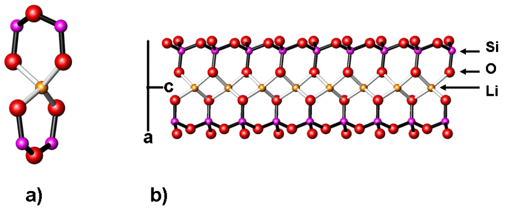

MS05-P14

Me$_2$Sn(HPO$_3$), Et$_2$Sn[HPO$_2$(OH)]$_2$ und ^{t}Bu$_2$Sn[HPO$_2$(OH)]$_2$ die ersten Diorganozinn(IV)-phosphonate

H. Reuter[1], M. Reichelt[1]
[1]*Universität Osnabrück, Institut für Chemie neuer Materialien, Osnabrück, Germany*

Die einzigen bisher bekannten Organozinn(IV)-phosphonate stammen von Chandrasekhar et al. [1, 2] und sind ausschließlich komplex aufgebaute Käfigverbindungen des Typs $[RSn]_6[HPO_3]_4[OR‘]_6O_2$. Bei den Titelverbindungen handelt sich um die ersten reinen Organozinn(IV)-phosphonate überhaupt und die ersten Phosphonate, $[HPO_3]^{2-}$, bzw. Hydrogenphsophonate, $[HPO_2(OH)]^-$, mit Diorganozinn(IV)-Baueinheiten.

Die Herstellung der Verbindungen erfolgte bei Raumtemperatur durch Umsetzung der entsprechenden Diorganozinn(IV)-dichloride, R_2SnCl_2 mit R = Me, Et und ^{t}Bu, mit Phosphonsäure, H_3PO_3, in einem Gemisch aus EtOH und THF.

In der Verbindung $Me_2Sn(HPO_3)$, **1** (Abb. 1), sind beide Zinnatome der asymmetrischen Einheit trigonal-bipyramidal koordiniert und durch dreizähnige Phosphonat-Baueinheiten zu eindimensionalen Bänder verknüpft. $C_2H_7O_3PSn$: monoklin, $P2_1/c$, a = 6.8226(3) Å, b = 13.8114(6) Å, c = 12.2158(6) Å, β = 91.108(2)°, V = 1150.88(9) $Å^3$, Z = 8, $R_1[I > 2(I)] = 0.0224$.

In der Verbindung $Et_2Sn[HPO_2(OH)]_2$, **2** (Abb. 2), sind die beiden Zinnatome der asymmetrischen Einheit trigonal-bipyramidal bzw. oktaedrisch koordiniert. Drei $[HPO_2(OH)]$-Ionen verbrücken jeweils zwei Et_2Sn-Baueinheiten zu eindimensionalen Bänder während das vierte nur an ein Zinnatom koordiniert. $C_4H_{14}O_6P_2Sn$: orthorhombisch, $I222$, a = 13.8536(3) Å, b = 14.9540(4) Å, c = 20.6374(6) Å, V = 4275.4(2) $Å^3$, Z = 16, $R_1[I > 2(I)] = 0.0126$.

^{t}Bu$_2$[H$_2$PO$_2$(OH)]$_2$, **3**, besteht aus trigonal-bipyramidal koordinierten Zinnatomen, die über ein zweizähniges Hydrogenphosphonat-Ion zu Ketten verknüpft sind, während das zweite $[HPO_2(OH)]$-Ion als einzähniger Ligand fungiert. $C_8H_{22}O_6P_2Sn$: triklin, P-1, a = 6.6698(2) Å, b = 8.9201(3) Å, c = 13.2188(5) Å, α = 79.928(2)°, β = 85.831(2)°, γ = 80.102(2)°, V = 762.07(4) $Å^3$, Z = 2, $R_1[I > 2(I)] = 0.0225$.

Keywords: Zinnverbindungen, anorganisch-organische Hybridmaterialien, Phosphonate

[1] V. Chandrasekhar, V. Baskar, and J. J. Vittal. *J. Amer. Chem. Soc.*, 125 (2003)**,** 2392.
[2] V. Chandrasekhar, V. Baskar, K. Gopal, and J. J. Vittal. *Organometallics*, 24 (2005), 4926.

Figure 1

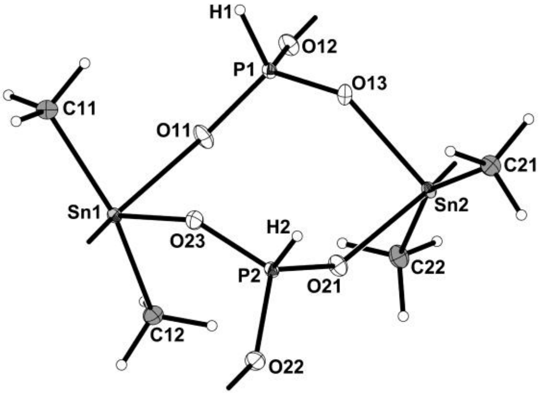

Figure 2

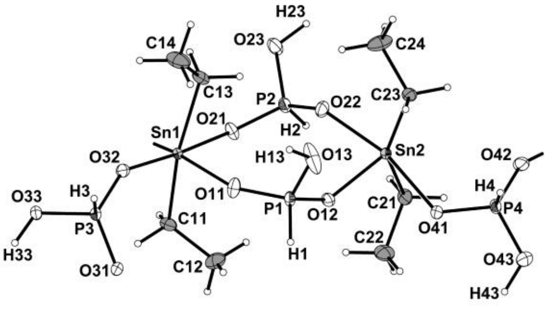

MS05-P15

Phase relations in the binary system Sm_2O_3 - P_2O_5

A. Neumann[1], A. Hirsch[1], J. Heuser[2], R. Faust[1], H. Schlenz[2], D. Bosbach[2], L. Peters[1], G. Roth[1]
[1]*Institut für Kristallographie, RWTH Aachen University, Aachen, Germany*
[2]*Forschungszentrum Jülich GmbH, Institute of Energy and Climate Research IEK-6, Jülich, Germany*

Phosphate based ceramics of the monazite type are very promising candidates for the immobilisation of the minor actinides, due to their outstanding properties considering waste loading capacities, thermal stability, and chemical durability. The minor actinides Am, Cm, and Np are problematic because they contribute to the extensive and long-lived radiotoxicity of high level nuclear waste.

We focus on Sm-monazite which exhibits compared to other Ln-monazites the lowest melting point (T_m = 1916 °C) [1]. The sintering process of such ceramics may profit from this circumstance considering energy and cost savings. It is therefore important to investigate the phase relations in the phase diagram Sm_2O_3-P_2O_5. Phase relations in this binary system are currently not well established.

We synthesised Sm-phosphate compounds which were stoichiometrically observed in the known system La_2O_3-P_2O_5 [2]. Our synthesis was carried out by solid state reactions. Sm_2O_3 and $NH_4H_2PO_4$ were used as starting reagents which were intimately mixed in an agate mortar to obtain a homogenous mixture which was then fired in ambient atmosphere. The monazite compound $SmPO_4$ was synthesised at 1250 °C. The phase purity was investigated by XRD and did not show any byproducts. For the synthesis of the other compounds, which were expected in the system Sm_2O_3-P_2O_5, we applied temperatures which were approx. 200 °C to 300 °C below the decomposition temperatures of the observed phases in the La_2O_3-P_2O_5 system. This approach was chosen because the melting point of the Sm-monazite is approx. 200 °C below than that of the La-monazite (2072 °C).

The synthesis of Sm_3PO_7 was carried out at 1000 °C and 1100 °C. At both temperatures the synthesis was successful and did not show any byproducts. Sm_3PO_7 is isostructural with Nd_3PO_7 [3] and crystallises in the space group (SG) *Cm*. The refined lattice parameters were smaller than those of the respective Nd compound. Assuming similar phase relations as reported for the La_2O_3-P_2O_5 system the expected Sm compound Ln_5PO_{10} was not observed. Instead, Sm_2O_3 and Sm_3PO_7 were formed.

The synthesis of SmP_3O_9 (SG $C222_1$) at 900 °C was partly successful as minor amounts of $SmPO_4$ were also present. This could be due to the loss of phosphate during the heating and decomposition of $NH_4H_2PO_4$, i.e. there was not sufficient phosphate present to form only the meta-phosphate. A similar observation was made for the synthesis of the ultra-phosphate LaP_5O_{14} (SG: *P2/c*) at 700 °C due to the loss of phosphate. Beside the ultra-phosphate, small amounts of the meta-phosphate were formed.

Forthcoming temperature dependent XRD experiments will be carried out in order investigate the phase transitions in the system Sm_2O_3 - P_2O_5.

[1] Y. Hikichi, T. Nomura, J. Amer. Ceram. Soc. 70 (10) (1987) C-252. [2] J. Kropiwnicka and T. Znamierowska, *Pol. J. Chem.*, **62** [7-12] 587-594 (1988) [3] Tselebrovskaya, E., Dzhurinskii, B., Lyamina, O., Izv. Akad. Nauk SSSR, Neorg. Mater., volume 33, page 59 (1997)

MS05-P16

Crystal structure of $CaMg_2P_6O_3N_{10}$

L. Neudert[1], A. Marchuk[1], O. Oeckler[2], W. Schnick[1]
[1]*LMU Munich, Munich, Germany*
[2]*Leipzig University, IMKM, Leipzig, Germany*

There are different synthetic routes to oxonitridophosphates, which are interesting materials with structural analogies to silicates. Oxonitridophosphates exhibit similar ability to form a plurality of structure types. However, only few representatives of this class of compounds are known.[1,2,3] Single-crystals of the new oxonitridophosphate $CaMg_2P_6O_3N_{10}$ were obtained from stoichiometric amounts of $Ca(N_3)_2$, Mg_3N_2, P_3N_5, and PON under high-pressure/high-temperature (HP/HT; 8 GPa and 1100 °C, additional NH_4Cl) conditions using a Walker-type multianvil assembly. Energy-dispersive X-ray spectroscopy confirms the composition and in FTIR spectra no OH vibration was observed. The crystals of $CaMg_2P_6O_3N_{10}$ are transparent and their habitus corresponds to partially truncated octahedra. Single-crystal X-ray diffraction (SCXRD) yields a crystal structure in the space group $I4_1/acd$ with lattice parameters a = 12.543(2) Å, c = 23.713(4) Å and Z = 16 (R1 = 0.0741). The structure consists of a three-dimensional network of Q^4-type and Q^3-type $P(O,N)_4$ tetrahedra and comprises two different Ca and one Mg position. This is the first example of a Ca (Ca1) with a twelvefold coordination by nitrogen in a slightly distorted cuboctahedron. The coordination of the other Ca atom

(Ca2) corresponds to a distorted octahedron consisting of six (4+2) mixed N/O positions with rather short (2.18 Å) average axial distances. However, Ca2 is displaced from the average position and exhibits a rather oblate displacement ellipsoid. The combination of SCXRD, high resolution transmission electron microscopy (HRTEM) and electron diffraction (selected area electron diffraction) unequivocally confirms the unit-cell dimensions, the space group assignment and the unusual position of Ca2. Simulated HRTEM defocus series further confirm the structure model. There are no pronounced short-range ordering phenomena. Additionally, bond-valence as well as lattice energy (MAPLE, Madelung part of lattice energy) calculations corroborate the displacement of Ca2 and confirm the electrostatic consistency of the crystal structure of $CaMg_2P_6O_3N_{10}$.

[1] S.J. Sedlmaier, E. Mugnaioli, O. Oeckler, U. Kolb, W. Schnick, *Chem. Eur. J.* 2011, *17*, 11258-11265.
[2] S.J. Sedlmaier, J. Schmedt auf der Günne, W. Schnick, *Dalton Trans.* 2009, 4081-4084.
[3] D. Baumann, S.J. Sedlmaier, W. Schnick, *Angew. Chem. Int. Ed.* 2012, *51*, 4707-4709.

MS05-P17

$Ce[AsO_3]$: Cerium(III) Oxoarsenate(III) with α-$Pb[SeO_3]$-Type Crystal Structure

F. Ledderboge[1], T. Schleid[1]
[1]*Institut für Anorganische Chemie der Universität Stuttgart, Stuttgart, Germany*

Water- and air-stable colourless single crystals of cerium(III) oxoarsenate(III) $Ce[AsO_3]$ were prepared by the solid-state reaction between elemental cerium (Ce) and arsenic sesquioxide (As_2O_3) with cesium chloride (CsCl) as fluxing agent in an evacuated silica ampoule at 750 °C over 4 days. $Ce[AsO_3]$ crystallizes monoclinically in the space group $P2_1/c$ and is isotypic with *α*-$Pb[SeO_3]$ [1]. The lattice constants are a = 902.89(8), b = 782.54(7), c = 829.68(7) pm and β = 103.392(3)° for Z = 8. Its crystal structure contains two crystallographically different cerium(III) cations. $(Ce1)^{3+}$ is coordinated by nine oxygen atoms ($d((Ce1)^{3+}\text{-}O^{2-})$ = 244 - 286 pm), while $(Ce2)^{3+}$ has only eight oxygen neighbours ($d((Ce2)^{3+}\text{-}O^{2-})$ = 240 - 273 pm). Both crystallographically different arsenic(III) cations form discrete $[AsO_3]^{3-}$ ψ^1-tetrahedra ($d(As^{3+}\text{-}O^{2-})$ = 174 - 179 pm), which are attached to the cerium(III) cations via edges and corners. A second monoclinic modification of $Ce[AsO_3]$ with the lattice constants a = 439.32(4), b = 529.21(5), c = 617.34(6) pm and β = 105.369(3)° for Z = 2 was obtained by high-pressure synthesis before [2]. Just like $La[AsO_3]$ [3] it adopts the space group $P2_1/m$, crystallizes isotypically with β-$Pb[SeO_3]$, $Pb[SO_3]$ (*scotlandite*) or $K[ClO_3]$ and exhibits ninefold coordinated Ce^{3+} cations exclusively ($d(Ce^{3+}\text{-}O^{2-})$ = 254 - 287 pm; $d(As^{3+}\text{-}O^{2-})$ = 175 - 176 pm) [2].

The Raman spectrum of α-$Pb[SeO_3]$-type $Ce[AsO_3]$ shows four bands between 600 and 900 cm^{-1}. Assigned to the stretching vibrations are the two strong bands (ν_1: 769 and 731 cm^{-1}), which represent the symmetric and two weaker bands (ν_3: 659 and 617 cm^{-1}) for the asymmetric vibrations. The symmetric bending mode vibrations emerge in the range of 340 to 410 cm^{-1} and the asymmetric bending modes range between 230 and 290 cm^{-1}.

Figure 1**:** Single crystal Raman spectrum of α-$Pb[SeO_3]$-type $Ce[AsO_3]$ recorded at λ = 638 nm.

Figure 2**:** View at the crystal structure of α-$Pb[SeO_3]$-type $Ce[AsO_3]$ along [001].

Further details of both crystal structure investigations for dimorphic $Ce[AsO_3]$ may be obtained from Fachinformationszentrum Karlsruhe, 76344 Eggenstein-Leopoldshafen, Germany, on quoting the deposition numbers CSD-423417 for $K[ClO_3]$-type $Ce[AsO_3]$ and CSD-426720 for α-$Pb[SeO_3]$-type $Ce[AsO_3]$ (http://www.fiz-karlsruhe.de/request_for_deposited_data.html fax: (+49)7247-808-666; e-mail: crysdata@fiz-karlsruhe.de,).

References

[1] M. Lahtinen, J. Valkonen, *Chem. Mater.* 2002, *14*, 1812-1817.
[2] S. J. Metzger, *Doctoral Thesis*, Univ. Stuttgart 2012.
[3] S. J. Metzger, G. Heymann, H. Huppertz, Th. Schleid, *Z. Anorg. Allg. Chem.* 2012, *638*, 1119-1122.

Figure 1

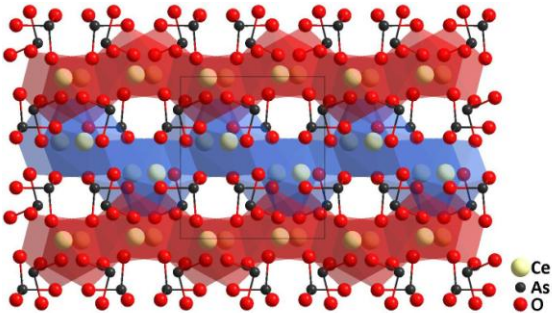

Figure 2

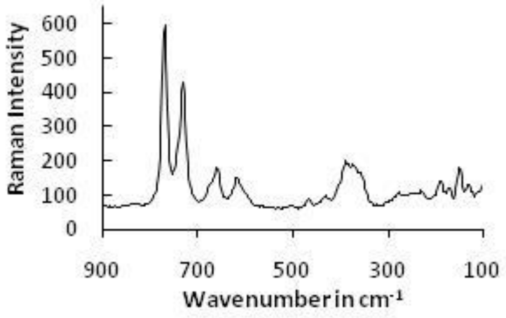

MS05-P18

(La, Sr, Ce) and (Sm, Ca, Ce) Monazite Solid Solutions

A. Neumann[1], A. Hirsch[1], J. Heuser[2], P. C. Jung[1], J. Zaddach[1], H. Schlenz[2], D. Bosbach[2], L. Peters[1], G. Roth[1]
[1]*Institut für Kristallographie, RWTH Aachen University, Aachen, Germany*
[2]*Forschungszentrum Jülich GmbH, Institute of Energy and Climate Research IEK-6, Jülich, Germany*

Monazite type ceramics (space group SG *P2₁/n*) are considered as an alternative waste matrix for high level nuclear waste. Natural monazites can accommodate considerable amounts of Th and U without becoming metamict in geological time scales. Furthermore, they exhibit an extensive chemical flexibility and durability [1].

Using $LaPO_4$ and $SmPO_4$ as endmembers, solid solutions were prepared, replacing 2 Sm^{3+} by Ca^{2+} and Ce^{4+}, and 2 La^{3+} by Sr^{2+} and Ce^{4+}. Ce was used as non-radioactive surrogate for the long-lived tetravalent minor actinoides.

The syntheses were carried out by solid state reactions. *Ln*-oxides, Ca-/Sr-carbonates and $NH_4H_2PO_4$ were used as starting reagents which were intimately mixed to obtain a homogenous mixture which was then fired in ambient atmosphere. The samples were characterised by XRD and IR spectroscopy.

The solid solution $Sm_{1-x}(Ca,Ce)_xPO_4$ was synthesised at 1000 °C. By substituting approx. 25 mol% of Sm by Ca and Ce the phase $Ca_2P_2O_7$ (b-Diphoshate, SG $P4_1$) was observed. At $x \geq 0.25$ the amount of CaP_2O_7 increased. IR spectroscopy supported these results because at $x \geq 0.25$ a new mode at 974 cm^{-1} evolved. A substitution limit of ~0.2 for Ce and Ca was reported by Pepin and Vance [2]. On heating $Sm_{0.85}(Ca,Ce)_{0.15}PO_4$, we observed the formation of whitlockite $Ca_3(PO_4)_2$ (SG *R-3c*) at 1200 °C. At 1400 °C whitlockite was not stable and in addition to monazite, the eulytite-type ($Ca_3(Sm,Ce)(PO_4)_3$, SG *I-43d*) was formed.

Another eulytite-type ($Sr_3(La,Ce)(PO_4)_3$) was observed in the system $La_{1-x}(Sr,Ce)_xPO_4$ (x=0-0.3). This solid solution series was synthesised at 1400°C and with 10 wt% $NH_4H_2PO_4$ excess in order to reduce the loss of the phosphate upon heating. $LaPO_4$ did not show any byproducts, whereas from x=0.05 to 0.3 eulytite was formed. The *a* parameter of eulytite was constant (approx. 10.185(2) Å), whereas its amount increased continuously.The lattice parameters of monazite *a*, *b*, and *c* decreased and *b* increased. Due to the constant Sr to *Ln* ratio of 3:1 in eulytite and the lack of any phase richer in *Ln* than monazite, the behaviour of the latter could be influenced by a change in the valancy of Ce (Ce^{4+}/Ce^{3+}). IR analysis of this series did not show any new modes, hence understanding the redox behaviour of Ce in this system remains an unsolved issue.

Solid solution series which were prepared at 1000 °C with 10 and 20 wt% $NH_4H_2PO_4$ excess showed that metaphosphate (LnP_3O_9, SG $C222_1$) or tristrontium tetraphosphate ($Sr_3(P_4O_{13})$, SG *P-1*) were formed. The solid solution with 10wt% excess phosphate were only pure for x=0.10 and 0.15.

[1] R. Ewing, L. Wang, Phosphates as nuclear waste forms in Reviews in Mineralogy and Geochemistry, 2002
[2] J. Pepin, E. Vance, Mat. Res. Bull., Vol. 16, pp. 627-633, 1981

MS05-P19

Mechanical and physical properties of monazite-type ceramics $La_{(1-x)}Eu_{(x)}PO_4$

A. Thust[1], Y. Arinicheva[2], E. Haussühl[1], S. Neumeier[2], L. Bayarjargal[1], B. Winkler[1]
[1]*Goethe-University Frankfurt am Main, Department of Geosciences, Frankfurt am Main, Germany*
[2]*Forschungszentrum Jülich, Institute of Energy and Climate Research IEK-6 Nuclear waste waste management, Jülich, Germany*

Natural monazites are orthophosphates which may contain significant amounts of radioactive thorium and uranium without showing significant metamictisation [1]. In addition to the radiation tolerance monazites exhibit high chemical durability and high mechanical stability. Hence synthetic monazite ceramics are considered as promising candidate materials for the conditioning of minor actinides and the disposal of nuclear waste [1,2]. Our research focuses on the mechanical and physical properties of lanthanum europium monazites $(La,Eu)PO_4$ where europium serves as a surrogate for trivalent actinides.

Powders with various La/Eu ratios were synthesized hydrothermally at the FZ Jülich. The dried precipitates were calcined for 2 h at 600°C. Afterwards the products were pelletized at ambient temperatures in an uniaxial press (15 kN to 35 kN) and finally hot pressed (uniaxial, 2 h, 1350°C, 3.9 kN). Final densities of up to 99% of the theoretical density were obtained. The pellets were analyzed by ultrasound spectroscopy, dilatometry and micro-calorimetry.

Young's moduli, *E*, were calculated from the elastic stiffness coefficients which were obtained by plane wave ultrasound spectroscopy. The Young's moduli increase linearly with increasing Eu concentration from 139(7) GPa for $LaPO_4$ to 157(8) GPa for $La_{0.1}Eu_{0.9}PO_4$. Hence, compared to waste glasses, where *E* are typically 80 - 90 GPa [3] monazite ceramics have significantly higher Young's moduli. Dilatometry (Netsch 402C) up to 773 K yielded coefficients of thermal expansion, *CTE*, (at 673 K) for $(La,Eu)PO_4$ between $8.8(3)\cdot10^{-6}$ K^{-1} ($La_{0.1}Eu_{0.9}PO_4$) and $10.0(3)\cdot10^{-6}$ K^{-1} ($La_{0.9}Eu_{0.1}PO_4$). There was no significant correlation of the *CTE* with the

Eu content. Heat capacities were obtained with a Quantum Design PPMS for temperatures 2 K < T 400 K. A slight increase in *C*p with increasing Eu content was observed. No evidence for a low temperature phase transition was found. At room temperature the *C*p for $La_{0.9}Eu_{0.1}PO_4$ is 103(1) J $mol^{-1}K^{-1}$, for $EuPO_4$ it is 109(1) J $mol^{-1}K^{-1}$. To a first approximation there is ideal mixing across the solid solution. The heat capacities of ceramics are significantly higher than those of glasses used as waste forms, where *C*p is around 50 J $mol^{-1}K^{-1}$ [4].

Literature:
[1] Schlenz H., Heuser J., Neumann A., Schmitz S., Bosbach D. (2013). Monazite as a suitable actinide waste form. Zeitschrift für Kristallographie, 228, 113-123.
[2] Montel J-M. (2011). Minerals and design of new waste forms for conditioning nuclear waste. Comptes Rendus Geoscience, 343, 230-236.
[3] Matzke Hj., Vernaz E. (1993). Thermal and physicochemical properties important for the long term behavior of nuclear waste glasses. Journal of Nuclear Materials, 201, 295-309.
[4] Linard Y., Yamashita I., Atake T., Rogez J., Richet P. (2001). Thermochemistry of nuclear waste glasses: an experimental determination. Journal of Non-Crystalline Solids, 286, 200-209.

MS05-P20

Thorium arsenates from high temperature solid state reactions

N. Yu[1], E. Alekseev[1], V. Klepov[1]
[1]*Institute of Energy and Climate Research (IEK-6) Forschungszentrum Jülich, Juelich, Germany*

Inorganic phases including thorium are under strict interests of scientific community. Thorium can be used as a modeling element for An^{4+} cations without serious difficulties in handling. Moreover, Th-fuel circle is revised in some countries (for example India) as the most perspective one. Previously, several researches were performed in thorium phosphate systems.[1-5] It was shown that several different phases can form within the alkali elements thorium phosphates. The coordination chemistry of arsenic is quite similar to phosphate, but the area of thorium arsenates is relatively unexplored. In this research, we focused on systematic study of solid phases formations in thorium-arsenate system: A^I-ThO_2-As_2O_5, where A^I - alkali cations and silver. We used high temperature solid state reactions for preparation of new compounds in mentioned system. Till date we obtained following new phases: $ATh_2(AsO_4)_3$ (A= K, Rb, Cs, Ag), $A_2Th(AsO_4)_2$ (A= Li, Na, K, Rb, Cs), $Li_2Th_2(AsO_4)_2(As_2O_7)$, $Na_5Th_4(AsO_4)_7$ and $Na_5Th(AsO_4)_3$. The crystal structures of these phases were characterized by using single crystal and powder X-ray diffraction. The DSC, IR and Raman spectra were measured on single crystals and pure powder samples. Significant structural changes were observed in $A_2Th(AsO_4)_2$ (A= Li, Na, K, Rb, Cs) series.

Reference:
(1) Matkovic, B. S., M.; Inorganica Chimica Acta 1970, 4, p571.
(2) Ruzic Toros, Z. K.-P., B.; Liminga, R.; Popovic, S. Inorganica Chimica Acta 1974, 8, p273.
(3) Matkovic, B. P., B.; Sljukic, M. Documenta Chemica Yugoslavica. Croatica Chemica Acta 1968, 40, p147.
(4) Kojic-Prodic, B. S., M.; Ruzic Toros, Z. Acta Crystallographica B(24,1968-38,1982) 1982, 38, p67.
(5) Krishnan, K. S., S.K.; Singh Mudher, K.D. Journal of Alloys Compd. 2006, 414, p310.

MS05-P21

$CoAs_2O_4$: synthesis and structural characterisation

A. Wittwer[1], T. Đorđević[1]
[1]*Universität Wien, Institut für Mineralogie und Kristallographie, Wien, Austria*

In order to understand the role of arsenic in the environment, one has to investigate structural features and stabilities of naturally occurring arsenic compounds. In addition, a study of mineral-related synthetic phases should be very helpful because they can appear as a result of human activities. $CoAs_2O_4$ was synthesised during an on-going research on natural and synthetic arsenic oxo-salts, with a focus on their structural and spectroscopic classification. Anhydrous arsenates of cobalt are well-established but arsenites of divalent cobalt are less known. Besides $Co_2As_2O_5$ [1], $CoAs_2O_4$ represents the second compound in the Co(II)-As(III)-O system.

$CoAs_2O_4$ was synthesized under mild hydrothermal conditions from a mixture of KCl, $Co(OH)_2$, As_2O_3 and distilled water in a 1:1:1 molar ratio (Teflon-lined steel autoclave, 12 days, autogeneous pressure, T_{max}= 493 K, pH = 6). $CoAs_2O_4$ forms transparent, dark pink, elongated prismatic crystals up to 1.8 mm in length (yield ca. 55 %) together with transparent, colourless hexagonal crystals of KAs_4O_6Cl (yield ca. 45 %) [2].

The crystal structure of $CoAs_2O_4$ was refined using single-crystal X-ray diffraction data (CCD detector, Mo*K*α radiation, 293 K, θ_{max} = 44.387 °) starting from the atomic coordinates of isotypic $CuAs_2O_4$ [3]. The refinement on $F_0{}^2$ with 22 parameters and 838 unique reflections yielded R_1 = 0.0306, wR_2 = 0.0455, and R_1 = 0.0229 for 719 observed reflections with $I \geq 2\sigma(I)$. *Crystal data*: a = 8.3453(1) Å, c = 5.6201(1) Å, V = 391.406(12) Å³, Z = 4.

$CoAs_2O_4$ crystallises in tetragonal space group $P4_2/mbc$. It is isostructural with the materials adopting general formula MSb_2O_4 (M^{2+} = Mg, Mn, Fe, Co, Ni, Zn) [4] and naturally occurring phase trippkeite, $CuAs_2O_4$ [3]. The crystal structure of $CoAs_2O_4$ contains chains of edge-linked CoO_6 distorted octahedra (<Co-O> = 2.0795 Å) running along [001], where the individual octahedra are oriented such that the apical bonds (Co-O1 = 2.1775(11) Å) lie perpendicular to [001] and are directed toward the adjacent chain. These chains are further interconnected via trigonal pyramidal AsO_3 units (<As-O> = 1.8079 Å). The distance between adjacent Co^{2+} cations in a single chain is 2.8140(5) Å, which is somewhat shorter than the Co-Co distance of 2.9619 Å in $CoSb_2O_4$ [4].

The magnetic properties of the isotypic MSb_2O_4 (M = Mg, Mn, Fe, Co, Ni, Zn) compounds containing the first row transition metals have been widely investigated [4 and references therein]. Further measurements of the magnetic properties of $CoAs_2O_4$ are in preparation.

Financial support of the Austrian Science Foundation (FWF) (Grant V203-N19) is gratefully acknowledged.

References**:**

[1] Lösel, S. and Hillebrecht, H. (2008): *Z. Anorg. Allg. Chem.* 634, 2299-2302.

[2] Pertlik, F. (1988): *Monatshefte für Chemie*. 119, 451-456.

[3] Pertlik, F. (1975): *Tschermaks Min. Petr. Mitt.* 22: 211-217.

[4] De Laune, B.P. and Greaves, C. (2012): *J. Solid State Chem.* 187: 225-230.

MS05-P22

New ternary molybdates in the *M*-Fe(II,III)-Mo-O systems with *M*=K, Rb

A. Sarapulova[1], O. Chimitova[1,2], D. Mikhailova[1], N. Kuratieva[3], A. Komarek[1], Y. Prots[1], H. Ehrenberg[4]

[1]*Max Planck Institute for Chemical Physics of Solids, Dresden, Germany*

[2]*Baikal Institute of Nature Management, Ulan-Ude, Russia, Russian Federation*

[3]*Nikolaev Institute of Inorganic Chemistry, Novosibirsk, Russia, Russian Federation*

[4]*Karlsruhe Institute of Technology , Eggenstein-Leopoldshafen, Germany*

New ternary molybdates $Rb_2Fe_2(MoO_4)_3$, $RbFe_5(MoO_4)_7$ and $KFe_4(MoO_4)_6$ were identified by single-crystal X-ray diffraction after annealing of several compositions from the Rb_2MoO_4-$FeMoO_4$-$Fe_2(MoO_4)_3$ and K_2MoO_4-$FeMoO_4$-$Fe_2(MoO_4)_3$ systems at elevated temperatures in evacuated sealed silica tubes. The selected single crystals were investigated at room temperature using Bruker Nonius X8Apex and Bruker D8 VENTURE diffractometers (Mo-Kα radiation).

The structure of cubic $Rb_2Fe_2(MoO_4)_3$ ($P2_13$, a = 10.7691(5) Å, Z = 4) is very similar to the structure of $Cs_2Fe_2(MoO_4)_3$ [1] and to the structure of pseudocubic $Cs_2Co_2(MoO_4)_3$ with a weak orthorhombic distortion [2]. $RbFe_5(MoO_4)_7$ crystallizes in a monoclinic symmetry ($P2_1/m$, a = 6.8987(4) Å, b = 21.291(1) Å, c = 8.6833(5) Å, β= 102.190(2)°, Z = 2) and is isostructural to $CsFe_5(MoO_4)_7$, which adopts its own structure type [1]. A three-dimensional framework of this structure contains three crystalographically independent Fe-sites and consists of isolated FeO_6-octahedra and Fe_4O_{18}-units of edge-sharing FeO_6-octahedra, which are connected with MoO_4-tetrahedra via corners.

Single crystals of the composition $KFe_4(MoO_4)_6$ were obtained after attempts to reproduce the synthesis of $NaFe_2(MoO_4)_3$ (S. G. P-1) [3]. In contrast to the Na-analog, the K-containing compound (Fig. 1) exhibits a deficit of potassium ions and crystallizes in a trigonal space group (R-3, a=9.0978(3), c= 24.2359(10) Å, Z=3). The structure is similar to the NASICON-type structure of arsenates $Na_3M_2(AsO_4)_3$ (M = AI, Ga, Cr, Fe) [4].

Since $RbFe_5(MoO_4)_7$ is isostructural to $CsFe_5(MoO_4)_7$, one can expect similar magnetic behavior for both compounds. It is known that $CsFe_5(MoO_4)_7$ represents a canted antiferromagnet with the complex magnetic structure, which was described by combination of two propagation vectors k=(1/2, 0, 0) and k=(0, 0, 0) [1]. Two magnetic-field induced transitions were observed at 0.25 T and 1.9 T at 2 K for the Cs-compound.

[1] T. Namsaraeva, B. Bazarov, D. Mikhailova, N. Kuratieva, A. Sarapulova, A. Senyshyn, H. Ehrenberg, *Eur. J. Inorg. Chem*. (2011) 2832-2841.

[2] S. F. Solodovnikov, R. F. Klevtsova, V. G. Kim, P. V. Klevtsov, *Zh. Strukt. Khim.* 27 (1986) 928-933.

[3] E. Muessig, K. G. Bramnik, H. Ehrenberg, *Acta Cryst. B59* (2003) 611-616.

[4] F. D'yvoire, E. Bretey, *Solid State lonics* 28-30 (1988) 1259-1264.

Figure 1. Crystal structure of $K_{0.5}Fe_2(MoO_4)_3$ with corner-sharing FeO_6-octahedra and MoO_4-tetrahedra. Potassium ions represent grey spheres.

Figure 1

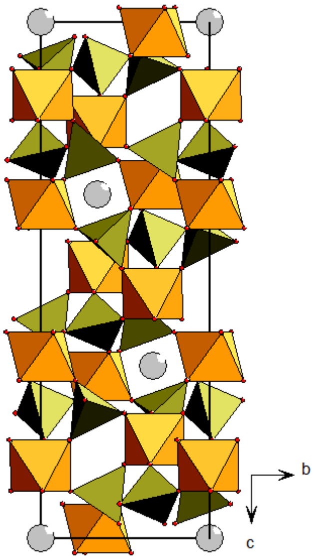

MS05-P23

Synthesis, structure and characterization of $Li_3AsW_7O_{25}$

P. Zhao[1], M. M. Murshed[1], E. V. Alekseev[1], T. M. Gesing[1]

[1]*Universität Bremen, Institut für Anorganische Chemie, Bremen, Germany*

$KAsW_2O_9$ [1] and the isotypic $NaAsW_2O_9$ [2] are the first two alkali arseno-tungstates crystalize in the non-centrosymmetric space group $P2_12_12_1$ showing non-linear optical (NLO) properties. To further investigate the effect of alkali ions on NLO properties, the alkali source KNO_3 or $NaNO_3$ was replaced by $LiNO_3$ during the synthesis. The new compound $Li_3AsW_7O_{25}$ was successfully produced using a solid state reaction and characterized by X-ray single crystal and powder diffraction, FTIR and Raman spectroscopy. Opposite to the sodium and potassium phases this compound crystallizes in the centrosymmetric space group *Pbca* with the metric parameters a = 0.72555(15) nm, b = 1.0081(2) nm, c = 4.9048(10) nm and V = 3.5824(13) nm^3. The structure consists of a three dimensional framework formed by WO_6 octahedra and AsO_4 tetrahedra (Fig. 1). The Li cations are located in channels running along **b**-direction. Two different channels are formed. One channel type consists of 4 WO_6 and 2 AsO_4 polyhedra where the tungsten atoms are found on a plane with its plane-normal nearly parallel to [0-11]. The tetrahedrally oxygen coordinated arsenic cations are above and below this plane. The other channel type is formed by 6 WO_6 octahedra where the tungsten atoms are placed (nearly) on a plane with its plane normal parallel to [011]. The angle between both planes is 100.6(3)°. Both channels are wide enough for fast lithium diffusion which indicates a promising application in Li-ion conductivity.

[1] E.V. Alekseev, O. Felbinger, S. Wu, T. Malcherek, W. Depmeier, G. Modolo, T.M. Gesing, S.V. Krivovichev, E.V. Suleimanov, T.A. Gavrilova, L.D. Pokrovsky, A.M. Pugachev, N.V. Surovtsev, V.V. Atuchin, J. Solid State Chem. 204 (2013) 59. [2] P. Zhao, M.M. Murshed, E.V. Alekseev, V.V. Atuchin, T.M. Gesing, submitted.

Figure 1: Structure plot of $Li_3AsW_7O_{25}$ with tungsten atom assignment to WO_6 octahedra chain contribution.

Figure 1

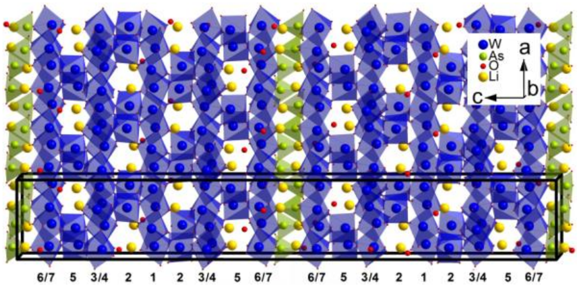

MS05-P24

Four novel organo-templated microporous compounds with DFT - type topology

T. Đorđević[1], L. Karanović[2], S. Šutović[2], D. Poleti[3]

[1]*Universität Wien, Institute für Mineralogie und Kristallographie, Wien, Austria*

[2]*University of Belgrade, Laboratory for Crystallography, Faculty of Mining and Geology, Belgrade, Serbia, Serbia*

[3]*University of Belgrade, Faculty of Technology and Metallurgy, Belgrade, Serbia, Serbia*

Four novel microporous compounds $[C_2H_4(NH_3)_2][ZnAsO_4]_2$ (**1**), $[C_2H_4(NH_3)_2][(Co_{0.1}Zn_{0.9})AsO_4]_2$ (**2**), $[C_2H_4(NH_3)_2]_{0.9}[C_2H_4(NH_2)_2]_{0.1}(Fe_{0.1}Zn_{0.9}AsO_4)_2$ (**3**) and $[C_2H_4(NH_3)_2][ZnPO_4]_2$ (**4**) containing ethylenediamine molecules $C_2H_4(NH_2)_2$ (en) and ethylenediammonium cations $[C_2H_4(NH_3)_2]^{2+}$ (H_2en^{2+}) have been synthesized by hydrothermal method and their crystal structures are reported. While **1**, **2** and **3** exhibit a twinned DFT-type structures [1] and crystallize in tetragonal $P4_2/n$ space group, **4** crystallizes in orthorhombic space group *Pcca*, which till now was not observed among known compounds with DFT-type framework topology. The main feature of the compounds **2** and **3** is their novel chemical composition, represented by cobalt blue and reddish brown colour and one mixed tetrahedral position occupied by Zn/Co and Zn/Fe, respectively. In the structure of **1**, the hydrogen atoms (previously not reported by Bu *et al*. [2]) were calculated and refined to reasonable positions using riding model.

The DFT anionic frameworks of **1** - **3** are built from AsO_4 tetrahedra alternating with ZnO_4 in **1**, $(Co_{0.1}Zn_{0.9})O_4$ in **2**, $(Fe_{0.1}Zn_{0.9})O_4$ in **3** and from PO_4 with ZnO_4 in **4**. They are linked through their vertices generating 4M, 6M and 8M tetrahedral rings, which produce three mutually perpendicular 8M ring channels (Fig. 1). At the intersections of these channels H_2en^{2+} ions are accommodated and hydrogen-bonded to the adjacent oxygen atoms of the anionic framework. Only in **3**, H_2en^{2+} is partly substituted by en to maintain electroneutrality. It was found that the DFT structures, which incorporate larger tetrahedral cations, have higher degree of lattice distortion and are more dissimilar to the ideal structural models derived from the aristotype.

Financial supports of the Austrian Science Foundation (FWF) (Grant V203-N19) and Ministry of Education, Science and Technological Development of the Republic of Serbia (grant No. III45007) are gratefully acknowledged.

References:

[1] Baerlocher, Ch., McCusker, L. B., Olson, D. H., (2007): Atlas of Zeolite Framework Types, pp. 112-113, Sixth revised edition, first impression 2007, Elsevier, Radarweg 29, PO Box 211, 1000 AE Amsterdam, The Netherlands, Linacre House, Jordan Hill, Oxford OX2 8DP, UK.

[2] Bu, X. H., Feng, P. Y., Gier, T. E., Stucky, G. D. (1998): J. Solid State Chem., 136, 210-215.

Figure 1. The tetragonal aristotype of the DFT-type structure: the 3D framework of corner-sharing tetratahedra and the 8M ring channels filled with H_2en^{2+} cations when viewed approximately along [100] (+*c* direction up, +a_2 direction right).

Figure 1

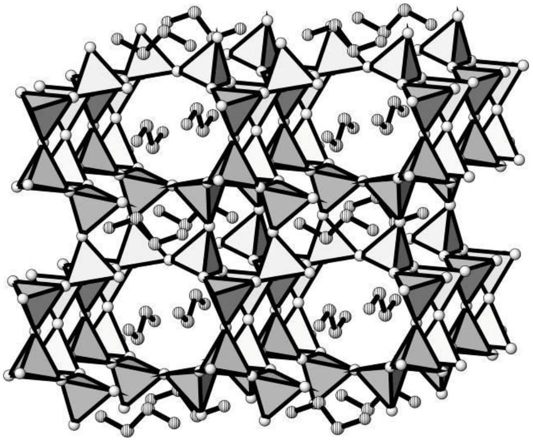

MS05-P25

Synthesis and Crystal Structure of New Hydrogen Carbonate Tungstates $Rb_3(HCO_3)(WO_4)$ and $Cs_3(HCO_3)(WO_4)$

E. Irran[1], J. Higuera-Serrano[1]
[1]*Technische Universität Berlin, Institut für Chemie, Berlin, Germany*

The new hydrogen carbonate tungstates $Rb_3(HCO_3)(WO_4)$ and $Cs_3(HCO_3)(WO_4)$ were prepared from solutions of H_2WO_4 in deionized water, to which surplus of RbOH and CsOH solutions, respectively, were added. These solutions were evaporated slowly at room temperature in air, so CO_2 from the air was able to be incorporated. The crystal structures of the colorless crystals were determined with single-crystal X-ray diffraction (Oxford Diffraction XcaliburS; space group: $Pna2_1$ (no. 33), a = 8.2471(2), b = 17.6437(4), c = 6.1905(2) Å ($Rb_3(HCO_3)(WO_4)$), a = 8.6106 (3), b = 18.2672 (6), c = 6.4191(3) Å ($Cs_3(HCO_3)(WO_4)$); Z = 4). In $Rb_3(HCO_3)(WO_4)$, the rubidium atoms are surrounded by eight or ten oxygen atoms and in $Cs_3(HCO_3)(WO_4)$, the cesium atoms are surrounded by eight, nine or ten oxygen atoms. In both compounds each tungsten atom is surrounded by four oxygen atoms forming a tetrahedron and each carbon atom is surrounded by two oxygen atoms and one OH^- group forming a triangle. The WO_4^{2-} tetrahedra and the HCO_3^- ions are linked by a hydrogen bond in both compounds.

MS05-P26

Solvochemical Synthesis and Structural Characterization of the Neodymium(III) Fluoride *Ortho*-Oxomolybdate(VI) NdF[MoO$_4$]

T. Schustereit[1], T. Schleid[1], I. Hartenbach[1]
[1]*University of Stuttgart, Institute for Inorganic Chemistry, Stuttgart, Germany*

The crystal structure of the rare-earth metal(III) fluoride *ortho*-oxomolybdates(VI) with the composition *RE*F[MoO_4] was determined for yttrium and the heavy lanthanoids (*RE* = Y [1], Sm - Tm [2]) in 2008 for the first time, while those for the light elements were not possible to be obtained via solid-state synthesis. A solvochemical synthesis route involving a final treatment for the precipitated product for six days 6 at 850 °C in evacuated fused silica ampoules yielded lilac, transparent single crystals of NdF[MoO_4] as first representative for the *RE*F[MoO_4] series with a larger RE^{3+} cation. The title compound crystallizes monoclinically in space group $P2_1/n$ (a = 694.02(4), b = 653.41(4), c = 933.10(5) pm and β = 106.161(3)°) with four formula units per unit cell. Based on the solvochemical synthesis it was also possible to prove the dimorphic character of the samarium representative SmF[MoO_4] by X-ray powder diffraction. Although a lot of similarities can be identified, its crystal structure differs from those of the well-known representatives with the smaller rare-earth metal cations. The structure contains crystallographically unique Nd^{3+} cations, which are surrounded by two F^- and six O^{2-} anions (d(Nd-F) = 233 - 234 pm, d(Nd-O) = 241 - 253 pm) each forming distorted bicapped trigonal prisms (CN = 8). These polyhedra are fused together via two common edges, which consist of two oxide anions to form strands running parallel to the [100] direction. Those strands are finally shared via fluoride vertices to build up a three-dimensional lattice, which leaves tetrahedral voids that to host the Mo^{6+} cations (d(Mo-O) = 172 - 182 pm, Figure 1). This is in contrast to the structure of the representatives with the smaller lanthanoids and yttrium which do not share common fluoride vertices, but F-F edges instead to form layers in between, which the Mo^{6+} cations reside in to interconnect them. This the YF[MoO4] structure comprises rhombus-shaped $[F_2Y_2]^{4+}$ units consisting of two edge-sharing $[FY_2]^{5+}$ boomerangs (Figure 2, left), whereas the NdF[MoO4] displays zigzag chains of vertex-sharing $[FNd_2]^{5+}$ boomerangs (Figure 2, right).

[1] Th. Schleid, S. Strobel, P. K. Dorhout, P. Nockemann, K. Binnemans, I. Hartenbach, *Inorg. Chem.* 2008, *47*, 3728.
[2] I. Hartenbach, S. Strobel , P. K. Dorhout, Th. Schleid, *J. Solid State Chem.* 2008**,** *181*, 2828.

Figure 1**.** View along the *b* axis of the structure of NdF[MoO_4].

Figure 2. Rhombus-shaped $[F_2Y_2]^{4+}$ unit in the structure of $YF[MoO_4]$ (left) and zigzag chain in the structure of $NdF[MoO_4]$ (right).

Figure 1

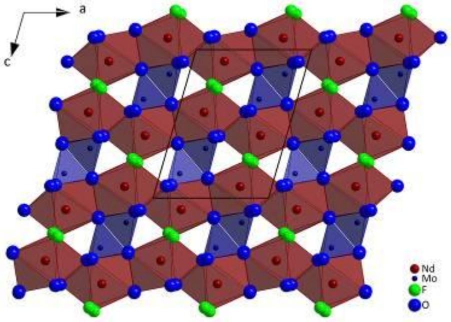

Figure 2

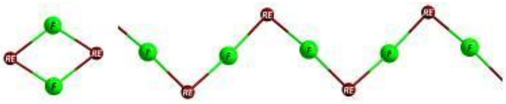

MS05-P27

In-doped multiferroic $MnWO_4$

U. Gattermann[1], S.- H. Park[1]
[1]*Ludwig-Maximilians-Universität München, Kristallographie, München, Germany*

Question
The naturally occurring mineral Huebnerite ($MnWO_4$) shows several transitions of its magnetic structure below its Neel temperature (~13K). The unpaired Mn^{2+} spins in the antiferromagnetic ordered phase AF2 (stable between 7.6K and 12.7K) show an elliptical spin spiral ordering, inducing an electric polarisation. In the present study the influence of In^{3+} substitution for Mn^{2+} on the atomic and magnetic structure of $MnWO_4$ was investigated.

Experimental
Polycrystalline $Mn_{1-1.5x}In_x\square_{0.5x}WO_4$ (x = 0, 0.04, 0.06, 0.10 and 0.14, □ = vacancy) was synthesized by solid-state reaction in the system MnO-WO_3-InO at 1050 °C in air. Chemical analysis was performed using electron microprobe measurements to confirm In substitution for Mn. The solid-solution $Mn_{0.88(4)}In_{0.08(4)}\square_{0.04}W_{0.98(2)}O_4$ was investigated using neutron powder diffraction at the beamline SPODI (FRM II) at 300 and 3.5 K. Rietveld-Analysis with X-Ray powder diffraction (XPD) data (GE X-ray Diffraction System XRD 3003 TT, Cu*K*α1) was performed to obtain accurate lattice parameters so that successful replacement of In^{3+} for Mn^{2+} in the solid-solutions $Mn_{1-1.5x}In_x\square_{0.5x}WO_4$ was confirmed.

Results
Rietveld-Analysis with XPD data show a steady change of lattice parameters with increasing amount of In_2O_3 introduced in the synthesis. Considering the smaller ionic radius of In^{3+} against Mn^{2+} we observed an anomaly of lattice parameter changes, a constant increase of a, b, c and a constant decrease of the monoclinic β (Figure 1). One third of the substituted Mn^{2+} positions remains unoccupied in our In:$MnWO_4$ compounds. Rietveld-Analysis with neutron powder diffraction data showed no disymmetrisation in nuclear and magnetic structure of In-doped $MnWO_4$ with respect to the undoped $MnWO_4$ (Figure 2).

Figure 1 The change of the lattice metric with increasing In doping in $MnWO_4$.

Figure 2 Graphical presentation of Rietveld calculation with neutron powder diffraction data at 3.5 K. Open circles correspond to data points, solid line is calculated with the refined models of the nuclear structures from $Mn_{0.88(4)}In_{0.08(4)}\square_{0.04}W_{0.98(2)}O_4$, In_2O_3, Mn_5O_8, Mn_2O_4 and the magnetic structures of $Mn_{0.88(4)}In_{0.08(4)}\square_{0.04}W_{0.98(2)}O_4$, Mn_5O_8, Mn_2O_4. Their respective reflection positions are marked as bars. The line at the bottom corresponds to the difference between the observed and calculated intensities.

Figure 1

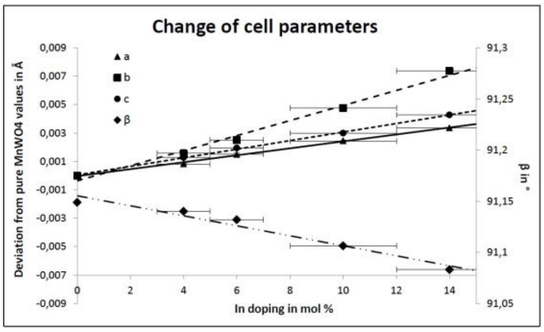

Figure 2

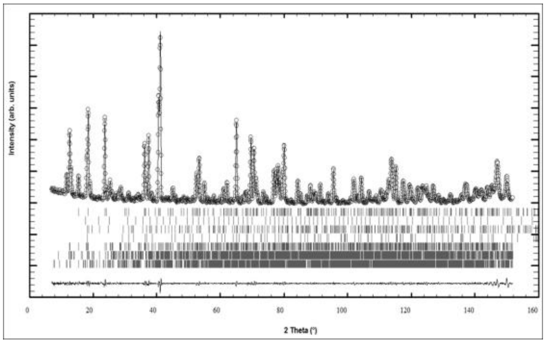

MS05-P28

New iodine polysulfates
Syntheses, crystal structures and characterization of $I_2(SO_4)_2(S_2O_7)$, $I_2(SO_4)_2(S_3O_{10})$, and a new modification of $(IO_2)_2(S_2O_7)$

L. V. Schindler[1], J. Bruns[1], M. S. Wickleder[1]
[1]*Institut für Chemie, Oldenburg, Germany*

There are a lot of research activities on the oxochemistry of halides throughout the years. With respect to iodine especially structural curiosities and SHG responses come into focus. In 1974 *Kjekshus* et al. were able to synthesize and characterize the first iodine-containing oxo-compound, exhibiting a polymeric iodosyl cation in the structure of $(IO)_2SO_4$.[1] Especially in the last 20 years remarkable new structures could be characterized.[2] $(IO_2)_2(S_2O_7)$[3], the first compound showing formally a iodyl-cation, was synthesized by the reaction of iodic acid with oleum at 195 °C. In course of our recent research activities on the chemistry of new polysulfates, we were able to synthesize the two heteroleptic iodine sulfates $I_2(SO_4)_2(S_2O_7)$, and $I_2(SO_4)_2(S_3O_{10})$, as well as a new modification of the iodylium disulfate $(IO_2)_2(S_2O_7)$ via the reaction of I_2O_5 with neat SO_3 or oleum at elevated temperatures. In the monoclinic structure of $I_2(SO_4)_2(S_3O_{10})$ ($I2/a$, a = 908.12(9) pm, b = 555.67(5) pm, c = 2819.86(3) pm, β = 94.394(1)°, V = 1.41876(3) nm³, Z = 4) the iodine atoms are linked by sulfate and trisulfate anions forming infinite layers in the *a*-*b*-plane with termination by sulfate anions in *c*-direction. The layers are therefore stacked along the crystallographic *c*-axis (Fig. 1, left). The non-centrosymmetric structure of $I_2(SO_4)_2(S_2O_7)$ ($P1$, a = 537.93(1) pm, b = 669.65(2) pm, c = 899.93(2) pm, α = 96.237(1)°, β = 94.769(1)°, γ = 109.130(1)°, V = 0.30202(1) nm³, Z = 1) also reveals infinite layers formed by sulfate and disulfate anions linking the trivalent iodine atoms. In the new orthorhombic modification of $(IO_2)_2(S_2O_7)$ ($Pna2_1$, a = 1816.43(6) pm, b = 452.59(1) pm, c = 1049.02(3) pm, V = 0.86240(4) nm³, Z = 4) the I-O-distances range almost continuously from 175.5(4) to 283.10(1) pm, so the structure can be described with two extremes: on the one hand as a ionic structure containing the iodyl-cation $(IO_2)^+$ and the disulfate-anion $(S_2O_7)^{2-}$, or on the other hand as a polymeric network (Fig. 1, right). The main difference compared with the already known monoclinic structure is the constitution of the iodyl-dimere. In both structures two iodine-atoms are connected by two bridging O-atoms. In the monoclinic structure the two terminal O-atoms on the two iodine-atoms are *cis*-orientated, in the orthothombic structure they are *trans*-orientated.

Figure 1**.** left: crystal structure of $I_2(S_3O_{10})(SO_4)_2$ (dashed lines for wide range I-O bonds with 242.8 pm); right: crystal structure of $(IO_2)_2(S_2O_7)$.

[1] S. Furuseth, K. Selte, H. Hope, A. Kjekshus, B. Klewe, *Acta. Chem. Scand. A,* 1974, *28***,** 71.
[2] M. Jansen. T. Kraft, *Chem. Ber. / Recueil* 1997*, 130*, 307.
[3] M. Jansen, R. Müller, *Z. Anorg. Allg. Chem.* 1997, *623*, 1055.

Figure

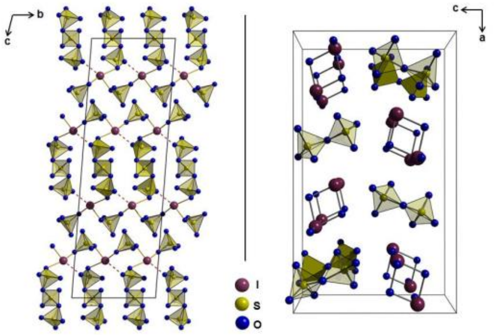

MS05-P29

Reactions of $B(OH)_3$ with sulfuric acid derivatives - The unprecedented layer structures of $B_2S_2O_9$ and $B_6O_9 \cdot CH_3SO_3H$

C. Logemann[1], M. S. Wickleder[1]
[1]Institut für Chemie, Carl von Ossietzky Universität Oldenburg, Oldenburg, Germany

Some years ago we started a research project regarding the synthetic potential of sulfuric acid and its derivatives in the preparation of new functional compounds. Throughout the years we were able to develop various synthetic routes using reactants like sulfuric acid, methanesulfonic acid, trifluoromethanesulfonic acid, chlorosulfonic acid, oleum, or even neat SO_3. Reactions with the latter yielded for example the first tetrasulfate $(NO_2)_2[S_4O_{13}]$[1] and the ferromagnetic disulfate $Pd(S_2O_7)$[2]. Usage of trifluoromethanesulfonic acid in the preparation of new gold compounds led to a number of complex gold salts, namely $M[Au(CF_3SO_3)_4]$ (M = Li, Na, K, Rb, Ag)[3]. Also main group elements came into our focus and we were able to prepare a plethora of compounds following the formulae $A_2[M(S_2O_7)_3]$ (A=Li, Na, K, Rb, Cs, Ag, NH_4; M=Si, Ge, Sn)[4].

Attempts to incorporate boron in oxoanionic compounds recently led to exiting new compounds, $B_2S_2O_9$, starting from boric acid and chlorosulfonic acid and $B_6O_9 \cdot CH_3SO_3H$, which could be obtained in the reaction of boric acid and methanesulfonic acid.

$B_2S_2O_9$ can be described as a layered framework of $[BO_4]$ and $[SO_4]$ tetrahedra[5]. In each layer $[BO_4]$ and $[SO_4]$ tetrahedra alternate (Fig. 1). Three out of four oxygen atoms of each $[SO_4]$- tetrahedron coordinate to neighboring boron atoms and one oxygen atom remains uncoordinated. Three out of four oxygen atoms of each $[BO_4]$ tetrahedron coordinate to sulfur atoms. Double layers are formed through linkage of two neighboring $[BO_4]$ tetrahedrons forming a B-O-B bridge using the fourth oxygen atom of each $[BO_4]$ tetrahedron.

The crystal structure of $B_6O_9 \cdot CH_3SO_3H$ is also of a layered type (Fig. 2). In this case planar B_6O_6 rings, showing the boron atom in trigonal planar coordination, are formed which are then linked to other B_6O_6 rings via an oxygen bridge. In this way puckered layers of electroneutral B_6O_9 units form, which are intercalated by methanesulfonic acid.

Literature:

[1] C. Logemann, T. Klüner, M.S. Wickleder, *Angew. Chem.* 2012, 124, 5082-5085; *Angew. Chem. Int. Ed.* 2012, 51, 4997-5000.

[2] J. Bruns, M. Eul, R. Pöttgen, M. S. Wickleder, *Angew. Chem.* 2012, 124, 2247-2250; *Angew. Chem. Int. Ed.* 2012, 51, 2204-2207.

[3] C. Logemann, T. Klüner, M. S. Wickleder, *Z. Anorg. Allg. Chem.* 2013, 639, *3-4*, 485-492.

[4] a) C. Logemann, J. Witt, D. Gunzelmann, J. Senker, M. S. Wickleder *Z. Anorg. Allg. Chem.* 2012**,** 638, *12-13*, 2053-2061; b) C. Logemann, D. Gunzelmann, T. Klüner, J. Senker, M. S. Wickleder, *Chem. Eur. J.* 2012, 18, 15495-15503.

[5] C. Logemann, M. S. Wickleder, *Angew. Chem.* 2014, in press.

Figure 1

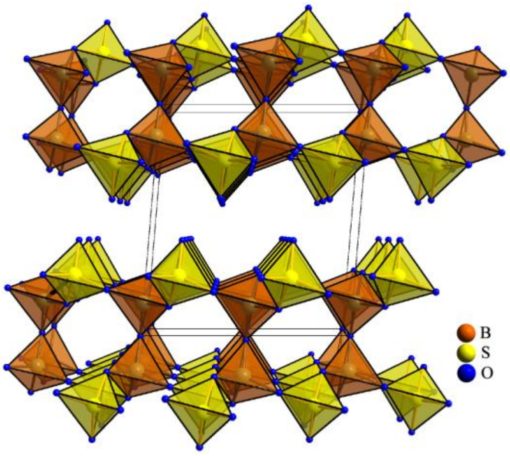

Double Layers in the structure of B_2S_2O

Figure 2

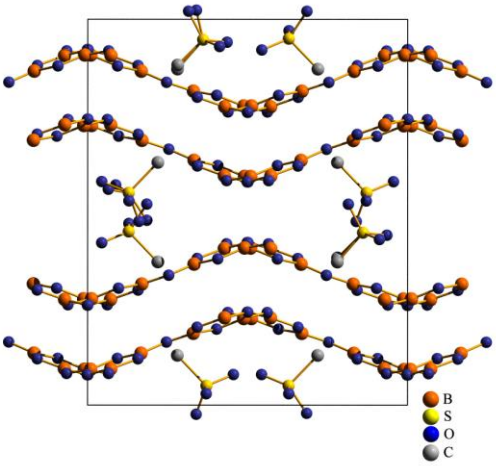

Layered structure of $B_6O_9 \cdot CH_3SO_3H$

MS05-P30

Syntheses, crystal structures and vibrational spectra of diselenates(VI) $A_2Se_2O_7$ (A = Li, Na, K, Rb, Cs)

M. Daub[1], H. Hillebrecht[1]
[1]*University Freiburg , Inorganic Chemistry, Freiburg, Germany*

While disulfates $A_2S_2O_7$ are well-known and characterized in detail [1-4], the analogue selenium (VI) compounds are not. Just the structure of $Na_2Se_2O_7$ was determined [5]. $Na_2Se_2O_7$ and $K_2Se_2O_7$ were characterized by vibrational spectra [6]. Reasons for that marked differences between sulfates and selenates(VI) is the much higher oxidation power of Se(VI) (S/SO_4^{2-}: E° = +0.158 V; Se/SeO_4^{2-}: E° = +1.15V) and sensitivity of selenates(VI) to moisture.

Single crystals of $A_2Se_2O_7$ were obtained from heating the corresponding carbonates with H_2SeO_4 to 573 K followed by slow cooling to RT. The colourless crystals are very sensitive to moisture. All diselenates are isotypic to the corresponding disulfates. They contain corner-sharing ditetrahedral units $Se_2O_7^{2-}$. The SeO_4 tetrahedra are nearly regular with shorter Se-O_{term} bonds (1.58–1.63Å) and longer Se-O_{br} bonds (1.75–1.81Å). Se-O_{br}-Se angles are between 117° and 126°. The coordination numbers of the *A* cations correlate to their size.

Raman and IR spectra show a great similarity with slight differences according to different *A* cations and symmetry. The modes can be assigned by comparison to other compounds containing ditetrahedral units $E_2O_7^{n-}$ [6].

The crystallographic data are as follows: $Li_2Se_2O_7$: orthorhombic, *Pnma*, $Z = 4$, $a = 13.815(3)$Å, $b = 8.452(2)$Å, $c = 5.0585(9)$Å; $Na_2Se_2O_7$: triclinic $P{-}1$, $Z = 2$, $a = 6.990(1)$Å, $b = 6.994(1)$Å, $c = 7.083(1)$Å, α=83.32(3)°, ß = 64.56(3)°, γ=81.18(3)°; $K_2Se_2O_7$: monoclinic, *C*2/*c*, $Z = 4$, $a = 12.851(3)$Å, $b = 7.568(2)$Å, $c = 7.500(2)$Å, ß = 93.35(3)°; $Rb_2Se_2O_7$: monoclinic, *C*2/*c*, $Z = 4$, $a = 13.118(3)$Å, $b = 7.796(2)$Å, $c = 7.781(2)$Å, ß = 94.03(3)°; $Cs_2Se_2O_7$: triclinic, $P{-}1$, $Z = 10$, $a = 7.7271(3)$Å, $b = 16.2408(8)$Å, $c = 18.4427(8)$Å, α=89.685(2)°, ß = 89.1923(2)°, γ=76.251(2)°.

[1] C. Logemann, J. Witt, M. S. Wickleder *Z. Kristallogr. NCS* 228(2013)159-160.

[2] Ståhl, K.; Balic-Zunic, T.; da Silva, F.; Eriksen, K. M.; Berg, R. W.; Fehrmann, R.: *J. Solid State Chem. 178(2005)1697-1704.*

[3] Lynton, H.; Truter, M. R.: *J. Chem. Soc*. (1960)5112-5118.

[4] Ståhl, K.; Berg, R. W.; Eriksen, K. M.; Fehrmann, R.: *Acta Crystallogr.* B65(2009)551-557.

[5] I. V. Morozov, S. I. Troyanov, A. Stiewe, E. Kemnitz *Russ. J. Inorg. Chem*. 44(1999)1536-1541.

[6] R. Paetzold, H. Amoulong, A. Ruzicka *Z. Anorg. Allg. Chem.* 336(1965)278-285.

MS05-P31

Synthesis and Crystal Structure of the Scandium(III) Fluoride Oxoselenate(IV) ScF[SeO_3]

S.- C. Chou[1], T. Schleid[1]
[1]*Institut für Anorganische Chemie, Uni Stuttgart, Stuttgart, Germany*

The scandium(III) fluoride oxoselenate(IV) ScF[SeO_3] can be synthesized through common solid-state reactions. So ScF[SeO_3] was obtained phase-pure by reacting mixtures of Sc_2O_3, ScF_3, and SeO_2 (molar ratio: 1 : 1 : 3) together with CsBr as fluxing agent in corundum crucibles embedded into evacuated glassy silica ampoules after firing at 700 °C for seven days. ScF[SeO_3] crystallizes monoclinically in space group $P2_1/m$ with a = 406.43(2), b = 661.09(4), c = 632.35(4) pm, β = 93.298(3)° and Z = 2. It is not isotypic with YF[SeO_3] [1] or LuF[SeO_3] at room temperature [2], but with the high-temperature form of LuF[SeO_3] [3]. Therefore the crystal structure contains only one crystallographically distinct type of Sc^{3+} cation, which is surrounded by five oxygen atoms from four $[SeO_3]^{2-}$ groups and two F^- anions forming a pentagonal bipyramid $[ScO_5F_2]^{9-}$. These $[ScO_5F_2]^{9-}$ polyhedra arrange as infinite strands 1D-$\{[ScO_{5/1}F_{2/2}]^{8-}\}$ along [100] by sharing common F^- vertices with F^--Sc^{3+}-F^- angles almost at 180°. The resulting strands are further connected with each other along the [010] direction through *trans*-oriented O2⋯O2 edges to build up 2D-$\{[Sc(O2)_{4/2}(O1)_{1/1}F_{2/2}]^{4-}\}$ layers. Finally, the charge balance and the three-dimensional interconnection of these 2D-$\{[Sc(O2)_{4/2}(O1)_{1/1}F_{2/2}]^{4-}\}$ layers occurs via Se^{4+} cations in discrete ψ^1-tetrahedral $[SeO_3]^{2-}$ anions. Worth noticing is that the whole crystal structure is strongly influenced by stereochemical lone-pair activity of these $[SeO_3]^{2-}$ groups. This provides another main structural feature of empty channels along [100], which are filled with the non-bonding lone-pair electrons at the Se^{4+} cations of the tripodal $[SeO_3]^{2-}$ anions.

[1] C. Lipp, Th. Schleid, *Z. Anorg. Allg. Chem.* 2008, *634*, 657-661.
[2] C. Lipp, Th. Schleid, *Z. Anorg. Allg. Chem.* 2007, *633*, 1429-1434.
[3] C. Lipp, R. E. Dinnebier, Th. Schleid, *Inorg. Chem.* 2013**,** *52*, 10788-10794.

Figure 1**.** The pentagonal bipyramids $[ScO_5F_2]^{9-}$ are connected with each other through common edges along [010] and common vertices along [100] forming 2D-$\{[Sc(O2)_{4/2}(O1)_{1/1}F_{2/2}]^{4-}\}$ layers in the crystal structure of ScF[SeO_3].

Figure 1

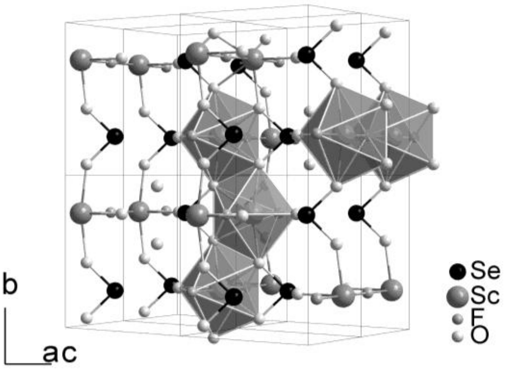

MS05-P32

On the first boroselenates(VI)

H. Hillebrecht[1], M. Daub[1]
[1]*University Freiburg , Inorganic Chemistry, Freiburg, Germany*

Recently the first borosulfates were synthesized and structurally characterised [1-3]. Their relation to silicates [4] and borophosphates [5] is obvious, but there are also some new features. The substitution of sulfate by selenate seems to be trivial, but the much higher oxidation power of Se(VI) (S/SO_4^{2-}: E° = +0.158 V; Se/SeO_4^{2-}: E° = +1.15V) is an experimental challenge.

Heating appropriate mixtures of boron acid H_3BO_3, selenium acid H_2SeO_4 and the corresponding carbonates A_2CO_3 in a silica crucible to 500-750 K followed by slow cooling to RT yielded in colourless, hygroscopic single crystals of the boroselenates. They were characterized by structure analyses, powder-XRD, Raman- and IR spectra.

$Rb_3[B(SeO_4)_3]$ (*Ibca*, Z = 8, a = 7.5079(15)Å, b = 15.249(3)Å, c = 23.454(5)Å) is isotypic to $Ba_3[B(PO_4)_3]$ [6] and $A_3[B(SO_4)_3]$ (A = K, Rb) [2].Each BO_4 tetrahedron is surrounded by four SeO_4 tetrahedra. Two of them connect by common corners to the next BO_4 tetrahedron while the two remaining ones are terminal. According to Liebau they are classified as open branched vierer single chains.

Monoclinic **$Cs_3[B(SeO_4)_3]$** ($P2_1/c$, Z = 4, a = 11.3553(4)Å, b = 7.9896(3)Å, c = 15.7692(6)Å, β = 101.013(1)°) represents a distorted variant of $Rb_3[B(SeO_4)_3]$. The symmetry reduction results from a concordant rotation of the chains.

The tetragonal structure of **$H_3ONa_6[B(SeO_4)_4(SeO_4)]$** (*I*-4, Z = 4, a = 8.9796(1)Å, c = 18.2614(2)Å) contains tetrahedral (open branched) pentameric $[B(SeO_4)]^{5-}$ units as they were also found in $K_5[B(SO_4)_4]$ [1] and $Na_5[B(SO_4)_4]$ [2]. Additionally, there are isolated SeO_4^{2-} tetrahedra. This structure principle is known from $A_6[B(PO_4)_4(PO_4)]$ (A = Sr, Pb) [7,8].

In triclinic **$HK_4[B(SeO_4)_4]$** (P–1, $Z = 6$, $a = 7.5303(1)$Å, $b = 7.7584(1)$Å, $c = 42.6359(1)$Å, α=88.741(1)°, ß = 89.118(1)°, γ=89.971(2)°) the pseudo-tetragonal structure contains isolated pentameric units arranged in layers in the *a-b* plane.

The boroselenates (VI) continue the series of silicate-analogue compounds with edge-sharing tetrahedra. The ratio BO_4/SeO_4 determines the topology of the structures. With a ratio 1:3 there are chains, with 1:4 isolated supertetrahedral units and with 1:5 supertetrahedra with additional SeO_4 units.

[1] H.A. Höppe, K. Kazmierczak, M. Daub, K. Förg, F. Fuchs, H. Hillebrecht, *Angew. Chem*, 2012, *124*, 6359.
[2] M. Daub, K. Kazmierczak, P. Gross, H. Höppe, H. Hillebrecht *Inorg. Chem.* 2013, *52*, 6011.
[3] M. Daub, K. Kazmierczak,H. Höppe, H. Hillebrecht *Chem. Eur. J.* 2013, *19*, 16954.
[4] F. Liebau Structural Chemistry of Silicates, Springer Verlag, Heidelberg, 1985.
[5] B. Ewald. Y.-X. Huang, R. Kniep *Z. Anorg. Allg. Chem.* 2007, *633*, 1517.
[6] R. Kniep, G. Goezel, B. Eisenmann, C. Roehr, M. Asbrand, *Angew. Chem. Int. Ed*. 1994 *33*, 749.
[7] E. L. Belokoneva, E. A. Ruchkina, O. V. Dimitrova, S. Yu. Stefanovich, *Russ. J. Inorg. Chem*. 2001, *46*,179.
[8]N. Shin, J. Kim, D. Ahn, K.-S. Sohn, *Crystallogr.* 2005, *C61*, i54.

MS05-P33

$Sc_2Te_3O_9$: A New Crystal Structure of the Rare-Earth Metal(III) Oxotellurates(IV) with the Composition $M_2Te_3O_9$

S.- C. Chou[1], T. Schleid[1]
[1]*Institut für Anorganische Chemie, Uni Stuttgart, Stuttgart, Germany*

Ternary rare-earth metal(III) oxotellurates(IV) with the chemical formula $M_2Te_3O_9$ are known with four different crystal structures depending upon the size of the involved M^{3+} cation: A1-type for M = La, Ce and A2-type for M = Pr, Nd [1], B-type for M = Y, Sm - Er [2, 3], and C-type for M = Tm - Lu [4]. Now we were able to synthesize a new $M_2Te_3O_9$ compound even with the last missing rare-earth metal, namely $Sc_2Te_3O_9$, from reactions of Sc_2O_3 with TeO_2 (molar ratio: 1 : 2) together with CsBr as fluxing agent in evacuated glassy silica ampoules after firing at 850 °C for ten days. $Sc_2Te_3O_9$ crystallizes monoclinically in space group $P2_1/n$ with $a = 523.34(4)$, $b = 243.81(2)$, $c = 686.43(6)$ pm, $\beta = 106.932(3)°$ and Z = 2. It represents a new D-type crystal structure for the composition $M_2Te_3O_9$ with all atoms residing at the *Wyckoff* position 4e (site symmetry: 2). The crystal structure contains two crystallographically distinct types of Sc^{3+} cations, which are both surrounded by six oxygen atoms forming $[ScO_6]^{9-}$ octahedra with d(Sc1-O) = 206 - 219 pm and d(Sc2-O) = 203 - 223 pm. The octahedra $[(Sc1)O_6]^{9-}$ share common O1⋯O1 and O4⋯O4 edges generating zig-zag chains, which are further grafted by the $[(Sc1)O_6]^{9-}$ octahedra through common O5 vertices to build up serrated 1D-$\{[Sc_2O_{17/2}]^{11-}\}$ chains running along the [100] direction (Figure. 1, *left*). These 1D-$\{[Sc_2O_{17/2}]^{11-}\}$ chains arrange in a staggered manner (ABA) parallel to the crystallographic b direction, where A and B are related to each other by the symmetry elements of the 2_1 screw axis and the n glide plane (Figure. 1, *right*). Finally, the crystal structure of $Sc_2Te_3O_9$ is completed by three crystallographically independent Te^{4+} cations with stereochemically active lone pairs in discrete ψ^1-tetrahedral $[TeO_3]^{2-}$ units (d(Te-O) = 184 - 191 pm).

[1] S.-C. Chou, S. Strobel, Th. Schleid, *Z. Anorg. Allg. Chem.* 2014, in preparation.
[2] S. F. Meier, P. Höss, Th. Schleid, *Z. Anorg. Allg. Chem.* 2009, *635*, 768-775.
[3] S.-C. Chou, Th. Schleid, *Z. Naturforsch.* 2014, in preparation.
[4] P. Höss, S. F. Meier, Th. Schleid, *Z. Anorg. Allg. Chem.* 2013, *639*, 2548-2553.

Figure 1. Strands of the composition 1D-$\{[Sc_2O_{17/2}]^{11-}\}$ running along [100] (left) and a view along [100] at the crystal structure of $Sc_2Te_3O_9$ (*right*).

Figure 1

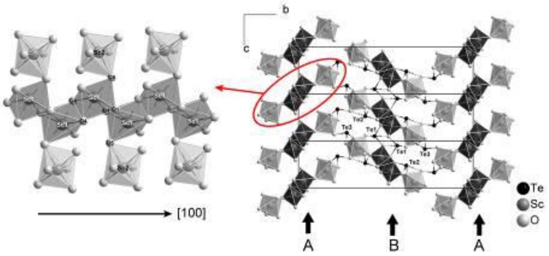

MS05-P34

The high pressure spinel-type Si3N4 phase and its capability for oxygen incorporation

A. Köhler[1], C. Schimpf[2], V. Klemm[2], D. Rafaja[2], T. Schlothauer[3], K. Keller[3], G. Heide[3], M. Schwarz[1], E. Kroke[1]
[1]*TU Bergakademie Freiberg, Institute of Inorganic Chemistry, Freiberg, Germany*
[2]*TU Bergakademie Freiberg, Institute of Materials Science, Freiberg, Germany*
[3]*TU Bergakademie Freiberg, Institute of Mineralogy, Freiberg, Germany*

The high pressure spinel-type γ-Si_3N_4 phase is known since almost 15 years [Zerr1999]. But the role of oxygen impurities which in reality occur in this material was not studied until now. By fabrication of shockwave synthesized samples, we present the chemical and structural characterization of γ-$Si_3(N,O)_4$ material with different degree of oxygen contamination. The samples were investigated by Elementary Analysis by Carrier Hot Gas Extraction (CHGE), XRD, Neutron Diffraction and TEM including EELS and EDX. The overall oxygen content measured by CHGE reaches from about 7 wt% to

12 wt% depending on the oxygen contamination of the starting material. Concomitantly to the spinel-type γ-Si_3N_4 phase an amorphous phase occurs. Its fraction increases with increasing the oxygen content By EELS measurements it was confirmed that the amorphous phase contains more oxygen than the crystalline phase. The incorporation of the oxygen into the spinel type γ-Si_3N_4 lattice in a possible metastable solid solution series $Si_{3-y}O_xN_{4-x}$ was investigated by Neutron Diffraction in more detail. The determined value of about $x = 0.4$ is similar to the value determined by CHGE after etching of the as-received powders by hydrofluoric acid. Thus, we conclude a small amount of oxygen can be incorporated in the spinel structure but an excess of oxygen leads to the formation of an amorphous phase. The deficiency of silicon determined by Neutron Diffraction is $y = 0.2$. The silicon vacancies only occur on the octahedral site which is in contrast to theoretical predictions [Kroll2003].

[Zerr1999] A. Zerr, G. Miehe, G. Serghiou, M. Schwarz, E. Kroke, R. Riedel, H. Fueß, P. Kroll, and R. Boehler. Synthesis of cubic silicon nitride. Nature 400 (1999), 340.

[Kroll2003] P. Kroll, M. Milko, Theoretical Investigation of the Solid State Reaction of Silicon Nitride and Silicon Dioxide forming Silicon Oxynitride under Pressure, Z. Anorg. Allg. Chem. 629 (2003) 1737.

MS05-P35

Phase transitions of perovskites with the chemical composition Ca(Ti,Fe,Mn)O_{3-d}

S. Stöber[1], H. Pöllmann[1]
[1]*Institut für Geowissenschaften, Halle (Saale), Germany*

Phases with perovskite and perovskite-type structures have a strong technical potential for example in the field of fuel cells, as catalysts, clinker phases in different types of cements. Because temperature is an important factor in all of those fields of technical interests, those phases were investigated for possible phase transitions, stability fields and disintegration temperatures.

Perovskite solid solutions with the chemical composition $CaFe_xTi_{(1-x)/2}Mn_{(1-x)/2}O_{3-d}$ with $0 \leq x \leq 0.33$ were synthesised by the Pechini process, applying Ca-, Fe-, Mn- nitrates and $C_{12}H_{28}O_4Ti$ together with citric acid and ethylene glycol. After sintering the precursors pure perovskites with space groups Pnma and I4/mcm were obtained. X-ray data were collected on a Panalytical X`pert and Empyrean system equipped with a HTK 16 and a HTK 1200 applying copper and molybdenum radiation.

The structures of those ternary perovskites are composed of octahedra, which belong to specific tilting systems described by Glazer (1972), Howard et al. (1998), Woodward (1997). Under the influence of non ambient temperatures phase transitions orthorhombic <=> tetragonal <=> cubic were detected and are related closely wit the Iron content of the perovskite solid solutions.

References
Glazer, A. (1972): „The classification of tilted octahedra in perovskites.“ Acta Crystallographica Section B 28(11): 3384-3392.
Howard C. J. and Stokes H. T. (1998): „Group-Theoretical Analysis of Octahedral Tilting in Perovskites.“ Acta Crystallographica Section B 54(6): 782-789.
Woodward, P. (1997): „Octahedral Tilting in Perovskites. I. Geometrical Considerations.“ Acta Crystallographica Section B 53: 32-43.
Woodward, P. (1997): „Octahedral Tilting in Perovskites. II. Structure Stabilizing Forces.“ Acta Crystallographica Section B 53: 44-66.

MS05-P36

Tantalum and vanadium substitution in potassium tungsten bronzes

M. S. Rahman[1], M. M. Murshed[1], T. M. Gesing[1]
[1]*Universität Bremen, Institut für Anorganische Chemie, Bremen, Germany*

Potassium tungsten bronzes $K_x(W^{6+}_{1-x}W^{5+}_x)O_3$ (0 < x < 1) show variety of phases depending on the concentration of x [1]. Crystal structures and physical properties of hexagonal potassium tungsten bronzes (K-HTB) draw particular attention for rich electrical properties [2] due to concomitant presence of W^{5+} and W^{6+} ions in the same crystallographic sites and K^+ cations in the hexagonal tunnels of the lattice. Similar crystal structures are formed when W^{5+} ions are substituted by ions of lower valence exhibit significant change of their second-harmonic generation, piezoelectric, pyroelectric, and ferroelectric properties [3]. Here we report on synthesis and characterizations of $K_{0.3}(W^{6+}_{0.7}W^{5+}_{0.3-x}M^{5+}_x)O_3$ (M = Ta^{5+} and V^{5+}; x = 0 - 0.3), where W^{5+} has been successively replaced by Ta^{5+} or V^{5+} to investigate the range of chemical miscibility using two different sizes of five-fold cations. Samples were prepared by solid state reactions using K_2WO_4, WO_2, WO_3, Ta_2O_5 and V_2O_5 at 1073 K. The polycrystalline Ta^{5+} and V^{5+} substituted bronzes show cream white and brown color, respectively, $K_{0.3}(W^{6+}_{0.7}W^{5+}_{0.3})O_3$ is deep blue. Space group $P6_322$ of $K_{0.3}(W^{6+}_{0.7}W^{5+}_{0.3})O_3$ has been established by X-ray powder diffraction along with Raman spectroscopy. In the K-HTB bronzes, W^{5+} was fully replaced by Ta^{5+}, whereas V^{5+} could only be substituted up to x = 0.15. Both Ta^{5+} and V^{5+} cations were statistically distributed on the W^{5+}/W^{6+} sites. Replacing smaller W^{5+} ions (62 pm [4]) by larger Ta^{5+} ions (64 pm [4]) in $K_{0.3}(W^{6+}_{0.7}W^{5+}_{0.3-x}Ta^{5+}_x)O_3$ the average W/Ta-O bond distances slightly increase from x = 0.05 to 0.20, the mean octahedral quadratic elongation scattered close to a mean value of 1.02, and the inter-octahedral W-O-W bond angle significantly decreases. These combined effects led to cooperative rotation of the ‘rigid unit’ like WO_6

octahedra, resulting in expansion of the *c*-axis, contraction of the *a*-axis and a total slight contraction of the cell-volume. Upon further increase of the tantalum concentration (x = 0.2 - 0.3) the WO_6 octahedra show 'quasi-rigid unit' like behavior with a steep increase of mean W-O bond distance leading to an overall increase of the cell-volume. The $K_{0.3}(W^{6+}{}_{0.7}W^{5+}{}_{0.3-x}V^{5+}{}_{x})O_3$ bronzes show similar behavior in terms of metric parameter change with respect to successive replacement of W^{5+} with V^{5+} however, limited to x = 0.15. In this series the observed cell-volume contraction is much higher than in $K_{0.3}(W^{6+}{}_{0.7}W^{5+}{}_{0.3-x}Ta^{5+}{}_{x})O_3$ with comparable x from 0 to 0.15. Incorporating Ta^{5+} and V^{5+} cations in the K-HTB structure led to distortions of the MO_6 octahedra driven by second order Jahn-Teller effects.

[1] P. G. Dickens, M. S. Whittingham, *Q. Rev. Chem. Soc*. 22 (1968) 30.
[2] K. S. Lee, D. K. Seo, M. H. Whangho, *J. Am. Chem. Soc*. 119 (1997) 4043.
[3] H. Y. Chang, T. Sivakumar, K. M. Ok, P. S. Halasyamani, *Inorg. Chem*. 47 (2008) 8511.
[4] R. D. Shannon, *Acta Crystallogr*. A32 (1976) 751.

MS05-P37

Synthesis and crystal structure of new mixed metal oxide fluorides with ReO_3-type structure

S. Nakhal[1]
[1]*Technische Universität Berlin, Institut für Chemie, Berlin, Germany*

In the last years several attempts have been made to increase the voltage of lithium ion batteries. For this reason fluorides and oxide fluorides as cathode materials became more and more in the focus of interest of battery research (e.g. [1]). Oxide fluorides with rutile-type structure (*M*OF, *M* = transition metal) are promising candidates also due to their high theoretical capacity. In addition, literature reports also transition metal oxide fluorides exhibiting the cubic ReO_3-type structure (for example NbO_2F and $TiOF_2$). Li-containing phases were prepared by treatment with *n-Bu*Li [2]. The electrochemical properties of $M(O,F)_3$ compounds were investigated and described [3].

New mixed metal ReO_3-type oxide fluorides $MNb_2O_3F_6$ (M = Mg, Zn), $MgTi_2OF_8$, and $TiNb_2O_5F_4$ were prepared by treatment of their corresponding oxides (MNb_2O_6 (M = Mg, Zn), $MgTi_2O_5$, $TiNb_2O_7$) as precursors with a 1:1 mixture of an aqueous solution of hydrofluoric acid HF and HNO_3. The mixture was stirred in a PTFE cask under constant heating until the solvent was evaporated. All the mentioned oxide fluorides crystallize in the ReO_3 type (cubic, space group *Pm*-3*m*). The prepared colorless powders were characterized by means of hot gas extraction and X-ray diffraction (XRD) incl. Rietveld refinement.

[1] E. Gonzalo, A. Kuhn, F. Garcia-Avarado, *J. Power Sources* 2010, 195(15), 4990-4996.
[2] D.W. Murphy, M. Greenblatt, R.J. Cava, S.M. Zahurak, *Solid State Ionics* 1981, 5, 327.
[3] M.V. Reddy, S. Madhavi, G.V. Subba Rao, B.V.R. Chowdari, *J. Power Sources* 2006, 162, 1312-1321.

Fig.1: X-ray powder diagrams of $MgNb_2O_3F_6$ (left) and $TiNb_2O_5F_4$ (right) with the results of the Rietveld refinements.

Figure1

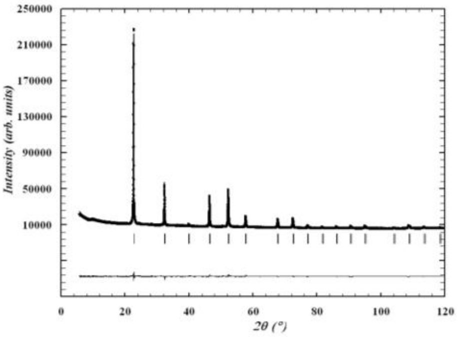

Figure 2

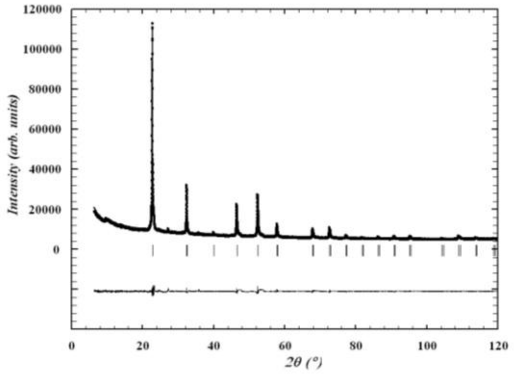

MS05-P38

Thermodynamics of Oxygen Incorporation into Bixbyite-Type Vanadium Sesquioxide

C. Reimann[1], T. Bredow[1]
[1]*University of Bonn, Mulliken Center for Theoretical Chemistry, Bonn, Germany*

During the preparation of metastable vanadium sesquioxide with bixbyite structure careful adjustment of the reaction conditions was necessary to prevent oxidation to higher valent vanadium oxides [1]. In order to study the thermodynamics of this oxidation process, we performed periodic quantum-chemical calculations at density-functional theory level [2]. Due to the complicated Mott-Hubbard physics of V_2O_3 that pure density functionals fail to describe properly, we checked our DFT results using a hybrid method with 12 % Hartree-Fock exchange.

Initially different defect structures for non-stoichiometric phases with the general composition V_2O_{3+x} were examined. These have been obtained either by removing single atoms from their respective lattice positions or by introducing additional atoms into otherwise empty lattice sites. Concluding that the stoichiometric phase is likely to incorporate excess oxygen into the empty *16c* Wyckoff position, we next investigated these non-stoichiometric phases in greater detail. It turned out that insertion of up to 0.7 equivalents of oxygen is possible into bixbyite-type V_2O_3 without significant structural transformations.

Performing frequency calculations to include vibrational and entropic contributions, we found that incorporation of additional oxygen atoms is preferred thermodynamically at ambient pressure. Therefore it is necessary to shift the equilibrium towards the stoichiometric phase during the synthesis, which can be accomplished by taking the oxygen partial pressure $p(O_2)$ into account explicitly. Our calculated value for $p(O_2)<10^{-17}$ bar necessary for stabilization of pure V_2O_3 under reaction conditions (T=873 K) is in semi-quantitative agreement with the experimental observation.

[1] D. Weber, A. Stork, S. Nakhal, C. Wessel, C. Reimann, W. Hermes, A. Müller, T. Ressler, R. Pöttgen, T. Bredow, R. Dronskowski, M. Lerch, Inorg. Chem. **50**, 6762-6766 (2011).
[2] C. Reimann, D. Weber, M. Lerch, T. Bredow, J. Phys. Chem. C 117, 20164-20170 (2013).

Figure 1: Conventional unit cell of bixbyite-type V_2O_3 (larger blue spheres: V, smaller red spheres: O). The yellow tetrahedra mark the 16c Wyckoff position.

Figure 1

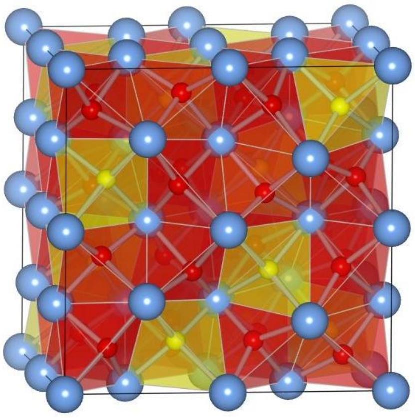

MS05-P39

The effects of cooling process on the phases and particle sizes of vanadium slag

L. Li[1], W. Ge[1], L. Chen[1], Y. Chen[1]
[1]*PanGang Group Research Institute Co., Ltd., Panzhihua, China*

The vanadium slag is recovered from vanadium-containing hot metal by combined-blowing converter, which is cooled in the slag tank. The effects of cooling time on the different phases and particle size of vanadium slag were investigated. The experimental results show that the holding times of vanadium slag in the slag tank increase from 8 hours to 48 hours, the grain sizes of 60% vanadium spinel increase from about 45 microns to approximately 65 microns, and the spinel phase contents remain at 40-46%. The crystalline phases in silicate are iron manganese olivine, ferromanganese olivine and pyroxene. Where the grain size of square, bar-shaped ferromanganese olivine is up to 200 microns, the grain size of square-shaped iron manganese olivine is nearly 180 microns. The cryptocrystalline structure and fine grain are appeared in pyroxene. The difference of cooling rate makes temperature fluctuations of the phase formation in vanadium slag, resulting in different nucleation ratio. The particle sizes of phases in vanadium slag grow with the increase of cooling time.

MS05-P40

Nanoindentation and crystallographic/spectroscopic characterization of Ta_2TiO_7 single-crystals and ceramics

L. Perfler[1], V. Kahlenberg[1], C. Wikete[2], R. Kaindl[3]
[1]*University of Innsbruck, Institute of Mineralogy and Petrography, Innsbruck, Austria*
[2]*University of Innsbruck, Insitute for Structural Engineering and Material Sciences, Innsbruck, Austria*
[3]*JOANNEUM RESEARCH, Materials - Institute for Surface Technologies and Photonics, Niklasdorf, Austria*

Ta_2TiO_7 shows interesting chemical and physical properties, for example, as promising anode materials for Li-ion batteries [1]. Since Ta_2TiO_7 is expected to have high refractive indices (n > 2,25) we tried to characterize this material in more detail using single-crystal X-ray diffraction, Raman spectroscopy as well as nanoindentation and electron microprobe analysis.

Colorless single-crystals of Ta_2TiO_7 were grown directly from melt at 1700°C. Stoichiometric amounts of the dried starting materials (Alfa Aesar, Nb_2O_5 99.999%, Ta_2O_5 99.85%, TiO_2 > 99%) were homogenized in a planetary ball mill with ethanol. The pressed starting mixture was placed on an iridium foil and fired in a muffle furnace from 1000 to 1700°C with a heating ramp of 5°C/min. After a dwell time of 10 min the melt was cooled down from 1700 to 900°C with a ramp of 0.5°C/min and subsequently quenched in air. Polycrystalline Ta_2TiO_7 was additionally prepared by solid-state reactions in a platinum crucible at 1500 and 1350°C, respectively. After a dwell time of 48h the samples were cooled down to 100°C with a ramp of 1.5°C/min.

Structure analysis of the Ta_2TiO_7 single-crystals resulted in the following crystallographic data: monoclinic symmetry, space group *I2/m*, a = 17.6813(12), b = 3.8044(2), c = 11.8448(8) Å, ß = 95.127(6)°, V = 793.57(9) $Å^3$, Z = 6. The crystal structure consists of distorted $(Ta,Ti)O_6$ octahedra sharing corners and edges. Among the different octahedral sites the Ti^{4+} and Ta^{5+} cations are distributed randomly.

From the selection rules of factor group C_{2h} a total number of 114 vibrational modes are predicted for monoclinic Ta_2TiO_7 with the following irreducible representations: $\Gamma_{opt.} = 36A_g + 20A_u + 18B_g + 40B_u$. These calculations for the monoclinic structure show that 54 modes ($36A_g + 18B_g$) are Raman-active while 60 modes are IR-active ($20A_u + 40B_u$). As a result only non-degenerated modes are expected in the Raman spectrum of Ta_2TiO_7. Raman spectra, excited with the 532 nm emission line of a frequency doubled Nd:YAG laser, exhibit strong Raman bands at 1020, 360, 280, 273, 116, 97, 79, 75 cm^{-1}, medium bands at 900, 717, 693, 674, 577, 384, 334, 318, 299, 244, 223, 207, 185, 143, 138, 130, 68 cm^{-1} and weak bands at 1059, 506, and 432 cm^{-1}.

Nanoindentation experiments were performed with a Berkovich diamond indenter tip to determine the hardness and elastic modulus of Ta_2TiO_7. For sample preparation the Ta_2TiO_7 single-crystals were embedded in resin and polished to a mirror-like flat surface. 54 indents (9x6 grid) with a distance of 10 µm were made with a maximum load of 20 mN. Atomic force micrographs displayed indents with a max. depth of 300 ± 6.8 nm . Analysis of the load-displacement curves revealed a hardness of 8.95 ± 0.54 GPa and a reduced elastic modulus of 149 ± 7.63 GPa.

[1] Saritha D., Varadaraju U. V., Materials Research Bulletin 2013, Vol. 48, p2702-2706.

MS05-P41

Crystalline phase formation during the atomic layer deposition of TiO_2

B. Abendroth[1], S. Rentrop[1], T. Moebus[1], J. Dietel[1], H. Stöcker[1], D. C. Meyer[1]
[1]*TU Bergakademie Freiberg, Institut für Experimentelle Physik, Freiberg, Germany*

TiO_2 is a wide gap semiconductor and is, based on its optical and electronic properties, widely used in various applications. For its use as thin dielectric layer in microelectronic data storage or in electrochemical energy storage devices, TiO_2 is commonly produced by atomic layer deposition (ALD). In this work we present the deposition of TiO_2 thin films by ALD from tetrakis(dimethylamino) titanium and water on silicon and polycrystalline TiN substrates for the use in metal - insulator - metal resistive switching random access memory cells. For this application, amorphous TiO_2 layers are desirable to minimize leakage currents, however, other applications of TiO_2 layers, such as a high k gate dielectric or photocatalysis require crystalline structures of either rutile or anatase polymorph. Here, the crystalline phases of TiO_2 ALD layers of 5 to 100 nm thickness are investigated by glancing angle x-ray diffraction. For the deposition of TiO_2 on silicon substrates with an amorphous native oxide layer by our ALD process, we find a dependence of crystallisation of anatase and rutile on the deposition temperature and layer thickness. A survey of literature data on TiO_2 ALD based on various precursors, shows that our results are representative for thermal ALD of TiO_2 on silicon substrates and can be summarized in a general thickness - temperature - phase diagram.

The initiation for crystalline growth is much stronger on crystalline substrates. For example, using RuO2 interlayers, which provide already a surface with rutile structure and small lattice mismatch, ALD of TiO_2 results exclusively in rutile phase [1]. In this work it is shown, that a polycrystalline TiN surface broadens the stability window for the ALD of anatase with respect to deposition temperature and layer thickness.

Reference
1: M. Popovici et al., Microelectronic Engineering 88 (2011) 1517.

MS05-P42

Synthesis and crystal structure of new mixed metal oxide fluorides AB_2OF_8 (A = Mg, Ti; B = Ti, Zr, Fe)

S. Nakhal[1]
[1]*Technische Universität Berlin, Institut für Chemie, Berlin, Germany*

In recent years, fluorides and oxide fluorides have become more and more in focus of interest as cathode materials for lithium-ion batteries (e.g. [1]). Theoretical work clearly point to a significant increase of the redox potential by partial or total substitution of oxygen by fluorine in oxide materials [2].

The new oxide fluorides $MgTi_2OF_8$, $MgZr_2OF_8$, and Fe_2TiOF_8 were prepared by treatment of their corresponding oxides with a 1:1 mixture of an aqueous solution of hydrofluoric acid HF and HNO_3, stirred in a PTFE cask under constant heating until the solvent was evaporated. $MgTi_2OF_8$ and $MgZr_2OF_8$ crystallize in the $NaSbF_6$ type (cubic, space group *Fm*-3*m*), Fe_2TiOF_8 in the VF_3 type (rhombohedral, space group *R*-3*c*). Both crystal structures types are derived from the simple cubic ReO_3 type. The prepared white powders have been investigated by means of hot gas extraction and X-ray diffraction (XRD) incl. Rietveld refinement (Fig.1).

[1] E. Gonzalo, A. Kuhn, F. Garcia-Avarado, *J. Power Sources* 2010, 195(15), 4990-4996.
[2] Y. Koyama, I. Tanaka and H. Adachi, *J. Electrochem. Soc.* 2000, 147, 3633.

Fig.1: X-ray powder diagrams of $MgZr_2OF_8$ (left) and Fe_2TiOF_8 (right) with the results of the Rietveld refinements.

Figure 1

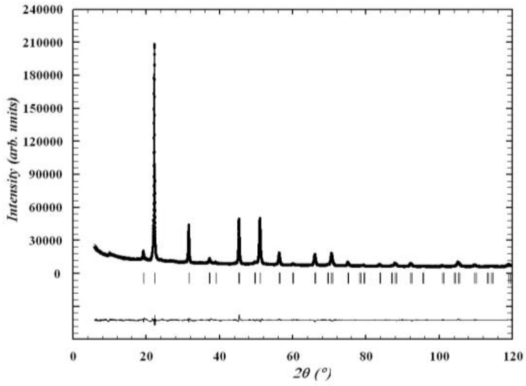

Figure 2

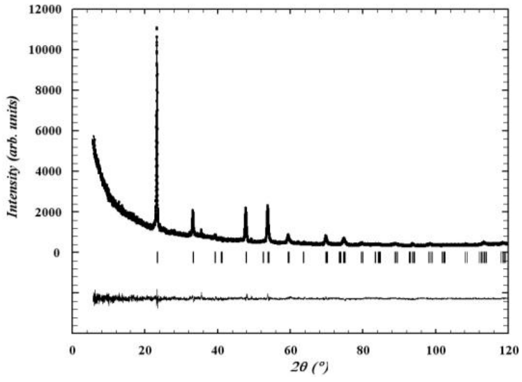

MS05-P43

Pressure-induced phase transitions in VOCl

M. Bykov[1], E. Bykova[1,2], L. Dubrovinsky[2], M. Hanfland[3], S. van Smaalen[1]
[1]*University of Bayreuth, Laboratory of Crystallography, Bayreuth, Germany*
[2]*University of Bayreuth, Bayerisches Geoinstitut, Bayreuth, Germany*
[3]*ESRF, Grenoble, France*

The phase transitions of transition metal oxychlorides with general formula *M*OCl (*M* = Ti, V, Cr, Fe) have been recently intensively studied at low-temperatures and high pressures [1 - 7]. At ambient conditions these compounds are isostructural and possess an orthorhombic space group *Pmmn*. *M*OCl structure consists of double *M*-O layers, which are separated by the bilayers of Cl atoms. These layers are weakly interconnected by the van der Waals interactions. Structural studies at low temperatures allowed systematic examination of the low-dimensional magnetic properties of *M*OCl. Of particular interest was the assessment of the role of the number of *d*-electrons on the dimensionality of the system, on allowed magnetic interactions, and on related structural distortions.

The recent studies on TiOCl, FeOCl and CrOCl have shown the high sensitivity of their properties regarding the application of high pressure. While the high-pressure properties of TiOCl are essentially related to its magnetism, FeOCl and CrOCl undergo pressure-induced phase transitions in the vicinity of 15 GPa, related to weak Cl - Cl interactions [5 - 7]. Despite the similar mechanism of the phase transition, there are noticeable differences in the high-pressure structures of FeOCl and CrOCl and in their compressional behavior. These differences are related to the differences in the ambient-pressure packing of Cl atoms, and to the elasticity of *M*-O framework. In order to extend the understanding of pressure-induced phenomena in *M*OCl and to find out the systematic relations between their high-pressure behavior, we have carried out a single-crystal X-ray diffraction study of VOCl between 0.0001 and 51 GPa.

Below 14 GPa VOCl shows an expected high-pressure behavior characterized by large anisotropic compression of lattice parameters. Between 14 and 16 GPa it undergoes a phase transition similar to those found in FeOCl and CrOCl. Further compression revealed the volume discontinuity, which was not previously observed in *M*OCl. This volume drop is a consequence of the connectivity changes in the structure. So, strong V - Cl bonds appear between the neighboring layers. This phase is stable up to 51 GPa and is not quenchable on decompression. Here we will present the description of all the high-pressure phases of VOCl and will focus on the interpretation of differences and similarities between high-pressure behavior of *M*OCl.

[1] A. Seidel *et al.* Phys. Rev. B. 67, 020405(R) (2003).
[2] J. Angelkort *et al.* Phys. Rev. B. 80, 144416 (2009).
[3] A. Schönleber *et al*. Phys. Rev. B. 80, 064426 (2009).
[4] J. Zhang *et al.* Phys. Rev. B. 86, 134428 (2012).
[5] S. Blanco-Canosa *et al*. Phys. Rev. Lett. 102, 056406 (2009).
[6] M. Bykov *et al* . Phys. Rev. B. 88, 014110 (2013).
[7] M. Bykov *et al*. High Press. Res. 33, 501 (2013).

MS05-P44

Crystal Structures of Group 14 Element Tetrachloridoaluminates

S. Schloots[1], W. Frank[1]
[1]*Heinrich-Heine-Universität Düsseldorf, Institut für Anorganische Chemie und Strukturchemie II, Düsseldorf, Germany*

Thermal analysis of the system $SnCl_2$-$AlCl_3$[1] has revealed the existence of crystalline intermediate compounds of this system and there is some evidence of compound formation in the system $PbCl_2$-$AlCl_3$ from own experiments.

However, no crystal structures of group 14 element tetrachloridoaluminates are reported in the literature, with the exception of some solvates with stabilizing arenes, *e.g.* (arene)$SnCl(AlCl_4)$ and (arene)$Sn(AlCl_4)_2$. arene[2-7] as well as $(arene)_2Pb(AlCl_4)_2$ and (arene)$Pb(AlCl_4)_2$ · arene[8-9].

Here we report on the syntheses and the crystal structures of $Sn(AlCl_4)_2$ (**1**) and $SnCl(AlCl_4)$ (**2**) just as $Pb(AlCl_4)_2$ (**3**) as well as $(Ge_2Cl_3)AlCl_4$ (**4**). Single crystals of **1-3** suitable for X-ray structure analysis were obtained by heating stoichiometric quantities of MCl_2 and sublimated $AlCl_3$ (M=Sn, Pb) to 250 °C for $SnCl_2$ and 400 °C for $PbCl_2$ in evacuated glass ampoules and adjacent cooling (1 °C/h) to room temperature. Single crystals of **4** were received via heating of stoichiometric quantities of $GeCl_4$ and Ge with $AlCl_3$ for 12 hours at 680 °C in quarz glass ampoules and subsequent cooling with 5 °C/h. Crystallographic data of **1 - 4** can be found in the table below.

According to the phase diagram[1] of the system $SnCl_2$-$AlCl_3$, compounds **1** and **2** could be crystallized from the melt.

The solid of **1** contains two crystallographically independent $[AlCl_4]^-$ units, each slightly distorted tetrahedral and one Sn^{2+} distorted triple-capped trigonal prism surrounded by nine Cl atoms and form a 3D network with varying distances Sn-Cl of 2.7245(11) to 3.4841(12) Å.

In the cationic partial structure of **2** $[SnCl]^+$ units build up a waved “ladder structure” perpendicular to the crystallographic *a*-axis. These are linked by the $[AlCl_4]^-$ tetrahedra to form a 3D network.

3 is isotypic to the above-mentioned $Sn(AlCl_4)_2$, as could be expected due to the similar ionic radii of Sn^{2+} (118 pm)[10] and Pb^{2+} (119 pm)[10].

The structure of **4** can be described as an arrangement of cyclic $[Ge_2Cl_2]^{2+}$ fragments bridged by additional Cl^- ions to form polymeric strands. Ge-Cl distances in this polymeric building block are between 2.3918(13) and 2.4738(12) Å. $[AlCl_4]^-$ tetrahedra are located between these strands and build up a 3D network with varying secondary distances Ge-Cl of 3.0282(13) to 3.6233(15) Å.

[1] Y. P. Afinogenov, L. P. Belozerova, *Russ. J. Inorg. Chem.* 1969, 14, 1168.
[2] H. Schmidbaur, T. Probst, B. Huber, G. Müller, C. Krüger, *J. Organomet. Chem.* 1989, 365,53.
[3] H. Schmidbaur, T. Probst, O. Steigelmann, G. Müller, *Heteroatom Chem.* 1990, 2, 161.
[4] M. S. Weininger, P. F. Rodesiler, E. L. Amma, *Inorg. Chem.* 1979, 18, 751.
[5] M. S. Weininger, P. F. Rodesiler A. G. Gash, E. L. Amma: *J. Am. Chem. Soc.* 1972, 94, 2135.
[6] W. Frank, *Z. Anorg. Allg. Chem.* 1990, 585, 121.
[7] H. Schmidbaur , O. Steigelmann, T. Probst, *Organometallics* 1991, 10, 3176.
[8] W. Frank, F.-G. Wittmer, *Chem. Ber.* 1997, 130, 1731.
[9] A. G. Gash, P. F. Rodesiler, E. L. Amma, *Inorg. Chem.* 1974, 13, 2429.
[10] R.D. Shannon, *Acta Crystallogr.* 1976, A32, 751.

Figure 1

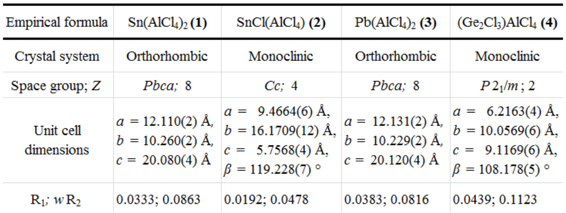

Empirical formula	$Sn(AlCl_4)_2$ **(1)**	$SnCl(AlCl_4)$ **(2)**	$Pb(AlCl_4)_2$ **(3)**	$(Ge_2Cl_3)AlCl_4$ **(4)**
Crystal system	Orthorhombic	Monoclinic	Orthorhombic	Monoclinic
Space group; *Z*	*Pbca;* 8	*Cc;* 4	*Pbca;* 8	$P2_1/m$; 2
Unit cell dimensions	*a* = 12.110(2) Å, *b* = 10.260(2) Å, *c* = 20.080(4) Å	*a* = 9.4664(6) Å, *b* = 16.1709(12) Å, *c* = 5.7568(4) Å, *β* = 119.228(7) °	*a* = 12.131(2) Å, *b* = 10.229(2) Å, *c* = 20.120(4) Å	*a* = 6.2163(4) Å, *b* = 10.0569(6) Å, *c* = 9.1169(6) Å, *β* = 108.178(5) °
R_1; wR_2	0.0333; 0.0863	0.0192; 0.0478	0.0383; 0.0816	0.0439; 0.1123

MS05-P45

Syntheses and crystal structures of $Rb_3Sn_2X_7$ (X = Cl, Br)

H. Hillebrecht[1], G. Thiele[1], B. Serr[1]
[1]*University Freiburg , Inorganic Chemistry, Freiburg, Germany*

Among the halogenometallates $A_xM_yX_z$ (*A* = Rb, Cs; *X* = Cl, Br, I) with *M*(II) = Ge, Sn, Pb the composition AMX_3 is by far the most frequent. The crystal structures can be assigned to a cubic perowskite structure or one of its lower-symmetric variants. This is in line with the ionic ratios. Marked exceptions are the systems Rb/Sn/Cl and Rb/Sn/Br, where no representatives of the composition AMX_3 are known. Precipitation from solutions of Sn(II) halogenides in aquous H*X* yielded the colourless compounds $Rb_3Sn_2Cl_7$ and $Rb_3Sn_2Br_7$. $Rb_3Sn_2Br_7$ is isotyp to the Ge(II)-compounds $(NH_4)_3Ge_2Br_7$ and $Rb_3Ge_2Br_7$ [1] ($P2_1/c$, *Z* = 4, *a* = 10.1759(5) Å, *b* = 12.9070(8) Å, *c* = 13.4969(7) Å, ß= 101.686(4)°). The structure contains two symmetry-independent $SnCl_6$ octahedra with a distortion to 3 + 3 (2.76/3.30 Å) and 2 + 1 + 1 + 2 (2.72/2.93/3.11/3.30 Å) pattern, respectively. In comparison to the Ge compound the differences between long and short distances is less pronounced (18% vs. 30%). The resulting $SnCl_3^-$ or $SnCl_2/SnCl_4^{2-}$ units are isolated, while the $SnCl_6$-octahedra form zig-zag chains of dimers running in (101) direction. These chains can be combines to layers in the a-c plane. The structure of $Rb_3Sn_2Cl_7$ ($P2_1/c$, *Z* = 12, *a* = 9.584(2)Å, *b* = 37.105(7)Å, *c* = 12.927(3)Å, ß = 100.63(3)°) represents a new structure type which is distortion variant of $Rb_2Sn_2Br_7$. The complex structure contains 6 independent Sn atoms with pseudo-octahedral surrounding. Again, the deviation from regularity results from a significant splitting of the Sn-Cl distances. Each 3 Sn atoms have 3 short (2.55-2.65 Å) and 3 long distances (3.15-3.45Å) or 2 short, 2 medium (2.80-3.00Å) and 2 long distances. The enlargement of the unit cell in relation to $Rb_3Sn_2Br_7$ is caused by a slight rotation of the pseudo-octahedral units and a more pronounced splitting on the Sn-Cl distances. As seen from the lattice parameter, the repeating unit in [010] direction are 6 layers.

[1] G.Thiele, H.W.Rotter, K.D. Schmidt Z. Anorg.Allg. Chem. 1989, 578, 149-158.

MS05-P46

Ho_3OFSe_3 and $Ho_3OF_3Se_2$: Two Surprising New Structure Types for Rare-Earth Metall(III) Oxide Fluoride Selenides

D. Zimmermann[1], T. Schleid[1]
[1]*University of Stuttgart, Institute for Inorganic Chemistry, Stuttgart, Germany*

Syntheses for all polymorphs of HoFSe [1] were carried out with holmium metal (Ho), its trifluoride (HoF_3) and selenium (Se) as educts. Standard solid-state reaction methods in glassy silica and tantalum or niobium ampoules caused a lot of problems, e. g. the formation of oxosilicates, oxotantalates or oxoniobates, however, thus corundum (aluminium sesquioxide) was tested as an alternative highly resistant reaction-vessel. Surprisingly, no traces of the desired product HoFSe could be detected in these container, but scattered crystals of the two new holmium oxide fluoride selenides Ho_3OFSe_3 and $Ho_3OF_3Se_2$ were formed instead. Up to now both structure types are only known for the erbium oxide fluoride sulfides Er_3OFS_3 and $Er_3OF_3S_2$ [2]. Mixed light-anion positions emerge as a structural feature of both compounds, but rare-earth metal(III) oxide fluoride selenides were so far known only with the compositions $M_6O_2F_8Se_3$ (M = La, Ce, Nd) and M_2OF_2Se (M = La, Pr, Nd, Sm, Gd - Ho) [3].

Ho_3OFSe_3 crystallizes tetragonally in the space group *I*4/*mmm* (no. 139) with the cell parameters a = 387.10(3), c = 2169.25(17) pm and two formula units per unit cell. Its crystals emerge as plate-shaped specimens with dark-red colour.

In the crystal structure (Figure 1) two crystallographically different Ho^{3+} cations are present. One is coordinated as distorted square antiprism by four Se^{2-} anions in one square and four mixed occupied light anions (F^-: O^{2-}-ratio of 1 : 1) forming the other. The second one is octahedrally coordinated by six Se^{2-} anions as $[HoSe_6]^{9-}$ octahedra generating layers by sharing four common edges. The light anions are centering tetrahedral $(Ho^{3+})_4$ which are units also forming layers by sharing four common edges.

$Ho_3OF_3Se_2$ crystallizes orthorhombically in the space group *Ccce* (no. 68) with the cell parameters a = 552.06(4), b = 1940.98(14), c = 551.84(4) pm and four formula units per unit cell. Its crystals occur as elongated plate-shaped specimens with transparent yellow colour. Again two crystallographically different Ho^{3+} cations are present in this crystal structure (Figure 2). One of them is coordinated as square antiprism by four Se^{2-} anions and four mixed occupied light anions (F^-: O^{2-}-ratio of 3 : 1) as described above, but in addition the square created by the heavy anions is capped by an additional Se^{2-} species. In contrast to Ho_3OFSe_3 the second Ho^{3+} position in $Ho_3OF_3Se_2$ is exclusively coordinated by eight light anions forming slightly twisted square prisms. The light anions are once again tetrahedrally surrounded by Ho^{3+} cations. These tetrahedra compose double layers, which are separated by two layers of Se^{2-} anions.

Figure 1 : Crystal structure of Ho_3OFSe_3 as viewed along [010].
Figure 2 : Crystal structure of $Ho_3OF_3Se_2$ as viewed along [101].

[1] H.-D. Nguyen, C. Dagron, P. Laruelle, *Acta Crystallogr.* 1975, *B 31*, 514-518.
[2] S. Strobel, A. C. Müller, Th. Schleid, *Z. Anorg. Allg. Chem.* 2009, *635*, 1940-1946.
[3] H. Grossholz, *Doctoral Dissertation*, Universität Stuttgart, 2003.

Figure 1

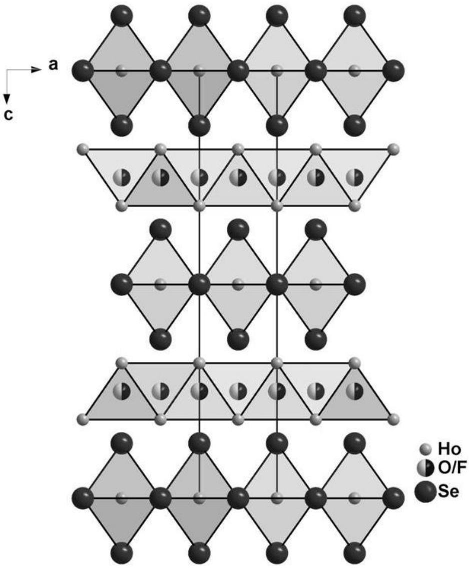

Figure 2

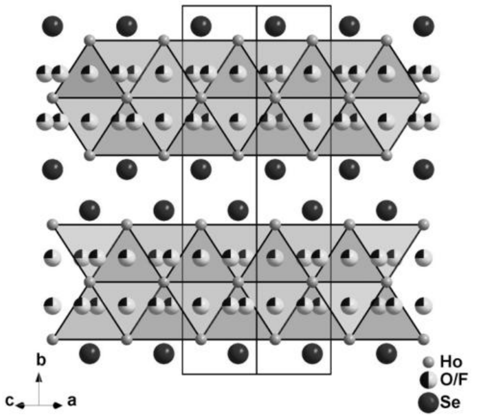

MS05-P47

Synthesis and Crystal Structures of the Dimorphic Holmium(III) Fluoride Selenide HoFSe

D. Zimmermann[1], T. Schleid[1]
[1] *University of Stuttgart, Institute for Inorganic Chemistry, Stuttgart, Germany*

Systems of three components containing rare-earth metal, fluorine and chalcogen with the compositions *M*FS [1], *M*FSe [2] and *M*FTe [2] are well-known to crystallize with the tetragonal PbFCl-type structure with only few trigonal or hexagonal exceptions [3].

Another exception was now found for the selenides with HoFSe, first described for YFSe [4] and later for ErFSe [5] in terms of crystal structures. It even occurs in both different prototypic structures. Both polymorphs of straw yellow HoFSe have planar $[FHo_3]^{8+}$ triangles as central building unit. The structure with the smaller unit cell (HoFSe-I) shows only monomeric strands of edge-sharing triangles, whereas the structure with the larger unit cell (HoFSe-II) exhibits trimeric strands. In HoFSe-I the unique Ho^{3+} cation is coordinated by two axial Se^{2-} and two Se^{2-} along with three F^- anions in the plane as pentagonal bipyramid. The same coordination is also found in HoFSe-II, but moreover a second Ho^{3+} position as octahedrally coordinated cation by only six Se^{2-} anions and even a third one, again coordinated axially by two Se^{2-} now with a hexagonal ring of six F^- anions forming a bipyramid like in the B- and C-type structures of YFS and LuFS [3], are present.

Both polymorphs crystallize orthorhombically with the space group *Pnma* and the lattice parameters a = 989.48(9), b = 408.16(3), c = 629.99(6) pm (Z = 4) for HoFSe-I or a = 993.45(6), b = 411.12(3), c = 1877.36(11) pm (Z = 12) for HoFSe-II, indicating type I as high-pressure form as judged from its higher density (6.86 g/cm^3 vs. 6.83 g/cm^3).

Figure 1. Fractional atomic coordinates and equivalent isotropic displacement parameters for HoFSe-I (top) and HoFSe-II (bottom).

Figure 2**.** Orthorhombic unit cells of both HoFSe polymorphs (I: left, II: right) as (010) projections.

References
[1] H. Grossholz, Th. Schleid, *Z. Anorg. Allg. Chem.* 2001, *627*, 2693-2699.
[2] V. S. Filatkina, G. N. Kustova, S. S. Batsanov, *Izv. Akad. Nauk SSSR Ser. Khim.* 1972**,** 2171-2110.
[3] Th. Schleid, *Z. Anorg. Allg. Chem.* 1999, *625*, 1700-1706.
[4] H.-D. Nguyen, *Acta Crystallogr.* 1973, *B 29*, 2095-2097.
[5] H.-D. Nguyen, C. Dagron, P. Laruelle, *Acta Crystallogr.* 1975, *B 31*, 514-518.

Figure 1

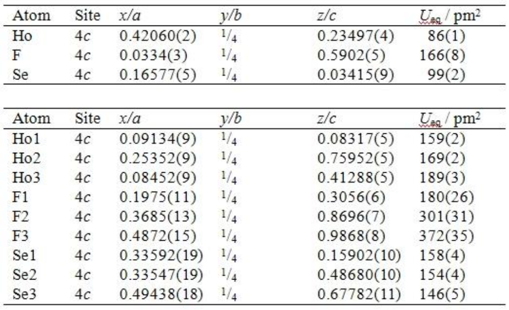

Atom	Site	*x/a*	*y/b*	*z/c*	U_{eq} / pm^2
Ho	4*c*	0.42060(2)	1/4	0.23497(4)	86(1)
F	4*c*	0.0334(3)	1/4	0.5902(5)	166(8)
Se	4*c*	0.16577(5)	1/4	0.03415(9)	99(2)

Atom	Site	*x/a*	*y/b*	*z/c*	U_{eq} / pm^2
Ho1	4*c*	0.09134(9)	1/4	0.08317(5)	159(2)
Ho2	4*c*	0.25352(9)	1/4	0.75952(5)	169(2)
Ho3	4*c*	0.08452(9)	1/4	0.41288(5)	189(3)
F1	4*c*	0.1975(11)	1/4	0.3056(6)	180(26)
F2	4*c*	0.3685(13)	1/4	0.8696(7)	301(31)
F3	4*c*	0.4872(15)	1/4	0.9868(8)	372(35)
Se1	4*c*	0.33592(19)	1/4	0.15902(10)	158(4)
Se2	4*c*	0.33547(19)	1/4	0.48680(10)	154(4)
Se3	4*c*	0.49438(18)	1/4	0.67782(11)	146(5)

Figure 2

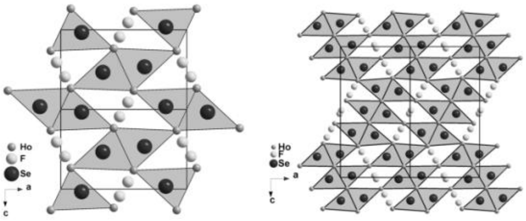

MS05-P48

$SrCuNdS_3$: A New Compound With Two Different Crystal Structures

M. Eberle[1], S. Strobel[1], T. Schleid[1]
[1] *Universität Stuttgart, Institut für Anorganische Chemie, Stuttgart, Germany*

In order to find new synthetic methods using premanufactured compounds, *e.g.* $CuNdS_2$ [1], the new quaternary sulfide $SrCuNdS_3$ emerged, showing up in two different crystal structures. Purple-coloured B-type $SrCuNdS_3$ crystallizes in the orthorhombic space group *Pnma* (a = 1056.93(7), b = 400.72(3), c = 1289.05(9) pm, Z = 4) and is isotypic with Eu_2CuS_3 (≡ $Eu^{II}Cu^{I}Eu^{III}S_3$) [2]. So $[NdS_6]^{9-}$ octahedra share common edges and vertices, establishing layers parallel to the (001) plane. Indentations between octahedra within these layers embed Cu^+ cations forming $[CuS_4]^{7-}$ tetrahedra, which are linked by common vertices building straight chains along [010]. In between the layers, build up by $[NdS_6]^{9-}$ octahedra, Sr^{2+} cations are situated, which have seven S^{2-} neighbours and are therefore centering capped trigonal prisms. Their fusion via common faces and caps leads to the formation of strands along [010]. A-type $SrCuNdS_3$ also has a purple colour and crystallizes in the orthorhombic space group *Pnma* (a = 1106.63(8), b = 408.86(3), c = 1146.25(8) pm, Z = 4) as well, but is isotypic with α-$BaCuLaSe_3$ [3]. Its structure can be described with two interpenetrating three-dimensional frameworks. In contrast to B-type $SrCuNdS_3$, where the Nd^{3+} cations are located in $[NdS_6]^{9-}$ octahedra, Nd^{3+} is now coordinated by seven S^{2-} anions forming capped trigonal prisms. Linkage via common edges, faces and caps results in a framework with large cavities. The Sr^{2+} cations also have more S^{2-} ligands than in the crystal structure of B-type $SrCuNdS_3$ as they reside in the center of bicapped trigonal prisms. Again, a framework is erected by using common faces and caps of these

$[SrS_{7+1}]^{13-}$ prisms. Even in combination both frameworks leave enough empty space to host Cu^+ cations in $[CuS_4]^{7-}$ tetrahedra, which are fused by common vertices to form chains along [010] just like in the B-type structure of $SrCuNdS_3$.With increasing coordination numbers comes an increase of density (4.76 g/cm^3 for B- *vs.* 5.02 g/cm^3 for A-type $SrCuNdS_3$), which identifies the A-type structure as high-pressure phase.

Figure 1: Crystal structure of B-type $SrCuNdS_3$.
Figure 2**:** Crystal structure of A-type $SrCuNdS_3$.

References
[1] S. Strobel, P. Lauxmann, Th. Schleid, *Z. Naturforsch.* 2005, *60 b*, 917-923.
[2] P. Lemoine, D. Carré, M. Guittard, *Acta Crystallogr.* 1986, *C 42*, 390-391.
[3] A. E. Christuk, P. Wu, J. A. Ibers, *J. Solid State Chem.* 1994, *110*, 330-336.

Figure 1

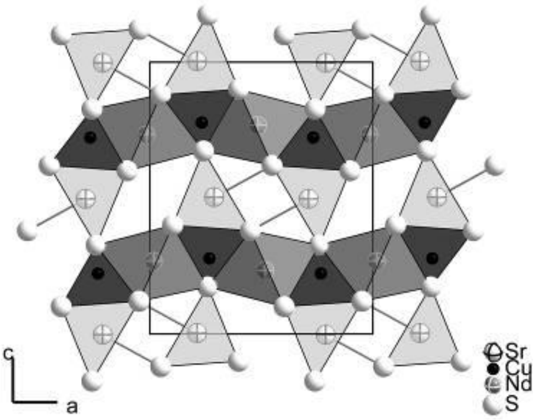

Figure 2

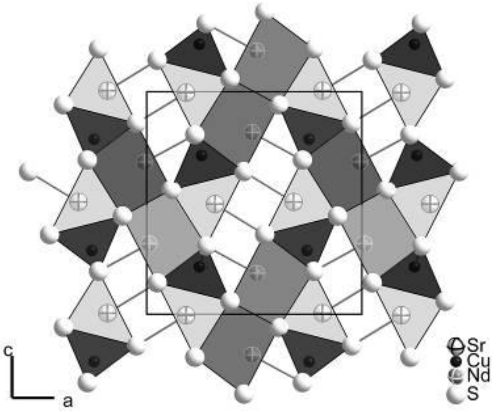

MS05-P49

Crystal structure study of naturally occurring phases $Ag_4Pd_3Te_4$ and $Pd_{14}Ag_2Te_9$

F. Laufek[1], A. Vymazalova[1], M. Drabek[1], J. Drahokoupil[2], M. Dusek[2]
[1]*Czech Geological Survey, Prague, Czech Republic*
[2]*Institute of Physics, Prague, Czech Republic*

Within the research of phase relations in the Pd-Ag-Te system, the synthetic analogues of the mineral sopcheite $Ag_4Pd_3Te_4$ and a new phase $Pd_{14}Ag_2Te_9$ (also termed as Pd_6AgTe_4) were synthesized and structurally characterized. The mineral sopcheite was discovered in the Cu-Ni sulphide ores of the Sopcha massif, Kola peninsula, Russia by [1], where it occurs as veins with size not exceeding of 0.02 mm included in chalcopyrite. The $Pd_{14}Ag_2Te_9$ phase was observed in the form of small anhedral grains (<0.1 mm) by [2,3] from the Lukkulaisvaara pluton in Karelia, Russia. In order to understand the behavior of these phases in natural conditions and to elucidate the mechanisms of various chemical substitutions, the crystal structures of both phases have been determined.

Because of very low amount of natural samples and difficulties connected with their isolation, both phases were synthesized from elements by conventional solid-state reactions. Stoichiometric amounts of individual elements were sealed in the silica glass tubes and resultant mixtures were heated at 350°C for 4 months. After heating, the samples were quenched in a cold-water bath. The crystal structure of synthetic analogue of sopcheite $Ag_4Pd_3Te_4$ was solved from single-crystal X-ray diffraction data, whereas structure of $Pd_{14}Ag_2Te_9$ was solved from the powder X-ray diffraction data.

$Ag_4Pd_3Te_4$: Space group *Cmca*, a = 12.22 Å, b = 6.14 Å, c = 12.23, V = 918 Å^3 and Z = 4. In the layered structure of $Ag_4Pd_3Te_4$, the Pd atoms show a square planar coordination by the four Te atoms. The $[PdTe_4]$ squares share two opposite Te-Te edges with adjacent $[PdTe_4]$ squares forming layers parallel to (100). In addition, each Pd atom has four short contacts with the Ag atoms. The layers of edge-sharing $[PdTe_4]$ squares are connected by number of Ag-Te bonds running approximately in the [100] direction.

$Pd_{14}Ag_2Te_9$: Space group *I*4/*m*, a = 8.96 Å, c = 11.82 Å, V = 949 A^3 and Z = 2. The three-dimensional framework structure of Pd_{14} Ag_2Te_9 consists of $[PdTe_4]$ squares and $[(Pd/Ag)Te_4]$ flattened tetrahedra. The squares and tetrahedra form slabs parallel to (001), which regularly alternate along the *c*-axis. The flattened tetrahedra are a typical feature of this crystal structure.

[1] D. A. Orsoev, S. A. Rezhenova, A. N. Bogdanova, *Zap. Vses. Mineralog. Obshch*., 111
(1982), 114.

[2] T.L. Grokhovskaya, Distler, V.V. Klyunin, S.F. Zakharov, A.A. Laputina, I.P.
Int.Geol.Rev. 34 (1992), 503.
[3] A. Y. Barkov, R. F,. Martin, M. Tarkian, G. Poirier, Y. Thibault, *Can. Mineral.*, 39**,**
(2001) 639.

Figure 1. The crystal structure of the $Ag_4Pd_3Te_4$ phase in a polyhedral representation. The [$PdTe_4$] squares are emphasized.
Figure 2. Polyhedral representation of the $Pd_{14}Ag_2Te_9$ crystal structure. Note the [$PdTe_4$] squares and [$(Pd/Ag)Te_4$] flattened tetrahedral

Figure 1

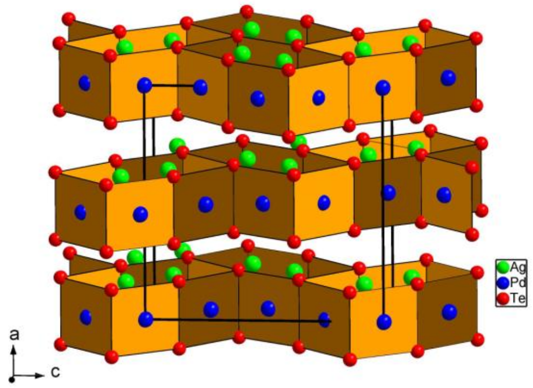

Figure 2

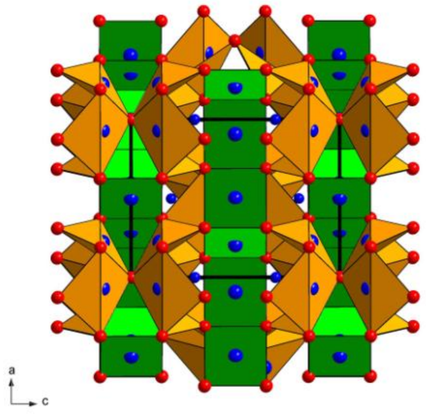

MS05-P50

Two New Nitride Tellurides of Dysprosium: Dy_3NTe_3 and $Dy_4N_2Te_3$

M. Foltin[1], F. Lissner[1], T. Schleid[1]
[1]*University of Stuttgart, Institute for Inorganic Chemistry, Stuttgart, Germany*

Most systems for the ternary compounds M_3NCh_3 (M = La − Ho; Ch = S, Se) [1] and $M_4N_2Ch_3$ (M = La − Nd, Tb; Ch = S, Se, Te) [1] are well investigated and known for their structural diversity. On the one hand, vertex-connected lanthanido-ammonium tetrahedra serve as main structural feature in the nitride-poor compounds M_3NCh_3, and on the other hand, the $M_4N_2Ch_3$ series shows different chains and layers containing $[NM_4]^{9+}$ tetrahedra with common edges or edges and vertices. In contrast, Ho_3NSe_3 [2] is special for its discrete $[N_2Ho_6]^{12+}$ bitetrahedra and these isolated units (Fig. 1) are also seen in the new structure of Dy_3NTe_3, the first nitride telluride of the lanthanides with this composition. It crystallizes monoclinically in space group $P2_1/c$ with the lattice parameters a = 806.63(6), b = 1182.51(8), c = 860.72(6) pm, β = 109.038(3)° and Z = 4. Not only a space group change compared to Ho_3NSe_3 (monoclinic, $C2/c$) [2] occurs, but the three crystallographically different Dy^{3+} cations are coordinated by the anions (N^{3-} and Te^{2-}) as two distorted octahedra and one trigonal prism.

$Dy_4N_2Te_3$, another nitride-rich example for the composition $M_4N_2Te_3$ (M = La − Nd) [3], extends the systematics and shows infinite $[NM^{e}_{4/2}\ ]^{3+}$ chains of $[NM_4]^{9+}$ tetrahedra, which share two *trans*-oriented edges (Fig. 2). But unlike the orthorhombic light representatives (space group: $Pnma$) [3], it crystallizes monoclinically in space group $P2_1/n$ with the lattice parameters a = 719.56(5), b = 1164.05(8), c = 1097.34(7) pm, β = 91.327(3)° and Z = 4. Each Dy^{3+} cation is coordinated by four Te^{2-} and two N^{3-} anions in the shape of three distorted octahedra and one trigonal prism.

Both compounds were obtained by reactions of dysprosium metal with tellurium, sodium azide, iodine and sodium iodide as flux in evacuated silica tubes. Appropriate molar ratios were chosen for the reactions, which ran for seven days at 950 °C. After subsequent slow cooling, red ($Dy_4N_2Te_3$) and black (Dy_3NTe_3) crystals could be detected and selected for single crystal X-ray diffraction studies.

Figure 1**.** Discrete $[N_2Dy_6]^{12+}$ bitetrahedron in Dy_3NTe_3.
Figure 2**.** Infinite $[NDy^{e}_{4/2}]^{3+}$ chain of edge-shared $[NDy_4]^{9+}$ tetrahedra in $Dy_4N_2Te_3$.

Figure 1

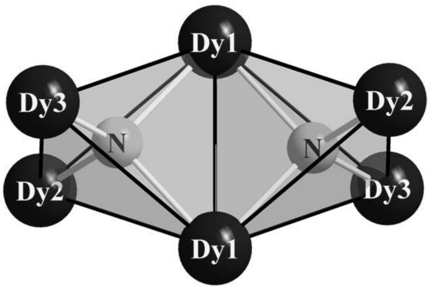

Figure 2

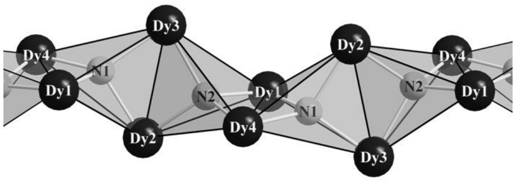

MS05-P51

Ln_2NBi (Ln = La - Nd): The First Nitride Bismuthides of the Lanthanides

K. K. Wolff[1], F. Lissner[1], J. Köhler[2], T. Schleid[1]
[1]*University of Stuttgart, Institute of Inorganic Chemistry, Stuttgart, Germany*
[2]*Max Planck Institute for Solid State Research, Stuttgart, Germany*

All binary nitrides of the rare-earth elements with the composition MN (M = Sc, Y, La; Ce - Lu) [1] crystallize with the rock-salt structure of NaCl. In ternary derivatives of the mononitrides with chalcogenide (Ch^{2-} = S^{2-} - Te^{2-}) and/or halogenide anions (X^- = Cl^- - I^-) [2] the coordination number of the bulky Ln^{3+} cations (Ln = La - Nd, Sm, Gd - Ho) increases considerably, while N^{3-} settles with a tetrahedral Ln^{3+} coordination (CN = 4). Now the question arises, whether mononitrides (LnN) and monobismuthides (LnBi), both crystallizing with the rock-salt structure, form solid solutions or compounds with an own structure.

The preparation of the first representatives of the new class of compounds with the formula Ln_2NBi (Ln = La - Nd) was carried out by flux syntheses in molten CsCl with the metallic elements (Ln and Bi) and caesium azide (CsN_3) as nitrogen source at 900 °C. The obtained black, prismatic, extremely air- and moisture-sensitive crystals were analyzed by means of X-ray diffraction. All compounds of the composition Ln_2NBi (Ln = La - Nd) are crystallizing tetragonally in the space group $P4/nmm$ with Z = 2 (Ln = La: a = 480.61(4), c = 948.34(9) pm, Ln = Ce: a = 475.48(4), c = 938.76(9) pm, Ln = Pr: a = 471.80(4), c = 929.51(9) pm, Ln = Nd: a = 468.13(4), c = 921.08(9) pm). From the four crystallographically different ions, $(Ln1)^{3+}$ occupies the 2b site, the others are located at 2c. Thereby the Ln_2NBi phases form a layered structure (Figure 1), following an *anti*-$BaNiS_2$-type arrangement [3]. It consists of square double sheets of bismuthide anions (Bi^{3-}) and layers of nitrogen-centered square pyramids erected by Ln^{3+} cations. These pyramids, in which the basis is built from $(Ln1)^{3+}$ (d(Ln1-N) = 249 - 253 pm) and the top from $(Ln2)^{3+}$ cations (d(Ln2-N) = 218 - 232 pm), are connected via all their basal edges to two-dimensional infinite layers. Both of the crystallographically independent Ln^{3+} cations are surrounded by the two types of anions eight- and sixfold, respectively (Figure 1). $(Ln1)^{3+}$ is coordinated in the shape of a square antiprism out of four N^{3-} and Bi^{3-} anions each (d(Ln1-Bi) = 365 - 374 pm), while $(Ln2)^{3+}$ is surrounded by a distorted octahedron built from one N^{3-} and five Bi^{3-} anions (d(Ln2-Bi) = 332 - 350 pm).

[1] W. Klemm, G. Winkelmann, *Z. Anorg. Allg. Chem.* 1956, *288*, 87-90. [2] Th. Schleid, F. Lissner, *J. Alloys Compds.* 2008, *451*, 610-616. [3] I. E. Grey, H. Steinfink, *J. Am. Chem. Soc.* 1970, *92*, 5093-5095.

Figure 1**:** Crystal structure of the lanthanide nitride bismuthides Ln_2NBi (Ln = La - Nd) (*left*) and coordination polyhedra around the four involved crystallographically independent ions (*right*).

Figure 1

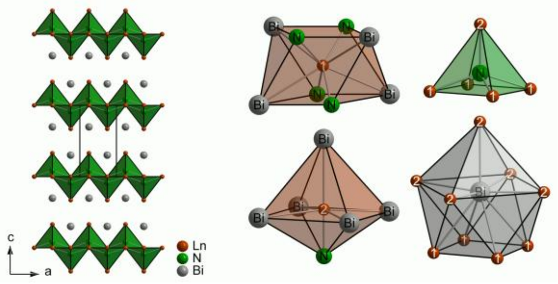

MS05-P52

Crystallographic peculiarities in the solid solution series $La_{1-x}Ce_xOBiS_2$

E. Ahrens[1], T. Doert[1]
[1]*Technische Universität Dresden, Dep. of Chemistry and Food Chemistry, Dresden, Germany*

Recently, several BiS_2-layered superconductors, particularly $REO_{1-x}F_xBiS_2$ compounds (RE = La, Ce, Pr, Nd) with critical temperatures up to 10 K were found [1]. The structure contains REO blocking layers separating the superconducting BiS_2 slabs. On this background we are interested in the substitution series $La_{1-x}RE_xOBiS_2$ to look for superconducting fluorine-free samples. In this contribution, we present the influence of the isovalent substitution of La by Ce on the atomic structure, especially in the REO layers.

Single crystals of $La_{1-x}Ce_xOBiS_2$ are obtained by reaction of stoichiometric amounts of the RE metals, Bi, S and Bi_2O_3 in a KI/KCl flux in sealed silica ampoules with glassy carbon crucibles at 800° C. The products can be separated by removing the halide flux with distilled water and ethanol. The quality of the single crystals allows a considerably deeper insight into the structural details compared to the Rietveld analyses discussed in [2].

The samples $La_{1-x}Ce_xOBiS_2$ ($0 \leq x \leq 1$) form a complete solid solution series, all samples crystallize in space group $P4/nmm$ (no. 129). The lattice parameters determined from powder X-ray diffraction data vary between 4.0575(1) Å and 4.0133(1) Å for a and between 13.7902(4) Å and 13.6041(2) Å for c. Going from $LaOBiS_2$ to $CeOBiS_2$, the lanthanide contraction of approximately 1.5% (La^{3+}: 1.16 Å, Ce^{3+}: 1.14 Å; eff. ionic radii for 8-fold coordination, [3]), is mirrored in a linear shrinkage of the lattice parameter a, whereas for c a significant deviation from Vegard's rule can be observed for samples with low amounts of Ce, figure 1.

The Fourier maps (F_{obs}) around the RE site (Wyckoff sites 2c, ¼, ¼, z with $z \approx 0.58$) in crystals of the mixed compounds have a pronounced prolate shape. We take this as a hint for two distinct sites for La and Ce rather than one site *RE* with mixed occupancy. The structure refinements with two *RE* positions at different *z*-values converge to much better residuals and featureless difference Fourier maps. As a result, two different *RE*-O distances are calculated for the mixed compounds. For $La_{0.75}Ce_{0.25}OBiS_2$, as one example (Figure 2), the *z*-values are computed to 0.5968(1) for La and 0.5788(1) for Ce, resulting in a La-O distances of 2.411(1) Å and a Ce-O distance of 2.286(1) Å. The La-O distances in the mixed compounds are generally larger than those of pure $LaOBiS_2$ of 2.395(1) Å. Distinct *z* values for La and Ce and different *RE*-O distances are confirmed by SCF-DFT calculations (FPLO code, [4])

References
[1] M. Nagao, A. Miura, S. Demura, K. Deguchi, S. Watauchi, T. Takei, Y. Takano, N. Kumada, I. Tanaka, *Solid State Comm*. 2014, *178*, 33.
[2] Y. Mizuguchi, S. Demura, K. Deguchi, Y. Takano, H. Fujihisa, Y. Gotoh, H. Izawa, O. Miura, *J. Phys. Soc. Jpn*. 2012, *81*, 114725.
[3] R. D. Shannon, *Acta Cryst.* 1976, *A32*, 751.
[4] K. Koepernik, H. Eschrig, *Phys. Rev. B* 1999, *59*, 1743.

Figure 1

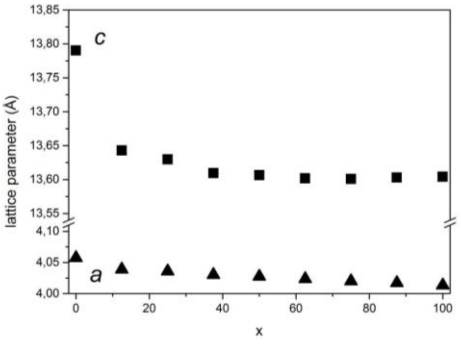

Plot of the lattice parameters vs. the Ce amount *x*.

Figure 2

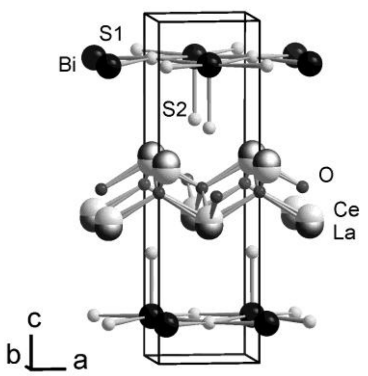

Crystal structure of $La_{0.75}Ce_{0.25}OBiS_2$.

MS05-P53
Low-temperature route to crystalline Cu_2ZnSnS_4

A. Ritscher[1], M. Lerch[1]
[1]*Technische Universität Berlin, Institut für Chemie, Berlin, Germany*

Cu_2ZnSnS_4 (CZTS) is a promising semiconductor material and a potential compound for future thin film photovoltaic applications. It can be considered as suitable material for absorber layers because it consists of non-toxic, abundantly available and low-cost elements. CZTS crystallizes in the kesterite-type structure (space group I-4) and is derived from currently used chalcopyrite-type absorbers [1]. However, attempts to prepare single-phase CZTS have been met with varying levels of success. The existence of a large number of secondary phases and the rather small homogeneity region [2] of the quaternary sulfide are main problems.

The motivation of the here-presented research is the development of new chemical routes for the synthesis of phase-pure kesterite powders. The main idea is to create a low-temperature formation process to avoid thermal segregation and formation of secondary phases such as ZnS. In a promising precursor the elements should be already mixed at room temperature at an atomic level. This can be realized by a mechanochemical treatment of the corresponding binary sulfides in a high-energy ball mill. In a second step, the poorly crystalline product is annealed at elevated temperatures to get a well crystalline and ordered product. In order to minimize oxygen contamination, the annealing process is carried out in H_2S atmosphere. It should be mentioned that the mechanochemical step is essential. Without this pretreatment procedure additional phases are observed.

The prepared powders have been investigated by means of X-ray diffraction (XRD) incl. Rietveld refinement. As an example, the diffraction pattern of an apparently ZnS-free material is shown in Fig.1a. The small diagram at the top right corner (b) represents the precursor after the milling step. However, using XRD it is difficult to exclude the presence of secondary phases such as ZnS unambiguously. Consequently, further characterization of the material (EDX/WDX, neutron diffraction) is necessary.

[1] S. Schorr; Thin Solid Films, 515, 2007, 5985
[2] I.D. Olekseyuk; I.V. Dudchak; L.V. Piskach; J. Alloys Compd., 368, 2004, 135

Fig.1:

a) XRD pattern of the final material with the results of a Rietveld refinement

b) Diffraction pattern of the as-prepared sample (precursor) after ball-milling

Figure 1

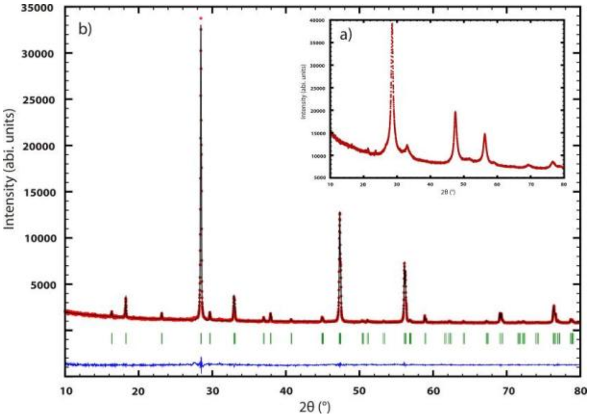

MS05-P54

Microstructure and crystallization behavior of the amorphous thermoelectrics $(GeSe_{3.5})_{88}M_{12}$ (M = Bi, Sb)

R. Schlegel[1], G. Wagner[1], O. Oeckler[1]
[1]*Universität Leipzig, IMKM, Leipzig, Germany*

Thermoelectric materials for effective power generation from waste heat become increasingly important, and various classes of compounds have been discussed.[1] The efficiency depends on the figure of merit $ZT = S^2\sigma T/\kappa$ (S = Seebeck coefficient in μV/K, σ = electrical conductivity in S/cm, T = temperature in K, κ = thermal conductivity in W/cmK). Much current research focuses on crystalline materials with good electrical conductivity and aims at reducing their thermal conductivity. Glasses, on the other hand, exhibit low thermal conductivities. In contrast to most of them, amorphous phases $(GeSe_{3.5})_{88}M_{12}$ [2,3] exhibit electrical conductivities of about 1300 S/cm for M = Sb and 310 S/cm for M = Bi. The Seebeck coefficient of $(GeSe_{3.5})_{88}Bi_{12}$ lies in the range of semiconductors (-1100 μV/K),[4] and related samples have also been discussed as thermoelectric materials.[5]

Bulk samples of $(GeSe_{3.5})_{88}M_{12}$ were prepared by melting stoichiometric amounts of the elements in silica glass ampoules sealed under Ar and subsequent quenching in water. Some samples were further annealed at ~350 °C. X-ray powder diffraction patterns of quenched samples exhibit no Bragg reflections and selected-area electron diffraction patterns show diffuse rings as expected for glasses.

Quenched $(GeSe_{3.5})_{88}Bi_{12}$ contains droplets of amorphous Se in a matrix of the ternary glass. Upon annealing this glass for one week, Ge-doped crystals of Bi_2Se_3 (according to EDX) precipitate and grow.[6] They exhibit the Bi_2Te_3 structure type (space group *R*`3*m*), 15 % of Bi can be substituted by Ge. TEM-EDX mapping shows the precipitation of Bi-rich micro- and nanocrystals in a homogenous matrix. According to SAED this turns into crystalline Ge_4Se_9, which forms a structure type with one diselenide entity per formula unit (space group $Pca2_1$).

In contrast, quenching of $(GeSe_{3.5})_{88}Sb_{12}$ yields a homogeneous glass, whose chemical composition (measured by SEM-EDX) is consistent with the weighted samples. Annealing leads to Ge_4Se_9 crystals in a glassy matrix with a final composition of $Sb_{0.06}Ge_{0.2}Se_1$. (confirmed by TEM-EDX). The present study aims at discussing the thermoelectric properties, as a function of the composition of the glass and the amount of crystals in the glass.

[1]J. R. Sotsman, D. Y. Chung, M. G. Kanatzidis, *Angew. Chem. Int Ed.* 2009, *48*, 8616.
[2]A. Giridhar, P. S. L. Narasimham, S. Mahadevan, *J. Non-Cryst. Solids* 1980, *37*, 165.
[3]N. Tohge, T. Minami, Y. Yamamoto, M. Tanaka, *J. Appl. Phys.* 1980, *51*, 1048.
[4]P. Nagels, L. Tichy, A. Triska, H. Ticha, *J. Non-Cryst. Solids* 1983, *59&60*, 1015.
[5]F. Shangguan, J. Xie, Z. Wu, J,. Xing, B. Zhao, Y. Liu, G. Chen, *Key Eng. Mater.* 2012, *509*, 235.
[6]Y. Liu, S. Yuan, J. Xie, F. Shangguan, J. Ren, G. Chen, *J. Am. Ceram. Soc.* 2013, *96*, 21241.

MS05-P55

X Marks the Path—Diffusion Pathways in 3R-Li_xTiS_2 as a Function of Lithium Content

D. Wiedemann[1], S. Nakhal[1], A. Senyshyn[2], M. Lerch[1]
[1]*Technische Universität Berlin, Institut für Chemie, Berlin, Germany*
[2]*Technische Universität München, ZWE FRM II, München, Germany*

With respect to battery materials, lithium-ion conductors have been a focus of interest in recent years. Yet, compared to the enormous effort put in optimizing batteries, basic understanding of lithium diffusion in solids is still lacking. The influence of lithium content and surrounding coordination polyhedra on diffusion pathways can be studied excellently on 2D conductors of the general formula Li_xMS_2 ($x \leq 1$, M: transition metal). These compounds exhibit layered structures varying in the stacking sequence of sulfur atoms, the most prominent being the so-called 1T-, 2H- and 3R-types. Preliminary theoretical work on such materials has proposed two different viable lithium diffusion-pathways: one “directly” within the layer, one “indirectly” through adjacent tetrahedral voids. Further, the predominance of a pathway is predicted to be a function of lithium content.[1]

1T-TiS_2 was synthesized by controlled heating of the elements in an evacuated ampoule and subsequently chemically lithiated using 1-butyllithium. The resulting compounds 1T-Li_xTiS_2 (x = 0.7, 0.9) reversibly transformed into 3R-Li_xTiS_2, when heated above ca. 500 °C. Rietveld refinement of powder neutron-diffractograms acquired at 600 and 700 °C allowed modelling of the lithium Debye-Waller factors including anharmonic terms. Probability-density functions (PDFs) and one-particle potentials (OPPs) were derived.

The PDF is distributed in plane with the lithium-ion layer for $x = 0.7$, but sprawls towards the tetrahedral voids for $x = 0.9$ (Fig. 1). The OPPs indicate that, at 600 °C, only the “direct”/“indirect” path with energy barriers of 0.37 eV/2.00 eV is allowed for $x = 0.7/0.9$ (Fig. 2). Hence, 3R-Li_xTiS_2 indeed shows a variation of lithium-diffusion pathways as function of lithium content: one in-plane and one through tetrahedral voids. The former is dominant in 3R-$Li_{0.7}TiS_2$, the latter in 3R-$Li_{0.9}TiS_2$. Theoretical work on these phases is in progress and shall be further contextualized in view of *in-situ* solid-state-NMR-measurements and impedance spectroscopy at high temperatures.

Financial support from Deutsche Forschungsgemeinschaft (FOR 1277) is gratefully acknowledged.

[1] M. M. Islam, T. Bredow, *Z. Phys. Chem.* 2012, *226*, 449-459.

Fig. 1**.** Detail of the crystal structure of 3R-$Li_{0.7}TiS_2$ (top) and 3R-$Li_{0.9}TiS_2$ (bottom) at 600 °C (yellow: sulfur, red: lithium).

Fig. 2. OPP contour-plot of 3R-$Li_{0.7}TiS_2$ (top) and 3R-$Li_{0.9}TiS_2$ (bottom) at 600 °C in view of (018) with origin at 0,0,0.5. Deep red signifies low, pure white infinitely high potential (Li, Li’: lithium, M: octahedron-edge center, T: tetrahedral void center).

Figure 1

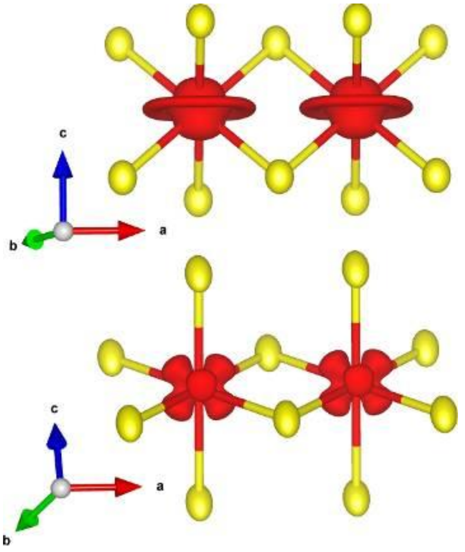

Figure 2

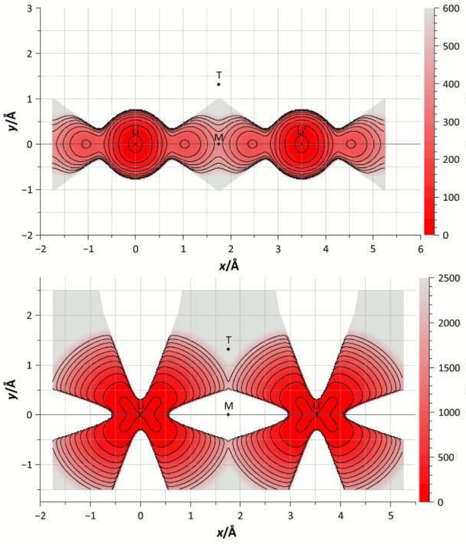

MS05-P56

The crystal chemistry of $CsAlS_2$

V. Winkler[1]
[1]*University of Regensburg, Inorganic Chemistry, Regensburg, Germany*

Two different structure types are well known in the family of MTQ_2 compounds (*M:* alkali metal; *T:* Al, Ga, In; *Q:* S, Se, Te): Monoclinic $CsGaSe_2$-I [1] for example crystallizes in the $KFeS_2$ structure type [2] and hence contains linear, polymeric $^1_\infty[GaSe_2^-]$ anions. Tetragonal $CsGaSe_2$-II [3] features adamantane-like super-tetrahedra $[Ga_4Se_{10}]^{8-}$ and is isotypic to $KInS_2$ [4].

A new member of the MTQ_2 family was obtained by the reaction of a stoichiometric mixture of elemental aluminum, sulfur, and cesium azide. $CsAlS_2$ is highly air sensitive and crystallizes in the $KFeS_2$ structure type [2] with the unit cell dimensions: a = 7.4269(6) Å, b = 12.1916(7) Å, c = 5.7646(5) Å, β = 112.534(9)°, and V = 482.11(6) Å^3 ($Z = 4$). The 3D periodic crystal structure of the compound is dominated by linear infinite polymeric $^1_\infty[AlS_2^-]$ anions of edge-linked tetrahedra (Fig. 1). These polymers are surrounded by cesium. Each cesium atom is coordinated by eight sulfur atoms. The one-dimensional $^1_\infty[AlS_2^-]$ anions are positioned within hexagons of Cs^+, arranged with the motif of a hexagonal rod packing.

Electronic band structure-calculations (DFT-GGA) [5] reveal a direct band gap of 3.1 eV. Bonding is analyzed with the electron localization function (ELF) and Bader´s theory of atoms in molecules (AIM). Experimentally determined Raman spectra of $CsAlS_2$ are interpreted from calculated vibrational data.

A tetragonal structure (a = 8.4897(1) Å, c = 63.229(1) Å, V = 4557.2(1) Å^3) [6] with the general composition MTQ_2 was obtained besides the monoclinic phase of $CsAlS_2$. The expected layer structure with adamantane-like super-tetrahedra $[T_4Q_{10}]^{8-}$ turns out to be a composite modulated structure, which shows also linear, one-dimensional $^1_\infty[\mathrm{AlS_2}^-]$ anions embedded between cesium cations but no super-tetrahedra. The structure is described in the superspace group *P4/nnc(00γ)*, *γ=6/7* as a commensurately modulated composite structure. While the atoms in the strands $^1_\infty[\mathrm{AlS_2}^-]$ can be described by a simple harmonic modulation wave affecting only atom positions and harmonic ADPs, the Cs atoms making a parallel column are strongly modulated and for a full description the modulation of ADPs up to 4th order are to be used. An alternative refinement in the supercell *(a,a,7c)* leads to the almost identical solution but with advantage to handle each Cs atom individually. This makes possible to describe two of five independent Cs atoms in the harmonic approximation which reduces the number of refined parameters.

References:
[1] A. Kyas, *Thesis Univ. Aachen* 1981.
[2] W. Bronger, P. Müller, *Z. Anorg. Allg. Chem.*, 1968, *359*, 225.
[3] H.J. Deiseroth, *Z. Kristallogr.*, 1984, *166*, 283.
[4] B. Eisenmann, A. Hofmann, *Z. Kristallogr.*, 1991, *195*, 318.
[5] R. Dovesi, R. Orlando, B. Civalleri, C. Roetti, V. R. Saunders, C. M. Zicovich-Wilson, *Z. Kristallogr.*, 2005, *220*, 571.
[6] J. Weiß, H. Schäfer, G. Schön, *Z. Naturforsch, B: Chem. Sci.*, 1976, *31b*, 1336.

Figure 1

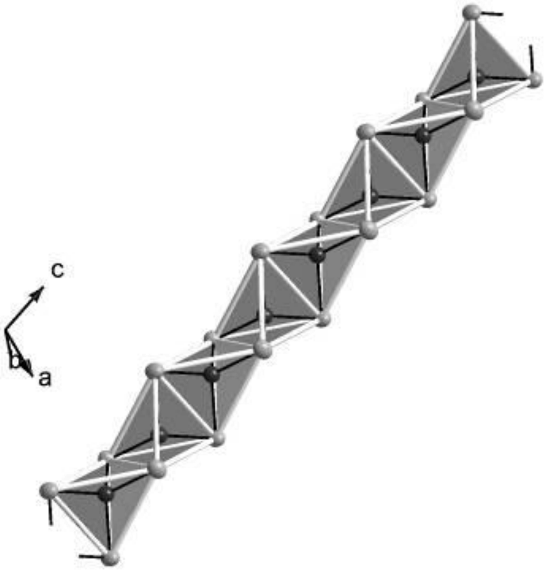

Figure 1 A linear chain $^1_\infty[\mathrm{AlS_2}^-]$ of edge-sharing tetrahedra in $\mathrm{CsAlS_2}$ (ellipsoids represent 95% probability).

Figure 2

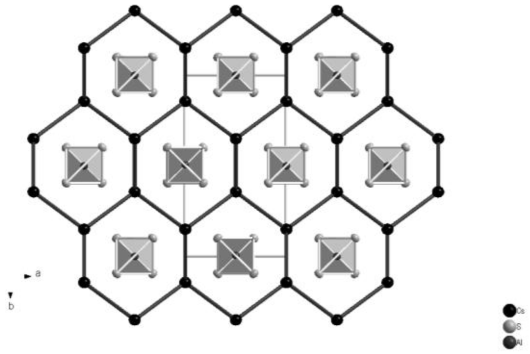

Figure 2 Projection of the crystal structure of $\mathrm{CsAlS_2}$ along [001].

MS05-P57

Synthesis and characterization of $\mathrm{Cs_2Ga_2S_5}$ and $\mathrm{Cs_2Ga_2Se_5}$

D. Friedrich [a], *M. Schlosser* [a], *A. Pfitzner* [a]*
*Prof. Dr. Arno Pfitzner
[a] Univeristät Regensburg, Institut für Anorganische Chemie, Universitätsstraße 31, 93040 Regensburg, Deutschland
D. Friedrich[1]
[1] *Universität Regensburg, Institut für Anorganische Chemie, Regensburg, Germany*

Two new chalcogenometallates of group 13 metals with alkali metal cations were synthesized and characterized. The crystal structures of $\mathrm{Cs_2Ga_2S_5}$[1] and $\mathrm{Cs_2Ga_2Se_5}$ were determined by single-crystal X-Ray diffraction. Both compounds crystallize in the monoclinic space group $C2/c$ (No. 15) with a = 12.682(3) Å, b = 7.199(1) Å, c = 12.375(4) Å, β = 108.28(2)°, V = 1072.7(5) Å^3, and Z = 4 for $\mathrm{Cs_2Ga_2S_5}$[1], and a = 15.4660(5) Å, b = 7.4048(1) Å, c = 13.0160(4) Å, β = 126.588(4)°, V = 1196.89(6) Å^3, and Z = 4 for $\mathrm{Cs_2Ga_2Se_5}$. The chalcogenometallate anions present in both compounds consist of infinite one-dimensional chains $^1_\infty[\mathrm{Ga_2}Q_3(Q_2)^{2-}]$ (Q = S, Se) composed of edge- and corner sharing GaQ_4 tetrahedra (Fig. 1). The optical band gaps of 3.26 eV ($\mathrm{Cs_2Ga_2S_5}$) and of 1.95 eV ($\mathrm{Cs_2Ga_2Se_5}$) were determined by UV/Vis diffuse reflectance spectroscopy. The Raman spectra show peaks for dichalcogenide units (Q_2^{2-}) at 493 cm^{-1} for $\mathrm{Cs_2Ga_2S_5}$ and at 236 cm^{-1} for $\mathrm{Cs_2Ga_2Se_5}$.

Figure 1: The anionic chain $^1_\infty[\mathrm{Ga_2}Q_3(Q_2)^{2-}]$ (Q = S, Se) present in $\mathrm{Cs_2Ga_2S_5}$ and $\mathrm{Cs_2Ga_2Se_5}$ showing the linkage of the GaQ_4 - tetrahedra. The bonds within the dichalcogenide units are emphasized.

[1] D. Friedrich, A. Pfitzner, M. Schlosser, *Z. Anorg. Allg. Chem.* 2012, *638*, 1572.

Figure 1

MS05-P58
Synthesis and Structural Characterization of a Polar Framework of Thiogallato-*closo*-Dodecaborate Anions Containing Rare-Earth Metal(III) Cations

R. Stromsky[1], F. M. Kleeberg[1], L. W. Zimmermann[1], T. Schleid[1]
[1]*Universität Stuttgart, Institut für Anorganische Chemie, Stuttgart, Germany*

Only a few examples of dodecachalcogeno-*closo*-dodecaborates are known in the literature [1]. Among these there is only one rare-earth metal dodecachalcogeno-*closo*-dodecaborate with the formula $(K_3I)Sm[B_{12}(GaS_4)_3]$, which was published in 2009 [2].

We now report the synthesis and structural characterization of three further rare-earth metal dodecachalcogeno-*closo*-dodecaborates of the same formula with scandium, yttrium and lanthanum. All compounds with the composition $(K_3I)RE[B_{12}(GaS_4)_3]$ (RE = Sc, Y and La) crystallize in the polar hexagonal space group $P6_322$, thus isotypically to the already known samarium prototype [2].

The crystal structure contains B_{12} icosahedra, which consist of two crystallographically different boron atoms. To each of these B_{12} clusters six GaS_4 tetrahedra are bound via one edge each, while the corresponding *trans*-edge of all tetrahedra is connected to another B_{12} cluster erecting a three-dimensional 3D-$\{(B_{12}(S_2GaS_2)_{6/2}]^{5-}\}$ framework. The $[B_{12}S_{12}]^{14-}$ clusters are additionally interconnected to chains along [001] via the rare-earth metal cations (RE^{3+}), which reside in sixfold coordination of sulfur atoms arranged as trigonal antiprisms. Moreover hexagonal channels occur parallel to the crystallographic c-axis, ready to take up columns 1D-$\{IK_{6/2}]^{2+}\}$ of *trans*-face sharing $[IK_6]^{5+}$ octahedra. Since the RE^{3+} cations are only relevant for the stiffening of the framework along [001], the a and b axes (about 1290 pm long) remain pretty much the same for all three rare-earth metal compounds, but the c axes vary ($c \approx 908$ pm for RE = Sc, $c \approx 925$ pm for RE = Y, $c \approx 956$ pm for RE = La) to fulfill the coordinative demands of the differently sized cations (d(Sc-S) = 267 pm, d(Y-S) = 278 pm, d(La-S) = 293 pm) within their sulfur octahedra.

Figure 1**:** Crystal structure of $(K_3I)RE[B_{12}(GaS_4)_3]$ (RE = Sc, Y and La) as viewed along [001].

References

[1] A. Hammerschmidt, M. Döch, S. Pütz, B. Krebs, *Z. Allg. Anorg. Chem.* 2005, *631*, 1125-1128.
[2] S.-P. Guo, G.-C. Guo, M.-S. Wang, J.-P. Zou, H.-Y. Zeng, L.-Z. Cai, J.-S. Huang, *Chem. Commun.* 2009, *2009*, 4366-4368.

Figure 1

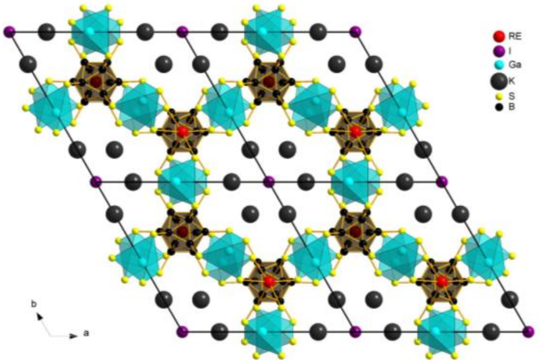

MS05-P59
Kettenstücke, (Doppel-)Ketten und Supertetraeder: Neue Caesiumsulfidoferrate $Cs_8[Fe_4S_{10}]$, $Cs_7[FeS_2]_2[Fe_2S_3]_2$ und $Cs_7[Fe_4S_8]$

M. Schwarz[1], C. Röhr[1]
[1]*Albert-Ludwigs-Universität Freiburg, Freiburg im Breisgau, Germany*

Die Strukturchemie der höher verknüpften Cs-Sulfidoferrate wird von der Kantenverknüpfung von FeS_4-Tetraedern bestimmt. In den bekannten Verbindungen $Cs_6[Fe_2S_6]$ [1], $Cs[FeS_2]$ [2] und $Cs_3[FeS_2]_2$ [3] liegen Dimere bzw. Stränge kantenverknüpfter FeS_4-Einheiten vor, in $Cs[Fe_2S_3]$ [4] sind diese Stränge kondensiert zu Doppelsträngen.

Durch Synthese aus den Elementen Fe und S und Cs_2S_2 mittels Schmelzreaktion bei 800°C konnten der Reihe drei weitere Glieder hinzugefügt werden:

Das Tetraferrat $Cs_8[Fe_4S_{10}]$ (P-1, a=7.6783(10), b=8.8557(12), c=10.677(2) Å, α=79.013(6), β=85.151(6), γ=80.185(6)°), isotyp zur Rb-Verbindung [5], besteht aus $[Fe^{III}{}_4S_{10}]^{8-}$-Kettenstücken (Abb. links), die in einer hexagonalen Stabpackung längs der Raumdiagonalen [-111] angeordnet sind.

$Cs_7[FeS_2]_2[Fe_2S_3]_2$ ($C2/m$, a=30.838(2), b=5.5903(3), c=7.6157(4) Å, b=95.829(4)°) enthält parallel zueinander verlaufende $FeS_{4/2}$-Ketten neben Doppelketten $Fe_2S_{4/2}S_{2/2}$, die aus $CsFe_2S_3$ [4] bereits bekannt sind. Von einer einfachen Ausordnung von Fe^{II}/Fe^{III} ist aufgrund der Anzahl kristallographischer Lagen nicht auszugehen.

$Cs_7[Fe_4S_8]$ ($C2/c$, a=18.9171(8), b=8.5287(3), c=16.6897(7) Å, β=117.968(2)°), ist aus $[Fe_4S_8]^{7-}$-Supertetraedern aufgebaut, worin sich jedes FeS_4-Tetraeder drei Kanten mit den benachbarten Tetraedern (Abb. rechts) teilt. Die Verbindung reiht sich damit in die

Strukturchemie kantenverknüpfter Tetraeder ein, jedoch - trotz Fe:S = 1:2 - nicht in die Kettenstrukturen [5], was vermutlich auf die verringerte Ladung der Eisenkationen (Fe^{II}:Fe^{III} = 3:1) zurückzuführen ist. Das Anion ist vergleichbar mit den 4Fe4S-Clustern aus Ferredoxinen [6], die über Protein-S-Reste an dieselben gebunden vorliegen und die Funktion des Elektronentransportes übernehmen [7]. Zum ersten Mal ist es damit gelungen, dieses Strukturelement als nicht funktionalisiertes Anion in rein anorganischer Umgebung darzustellen [8].

[1] W. Bronger, U. Ruschewitz, P. Müller, J. Alloys Compd. 1992, *187*, 95.
[2] W. Bronger, Z. Anorg. Allg. Chem. 1968, *359*, 225.
[3] W. Bronger, U. Ruschewitz, P. Müller, J. Alloys Compd. 1995, *218*, 22.
[4] R. H. Mitchell, K. C. Ross, E. G. Potter, J. Solid State Chem. 2004, *177*, 1867.
[5] M. Schwarz, M. Haas, C. Röhr, Z. Anorg. Allg. Chem. 2013, *639*, 360.
[6] H. Beinert, R. H. Holm, E. Münck, Science, 1997, *277*, 653.
[7] C. Wittekindt, M. Schwarz, Th. Friedrich, Th. Koslowski, J. Am. Chem. Soc. 2009, *131*, 8134.
[8] P. Venkateswara Rao, R. H. Holm, Chem. Rev. 2004, *104*, 527.

Figure 1

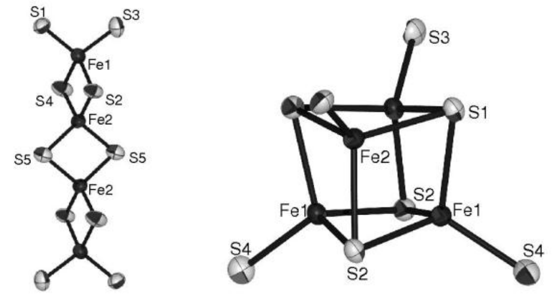

MS05-P60

Hole-doped $Ca_{1-x}Na_xFFeAs$: A New Iron-Arsenide Based Superconductor

K. K. Wolff[1], L. Shlyk[1], M. Bischoff[1], E. Rose[2], R. Niewa[1], T. Schleid[1]
[1]*University of Stuttgart, Institute of Inorganic Chemistry, Stuttgart, Germany*
[2]*University of Stuttgart , 1. Physics Institute, Stuttgart, Germany*

In 2008 with the detection of superconductivity in iron pnictides [1], a new class of high-temperature superconductors was found more than two decades after the discovery of this phenomenon in oxocuprates [2]. The first compounds can be derived from LaOFeAs with a tetragonal ZrSiCuAs-type structure, in which topologically equivalent cationic $[OLa_{4/4}]^+$ and anionic $[FeAs_{4/4}]^-$ layers are alternating (see Figure 1). Meanwhile, several structurally related types of these iron pnictides became known. As another 1111-phase besides LaOFeAs a representative of the fluoride-containing compounds, namely CaFFeAs [3] (tetragonal, *P*4/*nmm*: a = 387.828(4) pm, c = 859.29(1) pm, c/a = 2.216, Z = 2) as seen in Figure 1, was hole-doped with sodium for the first time. The approaches for the target series $Ca_{1-x}Na_xFFeAs$ with x = 0.1 - 0.2 have been implemented with classical solid-state reactions in sealed niobium ampoules at 1000 °C. $Ca_{1-x}Na_xFFeAs$ consists of small, platelet-like crystals, which are sufficient in size for single crystal X-ray diffraction (about 0.1 × 0.1 mm^2). However, for $x \geq 0.1$ an increasingly larger proportion of secondary phases arises. Bigger single crystals for directional physical measurements could be grown in a flux of sodium chloride additionally. EDX analyses confirm a certain amount of the substituent in the obtained crystals. They exhibit compositions in a narrow range of $Ca_{0.99}Na_{0.01}FFeAs$ to $Ca_{0.86}Na_{0.14}FFeAs$ depending on the sodium amount used. For this series X-ray diffraction data from single crystals can be structurally refined with the values from the EDX analyses. Magnetic measurements on on the powder samples $Ca_{1-x}Na_xFFeAs$ (x = 0.1 - 0.2) indicate the occurrence of superconductivity with a transition temperature of 34 K, however, highly substituted $Ca_{1-x}Na_xFe_2As_2$ detected as a side phase in all samples was previously reported to exhibit superconductivity with T_c up to 34 K [4]. Afore known hole-doped oxide compounds of the "1111 class" show rather low transition temperatures ($La_{0.87}Sr_{0.13}OFeAs$: T_c = 25.6 K [5], $Pr_{0.75}Sr_{0.25}OFeAs$: T_c = 16.3 K [6]). Resistivity as well as directional physical measurements of the magnetic susceptibility have been performed on a larger single crystal of $Ca_{0.89}Na_{0.11}FFeAs$ grown in NaCl flux (Figure 2). The critical temperature apparent at 34.5 K shows that hole-doped CaFFeAs with a sodium content of 11 % exhibits almost the same T_c as $Ca_{1-x}Na_xFe_2As_2$ ($x \approx 0.66$) incidentally.

[1] Y. Kamihara, T. Watanabe, M. Hirano, H. Hosono, *J. Am. Chem. Soc.* 2008, *130*, 3296-3297. [2] J. G. Bednorz, K. A. Müller, *Z. Phys.* 1986, *B 64*, 189-193. [3] S. Matsuishi, Y. Inoue, T. Nomura, H. Yanagi, M. Hirano, H. Hosono, *J. Am. Chem. Soc.* 2008, *130*, 14428-14429. [4] K. Zhao, Q. Q. Liu, X. C. Wang, Z. Deng, Y. X. Lv, J. L. Zhu, F. Y. Li, C. Q. Jin, *Phys. Rev. B* 2011, *84*, 184534. [5] H.-H. Wen, G. Mu, L. Fang, H. Yang, X. Zhu, *Europhys. Lett.* 2008**,** *82*, 17009. [6] G. Mu, B. Zeng, X. Zhu, F. Han, P. Cheng, B. Shen, H.-H. Wen, *Phys. Rev. B* 2009, *79*, 104501.

Figure 1**:** Crystal structure of $Ca_{1-x}Na_xFFeAs$.

Figure 2: Magnetic susceptibility ($\mu_0 H$ = 100 Oe) (*top*) and resistivity (*bottom*) of an oriented single crystal of $Ca_{0.89}Na_{0.11}FFeAs$.

Figure 1

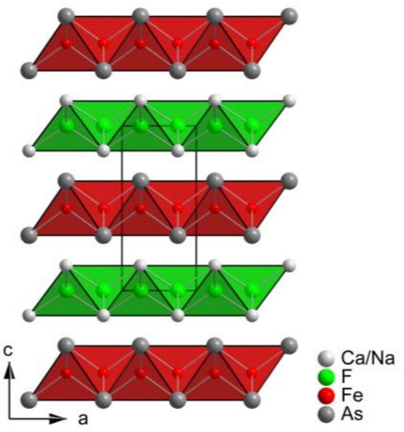

Figure 2

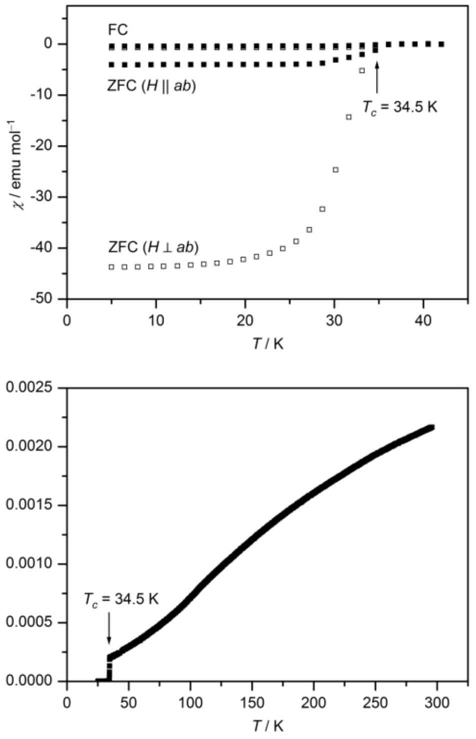

MS05-P61

Eine neue Modifikation von $CaGe_2$

M. Jehle[1], J. Steckhan[1], C. Röhr[1]
[1]*Universität Freiburg, Freiburg i. Br., Germany*

Im Rahmen der Untersuchung gemischter Erdalkalimetall-Tetrelide [1] konnte im System Ca-Ge-Pb (Ca:Ge:Pb=1:1.2:0.4) eine dritte Modifikation des Digermanids $CaGe_2$ (SmSI-Typ, *hR*9, Raumgruppe *R*-3*m*, *a*=396.7(1); *c*=1581.5(8) pm, *V*=215.2(2) 10^6 pm^3, *R*1=0.034) erhalten werden. Von $CaGe_2$ waren bisher zwei Modifikationen bekannt. Die erstmals 1944 beschriebene Form ($CaSi_2$-Typ, *hR*18, Raumgruppe *R*-3*m*, *a*=399.0(1), *c*=3060.2(9) pm, *V*=421.9(1) 10^6 pm^3 [2]) kann aus stöchiometrischen Schmelzen erhalten werden. Die zweite berichtete Modifikation (N_2W-Typ, *hP*6, Raumgruppe $P6_3mc$, *a*=399.7(1), *c*=1021.1(4) pm, *V*=121.2(1) 10^6 pm^3 [3]) wurde aus einer Indium-Schmelze kristallisiert (Ca:Ge:In=1:1:10). Alle drei polymorphen Formen weisen gewellte Ge-Sechseckschichten auf. Es unterscheiden sich lediglich deren Stapelfolgen: In der im N_2W-Typ kristallisierenden Phase lautet sie |:AB:|, in der *hR*9-Phase |:ABC:| und in der *hR*18-Phase |:AA'BB'CC':|. Während die beiden bereits bekannten Phasen zwei kristallographisch unterschiedliche Ge-Lagen aufweisen liegt in der neuen Form nur eine kristallographische Ge-Lage vor (alle 3m, 0,0,*z*). Die Ge-Ge-Abstände betragen in der *hR*9-Phase 254.5(1) pm. Die beiden anderen Modifikationen weisen Ge-Ge-Abstände von 251.9(1) bis 255.1(1) pm (*hP*6) und 251.4(1) bis 255.2(1) pm (*hR*18) auf. Während sich die Ge-Ge-Abstände der einzelnen Formen nicht gravierend unterscheiden, weist die Koordination der Ca-Ionen, die jeweils nur eine Wyckoff-Lage besetzen, deutliche Unterschiede auf. So besitzt Ca in der *hR*9-Phase eine Ge-Koordinationszahl von 6+2 (309.7(2) und 318.7(3) pm). Bei den anderen beiden Modifikationen beträgt sie (3+3)+1+3. In diesen nehmen die Ca-Ge-Abstände mit 300.4(1) bis 375.2(1) pm deutlich unterschiedliche Werte an. Das auf die Zahl der Formeleinheiten normierte Volumen ist für die *hR*9-Phase am größten, das für die *hP*6-Phase ist um 1.7% kleiner, das der *hR*18-Phase um 2.1%. Eine in [4] durchgeführte Geometrieoptimierung, im Fall der *hR*9-Phase ausschließlich anhand theoretischer Daten, liefert den gleichen Trend. Vergleicht man nun die Koordinationszahlen der einzelnen Phasen und deren Volumina, so liegt der Schluss nahe, dass es sich bei der neuen *hR*9-Phase um die Hochtemperatur-Phase von $CaGe_2$ handelt.

[1] M. Jehle, J. Steckhan, C. Röhr, *Acta Crystallogr.* A69, 502 (2013). [2] H. J. Wallbaum, *Naturwiss.*, 32, 76 (1944). [3] P. H. Tobash, S. Bobev, *J. Sol. State Chem.*, 180, 1575-1581 (2007). [4] H. Bouderba, Y. Djaballah, A. Belgacem-Bouzida, R. Beddiaf, *Intermet.*, 28, 108-119 (2012).

MS05-P62

Intermetallische Phasen des quasibinären Schnitts $SrIn_4$-$SrHg_4$

C. Röhr[1], M. Wendorff[1]
[1]*Institut für Anorganische und Analytische Chemie, Universität Freiburg, Freiburg, Germany*

In Erweiterung der strukturell vielfältigen und bindungstheoretisch sehr interessanten Ba-In-Mercuride [1-3] wurden nun auch vergleichbare Sr-Phasen, zunächst des Schnittes SrIn4-SrHg4, synthetisiert und strukturell charakterisiert, da sich sowohl die binären Sr-Indide als auch die reinen Sr-Mercuride sehr deutlich von den entsprechenden Ba-Verbindungen unterscheiden. In dem nahe der 1:4-Zusammensetzung liegenden binären Indid Sr_3In_{11} (La_3Al_{11}-Typ, Abb. b [4]) läßt sich nur ein sehr kleiner Teil des Indiums durch Quecksilber ersetzen. Ausgehend von der ebenfalls bekannten binären

Randphase $SrIn_4$, die im monoklinen $EuIn_4$-Strukturtyp kristallisiert (Abb. c, [5]), konnten ohne Strukturwechsel 14% des Indiums durch Quecksilber substituiert werden. Bei weiter erhöhten Hg-Anteilen wird ab einem Gehalt von 24 % der einfache $BaAl_4$-Typ (Abb. a) stabil, der auch im analogen Ba-System beobachtet wurde [1] und der bis zur vollständig geordneten Verbindung $SrIn_2Hg_2$ (50 % Hg) reicht. Überraschenderweise tritt dann bei weiter erhöhten Hg-Gehalten zwischen 71 und 76 % wiederum der EuIn4-Typ auf, in diesem Fall jedoch mit deutlich geänderten Achs- und Bindungsverhältnissen. Proben mit Hg-Gehalten zwischen 50 und 70 % führen dagegen zu von der 1:4-Stöchiometrie abweichenden Phasen, die (a) entweder aus dem Ba-System bekannt sind (z.B. $Sr(In/Hg)_6$, vgl. [2]), (b) ternäre Varianten binärer Sr-Mercuride darstellen oder (c) in neuen Strukturtypen kristallisieren (z. B. die 1:3-Phase $SrIn_{1.2}Hg_{1.8}$: monoklin, *C*2/*m*, *a*=1169(1), *b*=487.0(4), *c*=1471(2) pm, β=92.07°, *R*1=0.0818; Abb. d). Für die neuen Sr-In-Mercuride werden die strukturellen Gemeinsamkeiten (Pyramindenschichten, KHg_2-Strukturelemente, Hg-Rhomben, s. Abb.), die elektronische Strukturen (auf der Basis von FP-LAPW Bandstrukturrechnungen) und die In/Hg-Verteilung (Kolorierung des Anionennetzes) diskutiert.

[1] M. Wendorff, C. Röhr, Z. Naturforsch. 68b, 307-322 (2013).

[2] M. Wendorff, C. Röhr, J. Alloys Compd. 546, 320-328 (2012).

[3] M. Wendorff, C. Röhr, J. Solid State Chem. 203, 297-303 (2013).

[4] J.-G. Mao, A. M. Guloy, J. Alloys Compd. 363, 143-149 (2004).

[5] D.-K. Seo, J. D. Corbett, J. Am. Chem. Soc. 122, 9621-9627 (2000).

Figure 1

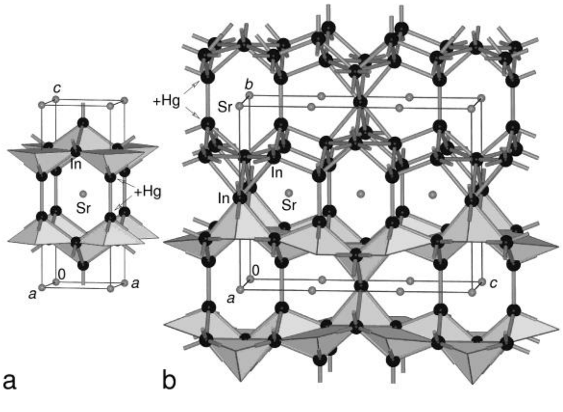

Figure 2

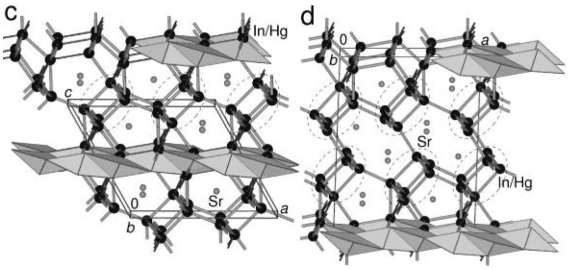

MS05-P63

New intermetallics in the system Ta/Ga

A. Koffi[1], M. ade[1], H. Hillebrecht[1]
[1]*University Freiburg , Inorganic Chemistry, Freiburg, Germany*

Phase equilibria in intermetallic systems of metals with strongly unequal melting points are afflicted with uncertainties. The approach to the thermodynamic equilibrium can be prevented or delayed by kinetic reasons. The system Ta/Ga is one example for this situation. Using sufficient long times for reaction and cooling we succeeded to obtain new compounds in the system Ta/Ga and characterized their stuctures based in single crystal data.

Ta_8Ga_{41} (*R* , *Z* = 3, *a* = 14.299(9) Å, *c* = 15.317(8) Å) crystallizes with Mo_8Ga_{41} structure [1]. Ta shows a 10-fold coordination as a “centaur” polyhedron (half cube, half icosahedron). These polyedra are connected by common vertices to cube-shaped octameric units $TaGa_{10/2}$. In the center there is one additional Ga-atom with cuboctahedral surrounding. The other Ga-atoms perform coordination numbers between 10 and 12 (*Ga*Ga_8Ta_2, *Ga*Ga_9Ta_2, *Ga*$Ga_{10}Ta_2$).

Triclinic Ta_6Ga_{31} (*P* , *Z* = 2, *a* = 9.681(5) Å, *b* = 9.708(6) Å, *c* = 14.843(9) Å, α = 80.75(5)°, ß = 85.21(4)°, γ = 85.21(4)°) is isotypic to triclinic Mo_6Ga_{31} [2]. Similar to rhombohedral Ta_8Ga_{41} there are octameric units of centaur-polyhedra with a single Ga atom in the center. According to the increased Ta-content, the “supercubes” form dimers in sharing a common face. These dimers are all parallel orientated in direction [001]. In monoclinic Mo_6Ga_{31} [3] the “dimers” of the octameric units are orientated in an orthogonal pattern.

Ta_2Ga_5 belongs to the well-known Mn_2Hg_5 type (*P*4/*mbm*, *a* = 9.321(1)Å, *c* = 2.7572(6)Å), which is also realized by other Ga-compounds like V_2Ga_5. The Ga atoms form a layer of triangles, squares and pentagons. Ta is in a pentagonal prism Ga_{10} with two capping Ta atoms.

The tetragonal structure of Ta_5Ga_4 represents a new structure type (*tP*144, *P*4$_2$/*mnm*, *Z* = 16, *a* = 11.7883(5)Å, *c* = 16.9849(9)Å). The complex structure contains Ta-Ta, Ta-Ga, and Ga-Ga contacts with a great variety of distances. Interestingly, one of the Ga-Ga bonds is nearly as short (2.56 Å) as in elemental Ga (2.49 Å). Coordination numbers range from 11 to 14 (Ta) and 8 to 11 (Ga), respectively.

[1] K. Yvon, *Acta Crystallogr.* B31(1975)117-120.
[2] R. Lux, PhD thesis university Freiburg, 2004.
[3] K. Yvon, Acta Crystallogr. B30(1974)853-861

MS05-P64

Alkaline-Earth Metal Amides as Mineralizers for Ammonothermal GaN Crystal Growth: $Ba[Ga(NH_2)_4]_2$ as Intermediate

J. Hertrampf[1], S. Zhang[1], N. S. A. Alt[2], E. Schlücker[2], R. Niewa[1]
[1]*University of Stuttgart, Institute of Inorganic Chemistry, Stuttgart, Germany*
[2]*University of Erlangen-Nuremberg, Institute of Process Machinery and Systems Engineering, Erlangen, Germany*

Single crystals of metal nitrides are of great importance for semiconductor industries. Gallium nitride is characterized by its wide bandgap (3.2 ~ 3.4 eV), high chemical and thermal durability. Those features are needed in a number of applications such as blue laser diodes, transistors or high power amplifiers [1,2].

Ammonothermal synthesis (critical point of ammonia: $p \geq 11.3$ MPa, $T \geq 403.5$ K) of GaN is suitable for growth of high-quality wafers of several inch. Within this technique, mineralizers are responsible for reasonable solubility of GaN in ammonia, thus, for material transport (ammono-basic: alkali metals, their amides or azides, ammono-acidic: gallium halides or ammonium halides) [3-5]. The chemical nature of dissolved species in general is still in question, although several potential intermediates have been recently characterized [6,7]. Under ammono-basic conditions possible intermediates $Li[Ga(NH_2)_4]$ and $Na_2[Ga(NH_2)_4]NH_2$ were obtained and characterized with $LiNH_2$ an $NaNH_2$ as mineralizers [6].

To the best of our knowledge no studies report GaN crystal growth using alkaline-earth metal amides as mineralizers so far. We report GaN transport under ammono-basic conditions as well as formation and characterization of $Ba[Ga(NH_2)_4]_2$ as possible intermediate with $Ba(NH_2)_2$ as mineralizer. $Ba[Ga(NH_2)_4]_2$ crystalizes tetragonal with: $a = 9.1019(3)$ Å, $c = 6.5664(2)$ Å, $Z = 2$, in P -4 . The compound contains isolated tetramidogallat ions $[Ga(NH_2)_4]^-$. Barium is coordinated by eight amide ions in a two-fold capped octahedron.

[1] O. Ambacher, *J. Phys. D. Appl. Phys.* 1998, *31*, 2653.
[2] M. R. Krames, O. B. Shchekin, R. Müller-Mach, G. O. Müller, L. Zhou, G. Harbers, M. G. Craford, *J. Disp. Technol.* 2007, *3*, 160.
[3] R. Dwilinski, R. Doradzinski, J. Garczynski, L. Sierzputowski, R. Kucharski, M. Zajac, M. Rudzinski, R. Kudrawiec, J. Serafinczuk, W. J. Strupinski, *J. Cryst. Growth* 2010, *312*, 2499.
[4] H. W. Xiang, *J. Phys. Chem. Ref. Data* 2004, *33*, 1005.
[5] D. Ketchum, J. Kolis, *J. Cryst. Growth* 2001, *222*, 431.
[6] S. Zhang, N. S. U. Alt, E. Schlücker, R. Niewa, *J. Cryst. Growth* 2014, submitted.
[7] S. Zhang, F. Hintze, W. Schnick, R. Niewa, *Eur. J. Inorg. Chem.* 2013, *31*, 5374.

MS05-P65

Crystal Structure of Hexaphenyldisilane $Si_2(C_6H_5)_6$

L. Fink[1], T. Bernert[2], J. Glinnemann[1], E. Alig[1], M. Berger[1], M. U. Schmidt[1]
[1]*Universität Frankfurt, Anorg. Analyt. Chemie, Frankfurt, Germany*
[2]*Universität Frankfurt, Geowissenschaften, Frankfurt, Germany*

The title compound is a common reactant in organic and organometallic synthesis.

Up to now no suitable crystals for single-crystal X-ray structure determination could be obtained.

Therefore the crystal structure was solved from synchrotron X-ray powder diffraction data. The Rietveld refinement confirmed the orthorhombic space group $P2_12_12_1$ (19), lattice parameters $a = 16.9602(3)$ Å, $b = 20.2889(3)$ Å, $c = 8.55060(8)$ Å at ambient, and $Z = 4$. No phase transition could be observed in the temperature range from 4 to 400 K.

Fig. 1 gives a projection of the structure along [001], the direction of the Si-Si bond in the molecules. From the arrangement of the molecules a pseudohexagonal metric in the (a,b)-plane results, with $a/2 \bullet \sqrt{3} \approx b$. The phenyl rings exhibit a staggered paddle-wheel arrangement around the molecular Si-Si axis (Fig. 2). Due to the interlock of the paddle wheels of neighbouring molecules, interesting structure-property relations were discovered. These will be the topic of another contribution by Th. Bernert during the conference.

Appropriate to the general position (the lone position) in space group $P2_12_12_1$, the molecule clearly exhibits only point-group symmetry 1 (C_1).

Figure 1

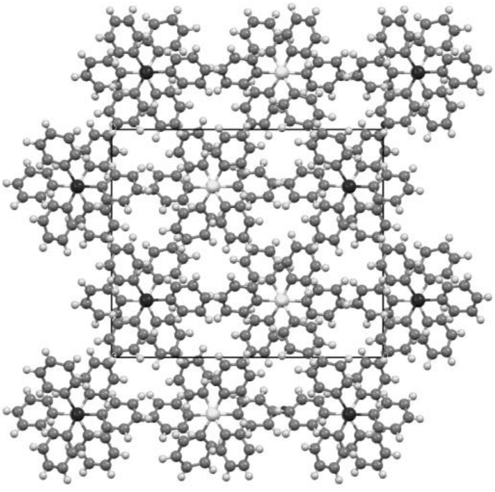

Figure 2

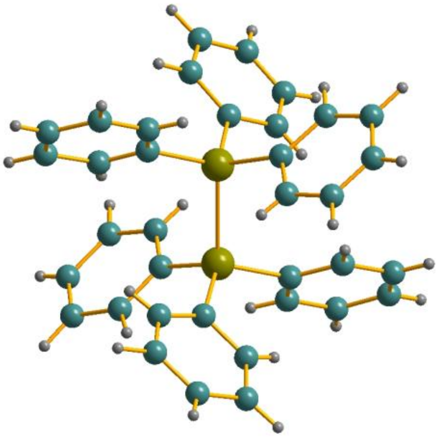

MS05-P66

Crystal Structures of New Cu(II) Coordination Polymers from X-ray Powder Data

H. Zhao[1], L. Fink[1], Y. Krysiak[1], J. Glinnemann[1], E. Alig[1], M. U. Schmidt[1]

[1]*Goethe Universität Frankfurt am Main, Institut für Anorganische und Analytische Chemie, Frankfurt am Main, Germany*

Coordination polymers have attracted increasing interest in recent years because of their properties derived from their polymeric structures und applications in many areas. The coordination compounds, $[CuCl_2py]_n$ (**1**) and $[CuCl_2(4\text{-}CNpy)]_n$ (**2**), were prepared by thermal decomposition of $[CuCl_2L_2]_n$ (L = pyridine, 4-cyanopyridine) under different conditions. Due to a mixture of two polymorphic phases in both compounds, we shifted the X-ray intensities by smart variations of sample preparations in that way, that the assignment of the powder diagrams to its respective phase was possible. The crystal structures were determined with direct-space methods and confirmed by Rietveld refinements. For both coordination compounds with polymeric chains a triclinic (P-1, Z=2) and a monoclinic phase ($P2_1/n$, Z=4) are obtained. Unexpectedly, in (**2**) cyanopyridine acts as a monodentate ligand via the N_{py}-donor only. While the arrangements of the polymeric chains in both triclinic phases are quite similar, the arrangements are rather different in both monoclinic phases.

Figure 1

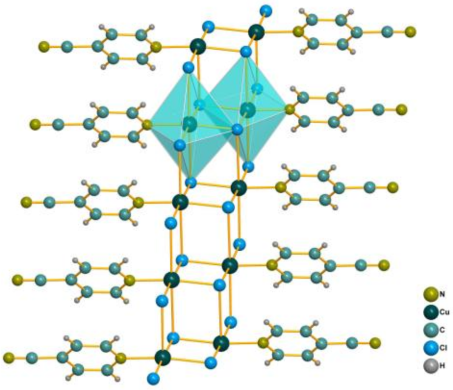

Polymeric chain in triclinic phase of compound (**2**)

MS05-P67

Crystal Structure of Lead(II) Methanesulfonate Monohydrate

T. Trella[1], W. Frank[1]

[1]*Heinrich-Heine-Universität Düsseldorf, Institut für Anorganische Chemie und Strukturchemie II, Düsseldorf, Germany*

Regarding catalysis and crystal engineering, the properties of methanesulfonates as eco-friendly Lewis acids[1] and as components of layered inorganic-organic hybrid materials[2] have been increasingly investigated during the last decade. Methanesulfonates are throughout excellently water-soluble, stable up to about 400 °C and practically inert against hydrolyzing, oxidizing or reductive agents.[3,4] Particularly in electroplating processes, a medium based on an aqueous solution of lead(II) methanesulfonate has largely replaced systems resting upon fluoroboric, fluorisilicic or sulfamic acid, for example.[5,6] Moreover, it has been suggested as an efficient electrolyte for novel flow batteries.[7] The structure of lead(II) methanesulfonate monohydrate which is obtained from aqueous solutions at room temperature shall be presented here to give further information concerning the crystal chemistry of this technically interesting compound.

Colourless, platelet-like crystals of lead methanesulfonate monohydrate, $Pb(CH_3SO_3)_2 \cdot H_2O$ (**1**), were prepared by the reaction of lead carbonate with an aqueous solution of equimolar methanesulfonic acid and subsequent evaporation of the solvent at room temperature. The crystallographic data for **1** are summarized in Table 1.

The solid state structure of **1** consists of two different kinds of layers: one hydrophobic region with methyl groups being geared into each other and one hydrophilic part containing ninefold coordinated Pb^{2+} ions. The coordination polyhedron is a tricapped pentagonal pyramid that is slightly distorted by the cations' lone pair and weak to medium strong O—H···O hydrogen bonding as indicated by the O···O distances of 2.7-3.1 Å. Along [010] the cations are connected to each other by the sulfonate groups *via* Pb—O—Pb and Pb—O—S—O—Pb sequences, forming a double chain array. Hydrogen bonding between the water ligands and the —SO_3 groups links these chains in *c* direction. Perpendicular to [010], the polar layers are connected by *van der Waals* interactions between the methyl groups. Despite of considerably different cell parameters, there is a significant analogy to the solid state structure of strontium methanesulfonate monohydrate.[8]

Table 1. Crystallographic data for $Pb(CH_3SO_3)_2 \cdot H_2O$ (**1**).

[1] M. Wang, G. F. Tian, Z. G. Song, H. Jiang, *Chin. Chem. Lett.* 2009, *20*, 1034.
[2] T. Trella, W. Frank, *Acta Crystallogr.* 2012, *E68*, m1136.
[3] M. D. Gernon, M. Wu, T. Buszta, P. Janney, *Green Chem.* 1999, *1*, 127.
[4] E. M. Aricó, L. B. Zinner, C. Apostolidis, E. Dornberger, B. Kanellakopulos, J. Rebizant, *J. Alloys Compd.* 2001, *323-324*, 39.
[5] W. L. Hsueh, C. C. Wan, *B. Electrochem.* 1990, *6*, 790.
[6] M. D. Capelato, J. A. Nóbrega, E. F. A. Neves, *J. Appl. Electrochem.* 1995, *25*, 408.
[7] A. B. Velichenko, R. Amadelli, E. V. Gruzdeva, T. V. Luk'yanenko, F. I. Danilov, *J. Power Sources* 2009, *191*, 103.
[8] T. Trella, W. Frank, *Z. Krist. Suppl.* 2012, *32*, 112.

Figure 1

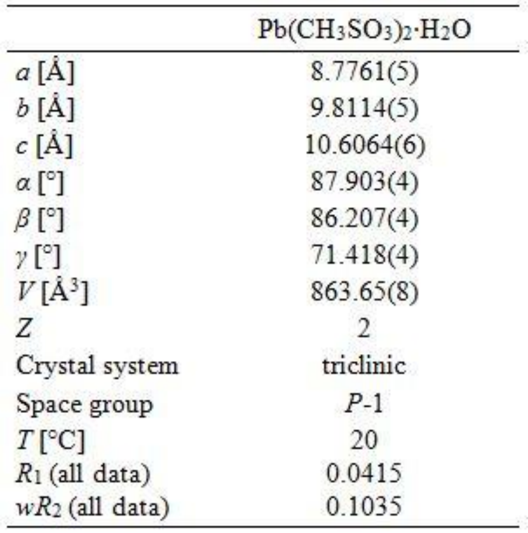

	$Pb(CH_3SO_3)_2 \cdot H_2O$
a [Å]	8.7761(5)
b [Å]	9.8114(5)
c [Å]	10.6064(6)
α [°]	87.903(4)
β [°]	86.207(4)
γ [°]	71.418(4)
V [Å^3]	863.65(8)
Z	2
Crystal system	triclinic
Space group	*P*-1
T [°C]	20
R_1 (all data)	0.0415
wR_2 (all data)	0.1035

MS05-P68

Crystal Structure of 4-Aminopyridin-1-ium Hydrogen (9-Phosphonononyl)phosphonate

M. van Megen[1], G. J. Reiß[1], W. Frank[1]
[1]*Heinrich-Heine-Universität Düsseldorf, Institut für Anorganische Chemie und Strukturchemie II, Düsseldorf, Germany*

Investigations on diphosphonic acids in the context of supramolecular chemistry and crystal engineering have been limited mainly to metal phosphonates [1-3]. Studies on organic aminium salts of diphosphonic acids [4-7] have shown that they exhibit similar structural features to their inorganic counterparts. The structure-directing elements of the phosphonate moieties are their three-dentate character and their trigonal geometry. Hence, organic aminium salts of diphosphonic acids have the ability to form extended hydrogen bonded assemblies which can be utilized for the design of new solid materials with 1D, 2D, and 3D coordination polymeric structures.

Thin, colourless platelets of 4-aminopyridin-1-ium hydrogen (9-phosphonononyl)phosphonate, $[C_5H_7N_2][(HO)_2OP(CH_2)_9PO_2(OH)]$, were grown from a methanolic solution of 4-aminopyridine and nonane-1,9-diphosphonic acid by slow evaporation of the solvent under ambient conditions. The title compound crystallises in the triclinic space group *P*-1 with a = 6.7275(4) Å, b = 6.8963(4) Å, c = 20.0643(10) Å, α = 97.956(4)°, β = 98.767(4)°, γ = 94.309(5)°, V = 906.73(9) Å^3, Z = 2, R_1 = 0.0337, wR_2 = 0.0743, 3163 reflections and 301 parameters.

The asymmetric unit of the title compound consists of one 4-aminopyridin-1-ium cation and one hydrogen (9-phosphonononyl)phosphonate anion both in general positions. The (9-phosphonononyl)phosphonate anion exhibits an all-*transoid* conformation within the limits of experimental uncertainties and shows, as well as the 4-aminopyridin-1-ium cation, common values for the intermolecular bond lengths and angles. The structure of the title compound can be described as a three-dimensional hydrogen bonded network with clearly separated anionic and cationic layered regions stacked along the *c* direction. Within the anionic layers, the end groups of the hydrogen (9-phosphonononyl)phosphonates form two-dimensional hydrogen bonded networks in the *ab* plane consisting of strong charge supported P-O$^-$···H-O (d(D···A) = 2.497(2) - 2.507(2) Å) and medium-strong P=O···H-O hydrogen bonds (d(D···A) = 2.621(2) Å). The basic hydrogen bonded motifs occurring in these networks are $R_6^6(24)$ rings [8] which are arranged like bricks in a wall. The two hydrogen bonded networks belonging to one anionic layer are connected by alkyl chains. The alkyl chains themselves are aligned along the *c* axis interacting with each other only by *van der Waals* forces. Within the cationic layers, the predominant intramolecular forces between the 4-aminopyridin-1-ium ions are arene-arene interactions. Neighbouring arenes are packed in a parallel displaced face-to-face arrangement with a plane to plane distance of 3.3252(8) Å and an offset of 2.2703 Å. The anionic and cationic layers are linked along the *c* axis *via* medium-strong N-H···O hydrogen bonds (d(D···A) = 2.697(2) - 2.808(3) Å) accomplishing the three-dimensionality of the network.

Figure 1. Literature.

Figure 1

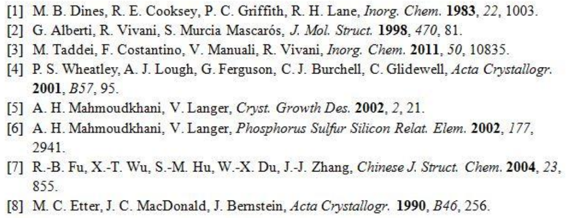

[1] M. B. Dines, R. E. Cooksey, P. C. Griffith, R. H. Lane, *Inorg. Chem.* **1983**, *22*, 1003.
[2] G. Alberti, R. Vivani, S. Murcia Mascarós, *J. Mol. Struct.* **1998**, *470*, 81.
[3] M. Taddei, F. Costantino, V. Manuali, R. Vivani, *Inorg. Chem.* **2011**, *50*, 10835.
[4] P. S. Wheatley, A. J. Lough, G. Ferguson, C. J. Burchell, C. Glidewell, *Acta Crystallogr.* **2001**, *B57*, 95.
[5] A. H. Mahmoudkhani, V. Langer, *Cryst. Growth Des.* **2002**, *2*, 21.
[6] A. H. Mahmoudkhani, V. Langer, *Phosphorus Sulfur Silicon Relat. Elem.* **2002**, *177*, 2941.
[7] R.-B. Fu, X.-T. Wu, S.-M. Hu, W.-X. Du, J.-J. Zhang, *Chinese J. Struct. Chem.* **2004**, *23*, 855.
[8] M. C. Etter, J. C. MacDonald, J. Bernstein, *Acta Crystallogr.* **1990**, *B46*, 256.

MS05-P69

Crystal Structures of Two Transition Metal Methanesulfonate Hydrates

<u>T. Trella</u>[1], W. Frank[1]
[1]*Heinrich-Heine-Universität Düsseldorf, Düsseldorf, Germany*

Regarding catalysis and crystal engineering, the properties of methanesulfonates as eco-friendly Lewis acids[1,2,3] and as components of layered inorganic-organic hybrid materials[4] have been increasingly investigated during the last decade. Methanesulfonates are throughout excellently water-soluble, stable up to about 400 °C and practically inert against hydrolyzing, oxidizing or reductive agents.[5,6] The structures of manganese(II) and iron(II) methanesulfonate hydrates that are obtained from aqueous solutions at room temperature shall be presented here to give further information concerning the crystal chemistry of transition metal methanesulfonates.

Rose, platelet-like crystals of manganese(II) methanesulfonate dihydrate, $Mn(CH_3SO_3)_2{\cdot}2H_2O$ (**1**), were grown from aqueous solutions of methanesulfonic acid and manganese carbonate by slow evaporation of the solvent at room temperature. The crystallographic data for all compounds are summarized in Table 1. In case of **1**, the unit cell parameters are in good agreement with the literature.[7]

The Mn^{2+} cation is octahedrally surrounded by oxygen atoms of two water molecules and four methanesulfonate anions, two of which are in axial position. In *a* direction the cations are associated by two sulfonate groups in a Mn—O—S—O—Mn sequence, forming an infinite chain. Along *b* these chains are connected to polar layers by O—H···O hydrogen bonding between one water ligand and two anions, respectively. In total, each sulfonate group is involved in the monodentate coordination of two cations and in a hydrogen bond to two aqua ligands with its remaining oxygen atom. Within the *ac* plane, the polar layers are connected by *van der Waals* interactions between the anions' methyl groups.

Iron(II) methanesulfonate tetrahydrate, $Fe(CH_3SO_3)_2{\cdot}4H_2O$ (**2**), crystallizes as pale blue platelets from an aqueous solution of methanesulfonic acid and iron powder. The synthesis was carried out under nitrogen atmosphere to prevent the cation from oxidation by oxygen. Due to the very similar ion radii, the solid state structure of **2** is isostructural to the respective copper(II)[8] and zinc(II)[9] methanesulfonate tetrahydrates.

The characteristic building block of **2** is a centrosymmetric unit containing a Fe^{2+} cation that is octahedrally coordinated by oxygen atoms of four aqua ligands in square-planar and two sulfonate groups in apical position. Medium-strong hydrogen bonding of the type —O—H···O—S—O···H—O— links these units to a two-dimensional network within the *bc* plane. In terms of graph-set analysis,[10] one remarkable helical path of hydrogen bonding can be characterized by $C^4_4(24)$ (H5A, H5B). While spiraling around the 2_1 axis and connecting five octahedra on its way, it also coincides with components of extensive cyclic graphs like $R^6_6(36)$ (H5A, H5B). As already known from above, the polar networks are alternately separated by hydrophobic layers.

Table 1. Crystallographic data for $Mn(CH_3SO_3)_2{\cdot}2H_2O$ (**1**) and $Fe(CH_3SO_3)_2{\cdot}4H_2O$ (**2**).

Figure 1

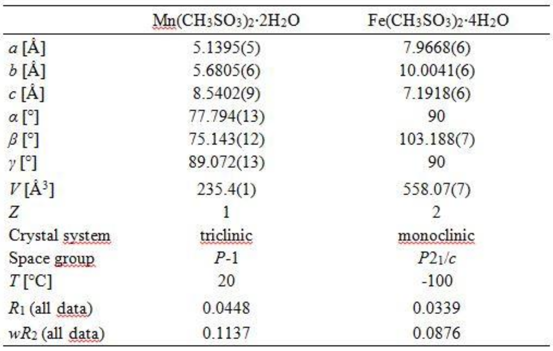

	$Mn(CH_3SO_3)_2{\cdot}2H_2O$	$Fe(CH_3SO_3)_2{\cdot}4H_2O$
a [Å]	5.1395(5)	7.9668(6)
b [Å]	5.6805(6)	10.0041(6)
c [Å]	8.5402(9)	7.1918(6)
α [°]	77.794(13)	90
β [°]	75.143(12)	103.188(7)
γ [°]	89.072(13)	90
V [Å³]	235.4(1)	558.07(7)
Z	1	2
Crystal system	triclinic	monoclinic
Space group	*P*-1	$P2_1/c$
T [°C]	20	-100
R_1 (all data)	0.0448	0.0339
wR_2 (all data)	0.1137	0.0876

Figure 2

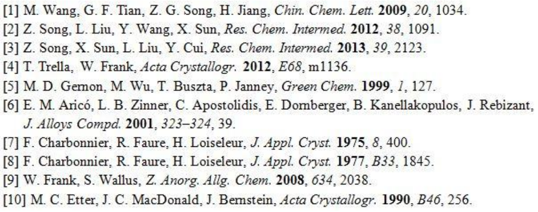

[1] M. Wang, G. F. Tian, Z. G. Song, H. Jiang, *Chin. Chem. Lett.* **2009**, *20*, 1034.
[2] Z. Song, L. Liu, Y. Wang, X. Sun, *Res. Chem. Intermed.* **2012**, *38*, 1091.
[3] Z. Song, X. Sun, L. Liu, Y. Cui, *Res. Chem. Intermed.* **2013**, *39*, 2123.
[4] T. Trella, W. Frank, *Acta Crystallogr.* **2012**, *E68*, m1136.
[5] M. D. Gernon, M. Wu, T. Buszta, P. Janney, *Green Chem.* **1999**, *1*, 127.
[6] E. M. Aricó, L. B. Zinner, C. Apostolidis, E. Dornberger, B. Kanellakopulos, J. Rebizant, *J. Alloys Compd.* **2001**, *323–324*, 39.
[7] F. Charbonnier, R. Faure, H. Loiseleur, *J. Appl. Cryst.* **1975**, *8*, 400.
[8] F. Charbonnier, R. Faure, H. Loiseleur, *J. Appl. Cryst.* **1977**, *B33*, 1845.
[9] W. Frank, S. Wallus, *Z. Anorg. Allg. Chem.* **2008**, *634*, 2038.
[10] M. C. Etter, J. C. MacDonald, J. Bernstein, *Acta Crystallogr.* **1990**, *B46*, 256.

MS05-P70

Dinuclear Transition Metal Complexes with Pyrazolato-Bridged Imidazolium-Based Ligands

S. A. Reindl[1], A. Pöthig[1], F. E. Kühn[1], W. A. Herrmann[1]
[1]*Technische Universität München, Catalysis Research Center, Garching, Germany*

Pyrazolato-bridged dinuclear complexes of different transition metals were synthesized from *N*-heterocyclic carbene (NHC) precursors, 3,5-bis(methylimidazolium-1-ylmethyl]-1*H*-pyrazole bishexafluorophosphate and the respective metal precursors. Depending on the reaction conditions, dinuclear imidazolium complexes or the corresponding NHC complexes were formed. Cyclic voltammetry (CV) experiments were carried out to detect possible electronic coupling between the metal centers. One of the synthesized compounds, a Ru-bis(NHC) complex, shows three reversible redox-processes. Density functional theory (DFT) calculations were used to verify the processes during CV.

Figure 1

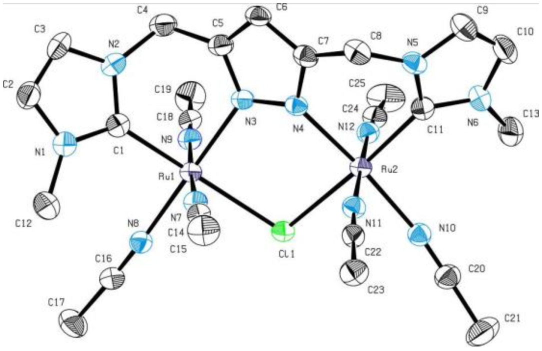

Figure 2

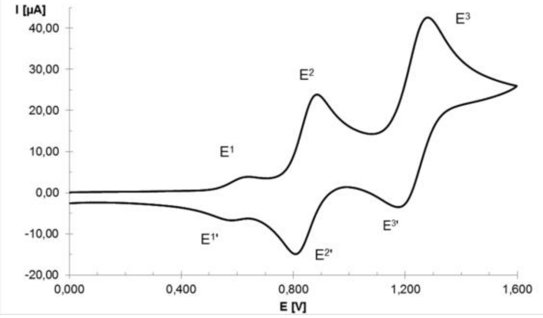

MS05-P71

Synthesis and Crystal Structure of $Sr_2Cl_2[C_2O_4] \cdot 6\ H_2O$

H. Henning[1], T. Schleid[1]
[1]*Universität Stuttgart, Anorganische Chemie, Stuttgart, Germany*

In an attempt to gain a crystalline sample of the intermediate hydrate $Sr[C_2O_4] \cdot H_2O$, which occurs during the complete thermal decomposition of $Sr[C_2O_4] \cdot 2\ H_2O$ [1], aqueous solutions of strontium chloride ($SrCl_2$) and oxalic acid ($H_2C_2O_4$) were mixed. X-ray diffraction of the resulting solid revealed an additional unexpected phase. Upon further investigations, brick-shaped singlecrystals of $Sr_2Cl_2[C_2O_4] \cdot 6\ H_2O$ were found and identified.

The only other known example for an alkaline earth metal oxalate chloride is the mineral *novgorodovaite* ($Ca_2Cl_2[C_2O_4] \cdot 2\ H_2O$), which has been described by *Rastsvetaeva et al.* recently [2]. Unlike the title compound, which has six water molecules in one formula unit and five in the Sr^{2+} coordination sphere, *novgorodovaite* has only two, which greatly influences the structural motifs in comparison to $Sr_2Cl_2[C_2O_4] \cdot 6\ H_2O$.

$Sr_2Cl_2[C_2O_4] \cdot 6\ H_2O$ crystallizes in the monoclinic space group $P2_1/c$ with the lattice parameters a = 984.65(7), b = 913.74(6), c = 753.69(5) pm, β = 110.998(3)° and Z = 2. The crystal structure contains one crystallographically unique Sr^{2+} and Cl^- ion each, two distinguishable oxygen atoms and one carbon atom, forming the complex oxalate anions, and finally three different oxygen atoms and their respective hydrogen atoms, which constitute the water molecules. Whereas in *novgorodovaite* the Ca^{2+} is coordinated by eight ligands, two Cl^- ions, two water molecules and four oxygen atoms of the oxalate, in $Sr_2Cl_2[C_2O_4] \cdot 6\ H_2O$ Sr^{2+} exhibits nine ligands in total. This coordination sphere consists of five water molecules (d(Sr−O) = 261 - 277 pm), via edges to one oxalate anion (d(Sr−O) = 256 - 265 pm) and via corners to two more oxalate anions (d(Sr−O) = 257 - 276 pm), respectively (Figure 1). Each oxalate anion by itself is coordinates via edges to two Sr^{2+} cations and via corners to four more of them. This forms corrugated layers in the (100) plane, between which the Cl^- anions are located and fixed by hydrogen bonds originating from the water molecules (d(Cl···H) = 229 - 249 pm) (Figure 2).

Figure 2: View at the crystal structure along [001].

[1] K. Nagase, K. Sato, N. Tanaka, *Bull. Chem. Soc. Jpn.* 1975, *48*, 439.
[2] R. K. Rastsvetaeva, N. V. Chukanov, Yu. V. Nekrasov, *Dokl. Chem.* 2001, *381*, 329.

Figure 1

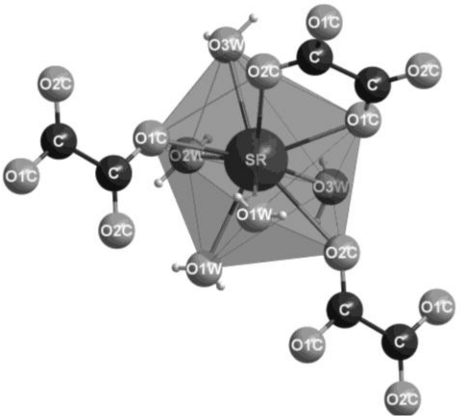

Coordination enviroment of Sr^{2+}.

Figure 2

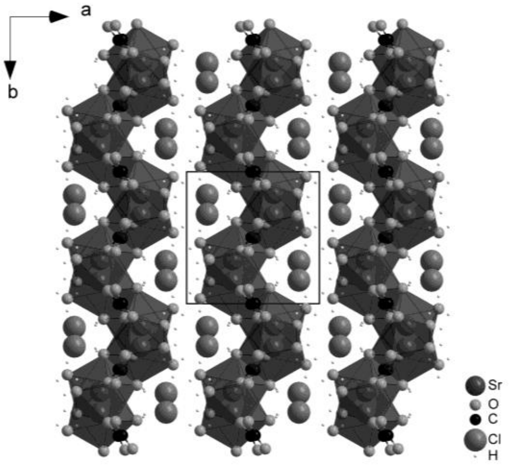

MS05-P72
The crystal structure of 4,4‘-bipyridinium-pentachlorooxomolybdate(V)

J. van Megen[1], W. Frank[1]
[1]*Heinrich-Heine-Universität Düsseldorf, Institut für Anorganische Chemie und Strukturchemie II, Düsseldorf, Germany*

By the reaction of 4,4’-bipyridine and molybdenum(V) chloride in concentrated hydrochloric acid, a green solution is obtained, from which the title compound, [4,4’-H_2bipy][$MoOCl_5$], crystallizes in the orthorhombic space group *Pbca* with $a = 7.9291(3)$ Å, $b = 14.7932(5)$ Å, $c = 25.6716(9)$ Å, $Z = 8$; $R_1 = 0.0444$, $wR_2 = 0.0947$, 2649 reflections and 213 parameters. The asymmetric unit of 4,4‘-bipyridinium-pentachlorooxomolybdate(V) consists of one [4,4’-H_2bipy]$^{2+}$ ion and one [$MoOCl_5$]$^{2-}$ ion, both in general position. N-C, C-C, Mo=O and Mo-Cl bond lengths are in line with expectations (Orpen *et al.*, 2001, Jalilehvand *et al.*, 2007) and the bipyridinium ion, [4,4’-H_2bipy]$^{2+}$, exhibits regular geometry.

In search of reliable strategies for crystal engineering, a key goal is the identification and exploitation of robust synthons[3] to control the formation of the solid. While in some cases global packing forces are sufficient to afford control over the crystal structure or even the periodic network formed by synthons, in other cases local interactions (such as hydrogen bonds) might be necessary.

In this abstract we explore the structural relationships between 4,4‘-bipyridinium-pentachlorooxomolybdate(V) (**1**) and known 4,4’-bipyridinium salts of [MCl_6]$^{2-}$ [M = Os (**2**), Pt (**3**)][1], with similar molecular components and closely related hydrogen bond based synthons. Crystals of **2** and **3** include metal ions in essentially regular octahedral coordination. Their structures contain hydrogen bond motifs **A** (see Figure 1) setting up linear ribbons along the *b*-axis, which are cross-linked by the metal ions (see **B** in Figure 1) forming layers in the *b*,*c* plane. In contrast, the solid of **1** includes molybdate ions in distorted octahedral coordination which are less symmetrical because of the substitution of one chlorido ligand with an oxido ligand. As a result its structure contains hydrogen bond motives **C** (see Figure 1) setting up linear ribbons along the c-axis, built up by simple instead of double hydrogen bond bridgings, and arranged without layer forming cross-linking (see Figure 2). Details of construction of units **C** for **1** and **B** for **2** and **3** are given in Table 1. Although directed bonding between oxido O atoms and N-H functions of the neighboring bipyridinium ions has to be excluded, falling into account the geometric parameters (O···HN: 3.17 Å; 2.98 Å), there are close structural relationships, so that **1** and **2** as well as **1** and **3** can be considered as homotypic, the solid state arrangement mainly determined by the size and shape of its components.

Table 1: Selected hydrogen bond lengths, angles and Cl···Cl distances.

	1 (M = Mo)	**2** (M = Os)[1]	**3** (M = Pt)[1]
Cl···HN/Å	2.41; 2.46	2.59	2.59
M-Cl···HN/°	113; 114	127	126
MCl···H-N/°	165; 163	143	144
Cl···Cl/Å		3.107	3.044

[1] B. Dolling, A. L. Gillon, A. G. Orpen, J. Starbuck, X.-M. Wang, *Chem. Commun.* 2001, 567.
[2] F. Jalilehvand, V. Mah, B. O. Leung, D. Ross, M. Parvez, R. F. Aroca, *Inorg. Chem.* 2007**,** *46*, 4430.
[3] G. R. Desiraju, *Angew. Chem., Int. Ed. Engl.* 1995, *34*, 2311.

Figure 1

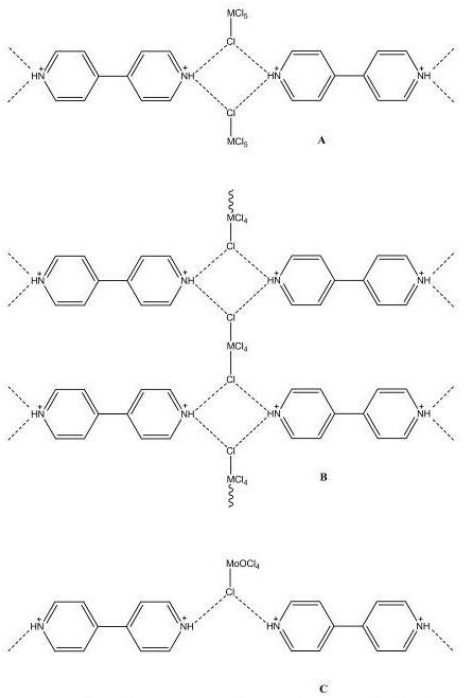

Figure 1: Hydrogen bond motives found in crystal structures of [4,4'-H_2bipy][$MoOCl_5$] (**1**), [4,4'-H_2bipy][$OsCl_6$] (**2**) and [4,4'-H_2bipy][$PtCl_6$] (**3**).

Figure 2

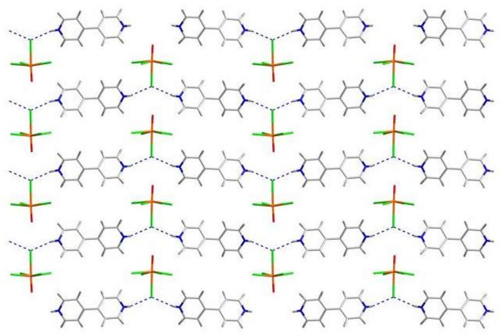

Figure 2: Hydrogen bonded ribbons present within the crystal structure of [4,4'-H_2bipy][$MoOCl_5$] (**1**). Compounds **2** and **3** are homotypic with **1**.

MS05-P73

A comparative study of long chain alkaline earth metal carboxylates

J. Volk[1], W. Frank[1]
[1]*Heinrich-Heine-Universität Düsseldorf, Institut für Anorganische Chemie und Strukturchemie II, Düsseldorf, Germany*

The alkaline earth metal soaps are widely used in industrial applications as softeners, lubricants, pharmaceuticals and detergents. Therefore the structural chemistry of alkaline earth metal carboxylates is of general and practical interest. However, only very few single crystal structures of long chain alkaline earth metal soaps have been successfully determined, so far. [1-3]
Soap crystals are usually obtained as extremely thin, colourless plates that are bent very easily. Any kind of mechanical stress has to be avoided to get crystals of sufficient quality for X-ray structure determinations. Due to ordering problems the quality indicators for soap structures usually are very high.
In the table below crystallographic data for Mg, Ca, Sr, and Ba pelargonates (**1**-**4**) are presented. Crystals of the compounds were obtained by slowly cooling heated aqueous solutions of ammonium pelargonate and the corresponding metal chloride to room temperature.
The solids of **1**-**4** can be described as layer-like with stacking of sheets perpendicular to the longest crystallographic axis. The metal ions with coordinated O atoms build up the inorganic basis of the lamellar structure. This part is dominated by Coulomb interactions (incl. hydrogen bonds (**1**-**2**)). The organic fragments of the solids are characterized by the long alkyl chains located perpendicular and on both sides of the metal-oxygen planes. The layers are linked by *van der Waals* interactions between the terminal -CH_3 groups of the aliphatic chains.
In contrast to **3** and **4**, Ca and Mg soaps contain water of hydration. The Mg atoms in solid **1** have a distorted octahedral coordination given by three O atoms of carboxylate ions and by three O atoms of water molecules. These octahedra are connected by hydrogen bonding between the water molecules. The carboxylates are unidendate and bidendate bridging ligands and link the metal atoms perpendicular to the longest axis.
In case of solid **2** the Ca atoms are pentagonal-bipyramidal coordinated by six O atoms of carboxylate groups and one of a water molecule. The Ca atoms are linked by oxygen atoms from chelating and bridging carboxylates. Hydrogen bonds of the water molecules within the layers give significant contributions additional to the electrostatic Ca-O intralayer bonding forces.
The solids of **3** and **4** are anhydrous. The metal cations Sr and Ba are coordinated by eight oxygen atoms of the carboxylate ions. The metal ions are linked along *a*- and *b*- axis by chelating and bridging carboxylates.

[1] Mesbah, A., Juers C., Lacouture F., Mathieu S., Rocca E., François M., Steinmetz J., *Solid State Sci.*, 2007, *9*, 322-328.
[2] Morley, W. M., Vand, V., *Nature*, 1949, *163*, 285.
[3] Stanley, E., *Nature*, 1964, *203*, 1375-1376.

Figure 1

Formula	$Mg(C_9O_2H_{17})_2(H_2O)_3$ **1**	$Ca(C_9O_2H_{17})_2(H_2O)$ **2**	$Sr(C_9O_2H_{17})_2$ **3**	$Ba(C_9O_2H_{17})_2$ **4**
a (Å)	30.129(2)	5.8410(6)	4.1911(4)	4.3768(4)
b (Å)	8.3385(5)	6.7629(6)	4.5231(5)	4.6444(3)
c (Å)	9.0700(5)	26.744(32)	25.710(22)	25.420(21)
α (°)			88.165(7)	87.495(9)
β (°)	91.840(5)	92.76(14)	89.281(7)	89.60(10)
γ (°)			81.628(7)	81.174(9)
Space group	$P2_1/c$	$P2_1$	$P\bar{1}$	$P\bar{1}$
Z	4	2	1	1
R_1; wR_2	0.1283; 0.2516	0.1548; 0.3769	0.0588; 0.1555	0.0269; 0.0646

MS05-P74

Unusual tetraazaadamantane ligand in a series of manganese(IV) dimers with varying bridging ligands

D. Premužić[1], M. Hołyńska[1]
[1]*Philipps-Universität Marburg, Fachbereich Chemie, Marburg, Germany*

Investigation of the magnetic exchange interaction plays an important role in the coordination chemistry of polynuclear metal complexes. Its understanding based on studies of simple dimeric complexes is the key to tuning of the magnetic properties of multinuclear systems in a systematic way. Simple [Mn_2] dimers are also used as model systems for Photosystem II.[1]

Tris(1-propan-2-onyl oxime)amine (Ox_3H_3) is a polydentate ligand containing three oxime groups, being good linkers. A variety of mononuclear and dinuclear complexes with this ligand is known.[2,3] An unusual cyclization into a tetraazaadamantane ligand has also been described,[4] yet no metal complexes have been reported. Herein we present structure and properties of the first examples of dimeric Mn(IV) complexes with this tetraazaadamantane ligand, comprising dimers bridged by small ligands like oxalate or azide (Fig. 1).

Fig. 1 Structure of the title complexes with different bridging ligands.

[1] M. Hirahara, A. Shoji, M. Yagi, DOI: 10.1002/ejic.201300683. [2] R. M. Jones, M. J. Goldcamp, J. A. Krause, M. J. Baldwin, *Polyhedron*, 2006, *25*, 3145-3158. [3] S. E. Edison, S. D. Conklin, N. Kaval, L. E. Cheruzel, J. A. Krause, C. J. Seliskar, W. R. Heineman, R. M. Buchanan, M. J. Baldwin, *Inorg. Chim. Acta*, 2008, *361*, 947-955. [4] A. N. Semakin, A. Yu. Sukhorukov, A. V. Lesiv, S. L. Ioffe, K. A. Lyssenko, Y. V. Nelyubina, V. A. Tartakovsky, *Org. Lett.*, 2009, *11*, 4072-4075.

Figure 1

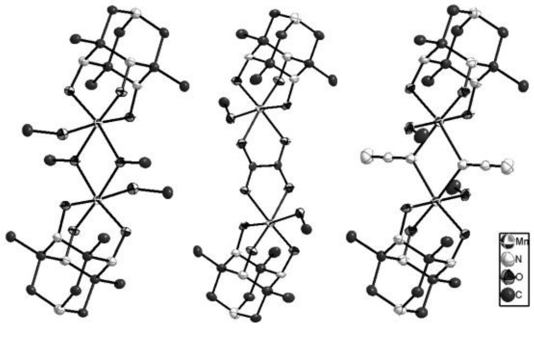

MS05-P75

A new isomer of the classical [Mn^{III}_6] SMMs

M. Holynska[1]
[1]*Philipps University Marburg, Chemistry, Marburg, Germany*

Oxime-bridged hexanuclear manganese(III) complexes are an established group of materials, often displaying Single Molecule Magnet behavior [1]. In the case of [$Mn^{III}_6O_2(Etsao)_6(O_2CPh(Me)_2)_2(EtOH)_6$] ($saoH_2$ = salicylaldoxime) compound [1a] the record values for blocking temperature and energy barrier long held by the famous mixed-valence [Mn_{12}] complex [2] could be improved. A magnetostructural correlation was found showing the importance of the Mn-N-O-Mn torsion angles values with the possibility to switch the dominating magnetic coupling from ferro- to antiferromagnetic below the magical value of 31^0 [1b]. In this contribution a new isomer of the classical [Mn_6O_2]-core oxime-bridged SMMs is introduced with a modified stacking arrangement of the [Mn_3O] units (see Figure 1). The bridging oxime ligand used was 1-(1-hydroxynaphthalen-2-yl)-ethanone oxime newly introduced in our Group [3]. Studies of the magnetic properties show that the title compound is an SMM with a two-step relaxation process of magnetization, where the higher-temperature component can be assigned an energy barrier of 76 K.

Figure 1. (a) The novel stacking arrangement of the triangular [Mn_3O] units in the title compound. (b) The classical [$Mn^{III}_6O_2$] core. (c) Overlap of (a - solid line) and (b - dashed line).

References
[1] (a) C. J. Milios, C. P. Raptopoulou, A. Terzis, F. Lloret, R. Vicente, S. P. Perlepes, A. Escuer, Angew. Chem. 2004, 43, 210; (b) C. J. Milios, R. Inglis, A. Vinslava, R. Bagai, W. Wernsdorfer, S. Parsons, S. P. Perlepes, G. Christou, E. K. Brechin, J. Am. Chem. Soc. 2007, 129, 12505. [2] (a) T. Lis, Acta Cryst., 1980, B36, 2042; (b) R. Sessoli, H. L. Tsai, A. R. Schake, S. Wang, J. B. Vincent, K. Folting, D. Gatteschi, G. Christou, and D. N. Hendrickson, J. Am. Chem. Soc., 1993, 115, 1804. [3] (a) M. Hołyńska, N. Frank, S. Dehnen, Z. Anorg. Allg. Chem. 2012, 638, 2248; (b) M. Hołyńska, N. Frank, C. Pichon, I.-R. Jeon, R. Clerac, S. Dehnen, Inorg. Chem. 2013, 52, 7183.

Figure 1

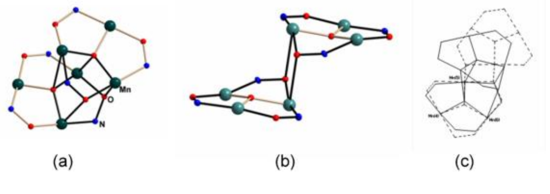

MS05-P76

Synthesis and characterisation of oxygenated

magnsium phthalocyanine

J. Janczak[1], R. Kubiak[1]
[1]*Institute of Low Temperature and Structure Research, Polish Academy of Sciences, Crystallography, Wroclaw, Poland*

Interest of magnesium phthalocyanine, MgPc and its axially or biaxially ligated complexes, MgPcL and $MgPcL_2$ (L is a N or O donor ligand), arises from their similarity and relationship to chlorophyll and they can be used as its synthetic model. Magnesium phthalocyanine similar to other M(II)Pc complexes (M(II)Pc) crystallises in two crystallographic modifications - α and β. However the single crystal structure has been determined only for β-modification [1]. Within the b-M(II)Pc complexes, the magnesium phthalocyanine is exceptional and unusual. It has been stated that the crystals of MgPc are unstable in ambient atmosphere and absorb O_2 and/or N_2 forming complexes with the composition of $(MgPc)_2O_2$ and $(MgPc)_2N_2$ [2]. The differences in the crystal structure of MgPc, relatively to other b-M(II)Pc complexes, establish a chemical feature of MgPc that is responsible for its catalytic properties [3]. Several magnesium phthalocyaninato complexes are used as photosensitisers for photodynamic cancer therapy (PDT) due to their possibility to generate oxygen in the singlet state and their non-toxicity. During photodynamic therapy with phthalocyanines as photosensitisers, they are first excited to the triplet state and than transfer the energy to the ground-state triplet oxygen (O_2, $^3\Sigma_g$), generating the excited-state singlet oxygen (O_2, $^1\Delta_g$). Their activities decrease in the order ZnPc > MgPc > CuPc > MnPc > CoPc > FePc [4]. The molecular oxygen O_2 plays a great and significant role in many photobiological and photochemical processes such as photooxidation, photodegradation or photoaging [5]. In this context, we used magnesium phthalocyanine as a synthetic model of chlorophyll, to investigate the interaction of molecular oxygen with MgPc and the formation of oxygenated magnesium phthalocyanine. The results will be helpful for understanding the nature of the interaction between the molecular oxygen and MgPc.

Two crystals of oxygenated magnesium phthalocyanine complex $(MgPc)_2O_2$ with a composition of $(MgPc)_2O_2{\cdot}2(MgPcDBU){\cdot}2DBU$ - crystal **1** (DBU=1,8-diazabicyclo[5.4.0]undec-7-ene) and $(MgPc)_2O_2{\cdot}4$(4-Mepy) - crystal **2** were obtained, and the structural characterisation will be presented.

Figure 1. View of the molecular structure of oxygenated magnesium phthalocyanine $(MgPc)_2O_2$.

Literature

[1] J. Janczak, R. Kubiak, *Polyhedron* 20 (2001) 2901-2909.

[2] R. Kubiak, J. Janczak, K. Ejsmont, *Chem. Phys. Lett.* 245 (1995) 249-252.

[3] J. Janczak, *Polyhedron* 38 (2012) 75-87.

[4] (a) T. Nyokong, *Pure Appl. Chem.* 83 (2011) 1763-1779; (b) R. Bonnett, Chemical Aspects of Photodynamic Theraphy, pp. 199-222, Gordon and Breach, Amsteldijk, Nederlands, 2000.

[5] (a) S, Mitra, T.H. Foster, *Biophys. J.* 78 (2000) 2597; (b) M.R. Badger, S. Caemmererm S. Ruuska, H. Nakano, *Phil. Trans. R. Soc. London*, B355 (2000) 1433-1446; (c) D.R. Ort, N.R. Baker, *Curr. Opin. Plant Biol*. 5 (2002) 193-198.

Figure 1

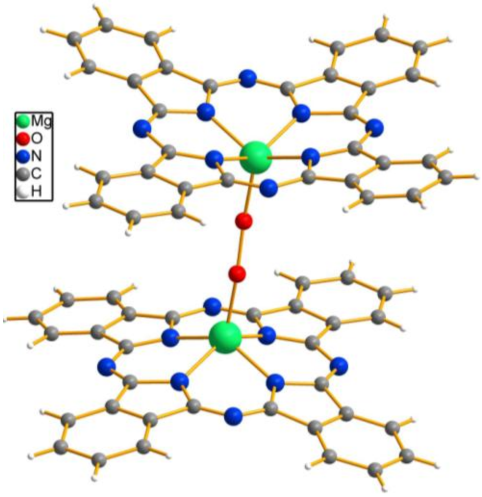

MS05-P77

Square-planar organoplatinum complexes: Crystal structures of three pharmaceutically relevant compounds

W. Raven[1], U. Englert[1], I. Kalf[1], P. Hermes[1]
[1]*RWTH Aachen University, Institute for inorganic Chemistry, Aachen, Germany*

The cycloplatination of primary amines became possible in 2008[1]. An easily accessible intermediate aqua complex has opened up a variety of substitution reactions under mild conditions; we here present two cationic and a neutral derivative. We discuss the intra-complex features such as the strong *trans* effect exerted by the Pt-C bond and the planarity of the coordination environment around the Pt(II) cation, and we address packing and inter-molecular interactions, in particular hydrogen bonds.

Figure 1: Molecular structure of the organoplatinum isocyanato complex in the crystal; displacement ellipsoids are drawn at 50% probability.

[1] B. Calmuschi-Cula and U. Englert, *Organometallics* 27, 3124-3130, 2008

Figure 1

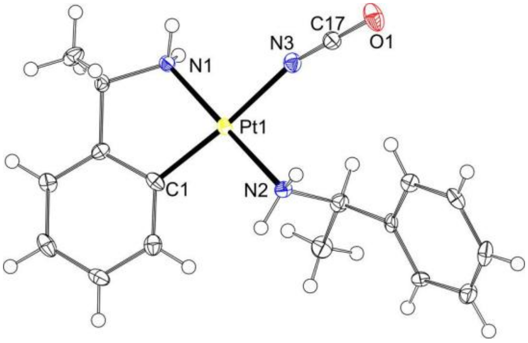

MS06 – Structure property relations in materials scienes

MS06-P01

New Mn(II) coordination polymers employing 2,2’-bipyridine-3,3’,6,6’-tetracarboxylate as a ligand

A. Kochel[1], M. Hołyńska[2]
[1]*University of Wrocław, Faculty of Chemistry, Poland, Poland*
[2]*Fachbereich Chemie and Wissenschaftliches Zentrum für Materialwissenschaften, Philipps-Universität Marburg, Marburg, Germany*

One of the ligands combining the presence of *N*-donor centres and more than one carboxylic group is 2,2’-bipyridine-3,3’,6,6’-tetracarboxylic acid (*bptH₄*). This ligand has already been proved useful in the design of new magnetic/luminescent materials [1].

Two new coordination polymers employing 2,2’-bipyridine-3,3’,6,6’-tetracarboxylate (*bptc*) as a ligand will be presented: $[Mn_2(H_2O)_5(bptc)]_n$ (**1**), $[Mn_2(H_2O)(bptcH_2)]_n$ (**2**). Both **1** and **2** are 2D coordination polymers stabilized by Mn-O coordination bonds obtained under solvothermal conditions. **1** and **2** are characterized by X-ray diffraction studies, IR spectra, elemental analysis, TGA and magnetic properties measurements. Both compounds exhibit the presence of weak antiferromagnetic interactions.

References

[1] (a) U. Dawid, F. P. Pruchnik, R. Starosta, *Dalton Trans.* 2009, 3348; (b) A. Kochel, M. Hołyńska, K. Twaróg, *Inorg. Chem. Commun.* 2012, 24, 47; (c) B. Ji, D. Deng, X. He, B. Liu, S. Miao, N. Ma, W. Wang, L. Ji, P. Liu, X. Li, *Inorg. Chem.* 2012, 51, 2170; (d) W. Mingyan, J. Feilong, Z. Youfu, F. Rui, C. Lian, H. Maochun, *Inorg. Chem. Commun.* 2012, 15, 25.

Figure 1

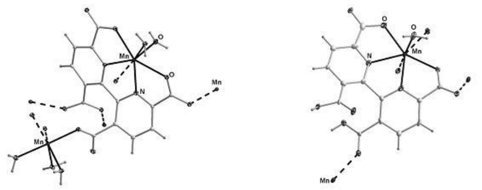

Figure 1. Molecular structure of **1** (left) and **2** (right). Thermal ellipsoids are plotted at 30% probability level. Coordination bonds to Mn are denoted in black. Bonds leading to extension of the coordination polymer are shown as black dashed lines.

MS06-P02

Neutron Diffraction Studies of Pressure Effects on Crystal and Magnetic Structure of $La_{0.5}Ba_{0.5}CoO_{2.8}$

V. Sikolenko[1], I. Troyanchuk[2], D. Többens[1], C. Ritter[3], T. Hansen[3], V. Efimov[4], S. Schorr[1,5]
[1]*Helmholtz-Zentrum Berlin, Crystallography, Berlin, Germany*
[2]*Scientifical-Practical Materials Research Centre, Minsk, Belarus*
[3]*Institute Laue Langevin, Grenoble, France*
[4]*Joint Institute for Nuclear Research, Dubna, Russian Federation*
[5]*Free University Berlin, Berlin, Germany*

The oxygen deficient cobaltite $La_{0.5}Ba_{0.5}CoO_{2.8}$ have been studied in large region of temperature (2 - 300K) and external pressure (up to 6.5 GPa) by neutron powder diffraction. At ambient pressure the compound is cubic and antiferromagnetic below 250K. External pressure suppresses antiferomagnetic ordering and induced ferromagnetism. This transition is not accompanied by changes in crystal symmetry. We suppose that the origin of transition is associated with cobalt ion spin state crossover from a mixed High spin/ Low spin into Intermediate spin/ Low spin state.

MS06-P03

Polarized optical absorption spectra and crystal field Superposition Model calculations of the multiferroic compound Co_3TeO_6

D. Reichartzeder[1], M. Wildner[1]
[1]*Universität Wien, Institut für Mineralogie und Kristallographie, Wien, Austria*

Since the first description of the novel cobalt tellurate Co_3TeO_6 by Becker et al. (2006), this compound has gained much interest due to its multiferroic properties at low temperatures. Besides, the spinel-related monoclinic structure of Co_3TeO_6 is highly interesting from a crystal chemical point of view, comprising five crystallographically different sites of Co^{2+} cations coordinated by [4], [5] and [6] oxygen atoms. The coordination polyhedra exhibit strong to extremely strong distortions from respective ideal polyhedral shapes, thus potentially allowing (i) to resolve low-symmetry crystal field splittings of d-d electronic transitions of Co^{2+}, and furthermore (ii) to test the applicability of the semi-empirical Superposition Model of crystal fields (Newman, 1971) for "multi-polyhedral" cases, when using only a single basis set of Superposition Model intrinsic and power-law parameters.

Polarized optical absorption spectra were measured using microscope-spectrometric techniques in the IR to UV range between 500 and 34000 cm^{-1}. The extreme strong absorption necessitates laborious multi-step preparation of single crystals, and so far spectra of a thin *a*-b* slab could be measured at ambient conditions (Fig. 1); temperature- and pressure-dependent measurements are planned.

According to the Laporte selection rule, the strongest contribution to absorbance (Fig. 1) is expected to originate from the pseudo-tetrahedrally coordinated Co5 site with ground state $^4A_2(F)$, dominating the visible spectral range with the split (cubic) $^4T_1(P)$ level, but also contributing to the IR- and NIR- range. The uncommonly strong band in the UV around 27000 cm^{-1} may be attributed to the [5]-coordinated Co3 site. Depending on the degree of octahedral distortion, the [6]-coordinated sites with cubic ground state $^4T_{1g}(F)$ will more (Co4 and Co2) or less (Co1) contribute to the absorption in the NIR range (cubic $^4T_{2g}(F)$ state) and add minor peaks and shoulders in the visible part (cubic $^4T_{1g}(P)$ state). As a consequence of the strong splitting of spin-allowed crystal field levels, certain spin-forbidden states are expected to play an important role due to "intensity-stealing", thus further complicating reliable band assignments.

Crystal field calculations are still in progress and results will be presented with detailed energy level assignments at a later stage.

References:
Becker R, Johnsson M, Berger H (2006) Acta Crystallogr C62, i67-i69
Newman DJ (1971) Adv Phys 20, 197-256

Figure 1

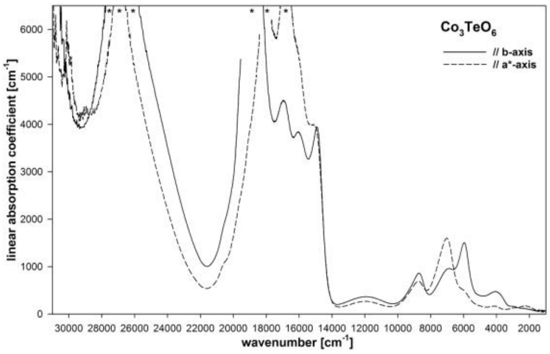

Polarized optical absorption spectra of Co_3TeO_6 (asterisks denote absorption bands still exceeding the sensitivity range of the instrument at a sample thickness of 4µm).

MS06-P04

Temperature-dependent behavior of $|Na_8(NO_2)_2|[AlSiO_4]_6$ in air and carbondioxide

M. Šehović[1], L. Robben[1], T. M. Gesing[1]
[1]*University Bremen, Chemistry, Bremen, Germany*

The three-dimensional highly flexible framework of sodalites forming *toc*-cages (better known as β-cages) is used as a model system for various zeolites, such as LTA, LSX and the Faujasite-type zeolite. Anionic or neutral templates can be incorporated which are charge balanced, as the framework, by cations, all located in the β-cages. We have investigated the temperature-dependent behavior of alumosilicate NO_2^--sodalite in air and CO_2. While heating the NO_2^--sodalite in air a phase transition from $P\bar{4}3n$ to $Pm\bar{3}n$ at 937(3) K is observed explained by the full expansion of the framework, expressed in a tilt angle [1] of φ = 0. This type of phase transition was earlier described for the respective NO_3^--sodalite [2], too. Opposite, the NO_2^--sodalite undergoes a phase transformation towards the CO_3-Nosean, along with a symmetry lowering from P3n to P23, while heating in a CO_2 atmosphere [3]. We have investigated the latter phase transition by in-situ temperature-dependent X-ray powder diffraction, simultaneous thermal analysis and Raman spectroscopy.

Comparing the departure-dependent behavior in air and in a CO_2 atmosphere, a cell-volume expansion of the NO_2^--sodalite from 890 K on can be observed in air (Figure 1). This is most likely caused by an oxidation of NO_2^- to NO_3^- [4]. In contrast to this behavior a delay in the respective expansion in CO_2 is observed. These investigations are aimed to establish the reaction kinetics. After the transformation while heating the CO_3-Nosean in air the partially collapsed (low temperature) to fully expanded (high temperature) framework phase-transition could also be observed. Nevertheless, in this case it must be described as a P23 to P23 phase-transition.

Figure 1. Temperature-dependent cell-volume of nitrite-sodalite (blue) and carbonate-nosean (red) in air. For the nitrite-sodalite treatment in CO_2 (gold) each data point corresponds to a measurement time of 7 minutes.

[1] W. Depmeier, *Acta Crystallogr.* B40 (1984). 434-436. [2] C. H. Rüscher, Th. M. Gesing, J.-Ch. Buhl, *Z. Kristallogr.* 218 (2003) 332-344. [3] Th. M. Gesing, Buhl J.-Ch., *Eur. J. Mineral.* 10 (1998) 71-77. [4] M. T. Weller, G.Wong, C. L. Adamson, S. M. Dodd, J. J. B. Roe, *J. Chem. Soc. Dalton Trans.* (1990) 593-597.

Figure 1

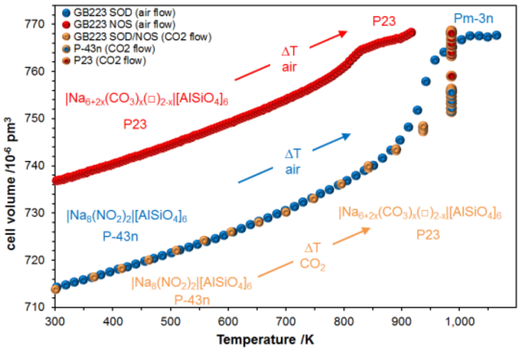

MS06-P05

The Influence of Boron on the Crystal Structure and Properties of Mullite - Investigations at Ambient, High-Pressure, and High-Temperature Conditions

H. Lührs[1], R. X. Fischer[1], H. Schneider[1], S. P. King[2], J. V. Hanna[2], P. E. Kalita[3], K. Lipinska[3], S. Söllradl[4], J. Konzett[5]
[1]*Universität Bremen, Geowissenschaften, Bremen, Germany*
[2]*University of Warwick, Coventry, United Kingdom*
[3]*University Nevada, Las Vegas, United States*
[4]*FRM II, Garching, Germany*
[5]*Universität Innsbruck, Innsbruck, Austria*

Mullite is one of the most important synthetic compounds for advanced structural and functional ceramic materials. The crystal structure of mullite with the composition $Al_2[Al_{2+2x}Si_{2-2x}]O_{10-x}$, $0.2 < x < 0.9$ [1], can incorporate a large variety of foreign cations [2,3]. The influence of boron on the crystal structure and selected properties of mullite was investigated under ambient, high-pressure, and high-temperature conditions.

An anisotropic development of lattice parameters upon boron incorporation is reported [4-6] and explained based on crystal-chemical considerations [7]. Whereas lattice parameters *a* and *b* show minor changes only, a linear relationship between lattice parameter *c* and the amount of boron in the crystal structure was established on the basis of prompt gamma activation analyses (PGAA) and Rietveld refinements. According to this relationship about 15% of the silicon in mullite can be replaced by boron yielding single-phase B-mullite. B-mullites with significantly higher (~ factor 3) boron contents in the mullite structure were also observed but the respective samples contain alumina impurities.

The incorporation of boron results in a reduction of the volume thermal expansion coefficient of 16%, which makes B-mullites a potential candidate for technical applications in the temperature range below 1000°C [5]. Furthermore, boron incorporation is associated with the formation of additional oxygen vacancies which reduces the mechanical stability of the mullite structure at high pressure. A slight increase of the overall (volume) compressibility of B-mullite compared to boron-free mullite is observed. The compressibility in mullite is anisotropic with the **a**-axis being the most and the **c**-axis being the least compressible one. The increasing divergence with pressure between the compressibilities in **a**- and **b**-direction can be explained by a rotation of the octahedra and the increasing inclination angle ω between the octahedral axes of neighboring AlO_6 octahedra in the **ab**-plane.

Single-phase B-mullite with 40% replacement of silicon by boron was synthesized at 10 kbar and 875°C [8]. Based on XRD, ^{11}B MAS NMR, and PGAA data, it was shown that some aluminum in the AlO_4 tetrahedra is replaced by boron as well in addition to the established silicon-boron substitution mechanism.

References:
[1] Fischer, R.X., et al. (1996) J Europ Ceram Soc, 16(2), 109-113.
[2] Schneider, H., in *Mullite*, H. Schneider and S. Komarneni, Editors. 2005, WILEY-VCH: Weinheim. p. 70-93.
[3] Schneider, H., et al. (2008) J Europ Ceram Soc, 28(2), 329-344.
[4] Griesser, K.J., et al. (2008) Miner Petrol, 92(3-4), 309-320.
[5] Lührs, H., et al. (2012) Mater Res Bull, 47, 4031-4042.
[6] Zhang, G.M., et al. (2010) J Europ Ceram Soc, 30(12), 2435-2441.
[7] Lührs, H., et al. (2013) Z Kristallogr, 228(9), 457-466.
[8] Lührs, H., et al. (2013) Cryst Res Technol, in press, DOI: 10.1002/crat201300210.

MS06-P06

Characterization of the hydrides in Mg-Dy alloy using synchrotron radiation

Y. Huang[1], L. Yang[1], K. U. Kainer[1], N. Hort[1], W. Gan[1]
[1]*helmholtz-Zentrum Geesthacht, Geesthacht, Germany*

An unexpected precipitate phase was observed in Mg-20 wt.% Dy alloy, with cuboid morphology not compatible with anyone shown in Mg-Dy binary phase diagram. As observed by SEM-EDX, the ratio of atomic percent of Dy to Mg is very high for those particles, probably due to the poor spatial resolution of that technique but already showing the mismatch with any previously characterized Mg-Dy compound. High-brilliance synchrotron diffraction (HEMS, DESY) and transmission electron microscopy experiments confirmed that these particles are composed of DyH_2. They were formed during sample preparations at room temperature when hydrogen-containing sources, such as water.

Furthermore, the heat treatments such as solid solution or ageing treatments have no influence on the formation of hydrides for the present Mg-Dy materials. The formation mechanism of DyH_2 has been explained. In contrast, the formation of hydrides is prevented in the specimens if they are machined and polished in a dry environment.

MS06-P07

Thermal expansion across phase-transitions.

T. M. Gesing[1], M. M. Murshed[1], L. Robben[1]
[1]*Chemische Kristallographie fester Stoffe, Institut für Anorganische Chemie, Universität Bremen, Bremen, Germany*

The description of a Landau phase-transition considers group-subgroup relation with respect to the initial structure in the thermodynamic equilibrium. Accordingly, the Gibbs free energy (G) is expanded in terms of an order parameter Q [1] as $G(P, T, Q) = G_O(P, T) + G_L(P, T, Q)$ with G_O the Gibbs free energy of the high-temperature phase and G_L the Landau free energy. For isobaric thermal expansion, $G(T) = G_O(T) + a(T-T_c)Q^2/2 + bQ^4/4 + cQ^6/6$ (a, b, c are the temperature independent thermodynamic relative quantities). A first order phase transition (2-4-6 potential) has a jump in the order parameter whereas a second order phase transition (2-4-potential) and the tricritical behavior (2-6- potential) could be described as $Q = (1 - T/T_c)^n$ with n = 0.5 and 0.25, respectively. Data collections in a thermodynamic equilibrium are quite difficult and describing the phase-transitions using the Landau theory leads quite often to a deviation of the observed data with respect to the calculated one close to T_c due to kinetic effects. Additionally, evaluating the order parameter could be a challenge. In most cases the order parameter is proportional correlated to the unit-cell volume of the sample. Therefore the same effect could be seen while evaluating the phase volume using Debye quasi-harmonic (U_{Di}), Einstein harmonic (U_{Ei}) and anharmonic (U_A) internal energy (DEA-model) contributions with M = V as given in the formula in Fig. 1 [2]. Fitting the temperature-dependent volume change with a DEA-model gives the possibility to compare the experimental thermal expansion coefficient (TEC) with the theoretical one (Figure 1). For example in dehydrated carbonate-nosean [3] the kinetic effect close to the P23-P23 phase-transition could be seen in a decrease of the TEC over several data points around 800 K (a pure Landau transition would drop the TEC without intermediate values). These deviations in the experimental data could be theoretically modeled by overlapping the TEC's of the low-temperature (TEC_{LT}) and the high-temperature (TEC_{HT}) phase using a sigmoidal function $f_s(T)$ $\{0 < f_s(T) < 1\}$ as $f_s(T) \bullet TEC_{low} + (1- f_s(T)) \bullet TEC_{high}$. The slope of this sigmoidal function corresponds to the deviation of the models used for the volume calculation close to the phase-transition and therefore carries kinetic information. The same could be calculated for the dehydration process of the hydrated carbonate-nosean $|Na_8(CO_3)(H_2O)_4|[AlSiO_4]_6$ around 400 K. The hydrated and the dehydrated phase are fitted with two different DEA models and correlated.

[1] A. Putnis: *Introduction to Mineral Sciences.* Cambridge University Press 1992, chapter 8.6 PP. [2] Th. M. Gesing, C. B. Mendive, M. Curti, D. Hansmann, G. Nénert, P. E. Kalita, K. E. Lipinska, A. Huq, A. L. Cornelius, M. M. Murshed, *Z. Kristallogr.* 228 (2013) 532-543. [3] Th. M. Gesing, J.-Ch. Buhl, *Eur. J. Mineral.* 10 (1998) 71-77.

Figure 1. Temperature-dependent thermal expansion coefficients across the dehydration and the P23-P23 phase-transition of $|Na_8(CO_3)|[AlSiO_4]_6$ with sigmoidial overlap calculations.

Figure 1

$$M(T) = M_0 + \sum_{i=1}^{d} k_{Di} U_{Di}(T) + \sum_{i=1}^{e} k_{Ei} U_{Ei}(T) + k_A U_A(T)$$

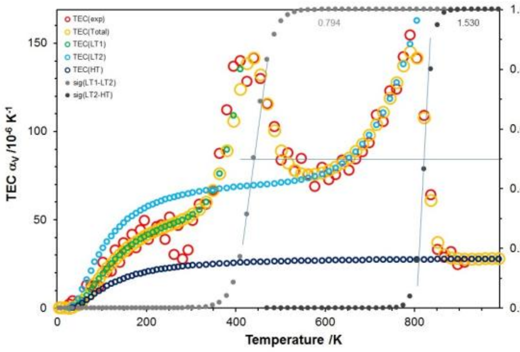

MS06-P08

A ^{57}Fe Mössbauer Study of Local Structure and Cation Distribution in Mullite-type $Bi_2(Fe_xMn_{1-x})_4O_{10}$ and $Bi_2(Fe_xM_{1-x})_4O_9$, M=Al, Ga, Mn

S.- U. Weber[1], T. Gesing[2], M. Lufaso[3], H. Schneider[4], F.- J. Litterst[5], K.- D. Becker[1]
[1]*Technische Universität Braunschweig, Institute of Physical and Theoretical Chemistry, Braunschweig, Germany*
[2]*University of Bremen, Institute of Crystallography, Bremen, Germany*
[3]*University of North Florida, Department of Chemistry, Jacksonville, United States*
[4]*University of Köln, Institute of Crystallography, Köln, Germany*
[5]*Technische Universität Braunschweig, Institute of Condensed Matter Physics, Braunschweig, Germany*

In the present work, the local structure of solid solutions of $Bi_2(Fe_xMn_{1-x})_4O_9$ (designated as O9-phases) with M=Al, Ga, and Mn and of $Bi_2(Fe_xMn_{1-x})_4O_{10}$ (designated as O10-phases) is studied by ^{57}Fe Mössbauer spectroscopy. Spectra are composed of two quadrupole doublets due to iron located on octahedrally and tetrahedally coordinated sites, see Fig. 1, where the smaller of the two splittings is always due to octahedrally coordinated species. The spectra yield quantitative information on the iron occupancy of the two structural sites in the mullite-type lattices. In the Fe-Al system, the distribution of cations is found to be almost random, whereas in the Fe-Ga system, gallium ions are found to develop a strong preference for the occupation of tetrahedral sites, thus displacing Fe cations to the octahedral sites. In the Fe-Mn system, manganese ions reveal a strong preference for the octahedral position: in the O9-solid solution phase Mn ions are found to exclusively occupy this site, whereas the tetrahedrally coordinated sites are completely filled by Fe. In the O10-phase, the Fe occupancy of the pyramidal site is twice as big as that of the octahedral sites.

Hyperfine parameters (isomer shifts, and quadrupole splittings) derived from the spectra as a function of composition provide , e.g., evidence for a strong distortion of the iron sites at low iron concentrations in the Fe-Al system. In addition to measurements at room temperature, high-temperature in-situ Mössbauer spectroscopy provides information on the temperature dependence of the cation distribution of Fe, Al, and Ga on the two inequivalent lattice sites of the O9-structure. In both solid solutions, cation distributions show almost no temperature dependency, yielding site exchange energies close to zero. However, the mass action constants take values close to one for the random distribution in the Fe-Al system and of about 0.4 for the Fe-Ga system. The temperature-dependent study of the Fe-Mn system exhibits also no temperature dependency of the cation distribution.

Fig.1: Mössbauer spectrum of $Bi_2Fe_4O_9$

Figure 1

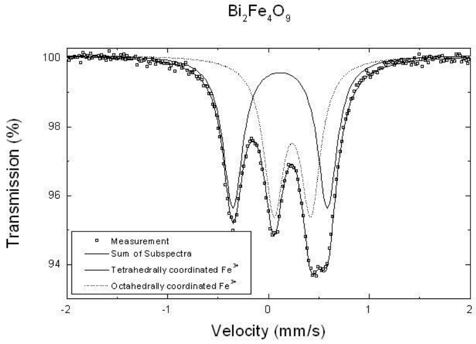

MS06-P09

Stimulated Raman scattering in lead carbonate crystals - $PbCO_3$ (cerussite) and $Pb_2CO_3Cl_2$ (phosgenite)

A. A. Kaminskii[1], H. Rhee[2], A. Kaltenbach[2], O. Lux[2], H.- J. Eichler[2], L. Bohatý[3], P. Becker-Bohatý[3]
[1]*Russian Academy of Sciences, Institute of Crystallography, Moscow, Russian Federation*
[2]*Technische Universität Berlin, Institut für Optik und Atomare Physik, Berlin, Germany*
[3]*Universität zu Köln, Institut für Kristallographie, Köln, Germany*

With the ongoing research on stimulated Raman scattering (SRS) of $\chi^{(2)}$- and $\chi^{(3)}$-active crystals a variety of nonlinear laser photon-phonon interactions and some of their relation to structural features could be found. In particular, the observation of high SRS efficiency frequently goes in hand with the presence of isolated building units in the crystal structure, such as $[SO_4]$, $[WO_4]$, $[MoO_4]$, $[NO_3]$ or $[CO_3]$, where the fully symmetric breathing mode of these groups usually promotes SRS. Especially in the case of carbonates with coplanar $[CO_3]$ groups in their crystal structure, the A_{1g} mode of this group usually acts as the dominant SRS-promoting vibration mode, with an energy shift of around 1050 to 1090 cm^{-1}. In crystals with calcite- or aragonite-type structures this mode can be accompanied by further low-energy modes [1-3]. $PbCO_3$ (cerussite) with aragonite-type structure follows this general habit, showing SRS and Raman induced four wave mixing (RFWM) processes related to the A_{1g} mode with $\omega_{SRS} \approx 1054$ cm^{-1} [4]. The detected rather high steady state Raman gain coefficient of ≥ 4.6 cm· GW^{-1} proves $PbCO_3$ to be an attractive material for Raman frequency conversion.

In contrast to the aragonite (and also calcite) structure type, the crystal structure of $Pb_2CO_3Cl_2$ (phosgenite) shows a very different arrangement of $[CO_3]$ groups, with the planes of the $[CO_3]$ groups lying parallel to the diagonal mirror planes of the tetragonal phosgenite structure [5]. Our SRS investigations reveal, that in phosgenite efficient Stokes and anti-Stokes generation is related to two active vibration modes, the A_{1g} mode of $[CO_3]$ groups with $\omega_{SRS1} \approx 1062$ cm^{-1} and a second mode with $\omega_{SRS2} \approx 86$ cm^{-1} [6]. Using an excitation geometry $q(pp)q$, with $\boldsymbol{q} = (\boldsymbol{b} - \boldsymbol{a})$ and $\boldsymbol{p} = (\boldsymbol{a} + \boldsymbol{b})$, the low-energy mode with $\omega_{SRS2} \approx 86$ cm^{-1} contributes exclusively to the SRS activity of phosgenite crystals without involvement of the A_{1g} vibration mode. This is the first case of a carbonate crystal, where the SRS activity of the otherwise dominant A_{1g} mode can be suppressed completely. In the present contribution a comparison of SRS and RFWM nonlinear properties of the two lead carbonate crystals, $PbCO_3$ and $Pb_2CO_3Cl_2$ is presented.

[1] J.A. Giordmaine, W. Kaiser, Phys. Rev. 144 (1966) 676-688.
[2] L. Bohatý, P. Becker, H. Rhee, O. Lux, H.J. Eichler, H. Yoneda, A.A. Kaminskii, Laser Phonon. Rev. 6 (2012) 690-701.
[3] A.A. Kaminskii, H. Rhee, O. Lux, H.J. Eichler, V.V. Koltashev R. Kleinschrodt, L. Bohatý, P. Becker, Laser Phys. Lett. 9 (2012)259-284.
[4] A.A. Kaminskii, L. Bohatý, H. Rhee, A. Kaltenbach, O. Lux, H.J. Eichler, R. Rückamp, P. Becker, Laser Photon. Rev. **7** (2013) 425-431.
[5] G. Giuseppetti, C. Tadini, Mineral. Petrol. 21 (1974) 101-109.
[6] L. Bohatý, P. Becker, H. Rhee, A. Kaltenbach, H.J. Eichler, H. Yoneda, A. Shirakawa, K. Ueda, A.A. Kaminskii, Phys. Status Solidi RRL **7** (2013) 429-433.

MS06-P10

Efficient $\chi^{(2)}$- and $\chi^{(3)}$-nonlinear optical processes in single crystals of guanylurea(1+) hydrogen phosphite (GUHP)

A. A. Kaminskii[1], H. Rhee[2], O. Lux[2], A. Kaltenbach[2], H.- J. Eichler[2], I. Nemec[3], M. Fridrichová[3], P. Becker-Bohatý[4], L. Bohatý[4]
[1]*Russian Academy of Sciences, Institute of Crystallography, Moscow, Russian Federation*
[2]*Technische Universität Berlin, Institut für Optik und Atomare Physik, Berlin, Germany*
[3]*Charles University in Prague, Department of Inorganic Chemistry, Prague, Czech Republic*
[4]*Universität zu Köln, Institut für Kristallographie, Köln, Germany*

Guanylurea(1+) hydrogen phosphite, $(NH_2)_2CNHCO(NH_2)H_2PO_3$ (abbreviated GUHP), crystallizes in the monoclinic space group *Cc* [1]. This non-centrosymmetric symmetry allows both, $\chi^{(3)}$- and $\chi^{(2)}$-based nonlinear optical processes. Crystals of this compound show efficient second harmonic generation (SHG) [2], as well as sum- and difference frequency mixing and stimulated Raman scattering (SRS) [3]. The simultaneous $\chi^{(2)}$- and $\chi^{(3)}$-activity of GUHP gives rise to a variety of cascaded $\chi^{(2)} \leftrightarrow \chi^{(3)}$ and cross-cascaded $\chi^{(3)} \leftrightarrow \chi^{(3)}$ processes.

For the nonlinear optical investigation (and potential application) of GUHP the main obstacle is the availability of large single crystals of optical quality. Being soluble in water, alcohols and several further organic solvents GUHP can be grown by the solution growth method. To overcome the problem of usually thin-platy growth habit of GUHP crystals a series of growth experiments with different solvents and growth conditions were carried out. Best growth results were achieved by crystal growth from aqueous solution within the temperature range from 50°C - 35°C, resulting in single crystals of optical grade with dimensions up to 60 x 40 x 4 mm^3.

Refractive indices and their dispersion were measured by the prism method in the wavelength range 365 - 1083 nm. Based on these results a detailed analysis of phase matching properties for collinear and non-collinear SHG as well as for selected sum- and difference frequency generation (SFG / DFG) processes were performed. Our SRS investigation of GUHP crystals gave evidence of nine SRS-active vibration modes and one combined mode, which can contribute to multi-phonon SRS processes of the crystal. Using excitation at 1064 nm, 532 nm as well as dual-wavelength pumping octaves-spanning Stokes and anti-Stokes combs, SHG, THG (third harmonic generation) and SFG were observed.

[1] M. Fridrichová, I. Němec, I. Císařová, P. Němec, Cryst. Eng. Commun. 12 (2010) 2054-2056.
[2] M. Fridrichová, J. Kroupa, I. Němec, I. Císařová, D. Chvostová, Phase Transitions 83 (2010) 761-767.
[3] A.A. Kaminskii, P. Becker, H. Rhee, O. Lux, A. Kaltenbach, H.J. Eichler, A. Shirakawa, H. Yoneda, I. Němec, M. Fridrichová, L. Bohatý, Phys. Status Solidi B 250 (2013) 1837-1856.

MS06-P11

Multiferroic and linear magnetoelectric properties of erythrosiderite-type and related compounds $A_2[FeCl_5(H_2O)]$ with A = NH_4, K, Rb, Cs

M. Ackermann[1], D. Brüning[2], T. Lorenz[2], P. Becker[1], L. Bohatý[1]
[1]*Universität zu Köln, Institut für Kristallographie, Köln, Germany*
[2]*Universität zu Köln, II. Physikalisches Institut, Köln, Germany*

Magnetoelectric effects, describing magnetic response of a material to an applied electric field, or, vice versa, electric response to an applied magnetic field, have attracted considerable interest during the last decade, particularly in connection with the discovery of spin-driven magnetoelectric multiferroicity in systems with frustrated magnetic order. In the family of orthorhombic (space group *Pnma* or *Cmcm* [1-3]) erythrosiderite-type and structurally closely related compounds of the general composition $A_2[FeCl_5(H_2O)]$ (A = NH_4, K, Rb or Cs) magnetic properties have been studied in the past, showing that most of the family members studied so far have collinear antiferromagnetic order with Néel temperatures ranging from ~6 K to ~23 K and with the ***a***-axis as magnetic easy axis [4-6].

The crystal structures of these $A_2[FeCl_5(H_2O)]$-type compounds basically consist of isolated $[FeCl_5(H_2O)]^{2-}$ groups, where Fe^{III} is octahedrally coordinated by one H_2O and five Cl ligands, and the respective A^+ counterions. Besides ionic bonds between these structural building units neighboring $[FeCl_5(H_2O)]$ groups are linked by strong hydrogen bonding via O-H-Cl [1-3]. The H-bonded $[FeCl_5(H_2O)]$ octahedra form zig-zag chains along the ***b***-axis. Single crystals of $A_2[FeCl_5(H_2O)]$-type compounds with A = NH_4, K, Rb and Cs were grown from aqueous solutions with a surplus of HCl by controlled slow evaporation of the solvent, using a stoichiometric ratio of the educts and a growth temperature of 323 K for the compounds with A = Rb and Cs, and a surplus of $FeCl_3$ and a growth temperature of 311 K for the compounds with A = NH_4 and K.

By detailed magnetic and dielectric investigations the ammonium compound $(NH_4)_2[FeCl_5(H_2O)]$ was found recently to be a multiferroic material with a strong magnetoelectric coupling and complex magnetic field versus temperature phase diagrams [7]. Our investigations of dielectric, magnetic and magnetoelectric properties of crystals of the alkalimetal compounds $K_2[FeCl_5(H_2O)]$, $Rb_2[FeCl_5(H_2O)]$ and $Cs_2[FeCl_5(H_2O)]$ and their anisotropy in applied magnetic fields up to 14 T give evidence, that they are linear magnetoelectric materials. In the present contribution detailed magnetic field versus temperature phase diagrams and the linear magnetoelectric tensors of the alkali compounds in comparison to the respective magnetic field versus temperature phase diagrams of the multiferroic ammonium compound are presented.

[1] B.N. Figgis, C.L. Raston, R.P. Sharma, A.H. White, Aust. J. Chem. 31 (1978) 2717-2720.
[2] C.J. O'Connor, B.S. Deaver jr., E. Sinn, J. Chem. Phys. 70 (1979) 5161-5167.
[3] J.E. Greedan, D.C. Hewitt, R. Faggiani, I.D. Brown, Acta Cryst. B 36 (1980) 1927-1929.
[4] J.N. McElearny, S. Merchant, Inorg. Chem. 17 (1978) 1207-1215.
[5] R.L. Carlin, F. Palacio, Coord. Chem. Rev. 65 (1985) 141-165.
[6] J. Campo, J. Luzón, F. Palacio, G.J. McIntyre, A. Millán, A.R. Wildes, Phys. Rev. B 78 (2008) 054415.
[7] M. Ackermann, D. Brüning, T. Lorenz, P. Becker, L. Bohatý, New J. Phys. 15 (2013) 123001.

MS06-P12

Crystal structures of Pigment Red 57:1 ($C_{18}H_{12}CaN_2O_6S \cdot n\ H_2O$) determined by X-ray powder diffraction

S. M. Hammer[1], S. Bekö[1], M. U. Schmidt[1]
[1]*Goethe Universität, Inst. f. Anorg. u. Analyt. Chemie, Frankfurt, Germany*

Worldwide most journals and newspapers are printed with Pigment Red 57:1 ($C_{18}H_{12}CaN_2O_6 \cdot n\ H_2O$ with n = 0,1,3, figure 1). Pigment Red 57:1 has been industrially produced for more than 100 years with a production today of more than 50.000 t per year and an annual sales volume of more than 200 Mio Euro per year.[1]

Its crystal structures and hydration states were finally unravelled.[2]

The compound exhibits three hydration states: The trihydrate and the monohydrate of Pigment Red 57:1 are both kinetically stable at ambient conditions. Heating the monohydrate at temperatures higher than 190 °C lead to the hygroscopic anhydrous phase.

The crystal structures of all three phases were determined from X-ray powder data measured in transmission mode with Cu-Kα_1 radiation (STOE-Stadi-P diffractometer).

The data could be indexed without ambiguity. The structures were solved by real-space methods with simulated annealing using the program *DASH*[3]. The Rietveld refinements were performed with the program *TOPAS*[4].

These three different hydration states crystallize in $P\ 2_1/c$, Z = 4, with a similar molecular arrangement. The trihydrate and the monohydrate show eightfold and the anhydrate a sevenfold coordination geometries.

In the trihydrate the calcium ion is coordinated by the sulfonate, the keto and the carboxylate group of one anion, by the carboxylate group of a second anion and by four water molecules (two are shared by two calcium ions). The monohydrate is coordinated by only one water molecule instead of four. Therefore it is additional coordinated by a sulfonate group of a third anion and by a carboxylate group of a fourth anion as a bidentate group.

The anhydrate has the same coordination as the monohydrate only the water molecule is absent.

In the crystal structures a double-layer structure with a polar and a nonpolar layer is formed. The polar layer is dominated by hydrogen bonds and Coulomb interactions and consists of water molecules, calcium ions, sulfonate, keto and carboxylate groups. The nonpolar layer contains naphthalene and toluene moieties.

References:

[1] W. Herbst, K. Hunger, Industrial Organic Pigments, 3rd ed., Wiley-VCH, Weinheim, 2004.
[2] S. L. Bekö, S. M. Hammer, M. U. Schmidt, *Angew. Chem.* 2012**,** *124*, 4814−4818, *Angew. Chem. Int. Ed.* 2012, *51*, 4735−4738.
[3] W. I. F. David, K. Shankland, J. van de Streek, E. Pidcock, W. D. S. Motherwell, J. C. Cole, *J. Appl. Cryst.* 2006**,** *39*, 910−915.
[4] A. A. Coelho, *TOPAS Academic 4.1*, 2007, http://www.topas-academic.net.

Figure 1: Chemical structure of Pigment Red 57:1 ($C_{18}H_{12}CaN_2O_6 \cdot n\ H_2O$ with n = 0,1,3).

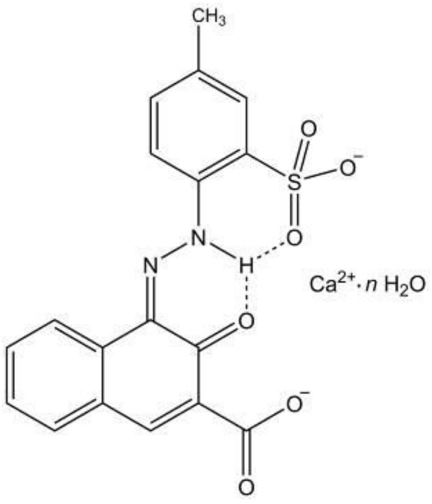

MS06-P13

Structural and Magnetic Characterization of the Diluted Ferromagnet $Sn_xFe_{4-x}N$ ($0 < x \le 1$)

T. Scholz[1], A. Houben[2], A. Houben[1], R. Dronskowski[1]
[1]*Institute of Inorganic Chemistry, RWTH Aachen University, Aachen, Germany*
[2]*Forschungszentrum Jülich GmbH, Institut für Energie- und Klimaforschung – Plasmaphysik, EURATOM Association, Jülich, Germany*

The ferromagnetic phase γ'-Fe_4N exhibits fascinating magnetic properties. Its very large saturation magnetization M_S = 208 A m^2 kg^{-1} (close to α-Fe: M_S = 218 A m^2 kg^{-1}) and its low coercive field ($H_C \approx 460$ A m^{-1}) have attracted early attention. γ'-Fe_4N adopts the simple perovskite-like structure in space group *Pm*-3*m*, wherein iron atoms occupy the cube corners (Wyckoff position 1*a*) and the faces (3*c*) while nitrogen is located in the octahedral centers (1*b*). This structure can also be derived from fcc γ-Fe by filling nitrogen atoms into a quarter of the empty sites in the Fe octahedra. The nitrogen alters the magnetism from antiferromagnetism (γ-Fe) to ferromagnetism (γ'-Fe_4N) due to lattice expansion and the difference in electron count. Through systematically substituting iron in γ'-Fe_4N by other metal atoms according to the general formula $M_xFe_{4-x}N$ ($0 < x \leq 1$), the magnetic properties of such ternary nitrides can be tuned and improved with regard to a desired application. Within the past sixty years a large number of ternary iron nitrides with the general formula $M_xFe_{4-x}N$ and also the archetypal phase γ'-Fe_4N have been studied with respect to synthesis and magnetic properties using experimental and theoretical methods. Among these ternary nitrides, the tin-substituted $Sn_xFe_{4-x}N$ was both synthesized, through ammonolysis of intermetallic compounds, and structurally described by Stadelmaier and Fraker already in 1962. Herein, we present the challenges of synthesizing such nitrides via a two-step ammonolytic reaction directly from iron(II) oxide and tin. Using XRPD Rietveld refinements we have derived the Vegard-like evolution of the lattice parameter for the entire series of compounds. We have also carried out the first extensive magnetic characterization of these nitrides which yields, first of all, a drastic but non-linear weakening of the ferromagnetic coupling through an increasing tin concentration. Furthermore, we performed a.c. susceptibility measurements at different frequencies to evaluate the short-range magnetic interaction in the highly tin-diluted $Sn_xFe_{4-x}N$. The stability, structure and magnetic properties are compared with results from first-principles electronic-structure calculations.

MS06-P14

DFT investigations on different magnetic configurations of $PbFeBO_4$

M. Murshed[1], C. Mendive[2], M. Curti[3], T. Gesing[1]
[1]*Universität Bremen, Bremen, Germany*
[2]*Universidad Nacional de Mar del Plata, Mar del Plata, Argentina*
[3]*,, Argentina*

The crystal structure of $PbFeBO_4$ is built of edge-sharing FeO_6 octahedra running parallel to **c**-axis of the orthorhombic system (*Pnam*) linked by BO_3 and PbO_4 groups [1, 2]. Between two BO_3 groups Pb^{2+} cation locates at the apex of a distorted PbO_4 square pyramid, where the $6s^2$ lone electron pair of Pb^{2+} is stereochemically active. The edge-sharing FeO_6 octahedra were described as Heisenberg 1-D uniform chain model [1]. The density functional theory (DFT) calculations of the spin exchange parameters agree well with the reported ones [3], confirming that the dominant spin exchange interaction is antiferromagnetic (AFM). Periodic calculations were performed with the crystalline orbital program CRYSTAL09 [4, 5], employing the PW1PW hybrid Hartree Fock-Density Functional Theory (HF-DFT) method [6]. Structures were optimized starting from the experimental data, however, using four different high spin configurations by arranging the spin of the Fe^{3+} atoms within a super cell of 12 unit cells, namely, FM, AFM1, AFM2 and AFM3 (Figure 1). For each configuration, the constant pressure constrained geometry optimizations were performed at different pressures. Optimizing the lattice parameters followed by energy fitting, the bulk modulus and the zero-pressure volume (V_0) were calculated which slightly differ from each other. Of them, values calculated for a given spin configuration agree well with the respective experimental ones [2]. The obtained data helped guide to chose V_0 for thermal expansion modeling using Debye-Einstein-Anharmonicity (DEA) approach [2]. Harmonic frequencies of the infrared and Raman modes were calculated by computing numerically the second derivatives of the energy with respect to the atomic positions, and diagonalizing the mass-weighted Hessian matrix in Cartesian coordinates. The associated mode-Grüneisen parameters (γ_i) were calculated from the pressure derivatives. The non-linear behavior of the experimental γ_i has been considered belonging to the intrinsic anharmonicity. However, whether the spin configuration plays role for such anharmonicity these DFT calculated dataset would shed light to understand the mechanism at microscopic level.

[1] Park et al. Chem. Mater. 15 (2003) 1703. [2] Murshed et al. Mat. Res. Bull (2013) submitted. [3] Koo & Whangbo, Solid State Comm. 149 (2009) 602. [4] Dovesi et al. Z. Kristallogr. 220 (2005) 571. [5] Dovesi et al. CRYSTAL09 (2009) CRYSTAL09 User's Manual. University of Torino, Torino. [6] Bredow & Gerson, Phys. Rev. B61 (2000) 5194.

Figure 1: The four $PbFeBO_4$ configurations respect to the Fe^{3+} spin arrangements of the 1-D FeO_6 chain in a super cell of 12 unit cells. (a) Ferromagnetic (FM), (b) antiferromagnetic (AFM1), (c) antiferromagnetic (AFM2), (d) antiferromagnetic (AFM3).

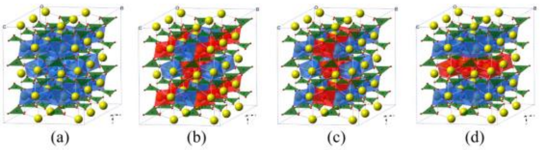

MS06-P15

Magnetic ordering in the system $Cu_{1-x}Ni_xCr_2O_4$ studied by neutron powder diffraction

M. Reehuis[1], M. Tovar[1], D. Többens[1]
[1]*Helmholtz-Zentrum Berlin, M-AQM, Berlin, Germany*

In the present work we have investigated the structural and magnetic properties of $Cu_{1-x}Ni_xCr_2O_4$ in the range $0 \leq x(\mathrm{Cu}) \leq 0.30$ by neutron powder diffraction. The end members $NiCr_2O_4$ and $CuCr_2O_4$ crystallize at room temperature in the tetragonal space group $I4_1/amd$ due to a cooperative distortion of the NiO_4- and CuO_4-tetrahedra through the Jahn-Teller effect [1,2]. The tetrahedral crystal field around Ni^{2+} ($3d^8$) and Cu^{2+} ($3d^9$) results in fully occupied low-energy e_g-levels, while the tetragonal distortions are driven by the orbital degeneracy of the nongenerate t_{2g}-states (Ni^{2+} t_{2g}^4; Cu^{2+} t_{2g}^5). In this structure type the CuO_4 tetrahedra are compressed toward a square-planar configuration, whereas the NiO_4 tetrahedra are elongated. In the system $Cu_{1-x}Ni_xCr_2O_4$ a partial compensation of both effects can be reached for $Cu_{0.15}Ni_{0.85}Cr_2O_4$, where two of the four enlarged (shortened) tetrahedron angles in $NiCr_2O_4$ ($CuCr_2O_4$) change to 109.6° very close to the ideal value of 109.4° [2]. In comparison to $NiCr_2O_4$ (b/a = 0.998) the b/a ratio of $Cu_{0.15}Ni_{0.85}Cr_2O_4$ (b/a = 1.032) was found to be significantly enlarged and therefore the orthorhombic distortions are stronger pronounced. This can be ascribed to the fact that four of the six tetrahedron angles in $NiCr_2O_4$ are similar, while in $Cu_{0.15}Ni_{0.85}Cr_2O_4$ one finds three different angles.

For the end members $NiCr_2O_4$ a ferrimagnetic transition was observed at T_C = 74 K [1,2]. This transition is accompanied by a change to an orthorhombic structure with the space group *Fddd*. For $Cu_{0.15}Ni_{0.85}Cr_2O_4$ this structural transition was observed at much higher temperature (T_S = 300 K), but in contrast the ferrimagnetic transition sets in well below at T_C = 150 K. Here it can be noticed that stronger orthorhombic distortions alleviate frustrations in the Cr^{3+} sublattice. However, in both chromites the same type of ferrimagnetic ordering was observed, where the magnetic moments of the Cr- and Ni- atoms are coupled antiparallel within the *ab* plane. The Ni atoms in both chromites almost reach the same moment values: μ_{ab}(Ni) = 1.83(9) μ_B ($NiCr_2O_4$) and μ_{ab}(Ni) = 1.84(14) μ_B ($Cu_{0.15}Ni_{0.85}Cr_2O_4$). The Cr-moment m_{ab}(Cr) = 1.28(10) μ_B of $Cu_{0.15}Ni_{0.85}Cr_2O_4$ was found to be slightly larger than μ_{ab}(Cr) = 0.90(7) μ_B of $NiCr_2O_4$. Interestingly both $NiCr_2O_4$ and $Cu_{0.15}Ni_{0.85}Cr_2O_4$ undergo a second magnetic transition at 27 and 50 K, where one finds for the Cr-moments an additional antiferromagnetic order parallel to the *c*-axis. In both compounds the same spin sequence was found for the four Cr-atoms in the unit cell. But in contrast to $NiCr_2O_4$ the magnetic structure of $Cu_{0.15}Ni_{0.85}Cr_2O_4$ does not violate the *F*-centering. The chromium moment μ_c(Cr) = 1.89(4) μ_B of $Cu_{0.15}Ni_{0.85}Cr_2O_4$ is somewhat larger than μ_c(Cr) = 1.19(4) μ_B of the undoped chromite resulting in total moments of μ_{tot}(Cr) = 2.28(7) μ_B and μ_{tot}(Cr) = 1.49(5) μ_B, respectively.

[1] M. Tovar, R. Torabi, C. Welker, F. Fleischer, Physica B 385 (2006) 196.
[2] M. R. Suchomel, D. P. Shoemaker, L. Ribaud, M. C. Kemei, R. Seshadri, Phys Rev. B 86 (2012) 054406.

MS06-P16

A treatment for theoretical determination of defocusing curves and its application for the adjustment of an Eulerian goniometer

J. Palacios Gomez[1]
[1]*Instituto Politecnico Nacional, Fisica, Mexico City, Mexico*

Using a strictly geometrical approach, characteristics of a beam diffracted by a sample during the measurement of a defocusing curve is calculated. A parallel incident beam is assumed, and an elliptical cross section for the diffracted beam is obtained, whose parameters depend on the sample inclination and the Bragg angle, but they are also affected by misalignment of the goniometer. The ellipse parameters can be obtained through measurement of defocusing curves for low index reflections and detector scans of a model sample. As a result, a process is obtained to simulate defocusing general curves, and also to identify errors of zeros in Eulerian goniometer.

MS06-P17

Investigation of precipitation behavior in micro-alloyed steels

I. Janßen[1], H. Klein[1], C. Klinkenberg[2]
[1]*Universität Göttingen, GZG, Kristallographie, Göttingen, Germany*
[2]*SMS Siemag AG, Düsseldorf, Germany*

The precipitation and dissolution behavior of niobium carbo-nitrides in micro-alloyed high strength low alloy (HSLA) steels is of particular interest for many technical applications. Reasonable equations for the solubility product at thermal equilibrium can be taken from literature but kinetics is largely unknown. Investigation of nano-scale niobium precipitates by TEM analysis or chemical extraction methods is common practice. However, TEM suffers from statistical relevance and chemical extraction will not give information on particle distribution and orientation. Information on kinetics is difficult to obtain from both methods, as samples have to be quenched from soaking to room temperature. Besides the considerable experimental effort the situation at soaking temperature is evaluated from the room temperature state. The most important role of niobium as a micro-alloying element in thermo-mechanically rolled steel is the retardation of austenite recrystallization, which provides more nuclei for the γ/α-Fe transformation and thus a finer grain size. Besides niobium’s role in solid solution by delaying all diffusion controlled processes, its tendency to form carbides provides the dominant effect [1].

Investigations with high-energy synchrotron radiation (E~60 keV) offers statistical relevance as volumes of several cubic millimeters are examined [2]. The short wavelength (l~0.2 Å) enables to analyze nanometer particles. This technique permits in situ observation of the precipitation state as i.e. chemical and phase composition, orientation and tilt towards the surrounding austenitic or ferritic matrix. In addition, high-energy synchrotron experiments allow in situ investigations of the precipitation kinetics under high-temperature conditions.

Synchrotron investigations on laboratory and industrial samples have been carried out at DESY in Hamburg. The results establish this technology for qualitative and quantitative analysis of nano-scale niobium carbo-nitride precipitates.

References
[1] C. Klinkenberg, K. Hulka, W. Bleck (2004). Niobium carbide precipitation in micro-alloyed steel. Steel Research int. **75**, 1-11.
[2] H. Klein (2009). Principles of highly resolved determination of texture and microstructure using high-energy synchrotron radiation. Adv. Eng. Mat. 11, 6, 452-458

MS06-P18
Microstructural analysis and compositional examination of Cu(In,Ga)Se$_2$ thin films by grazing incidence X-ray diffraction

R. Gunder[1], J. Marquardt[1], S. Schorr[1]
[1]*Helmholtz-Centre Berlin, Crystallography, Berlin, Germany*

By now, the progress in manufacturing of Cu(In,Ga)Se$_2$ thin films as absorber layer in thin film solar cells has led to conversion efficiencies of more than 20%. In general, compound semiconductors own the possibility of adjusting the band gap by changing the composition of the solid solution, like in CuIn$_{1-x}$Ga$_x$Se$_2$, providing the advantage to exploit the solar energy spectrum optimally. During the 3-stage co-evaporation process of Cu(In,Ga)Se$_2$ thin film synthesis, the depth distribution of indium and gallium within the thin film depends on several process parameters and can be adjusted during the first and second stage. However, the third stage triggers recrystallization and ultimately redistributes the trivalent cations, i.e. Ga and In [1].

In our study we focused on two differently fabricated Cu(In,Ga)Se$_2$ thin films. One sample (3056-1B) has undergone a complete 3-stage co-evaporation process, whereas for the other sample (3056-4B) the process was stopped at the end of the second stage. The thin films have been characterized with respect to both, the microstructure as well as the phase content for various thin film depths, by means of grazing incidence X-ray diffraction (GIXRD). The microstructural analysis refers to the separation of size and strain induced peak broadening after the Williamson-Hall method [2]. Through measuring a standard reference material (LaB6, NIST-SRM 660b) the finite resolution of the XRD instrument was taken into consideration to solely obtain the microstructural information of the XRD pattern.

For sample 3056-1B it came out that both, the microstrain as well as the domain size, are increasing from the uppermost absorber layer to the absorber back-contact interface. In contrast to that, the other sample generally exhibits a lower microstrain and a smaller domain size. Also, the trend of the microstrain is reversed and the domain size remains virtually constant.

In both samples, detailed measurements in the vicinity of the 112 main reflection and the subsequent profile fitting revealed the presence of three distinguishable Cu(In,Ga)Se$_2$ phases and a variation of the Ga content for various sample depths. Since every incidence angle can be attributed to a corresponding X-ray attenuation length for a given composition and for a monochromatic X-ray beam (E=8.048 keV) by applying the Beer-Lambert law, the phases and the Ga content can be approximately allocated to specific sample depths. Sample 3056-1B clearly exhibits a three layer stack of differently composed Cu(In,Ga)Se$_2$ phases. Though sample 3056-4B also seems to contain three Cu(In,Ga)Se$_2$ phases, a fairly high density of stacking faults and a probably present binary phase make it more difficult to unambiguously discriminate the reflex positions of the profile fits.

[1] Barreau Net al.J. Acta Mater 2010;58:5572-5577
[2] Williamson GK, Hall WH. Acta Metall 1953;1:22-31

MS06-P19
Phase content analysis of off-stoichiometric Cu$_2$ZnSnS$_4$ (CZTS)

K. Neldner[1], S. Schorr[1]
[1]*Helmholtz-Zentrum Berlin, Berlin, Germany*

Quaternary chalcogenides have seen a rapid development in the last years leading to a world record efficiency for thin film solar cells based on Cu$_2$ZnSn(S,Se)$_4$ (CZTSSe) of 12% [1]. CZTSSe consist mostly of abundant and non-toxic elements, which is considered as a main advantage of the material for photovoltaic applications.

Cu$_2$ZnSnS$_4$ (CZTS) belongs to the $A^{I}_{2}B^{II}C^{IV}X^{IV}_{4}$ compound family and crystallizes in the tetragonal kesterite type structure, the certain ordering of the Cu and Zn cation layers results in the space group [2]. In the ternary phase diagram of Cu$_2$S, ZnS and SnS$_2$, CZTS can be found at the intersection point of 33.33 mol-% of each binary compound [3]. According to literature [3]the stability field of single phase CZTS is assumed to be quite narrow. Typical secondary phases coexisting with a quaternary kesterite type phase are ZnS, CuS, Cu$_2$S, SnS, Sn$_2$S$_3$, SnS$_2$ and Cu$_2$SnS$_3$. Nevertheless there is still a lack of knowledge about existing phases and phase relations in the vicinity of the intersection point of CZTS.

In literature [4] four different off-stoichiometric CZTS compounds, named A-, B-, C- and D-type, have been proposed. The A-type CZTS compound, we currently concentrating on, is Cu-poor and Zn-rich with an expected substitution mechanism 2 Cu → V_{Cu} + Zn_{Cu}

(V_{Cu} - copper vacancy, Zn_{Cu} - Zn on Cu anti site), which leads to the formula $Cu_{2-2x}Zn_{1+x}SnS_4$.

A-type CZTS was synthesized by solid state reaction. The pure elements, weighted in the calculated composition, are placed in a pyrolytic graphite boat and sealed in evacuated quartz ampoules. The tubes were placed in a one-zone furnace and heated with 10 K/h in 4 steps up to 750°C. After holding the final temperature for 240 h the samples were cooled to room temperature with 50 K/h. After a homogenization step and pressing pellets an annealing in evacuated silica tubes at 750°C for 240 h follows. The obtained powder samples have been characterized by X-ray diffraction (XRD) and wavelength-dispersive X-ray spectroscopy (WDX) using an electron microprobe system.The phase content analysis presented here considers the samples before (intermediate samples) as well as after the annealing step.

The results of the XRD and WDX analysis show that CZTS is the main phase in all samples synthesized. The CZTS grains in the intermediate samples exhibit a slight variation of the chemical composition. The presence of secondary phases like CuS, ZnS and Cu_2SnS_3 was noticed for all samples. Moreover a limited solubility of Cu and Sn in ZnS, Zn and Sn in ZnS as well as Zn in Cu_2SnS_3 was determined. These results have been assistant to understand the growth process of CZTS and to improve the solid state synthesis procedure.

[1] Winkler, et al., E. & E. Sc., 2013.
[2] Schorr, Sol. E. Mat. Sol. Cells, 2011. **95**(6): 1482-1488.
[3] Olekseyuk, et al., J. All. Com., 2004. 368(12): 135-143.
[4] Lafond, et al., ZAAC, 2012. 638(15): 2571-2577.

MS06-P20

Chemical and structural characterization of off-stoichiometric $Cu_2ZnSnSe_4$

L. E. Valle Rios[1], S. Schorr[1,2]
[1]*Freie Universität Berlin, Department of Geosciences, Berlin, Germany*
[2]*Helmholtz-Zentrum Berlin, Department Crystallography, Berlin, Germany*

Quaternary $Cu_2ZnSnSe_4$ (CZTSe) is a promising low cost alternative absorber material for thin film solar cells. A record efficiency of 12% was reported for a $Cu_2ZnSn(S,Se)_4$ (CZTSSe) based thin film solar cell [1]. The polycrystalline CZTSSe absorber layer exhibits an off-stoichiometric composition which causes intrinsic point defects (vacancies, anti sites, interstitials). These defects determine the electronic properties of the material in a crucial way.

This work focuses on off-stoichiometric CZTSe. In literature [2] different types of off-stoichiometric CZTSe have been suggested, amongst them A-type Cu-poor/Zn-rich $Cu_{2-2x}Zn_{1+x}SnSe_4$ (x=0.025-0.125) and B-type Cu-poor/Sn-poor $Cu_{2-2y}Zn_{1+3y}Sn_{1-y}Se_4$ (y=0.025-0.075). All powder samples were synthesized by solid state reaction from pure the elements in sealed evacuated silica tubes in a one zone furnace. The first reaction took place at a temperature of 750°C with several temperature holding steps (250°C, 450°C, 600°C) in between. After reaction all samples were grinded, pressed in pellets and annealed again in evacuated and sealed silica tubes at 750°C.

According to the ternary Cu_2Se-ZnSe-$SnSe_2$ phase diagram [3], the region of single-phase CZTSe is very narrow, therefore the formation of secondary phases is highly expected. To determine phase content and chemical composition of the obtained samples, an electron microprobe system equipped with wavelength dispersive X-ray (WDX) analysis was used. The measurements proved the presence of CZTSe as main phase in all synthesized samples. In samples located near the stability single phase region, no secondary phases were detected. Concerning the occurrence of secondary phases it can be stated that, for instance in A-type samples, ZnSe and $SnSe_2$ was found in samples located in the Sn-rich/Cu-poor region of the phase diagramm and CuSe, $CuSe_2$ and ZnSe in the Cu-rich/Sn-poor region of the phase diagramm. Thereby the cation ratio Cu/(Zn+Sn) of the CZTSe main phase varies from 0.978 to 0.815.

The lattice parameters a and c of the CZTSe main phase were determined by Rietveld analyses of XRD data collected using a PANalytical X'pertPro MPD diffractometer. The Rietveld analyses were performed using the FullProf software [4]. The kesterite structure model was used for the refinement procedure, because stoichiometric CZTSe crystallizes in the kesterite type structure [5]. A correlation between the occurrence of secondary phases and a variation of the lattice parameters could be noticed. For instance in A-type samples the $c/2a$ ratio values decrease as the secondary phase content increases.

[1] M.T. Winkler, *Energy & Environ. Sci. (2013)*
[2] A. Lafond, *Z.Anor.Allg.Che* 638, (2012) 2571-2577
[3] Oleksyuk et al., J. *Alloys Comp*. 368 (2004) 135-143
[4] J.Rodriguez-Carvajal and T.Roisnel,www.ill.eu/sites/fullprof/
[5] S. Schorr, *Solar Energy Materials & Solar Cells* 95 (2011) 1482-1488

MS06-P21

Structural and microstructural characterisation of $Cu_2ZnSn(S_{1-x}Se_x)_4$ thin films

G. Gurieva[1], M. Dimitrievska[2], R. Günder[1], H. Xie[2], V. Izquierdo-Roca[2], A. Pérez-Rodríguez[2], E. Saucedo[2], S. Schorr[1,3]
[1]*Helmholz Zentrum Berlin, Berlin, Germany*
[2]*Catalonia Institute for Energy Research , Barcelona, Spain*
[3]*Freie Universität Berlin, Institute of Geological Sciences, Berlin, Germany*

Quaternary chalcogenides of the type Cu_2ZnSnX_4, where X = S or Se (CZTSSe) have the suitable optical band-gap energy of 1.0 -1.5eV, which match the preferred range of solar irradiation. Moreover they exhibit a large optical absorption coefficient of 10^4 cm^{-1} [1,2] and contain only abundant elements, which makes these materials promising candidates for engineering on their base of different high-efficient and low-cost photovoltaic devices. The highest efficiency up to 12% was observed in $Cu_2ZnSn(S_{1-x}Se_x)_4$ solar cells [3] .

The studied CZTSSe thin films were processed in the following way: Cu/Sn/Cu/Zn metallic multi-stacks were deposited onto Mo coated soda lime glass by DC magnetron sputtering and annealed under S+Se+Sn atmosphere. Changing the S and Se fraction and the total pressure during the annealing, it was possible to tune the S/Se ratio in the range of 0 to 1. The Cu/(Sn+Zn) and Zn/Sn ratios were kept between 0.75-0.80 and 1.16-1.22 respectively. As grown sulphur rich samples were submitted to HC etching and selenium rich ones to $KMnO_4/H_2SO_4+Na_2S$ etching, aiming to remove ZnS and ZnSe secondary phases. The absence of secondary phases at the surface was confirmed by Raman spectroscopy with pre-resonant ultraviolet and blue excitations.

The structural characterization of the thin films was carried out by grazing incidence X-ray diffraction (GIXRD) and a subsequent Rietveld analysis of the diffraction data using the FullProf suite [4]. The kesterite structure (space group I-4) was used as starting model for the refinement procedure, because it was shown that both of the end members of $Cu_2ZnSn(S_{1-x}Se_x)_4$ solid solution adopt kesterite type structure [5]. Presence of Sn(S,Se) and $MoSe_2$ secondary phases was detected in some of the thin films and included in the refinements. The lattice parameters *a* and *c* of the thin films were obtained as result of the Rietveld analysis. The dependence of lattice parameters on S/S+Se ratio is in good agreement with Vergard's law. Microstructural analysis consisted in separation of strain and size effects for CZTSSe thin films, based on Williamson-Hall method [6]. The dependance of domain size and strain on the ratio of S/S+Se will be presented.

[1] J.M. Raulot, C. Domain, J.F. Guillemoles, J. Phys. Chem. Solids 66 (2005) 2019.
[2] P.A. Fernandes, P.M.P. Salomé, A.F. da Cunha, Phys. Status Solidi C 7 (2010) 901.
[3] M.T. Winkler, W. Wang, O. Gunawan , Energy and Envir. Science. (2014)
[4] Juan Rodriguez-Carvajal and Thierry Roisnel,www.ill.eu/sites/fullprof/
[5] Siebentritt, S. and Schorr, S. Prog. Photovolt: Res. Appl., 20, 512 (2012)
[6] G. K. Williamson, W. H. Hall, Acta Metall. 1, (1953), 22-31.

MS06-P22

Electrophretic deposition of yttria partially stabiloized zirconia on plasma spraying thermal barrier coating

M. Al-Tameemi[1], S. alrubaiye[2], H. Hussan[2,3]
[1]*Univ. of Technology, Production Engineering and Metallurgy, Baghdad, Iraq*
[2]*University of Technology, baghdad, Iraq*
[3]*University, Baghdad, Iraq*

The study investigated the effect of independent parameters of electrophoretic deposition (EPD) parameters on sealing the open porosity of air plasma sprayed (APS) yttria partially stabilized zirconia (YPSZ). EPD coatings were produced using different applying voltage, dispersion time, pH and sintering times in the range of 10-40 V, 4-8, 10-50 minutes and 700-900 °C respectively. Microstructural studies of plan view upper surface and transverse section EPD have been done using optical microscopy (OM), scanning electron microscopy (SEM), X ray diffraction (XRD) and atomic force microscopy (AFM) to evaluate the layer thickness, topography, phases, roughness and defects. The results show that the thickness and morphology of the deposited layers can be well controlled by proper selection of deposition parameters.

MS06-P23

Structural changes of strontium barium niobate $Sr_{0.53}Ba_{0.47}Nb_2O_6$ (SBN53) at the relaxor ferroelectric transition

H. A. Graetsch[1]
[1]*Ruhr-Universität Bochum, Institut für Geologie, Mineralogie & Geophysik, Bochum, Germany*

The average crystal structures of the ferroelectric and the intermediate paraelectric phases of SBN53 were refined at various temperatures up to 200 °C from single crystal X-ray diffraction data.Members of the $Sr_xBa_{1-x}Nb_2O_6$ (SBN100x) solution series in the compositional range x from 0.32 to 0.82 [1] crystallize with the tetragonal tungsten bronze type of structure [2]. Corner-sharing NbO_6 octahedra form a framework leaving space for three types of cavities. Two of them are incompletely filled with Sr^{2+} and Ba^{2+}. The niobium atoms are displaced in the same direction along the tetragonal *c*-axis away from the centers of the coordination octahedra. This is considered as the main cause of the ferroelectric properties [2].

No symmetry change was observed on crossing the relaxor ferroelectric (FE) phase transition near 95 °C. The major changes of the average structure are positional shifts and increased highly anisotropic atomic displacement parameters (ADP) of the niobium atoms and the Me2 site which is predominately occupied by Ba^{2+}. The ADP of Nb are largest parallel and those of Me2 perpendicular to the ***c***-axis. The niobium atoms are shifted closer to the centers of their coordinating oxygen octahedra. Both symmetrically non-equivalent Nb atoms behave differently. The separation of cations and oxygen atoms does not completely vanish at the FE transition so that a residual microscopic spontaneous electric polarization should persist in the paraelectric phase. The U_{33} atomic displacement parameter of Nb1 is enhanced by a factor of about 4 so that is becomes almost as high as the U_{11} parameter of Me2. Different temperature dependences of these parameters indicate a different nature of the structural disorder: density variation and distortions through incomplete occupation of the Me2 site by Ba^{2+} and Sr^{2+} and thermal fluctuations or static positional disorder of the fully occupied Nb1 site. The relaxor FE transition seems to consist mainly of microstructural changes such as mobilization or alternate orientations of static polar nanodomains which destroy the macroscopic polarization.

The structure is incommensurately modulated by a wavy tilting of the octahedra [3]. The amplitudes of the modulation decreases at elevated temperatures but the satellite reflections do not completely vanish at the FE transition.

Quenching SBN53 from high temperatures causes changes in the occupation of the Me1 and Me2 sites towards a less ordered cation distribution [4]. This in turn modifies the structural modulation.

[1] M. Ulex, R. Pankrath and K. Betzer, J. Cryst. Growth 271, 128 (2004)
[2] P. B. Jamieson, S. C. Abrahams, J. L. Bernstein, J. Chem. Phys. 48(11), 5048 (1968)
[3] T. Woike, V. Petříček, M. Dušek, N. K. Hansen, P. Fertey, C. Lecomte, A. Chapuis, M. Imlau and R. Pankrath, Acta Cryst. B59, 28 (2003)
[4] R. Guo, H. T. Evans Jr and A. S. Bhalla, Ferroelectrics 206(1), 123 (1998)

MS06-P24

Comparison of Neutron and NMR spectroscopic data for chalcopyrite $CuFeS_2$

R. R. Gainov[1,2], V. A. Golovanevskiy[3], V. V. Klekovkina[2], A. V. Dooglav[2], I. N. Pen'kov[2], R. R. Khassanov[2], M. Russina[1]
[1]*Helmholtz-Zentrum , Berlin, Germany*
[2]*Kazan Federal University, Kazan, Russian Federation*
[3]*Curtin University, Bentley, Perth, Australia*

Chalcopyrite $CuFeS_2$ is a well-known compound, with strong attention to it owing to several reasons. Natural chalcopyrite is one of the components of commercial copper ores and as such is of importance to the mining industry world-wide. At the same time, chalcopyrite is a parent compound for so-called CIGS-family of materials (copper indium gallium selenides), which are important for solar cell technologies development. However, in spite of the intensive study in the recent years, several electronic and magnetic properties of chalcopyrite are still not adequately understood. Among them are the nature of low-temperature phase transition and the details of the magnetic state. In particular, first Neutron diffraction studies at room temperature [1] suggested the presence of small magnetic moment for Cu (~ 0.2 μ_B or less) in addition to Fe moments (~ 3.8 μ_B) ordered in antiferromagnetic (AFM) manner below T_N = 823 K. Later, the results of temperature-dependent Neutron spectroscopic measurements [2] supported the presence of magnetic copper moments (~ 0.05 μ_B), which are probably ordered in AFM manner as well below T_{PT} = 52 K. This question has not been conclusively answered up to now due to, primarily, the technical limitations of conventional spectroscopy methods. On the other hand, complementary analysis by Neutron spectroscopy and ^{63,65}Cu nuclear magnetic resonance (NMR) methods could play a key role in understanding the low-temperature state of chalcopyrite. For instance, preliminary ^{63,65}Cu-NMR investigations [3] showed the capacity to extract the hyperfine fields at Cu nuclei and their fluctuations with high accuracy. In this report, recent low-temperature ^{63,65}Cu-NMR results are presented and discussed in the context of Neutron spectroscopic data. It is concluded that the reexamination by Neutron spectroscopy is essential to elucidate the fine properties of $CuFeS_2$.

This work is partly supported by RFBR (foundation No. 12-31282-mol-a).

[1] Donnay G. et al., Phys. Rev., v.112, p.1917-1923 (1958)
[2] Woolley J.C. et al., J.M.M.M., v.162, p.347-354 (1996)
[3] Gainov R.R. et al., Eur. J. Mineral., v.25, p.569-578 (2013)

MS06-P25

Use of a single crystal diffractometer for polycrystalline sample characterization

Z. Gál[1]
[1]*Oxford Industrial Park, Agilent Technologies LTD (UK), Yarnton, United Kingdom*

Whilst a diffractometer equipped with a micro-focus point source, 4-circle kappa goniometer and a 2D area detector is not primarily intended for polycrystalline / fibrous sample measurements, the convenience and the ease of use of the Agilent SuperNova System in combination with a number of cryo-devices easily lends itself to a wide variety of experiments outside of the single crystal domain.

Agilent's latest, S2 generation CCD detectors with Smart Sensitivity Control provide unprecedented levels of detectivity and accessible dynamic range. Combined with the brilliance of the Nova micro-focus Cu K-alpha source a few grains of material can prove sufficient for high quality data acquisition in transmission mode.

Starting from medium resolution phase identification to full-fledged Rietveld quality data collections, CrysAlis^{Pro} makes it straightforward to design the most optimal experiment strategy through its built-in ‘Powder Tools Module’, which is standard on all instruments. Using the language of powder diffractionists the dialogs allow for tuning the fully automated scans by simply selecting from pre-defined constraints and geometries to the full flexibility of crafting every scan by hand. Combined with the variable temperature module the instrument enables rapid scanning for phase transitions as well as tracking changes in unit cell parameters. Using the high resolution colour video microscope one is also able to record images during the temperature scans to be able to correlate any changes in the sample’s physical state.

Convenient data reduction tools are available for radial and azimuthal integrations based on accurately calibrated instrument models. Automated treatment (stitching and scaling) of multi-theta runs, export to a variety of external file formats as well as scripting for batch processing make Agilent’s single crystal diffractometers highly capable instruments for dealing with polycrystalline materials.

Figure 1

Figure 2

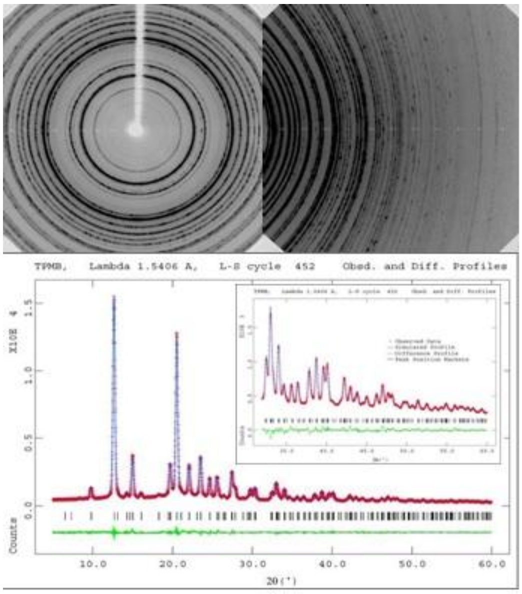

MS07 – Synchrotron opportunities and challenging structure determinations

MS07-P01

Data collection options for challenging samples at the Macromolecular Crystallography beamlines at Diamond Light Source

R. Flaig[1]
[1]*Diamond Light Source, Chilton, Didcot, United Kingdom*

Diamond Light Source [1] is the UK third generation synchrotron facility located south of Oxford and it started with the user programme in early 2007. Currently, there are five operational macromolecular crystallography (MX) beamlines that provide state of the art facilities to the user community and eventually there will be seven beamlines dedicated to MX [2].
All MX beamlines provide tools for standard data collection but given the increasing complexity and associated challenges with bigger macromolecular complexes, membrane proteins and smaller crystals, different approaches are often required to get the best possible data out of these samples.
Tools for sample location and characterization are a first step. Often, because of radiation damage and sample deterioration, multiple crystals are needed in order to obtain a complete data set and a number of tools and different experiment conditions that help to address this problem will be described, including fast data collection, crystal humidity control, *in situ* screening and use of a mini kappa goniometer. These tools enable new data collection strategies which can make the difference towards a successful structure determination.
Given the limited amount of beam time and ever faster data acquisition rates, quick decision making during the beam time becomes more important. Therefore, data collection strategies and crystal and diffraction image characterization are provided automatically. Very shortly after the data collection has finished the results from our automatic data processing routines are available and we also provide difference electron density map, molecular replacement and experimental phasing pipelines.
There are further challenges ahead and an outlook will be given of how new facilities will address these.

[1] http://www.diamond.ac.uk
[2] http://www.diamond.ac.uk/mx-home/

MS07-P02

Phasing strategies with HKL2MAP and SITCOM

F. Dall'Antonia[1], T. Schneider[1]
[1]*EMBL Hamburg, Hamburg, Germany*

The SHELXC/D/E software suite [1] is widely used for macromolecular crystallographic phasing, not the least due to the runtime speed, which makes these programs attractive for on-the-fly validation of diffraction data at synchrotron beam lines. The HKL2MAP [2] graphical user interface facilitates the input file and parameter setup as well as the result interpretation by means of intuitive graphs. In 2013, the new versions of the SHELX-programs were introduced and HKL2MAP 0.4 (0.3.i beta) now incorporates many of the novel features. With the new version of the interface, COOT [3] is employed as graphics program for the visualization of both SHELXE maps and auto-traced poly-ala models.

Here, we recapitulate the benefits of the recently added SHELX functionality: in particular multi-processor support by SHELXD and substructure site refinement as well as backbone auto-tracing for considerable electron density improvement with SHELXE. We present example cases of phasing scenarios on known structures, including sulfur-SAD and SAD/MAD with bromide-soaks, in order to demonstrate strategies that exploit the enhanced possibilities of SHELX phasing with HKL2MAP.

We also discuss the use of the program SITCOM [4] for substructure comparison and NCS analysis - both in the context of the "a posteriori" studies mentioned before and for the general usage during the solution of the phase problem for an unknown structure. SITCOM is an independent tool not bound to the SHELX suite; it can analyze and compare substructure solutions stemming from various software sources. The combined use of HKL2MAP/SHELX-2013 and SITCOM widens the tool set of experimental phasing. Their combined application can make the difference for successful structure solution from problematic experimental data. All of our programs are freely available for academic usage via download from http://webapps.embl-hamburg.de

[1] G. M. Sheldrick (2010). *Acta Cryst.* D66, 479-85.
[2] T. Pape & T. R. Schneider (2004). *J. Appl. Cryst.* 37, 843-4.
[3] P. Emsley et al. (2010). *Acta Cryst.* D66, 486-501.
[4] F. Dall’Antonia & T. R. Schneider (2006). *J. Appl. Cryst.* 39, 618-9.

MS07-P03

A systematic study of acyclic (L-Ala)n-OH peptides combining diffuse scattering, inelastic neutron scattering and DFT

M. Gutmann[1], S. Mukhopadyay[1], A. Wagner[1], M. von Zimmermann[2], L. Connor[3], A. Meents[2], A. Burkhardt[2], O. Gutowski[2]
[1]*Rutherford Appleton Laboratory, Chilton Didcot, Oxfordshire, United Kingdom*
[2]*Hamburger Synchortronstrahlungslabor HASYLAB, DESY, Hamburg, Germany*
[3]*DIAMOND Light Source, Chilton Didcot, United Kingdom*

Amino acids are the building blocks of proteins ubiquitous in living organisms. It would be desirable to know both the structure and dynamics to understand their behaviour. Whilst the structure of proteins is solved routinely by single crystal diffraction, the information about the dynamics, e.g. using spectroscopic methods, is rarely evaluated experimentally and often subject to crude computational studies. Dynamic information is contained in the diffraction pattern in the form of thermal diffuse scattering (TDS) which can easily be measured at a synchrotron source. This information is routinely discarded and only Bragg intensities are integrated to determine the average static structure. The reason for this is often a lack of expertise and software tools. Whilst the information contained in the TDS cannot directly be inverted to yield details of the real-space lattice dynamics, it can be calculated from models and compared against experiment. Here, we focus on a series of (L-Ala)n-OH where n=1,2,3 to study the systematic evolution of lattice dynamics as the peptide chains get longer. The crystal structure is obtained from combined neutron and X-ray data sets below 10K as an input to DFT computations and the phonons are used to compute the inelastic neutron spectra as obtained on powder samples on the TOSCA spectrometer at the ISIS spallation neutron source and complementarily X-ray diffuse scattering obtained on I12 at DIAMOND and P07 at PETRAIII to probe the phonons integrated in energy but resolved in momentum and away from the Gamma point. Experimental and theoretical large volumetric data sets have been obtained revealing an unexpected complexity and beauty of the diffraction patterns.

MS07-P04

The annealing behaviour of Eifel sanidine - Comparing results from neutron & X-ray diffraction experiments

J. Kaehn[1], D. Többens[1], M. Reehuis[2], J.- U. Hoffmann[2], S. Schorr[1]
[1]*Helmholtz-Zentrum Berlin, Crystallography, Berlin, Germany*
[2]*Helmholtz-Zentrum Berlin, Quantum Phenomena in Novel Materials, Berlin, Germany*

The alkali feldspar sanidine (K,Na,Ba)[$AlSi_3O_8$] is a monoclinic tectosilicate that occurs at two different modifications, low- and high-sanidine, which differ only in their Al/Si ordering. While disordering is usually acquired by long-term annealing at temperatures of 900°C and above, it is apparently possible to reach a nearly disordered state of Al/Si distribution at considerably lower temperatures and shorter annealing times, when annealing sanidine megacrysts from Volkesfeld/Eifel [1].

In order to investigate this unusual behaviour and to compare various approaches to obtain the Al/Si distribution, samples from different locations around the Eifel and, for comparison, Madagascar have been studied. The Al/Si order was determined by direct and indirect methods. These experiments include X-ray and neutron diffraction of both powder and single crystal samples.

The sanidine samples were annealed for 2 to 24 hours at temperatures up to 1050°C. Neutron scattering experiments were executed at the Berlin Research Reactor BERII. Neutron powder diffraction was performed at the Fine Resolution Neutron Diffractometer E9, single crystal neutron diffraction was done at the 4-circle diffractometer E5 and diffuse neutron scattering experiments were performed at the Flat-Cone diffractometer E2. Subsequently, Al/Si order was determined directly, refining site occupancies of tetrahedral sites by applying Rietveld refinement to powder diffraction data and using XTAL to evaluate data from single crystal experiments. This approach is not applicable when using data collected by X-ray diffraction due to similar atomic form factors of Al^{3+} and Si^{4+}. Thus indirect methods [2,3,4] have to be applied. X-ray powder diffraction was performed at Helmholtz-Zentrum Berlin, single crystal X-ray diffraction was done at Ruhr-University Bochum. Data from X-ray powder diffraction and single crystal X-ray diffraction were processed using Rietveld refinement and ShelXL software, respectively.

It was possible to verify a dependency of decreasing Al/Si order on increasing annealing times and temperatures. Interestingly we observed different results from direct and indirect methods, both for untreated and annealed samples. Applying the direct determination method, a stronger change of Al/Si distribution during annealing was revealed. Moreover, diffuse scattering of untreated and annealed sanidine samples was detected, which may arise from hydron (water) in the sanidines.

[1] Zeipert&Wondratschek, N.Jb.Miner.Mh. H.9, 407-415, 1981
[2] Kroll&Ribbe, Miner.Soc.Am. Rev. in Miner., 2nd ed., 57-99, 1983
[3] Kroll&Ribbe, Am.Miner. Vol.72, 491-506, 1987
[4] Carpenter&Salje, Am.Miner. Vol.79, 1084-98, 1994

MS07-P05

Room temperature macromolecular serial crystallography using synchrotron radiation

D. Oberthuer[1,2], F. Stellato[1], M. Liang[1], R. Bean[1], O. Yefanov[1], C. Gati[1], A. Barty[1], A. Burkhardt[3], P. Fischer[3], L. Galli[1], R. Kirian[1], J. Meyer[3], S. Panneerselvam[3], C. H. Yoon[1,4], T. A. White[1], C. Betzel[2]; A. Meents[3], H. N. Chapman[1,5,6]
[1]*CFEL - Coherent Imaging Division, DESY, Hamburg, Germany*
[2]*Institute of Biochemistry and Molecular Biology, University of Hamburg, Hamburg, Germany*
[3]*Photon Science, DESY, Hamburg, Germany*
[4]*European XFEL GmbH, Hamburg, Korea, Republic of*
[5]*Center for Ultrafast Imaging - CUI, University of Hamburg, Hamburg, Germany*
[6]*Department of Physics, University of Hamburg, Hamburg, Germany*

For the analysis of structure-function relations and rational drug discovery precise and accurate structural information of biological macromolecules is necessary. X-ray crystallography can yield this information at atomic resolution. However, the need to grow macroscopic crystals remains the bottleneck applying this method. Microfocus beamlines at third generation synchrotron sources allow obtaining diffraction from micron sized crystals, however due to radiation damage often datasets from several crystals have to be merged to obtain enough information for structure determination.

The method of Serial Femtosecond Crystallography (SFX) [1] exploits the ultra-short and intense X-ray pulses of Free-electron Lasers (FELs) to overcome the radiation damage limits in conventional crystallography, thus making it possible to determine protein structures to high resolution from crystals too small for synchrotrons. Recently it was shown [2] that combining advanced precision diffractometry at a microfocus beamline with SFX processing algorithms allows to solve the structure of Cathepsin B from *in vivo* grown microcrystals in a standard cryoloop at a synchrotron.

Here we present the application of serial crystallography methods at synchrotrons to room-temperature data collection. Using lysozyme microcrystals (6x6x6 µm^3) as a model system, over 50,000 single-crystal diffraction patterns were collected from more than 50,000 individual protein crystals, flowing rapidly and randomly oriented in their buffer across the X-ray beam. Applying data acquisition times of only 10 ms, diffraction from single crystals could be observed to the edge of the detector (2.0 Å). The data was merged after processing with CrystFEL and a structural model could be refined to 2.1 Å resolution. The final model was in excellent agreement with that obtained using standard X-ray data collection techniques. The presented method is well suited for even shorter exposure times and smaller crystals at future and upgraded synchrotron radiation facilities that may deliver beams with 1,000 times higher brightness than currently available.

[1] Chapman, H.N. et al. Femtosecond X-ray protein nanocrystallography. Nature 470, 73-77 (2011).
[2] Gati, C., Bourenkov, G., Klinge, M., Rehders, D., Stellato, F., Oberthur, D., Yefanov, O., Sommer, B. P., Mogk, S., Duszenko, M., Betzel, C., Schneider, T. R., Chapman, H. N. & Redecke, L. (2014). IUCrJ 1.

MS07-P06

Generating stereochemical restraints for SHELXL with Grade

J. Holstein[1], O. Smart[1], G. Bricogne[1]
[1]*Global Phasing Ltd., Cambridge, United Kingdom*

Restraints generated by Grade have a wide range of applications ranging from refinement of protein ligands, accurate modelling of supramolecular structures [1] and refining heavily disordered parts of small-molecule structures like solvent molecules or flexible alkyl chains. Grade generates stereochemical restraints for novel small molecules. It does so by querying the Cambridge Structural Database (CSD) as a main source of information about molecular geometry using Mogul, and then invoking quantum chemical procedures to obtain whatever information the CSD is unable to supply. Grade takes as input a SMILES string or a mol2 file containing 3D coordinates of all atoms. Restraint dictionaries produced by Grade can be directly used with Buster, coot or Refmac. A new routine to translate Grade restraint dictionaries into Shelxl syntax (DFIX, DANG and FLAT commands) has now been implemented and is available via the Grade Web Server. [2] The Grade Web Server is free to use and does not require a CSD license. For low-resolution or disordered small-molecule or supramolecular structures, Grade restraints enhance refinement stability and improve the geometrical quality of the final model. Further details on the use of GRADE and its application to structure refinement with SHELXL will be presented.

[1] T. K. Ronson, C. Giri, N. K. Beyeh, A. Minkkinen, F. Topić, J. J. Holstein, K. Rissanen, J. R. Nitschke, *Chem. Eur. J.* 2013, 19, 3374 - 3382
[2]Grade Web Server http://grade.globalphasing.org

MS07-P07

Microstructural and mechanical characterization of cold-drawn pearlitic steel wires using synchrotron X-ray diffraction

S. Djaziri[1], Y. Li[1], S. Goto[2], H. Springer[1], G. Dehm[1]
[1]*Max-Planck-Institut für Eisenforschung GmbH, Structure and Nano-/Micromechanics of Materials Department, Düsseldorf, Germany*
[2]*Akita University, Akita, Japan*

Cold-drawn pearlitic steel wires are widely used in several engineering applications as suspension bridges and tire cords. Indeed, they exhibit a strong tensile strength through the cold drawing process, where recently a strength of more than 6 GPa have been realized [1]. The pearlitic steel wires present a fine lamellar microstructure consisting of a soft ferrite matrix containing hard cementite lamellae with a lamellar spacing of several tens of nanometres. Upon cold drawing, the tensile strength of pearlitic wires increases with a refinement of the lamellar microstructure. It has been shown that the cementite is the strengthening phase in pearlitic steels which however decomposes during deformation at room temperature [1-4]. The decomposition process and redistribution of carbon may cause the outstanding mechanical properties. Moreover, the dislocation densities and vacancy cluster concentrations increase with increasing strain [5]. Transmission electron microscopy (TEM) and atom probe tomography (APT) studies on cold-drawn pearlitic steel showed the enrichment of carbon at ferrite dislocations and grain boundaries during deformation [1-2]. This phenomenon has been associated with the cementite decomposition upon cold-drawing of the pearlitic steel wires. Synchrotron X-ray diffraction measurements have been performed on pearlitic steel wires drawn at different strains. The results show how the internal stresses and the ferrite lattice parameter evolve as a consequence of cold-drawing. Moreover, *in-situ* tensile experiments have been carried out in order to reveal the stress distribution between the ferrite and the cementite phases. Synchrotron sources are of utmost importance for this study and especially for wires at ultra-high strength.

[1] Y.J. Li, P. Choi, S. Goto, C. Borchers, D. Raabe, R. Kirchheim, *Evolution of strength and microstructure during annealing of heavily cold-drawn 6.3 GPa hypereutectoid pearlitic steel wire*, Acta Materialia, 60, 4005-4016 (2012).
[2] Y.J. Li, P. Choi, C. Borchers, S. Westerkamp, S. Goto, D. Raabe, R. Kirchheim, *Atomic-scale mechanisms of deformation-induced cementite decomposition in pearlite*, Acta Materialia, 59, 3965-3977 (2011).
[3] V.G. Gavriljuk, *Decomposition of cementite in pearlitic steel due to plastic deformation*, Materials Science and Engineering, A345, 81-89 (2003).
[4] F. Wetscher, R. Pippan, S. Sturm, F. Kauffmann, C. Scheu, G. Dehm, *Microstructural evolution of a pearlitic steel during severe plastic deformation*, Met. Trans. A, 37A No.6 (2006) 1963-1968.
[5] Y.Z. Chen, G. Csiszár, J. Cizek, S. Westerkamp, C. Borchers, T. Ungár, S. Goto, F. Liu, and R. Kirchheim, *Defects in Carbon-Rich Ferrite of Cold-Drawn Pearlitic Steel Wires*, Metallurgical and Materials Transactions A, (2013).

MS07-P08

Structural biology using *in vivo* grown protein crystals

L. Redecke[1], M. Klinge[1], C. Gati[2], G. Bourenkov[3], R. Schönherr[4], K. Nass[2,5], D. Rehders[1], D. Oberthür[2,6], F. Stellato[2], B. Sommer[6,7], T. A. White[2], A. Barty[2], T. S. Schneider[3], J. Martinez-Costas[8], R. Duden[4], M. Duszenko[7], H. N. Chapman[2], C. Betzel[6]
[1]*University of Hamburg and University of Lübeck, Joint Laboratory for Structural Biology of Infection and Inflammation, Hamburg, Germany*
[2]*Center for Free-Electron Laser Science (CFEL), c/o DESY, Hamburg, Germany*
[3]*European Molecular Biology Laboratory (EMBL), Outstation Hamburg, Hamburg, Germany*
[4]*University of Lübeck, Institute of Biology, Lübeck, Germany*
[5]*University of Hamburg, Department of Physics, Hamburg, Germany*
[6]*University of Hamburg, Institute of Biochemistry and Molecular Biology, Hamburg, Germany*
[7]*University of Tübingen, Interfaculty Institute of Biochemistry, Tübingen, Germany*
[8]*University of Santiago de Compostela, Department of Biochemistry and Molecular Biology, Santiago de Compostela, Spain*

Spontaneous protein crystallization within living cells has been observed several times in nature, e.g. for storage proteins in seeds. *In vivo* crystal growth can also occur during gene over-expression, as particularly discovered in baculovirus-infected insect cells, but recently also in mammalian cells. However, *in vivo* grown crystals were not considered for structural biology at synchrotron sources so far, largely attributed to the small size that coincided with low diffraction capabilities and sensitivity to radiation damage. The realization of serial femtosecond crystallography (SFX) at X-ray free-electron lasers (XFELs) opened new opportunities to overcome these drawbacks (1). In a proof-of-principle study, we demonstrated the applicability of SFX on *in vivo* grown crystals by elucidation of the room-temperature 2.1 Å resolution structure of the precursor complex of the cysteine protease cathepsin B from the sleeping sickness causing parasite *Trypanosoma brucei* (TbCatB) that spontaneously crystallized within insect cells (2,3). Following this strategy, we additionally determined the 3 Å resolution structure of trypanosomal inosine monophosphate dehydrogenase (TbIMPDH) as a second example. Combining a highly brilliant micron-sized X-ray beam of a third-generation synchrotron source with high-precision diffractometry and a helical line scan approach, we recently demonstrated that suitable diffraction of TbCatB *in vivo* crystals can also be collected by a serial synchrotron crystallography approach (3), significantly extending the accessibility of suitable radiation sources. Inspired by the potential of the new technical implementations we analyzed the process of intracellular crystal growth in more detail applying live-cell imaging techniques, including proteins from firefly and avian reovirus. We investigated the impact of the intracellular environment on *in vivo* crystal growth by directing the proteins into different cellular compartments using specific signal sequences. The identification of the optimal compartment for intracellular crystallization is crucial to increase the success rate for spontaneous crystal growth of other proteins.

Our study demonstrates that high-resolution structural information can be obtained by irradiation of *in vivo* crystals with highly brilliant XFEL or synchrotron radiation. Consequently, *in vivo* grown crystals are suitable targets for structural biology, which offers exciting new possibilities for proteins that do not form crystals suitable for conventional X-ray diffraction *in vitro*.

(1) H.N. Chapman *et al*. *Nature* 470, 73-77 (2011).
(2) R. Koopmann*, K. Kupelli*, L. Redecke* *et al*. *Nat. Methods* 9, 259-262 (2012).
(3) L. Redecke*, K. Nass* *et al*. *Science* 339, 227-231 (2013).
(4) C. Gati*, G. Bourenkov* *et al*. *IUCrJ* (2013), in press

MS07-P09

The AGIPD photon detector for the Serial Femtosecond Crystallography Apparatus at the European XFEL

S. Stern[1], S. Raabe[1], H. Dadgostar[1], S. Ananthaneni[1], M. Liang[1], P. Vagovic[1], H. N. Chapman[1], L. Chavas[1], A. P. Mancuso[2], A. A. Aquila[2], G. Borchers[2], N. Reimers[2], K. Giewekemeyer[2], C. H. Yoon[2], J. Becker[3], F. Pithan[3], A. Delfs[3], H. Hirsemann[3], S. Smoljanin[3], H. Graafsma[3], D. Greiffenberg[4], B. Schmitt[4], X. Shi[4]
[1]DESY, CFEL, Hamburg, Germany
[2]European XFEL, Hamburg, Germany
[3]DESY, Hamburg, Germany
[4]PSI, Villingen, Switzerland

The European X-ray Free-Electron Laser (European XFEL) [1] will provide ultra-short, highly-intense, coherent x-ray pulses at high repetition rates and thereby revolutionize experiments in a variety of scientific areas, including new serial femtosecond crystallography experiments [2,3]

For serial femtosecond crystallography (SFX) experiments at the European XFEL, a dedicated SFX apparatus is being developed. It will be installed at the Single Particles, Clusters and Biomolecules (SPB) instrument [4,5] of the European XFEL and will house an Adaptive Gain Integrating Pixel Detector (AGIPD) [6-9]. To overcome some of the various challenges in XFEL crystallography, and to optimise the output for SFX experiments, an additional 4Mpixel AGIPD will be developed to consist of a hybrid-pixel detector system with 2048 x 2048 pixels of 200 x 200 µm^2 each. Requirements for operation at the SPB instrument include a high dynamic range of 0,1,...10^4 photons from a photon energy ranging from 3 to 16 keV, negligible pile-up of signal at the XFEL repetition rate of 4.5 MHz, and the ability to operate for doses covering up to 1 GGy.

We review the design of the AGIPD for the SFX apparatus at the European XFEL, show simulations of the expected performances, and present results of tests of the detector components.

[1] M. Altarelli, et al., Tech. Rep., DESY, Hamburg, Germany (2007), http://xfel.desy.de/technical_information/tdr/tdr/
[2] H. N. Chapman, et al., Femtosecond x-ray protein nanocrystallography, Nature 470, 73 (2011)
[3] J. C. H. Spence, U. Weierstall, and H. N. Chapman, X-ray lasers for structural and dynamic biology, Rep. Prog. Phys. 75, 102601 (2012)
[4] A. P. Mancuso, et al., Conceptual Design Report: Scientific Instrument SPB, 2011, XFEL.EU TR-2011-007, doi:10.3204/XFEL.EU/TR-2011-007
[5] A. P. Mancuso, et al, Technical Design Report: Scientific Instrument SPB, 2013, XFEL.EU TR-2013-004, doi:10.3204/XFEL.EU/TR-2013-004
[6] G. Potdevin, U. Trunk, and H. Graafsma, Performance simulation of a detector for 4th generation photon sources: The AGIPD, Nucl. Instrum. Meth. A 607, 51 (2009)
[7] B. Henrich, et al., The adaptive gain integrating pixel detector AGIPD a detector for the European XFEL, Nucl. Instrum. Meth. A 633, S11 (2011)
[8] J. Schwandt et al., Design of the AGIPD sensor for the European XFEL, JINST 8, C01015 (2013)
[9] J. Becker at al., Performance tests of an AGIPD 0.4 assembly at the beamline P10 of PETRA III, JINST 8, P06007 (2013)

MS07-P10

Capabilities of the Extreme Conditions Beamline at PETRA III, DESY

H.- P. Liermann[1], Z. Konôpková[1], K. Glazyrin[1], E. McBride[1], W. Morgenroth[2], A. Rothkirch[1], M. Wendt[1], A. Ehnes[1]
[1]Deutsches Elektronen-Synchrotron DESY, Photon Science, Hamburg, Germany
[2]Uni Frankfurt, Abt. Kristallographie, Hamburg, Germany

The Extreme Conditions Beamline (ECB) at PETRA III is dedicated to diffraction experiments at simultaneous high-pressures and high and low temperatures created in the Diamond Anvil Cell. The beamline has been open to general users since 2012 to conduct a variety of different experiments such as powder and single diffraction in the laser/resistive heated and cryogenically cooled Diamond Anvil Cell (DAC). Particularly attractive has been our ability to conduct diffraction experiments at high energies of 60 keV for pair distribution function (PDF) studies as well as the possibility to perform time resolved powder diffraction experiments at 26 and 43 keV with a maximum time resolution of 15 Hz. We are continuing to expand the time resolving capabilities by developing our own dynamic DAC system for fast compression (up to 500 GPa/s) as well as flash laser heating to reach in short time very high pressures and temperatures and study liquid/solid transitions as well as PDFs of liquids. Within we present some of the current capabilities of the beamline as well as future plans to promote single crystal diffraction at high pressures and temperatures using both monochromatic and pink beam.

Funding by the BMBF, Germany (projects 05K10RFA, 05KS7RF1 and 05K13RF1) is gratefully acknowledged.

MS07-P11

Structure Determination of Ho_2PdSi_3

M. Nentwich[1], M. Zschornak[1], C. Richter[1,2], D. C. Meyer[1]
[1]*TU Bergakademie Freiberg, Institute of Experimental Physics, Freiberg, Germany*
[2]*DESY/HASYLAB Hamburg, Hamburg, Germany*

Holmium-Palladium-Silicide Ho_2PdSi_3 is a member of rare earth transition metal silicides exhibiting a wide range of interesting magnetic and electrical properties like multiple transition temperatues. The crystal structure results from $HoSi_2$ by substitution of Si by Pd which is ordering commensurably with a 2 × 2 × 8 superstructure confirmed by a previous XRD and a *Diffraction Anomalous Fine Structure* (DAFS) measurement of the super structure reflection 1/2 1/2 3/8.

DAFS is an X-ray method combining the advantages of absorption and diffraction and hence offers the possibility of element and site selective studies. Thus, it was feasible to probe the local environment of Ho and Pd separately.

In the following, we will present a comparison of several structure proposals of Ho_2PdSi_3, which have been modeled with the finite difference code FDMNES, with experimental data from beamline E2 and BW1 of the former synchrotron DORIS III at DESY/HASYLAB.

MS07-P12

CrystFEL: software for crystallography using FEL sources

T. White[1]
[1]*Center for Free-Electron Laser Science, Hamburg, Germany*

Since the beginning of user operations at the world's first hard X-ray laser facilities — the Linac Coherent Light Source (LCLS) and more recently the Spring-8 Angstrom Compact Free-Electron Laser (SACLA) — crystallographic experiments on proteins have been a significant fraction of the experiments being performed. The very intense but very short X-ray pulses from these machines promise new opportunities to overcome radiation damage and study very fast chemical reactions, by allowing diffraction snapshots to be recorded with exposure times of only a few tens of femtoseconds.

However, the particular way in which such experiments must be carried out requires new approaches to crystallographic data analysis. To address these needs, CrystFEL has been developed. CrystFEL is a software suite which includes programs for indexing and integrating diffraction patterns, scaling and merging intensities, simulating patterns, calculating figures of merit, visualising the results and finally importing the processed data into conventional structure solution packages. CrystFEL is free and open-source software, available free of charge for all users and distributed under the GNU General Public License (v3). More information and download instructions can be found at http://www.desy.de/~twhite/crystfel/.

Code has been contributed to CrystFEL by Rick Kirian, Andrew Aquila, Andrew Martin, Lorenzo Galli, Kenneth Beyerlein, Chun Hong Yoon, Nadia Zatsepin, Cornelius Gati, Anton Barty and Fedor Chervinskii. The design of CrystFEL and its algorithms has been influenced by Henry Chapman, Petra Fromme, James Holton and John Spence.

MS07-P13

The Serial Femtosecond Crystallography user's consortia project at the European XFEL

P. Vagovic[1], L. Chavas[1], S. Stern[1], S. Raabe[1], H. Dadgostar[1], S. Ananthaneni[1], M. Liang[1], H. N. Chapman[1], A. P. Mancuso[2], A. Aquila[2], G. Borchers[2], N. Reimers[2], K. Giewekemeyer[2], C. H. Yoon[2], J. Becker[3], F. Pithan[3], A. Delfs[3], H. Hirsemann[3], S. Smoljanin[3], H. Graafsma[3], D. Greifenberg[4], B. Schmitt[4], X. Shi[4]
[1]*Center for Free-Electron Laser Science, Coherent Imaging Division, Hamburg, Germany*
[2]*European XFEL, Hamburg, Germany*
[3]*DESY, Hamburg, Germany*
[4]*PSI, Villigen, Switzerland*

The Serial Femtosecond Crystallography apparatus (SFX) as a parasitic apparatus for macromolecular crystallography is to be installed at the Single Particles, Clusters and Biomolecues (SPB) instrument of the European X-ray Free-Electron Laser facility (XFEL) [1]. It is planned to be constructed by the SFX consortium, in close collaboration with the European XFEL. Fourth generation light sources (Free Electron Lasers), due to their high brilliance (several orders higher than the third generation sources) and short, femto second pulses, potentially overcome common problems and bottlenecks encountered in structural biology experiments. Such as creating large crystals or dealing with radiation damages, and will enable the sub-picosecond time-resolved analysis. The key concept of SFX is based on the kinetic insertion of the samples (protein crystals in solution) *via* jet [2], and recording diffraction signals of individual randomly oriented crystals passing through the XFEL beam, firstly demonstrated by Chapman *et al.* [3]. The SFX apparatus will be located within the Single Particles, Clusters and Biomolecules (SPB) instrument [4,5] and will refocus the X-ray beam transmitted by the SPB instrument, thus allowing simultaneous operation of both SPB and SFX end-stations. The energy range of SPB instrument is in the range from 3 to 16 keV with SFX operating from 6 keV and higher. A 2k x 2k Adaptive Gain Integrating Pixel Detector (AGIPD) [6] will accept the scattering angles up to about 60° allowing for the resolution of 2 Å at 6keV to1Å at 16keV. We are aiming for high efficiency operation, collecting 3000 images per second. These images will contain both single crystal diffraction patters and empty patterns of pure liquid scattering due to the random nature of the crystals in the liquid jet. To improve the collection efficiency a fast veto system can be implemented removing empty patterns from the data collection. The huge data throughput, analysis and storage will be an important issue to solve and will be the subject of close collaboration with groups within the SFX user consortium, Diamond, and notably European XFEL. In this work, we review the overall design of the SFX apparatus and discuss the main parameters and challenges.

References:
[1] Technical Design Report: European X-Ray Free-Electron Laser - 2007
[2] D P DePonte et al. Phys. D: Appl. Phys. 41 (2008) 195505
[3] H. N. Chapman, et al., Femtosecond x-ray protein nanocrystallography, Nature 470, 73 (2011)
[4] A. P. Mancuso, et al., Conceptual Design Report: Scientific Instrument SPB, 2011, XFEL.EU TR-2011-007, doi:10.3204/XFEL.EU/TR-2011-007
[5] A. P. Mancuso, et al, Technical Design Report: Scientific Instrument SPB, 2013, XFEL.EU TR-2013-004, doi:10.3204/XFEL.EU/TR-2013-004
[6] B. Henrich et al. "The adaptive gain integrating pixel detector AGIPD a detector for the European XFEL," *Nuclear Instruments and Methods in Physics Research Section A*, vol. 633, p. 11, May 2011.

MS07-P14

TIME-RESOLVED X-RAY DIFFRACTION STUDY OF $Sr_{0.5}Ba_{0.5}Nb_2O_6$ UNDER EXTERNAL ELECTRIC FIELD

S. Gorfman[1], H. Choe[1], J. Dec[2], M. Ziolkowski[1], U. Pietsch[1], T. Łukasiewicz[3]
[1]*University of Siegen, Department of Physics, Siegen, Germany*
[2]*University of Silesia, Institute of Materials Science, Katowice, Poland*
[3]*Institute of Electronic Materials Technology, Warsaw, Poland*

$Sr_xBa_{1-x}Nb_2O_6$ (SBN) is the material with the tungsten-bronze type of a structure which attracts the interest due to its ferroelectric, electro-optical and piezoelectric properties [see for example 1]. SBNs are also interesting as model systems for the fundamental material science, as their crystallographic symmetry (paraelectric 4/mmm and ferroelectric 4mm) allows for the formation of 180° ferroelectric domains only. The absence of 90° (and other) types of domains simplifies the experiments / interpretation of the data and allows for the easier microscopic insight in the nature of ferroelectric and relaxor ferroelectrics properties. The aim of this work is to study the millisecond structural and domain dynamics of SBN(x=0.5) single crystal under periodically applied external electric field.

We implemented the specially developed measurement technique for the time-resolved X-ray diffraction study of single crystals under external perturbation. The technique (described in [2]) enables to record peak position and integrated intensity of selected Bragg reflections as function of time and the applied periodic electric field. It adopts the principle of stroboscopic data aquisition: where each detected X-ray photon is time-stamped and assigned to the time channel. The latter corresponds to a certain time delay with repect to the onset of the external high-voltage period. We applied triangular-shaped electric field (f=20 Hz; E_{max} = 2 kV/mm) and monitored the evolution of a Bragg rocking curve(s) within the 50 ms long high-voltage period. Figure 1 shows the contour map of the *0 0 7* Bragg rocking curve as function of time delay.

We will present the dynamics of the rocking curve in terms of intrinsic / extrinsic piezoelectric deformation and the ferroelectric domain formation.

1. Neurganorkar, R.R, Oliver, J.R., Cory, W.K., Cross, L.E., Viehland, D: Piezoelectricity in tungsten bronze crystals. Ferroelectrics. 1994; 165: 265-276
2. Gorfman S, Schmidt O, Ziolkowski M., Kozierowski M., Pietsch U: Time-resolved X-ray diffraction study of piezoelectric crystal response to a fast change of electric field. J. Appl Phys. 2010; 108:064911

Figure 1. Contour map of the *0 0 7* Bragg rocking curve as function of time delay

Figure 1

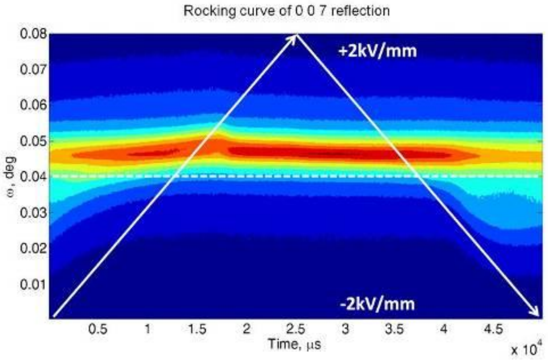

MS07-P15

EMBL P13 beamline for macromolecular crystallography at PETRA III @DESY, Hamburg, Germany

M. Cianci[1], G. Bourenkov[1], J. Kallio[1], G. Pompidor[1], S. Fiedler[1], T. Schneider[1]
[1]*EMBL, Hamburg, Hamburg, Germany*

The macromolecular crystallography P13 beamline is part of the European Molecular Biology Laboratory integrated infrastructure for life science applications at PETRA III.

P13 is tunable over the energy range from 4 to 17.5 keV to allow crystallographic data acquisition on a broad range of elemental absorption edges for experimental phase determination. In close proximity to the beam line laboratories, equipped for on-site heavy atom derivatization with a library of around ~150 compounds, and for sample preparation and characterization have been established.

An adaptive optics Kirk Patrick Baez focusing system provides an X-ray beam with a high photon flux (up to 10^{13} ph/sec), very low beam divergence (0.2 mrad (H) x 0.15 mrad (V)) and rapidly (few minutes) tunable focus size (15 to 100 mm) to adapt to diverse experimental situations. The MAATEL MicroDiffractometer2 with a mini kappa goniometer head (sphere of confusion ~2 mm) and the small focus beam facilitate the use of small crystals for data collection and allow precise 4D scans on needle-shaped crystals.

Data collections at energies as low as 4 keV (3.0996 Å) are possible due the optimized beam line design, which delivers a good flux (up to 10^{11} ph/sec at 4 keV) to the sample, the custom calibration applied to the PILATUS 6MF detector, and the availability of a Helium-path. At high energies, the high photon flux ($5*10^{11}$ ph/sec at 17.5 keV) allows data collection to atomic resolution (0.75 Å). Edge scans for MAD data sets are also possible with the Amptek X-100SDD/PX fluorescence detector. The miniKappa allows optimal orientation of the crystal for anomalous data collection and for 4D scans on long crystals. The new MARVIN sample changer has a capacity of 150 samples and duty-cycle under one minute.

We will show examples, taken for user operation, of how the variable beam size can resolve crystal imperfections, of SAD data collection and structure solution from small crystals, and high-resolution data collection.

MS07-P16

Macromolecular neutron diffraction at the FRM II neutron source

A. Ostermann[1], T. E. Schrader[2], M. Monkenbusch[3], B. Laatsch[4], P. Jüttner[1], W. Petry[1], D. Richter[3]
[1]*Technische Universität München, Forschungs-Neutronenquelle Heinz Maier-Leibnitz, Garching, Germany*
[2]*Forschungszentrum Jülich GmbH, Jülich Centre for Neutron Science (JCNS), Garching, Germany*
[3]*Forschungszentrum Jülich GmbH, Institute for Complex Systems, Jülich, Germany*
[4]*Forschungszentrum Jülich GmbH, Zentralabteilung Technologie, Jülich, Germany*

The research reactor Heinz Maier-Leibnitz (FRM II) is a modern high flux neutron source which feeds at the moment 26 state oft he art instruments. The newly build neutron single crystal diffractometer BIODIFF is especially designed to collect data from crystals with large unit cells. The main field of application is the structure analysis of proteins, especially the determination of hydrogen atom positions. BIODIFF is a joint project of the Forschungszentrum Jülich (FZJ/JCNS) and the FRM II. Typical scientific questions addressed are the determination of protonation states of amino acid side chains and the characterization of the hydrogen bonding network between the protein active centre and an inhibitor or substrate. BIODIFF is designed as a monochromatic instrument. By using a highly orientated pyrolytic graphite monochromator (PG002) the diffractometer is able to operate in the wavelength range of 2.4 Å to about 5.6 Å. Contaminations of higher order wavelengths are removed by a neutron velocity selector. To cover a large solid angle the main detector of BIODIFF consists of a neutron imaging plate system in a cylindrical geometry. A fast Li/ZnS scintillator CCD camera is available for additional detection abilities. The main advantage of BIODIFF is the possibility to adapt the wavelength to the size of the unit cell of the sample crystal while operating with a clean monochromatic beam that keeps the background level low. BIODFF is equipped with a standard Oxford Cryosystem "Cryostream 700+" which allows measurements in the temperature regime from 90K up to 500K.

MS07-P18

Solvent Exchange in Protein Crystals at Cryogenic Temperatures

A. Burkhardt[1], M. Warmer[1], A. Wagner[2], R. Reimer[3], H. Hohenberg[1], A. Meents[1]
[1]*Deutsches Elektronen-Synchrotron, Photon Science, Hamburg, Germany*
[2]*Diamond Light Source, Didcot, United Kingdom*
[3]*Heinrich Pette Institute, Leibniz Institute for Experimental Virology, Hamburg, Germany*

Biological samples are very sensitive towards ionizing radiation, such as X-rays or electrons. In electron microscopy the standard method to improve the radiation hardness of samples in order to prolong their lifetime in the electron beam is plastic-embedding [1]. This method first requires dehydration of the frozen samples by anhydrous organic solvents, such as ethanol, methanol or acetone to partially substitute the water inside the samples. In a second step the organic solvent is gradually replaced by a polymeric resin, such as EPON or Lowricyl, which can be subsequently polymerized by UV irradiation. Such an cryo-exchange is usually performed at temperatures below 243 K in order to preserve the ultrastructure of the biological samples.

We believe it would be of general scientific interest to know whether these cryofixation techniques from electron microscopy could also be applied to protein crystals. In an initial study plastic-embedded crystals of hen egg-white lysozyme diffracted to a resolution of 4.2 Å and showed a mosaicity of 1.0° [2].

Here, we report on the first successful data collection on freeze substituted protein crystals which we envision to be the first step towards more radiation-hard protein crystals. Hen egg-white lysozyme and thaumatin crystals were chosen as initial model systems to develop and establish an experimental cryo-exchange procedure.

Protein crystals are first drawn into quartz or cellulose tubes and high-pressure frozen at 210 MPa and 77 K using a Baltec HPM 010 high-pressure freezer [3, 4]. Protein crystals typically contain between 30 and 80%

solvent (mainly water) and are surrounded by their aqueous growth solution (mother liquor). The very high cooling rates provided by the Baltec HPM 010 device allow freezing the crystals directly in their mother liquor. The formation of hexagonal ice is suppressed and the water is converted to amorphous ice (vitrification) which does not destroy the crystal lattice.

The high-pressure frozen samples are transferred to a freeze substitution device (Leica AFS) and stored at 183 K for several days while being immersed in anhydrous ethanol. For X-ray data collection the tubes containing the crystals are mounted on standard cryo loops. The freeze substituted protein crystals diffracted to a resolution of up to 1.9 Å.

[1] M. Müller, Methods Microbiol. 20, 1-28 (1988); [2] R. B. G. Ravelli, U. Haselmann-Weiss, J. E. McGeehan, A. A. McCarthy, J. A. Marquez, C. Anthony, A. S. Frangakis, G. Stranzl, J. Synchrotron Rad. 14, 128-132 (2007); [3] A. Burkhardt, M. Warmer, S. Panneerselvam, A. Wagner, A. Zouni, C. Glöckner, R. Reimer, H. Hohenberg, A. Meents, Acta Cryst.F68, 495-500 (2012); [4] A. Burkhardt, A. Wagner, M. Warmer, R. Reimer, H. Hohenberg, J. Ren, E. E. Fry, D. I. Stuart, A. Meents, Acta Cryst. D69, 308-312 (2013).

MS07-P19

Engineering of the mechanics for the SFX sample delivery system.

S. K. Ananthaneni [1], L. Chavas [1]
[1]*DESY, CFEL, Hamburg, Germany*

Ananthaneni S[1], Adriano L[1], Beyerlein K R[1], Bartelmess M[1], Gumprecht L[1], Kirian R[1]. Bean R[1], Liang M[1], Stern S[1], Vagovic P[1], Raabe S[1], Dadgostar H[1], Hiraki M[1], Bajt S[1], Chavas L[1], Chapman H[1]

[1]*Center for Free-Electron Laser Science, Coherent Imaging Division, Hamburg (Germany)*
[2]*High Energy Accelerator Research Facility, Tsukuba (Japan)*

In Serial Femtosecond Crystallography experiments, vacuum causes the particles to freeze by evaporative cooling as they travel [1]. The injector must run for days without clogging, and must provide sub-micron positional stability to match the X-ray beam and particle size; as a consequence, the sample must be continuously refreshed. For this purpose, a six-nozzle cartridge has been developed for high-throughput sample delivery [2]. Each of the nozzles in the cartridge is connected to an individual sample liquid line that should be inserted into a liquid catcher to preserve high vacuum and prevent contamination of the sample chamber and other equipment by accumulating samples. Certain aspects of the nozzle system can be improved, such as the implementation of a proper alignment procedure, positioning feedback system, working with various orientations of the nozzle, or replacement of the whole cartridge when needed.

As an alternative, we propose here a design with the idea to automate the whole process at various levels.

In this system, a Stewart-Gough platform [3] (also known as hexapod) consisting of a fixed base plate and a top plate that can be moved relative to each other in six degrees of freedom will maneuver the nozzle attached to it. Since the nozzle dimensions are relatively small, the design of the Stewart platform becomes complex. For facilitating manipulation of the nozzle, a ball-and-socket joint [4], which possesses three degrees of freedom, can provide with a motion around an indefinite number of axes with one common center. The Stewart-Gough platform operating on the joint will allow holding in position the nozzle.

Nozzle clogging is a severe issue that seriously affects the flow of experiments by blocking sample jetting. The use of the six-nozzle cartridge partly deals with this problem, but challenges remain in designing larger cartridges. To overcome these limitations, robotic arms with the capability to operate in higher vacuum and on the tips of the nozzles are now being designed.

[1] Petra Fromme and John CH Spence, Femtosecond Nano crystallography using X-Ray lasers for membrane protein structure determination. 2011 August: 21(4): 509-516
[2] R. Bean, Multiple nozzle cartridge and integrated catcher [under review], CFEL Hamburg.
[3] Xiao-Shan Gao, et al., Generalized Stewart-Gough Platforms and their Direct Kinematics, IEEE TRANSACTIONS ON ROBOTICS, VOL. 21, NO. 2, APRIL 2005
[4] P. Baerlocher, et al., Parameterization and range of motion of the ball-and-socket joint, Computer Graphics Lab (LIG) EPFL-Lausanne, Switzerland

MS07-P20

A spectroscopic comparison of AOS thin films and TCO single crystals

J. Haeberle[1], D. Gaspar[2], P. Barquinha[2], S. Machulik[3], C. Janowitz[3], Z. Galazka[4], D. Schmeißer[1]
[1]*BTU Cottbus-Senftenberg, Applied science and Sensors , Cottbus, Germany*
[2]*New University of Lisbon and CEMOP-UNINOVA, Department of Materials Science Faculty of Sciences and Technology, Caparica, Portugal*
[3]*Humboldt-Universität zu Berlin, Institut für Physik, Berlin, Germany*
[4]*Leibnitz-Institut für Kristallzüchtung, Berlin, Germany*

Amorphous oxide semiconductors (AOS) and transparent conductive oxides (TCO) are today one of most attractive fields of research in many industrial products, like e.g. high definition, low cost, transparent, and flexible displays [1]. We got the unique possibility to measure a-GIZO and a-SnOx thin films and compare their electronic properties with those of In_2O_3, Ga_2O_3, ZnO, and SnO_2 single crystals. We use resPES to study the electronic properties. We report on the core levels, the VB PES data, partial Integrated Yield (pIY) and the XAS absorption data. From these we are able to derive the elemental ratio, the pDOS as well as the band scheme. At the O1s resonance we observe multiple Auger processes from which we deduce that a band of localized defect states is located between the Fermi energy and the CBM [2]. The resonant profiles taken at the corresponding metal edges indicate that metal states are involved in the DOS starting already below the Fermi energy [3].

[1] P. Barquinha, L. Pereira, G. Goncalves, R. Martins, and E. Fortunato; Journal of the Electrochemical Society, vol. 156, pp. H161-H168, 2009.
[2] Resonant Photoemission at the O1s threshold to characterize In2O3 single crystals; J. Haeberle, M. Richter, Z. Galazka, C. Janowitz, D. Schmeißer; Thin Solid Films, accepted, DOI: 10.1016/j.tsf.2013.03.036
[3] Electronic structure of amorphous ZnO films; D. Schmeißer, J. Haeberle, P. Barquinha, D. Gaspar, L. Pereira, R. Martins, and E. Fortunato; Phys. Stat. Sol.; submitted

MS07-P21
X-ray Optics

P. U. Pennartz[1], L. Jiang[1], B. Verman[1], N. Grupido[1], P. Oberta[2]
[1]Rigaku Innovative Technologies, Auburn Hills, United States
[2]Rigaku Innovative Technologies, Prague, Czech Republic

In the last 20 years, multilayer optics for the broad band of radiation from 40 eV to 100 keV have revolutionized the measurement capabilities and the experimental set ups for elemental analysis, diffraction and scattering equipment. Essential for the industrial production of excellent multilayer structure is the metrology of the coatings in regards to internal roughness on the atomic level while creating layered materials of defined thickness. Modern multilayers have d-spacings, synonymous for layer-pair thickness, which have to be produced uniform, laterally graded, depth graded or even a combination of both gradients: With d-spacings down to several tenth of nm thickness the technical capabilities and production equipments have to be weel characterized to keep costs in balance with performance. Core capabilities of high end producers are the knowledge of practical multilayer physics, beyond the simulation software, which was developed over the years and can now be applied even through web pages. The detailed knowledge of distinctive multilayer coating technology and their application in coating tools, optic engineering including optical system designs specific to instruments, the mounting and alignment of optics is the key for industrial success. Being able to coat numerous material systems working at different energy bands or having different performance characteristics makes almost all solution possible, high end science is asking for .

In the recent last years, the focus broadened and we developed technology for precise Johansson crystal manufacturing. Owing to its high precision, the monochromator has exceptionally high resolution both spatially and energy wise. When applied to x-ray diffractometry, for example the Cu-Kα2 radiation is strongly suppressed in the conditioned beam. The monochromator also provides excellent beam uniformity across the crystal's working area, and a small (10 µm to 40 µm) beam cross section at the crystal focus that results in low beam blurring. Rigaku Innovative Technologies is working on broadening the application of Johansson crystals in x-ray spectrometry and for EPMA spectrometers, particularly. A significant improvement in all major performances (intensity, resolution, and limit of detection) is expected. Results of the initial crystal tests will be presented.

On the other hand, replicated optics are becoming more and more popular. This kind of optics uses a unique optics manufacturing procedure which enables the creation of 3D optical devices suitable for EUV, XUV and X-ray radiation in a kind of mass production approach with severe production cost cut down. The replication technology enables us to create collimating (parabolic), focusing (elliptic) or custom made aspheric optics. The aperture ranges from just Ø 0.3 - 150 mm with a microroughness from 0.2 nm. We will show the latest results of our developments in all these areas.

MS07-P22
High-Efficiency SAXS/GISAXS/WAXS instrument for the Laboratory: Rigaku S-MAX 3000™

P. U. Pennartz[1], M. Degen[1], N. Grupido[1]
[1]Rigaku Innovative Technologies, Auburn Hills, United States

The Rigaku S-MAX 3000™ instrument provides excellent SAXS, GISAXS and simultaneous WAXS capabilities while maintaining maximum flexibility in controlling sample environment [1] and figure 1. This Instrument utilizes a high brilliance X-Ray microfocus source running at 40W of power. Its state-of-the art design concentrates the applied power into a tiny spot (20µm*20µm) which, when coupled with a confocal graded multilayer focusing optics, yields a high intensity x-ray beam comparable to conventional laboratory sources operating at kilowatt power. Combining this intense beam with three-pinhole collimation, a fully evacuated beam path and a photon-counting MSPC detector, this instrument is capable of making highly sensitive measurements from both isotropic and anisotropic materials without needing desmearing corrections. A photodiode embedded inside the beamstop allows continuous monitoring of the beam intensity yielding a direct measurement of the sample transmission. A second optional sample chamber allows exploration of a middle Q range without moving the detector or realigning the beam. High throughput SAXS measurements can be performed by running a user-friendly script, which automatically controls sample movement and environment. Simultaneous WAXS measurements can be collected on Image Plates at scattering angels up to 68°.An automated high weight sample stage for GISAXS provides better than 5 arc second angular precision and motion ranges of ±8° in plane, ±10° out of plane and ±12.5mm vertical. The high weight capacity can be utilized to support in-situ vessels or samples of all types. An alternative high precision stage is available with sub-arc second motion but lower weight capacity. Both stages are fully automated with automatics determination of the zero incident angles as well as automatic correction of the scattering data. The Rigaku S-MAX 3000™ is capable of characterizing a large variety of materials, ranging from colloids of all types, cements, nanoparticles, oils, polymers, plastics, proteins, surfactants, foods and pharmaceuticals. In this presentation, we demonstrate Rigaku SAXS/WAXS/GISAXS capabilities in studying various materials. The structural morphology from weak scattering polymer thin films can be determined using this laboratory setup.

References
[1] www.rigaku.com

Figure 1

Rigaku S-MAX 3000™ with dual sample chamber and offset detector position

MS07-P23

POWHOW: the proposed bispectral neutron powder diffractometer at the European Spallation Source

W. Schweika[1,2], N. Violini[1], K. Friese[1], K. Lieutenant[3], D. Nekrassov[3], C. Zendler[3], A. Houben[4], P. Jacobs[4], P. Henry[2]
[1]*Forschungszentrum Jülich, Jülich Centre for Neutron Science, JCNS, Jülich, Germany*
[2]*European Spallation Source ESS AB, Lund, Sweden*
[3]*Helmholtz-Centre , Berlin, Germany*
[4]*RWTH Aachen University, Inorganic chemistry, Aachen, Germany*

Within the ESS Design Update Programme funded by the German Federal Ministry of Education and Research, we have studied the new opportunities for powder diffraction at the long pulse spallation source ESS. This study led to the submission of the POWHOW instrument proposal which, after final successful ESS internal and diffraction advisory panel review, will be presented to the Scientific Advisory Committee in 2014 as a day-1 instrument concept.

The ESS design parameters provide truly new opportunities for science with neutrons. The peak brightness of the ESS is higher than any of the short pulse spallation sources, and more than an order of magnitude higher than the world’s leading continuous source. The time-integrated brightness at the ESS is similarly one to two orders of magnitude larger than today’s leading pulsed sources.

The instrument design of POWHOW effectively utilizes the specific source parameters to address the needs of a broad science community in powder diffraction. Key parameters for neutron diffraction are the particular sensitivity for light elements, magnetic diffraction, applications at low temperatures, and the high penetration depth. The high performance will also enable fast experiments on small samples.

By shaping the ESS pulse using choppers for adequate resolution, the instrument has gained a new flexibility in time resolution, tradable for intensity. The best time resolution yields a *d*-resolution of 2.8´10^{-4}Å for backscattering. There is further flexibility in the choice of wavelength band, covering simultaneously the peaks of the thermal and cold moderator fluxes (from 0.8 Å to 4.6 Å). Recent developments led to a new detector concept [1] based on ^{10}B coated cathodes, which is more than a substitute for today’s ^{3}He detectors. The detector covers 6 sr solid angle, almost free of any blind areas, with a high efficiency of 50 to 70%. The 2D high spatial resolution of 4 mm will support the recognition of prefered orientation and texture, and moreover, single crystal diffraction in a very efficient neutron time of flight Laue technique. A novel potential is the volume and time sensitivity of the detector to yield 4D data with better control and reduction of background while avoiding saturation effects, despite the high counts rates. Complementary to 2D Rietveld refinement for including texture [2], we are currently developing a 2D Rietveld code to exploit the varying resolution properties in diffraction angle and wavelength [3].

VITESS simulation of the whole instrument and benchmarking to currently world leading instruments demonstrates a far superior performance of POWHOW. For example, for medium resolution, the flux at the sample is 3.4´10^8 n/s/cm^2. For a small reference sample (0.4cm^3 NAC) 10^7 n/s are detected in total, and 10^6 n/s in the most intense peak.

[1] G. Modzel et al., accepted NIMA.
[2] L. Lutterotti, MAUD
[3] P. Jacobs et al., in preparation.

Fig.1. Simulated diffraction pattern of a reference sample (0.4 cm^3 $Na_2Ca_3Al_2F_{14}$) in medium resolution setting. Insets show examples of integrated peak profiles and intensities. The resolution *Dd (2p)*, is obtained from 2D Rietveld refinement for backscattering.

Figure 1

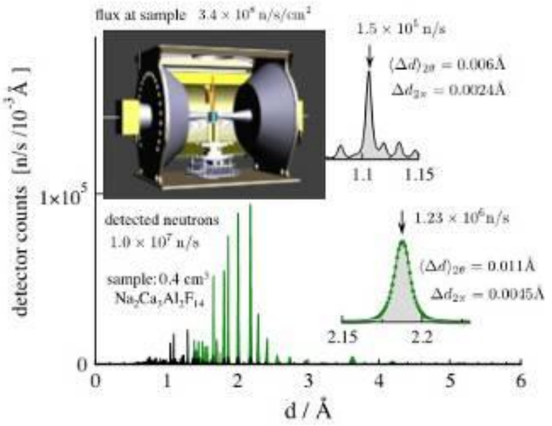

MS08 – Quasicrystals and incommensurate structures

MS08-P01
Modulated structure of Λ-Co(III) sepulchrate trinitrate in the second low temperature phase

S. Dey[1], A. Schönleber[1], S. van Smaalen[1], F. K. Larsen[2]
[1]*University of Bayreuth, Laboratory of Crystallography, Bayreuth, Germany*
[2]*Aarhus University, Department of Chemistry, Aarhus, Denmark*

Λ-cobalt(III) sepulchrate trinitrate, $[Co(C_{12}H_{30}N_8)](NO_3)_3$ crystallizes at room temperature in the hexagonal space group $P6_322$ [1,2]. Inside the sepulchrate cage, the Co^{3+} cation is six-coordinated by nitrogen atoms, while the sepulchrate cage is coordinated by six ordered and six disordered nitrate anions. The sepulchrate cages and the ordered anions are connected *via* N—H··O hydrogen bonds to form slabs, between the slabs are layers of disordered nitrate anions [1,2].

By optical microscopy and spectroscopic measurements, phase transitions at T_1 = 133 K and T_2 = 107 K were observed [3]. The phase transition at T_1 is interpreted as freezing of the disordered nitrate group into two non-equivalent configurations with the reduction of trigonal symmetry and destruction at T_2 [3]. Phase transitions have been observed as a function of temperature also by single crystal neutron diffraction [4]. Upon cooling, satellite reflections were observed at T_1 in the diffraction pattern followed by additional phase transitions at T_2 and T_3 = 98 K, respectively.

We found in the first low temperature phase between T_1 and T_2 a symmetry lowering from hexagonal to orthorhombic threefold twinning by analysis of the reflection intensities with possible superspace group $C222_1(\sigma00)000$.

Single crystal X-ray diffraction was performed at Hasylab/DESY (Hamburg, Germany) at T = 104 K and 100 K. At T = 104 K, main reflections are surrounded by satellite reflections up to 3rd order. All reflections can be indexed by a C-centred orthorhombic threefold twinned unit cell with a = 8.45 Å, b = 14.66 Å and c = 15.76 Å and the **q**-vector $(\sigma_1,0,0)$ where $\sigma_1 = 0.17$. A description of the twinned crystal structure is presented within the (3+1)-dimensional superspace approach.

[1] L. Dubicki, J. Ferguson, R. J. Geue, A. M. Sargeson, *Chem. Phys. Lett.* 74 (1980) 393-397.
[2] A. Schönleber, S. van Smaalen, F. K. Larsen, *Acta Crystallogr. C* 66 (2010) m107-m109.
[3] L. Dubicki, J. Ferguson, B. Williamson, *J. Phys. Chem.* 88 (1984) 4254-4258.
[4] F. K. Larsen, P. Jørgensen, R. H. Grønbæk, B. Lebech, R. Thomas, R. J. Geue, A. M. Sargeson, *Molecular Structure: Chemical Reactivity and Biological Activity*, Stezowski *et al*. (*ed*.) IUCr, Oxford University Press (1988) 499-504.

MS08-P02
Physical properties of incommensurate phase with multifractal distribution of defects

B. Gadjiev[1]
[1]*International University for Nature, Society and Man, SAM, Dubna, Russian Federation*

In the present paper the magnetic and ferroelectric phase transition with incommensurate phase in the system with multifractal defects distribution are considered [1,2,3]. We study the effect of the multifractal distribution of structural defects on the physical properties of crystals in the region of a sequence phase transitions high symmetry-incommensurate-commensurate phase. We used the maximum entropy principle for deriving the distribution function of defects and then show that in the case of the multifractal distribution of defects the equations of motion for the order parameters in the incommensurate phase takes the form of fractional differential equation. Spatial dependence of the order parameter in the incommensurate phase extensively reviewed. In particular, with decreasing the order differential equation occurs broadening of discommensurate and commensurate areas in a incommensurate phase. We study the neutron diffraction pattern in the region of existence incommensurate phase as a function of the generalized fractal dimension of the distribution of structural defects. We discuss the free energy functionals with and without the Lifshits invariants. By using the renormalization group method, we show that it is possible near the transition point due to defects set new critical regime which describes the new universal critical exponents.

References
1. Vik. S.. Dotrenko, Critical phenomena and quenched disordered , Physics-Uspekhi, 165, n.5, 481, (1995)
2. Leo P. Kadanoff, Theories of Matter: Infinities and Renormalization, arXiv:1002.2985v1 [physics.hist-ph] (2010)
3. B. R. Gadjiev, Phase transition in generalized inhomogeneous ‘cubic’ systems/ Proceedings of the XXVIII International Colloquium on Group-Theoretical Methods in Physics, Newcastle upon Tyne, 26-30 July 2010 (The IoP Journal of Physics Conference Series) —J. Phys.: Conf. Ser. 284 012026 (2011)

MS08-P03
Structure refinements of Al_3BC and Al_3BC_3 - Super structure versus modulation

P. Schultz[1], H. Hillebrecht[2]
[1]*Faculty for chemistry and mineralogy, Leipzig, Germany*
[2]*University Freiburg , Inorganic Chemistry, Freiburg, Germany*

Single crystals of Al_3BC [1] and Al_3BC_3 [2] were grown from the elements in an Al-melt. Both compounds crystallize with hexagonal unit cells (Al_3BC: a = 3.4849(7) Å, c = 11.520(2) Å; Al_3BC_3: a = 3.4075(9) Å, c = 15.900(2) Å) and show super structure reflections which demand the enlargement of the lattice parameter a by a factor √3 [3]. The refinement of the subcell in space group $P6_3/mmc$ revealed in both cases that the reason for the additional reflections is a shift of one Al-atom in direction [001]. This shift of about 0.2 Å changes the trigonal-planar coordination to 3 carbon atoms, which is energetically unfavourable. Conventional refinement (SHELX) of the super structure in space group *P c*1 resulted in a partially ordered structure with a reasonable model, but for 1/3 of the disordered Al-atoms the problem could not be solved. The symmetry reduction to *P*3c1 or even lower symmetry enables complete ordering of the Al-atoms but the ADP of the affected atoms remain questionable [4].

Treating the super structure reflections with the commensurate q-vector (1/3 1/3 0) based upon the mentioned subcells solves the ADP problems and reduces the number of parameters required to describe the structure significantly. Refinements of both structures in the super space groups *P* 1*c* (1/3 1/3 g) 000 and *P*31*c* (1/3 1/3 g) 000 were performed using the JANA2006 software package [5]. The structure description utilizing displacement modulation functions proved more precise and reduces the amount of refined variables. The main feature that results from the refinement as a modulated structure is a tilt of the trigonal pyramid CAl_5. The direction of the tilt follows one of the equivalent directions [100], [010], and [0] of the subcell. This explains the problems of the commensurate refinement based on a supercell, because the tilt is incompatible with an “up-down”ordering of the Al-atoms.

[1] KF. D. Meyer, H. Hillebrecht, *J. Alloys Compd.* 252(1997)98-102.
[2] H. Hillebrecht, F. D. Meyer *Angew. Chem.* 108(1996)2655-2657, *Angew. Chem. Int. Ed.* 35(1996)2499-2500.
[3] F. D. Meyer, PhD thesis, University Freiburg, 1998.
[4] P. Schultz, MSc thesis, University Freiburg, 2013.
[5] V. Petricek, M. Dusek, L. Palatinus (2006).Jana2006 - The crystallographic computing system. Institute of Physics, Praha, Czech Republic.

MS08-P04

Cell organelles with crystalloid inclusions and applicability in practice

A. CHESCA[1,2], A. CHESCA[1,2,3]
[1]*TRANSILVANIA UNIVERSITY OF BRASOV, ROMANIA, FACULTY OF MEDICINE, BRASOV, Romania*
[2]*Transilvania uNIVERSITY OF BRASOV, ROMANIA, FACULTY OF MEDICINE, BRASOV, Romania*
[3]*,, Romania*

Introduction: The present study show the implications of cell organelles with crystalloid inclusions, and their applicability in medical practice. In this context, the study is referring at peroxisomes. Peroxisomes are cell organelles with crystalloid inclusions, implied in pathology, taking into consideration their function in cellular digestia. From this point of view, we can mention peroxisomes as cell organellles with an important roles in lipid metabolism, taking into consideration the β-oxidation of fatty acids. Peroxisomes also play important roles in cholesterol and bile acid synthesis, in purine and polyamine catabolism and in prostaglandin metabolism. Finally, peroxisomes are cell organelles with implications in human diseases, most important at children, affecting life.

Methods: The purpose of the study is to observing pathology of peroxisomes, cell organelles with crystalloid inclusion, using transmision electron microscopy technique. We can mention three categories of peroxisomal disorders, for observing changes of this cell organelles. Using transmision electron microscopy, is possible to show ultrastructural particularities, in disorders as infantile Refsum disease and neonatal adrenoleukodystrophy. Microphotographs show particularities. Has been used TEM Philips, x1500-x5000.

Results : The medical diagnostic at aforementioned human diseases on neonatal infants and infants, is composed by a complexity of techniques, but for our study the electron microscopy technique, has been used for observing changes to necroptic tissues fragments. In this context, changes in peroxisomes and their crystalloid inclusions, have been observed.

Conclusion: Because the patients with the diseases, as neonatal adrenoleukodystrophy and Refsum disease, usually die within the first years after birth, the present study has been done easy with transmission electron microscopy technique, using necroptic fragments.

MS09 – Crystallography in geology – microstructures as indicators of rock forming processes

MS09-P01

Temperature, pressure and field induced processes/phase transitions

J. Stein[1], T. Cronert[1], J. Leist[2], K. Schmalzl[3], A. Nugroho[4], A. Komarek[5], G. Eckold[2], M. Braden[1]
[1]*II. Physikalisches Institut, Universität zu Köln, Köln, Germany*
[2]*Universität Göttingen, Institut für Physikalische Chemie, Göttingen, Germany*
[3]*JCNS at ILL, ..., France*
[4]*Institut Teknologi, Bandung, Indonesia*
[5]*MPI für chemische Physik fester Stoffe, Dresden, Germany*

Multiferroic crystals are promising materials for future memory devices with extremely low power consumption. The rise time between two states is a crucial parameter for a possible application and was investigated in the spiral spin multiferroic $TbMnO_3$.
Polarized neutron diffraction is able to determine the ratio of chiral domains, which can be controlled by an external electric field.
Using the stroboscopic technique we can follow the reversion of chiral domains in the timescale of a few hundred microseconds to hours.
In $TbMnO_3$ we find a clear logarithmic relation between the rise time and temperature that is fulfilled over 5 decades.

MS09-P02

Microstructural studies of *in situ* heated and deformed pure and silica gel-doped polycrystalline salt samples for long-term lithospheric rheology and radioactive waste disposal

C. E. Tommaseo[1]
[1]*Technical University Berlin, Department of Mineralogy, Berlin, Germany*

For the first time *in situ* deformation and heating experiments both on wet pure and silica gel-doped polycrystalline halite in uniaxial compression were performed to study the texture development and rheological behaviour in the mono- and bimineralic system and to better understand the most complex polymineralic systems present in the natural salt caverns used for Compressed Air Energy Storage (CAES) and final disposal of radioactive material.

In general a decrease in yield strength in the pure samples, which even decrease more with increasing temperature and grain size is observed. Under the same stress conditions the pure samples show a decrease in the Young's modulus and the yield strength and an extended plastic regime. All samples, irrespective of grain size, show a higher yield strength with silica gel additives. It is probable that some grains deform much more than others, resulting in a large variation in dislocation microstructure such as dislocation density and subgrain geometry. Silica gel additives in the halite bulk cause a lower strain accumulation, expressed through a larger Young's modulus, a strengthening of the samples, which correlates with a decrease in plasticity.

In the texture development a sustainability of the starting texture is observed, which correlates well with the mechanical behavior. The amorphous phase likely protects the single grains in the crystalline phase from deformation, alleviating strain accumulation by introduction of defects and therefore the preservation of the grain shape. The degree of stress and strain partitioning in the deforming salt depends strongly on the proportion of silica gel additive, as well as on the temperature and grain size dependencies, which bears important implications for long-term lithospheric rheology and radioactive waste disposal.

Furtheron the structural and microstructural results are in good correlation to each other. No matter which deformation, recrystallization processes the material went through, inhomogeneities in the textural development are highly correlated with structural changes in the material. With help of the EXAFS spectroscopy, a sensitive method for the detection of order/disorder in the structure, it was possible to show that the third and fourth coordination shells in the halite structure are mostly affected during the structural development. This is in good agreement with the microstructural development, in which (011)[0-11] and (011)[100] are the most active slip systems in the halite structure as shown with the EBSD method.

The observed structural and microstructural behavior in the simplified system is partly reproducible and nearly comparable with the natural samples, but it let also guess the complexity of processes taking place during recrystallization and deformation.

MS10 – Protein function and regulation

MS10-P01

Dynamic and conformational variability of the bacterial type-I fatty acid synthase Type-I

M. Enderle[1], M. Grininger[1], L. Ciccarelli[2]
[1]*University Frankfurt, BMLS, Frankfurt, Germany*
[2]*MPI of Biophysics, Structural Biology, Frankfurt, Germany*

Fatty acids are important molecules performing structural and functional tasks in all kingdoms of life except *Archaea*. Two types of fatty acid synthases (FAS) systems exist in nature. While type-I FAS have catalytic domains fused to polypeptide chains, type-II FAS carry catalytic activities on separate proteins. The type-I multienzyme system is highly organized and occurs in three different structural frames. Mammalian type-I FAS is a homodimer, the fungal type-I FAS a $\alpha_6\beta_6$ dodecamer and the bacterial type-I FAS a homohexamer [1].

The bacterial protein is a 1.9 MDa large barrel-shaped megacomplex with two reaction chambers. Each 320 kDa polypeptide chain carries a full set of functional domains [1,2,3].

Mycobacterium tuberculosis is the causative agent of tuberculosis (TB). There is a worldwide renaissance of TB. Reasons for a new threat of TB are deficiencies of immune systems as caused by HIV, and the occurrence of multi-drug resistant strains of *M. tuberculosis*. The WHO has launched a STOP-TB program in 2006. In our efforts of evaluating type-I FAS as a target for inhibition, we established the recombinant expression of the bacterial type-I FAS in *Escherichia coli* [4].

References:
[1] E. Schweizer and J. Hoffmann (2004). Microbial Type I Fatty Acid Synthases (FAS): Major Players in a Network of Cellular FAS Systems. Microbiol. Mol. Biol. Rev. 68, 501-517.
[2] D. Boehringer, N. Ban and M. Leibundgut (2013). 7.5-Å Cryo-EM Structure of the Mycobacterial Fatty Acid Synthase. JMB.425,841-849.
[3] L. Ciccarelli, S. Connell, M. Enderle, D. Mills, J. Vonck and M. Grininger (2013). Structure and conformational variability of the *Mycobacterium tuberculosis* fatty acid synthase multienzyme complex. Under Review.
[4] H. P. Stuible, G. Meurer and E. Schweizer (1997). Heterologous expression and biochemical characterization of two functionally different type I fatty acid synthases from Brevibacterium ammoniagenes. Eur J Biochem. 247, 268-273.

MS10-P02

Structural and functional analysis of the spliceosomal RNA helicase Brr2

C. Becke[1], E. Absmeier[1], K. Santos[1], M. Wahl[1]
[1]*Freie Universität Berlin, Laboratory of Structural Biochemistry, Berlin, Germany*

Pre-messenger RNA (mRNA) splicing, an essential step in gene expression, in which non-coding sequences (introns) are excised from pre-mRNAs and neighbouring coding sequences (exons) are joined, is catalyzed by the spliceosome, a multi-megadalton ribonucleoprotein machinery. For each splicing event, a spliceosome is assembled stepwise from its building blocks, five small nuclear ribonucleoprotein particles (snRNPs) and many non-snRNP factors, on its pre-mRNA substrate. Unlike other macromolecular machines, none of the building blocks contains a preformed catalytic centre. Eight highly conserved RNA helicases drive the remodelling events necessary to catalytically activate the spliceosome, enable it to perform the two-step splicing reaction and disassemble it after catalysis. Among these enzymes, the Brr2 protein is the key player in the catalytic activation process. While recent crystal structures provided insights into the molecular architecture and regulation of Brr2's helicase region (Mozaffari-Jovin et al., 2013; Nguyen et al., 2013; Santos et al., 2012), little is known about the structural organization and function of its N-terminal region comprising ca. 400 residues. In vivo studies in yeast showed that the N-terminal half of Brr2 can be crosslinked to U4, U5 and U6 small nuclear RNAs (snRNAs) and to pre-mRNA (Hahn et al., 2012), and certain mutations in the N-terminal region of Brr2 are synthetic lethal with mutations in U5 snRNA (Nancollis et al., 2013). Here, we present an atomic-resolution crystal structure of a folded domain within the N-terminal region of Chaetomium thermophilum Brr2 and a low-resolution structure of the yeast protein showing the domain in context of the helicase region bound to a fragment of Prp8, a key regulator of Brr2's helicase activity (Mozaffari-Jovin et al., 2013). Our structures confirm the presence of a PWI-like domain in the Brr2 N-terminal region as predicted bioinformatically. PWI domains in other spliceosomal proteins have been implicated in nucleic acid binding. Based on our structures we have investigated the functional consequences of progressive N-terminal truncations of Brr2.

Hahn, D., Kudla, G., Tollervey, D., and Beggs, J.D. (2012). Genes Dev. 26, 2408-2421.
Mozaffari-Jovin, S., Wandersleben, T., Santos, K.F., Will, C.L., Lührmann, R., and Wahl, M.C. (2013). Science 341, 80-84.Nancollis, V., Ruckshanthi, J.P.D., Frazer, L.N., and O'Keefe, R.T. (2013). J. Cell. Biochem. 114, 2770-2784.
Nguyen, T.H.D., Li, J., Galej, W.P., Oshikane, H., Newman, A.J., and Nagai, K. (2013). Struct. Lond. Engl.

1993 21, 910-919.
Santos, K.F., Jovin, S.M., Weber, G., Pena, V., Lührmann, R., and Wahl, M.C. (2012). Proc. Natl. Acad. Sci. U. S. A. 109, 17418-17423.

MS10-P03

Analysis of counter-ion effects in nonaqueous enzymology of subtilisin

M. Cianci[1], D. Lousa[2], B. Tomaszewski [3], A. Baptista[2], C. Soares[2], J. R. Helliwell[4], P. J. Halling[3]
[1]*EMBL, Hamburg, Hamburg, Germany*
[2]*Universidade Nova de Lisboa, Instituto de Tecnologia Química e Biológica, Lisboa, Portugal*
[3]*University of Strathclyde, WestCHEM, Glasgow, United Kingdom*
[4]*University of Manchester, Chemistry, Manchester, United Kingdom*

When enzymes are in low dielectric non-aqueous media, it would be expected that their charged groups would be more closely associated with counter-ions. There is evidence that these counter-ions may then affect enzymatic activity. We investigated the placement of several Cs^+ and Cl^- ions in crystals of the serine protease subtilisin Carlsberg through their anomalous diffraction using softer X-rays. Eleven defined sites for Cs^+ cations and eight Cl^- anions, some of which close to the mouth of the active site cleft, are identified around the protein molecule, with partial occupancy and non-specific binding sites. Cross-linked CsCl treated subtilisin crystals transferred to acetonitrile show catalytic activity several fold higher than the reference crystals containing Na^+. Pre-soaking with another large cation, choline, also increases the enzyme activity. The active site appears only minimally sterically perturbed by the ion presence around it, so alternative activation mechanisms can be suggested [1]. To address this question, we performed molecular dynamics (MD) simulations in acetonitrile, using the determined X-ray structure as starting point. Additionally we used a docking methodology to predict the ions' binding sites and performed similar simulations with this system. Our results indicate that chloride ions tend to stay close to the protein, whereas, cesium ions frequently migrate to the solvent. We also found that the distribution of the ions around the enzyme surface is not strongly biased by their initial locations. Replacing cesium by sodium ions showed that the distribution of the two cations is similar, indicating that Cs^+ can be used to find the binding sites of cations like Na^+ and K^+, which, unlike Cs^+, have physiological and biotechnological roles. Finally, we performed MD simulations of subtilisin in an aqueous solution containing 1.5 M of CsCl. The probability density maps of chloride and cesium ions obtained in water and acetonitrile show some differences, which indicates that the solvent influences the distribution of the ions around the protein [2].

[1] Cianci, M., Tomaszewski, B., Helliwell, J. R., Halling, P. J., J. Am. Chem. Soc. 132 (2010) 2293.

[2] Lousa, D.; Cianci, M.; Helliwell, J.R.; Halling, P.J.; Baptista, A. and Soares, C., J. Phys. Chem. B (2012) 116 (20), 5838-5848.

MS10-P04

Enthalpic cost of water removal from a hydrophobic glucose binding cavity on HK620 tailspike protein

U. Gohlke[1], N. Broeker[2], U. Heinemann[1], R. Seckler[2], S. Barbirz[2]
[1]*Max-Delbrück-Center for Molecular Medicine, Molecular Structure and Interactions, Berlin, Germany*
[2]*Universität Potsdam, Physikalische Biochemie, Golm, Germany*

Bacteriophage HK620 recognizes and cleaves the O-antigen polysaccharide of Escherichia coli serogroup O18A1 with its tailspike protein (TSP). HK620TSP binds hexasaccharide fragments with low affinity, but single and double amino acid exchanges generated a set of high-affinity mutants with submicromolar dissociation constants. Isothermal titration calorimetry showed that only small amounts of heat were released upon complex formation via a large number of direct and solvent-mediated hydrogen bonds between carbohydrate and protein. At room temperature, association was both enthalpy- and entropy-driven, emphasizing major solvent rearrangements upon complex formation. Crystal structure analysis of a nearly complete set of combinations of wildtype protein and point mutations with and without polysaccharide ligands was carried out. It could be shown that the extended sugar binding site can be dissected into two regions: first, a hydrophobic pocket at the reducing end with minor affinity contributions. Second, a region where the specific exchange of amino acids creates a site for additional water molecules. Sidechain rearrangements upon sugar binding lead to desolvation and additional hydrogen bonding which define this region of the binding site as the high-affinity scaffold.

This study is a major follow-up to and completes the analysis of experiments published recently (Broeker et al. (2013), Glycobiology 23, pp. 59-68).

MS10-P05

The class C Vps tethering complexes HOPS and CORVET

H. Behrmann[1], C. Ungermann[2], U. Heinemann[1]
[1]*MAX-DELBRÜCK-CENTRUM FÜR MOLEKULARE MEDIZIN (MDC) Berlin-Buch, Macromolecular Structure and Interaction, Berlin, Germany*
[2]*University of Osnabrück, Department of Biology/Chemistry, Biochemistry Section, Osnabrück, Germany*

Internal transport processes are among the hallmark developments separating eukaryotes from prokaryotes [1] as they are prerequisites for the higher complexity present in eukaryotes. This complexity allows, among other benefits, the spatial separation of cellular processes (e.g. energy production within mitochondria and transcription within the nucleus). However, this development comes at a price: Eukaryotic cells are divided into different internal membrane-enclosed compartments, which need to be connected via specific transport processes. Various proteins and protein complexes have evolved to coordinate the several steps necessary for intracellular transport. The main focus of this study is on protein complexes involved in the tethering step between vesicles and their target membranes, especially on the class C Vps tethering complexes HOPS and CORVET [2]. The reason for our interest is that, compared to the well-studied fusion process [3], little is known of the specific mechanisms of tethering. To date, knowledge is limited to the fact that they have to act as a bridge between the binding partners' GTPases and SNAREs leaving the exact mechanism to be uncovered.

To uncover these structural and functional mechanisms we are employing X-ray diffraction experiments in combination with biochemical assays to corroborate structural findings. A major obstacle precluding the analysis of membrane tethering complexes is that individual subunits are prone to aggregation and/or have limited half-lives in isolation. The exception to this trend proved to be Vps18, of which we were able to crystallize an N-terminal fragment and analyze its structure to 2.4 Å. The remaining subunits, however, were refractory to crystallization attempts in our hands. Therefore, we looked towards sub-complexes to improve the stability of our constructs. However, the lack of a reliable interaction network of the complex compounds co-expression of these potentially more stable sub-complexes. Consequently, we have implemented a sophisticated cloning strategy based on recombination [4] to facilitate the high-throughput generation of numerous sub-complex constructs. This approach has so far shown promise and resulted in the generation of crystals of a sub-complex comprising Vps11 and Vps39 constructs. Under the current crystallization conditions, diffraction is anisotropic and limited to 4.5 - 7.0 Å. Further trials to reduce anisotropy are undergoing.

References:
[1] Cavalier-Smith, *The phagotrophic origin of eukaryotes and phylogenetic classification of Protozoa.* Int J Syst Evol Microbiol, 2002. 52(Pt 2): p. 297-354.
[2] Epp, Rethmeier, et al., *Membrane dynamics and fusion at late endosomes and vacuoles--Rab regulation, multisubunit tethering complexes and SNAREs.* Eur J Cell Biol. 90(9): p. 779-85.
[3] Jahn and Scheller, *SNAREs--engines for membrane fusion.* Nat Rev Mol Cell Biol, 2006. **7**(9): p. 631-43.
[4] Bieniossek, Nie, et al., *Automated unrestricted multigene recombineering for multiprotein complex production.* Nat Methods, 2009. 6(6): p. 447-50

MS10-P06
APP-E1 in a new crystal form

S. Hoefgen[1], S. O. Dahms[1], M. E. Than[1]
[1]*Leibniz Institute for Age Research, FLI Jena, Protein Crystallography, Jena, Germany*

Alzheimer's disease (AD) is one of the most frequent forms of dementia in the elderly population affecting about 25 % of people in the age of 80 to 90 years. Due to the more and more ageing society the importance of dementia is increasing.

One important key player in the generation of AD is the type I transmembrane Amyloid Precursor Protein (APP). The neurotoxic Ab peptides that lead to AD typical plaques in the brain of affected patients are derived from APP by sequential cleavage of different proteases [1]. Beside its role in Alzheimer's pathology many physiological functions are discussed for APP [2]. But to understand the various functions it is important to know the molecular structure of APP.

Recently we could solve the structure of the APP-E1 domain and found that the two subdomains of E1, the growth factor like domain (GFLD) and the copper binding domain (CuBD) form one close entity. Additionally, we showed a dimeric arrangement of two E1-molecules [3]. Here we describe a new APP-E1 crystal form. Crystals diffracted up to 1.4 Å resolution at the synchrotron. During data analysis it turned out that the new crystal form is almost perfectly twinned. Using molecular replacement with the earlier E1 structure (pdb: 3ktm) we solved the new E1 structure and performed twin based refinement. Interestingly, this structure does not show the dimeric arrangement of two E1-molecules.

References
1. Selkoe, D.J. (2001). Alzheimer's Disease: Genes, Proteins, and Therapy. Physiological Reviews *81*, 741-766.
2. Thinakaran, G., and Koo, E.H. (2008). Amyloid precursor protein trafficking, processing, and function. J Biol Chem *283*, 29615-29619.
3. Dahms, S.O., Hoefgen, S., Roeser, D., Schlott, B., Gührs, K.-H., and Than, M.E. (2010). Structure and biochemical analysis of the heparin-induced E1 dimer of the amyloid precursor protein. Proceedings of the National Academy of Sciences *107*, 5281-5287.

MS10-P07

Structural Basis of Exosome-independent RNA 3’-5’ Degradation

Q. Ming[1], U. Heinemann[1]
[1] *MDC, Berlin, Germany*

Structural Basis of Exosome-independent RNA 3’-5’ Degradation
Qianqian Ming and Udo Heinemann
Max-Delbrück Center for Molecular Medicine Berlin-Buch, Germany

Regulated degradation plays a major role in determining the levels of both non-coding (miRNA) and coding (mRNA) transcripts. In humans, and possibly in most other eukaryotes, Dis3l2 together with Dis3 and Dis3l1 are the three homologs of Rrp44/Dis3 protein, which is the most prominent protein in RNA 3’-5’degradation. Function studies suggest that Dis3l2 plays a role in the genesis and development of Perlman syndrome and Wilms’ tumors[1] [2]. It has been only recently that pre-*let-7* was identified as the first physiological RNA substrate of this new exonuclease[3]. However, the precise mechanism of Dis3l2 is far from being elucidated. Bioactivity research defines Dis3l2 as a distinctively novel exoribonuclease, as it is exosomeindependent, shows affinity for oligo(U)-like sequences and is able to degrade structured substrates[4][5][6]. Therefore, it is also very interesting and meaningful to investigate the origin of the new features. Our project on Dis3l2 is carried out in two ways. One way is to take on a structural study of Dis3l2 and its complexes with oligo-nucleotides. The other line is to develop functional research on Dis3l2 and pre-*let-7* degradation. Up to now we have primarily tested expression and purification of different Dis3l2 constructs. The further purification and crystallization is undergoing. Bioactivity test will also be developed in the near future.

[1]Astuti, D. et al. (2012). Germline mutations in DIS3L2 cause the Perlman syndrome of overgrowth and Wilms tumor susceptibility. Nature Genet. 44, 277-284.
[2]Morris, M. R., et al. (2013). Perlman Syndrome: Overgrowth, Wilms Tumor Predisposition and DIS3L2. American Journal of Medical Genetics Part C: Seminars in Medical Genetics, Wiley Online Library.
[3]Chang, H. M., et al. (2013). A role for the Perlman syndrome exonuclease Dis3l2 in the Lin28-let-7 pathway. Nature 497(7448): 244-248.
[4]Lubas, M., et al. (2013). Exonuclease hDIS3L2 specifies an exosome-independent 3’-5’degradation pathway of human cytoplasmic mRNA. EMBO J 32(13): 1855-1868.
[5]Malecki, M., et al. (2013). The exoribonuclease Dis3l2 defines a novel eukaryotic RNA degradation pathway. EMBO Journal 32(13): 1842-1854.
[6]Ustianenko, D., et al. (2013). Mammalian DIS3L2 exoribonuclease targets the uridylated precursors of let-7 miRNAs. RNA. 497(7448):244-248.

MS10-P08

Structural studies of Terminal Uridylyl Transferases

A. Garg[1], U. Heinemann[1]
[1] *Max-Delbrück-Centrum für Molekulare Medizin (MDC), Crystallography, Berlin, Germany*

miRNAs are small, 22-nucleotide long non-coding RNAs that regulate the homeostasis of many target messenger RNAs (mRNA) through complementary base pairing and translational silencing, often coupled to target RNA degradation. The canonical process of miRNA biogenesis is well understood and is characterized by successive cleavage events catalyzed by RNase III enzymes. *Let-7* miRNAs are highly conserved regulators of developmental timing and stem cell differentiation. By down-regulating the expression of several oncogenes (including *RAS, HMGA2, cMYC, CDC25A* and *CDK6*) let-7 miRNA acts as a tumor suppressor.

The pluripotency factor Lin28 recruits terminal uridylyl transferase to the 3’-end of the pre-*let-7* molecule followed by the polyuridylation and destabilization of the miRNA. This addition of non-templated uridines to the 3’-ends of RNAs is an emerging form of RNA control that influences RNA stability and processing.

Terminal uridylyl transferases (TUTs; also known as poly(U) polymerases) are non-canonical ribo-nucleotidyl transferases (rNTases) of the DNA polymerase-β superfamily, which comprises enzymes that add nucleotides to a variety of substrates including miRNAs and histone mRNAs. Among the various TUTases only TUT4 and TUT7 are capable of polyuridylating pre-*let-7*, as these share several unique features essential for uridylation. Apart from the catalytic motif, which is common for all TUTases, TUT4 and TUT7 have three CCHC Zn-knuckles, a second, functionally inactive nucleotidyl transferase (NTP*) domain linked to a PAP-associated domain (PAP-asso), a putative C_2H_2 Zn-finger at the N terminus. It has been demonstrated that the NTP*/PAP-associated domain and N-terminal Zn-finger are essential for the Lin28-mediated pre-*let-7* polyuridylation, explaining why only TUT4 and TUT7 can polyuridylate pre-*let-7*.

We are particularly interested to understand how the small protein Lin28 accommodates a comparatively very large TUTase molecule in order to polyuridylate the substrate RNAs and by which molecular interactions between TUTase, Lin28 and pre-*let-7* the miRNA biogenesis is regulated.

References:

1) Thornton, J.E., Chang, H.M., Piskounova, E., Gregory, R.I. Lin28 mediated control of let-7 microRNA expression by alternative TUTase Zcchc11(TUT4) and Zcchc6(TUT7). RNA, 18, 1875-1885 (2012).

2) Schmidt, M.J., West, S., Norbury, C.J. The human cytoplasmic RNA terminal U-transferase Zcchc11 targets histone mRNAs for degradation. RNA, 17, 39-44 (2011).
3) Mayr, F., Schuetz, A., Doege, N., Heinemann, U. Lin28 cold shock domain remodels pre-let7 miRNA . Nucleic Acids Res, 40, 7492-7506 (2012).

MS10-P09

Structural basis of endoplasmic reticulum-associated degradation of misfolded proteins (ERAD)

S. Banchenko[1], U. Heinemann[1]
[1]*MDC, Berlin, Germany*

The ERAD process in eukaryotic cells serves to sequester and remove misfolded proteins from the endoplasmic reticulum (ER). We use structural characterization of luminal components of the HRD-E3 ligase, Yos9 and Hrd3 from *Saccharomyces cerevisiae, Chaetomium thermophilum* and *Lachancea thermotolerans*, to address the question, how the initial step in the ERAD pathway works.

The HRD (HMG-CoA reductase degradation) complex contains three membrane proteins: The E3 ubiquitin ligase Hrd1, Usa1, Der1 and two luminal proteins, Yos9 (yeast OS-9 homolog) and Hrd3. Degradation of misfolded proteins in the ER involves several steps. First, the ubiquitin ligase Hrd1 cooperates with recognition factors Yos9 and Hrd3 in substrate recognition (Hirsch et al., 2009). It is believed that Yos9 primarily recognizes specific sugar moieties of misfolded proteins and directly interacts with Hrd3's luminal domain. Hrd3 then recognizes and binds misfolded substrate proteins. Proteins are then exported into the cytosol via an as of yet unidentified channel. At the cytosolic face of the ER, the substrate is ubiquitinated by the E3 ligase Hrd1. Finally, the substrate is removed from the membrane and escorted to the 26S proteasome for degradation.

Yos9 from *Saccharomyces cerevisiae* contains two domains: a dimerization domain (DD) and an MRH (mannose receptor homology) domain. Since the Yos9 DD structure from *Saccharomyces cerevisiae* has been determined (Hanna et al. 2012), we initially aim to analyze the Yos9-MRH domain structure or the structure of variants containing both DD and the MRH domains together. This will allow us to understand better the initial steps of substrate protein recognition by Yos9 and Hrd3 proteins. For the interaction studies between Yos9 and Hrd3 we will to co-express and co-crystallize these proteins together. Functional activity tests with crystallized constructs and further experiments will be developed with our collaboration partners from the laboratory of Prof. Dr. Thomas Sommer (MDC).

Hanna, J., Schütz A., Zimmermann, F., Behlke, J., Sommer T., Heinemann, U. (2012). Structural and biochemical basis of Yos9 protein dimerization and possible contribution to self-association of the 3-hydroxy-3-methylglutaryl-coenzyme A reductase degradation ubiquitin-ligase complex. J. Biol. Chem. *287*, 8633-8640.

Hirsch, C., Gauss, R., Horn, S., Neuber, O., Sommer, T., (2009). The ubiquitylation machinery of the endoplasmic reticulum. Nature *458*, 453-460.

MS10-P10

Crystallographic insights into a cobalt (III) sepulchrate based alternative cofactor system of P450 BM3 monooxygenase

S. Panneerslevam[1], A. Shehzad[2], J. Mueller-Dieckmann[3], M. Wilmanns[1], M. Bocola[2], U. Schwaneberg[2]
[1]*DESY, HASYLAB, Hamburg, Germany*
[2]*RWTH, Lehrstuhl fur Biotechnologie, Aachen, Germany*
[3]*University Of Hamburg, Biocenter Klein Flottbek, Hamburg, Germany*

P450 BM3 is a 119-kDa water-soluble heme monooxygenase originating from *Bacillus megaterium*.[1] P450 BM3 and variants are known to oxidize structurally diverse substrates. However, the requirement for the natural cofactor, NADPH, limits cell-free applications of P450 BM3 in drug detection and synthesis, fuelling efforts to establish alternative cofactor systems.[2] Hence, P450 BM3 variants have been generated which circumvent the requirement for NADPH, and enabled P450 BM3 to be driven with cost-effective electron sources.[3]

Crystal structures of individual domains of P450 BM3 are available. However, the spatial organization of the full-length protein is unknown. In this study, crystal structures of the P450 BM3 M7 heme domain variant (substitutions: F87A, V281G, M354S)[4] with and without cobalt (III) sepulchrate are reported. Cobalt (III) sepulchrate acts as an electron shuttle in an alternative cofactor system employing zinc dust as the electron source. The crystal structure shows a binding site for the mediator cobalt (III) sepulchrate at the entrance of the substrate access channel. The mediator occupies a position which is far from the active site and distinct from the binding of the natural redox partner (FAD/NADPH binding domain). The unusual binding position suggests that the mediator shuttles electrons to the heme-centre through new routes. Electron transfer could occur by a 'through-protein' or a 'substrate-relayed' pathway. The latter seems more plausible since it would ensure efficient use of electrons only in the presence of a substrate in the active site. The structural evidence also indicates that the use of a positively charged mediator is important to effectively reduce the catalytic heme domain.

Understanding the mediator-monooxygenase interface opens new avenues for tailoring P450 BM3 to match application demands. Structural and molecular understanding of mediated electron transfer enables a paradigm shift from a mediator acceptance screening to a rational mediator design which considers only stability and electron transfer performance parameters.

1 L. O. Narhi and A. J. Fulco, *J Biol Chem*, 1986, 261, 7160-7169; L. O. Narhi and A. J. Fulco, *J Biol Chem*, 1987, 262, 6683-6690.
2E. O'Reilly, V. Kohler, S. L. Flitsch and N. J. Turner, *Chem Commun*, 2011, 47, 2490-2501.
3A. K. Udit, F. H. Arnold and H. B. Gray, *J Inorg Biochem*, 2004, 98, 1547-1550; J. Nazor and U. Schwaneberg, *ChemBioChem*, 2006, 7, 638-644; S. C. Maurer, K. Kuhnel, L. A. Kaysser, S. Eiben, R. D. Schmid and V. B. Urlacher, *Adv Synth Catal*, 2005, 347, 1090-1098; J. Nazor, S. Dannenmann, R. O. Adjei, Y. B. Fordjour, I. T. Ghampson, M. Blanusa, D. Roccatano and U. Schwaneberg, *Protein Eng Des Sel*, 2008, 21, 29-35; U. Schwaneberg, D. Appel, J. Schmitt and R. D. Schmid, *J Biotechnol*, 2000, 84, 249-257.
4 L. Q. Zhao, G. Guven, Y. Li and U. Schwaneberg, *Appl Microbiol Biotechnol*, 2011, 91, 989-999.

MS10-P11

Differential expression of activated protein kinase C receptor (LACK), alpha tubulin and protein disulfide isomerase in sensitive and resistant field isolates of *Leishmania tropica* by 2-Dimentional electrophoresis and Mass-spectrometry

H. Hajjaran[1], B. Vaziri[2], M. Mohebali[1], E. Kazemi-Rad[1], R. Hadighi[3]
[1]*School of Public Health, Tehran ,University of Medical Sciences, Medical Parasitology and Mycology, Tehran, Iran, Islamic Republic of*
[2]*Biotechnology Research Centre, Pasteur Institute of Iran, Protein Chemistry Unit, Tehran, Iran, Islamic Republic of*
[3]*Iran University of Medical Sciences, 3Department of Medical Parasitology and Mycology, School of Medicine, Tehran, Iran, Islamic Republic of*

Pantavalent antimonial remain the primary anti leishmanial drugs in most developing countries including Iran. In recent years, the rate of antimony resistance is increasing in endemic regions of Iran. In the present study, in order to define the protein expressional changes related to the process of meglumine antimoniate resistance in anthroponotic cutaneous leishmaniasis (ACL), we performed a comparative proteomics analysis on sensitive and resistant strains of *Leishmania tropica* isolated from Iranian CL patients.

Methods: Cell proteins were analyzed with 2-dimensional electrophoresis and differentially expressed proteins were identified by matrix-assisted laser desorption/ionization time-of-flight mass spectrometry (MALDI-Tof).

Results**:** Image analysis of the matched maps identified proteins that were either over- or down-expressed: activated protein kinase c receptor (LACK), alpha tubulin, protein disulfide isomerase. For more confirmation we used Real-time PCR for analysis the rate of expression of these proteins.

Conclusion**:** The study shows the usefulness of proteomics in identifying proteins that may express differences between sensitive and resistant *L. tropica* isolates. Our results suggest that differentially expressed above proteins, are important features of antimony resistance in *L. tropica*

MS10-P12

Structural Investigation of a Macromolecular Complex Formed by the AAA+ ATPase *At*CDC48, the UBX Adaptor Protein PUX1 and the SNARE SYP31 ***(Achtung, Text bitte bei Export mit Original Word tauschen!! SR)***

S. Petrović[1], U. Heinemann[1]
[1]*Max Delbrück Center for Molecular Medicine, AG Heinemann, Berlin, Germany*

The ATPase *At*CDC48, a p97/VCP homolog found in *Arabidopsis thaliana*, belongs to the family of AAA+ proteins (ATPases associated with diverse cellular activities). This essential and conserved protein family is involved in a broad range of cellular processes, such as cell cycle progression, ubiquitin-related protein degradation and homotypic membrane fusion (1-3). What enables AAA+ ATPases to act in various processes are adaptor proteins that recruit them to their sub-cellular sites of action, change their ATPase activity or remodel the quaternary structure from a commonly abundant hexameric structure to smaller oligomeric units (Arumughan et al., unpublished).

It has been found that *At*CDC48 interacts with the t-SNARE SYP31 in an ATP-dependent manner, as well as with the adaptor protein PUX1 (plant UBX domain containing protein 1) (4). SYP31, the plant homolog of human syntaxin 5, can be found in punctate membrane structures during interphase, and at the division plane during cytokinesis, which, supported by immuno-co-localization experiments, implies a putative role of *At*CDC48 as part of an alternative membrane fusion mechanism which may exist in parallel to that involving the NSF/α-SNAP pair (4). PUX1 binds to *At*CDC48 via the UBX domain, and the hexameric structure of *At*CDC48 is disassembled upon binding of the PUX1 N-terminus (5). However, the stoichiometry and conformational changes during the disassembly of *At*CDC48 by PUX1 remain unknown, and the exact nature of interaction between *At*CDC48, PUX1 and SYP31 is not clear.

As a starting point, we are currently investigating the interaction of PUX1 with different constructs of SYP31. The final aim of this work is to determine the crystal structure of *At*CDC48 in complex with its adaptor protein PUX1 and, for the first time, a substrate - the t-SNARE SYP31. This will enable us to propose a structure-based model that could be extended to other members of the well conserved AAA+ ATPase family.

- Meyer H, Bug M, Bremer S (2012) Emerging functions of the VCP/p97 AAA-ATPase in the ubiquitin system. Nat Cell Biol 14(2):117-123.
- Wang Q, Song C, and Li CC (2004) Molecular perspectives on p97-VCP: progress in understanding its structure and diverse biological functions. J Struct Biol 146: 44 -57.
- Woodman PG (2003) p97, a protein coping with multiple identities. J Cell Sci 116: 4283-4290.
- Rancour DM, Dickey CE, Park S, Bednarek SY (2002) Characterization of *At*CDC48. Evidence for multiple membrane fusion mechanisms at the plane of cell division in plants. Plant Physiol 130**:** 1241-1253
- Rancour DM, Park S, Knight SD, and Bednarek, S. Y. (2004) Plant UBX Domain-containing Protein 1, PUX1, regulates the oligomeric structure and activity of arabidopsis CDC48 J Biol Chem 279: 54264-54274

MS10-P13

Structural basis for methyl group transfer and acetyl-CoA synthesis in *Carboxydothermus hydrogenoformans*

S. Götzl[1], S. Hennig[1], J.- H. Jeoung[1], C. Teutloff[2], R. Bittl[2], H. Dobbek[1]

[1]*Humboldt Universität zu Berlin, Berlin, Germany*

[2]*Freie Universität Berlin, Berlin, Germany*

The anaerobic hydrogenogenic bacterium *Carboxydothermus hydrogenoformans* can convert CO_2 into cellular carbon compounds via the reductive acetyl-CoA pathway. Currently we are investigating the central proteins involved in the late steps of acetyl-CoA formation, namely corrinoid/iron-sulfur protein (CoFeSP), methyl-tetrahydrofolate:CoFeSP methyltransferase (MeTr) and acetyl-CoA synthase (ACS). The crystal structures of the individual proteins have been solved, giving insights into the structure-function relationship and substrate binding [1-3]. Recently, the complex structure of CoFeSP and its reductive activator (RACo) showed an extensive structural reorientation of the B12-capping domain of CoFeSP [4], which also seems to be mandatory for the methyl group transfer reaction involving MeTr and ACS. We performed FRET and PELDOR studies on bi-labeled CoFeSP and confirmed these structural changes in solution. To study the structural basis of acetyl-CoA formation, the active site containing C-terminal domain of ACS was purified and crystallized. Different high resolution structures illustrate the metal heterogeneity known to be problematic for ACS and give insights how the binding of CO and the methyl group could be facilitated at the proximal metal site.

[1] T. Svetlitchnaia, V. Svetlitchnyi, O. Meyer, H. Dobbek *Proc. Natl. Acad. Sci. USA* 2006; *103*,14331-14336.

[2] S. Goetzl, J.-H. Jeoung, S.E. Hennig, H. Dobbek *J. Mol. Biol.* 2011; *411*, 96-109.

[3] V. Svetlitchnyi, H. Dobbek, W. Meyer-Klaucke, T. Meins, B. Thiele, P. Römer, R. Huber, O. Meyer *Proc. Natl. Acad. Sci. USA* 2004; *101*,446-51.

[4] S.E. Hennig, S. Goetzl, J.-H. Jeoung, M. Bommer, F. Lendzian, P. Hildebrandt, H. Dobbek - to be *submitted*.

MS10-P14

Structure of the ubiquitin activating enzyme loaded with two ubiquitin molecules

A. Schaefer[1], H. Schindelin[1]

[1]*Rudolf Virchow Center for Experimental Biomedicine,University of Wuerzburg, Structural Biology, Wuerzburg, Germany*

The modification of proteins with ubiquitin is found in a broad variety of cellular processes like DNA repair and replication, cell signaling and trafficking and in the degradation of the target protein by the proteasome (1). Malfunctions in the ubiquitylation machinery are linked to a variety of human diseases including cancer as well as neurodegenerative and metabolic disorders (2,3). The activation of ubiquitin by the ubiquitin-activating enzyme Uba1 (E1) constitutes the first step in the covalent modification of target proteins with ubiquitin. This activation is a three-step process in which ubiquitin is adenylated at its C-terminal glycine, followed by the covalent attachment of ubiquitin to a catalytic cysteine residue of Uba1 and a subsequent adenylation of a second ubiquitin (4,5). With respect to the ubiquitin activating enzyme Uba1, structures of binary E1-ubiquitin complexes from Saccharomyces cerevisiae and Schizosaccharomyces pombe have been reported (6,7).

Here we present for the first time a ubiquitin E1 structure loaded with two ubiquitin molecules. While one ubiquitin is bound in its adenylated form to the active adenylation domain of E1, the second ubiquitin represents the status after transfer and is covalently linked to the active site cysteine. This doubly loaded E1 structure constitutes a missing link in the structural analyses of the ubiquitin transfer cascade.

(1) van der Veen, A. G. & Ploegh, H. L. (2012). *Annual review of biochemistry* 81, 323-357.

(2) Reinstein, E. & Ciechanover, A. (2006). *Annals of internal medicine* 145, 676-684.

(3) Petroski, M. D. (2008). *BMC biochemistry* 9 Suppl 1, S7.

(4) Haas, A. L. & Rose, I. A. (1982). *The Journal of biological chemistry* 257, 10329-10337.

(5) Haas, A. L., Warms, J. V., Hershko, A. & Rose, I. A. (1982). *The Journal of biological chemistry* 257, 2543-2548.

(6) Lee, I. & Schindelin, H. (2008). *Cell* 134, 268-278.

(7) Olsen, S. K. & Lima, C. D. (2013). *Molecular cell* 49, 884-896.

MS10-P15

Exploring Substrate and Product Channels in CO Dehydrogenase II of *Carboxydothermus hydrogenoformans*

L. Domnik[1], J.- H. Jeoung[1], J. Fesseler[1], H. Dobbek[1]
[1]*HU Berlin, AG Strukturbiologie/Biochemie, Berlin, Germany*

Rising of CO_2 levels in the earth's atmosphere demands the development of energy sources that are CO_2 neutral. Therefore understanding how microorganisms utilize C1-compounds will be of crucial importance in the future. The carbon monoxide dehydrogenase II (CODHII) of the thermophilic bacterium *Carboxydothermus hydrogenoformans* catalyses the reduction of CO_2 to CO using two protons and two electrons with a turnover of 15 s^{-1}. In order to guarantee an efficient supply of substrates (CO_2, protons and electrons) and final release of products (CO and water) controlled routes are needed to allow efficient transport of substrates and products within the enzyme [1, 2, 3]. Mutational studies have been applied to illuminate the putative proton and water transfer pathways together with crystallographic analysis. Exploiting the ability of xenon to bind hydrophobic protein cavities allowed determination of gas channels in CODHII.

References:
[1] Jeoung JH and Dobbek H (2007) Science 318(5855):1461-4
[2] Kim EJ, Feng J, Bramlett MR, Lindahl PA (2004) Biochemistry 43(19):5728-34
[3] Doukov TI, Blasiak LC, Seravalli J, Ragsdale SW, Drennan CL (2008) Biochemistry 47(11): 3474-3483.

MS10-P16

Tales from the Cloud Atlas: Structural insights into enzymatic CO_x-transformation

J. Fesseler[1], J.- H. Jeoung[1], H. Dobbek[1]
[1]*HU Berlin, Strukturbiologie/Biochemie, Berlin, Germany*

Carbon dioxide (CO_2) is considered as major cause of global warming and directly reflecting anthropogenic usage of carbon-based fuels since the beginning of the industrial era. Despite its high abundance in atmosphere, chemical usage of carbon dioxide is restricted due to its low reactivity. [1]

Nature's prime catalyst for CO_2 activation and reduction is cluster C of Ni,Fe-CO dehydrogenase, a complex metal cluster composed of a Ni-substituted cubane Fe_3S_4-cluster with an Fe-exo ligand. CODHs facilitate both, reduction of CO_2 as well as two electron oxidation of CO:

$CO_2 + 2\ e^- + 2\ H^+ <=> CO + H_2O$ (equation 1)

The structure of CODH from *Carboxydothermus hydrogenoformans* was solved at different redox potentials (-320 mV, -600 mV) and in presence of CO_2 revealed insights into CO_2-activation for the first time. [2]

Additional information on how cluster C interacts with its substrate or product CO, was deduced by comparison with the structure of its isoelectronic inhibitor CN^-. [3]

Optimization of crystallization conditions and employment of high brilliance synchrotron radiation allowed further clarification of geometries of cluster C complexed with its ligands and inhibitors (CO_2, NCO^- and CN^-) by extending diffraction data up to true-atomic resolution (d_{min} < 1.2 Å). The detailed description of coordination geometry of cluster C expands our understanding of the CO_2-activation of CODH.

Here we report insights into reactivity and composition of an enzymatic CO_x-transformer and reveal a blueprint for inorganic model compounds and industrial catalysts, operating with cost-effective and readily accessible metals nickel and iron.

References
1) Appel, A.M.; et al. *Chem. Rev*. 2013, *113* (8): 6621-6658.
2) Jeoung, J.-H.; Dobbek, H. *Science* 2007, *318* (5855):1461-4.
3) Jeoung, J.-H.; Dobbek, H. *J. Am. Chem. Soc.* 2009, 131(29):9922-3.

MS10-P17

Enzymology with multiple copies in the asymmetric unit: trapping reaction intermediates from a single crystal of homogentisate 1,2-dioxygenase

J.- H. Jeoung[1], M. Bommer[1], H. Dobbek[1]
[1]*Humboldt-Universität zu Berlin, Berlin, Germany*

The oxidative ring cleavage, the first catabolic reaction of homogentisate (2,5-hydroxy-phenylacetate, HG) in the degradation of Tyr and Phe is catalyzed by the enzyme homogentisate 1,2-dioxygenase (HGDO) that uses a mononuclear nonheme Fe^{2+} in 2-His-1-carboxylate facial triad motif to produce maleylacetoacetate. A deficiency of HGDO in human has been known to cause an autosomal recessive disorder, alkaptonuria (1).

Three crystal structures of HGDO from *Pseudomonas putida* at 1.7 - 1.98 Å resolution revealed five different reaction intermediates in the oxidative ring cleaveage cycle of HGDO, of which are an octahedral coordination for Fe^{2+} in resting state, monodentate binding of HG to Fe^{2+} (ES-complex), and three different reaction cycle intermediates trapped in different copies of a single crystal (superoxo:semiquinone-, alkylperoxo-, and product-bound states) (2). The observed structures demonstrate that extradiol-type dioxygenases using 2-His-1-carboxylate facial triad motif employ a common principal of reaction mechanisim to catalyze the oxdative cleavage of aromatic rings despite different structural folds and active site architectures.

(1) G. P. Titus et. Al *Nat Struct Biol* 7 (2000)
(2) J.-H. Jeoung, T.-Y. Lin, M. Bommer, and H. Dobbek, PNAS (2013)

MS10-P18
The world of CO dehydrogenases

Y. Dendra[1], J. Fesseler[1], J.- H. Jeoung[1]
[1]*HU Berlin, Institut für Biologie, Berlin, Germany*

There is no doubt that common air pollutants resulted from fossil fuel combustion have the undisputed negative impact on health and environment. Unfortunately, immense economical profit strongly inhibits the development of the alternative climate-neutral energy source, so the atmospheric level of exhausted gases linked to oil production (CO_2, CO, N_2, SO_2 etc.) will stay high for the nearest decades (1). In contrast diverse microorganisms developed highly efficient mechanisms for utilization of energetically useless and harmful carbon-containing compounds such as CO_2 and CO, using it as feedstock for synthesis of organic carbon (e.g acetic acid (2), acetyl-CoA (3).

In our group we focus on the key enzymes of Wood-Ljundahl pathways: CO dehydrogenase (CODH), reversibly oxidizing CO to CO_2, and acetyl-CoA synthase (ACS), catalysing the acetyl-CoA formation from CO, methylated corrinoid iron-sulfur protein and coenzyme A (4). Genome analysis of the phylogenetically distant microorganisms revealed the presence of more than one copy of Ni-CODH coding sequences, which points that this enzyme could be involved in multiple cellular processes (5). The sequence analysis of *Thermosinus carboxydivorans (6)* and *Acetonema longum (7)*, the anaerobic thermophilic bacteria, revealed a unique short-length Ni-CODH homologue (miniCODH) distinct from all known CODHs. The short length of miniCODH gene results from multiple deletions of various size, which however do not affect any structurally important domains of typical CODHs, suggesting it's fully functionality (6). It has been suggested that CODH-homologues functions with different enzymes, such as hydrogenase for energy generation, providing electrons for reduction of protons to H_2 (8), and ACS for carbon fixation by supplying CO for acetyl-CoA synthesis. The crystal structure of the CODH/ACS complex from *Moorella thermoacetica* has been solved at 2.2 angstrom (9). Here we give a small insight into the diverse world of CODHs, clarifying its important role in the global carbon cycle.

(1) S. Shafiee, E. Topal, 2009, Energy Policy, 37: 181-189
(2) Huber C., Wächterhäser G. 1997, Science, 276: 245 - 247
(3) Evans D. J. 2004, *Coord. Chem. Rev.*, 15-16: 1582-1595
(4) Ragsdale W.S., 2007, J. Inorg. Biochem., 101: 1657-1666
(5) Wu M. *et al.,* 2005, PloS Genet., 1: 563 -574
(6) Techtmann M.T. *et al.*, 2012, Front. Microbiol., 3: 132
(7) Altschul S.F. *et al*., 1997, Oxford Journals, 25: 3389 - 3402
(8) Singer S.W, Ludden P.W., 2006, Biochim. Biophys. Acta., 1757 :1582-1591
(9) Doukov T. I. *et al*., 2002, Science, 298: 567 - 572

MS10-P19
Transportmechanism of the Bacterial ABC-Transporter MsbA

A. Müller[1]
[1]*Ruhr-Universität Bochum, LS Biophysik AG Röntgenstrukturanalyse, Bochum, Germany*

ABC transporters form a ubiquitous family of integral transmembrane proteins responsible for the active transport of a wide variety of compounds across biological membranes (1). They share a common overall architecture consisting of two transmembrane domains (TMD), found to be responsible for substrate (allocrite) specificity, and two nucleotide binding domains (NBD), which power transport by ATP hydrolysis. We are working on the homodimeric E. coli ABC-Transporter MsbA located in the cytoplasmatic membrane of Gram-negative bacteria. It is essential for translocation of Lipid A from the inner to the outer membrane leaflet (2). MsbA exports similar xenobiotics as human P-Glycoprotein or other bacterial multidrug transporter like LmrA from Lactococcus lactis (3) and therefore can be used as a prokaryotic model for eukaryotic ABC-multidrug exporters. Despite the fact, that the X-ray structure of MsbA and other ABC-transporters were published over the last years, the molecular details of the mechanism are poorly understood. In a first step we applied time-resolved Fourier Transform Infrared Spectroscopy (trFTIR)to investigate isolated NBDs. We employed a cysteine-free MsbA-NBD mutant to obtainthe first time-resolved FTIR-spectra of the ATP hydrolysis reaction of an ABC transporter.This allowed us to kinetically follow the catalytic cycle of the NBD and determine two rateswhich characterize ATP binding and hydrolysis. We could identify a substrate-enzymecomplex intermediate. We also show that hydrolysis is the rate limiting step in this cycle.By comparing trFTIR and Xray structures in different states of the transport cycle, usingdifferent mutants, we want to elucidate the involved amino acids.Benefiting from the experience with the NBD, we want to apply the same methods on thefull length MsbA protein, obtaining detailed information of the mechanisms of coupling theATP-hydrolysis to movement of the TMD of ABC transporters. ATR-FTIR spectroscopyallows the investigation of hardly soluble transmembrane proteins. First results show thesuccessful immobilization of the full length transporter onto a germanium ATR-FTIRcrystal. This approach is expected to be applicable to other ABC-transporters. In order togain high resolution structures for deeper insight into the whole mechanism, we also workon the crystallization of full length MsbA.

1. Davidson, A. L., Dassa, E., Orelle, C., and Chen, J. (2008) Microbiol. MolBiol. Rev. 72, 317-364
2. Doerrler, W. T., Reedy, M. C., and Raetz, C. R. (2001) J. Biol. Chem. 276, 11461-11464
3. Reuter, G. (2003) J. Biol. Chem. 278, 35193-35198

MS10-P20

Design, structure and function of a novel ligand-binding globulin

K. Schmidt[1]
[1]*FAU Erlangen, Biology, Erlangen, Germany*

The computational design of novel functions onto existing scaffolds is still a field with a moderate number of success stories. In the current project an artificial steroid-binding pocket is introduced into the scaffold of alpha-1-antichymotrypsin (ACT) by computational design using MUMBO. Starting from the serpin corticosteroid-binding globulin (CBG) we transferred the ligand-binding site onto related ACT, thereby creating a novel ligand-binding globulin (*novel*LBG). Both CBG and ACT are members of the serine protease inhibitor (serpin) family and undergo a serpin-typical S-to-R transition upon cleavage of the reactive-center-loop (RCL) by proteases. For CBG it has been proposed that the S-to-R transition provides for an active steroid release mechanism at sites of inflammation.

*Novel*LBG variants can be produced in *E. coli* in high yields and bind steroids with micromolar affinity. Crystals obtained after 4 days in known conditions usually diffract to better than 2.0 Å. This allows us to continuously monitor and validate any progress of our computational design by solving crystal structures of designed variants.

While *novo*LBG variants still undergo the S-to-R transition, to our surprise, one variant completely loses its ligand-binding affinity after cleavage of the RCL. This opens the possibility that *novo*LBGs can be developed into a drug delivery shuttle that upon cleavage with tissue-specific proteases will locally release its cargo ligands. In current studies we focus on designing novel ligand-binding specificities into *novo*LBGs as well as redesigning the RCL loop that is targeted by cell specific proteases. Further variants aim at improving our understanding of the coupling between ligand release and the serpin-typical S-to-R conformational switch.

Klieber, M. A., Underhill, C., Hammond, G. L. & Muller, Y. A. (2007). Corticosteroid-binding globulin: Structural basis for steroid transport and proteinase-triggered release. J Biol Chem. 282, 29594-29603.

Lin, H.Y., Underhill, C., Gardill, B.R., Muller, Y.A., Hammond, G.L. (2009). Residues in the human corticosteroid-binding globulin reactive center loop that influence steroid binding before and after elastase cleavage. J Biol Chem. 284, 884-896.

Stiebritz, M. T., Muller, Y. A (2006). MUMBO: a protein-design approach to crystallographic model building and refinement. Acta Cryst. D62, 648-658.

Zhou, A., Wei, Z., Stanley, P.L., Read, R.J., Stein, P.E. & Carrell, R.W. (2008). The S-to-R transition of corticosteroid-binding globulin and the mechanism of hormone release. J Mol Biol. 380, 244-251.

Gardill, B. R, Vogl, M. R., Lin, H.-Y., Hammond, G. L. & Muller, Y. A. (2012). Corticosteroid-binding globulin: Structure-function implications from species differences. PLoS One 7, e52759 (PMID: 23300763).

MS10-P21

O_2-tolerant [NiFe] hydrogenase of *Ralstonia eutropha*: important amino acids in enzyme reactivation

J. Kalms[1], A. Schmidt[1], P. Scheerer[1]
[1]*Charite-Universitätsmedizin Berlin, Institut für medizinische Physik und Biophysik, Berlin, Germany*

Pollution, limited resources and steadily growing costs of fossil fuels raise the interest in renewable energy technologies e.g. enzymatic fuel cells. Enzymes such as hydrogenases produce hydrogen by catalysing the interconversion of H_2 into $2H^+ + 2e^-$. For an industrial application O_2-tolerance of the hydrogen producing enzyme is recommended. Only a small subgroup of hydrogenases evolved this feature [1]. One model organism for aerobic H_2-oxidation is *Ralstonia eutropha* H16. The gram-negative soil bacterium contains a membrane-bound [NiFe] hydrogenase (MBH). The MBH consists of a large subunit bearing the [NiFe] active site and a small subunit containing three different [FeS] clusters that direct electron flow to the respiratory chain [2]. In case of the MBH, oxygen-tolerance relies on the exceptional redox-properties of a unique six cysteine coordinated [4Fe3S]-cluster located proximal to the active site. Depending on the nature of the gas molecule attacking the active site, the proximal cluster operates as a bidirectional electron switch [3]. In case of H_2 approaching the active site through the gas channel (*Fig.1, blue dashes*), electrons and protons flow from the [NiFe] active site via the [FeS] clusters to the cytochrome b_{562}. Is oxygen attacking the active site, electrons as well as protons are needed for reducing oxygen to water. For a rapid reactivation of the enzyme water is released through the nearby water channels (*Fig.1, red dashes*). A feasible pathway via conserved histidines for the proton flow from the proximal cluster to the [NiFe] active site has been proposed (*Fig.2*) [4]. To understand the importance of the histidines in terms of activity, O_2-tolerance and structural changes, we studied several mutations in the proton pathway of the MBH with H_2-dependent methylene blue reduction activity assays, Protein film electrochemistry and protein X-ray crystallography.

References
[1] Fritsch, J., Lenz, O., Friedrich, B. (2013). Structure, function and biosynthesis of O_2-tolerant hydrogenases. *NatRevMicrobiol.* 2, 106-114.
[2] Bernhard, M., Benelli, B., Hochkoeppler, A., Zannoni, D., Friedrich, B. (1997). Functional and structural role of the cytochrome b subunit of the membrane bound hydrogenase complex of Alcligenes eutrophus H16*.* *EurJBiochem* 1, 179-86.
[3] Fritsch, J., Scheerer, P., Frielingsdorf, S., Kroschinsky, S., Friedrich, B., Lenz, O., Spahn, CM. (2011). The crystal structure of an oxygen-tolerant hydrogenase uncovers a novel iron-sulpher centre. *Nature* 479 (7372), 249-52.
[4] Frielingsdorf S, Fritsch J, Schmidt A, Hammer M, Löwenstein J, Siebert E, Pelmenschikov V, Jaenicke T, Kalms J, Rippers Y, Lendzian F, Zebger I, Teutloff C, Kaupp M, Bittl R, Hildebrandt P, Friedrich B, Lenz O§, and Scheerer P§. (2013). Redox-dependent structural and chemical transformation of the [4Fe3S] cluster in O2-tolerant [NiFe] hydrogenase. *in revision*.

Figure 1

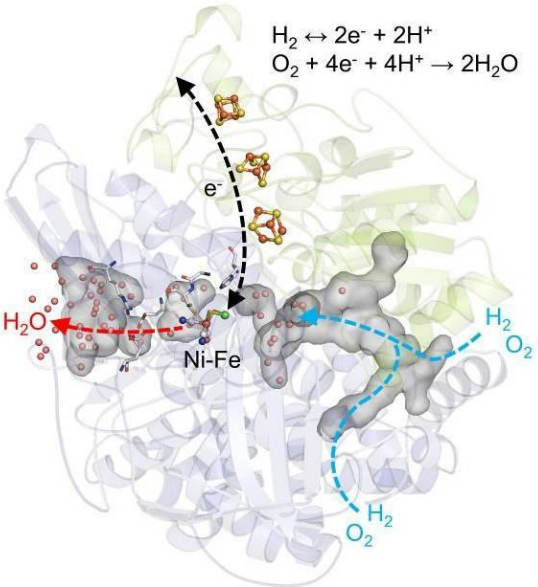

Figure 2

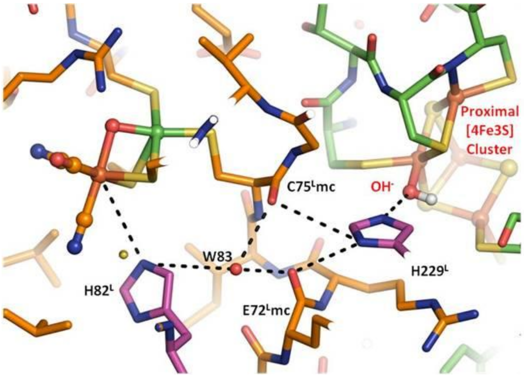

MS10-P22

Macrodomains of Middle-East Respiratory Syndrome Coronavirus

J. Lei[1], Q. Ma[1,2], J. R. Mesters[1,2], R. Hilgenfeld[1,2]
[1] *Institute of Biochemistry,Center for Structural and Cell Biology in Medicine,University of Lübeck, Ratzeburger Allee 160, 23562 Lübeck, Germany, Germany*
[2] *German Centre for Infection Research (DZIF), Lübeck, Germany*

The Middle-East Respiratory Syndrome coronavirus (MERS-CoV) was first identified in September 2012 (1,2). As of 02 December 2013, 163 cases of MERS have been recorded, with 71 deaths. We have identified two macrodomains within non-structural protein 3 of MERS-CoV. The first macrodomain is an X domain, similar to its counterparts in other coronaviruses (3,4). This macrodomain is immediately followed by a second one, which is similar to the middle subdomain of the SARS-unique domain (SUD_M). The exact functions of macrodomains in CoVs are still unclear. We found that the MERS-CoV X domain binds ADP-ribose with a K_D of about 2 μM. For the SUD_M-like macrodomain (SMLD), we detected binding to G_{10} but not A_{10}, T_{10}, or C_{10} oligonucleotides, similar to what we previously found for the SARS-unique domain (5). We determined crystal structures for the free MERS-CoV X domain and its complex with ADP-ribose. The domain consists of seven β strands and five α helices forming an α/β/α sandwich. We also constructed a homology model for the SMLD and will discuss possible functions of these macrodomains in viral replication and interaction with components of the infected host cell.

(1) Zaki, A.M., van Boheemen, S., Bestebroer, T.M., Osterhaus, A.D., Fouchier, R.A.: Isolation of a novel coronavirus from a man with pneumonia in Saudi Arabia. *N. Engl. J. Med.* 367, 1814-1820 (2012).
(2) Hilgenfeld, R., Peiris, M.: From SARS to MERS: 10 years of research on highly pathogenic human coronaviruses. *Antiviral Res.* 100, 286-295 (2013).
(3) Egloff, M.P., Malet, H., Putics, A., Heinonen, M., Dutartre, H., Frangeul, A., Gruez, A., Campanacci, V., Cambillau, C., Ziebuhr, J., Ahola, T., Canard, B.: Structural and functional basis for ADP-ribose and poly(ADP-ribose) binding by viral macrodomains. *J. Virol*. 80, 8493-8502 (2006).
(4) Piotrowski, Y., Hansen, G., Boomaars-van der Zanden, A.L., Snijder, E.J., Gorbalenya, A.E., Hilgenfeld, R.: Crystal structures of the X-domains of a Group-1 and a Group-3 coronavirus reveal that ADP-ribose-binding may not be a conserved property. *Prot. Sci.* 18, 6-16 (2009).
(5) Tan, J., Vonrhein, C., Smart, O.S., Bricogne, G., Bollati, M., Kusov, Y., Hansen, G., Mesters, J.R., Schmidt, C.L., Hilgenfeld, R.: The SARS-unique domain (SUD) of SARS coronavirus contains two macrodomains that bind G-quadruplexes. *PLoS Pathog.* 5, e1000428 (2009).

MS10-P23

Structural characterization of gephyrin by AFM and SAXS reveals a mixture of compact and extended states.

B. Sander[1], G. Tria[2], A. Shkumatov[2], E.- Y. Kim[3], J. Grossmann[4], I. Tessmer[1], D. Svergun[2], H. Schindelin[1]
[1]*Rudolf Virchow Center, Structural Biology, Würzburg, Germany*
[2]*EMBL, Hamburg, Germany*
[3]*Stony Brook University, Department of Biochemistry and Cell Biology, New York, United States*
[4]*University of Liverpool, Institute of Integrative Biology, Structural and Chemical Biology, Liverpool, United Kingdom*

Gephyrin is a trimeric protein involved in the final steps of molybdenum-cofactor (Moco) biosynthesis and in the clustering of inhibitory glycine and GABAA receptors at postsynaptic specializations. Each protomer consists of stably folded domains (referred to as the G and E domains) located at either terminus and connected by a proteolytically sensitive linker of ∼150 residues. Both terminal domains can oligomerize in their isolated forms; however, in the context of the full-length protein only the G-domain trimer is permanently present, whereas E-domain dimerization is prevented. Atomic force microscopy (AFM) and small-angle X-ray scattering (SAXS) reveal a high degree of flexibility in the structure of gephyrin. Further, the results imply an equilibrium between compact and extended conformational states in solution, with a preference for compact states, which is achieved by interactions of the linker with the G and E domains. Taken together, the data provide a rationale for the role of the linker in the overall structure and the conformational dynamics of gephyrin.

MS10-P24

Insights into the ATP-dependent Reductive Activation of the Corrinoid/Iron-Sulfur Protein of *Carboxydothermus hydrogenoformans*

S. E. Hennig[1], S. Götzl[1], J.- H. Jeoung[1], M. Bommer[1], F. Lendzian[1], P. Hildebrandt[1], H. Dobbek[1]
[1]*Humboldt Universität zu Berlin, Institut für Biologie, Strukturbiologie/Biochemie, Berlin, Germany*

The principle of coupling an exergonic to an endergonic reaction to enable the latter is a widespread strategy in biological systems. The reductive activation of the B_{12}-dependent corrinoid/iron-sulfur protein (CoFeSP) by transfer of one electron from an activating enzyme to the cobalamin cofactor is an energetically uphill process and is coupled to an ATPase reaction (1). How the energy transduction in the ATP-dependent reductive activation of CoFeSP is coupled to the hydrolysis of ATP, is scarcely understood.

We were able to determine the crystal structure of the complex formed between CoFeSP and its activator RACo at 2.5 Å resolution. The structure of the activation complex reveals besides large domain rearrangements of CoFeSP, conformational changes on RACo and offers an explanation for the observed redox-state-dependent partner recognition (1). We propose a mechanism for the interprotein electron transfer from the [2Fe2S] cluster of RACo to the cobalamin cofactor bound to CoFeSP, which will be discussed in detail on the poster.

(1) S. E. Hennig, J.-H. Jeoung, S. Goetzl, H. Dobbek, Redox-dependent complex formation by an ATP-dependent activator of the corrinoid/iron-sulfur protein. *Proc. Nat. Acad. Sci.U.S.A.* 109, 5235 (2012).

MS13 – Therapeutic targets and fragment-based drug discovery

MS13-P01

Automatic data processing using XDSAPP v1.0

K. Sparta[1], U. Müller[2], M. S. Weiss[2], U. Heinemann[3]
[1]*MDC / HZB MX, Macromolecular Crystallography, Berlin, Germany*
[2]*F-ISFM, Elektronenspeicherring BESSY-II, Macromolecular Crystallography (HZB-MX), Berlin, Germany*
[3]*Max Delbrück Center for Molecular Medicine, Macromolecular Structure and Interaction, Berlin, Germany*

Recent improvements in hardware at third generation synchrotrons have enabled the fast collection of diffraction images from protein crystals with exposure times below one second per image. We have developed the expert software XDSAPP (XDS Automation and Plotting Protocols) [1] in order to help synchrotron users analyze their diffraction data during measurements at the beamline with minimal effort. It mainly uses the diffraction data processing program XDS [2], along with additional software like POINTLESS from the CCP4 suite [3], XDSSTAT [4], SFCHECK [5] and PHENIX.XTRIAGE [6] for automatic decision making. Live statistic plots are generated as graphical output during data processing. XDSAPP also produces intensity files suitable for CCP4, CNS and SHELX.

The program is available free of charge.

References
[1] Krug, M. et al. (2012) J. Appl. Cryst. 45, 568-572
[2] Kabsch, W. (2012) Acta Cryst. D66, 125-132
[3] Collaborative Computational Project (1994) Acta Cryst. D50, 760-763
[4] Diederichs, K. (2006) Acta Cryst. D62, 96-101
[5] Vaguine, A. et al. (1999) Acta Cryst. D55, 191-205
[6] Adams, P.D. et al. (2010) Acta Cryst. D66, 213-221

MS13-P02

Fragment-screening by X-ray crystallography at the MX-beamlines of the Helmholtz-Zentrum Berlin

M. Weiss[1], M. Ühlein[1], U. Mueller[1], J. Linnik[1], A. Heine[2], G. Klebe[2]
[1]*HZB, Berlin, Germany*
[2]*Universität Marburg, Marburg, Germany*

Within the last decade, the fragment-based screening approach has been matured to a reliable and powerful instrument of pharmaceutical drug discovery. The success of a fragment screening experiment strongly depends on the quality of the chosen fragment library (100-200 Da) and the quality of the target protein diffraction. Further, it is of utmost importance to use high throughput methods for the screen application. A thorough crystallographic analysis of many protein-fragment complex structures and their binding modes has the perspective to result in the development of new potential lead structures and to map the interaction landscape of protein surfaces.

In order to develop a dedicated experimental facility for high throughput fragment screening at the BESSY II storage ring, we have recently assembled a fragment library of 96 compounds and have validated this library against two target proteins. These first results suggest that our library is capable of identifying binding partners at a hit rate of close to 10%. In the future, this library together with a fully automated beamline will be made accessible to users, thus enabling fragment-screening experiments on a much broader basis.

MS13-P03

Application of structure-based drug design to target histone demethylase enzymes.

D. Carter[1], E. Specker[2], J. Przygodda[1], M. Neuenschwander[2], C. Seyffarth[2], J. von Kries[2], U. Heinemann[1], U. Gohlke[1]
[1]*Max Delbrück Center for Molecular Medicine, Berlin, Germany*
[2]*Leibniz Institute for Molecular Pharmacology, Berlin, Germany*

Histone lysine demethylase (KDM) enzymes are an emerging class of therapeutic targets, known for their ability to regulate growth of various cancer cells. The Fe^{2+}- and α-ketoglutarate-dependent KDM4 family of isoenzymes comprises six members denoted KDM4A-F. Both KDM4A and KDM4C isoforms are known to stimulate growth of prostate cancer (PCa) cells by demethylating tri- and di-methylated forms of lysine 9, within histone H3. Importantly, knockdown of both isoforms was shown to halt growth of PCa cell lines and demonstrated their novelty as targets for development of small molecule inhibitors which may prove useful in a clinical setting. To address this possibility, we performed a high-throughput screening campaign to identify compounds that inhibit the most active KDM4 isoform, KDM4E. We identified several compounds that inhibit KDM4E with IC50 values in the mid- to low-micromolar range. In addition, we identified a smaller, less potent fragment with properties similar to, but still distinct from, a known KDM4 inhibitor. A crystal structure exists of this similar compound bound to KDM4A. The structure reveals a mode of binding, whereby the compound chelates the active site iron and hydrogen bonds to two neighboring residues. The structure also reveals regions within the active site topology which can be exploited through growth of a bound fragment. We aim to use structural information to grow our small molecule fragment into regions of KDM4 active sites that will further enhance inhibitor potency. Future studies are planned to introduce our compounds into PCa cell lines and to determine if they can prevent cell growth.

References.
1. Wissmann M, Yin N, Müller JM, Greschik H, Fodor BD, Jenuwein T, Vogler C, Schneider R, Günther T, Buettner R, Metzger E, Schüle R. Nat Cell Biol. 2007 Mar;9(3):347-53.

2. Couture JF, Collazo E, Ortiz-Tello PA, Brunzelle JS, Trievel RC. Nat Struct Mol Biol. 2007 Aug;14(8):689-95.
3. Ng SS, Von Delft F, Pilka ES, Kavanagh KL, Mcdonough MA, Savitsky P, Arrowsmith CH, Weigelt J, Edwards A, Sundstrom M, Schofield CJ, Oppermann U. PDB entry 2VD7, DOI:10.2210/pdb2vd7/pdb.

MS13-P04

Synthetic PhzB product analogues as inhibitors of a key step in phenazine biosynthesis

C. Diederich[1], J. Pletz[2], R. Breinbauer[2], W. Blankenfeldt[1]
[1]*Helmholtz Centre for Infection Research, Structure and Function of Proteins, Braunschweig, Germany*
[2]*Technical University Graz, Institute of Organic Chemsitry, Graz, Austria*

Pseudomonas aeruginosa is a widespread Gram-negative opportunistic pathogen, causing severe human infections. In order to provide a fitness advantage over other bacteria in its habitats, *P. aeruginosa* produces the blue pigment pyocyanin. This pigment belongs to a large class of nitrogen-containing heterocyclic metabolites called phenazines, which are versatile compounds involved in iron uptake and other redox reactions. As such, they exhibit broad-spectrum antibiotic activity as well as a high potency as virulence factors, causing major tissue damage upon human infection.[1,2] For this reason, understanding phenazine biosynthesis might help us to identify potential drug targets, hence to interfere with this important metabolic pathway and eventually fight infectious diseases caused by phenazine producing pathogens.

Phenazines are derived from chorismate by the products of at least five highly conserved genes (*phzBDEFG*), clustered in the *phz*-operon. A key step in the biosynthesis is the formation of the characteristic phenazine tricycle.[3] Although this step, which requires the symmetrical head-to-tail double condensation of two identical amino-cyclohexenone molecules, can proceed spontaneously *in vitro*, it could be shown in our group that PhzB is catalysing and thereby accelerating this condensation *in vivo.*[4]

In order to perform mechanistic studies, substrate analogues were designed, of which one binds with 51 nM affinity.[5] Based on this finding, a small compound library was synthesized and tested *in vitro*. Besides binding assays with isothermal titration calorimetry or microscale thermophoresis, an X-ray crystallography approach is used to confirm binding of these compounds to the active site of PhzB and to further develop the lead compounds in a rational design approach.

So far two high-resolution crystal structures with compounds derived from our best binder could be obtained as well as the structure of a complex with an afore described phenazine biosynthesis inhibitor, called Raloxifene, which surprisingly is structurally not related to phenazines.[2] The analysis of these structures provides crucial information on ligand binding modes and will enable us to derive new molecules with better affinity and inhibition activity.

References:

(1) Mavrodi, D. V.; Peever, T. L.; Mavrodi, O. V.; Parejko, J. A.; Raaijmakers, J. M.; Lemanceau, P.; Mazurier, S.; Heide, L.; Blankenfeldt, W.; Weller, D. M.; Thomashow, L. S. *Appl. Environ. Microbiol.* 2010, *76*, 866.
(2) Ho Sui, S. J.; Lo, R.; Fernandes, A. R.; Caulfield, M. D. G.; Lerman, J. A.; Xie, L.; Bourne, P. E.; Baillie, D. L.; Brinkman, F. S. L. *Int. J. Antimicrob. Agents* 2012, *40*, 246.
(3) Mavrodi, D. V.; Ksenzenko, V. N.; Bonsall, R. F.; Cook, R. J.; Boronin, A. M.; Thomashow, L. S. *J. Bacteriol.* 1998, *180*, 2541.
(4) Ahuja, E. G.; Janning, P.; Mentel, M.; Graebsch, A.; Breinbauer, R.; Hiller, W.; Costisella, B.; Thomashow, L. S.; Mavrodi, D. V.; Blankenfeldt, W. *J Am Chem Soc* 2008, *130*, 17053.
(5)Mentel, M.; Blankenfeldt, W.; Breinbauer, R. *Angew. Chem. Int. Ed.* 2009, *48*, 9084.

MS13-P05

Crystals in renal diseases

A. CHESCA[1,2]
[1]*TRANSILVANIA UNIVERSITY OF BRASOV, ROMANIA, FACULTY OF MEDICINE, BRASOV, Romania*
[2]*transilvania university of brasov, romania, faculty of medicine, brasov, Romania*

Introduction: The present study show the importance for the crystals studies implied in different renal diseases. The study is according with different types of renal pathology, depending of dietary, a determinant factor for renal diseases and their complications in case if the disease has not been well diagnosed from the first signs corresponding to a renal disease.

Material and Method: The purpose of the present study is to find different types of crystals to the patients, interested to know if are ill with a renal disease, according with their daily diet. For doing this study we collected urine from patients interested to know their healthy status, according with our interest in the study, The samples of urine were examined in the laboratory, using routine techniques. The study has been done to the patients from the last trimester of 2013 year, at one of the private laboratory from my county, for 2000 urine samples.

Results: According with the purpose of the study we found in urine samples, different types of crystals, as amorph urate, oxalate, being the most common in this study. The diagnostic of the crystals has been possible, using the laboratory techniques and a well known medical practice for urine samples results interpretation.

Conclusion: As a result of this study, has been observed urine crystals to patients apparently healthy but with a particular type of diet and life style. So, the examination and signs for possibles renal diseases, will be implied in changes for the daily diet of patients and a new life stile for being healthy.

MS13-P06

Small-molecule inhibitors of protein-protein interactions - application to Ena/VASP proteins

Y. Roske[1], M. Barone[2], R. Opitz[2], R. Kühne[2]
[1]*Max-Delbrück-Centrum, Berlin-Buch, Germany*
[2]*Forchungsinstitute für molekulare Pharmakologie, Berlin, Germany*

The cell‘s actin cytoskeleton is of central importance in the organization of morphogenesis, phagocytosis, endocytosis, cytokinesis and motility. Its dynamics is controlled by a vast number of proteins including the Ena/VASP family proteins. Ena/VASP proteins comprise of Ena/VASP homology domains 1 (EVH1) and 2 (EVH2) separated by a proline-rich region. While EVH2 binds to the barbed end, the proline-rich region recruits profilin and other proteins. In contrast, EVH1 binds to many proteins, e.g. zyxin or lamellipodin, mostly containing repeats of FPxxP motifs adopting a left-handed polyproline II helix (PPII). How EVH1 mediated protein-protein interactions influence the dynamics of the actin cytoskeleton by modulating the assembly of multiprotein complexes is not yet entirely understood. Until now, no small molecule and cell permeable inhibitor of the Ena/VASP EVH1 domain is availaible for dissecting its role in modulation of actin dynamics. Here we present for the first time efficiently binding EVH1 inhibitors based on rationally designed PPII-mimicking fragments. This set of novel small-molecule fragments forms a general toolkit for designing PPII competitors. We developed a 678 Da non-peptidic Ena/VASP EVH1 inhibitor, whose ester derivative exhibits cell permeability. The colon carcinoma cell line HCT 116 incubated with the cell permeable derivative exhibited significantly reduced numbers of stress fibers and displacement of Ena/VASP proteins from focal adhesions. Our results demonstrate the potency of our ligand design approach, by using the novel PPII-mimicking building blocks. The presented approach makes so far intractable targets such as src homology 3 (SH3) and WW domains, situated in hundreds of important signalling proteins, accessible for pharmacological interference.

MS13-P07

Structure-Based Drug Design Targeting the Main Protease of Human Coronavirus NL63

L. Zhang[1,2], D. Lin[1,2,3], Q. Ma[1,2], Y. Xiao[1,2], H. Liu[3], R. Hilgenfeld[1,2,3]
[1]*University of Luebeck, Biochemistry, Luebeck, Germany*
[2]*German Center for Infection Research (DZIF), Luebeck, Germany*
[3]*Shanghai Institute of Materia Medica, Shanghai, Germany*

Coronaviruses cause respiratory-tract and gastroenteritis diseases in mammals and birds. They are classified into four genera: *Alphacoronavirus, Betacoronavirus, Gammacoronavirus,* and the yet to-be-approved *Delta-coronavirus*. Human coronavirus NL63 (HCoV NL63), which was first isolated from a seven-month old infant suffering from respiratory symptoms, belongs to the alphacoronaviruses (1). HCoV NL63 has been shown to infect mainly children and immunocommpromised patients, with either mild upper- respiratory symptoms or more serious lower respiratory tract involvement.

The main protease (M^{pro}, also called 3C-like protease) of coronaviruses has been an appealing antiviral target since our earlier work on the M^{pro} of HCoV 229E and SARS-CoV (2-4), because it is essential for cleaving the viral polyproteins to yield functional subunits of the replication/transcription complex, and because proteases with a similar specificity are absent from the host. We have determined the crystal structure of the main protease of HCoV NL63 at 1.5 Å resolution, thereby providing sufficient structural detail for the design of inhibitors. We have designed a series of reversible alpha-ketoamide inhibitors, some of which show comparatively good *in-vitro* efficiency, with IC_{50} values of less than 10 mM. Furthermore, we have determined the crystal structure of HCoV-NL63 M^{pro} in complex with one of these compounds (RH01) at 2.5Å resolution. This structure will help improve the present lead compounds.

(1) van der Hoek, L., Pyrc, K., Jebbink, M.F., Vermeulen-Oost, W., Berkhout, R.J., Wolthers, K.C., Wertheim-van Dillen, P.M., Kaandorp, J., Spaargaren, J., Berkhout, B.: Identification of a new human coronavirus. *Nat. Med*. 10, 368-373 (2004).
(2) Anand, K., Ziebuhr, J., Wadhwani, P., Mesters, J.R., Hilgenfeld, R.: Coronavirus main proteinase ($3CL^{pro}$) structure: basis for design of anti-SARS drugs. *Science* 300, 1763-1767 (2003).
(3) Yang, H., Yang, M., Ding, Y., Liu, Y., Lou, Z., Zhou, Z., Sun, L., Mo, L., Ye, S., Pang, H., Gao, G.F., Anand, K., Bartlam, M., Hilgenfeld, R., Rao, Z.: The crystal structures of severe acute respiratory syndrome virus main protease and its complex with an inhibitor. *Proc. Natl. Acad. Sci. USA* 100**,** 13190-13195 (2003).
(4) Hilgenfeld, R., Peiris, M.: From SARS to MERS: 10 years of research on highly pathogenic human coronaviruses. *Antiviral Res.* 100, 286-295 (2013).

MS15 – Charge density for understanding chemical bonding in organic and inorganic structures (dedicated to Prof. Luger)

MS15-P01

A Bis(ylidic) or a Delocalized π-System? Charge Density Study of the First Mixed-Valent Tetraphosphete

V. Breuers[1], C. W. Lehmann[2], W. Frank[1]
[1]*Heinrich-Heine-Universität Düsseldorf, Institut für Anorganische Chemie und Strukturchemie II, Düsseldorf, Germany*
[2]*Max-Planck-Institut für Kohlenforschung, Mülheim an der Ruhr, Germany*

The first λ^3,λ^5-Tetraphosphete contains a 4π-electron four-membered ring as the central structural unit of a dispirocyclic system and can thus be classified as an analogue to diphosphetes and cyclodiphosphazenes. According to its crystal structure the central P_4 unit exhibits not only rhombic distortion but also P-P bonds which are of equal length.[1] Therefore its electronic structure cannot be described as “Phosphacyclobutadiene” but either as a bis(ylide) or as a system with delocalized double bonds. In contrast to quantum chemical calculations and an extensive examination of its reaction and coordination behavior a combined experimental and theoretical study of its charge density distribution has answered this question.[2] A detailed analysis of its topological properties and an inspection of the Laplacian reveal mainly polar Si-N and P-N bonds and two sp^3-hybridized phosphorus atoms. The results illustrate the unique bonding situation in the P_4 unit combining a high ylidic character with unusual not exclusively sigma-like P-P bonds.

[1] W. Frank *et al., Angew. Chem.* 1996, *108*, 1616; *Angew. Chem. Int. Ed.* 1996, *35*, 1512.
[2] A. Volkov *et al., XD2006,* 2006.
[3] A. Stash, V. Tsirelson, *J. Appl. Crystallogr.* 2002, *35*, 371.

Figure 1: Isosurface representation of the deformation density in the P_4 unit (0,175 $e\text{Å}^{-3}$).[3]

Figure 1

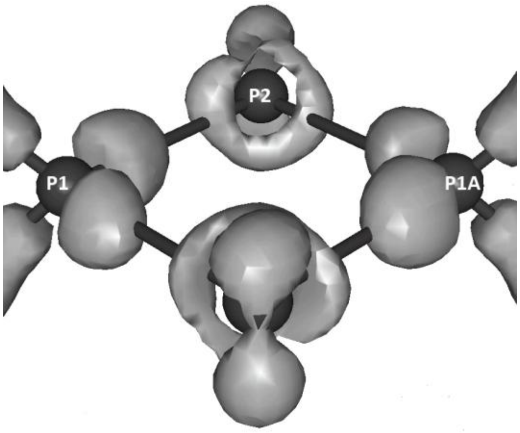

MS15-P02

Peri-Substituted (Ace)Naphthylphosphinoboranes. Regular vs. Frustrated Lewis Pairs Evaluated by Structural Parameters and Real Space Bonding Indicators

J. Beckmann[1], E. Hupf[1], E. Lork[1], S. Mebs[2]
[1]*Bremen University, Biology & Chemistry, Bremen, Germany*
[2]*Free University of Berlin, Chemistry & Pharmacy, Berlin, Germany*

Peri-substituted naphthyldiphenylphosphinoboranes 1-Ph_2P-8-Mes_2B-Nap (**1**) and ace-naphthyldiphenylphosphinoboranes 6-Ph_2P-5-Mes_2B-Ace (**2**) feature significant transannular interactions between the substituents in 1,8- and 5,6-positions that are attractive in **1** due to donor-acceptor bonding and repulsive in **2** due to steric congestions of the substituents, which is reflected in different *peri*-distances of 2.162(2) in **1** and 3.050(3) Å in **2**.[1] Due to the identical substituents and similar backbones electronic reasons can be ruled out for the significant structural differences. The most obvious difference between both molecular structures is the orientation of the phenyl ring attached to the P atom, which is marked by an arrow in the left Figure. In **1**, the phenyl ring is pointing between the rings of the two mesityl substituents, which allows to accommodate a close proximity of the P atom and the B atom. In contrast, in **2**, this phenyl ring is oriented almost perpendicular, which prevents a closer P-B contact. This is reflected in all real-space bonding descriptors utilizing the AIM,[2] Hirshfeld[3] and ELI-D[4] space partitioning schemes. In **1**, the short P-B distance gives rise to the formation of a P-B bond critical point (bcp) with an ED value of 0.54 $e\text{Å}^{-3}$, whereas for **2** no such bcp is observed. The results of the bond topology are supported by the curvedness mapped on the Hirshfeld surfaces of atomic fragments in that only for **1** a significant curvedness is found in direction of the P-B axis. Moreover, the atomic Hirshfeld fragments are connected in case of **1**, whereas in **2** the Hirshfeld surfaces of the P and B atom are clearly separated from each other. In agreement to the results of the topological AIM and Hirshfeld surface analysis, no ELI-D disynaptic P-B valence basin (V_2(P,B)) is observed in **2**. Instead, an isolated lone-pair basin V_1(P) is found. By mapping the ELI-D on the basin surfaces distinct effects of electron localizability become visible (see Figures in the middle and at the right side). Only in **1** a ring-shaped region of increased electron localizability is located at the side pointing towards the B atom. Consequently, **1** and **2** comprise straightforward cases of regular and frustrated Lewis pairs.

1. J. Beckmann, E. Hupf, E. Lork, S. Mebs, *Inorg. Chem 52* (2013) 11881.
2. R.F.W. Bader, *Atoms in Molecules: A Quantum Theory*, Cambridge University Press, Oxford U.K., 1991.
3. Spackman, M. A.; Byrom, P. G. *Chem. Phys. Lett*. 267 (1997) 215.
4. M. Kohout, *Int. J. Quantum Chem. 97* (2004) 651.

Left side: superposition of the X-ray structures of 1 and 2. Middle and right side: electron localizability mapped on the V_2(P,B) basin in 1 and the V_1(P) in 2.

Figure 1

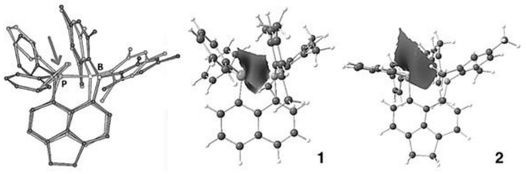

MS15-P03

Visualization Tools development started at Peter Luger's group

C. Hübschle[1], B. Dittrich[2], S. van Smaalen[1]
[1]*Universität Bayreuth, Lehrstuhl für Kristallographie, Bayreuth, Germany*
[2]*Universität Hamburg, Institut für Anorganische und Angewandte Chemie, Hamburg, Germany*

The program "MolIso - A Program for Colour-Mapped Iso-Surfaces [1]" was developed in the group of Peter Luger. Since it's first official release in 2006 it has been further developed and its functionalities have meanwhile been implemented into the more user friendly program called MoleCoolQt [2]. MoleCoolQt can help users to setup the XD input files for charge density refinement. It visualizes the local-coordinate systems, critical points, residual peaks and holes and residual maps as 3D iso-surfaces. A difference map between two models is also visualized. This difference map can show the difference between the IAM and the multipole to provide a quick deformation density representation or it is possible to visualize the difference between thermal models for example when anharmonic motion has to be refined. The probability density function of atoms can be visualized superimposed on to a model of the structure. Beside of the mentioned visualization features MoleCoolQt is able to do an Invariom transfer, like the program InvariomTool [3], which was developed in Peter Luger's group together with B. Dittrich. The Invariom transfer can be performed for XD and MoPro input files[4].

Recently MoleCoolQt is able to visualize the dynamic charge density calculated by the Maximum Entropy program BayMEM. The Maximum Entropy Method (MEM) provides a probable dynamic electron density without the need of an explicit model. The MEM was applied to a 20 K data set of the nucleoside thymidine[5]. With the Prior program of the BayMEM suite it is possible to calculate the dynamic charge density from multipole models. So calculated dynamic charge density results from [5] are compared with the MEM results.

[1] C. B. Huebschle and P. Luger J. Appl. Cryst. (2006). 39, 901-904.
[2] C. B. Huebschle and B. Dittrich J. Appl. Cryst. (2011). 44, 238-240.
[3] C. B. Huebschle, B. Dittrich and P. Luger J. Appl. Cryst. (2007). 40, 623-627.
[4] B. Dittrich, C. B. Huebschle, K. Proepper, F. Dietrich, T. Stolper and J. J. Holstein Acta Cryst. (2013). B69, 91-104.
[5] C. B. Huebschle, B. Dittrich, S. Grabowsky, M. Messerschmidt, and P. Luger Acta Cryst. (2008). B64, 363-374.

MS15-P04

Point charges for force-field parametrization from the invariom database

C. M. Orben[1], B. Dittrich[2]
[1]*University Goettingen, Inorganic Chemistry, Goettingen, Germany*
[2]*University Hamburg, Inorganic and Applied Chemistry, Hamburg, Germany*

The invariom database [1] is known to provide aspherical scattering factors for atoms in different chemical environments. It contains more than 1400 geometry optimized model compounds. Underlying the database is the formalism of assigning the atoms according to their local bonding situation. This formalism provides the opportunity to supply point charges according to those environments for organic compounds as soon as 3D-coordinates are available.

This could be especially useful for potential pharmaceutical molecules, because their point charges often have to be added to molecular mechanics simulations using force fields like the well established Amber force field [2]. Their charges currently come either from a DFT calculation, run especially for this purpose, or from a general atom force field (in case of Amber the GAFF [3]). Depending on the size of the molecule the first approach can take a long time, needs computational resources and the use of a quantum chemistry program. Using data from tables is easier and quicker, but the GAFF is rather general and therefore not very specific of the bonding situation.The invariom classification provides a more detailed description especially for hydrogen atoms.

Since the database already contains optimized geometries of model compounds and their electron density, a restrained fit to the electrostatic potential (resp) [4] yields charges, which were designed to be transferable and are therefore ideally suited for an application in force fields. Amber suggests the use of hf/6-31g* resp calculations. The model compounds in the invariom database have been optimized using more extensive basis functions and density functional theory. For coverage of heavier atoms a revision of the data base with a new basis set and functional will be provided. Some improvements to the invariom notation will be reported as well. Invariom point-charges will be presented for a series of tripeptides and compared with those from existing methods.

[1] B. Dittrich, C. B. Hübschle, K. Pröpper, F. Dietrich, T. Stolper, J. J. Holstein, *Acta Cryst.* (2013), B69, 91-104.
[2] W. D. Cornell , P. Cieplak , C. I. Bayly , I. R. Gould , K. M. Merz , D. M. Ferguson , D. C. Spellmeyer , T. Fox , J. W. Caldwell , P. A. Kollman,J. Am. Chem. Soc., (1995), 117 (19), 5179-5197.
[3] J. Wang, R. M. Wolf, J. W. Caldwell, P. A. Kollman, D. A. Case, *J. Comp. Chem.* (2004) 25, 1157-1174.
[4] C. I. Bayly, P. Cieplak, W. D. Cornell, P. A. Kollman, *J. Phys. Chem.* (1993), 97, 10269-100280.

MS15-P05

Efficient data collection with software and hardware features from Agilent Technologies

Z. Gál[1]
[1]*Oxford Industrial Park, Agilent Technologies LTD (UK), Yarnton, United Kingdom*

With the recent improvements in source brightness more samples are becoming viable candidates to be measured on in-house diffractometers. To cope with the resulting increase in workload it is important to be able to collect excellent, publishable-quality data as quickly and efficiently as possible.

Agilent Technologies develop and supply X-ray systems for single-crystal diffraction research, which includes the Nova and Mova sealed-tube micro-focus X-ray sources, as well as our new range of Atlas S2, Eos S2, and Titan S2 CCD detectors. Technological improvements allow us to make use of the high brilliance of the sources, and the large dynamic range and low signal-to-noise of our detectors to push the boundaries of what samples can be measured.

The new S2 detectors incorporate an Intelligent Measurement System, where the exposure time, binning mode, and gain settings are automatically chosen for each sample. High binning and gain modes are chosen to boost the detectivity for weakly-diffracting data, whereas low binning and gain modes are selected to increase the dynamic range for well-diffracting samples. This flexibility makes it very easy to collect high-quality, publishable datasets for a very large range of samples.

In conjunction, our innovative, user-friendly CrysAlisPro software is constantly being updated to make use of all new hardware improvements, as well as making it as easy as possible for the user to effectively screen their samples, gather enough preliminary information quickly, and run the most suitable experiments.

MS17 – Spectroscopy as supporting method in structure determination

MS17-P01

Crystallograc orientation of hydrogen defects in lithium niobate and lithium tantalate

T. Köhler[1], E. Mehner[1], J. Hanzig[1], G. Gärtner[1], H. Stöcker[1], D. C. Meyer[1]
[1]*Technische Universität Bergakademie Freiberg, Institut für Experimentelle Physik, Freiberg, Germany*

Pyroelectric crystals are used in many optical devices, therefore, understanding the structural defects is helpful to control optical and electrical properties. It is easy to incorporate hydrogen in air-grown $LiNbO_3$ and $LiTaO_3$ crystals, however, the exact processes are only partially understood. The incorporation of hydrogen in the two materials is investigated crystal axis resolved and polarization-dependent by FT-IR spectroscopy. In the congruent material systems the hydrogen defect causes an OH band with several sub-bands, at different spectral positions for both materials.

The examined congruent crystals are cube shaped, cut and polished along the [001], [100] and [110] directions. The OH band show a significantly weaker signal for the [100] and [110] directions than for the [001] direction of the crystal cubes. Further measurements were made in the far infrared range. The aim of the crystal axis resolved and polarization-dependent study is the development of a structural model for the orientation of the OH defects of the two pyroelectric materials.

MS17-P02

XRD and ^{29}Si NMR study of metamict minerals

P. Zietlow[1], T. Beirau[1], M. Fechtelkord[2], L. A. Groat[3], C. Paulmann[1], U. Bismayer[1]
[1]*Universität Hamburg, Mineralogisch-Petrographisches Institut, Hamburg, Germany*
[2]*Ruhr-Universität Bochum, Institut für Geologie, Mineralogie und Geophysik, Bochum, Germany*
[3]*University of British Columbia, Department of Earth, Ocean and Atmospheric Sciences, Vancouver, Canada*

Radiation damaged natural minerals show a domain structure consisting of crystalline, quasi amorphous and fully disordered clusters resulting from alpha decay of built-in uranium and thorium. Structural damages and their behaviour as a function of thermal annealing can be of interest for material sciences, especially for the better understanding of embedding materials of actinides from radioactive waste. Titanite and pyrochlore ceramics are among discussed embedding materials and occur as metamict minerals in nature. [1], [2]

We studied the recrystallisation behaviour of pyrochlores exposed to different radiation doses on annealing using X-ray diffraction (XRD), and ^{29}Si magic angle spinning nuclear magnetic resonance (NMR) spectroscopy in the case of heavily damaged titanite. Since XRD is sensitive to long range order and ^{29}Si NMR just to the local Si environment up to the second coordination sphere, both methods are complementary to study structural changes stemming from metamictisation. [3]

Recrystallisation temperatures are sensitive to crystal chemistry and structural topology; hence pyrochlores differ considerably in partly crystalline and completely XRD amorphous pyrochlores and from titanite. ^{29}Si NMR signals of heavily metamict titanite decrease in full width at half maximum upon annealing, indicating restructuring in the direct Si vicinity.

[1] Ewing, R. C., Meldrum, A., Wang, L.M., Wang, S.X. (2000): Radiation-Induced Amorphization, Reviews in Mineralogy and Geochemistry, Ed. P.H. Ribbe, Min. Soc. America 39, 319-361.
[2] Hawthorne, F.C., Groat, L.A., Raudsepp, M., Ball, N.A., Kimata, M., Spike, F., Gaba, R., Halden, N.M., Lumpkin, G.R., Ewing, R.C., and others. (1991): Alpha-decay damage in titanite. American Mineralogist, 76, 370-396.
[3] Zietlow, P., Beirau, T., Fechtelkord, M., Groat, L. A., Paulmann, C., Bismayer, U. (submitted): ^{29}Si NMR study of metamict titanite. Zeitschrift für Kristallographie

MS17-P03

Impact of temperature and barometric pressure fluctuations on X-ray beam intensities

T. Weigel[1], M. Herrmann[1], M. Zschornak[1], T. Leisegang[1], D. C. Meyer[1]
[1]*TU Bergakademie Freiberg, Institut für Experimentelle Physik, Freiberg, Germany*

Essential to X-ray experiments as diffraction and spectrometry as prominent examples is a highly reproducible and stable operating X-ray source. Often, the primary beam needs to path several centimeters of air until a sample or a detector is reached. Besides electronically induced variations of the X-ray primary intensity the ambient conditions and their changes are of particular importance. This includes humidity, barometric pressure and temperature. These parameters influence the air density and thus its linear attenuation coefficient that in turn changes the transmission of the primary beam. As a consequence the diffracted intensities for example are affected so misinterpretation or at least errors in a structure model occurs.

Here we report on the impact of temperature, barometric pressure and humidity fluctuations on X-ray beam intensities of a conventional sealed tube X-ray source with copper anode detected by a scintillation counter. The laboratory as well as external conditions has been investigated. Their individual influence but also their correlations have been evaluated by statistical analysis including time lag. Furthermore, simulation of air density and attenuation coefficient changes taking characteristic cobalt, copper and molybdenum radiation energy as well as paths lengths into account has been performed.

A qualitative as well as quantitative overview of the results is given. The main parameters affecting the primary beam intensity, the impact on X-ray intensity and time scales are presented.

MS17-P04

IR and ^{11}B MAS NMR investigations on $H_{4-x}B(OH)_x$ species in the sodalite cage

L. Schomborg[1], C. H. Rüscher[1], J.- C. Buhl[1], M. Fechtelkord[2]
[1]*Leibniz Universität Hannover, Institut für Mineralogie, Hannover, Germany*
[2]*Ruhr-Universität Bochum, Institut für Geologie, Mineralogie und Geophysik, Bochum, Germany*

Hydrogen release from BH_4-SOD ($Na_8Al_6Si_6O_{24}(BH_4)_2$) could form the intermediates $H_{4-x}B(OH)_x$ with x = 1,.., 4 in four consecutive steps in the reaction with H_2O. Dehydration of the $B(OH)_4$-cage filling occurs in two steps revealing $BO(OH)_2^-$ and BO_2^- species[1]. A further investigation is carried out by the combination of ^{11}B MAS NMR and FTIR spectroscopic method.

Parts of the as synthesized BH_4-SOD sample (a) were heated for 1 h at 250°C (b), 300°C (c) and 400°C (d). A part of the as synthesized $B(OH)_4$-SOD sample (e) was also heated for 1 h at 250°C (f) for reference purposes. Above the sodalite framework vibrations range, characteristic vibrations of the cage filling species appear in FTIR spectra (Fig. 1). $B(OH)_4$-cage filling species are identified by the OH peak at 3640 cm^{-1} (e). The intermediate dehydration step $BO(OH)_2$-SOD (f) is identified by the peaks at 1235 cm^{-1} (B-OH) and 1475 cm^{-1} (B-O). The corresponding OH vibrations now appear at 3590 cm^{-1}. Some amount of $B(OH)_4^-$ cage filling is still be identified by the OH peak at 3640 cm^{-1}. The BH_4^- cage fillings in samples a-d are identified by the peaks at 1130, 2240, 2287 and 2390 (all in cm^{-1}). Heating of sample "a" at 250°C (b) reveals decreasing intensity of the BH_4-peaks and new peaks at 1290 and 1310 cm^{-1} (A in Fig. 1). Heating at 300°C (b) reveals a further intensification of peaks A and some intensity B. We may relate peaks A and B with the appearance of intermediates as described above. At 400°C (d) some weak but significant peaks appear at around 1230 and 1470 which can be related to the formation of $BO(OH)_2^-$ cage filling species. According to this it could be suggested that also $B(OH)_4^-$ cage filling species should appear to be identified at 3440 cm^{-1}.

The cage filling species are further identified by ^{11}B MAS NMR. BH_4-SOD and the heated BH_4-SOD all show the ^{11}B signal at -49 ppm. The heated samples (b-d) show additional intensity between 20 and -5 ppm (Fig. 2), which increases with heating temperature. The intensity variation has been referenced to the ^{11}B total intensity. The relative intensity between 20 and -5 ppm can be estimated to about 3 % for b, 5 % for c and 20 % for d. The peak structure between 20 and -5 ppm observed for the BH_4-SOD heated at 250°C is related to the $H_{4-x}B(OH)_x^-$ intermediates. Further heating shows the upcoming $B(OH)_4^-$cage fillings, which can be observed at the lowest level reaction at around 1.5 ppm, too. Additionally, the intermediate dehydration step $BO(OH)_2^-$ is also clearly identified in sample "d" by the intensity distribution between 18 and 12 ppm. Both $B(OH)_4^-$ and $BO(OH)_2^-$ specification can clearly be justified by comparison with the spectra obtained for the $B(OH)_4$-SOD (e) and the sample heated at 250°C (f).

[1]Buhl, J.-Ch., Schomborg, L., Rüscher, C.H. (2012): Hydrogen Storage, Jianjun Liu (Ed.), InTech, pp. 49-90, ISBN: 978-953-51-0731-6

Fig. 1 IR absorption spectra of samples „a-f".

Fig. 2 ^{11}B MAS NMR chemical shifts relative to BF_3-OEt_2 of samples „a-f".

Figure 1

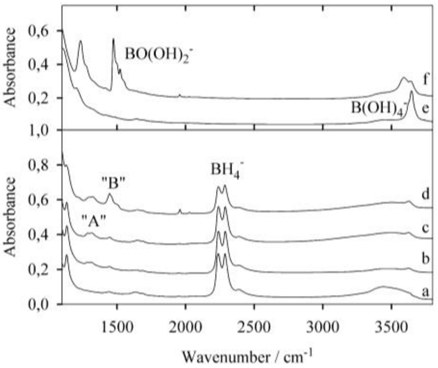

Figure 2

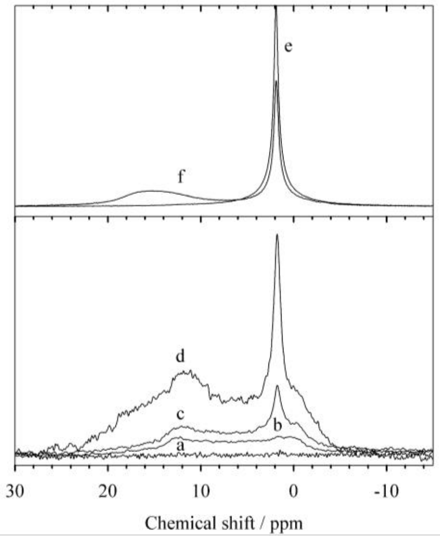

MS17-P05

The morpholog and ultra - structure of a new 2 - methoxyethanol utilizing Pseudomonas sp.

F. O. Ekhaise[1,2]
[1]University of Benin, Microbiology, Benin City, Nigeria
[2],, Nigeria

A new strain of Pseudomonas designated as Pseudomonas sp. strain VB degrading 2 - methoxyethanol was isolated from anaerobic sewage sludge. The cells are rod shaped, motile with polar lophotrichous flagella numbering between 7 and 9. Electron microscopy revealed cells aggregating yo form a network connected by interconnecting filaments. A thin section of the filaments showed an outer sheath surrounding a core area and an inner electron dense area. A thin section of the cell showed the typical Gram negative bacterial cell structure.

Keywords. Pseudomonas sp. strain VB, electron microscope, morphology and ultrastructure

MS18 – Crystallography in archeometry

MS18-P01

Collections of Crystal Models at TU Berlin

S. F. Herting-Agthe[1]
[1]*Technische Universität Berlin, Mineralogische Sammlungen, Berlin, Germany*

Since 1770, the foundation of the Bergakademie Berlin (mining academy), teaching collections have been indispensable for the education of geoscientists at the successor organisation: Technische Universität Berlin. Crystal models have been an integral part of mineralogical teaching until today: nothing better than a wooden model of an octahedron to understand cubic symmetries, to get a feeling for mirror planes and rotation axes.

Thus, the collections at TU Berlin are housing today app. 3500 models of crystals, mainly of natural occurring minerals - a treasure only few universities worldwide are able to provide. Most of these models are 4-6 cm in size, mainly made of pear wood, a minority made of maple wood or others.

The oldest wooden models exhibit the engraved letters KTH (Königlich Technische Hochschule, predecessor of TU Berlin, 1879-1916). The main and most precious collection consists of 743 different crystal models, after Prof. Dr. Paul Heinrich von Groth 1880, who studied mineralogy and crystallography among others in Berlin under the renowned Prof. Gustav Rose and became docent at the Bergakademie (1871-1872). This collection contains also twin models, contact twins rotatable, even up to eightlings. (fig. 1.).

Several other collections of wooden models are kept at TU Berlin, even of black-and-white-symmetries. Few models are made of gypsum, after Prof. F.X.Zippe (1791-1863), Prague/Vienna (fig. 2.). Further important teaching collections contain pasteboard crystal models and crystal structure models (steel bars and wooden balls).

References

GROTH, P. (1880): Mineralogisch-krystallographische Sammlung von 743 Krystallmodellen in Birnbaumholz.- Katalog Nr. 5, Dr. F. Krantz Rheinisches Mineralien-Contor, Universitäts-Buchdruckerei Carl Georgi Bonn, 50 S.

GROTH, P. (1885): Physikalische Krystallographie (und Einleitung in die krystallographische Kenntniss der wichtigeren Substanzen).- Leipzig, Verlag von Wilhelm Engelmann, 710 S. und 1 Tafel.

KJELLMAN, J. (2012): A quarter millenium of morphological Crystal Models - the makers, the materials, the collections - a current project on retrieving their history.- Senckenberg, Schriften Mus. Min. und Geol. Dresden, **18**, 106-107.

TANDY, P. (1998): Crystallography and the geometric modelling of minerals: a reflection on the models in the NaturalHistoryMuseum, London.- The Geological Curator **6** (9), 333-338.

TOURET, L. (2004):Crystalmodels: milestone in the birth of crystallography and mineralogy as sciences.- In: VISSER, R.W. & TOURET, J. [eds.]: Pioneers of the Earth Sciences.- (in Dutch), Koninklijke Nederlandse Akademie van Wetenschappen,Amsterdam, pp. 43-58.

www.mineralogische-sammlungen.de

Figure 1

Crystal model of Stephanite, rotatable twin on (110), pear wood, 5 cm. No. 405, coll. of 743 models after GROTH 1880.

Figure 2

Crystal models of calcite and ilvaite, size up to 9 cm, gypsum, after ZIPPE.

Index of Authors

ISBN 978-3-981-6508-2-2